



**Università  
degli Studi  
di Ferrara**

**DOCTORAL COURSE IN  
CHEMICAL SCIENCES**

CYCLE XXXII

DIRECTOR Prof. Cavazzini Alberto

***PROPERTIES OF ADSORBENT MATERIALS AND THEIR APPLICATIONS IN  
ENVIRONMENTAL AND SUSTAINABLE CHEMISTRY***

Scientific/Disciplinary Sector (SDS) CHIM/01

**Candidate**

Dott. Chenet Tatiana

**Supervisor**

Prof. Pasti Luisa

Years 2016/2019

# CONTENTS

<b>1 INTRODUCTION</b>	1
1.1 Environmental and sustainable applications of adsorbent materials	1
1.2 Aim of the work	3
<b>2 HEAVY METALS</b>	5
2.1 Cadmium	7
2.2 Lead	12
2.3 Nickel	15
2.4 Removal of heavy metals	17
2.5 References	20
<b>3 ORGANIC CONTAMINANTS</b>	22
3.1 Volatile organic compounds	22
3.1.1 Toluene	22
3.1.2 n-Hexane	23
3.2 Organochlorine compounds	26
3.2.1 Chlorobenzene	26
3.2.2 Metolachlor	27
3.3 References	30
<b>4 ADSORPTION</b>	32
4.1 Adsorption isotherms	33
4.2 Adsorption kinetics	37
4.3 References	42
<b>5 ADSORBENT MATERIALS</b>	43
5.1 Mollusc shells	43

5.2 Microporous materials	50
5.3 References	64
<b>6 EXPERIMENTAL</b>	<b>68</b>
6.1 Scallop shells as adsorbent material for the removal of heavy metals from aqueous solution	68
6.2 Adsorption of toluene from aqueous solutions onto zeolites	100
6.3 Adsorption of toluene and n-hexane onto zeolites, evaluation of competitive behaviour between aromatic and aliphatic compounds	114
6.4 Adsorption of chlorobenzene onto zeolites	132
6.5 Adsorption of the Metolachlor metabolite EMA onto zeolite ZSM-12 from aqueous solutions	149
6.6 Gallium-exchanged zeolites	172
<b>7 MICROPLASTICS</b>	<b>195</b>
<b>8 CONCLUSIONS</b>	<b>226</b>
<b>9 PAPERS</b>	<b>228</b>

# 1 INTRODUCTION

## 1.1 Environmental and sustainable applications of adsorbent materials

Most industrial processes are devoted to separate the components of large quantities of chemical mixtures into pure or purer forms. These processes are often based on energy consumption technologies. The development of economic, effective, safe and rapid separation techniques in many industrial sectors at a large scale is still a challenging issue. Among the different separation techniques, adsorption, a consolidated technology, is still considered to be a reliable and robust method to purify fluids at low cost and with high efficiency. One of the main advantage of adsorption based technologies is that they are capable of removing contaminants in very low concentrations range, an operative condition where most other separation techniques are scarcely efficient due to the small concentration gradients involved. The ability to treat dilute solutions is particularly relevant in the recovery of substances from solutions since often, the price of solutes is inversely correlated with the concentration of the various products. Additionally, adsorption is a versatile method that can simultaneously remove many different organic and inorganic compounds, providing a suitable mixture of adsorbent materials is employed. A characteristic feature of adsorption systems is that many components of the solution can interact with the sorbent surface, and generally their behaviour can differ in the strength and location of the interaction with the adsorbent. In addition, the adsorbent surface may show affinity also toward the solvent. As a result, adsorption is, in the majority of cases, a multicomponent process, even if a single solute is considered.

Adsorption based technologies have been successfully employed in many fields and among them in environmental remediation methodologies. In such a case the adsorbent may be of mineral, organic or biological origin. Activated carbon is the preferred material at industrial scale and is extensively used not only for removing pollutants from wastewater streams but also for adsorbing contaminants from drinking water sources (e.g. rivers, lakes or reservoirs). However, its widespread use is restricted due to high cost and limited regeneration of exhausted material. In the last three decades, numerous approaches have been studied for the development of cheaper and more effective adsorbents capable to eliminate pollutants at trace levels. The preservation of fresh water as a source of potable water and the safeguard of natural waters as life preservation systems (cultivation of aquatic food and reservoir of evolutionary diversity) has become important objectives.

In general, water is referred as polluted when it is compromised by anthropogenic contaminants which can alter the quality of water destined to human use, such as drinking water, or make natural water bodies not suitable for the nourishment of biotic communities.

Water pollutants include a wide spectrum of chemicals, they may be organic or inorganic substances.

The main categories of organic substances that commonly pollute the aquatic environment are: detergents, disinfection by-products, pesticides, petroleum hydrocarbons, volatile organic compounds, chlorinated solvents and drug pollution which involve pharmaceuticals and their metabolites.

Inorganic contaminants include acids originating from industrial discharges, ammonia, fertilisers containing nutrients such as nitrates and phosphates (causing nutrient pollution), heavy metals from motor vehicles and acid mine drainage.

Among the many classes of contaminants found in all environmental compartments, in this work we focused on heavy metals, volatile organic compounds, and microplastics.

Water pollution can originate from a variety of sources, either point sources and non-point sources. Pollutants can enter water directly, through both legal and illegal discharges from factories, for example, or water treatment plants. Spills and leaks from oil pipelines or hydraulic fracturing (fracking) operations can degrade water bodies. Weather conditions such as wind, storms, and littering—especially of plastic waste—can also send debris into waterways.

The safeguard of water supplies is important because even though nearly 70 percent of the world is covered by water, only 2.5 percent of it is freshwater. Moreover, just 1 percent of freshwater is easily accessible, with the majority stored in remote glaciers and snowfields.

Water is a common good and a limited source that needs to be protected in terms of both quality and quantity. The European Union has established two main legal frameworks for the protection and management of freshwater and marine resources: the Water Framework Directive (WFD) and the Marine Strategy Framework Directive (MSFD).

The Water Framework Directive regards the protection of inland surface waters, transitional waters, coastal waters and groundwater. The objectives of the WFD are to reduce and prevent pollution, promote sustainable water use, protect and improve the aquatic environment and mitigate the effects of floods and droughts. The Water Framework Directive is complemented by more specific directives, such as the Groundwater Directive, the Drinking Water Directive, the Bathing Water Directive, the Nitrates Directive, the Urban Waste Water Treatment Directive, the Environmental Quality Standards Directive and the Floods Directive.

The Marine Strategy Framework Directive aims to achieve “good environmental status” of the EU’s marine waters by 2020, to continue its protection and preservation, and to prevent subsequent deterioration (<https://www.europarl.europa.eu/factsheets/en/sheet/74/water-protection-and-management>).

In such a framework, adsorption based technologies can contribute to reach the objectives of preservation of natural water as a source of potable water and assuring the environmental water quality standards. In this work a brief overview of liquid-solid adsorption processes using conventional and non-conventional materials for pollutant removal is presented. Since the efficiency of the adsorption process is related to the number and type of interactions between the adsorbent and the adsorbate, different microscopic mechanisms involved in the adsorption phenomena are also recalled.

## **1.2 Aim of the work**

The main objective of this work of thesis is to evaluate the efficiency of different adsorbent materials in the removal of some classes of contaminants from aqueous matrices. The adsorption process was studied in each case to determine both kinetics and thermodynamics properties of the adsorption process. In addition, structural investigation approaches have been adopted to enlighten the mechanisms underlying the process.

The selected adsorbent materials employed in the present study differs from each other in structure and chemical composition. They can be categorised in two main classes: (i) silico aluminate synthetic microporous adsorbent (zeolites) and (ii) carbonatic based bioadsorbent (scallop shell).

In particular, scallop shells composed of biogenic calcium carbonate, were chosen as bio-adsorbents for the removal of heavy metals from water solution. Mollusc shells represent a waste originating from seafood processing, the features of the shell matrix such as the disposition of the  $\text{CaCO}_3$  layers and the presence of organic components, make mollusc shells a suitable material for the uptake of metal ions improving the quality of water bodies. The adsorption of cadmium, lead and nickel was studied considering different factors that can affect the adsorption process, such as temperature, pH and salinity. In addition, we investigate the modification of the structure of the shells after the adsorption of the cations. This information can give useful insight on the effects of certain metals on shells, especially in monitoring studies in which such specimens are employed as bioindicator.

Zeolites, which are aluminosilicate microporous materials, were instead employed for the adsorption of organic contaminants, in specific for the removal from aqueous solutions of toluene, hexane, chlorobenzene and the metabolite EMA (2-ethyl-6-methylaniline) originating from the degradation of the pesticide metolachlor.

Zeolites are classified according to the typology of the framework, every zeolite is characterised by regular channels and cavities systems with different dimensions. Moreover, the hydrophobic/hydrophilic behaviour of these materials can be tuned by varying the silica/alumina ratio (SAR): the higher the content of  $\text{Al}_2\text{O}_3$  in the zeolite structure, the

lower the SAR, a zeolite with a SAR lower than 5 is hydrophilic, whereas a zeolite with a SAR higher than 5 is hydrophobic.

In this work, zeolites with different framework typologies and SAR were selected to optimise the adsorption of the different organic contaminants considered.

Among the many applications in which zeolites are employed, their use as catalysts is one of the most common. To improve the catalysis efficiency, sometime zeolites are modified introducing heteroatoms, mainly metals, in the framework structure. This study includes a work on gallium substituted zeolites; gallium was introduced by wet impregnation (adsorption) on three different zeolites and the obtained materials were characterised combining adsorption isotherms, X ray powder diffraction and X ray absorption spectroscopy to determine the nature and structure of the Ga<sup>3+</sup> sites. In such a case adsorption has been used to generate a material with interesting characteristics and potential application in the sustainable chemistry field concerning the biomass conversion in platform chemicals.

The final part of this work of thesis includes a study on the presence of plastic debris in a species of fish of the Mediterranean Sea, the small-spotted catshark (*Scyliorhinus canicula*, Linnaeus, 1758). The accumulation of plastic debris in the environment, especially in water, has become an issue of major concern all around the world, the existence of plastic trash in the marine environment has been reported since the 80's. The durability that characterise plastic materials makes them resistant to degradation, resulting in long resident times in the environment leading to adverse effects on wildlife, wildlife habitats and, eventually, humans. In this work, the occurrence of plastics in the gastro-intestinal tract of the small-spotted catshark collected near Mazara del Vallo and Lampedusa (Sicily, Italy) was evaluated, and the effects of plastic presence on the health status of *Scyliorhinus canicula* were investigated through the analysis of the expression levels of key genes involved in immune response.

## 2 HEAVY METALS

The term “heavy metal” refers to those metallic elements that have a high atomic weight and a density at least five times higher than that of water [1].

With the growth and spread of industries since the Industrial Revolution and the increasing population, anthropogenic pollution has become a serious environmental issue.

Among the different groups of pollutants that have lasting effects on the natural balance of aquatic systems, heavy metals represent a major concern worldwide.

Metal pollutants are introduced into the environment, due to their wide use, via various sources, among them: smelting processes, fuel combustion, leaks, effluents and dumping activities [2].

### *Metal toxicity*

Elements can be classified in three categories, according to their toxicity and availability (table 2.1)

Non critical			Toxic but very insoluble or very rare		Very toxic and relatively accessible		
Na	C	F	Ti	Ga	Be	As	Au
K	P	Li	Hf	La	Co	Se	Hg
Mg	Fe	Rb	Zr	Os	Ni	Te	Tl
Ca	S	Sr	W	Rh	Cu	Pd	Pb
H	Cl	Al	Nb	Ir	Zn	Ag	Sb
O	Br	Si	Ta	Ru	Sn	Cd	Bi
N			Re	Ba		Pt	

Table 2.1 Classification of elements based on toxicity and availability.

For the human body, twenty elements are classified as essential; among them at least ten are metals [3]. In the absence of the essential trace element, the organism fails to grow or to complete its life cycle, but if the concentration of the element exceeds that required for the correct nutritional response, it becomes toxic as showed in the dose – response diagram displayed in figure 2.1a [2].

Regarding toxicity, two categories can be distinguished: i) elements that are not necessary for life due to their low abundance and low bioavailability, and ii) elements for which only negative effects have been observed even at low concentrations [3].

In any case, all metals are potentially hazardous to organisms depending on their concentration levels, as displayed by the dose – response diagrams in figure 2.1.

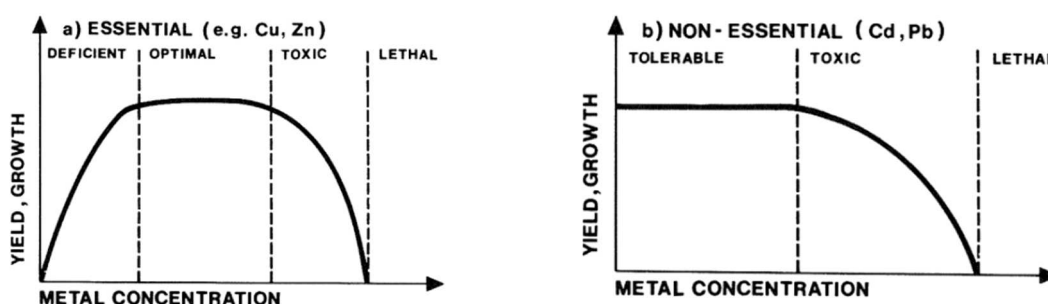


Figure 2.1 Dose - Response diagram for essential (a) and non - essential (b) trace elements [2].

In general, the toxic effects of heavy metals are due to the fact that they bind to protein sites normally occupied by other cations (essential trace elements) causing cell malfunctioning and, eventually, apoptosis. Figure 2.2 illustrates the oxidative stress caused by the increase in the production of reactive oxygen species (ROS) and the decrease of the production of antioxidant as consequence of heavy metal contamination.

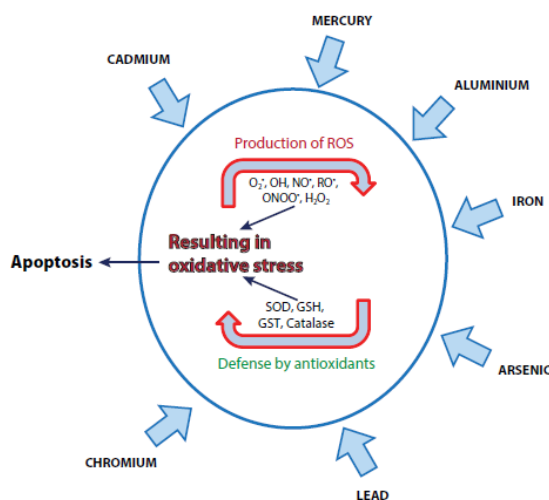


Figure 2.2 Heavy metals effect on a cell [4].

In this thesis, cadmium, lead and nickel were taken as representative of heavy metal pollutants found in water bodies, and its removal from aqueous solution via adsorption onto bio-adsorbents was studied.

## 2.1 Cadmium

### *Cadmium properties*

Cadmium, with symbol Cd, is a d-block element belonging to group 12 of the periodic table along with zinc and mercury. It has atomic number 48 and atomic weight 112.41 amu, its electronic configuration is  $[\text{Kr}]4d^{10}5s^2$  and shows intermediate chemical properties between Zn and Hg. The main oxidation state is +2, but there is evidence of existence of Cd(I) in  $\text{Cd}_2^{2+}$  species.

The concentration of Cd in the crust of Earth is about 0.2 ppm, with lower levels occurring in igneous rocks, sandstones and limestone, and higher concentrations in sedimentary rocks associated with organic material [5].

Only three cadmium minerals are known: greenockite and hawleyite are hexagonal and isometric polymorphic forms of cadmium sulphide, CdS, while the mineral otavite is composed of cadmium carbonate. None of these minerals, although, are found in nature in sufficient concentration to be extracted alone as an ore [6].

Cadmium is found in nature mainly associated with zinc and, in less extent, with lead and copper; it is obtained as a by-product of the extraction of their sulphide ores [5-6].

### *Cadmium speciation in the environment*

The natural occurrence of cadmium in the different environmental compartments is relatively low and variable with higher concentrations found in zinc ores ( $1 - 12 \text{ g kg}^{-1}$ ) and lower levels in sea and river waters ( $< 0.01 - 0.1 \text{ } \mu\text{g kg}^{-1}$ ). Larger cadmium concentrations are found nearby urban or industrialised areas; even though Cd emissions probably will increase in the next years in developing countries, a general decreasing annual trend is observed [7].

Cadmium is a persistent contaminant, but physical and chemical processes can affect its mobility, bioavailability and residence time in the different environmental compartments.

### *Atmosphere*

The contribution to cadmium content in the atmosphere comes from both natural and anthropogenic sources, the latter mainly deriving from the combustion of fossil fuels and pyro-metallurgical non-ferrous metal industries.

The first parameter to consider that controls deposition, transport and inhalation processes is the size of atmospheric aerosols; cadmium is mainly present in fine particles ( $0.6 - 1.3 \text{ } \mu\text{m}$ ) with percentages up to 60%, but cadmium can be found also in  $\text{PM}_{2.5}$  and  $\text{PM}_{10}$ .

Cadmium is found in air in a wide concentration range, from 0.1 to 5 ng m<sup>-3</sup> in rural areas, from 2 to 15 ng m<sup>-3</sup> in urban areas and up to 300 ng m<sup>-3</sup> in major cities.

Atmospheric cadmium compounds are easily solubilised/removed by wet or dry deposition, in particular, inorganic cadmium species commonly found in particulate form are characterised by a relatively short residence time (from 1 to 4 weeks). Elemental cadmium or Cd oxides, usually in the form of mixed oxides with other metals, are emitted in the atmosphere as consequence of combustion processes or iron and steel manufacturing, while CdCl<sub>2</sub> is the predominant species from refuse incineration. Other cadmium species present in the atmosphere are CdS and CdSO<sub>4</sub>, both coming from the dust emitted by lead smelter or formed by coal combustion and non-ferrous metal production.

In general, cadmium and many of its compounds are quite volatile, so condensation on aerosols can occur after emission from high temperature processes. The presence of cadmium species on particles surface may results in an increase of their bioavailability [7].

#### *Natural waters*

According to the HSAB theory, cadmium is a soft acid characterised by large atomic/ionic radius, high polarizability and a tendency to form covalent bounds. Being a soft acid, it reacts more strongly with soft or borderline ligands (Cl<sup>-</sup>, SCN<sup>-</sup>, I<sup>-</sup>, Br<sup>-</sup>) and to a lesser extent with oxygen-donor ligands (OH<sup>-</sup>, CO<sub>3</sub><sup>2-</sup>, SO<sub>4</sub><sup>2-</sup>).

In figure 2.3 the cadmium speciation diagrams for Cd + ligand (Cl<sup>-</sup>, OH<sup>-</sup>, CO<sub>3</sub><sup>2-</sup>) binary systems are shown. These diagrams are based on recommended and provisional values of stability constants at 25°C and ionic strength of 0 mol kg<sup>-1</sup> [8].

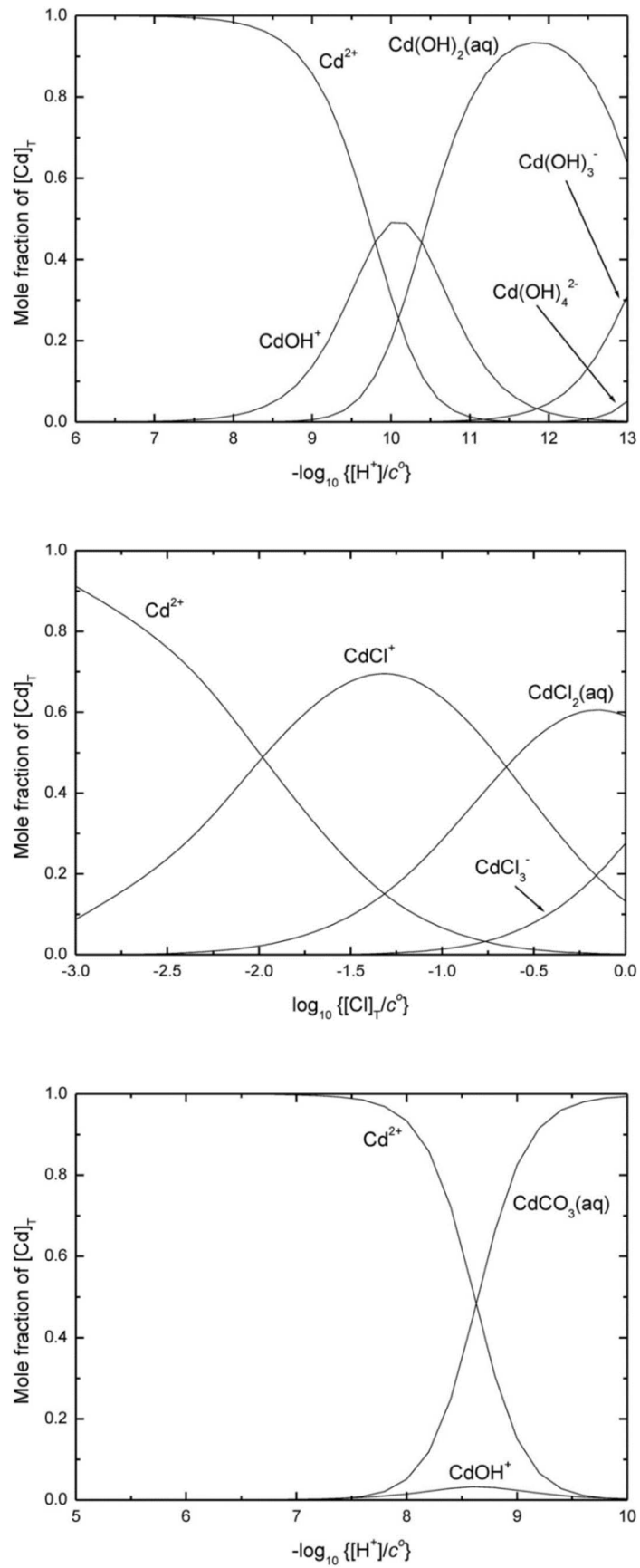


Figure 2.3 Speciation diagram for (a) binary Cd<sup>2+</sup> + OH<sup>-</sup> system, (b) binary Cd<sup>2+</sup> + Cl<sup>-</sup> system, (c) ternary Cd<sup>2+</sup> + H<sup>+</sup> + CO<sub>3</sub><sup>2-</sup> system [8].

As concern natural waters, metal speciation depends on different factors such as chemical composition of the water matrix, pH, salinity and temperature. The distribution of inorganic cadmium species varies strongly from fresh waters to hypersaline waters as can be seen from the diagrams reported in figure 2.4.

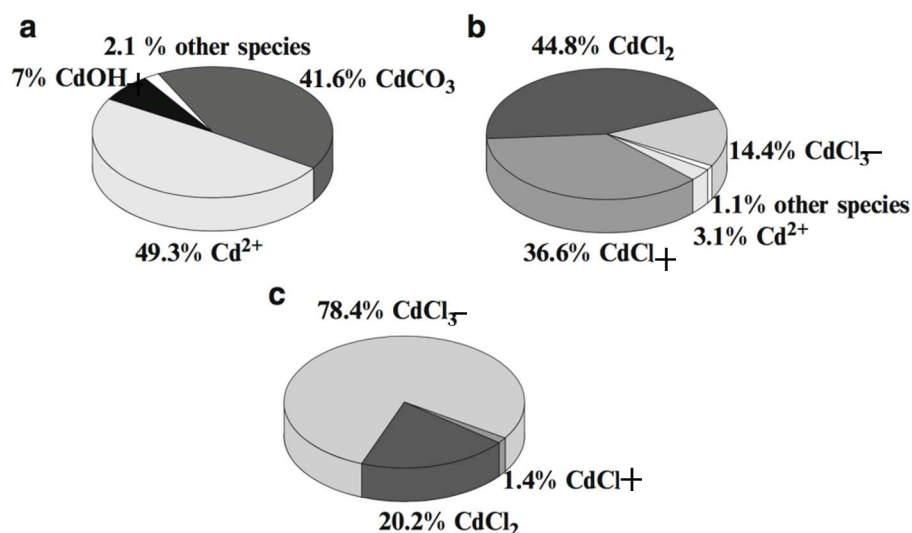


Figure 2.4 Distribution of inorganic Cd<sup>2+</sup> species in different natural waters: (a) fresh water at pH = 9 and I = 0,0015 mol L<sup>-1</sup>; (b) seawater at pH = 8,1 and I = 0,67 mol L<sup>-1</sup>; (c) hypersaline water at pH = 6,4 and I = 6,3 mol L<sup>-1</sup> [7].

### Soils and sediments

Generally, when metals are present in subsurface systems, they are relatively immobile and they are retained in the solid phase by different mechanisms, such as ion exchange, outer- and innersphere surface complexation/adsorption, precipitation or co-precipitation.

The metal bound to particulate solid phase can be divided into different fractions based on physicochemical properties:

- *Acid soluble fraction*: it is composed by exchangeable and carbonate phases, it is the fraction most subject to variations because it is sensitive to pH changes;
- *Reducible fraction*: in this fraction the metal is bound mainly to Fe-Mn oxides;
- *Oxidizable fraction*: cadmium is bound to organic matter and sulfur and it can be released under oxidative conditions;
- *Residual fraction*: in this fraction chemically stable and biologically inactive metal forms are found.

### Cadmium uses and toxicity

Due to its toxicity the use of cadmium has been significantly reduced in the industrialised countries over the last years with consequent less release of the metal into the environment, on the other hand, cadmium consumption in developing countries has continued or even

increased, so a non-negligible amount of cadmium is still released into the environment resulting in health and environmental risks related to the use, management and disposal of Cd-containing products.

The main uses of cadmium are reported in table 2.2.

<b>Common uses of cadmium and cadmium compounds</b>	
Nickel-cadmium batteries	Rechargeable Ni-Cd batteries are the main application of Cd. The use of these batteries is now limited by EU battery directive 2006/66/EC except when no alternative is available.
Coating and solder alloys	Due to its advantageous properties (i.e. it reduces the working temperature required) 16-25% of Cd is present in Cd-containing silver solder. Nowadays, Cd is still used in solder alloys but only for particular applications (aerospace and defence industries).
Pigments	CdS and CdS/CdTe are used as pigments in different applications including paints, glasses, ceramics and plastics.
Stabilisers in plastics	Cadmium stearate and cadmium laurate have been used as PVC stabilisers because of the high heat stability and weatherability that they confer to plastic products.
Solar cells	Due to its low cost and less toxicity than other Cd compounds, CdTe is the second most widely used materia in solar cells, after silicon.
Phosphate fertilisers	Cadmium is present, with concentration up to 0.01%, in phosphate fertilisers which are used widely used in agriculture. No general EU rule (2016)

**Table 2.2 Cadmium uses [9].**

According to the ATSDR (Agency for Toxic Substances & Disease Registry) ranking cadmium is the seventh most toxic heavy metal. Due to its wide use, humans and animals may get exposed at work or through the environment. The primary ways of Cd uptake are through inhalation and ingestion leading to acute or chronic intoxications [4].

## 2.2 Lead

### *Lead properties*

Lead is a chemical element with symbol Pb, atomic number 82 and atomic weight 207.2 amu. It is a heavy metal denser than most common materials, Pb is soft and malleable with a relatively low melting point (327.46°C). When freshly cut, it appears silvery with a hint of blue, but when exposed to air it turns into a dull grey colour. Lead electronic configuration is  $[\text{Xe}]4f^{14}5d^{10}6s^26p^2$  and is usually found in the +2 oxidation state rather than +4 oxidation state which is mostly limited to organolead compounds.

More than 200 lead minerals are known, but the more significant three are galena (PbS), cerrusite (PbCO<sub>3</sub>) and anglesite (PbSO<sub>4</sub>) and of these, galena is the mineral used for the extraction of lead.

Pb is found in the crust of Earth in concentration of about 13 ppm with high levels in coal and organic shales presumably due to the formation of complexes with organic compounds [5].

### *Lead speciation in the environment*

The main input of lead into the environment comes from anthropogenic emissions; the extensive use of this metal in industry and consumer products since the Industrial revolution until the introduction of regulations, has resulted in severe contamination of urban areas. Around the world, a wide variety of consumer products still contain lead resulting in a continuous release of the heavy metal into the environment to which humans continue to be exposed [10].

### *Atmosphere*

Lead is one of the most prominent pollutants in the atmosphere mainly because of the large use of leaded petrol worldwide. Even though thanks to the introduction of lead-free petrol the atmospheric Pb concentrations have decreased, the atmospheric pollution by Pb is still regarded as a potential health problem [11].

Lead and its sulphur and oxygen compounds are found predominantly as particulate, in many places Pb is present on particles with a diameter smaller than 1 µm (Belgium, Hungary, Korea, Spain) whereas larger particle sizes were recorded in Mumbai and Zürich where most of the lead was found on particles with a diameter larger than 2.5 µm. Lead can also be present in particles smaller than 1 µm as found in the Los Angeles near an industrial area; the occurrence of Pb on sub-micrometre particles is particularly concerning because it can be efficiently inhaled [12].

The main lead species originating from the exhausts of cars is PbClBr, but PbO, Pb(OH)X (with X = Cl, Br), PbSO<sub>4</sub>, Pb<sub>3</sub>(PO<sub>4</sub>)<sub>2</sub>, PbO·PbSO<sub>4</sub> and Pb can occur in larger particles, whereas α and β NH<sub>4</sub>Cl·2PbClBr and 2NH<sub>4</sub>Cl·PbClBr are found in smaller particles. Particulate materials originated from smelters contain PbS (coming from the primary ore), PbSO<sub>4</sub>, and PbO·PbSO<sub>4</sub>, PbO and Pb [5].

#### *Natural waters*

In aqueous solution, lead occurs in two oxidation states: +2 and +4, the former is the most commonly found. In figure 2.5 the speciation diagrams of lead and inorganic ligand systems are depicted. The natural concentration of lead in the water bodies is low, since its salts (carbonates, sulfates and phosphates) are poorly soluble in water. Pb can enter the natural water systems from industrial wastewaters, corrosion of tanks and piping, and from materials containing lead. Pb can also enter water from the air because of the emissions from road transport, since lead is still an additive found in petrol, even though in much lower concentrations.

In soluble form, lead occurs mainly as Pb<sup>2+</sup> and PbCO<sub>3</sub>(aq), and in alkaline medium also as [Pb(CO<sub>3</sub>)<sub>2</sub>]<sup>2-</sup>, Pb(OH)<sub>2(aq)</sub> and [Pb(OH)]<sup>+</sup> [13].

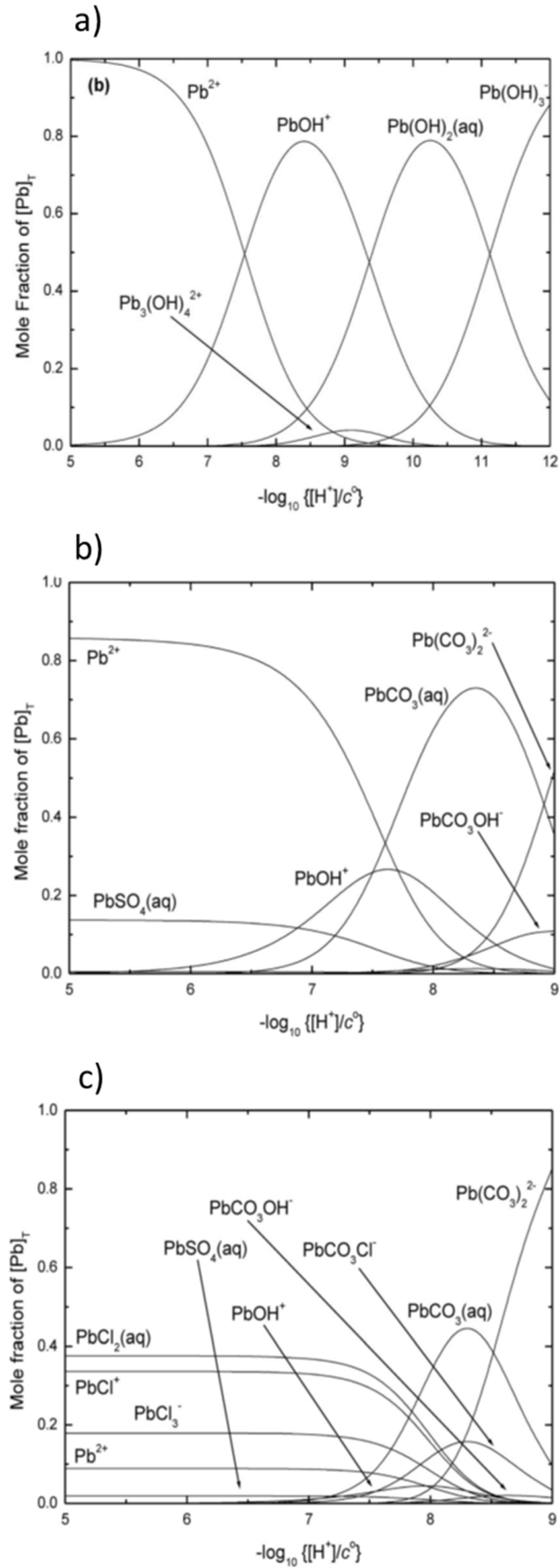


Figure 2.5 Speciation diagram for a)  $\text{Pb}^{2+} + \text{OH}^-$  binary system at a total  $\text{Pb}^{2+}$  conc of  $1 \text{ mg kg}^{-1}$ ; b) simulated freshwater medium; and c) simulated seawater medium [14].

### *Soils and sediments*

Lead is commonly found in soils, with an average concentration ranging from 10 to 20 mg kg<sup>-1</sup>, with levels higher than 100 mg kg<sup>-1</sup> indicating contamination. Moreover, Pb tends to be found in higher concentration in organic soils rather than mineral soils.

In sediments, PbCO<sub>3</sub>, PbSO<sub>4</sub>, PbS and Pb<sub>5</sub>(PO<sub>4</sub>)<sub>3</sub>Cl are commonly found originating from automobile aerosol. PbCO<sub>3</sub> and Pb<sub>3</sub>(CO<sub>3</sub>)<sub>2</sub>(OH)<sub>2</sub> are also commonly found in sediments, the latter formed as a precipitate in lead water pipes. The lead compounds vary according to the redox properties of the sediment, changing from oxy-compounds to PbS as the system becomes anoxic. Lead is found not only in mineral species, but also bound to organic matter, in fact, around 3 – 12% of lead is associated with surface active organic material in seawater [5].

### *Lead uses and toxicity*

Lead is a metal used since ancient times due to its malleability, resistance to corrosion and low melting point. The coloured lead-based pigments have been extensively used worldwide in ceramics, paint and cosmetics.

In the 20<sup>th</sup> century the use of lead increased significantly, tetraethyl- and/or tetramethyllead have been added to petrol to increase the octane rating of the fuel. The use of lead compounds as additives in petrol reached a peak in the 1970s, but nowadays the use of this metal in many applications is in decline due to its toxicity [5, 15].

Lead is classified as a possible human carcinogen (group 2B) by the International Agency for Research on Cancer (IARC). The organ systems affected by lead include the central and peripheral nervous systems, the red blood cells, the kidneys, the cardiovascular system, and the male and female reproductive organs. The main symptoms caused by lead poisoning are convulsions, wrist drop, renal failure, anemia, while reduced intelligence, slowed nerve conduction, impaired biosynthesis of heme, and altered excretion of uric acid represent their subclinical correlates [15].

## **2.3 Nickel**

### *Nickel properties*

Nickel is an element of the period table with symbol Ni, atomic number 28 and atomic weight 58.69 amu. It is a silvery-white lustrous metal with a slight golden tinge. Nickel has two electronic configurations, [Ar] 3d<sup>8</sup>4s<sup>2</sup> and [Ar] 3d<sup>9</sup>4s<sup>1</sup>, which are very close in energy, and its main oxidation state is +2, other oxidation states (-1, +1, +3 and +4) are also found, but to a much less extent.

Pure nickel is rarely found in nature, it usually occurs in mineral form such as limonite, pentlandite and a mixture of Ni-rich natural silicates known as garnierite. Ni is also found in meteors in combination with iron.

Nickel is an essential trace element for several animal species, microorganisms and plants, therefore either deficiency or toxicity effects can occur in presence of too low or too high concentration levels, respectively.

#### *Nickel speciation in the environment*

Nickel is a trace metal widely distributed in all environmental compartments, with input from both natural and anthropogenic sources.

#### *Atmosphere*

The introduction of nickel into the atmosphere from natural sources is caused by wind-blown dust derived from the weathering of rocks and soils, volcanic emissions, forest fires and vegetation. The anthropogenic activities responsible of atmospheric pollution include the combustion of coal, diesel oil and fuel oil, the incineration of waste and sewage, and other various sources.

Indeed, higher levels of Ni in ambient air are found in the proximity of highly industrialised areas. Typical mean values of airborne Ni are: 0.01 – 3 ng m<sup>-3</sup> in remote areas; 3 – 30 ng m<sup>-3</sup> in urban areas without metallurgical activities nearby; 70 – 770 ng m<sup>-3</sup> in nickel processing areas. The speciation of nickel depends on the kind of activity and process in which Ni is used; workers may be exposed to the following substances: dust of relatively insoluble nickel compounds, aerosols originating from nickel solutions (soluble nickel species) and gaseous forms containing nickel [16].

#### *Natural waters*

The main source of Ni pollution in the aquatic environment are domestic wastewater effluents and non-ferrous smelters. In freshwater, the ionic form and nickel associated with organic matter are the predominant species [16].

Nickel levels in groundwater depend on pH and soil use, acid rain enhance the mobility of Ni in the soil leading to a possible increase of its concentration in the water matrix; higher Ni concentrations (100 – 2500 µg L<sup>-1</sup>) in groundwater and municipal tap water in polluted areas and areas in which natural nickel was mobilised have been reported [17].

### *Soils and sediments*

In soils nickel can be present in many forms, inorganic crystalline minerals or precipitates, complexed or adsorbed on organic cation exchange surfaces or inorganic cation exchange surfaces, free-ion or chelated metal complexes in soil solution [16].

### *Nickel uses and toxicity*

Nickel is used in many applications including the production of stainless steel and nickel alloys, electroplating, electroforming, nickel-cadmium batteries, catalysts and electronic equipment. Nickel alloys are widely used in jewellery, and the associated products are the cause of contact dermatitis in a substantial part of the population who are sensitive to nickel [18].

Nickel is an essential element, especially for some plants, but when it is present in high concentrations it becomes toxic for the organisms.

According to the International Agency for Research on Cancer (IARC), metallic nickel and alloys belong to the group 2B (possibly carcinogenic to humans), while nickel compounds are classified in the group 1 (carcinogenic to humans).

The major effect that nickel has on the general population is allergic contact dermatitis; symptoms caused by acute exposure to nickel were reported to be nausea, vomiting, diarrhoea, giddiness, lassitude and shortness of breath in workers who accidentally drank water contaminated with nickel sulfate and nickel chloride [17].

## **2.4 Removal of heavy metals**

Environment pollution is a growing problem that needs to be controlled, especially in the case of persistent contaminants such as heavy metals.

Several physical and chemical approaches have been reported to remove heavy metals from different environmental matrices, regarding cadmium, the main methods employed are here reported.

*Precipitation:* the most commonly used method to remove heavy metals is by precipitation due to the low cost and simplicity of the process.

Hydroxide precipitation is the most widely used process because of its relative simplicity, low cost and ease to control pH, it involves the formation of metal hydroxide that precipitates, but the precipitate formation can be inhibited by the presence of complexing agents in the water matrix. This type of precipitation produces large volumes of relatively low density sludge with consequent disposal problems; moreover, some metal hydroxides show amphoteric behaviour enhancing the solubility of other metal hydroxides and releasing

the metal ion back to the solution. On the other hand, carbonate precipitation generally shows high removal efficiency and the metal carbonate precipitates are denser when compared to metal hydroxide precipitates.

Another precipitation method involves the formation of metal sulphide, the main advantages of this method are that the solubility of the products are lower than the relative hydroxides, and a high degree of metal removal is obtained over a wide range of pH. One of the disadvantages of this method is that sulphide sludge is prone to oxidation that can lead to resolubilisation of the metal into the solution.

*Cementation:* cementation process in wastewater remediation applications involves the deposition of a toxic metal which is reduced by a less toxic metal, for cadmium removal the reaction that takes place is:  $\text{Cd}^{2+} + \text{Zn} \rightarrow \text{Cd} + \text{Zn}^{2+}$ , this reaction is spontaneous since the redox potentials of cadmium and zinc are 0.76 and 0.31 V respectively. The disadvantages of this process are the sufficiency of redox potential and the consumption of sacrificing metals.

*Coagulation/flocculation:* this process, followed by sedimentation, uses coagulants such as aluminium, ferrous sulfate and ferric chloride for the destabilisation of colloids by neutralising the forces that keep them apart. Electrocoagulation is an effective method for the removal of heavy metals (i.e. removal of cadmium ions from electroplating rinse water) that produces in situ coagulants by sacrificial electro-oxidation of the anode, generally made of iron or aluminium.

*Flotation:* foam flotation, dissolved air flotation, precipitation flotation and adsorbing colloid flotation are processes extensively used for the removal of heavy metals in wastewater treatment. Even though this method is very efficient in a wide range of pH and initial concentrations, it involves high initial costs as well as high operational and maintenance costs.

*Solvent extraction:* this method is used mainly to recover and separate metal ions from highly concentrated aqueous media to obtain pure solutions. The disadvantage of this method is the discharge of large amounts of toxic solvents that needs to be replenished through a costly stripping test.

*Ion exchange:* another commonly used method that is based on the exchange mechanism between an electrolyte present in a solution, and an insoluble electrolyte. Ion exchange methods are advantageous because of their high treatment capacity, high removal

efficiency and fast kinetics. However, this technique requires expensive equipment and high operational costs for the resin regeneration.

*Membrane separation:* different types of membrane processes can be employed for the removal of cadmium, such as liquid membranes, hollow-fiber-supported liquid membranes and emulsion liquid membranes. The limitations of this technique are mainly due to fouling resulting from the presence in the wastewaters of inorganic and organic substances, and reduced durability and instability under salty or acidic conditions.

*Adsorption:* The more conventional treatment technologies mentioned above involve the use of large amounts of chemicals and/or present high operational or maintenance costs. Hence, the development of eco-friendly and cost-effective technologies for water remediation is of great importance. Adsorption nowadays is the most effective and economic method for the removal of cadmium from wastewater, this process offers flexibility in the design and operation, and a vast variety of naturally found adsorbent materials can be used. Moreover, in some cases the adsorption can be reversible, allowing the regeneration of the adsorbent material by a suitable desorption process.

The most common material used in adsorption technologies is activated carbon, sometimes treated chemically by acid, base, oxidising and reducing agent to improve its adsorption efficiency.

Biosorption using natural adsorbents is an area extensively studied worldwide in order to come up with sustainable alternatives for the removal of cadmium from aqueous matrices. Several possible biosorbents have been studied, they can be obtained from different sources: i) natural minerals, industrial and municipal wastes include zeolites, hydroxyapatite, fly ash, granular red mud and dried sludge; ii) agro-adsorbents that showed high cadmium removal efficiency comprise cedar wood, black gram husk, wheat bran and maize corncob; iii) fungi, algae and animal biomass including egg shell waste, bone char and invasive snail [19].

## 2.5 References

- [1] Tchounwou P.B., Yedjou C.G., Patlolla A.K., Sutton D.J. (2012) Heavy Metal Toxicity and the Environment. Luch A. (eds) Molecular, Clinical and Environmental Toxicology. *Experientia Supplementum*, vol 101. Springer, Basel.
- [2] Förstner U., Wittmann G. T. W. (1983) *Metal Pollution in the Aquatic Environment*. 2<sup>nd</sup> Revised Edition, Springer – Verlag, Berlin Heidelberg New York Tokyo.
- [3] Zoroddu M. A., Aaseth J., Crisponi G., Medici S., Peana M., Nurchi V. M. (2019) The essential metals for humans: a brief overview. *Journal of Inorganic Biochemistry*, 195, 120 – 129.
- [4] Jaishankar M., Tseten T., Anbalagan N., Mathew B. B., Beeregowda K. N. (2014) Toxicity, mechanism and health effects of some heavy metals. *Interdisciplinary Toxicology*, 7(2), 60 – 72.
- [5] Fergusson J. E. (1990) *The heavy elements: chemistry, environmental impact and health effects*. Pergamon Press.
- [6] Butterman W.C., Plachy J. (2004) *Mineral Commodity Profiles: Cadmium*. U.S. Geological Survey Open-File Report 02-238, Version 1.0, 1 – 25.
- [7] Crea F., Foti C., Milea D., Sammartano S. (2013) Chapter 3. Speciation of Cadmium in the Environment. in *Cadmium: From Toxicity to Essentiality, Metal Ions in Life Sciences 11*, Sigel (eds.).
- [8] Powell K. J., Brown P. L., Byrne R. H., Gajda T., Hefter G., Leuz A.-K., Sjöberg S., Wanner H. (2011) Chemical speciation of environmentally significant metals with inorganic ligands. Part 4: The  $\text{Cd}^{2+} + \text{OH}^-$ ,  $\text{Cl}^-$ ,  $\text{CO}_3^{2-}$ ,  $\text{SO}_4^{2-}$ , and  $\text{PO}_4^{3-}$  systems (IUPAC Technical Report). *Pure and Applied Chemistry*, 83(5), 1163 – 1214.
- [9] Remelli M., Nurchi V. M., Lachowicz J. I., Medici S., Zoroddu M. A., Peana M. (2016) Competition between Cd(II) and other divalent transition metal ions during complex formation with amino acids, peptides, and chelating agents. *Coordination Chemistry Reviews*, 327 – 328, 55 – 69.
- [10] Smith D. R., Flegal A. R. (1995) Lead in the Biosphere: Recent Trends. *Ambio*, 24(1), 21 – 3.
- [11] Sakata K., Sakaguchi A., Tanimizu M., Takaku Y., Yokoyama Y., Takahashi Y. (2014) Identification of sources of lead in the atmosphere by chemical speciation using X-ray adsorption near-edge structure (XANES) spectroscopy. *Journal of Environmental Sciences*, 26, 343 – 352.
- [12] Murphy D. M., Hudson P. K., Cziczo D. J., Gallavardin S., Froyd K. D., Johnson M. V., Middlebrook A. M., Reinard M. S., Thomson D. S., Thornberry T., Wexler A. S. (2007)

Distribution of lead in single atmospheric particles. *Atmospheric Chemistry and Physics*, 7, 3195 – 3210.

[13] Namieśnik J., Rabajczyk A. (2010) The speciation and physicochemical forms of metals in surface waters and sediments. *Chemical Speciation & Bioavailability*, 22:1, 1 – 24.

[14] Powell K. J., Brown P. L., Byrne R. H., Gajda T., Hefter G., Leuz A.-K., Sjöberg S., Wanner H. (2009) Chemical speciation of environmentally significant metals with inorganic ligands. Part 3: The  $\text{Pb}^{2+} + \text{OH}^-$ ,  $\text{Cl}^-$ ,  $\text{CO}_3^{2-}$ ,  $\text{SO}_4^{2-}$ , and  $\text{PO}_4^{3-}$  systems (IUPAC Technical Report). *Pure and Applied Chemistry*, 81(12), 2425 – 2476.

[15] Landrigan P. J., Boffetta P., Apostoli P. (2000) The Reproductive Toxicity and Carcinogenicity of Lead: A Critical Review. *American Journal of Industrial Medicine*, 38, 231 – 243.

[16] Cempel M., Nikel G. (2006) Nickel: A Review of Its Sources and Environmental Toxicology. *Polish Journal of Environmental Studies*, 15(3), 375 – 382.

[17] World Health Organization (2007) Nickel in Drinking-water. WHO Guidelines for Drinking-water Quality.

[18] Barceloux D. G., Barceloux D (1999) Nickel. *Journal of Toxicology: Clinical Toxicology*, 37:2, 239 – 258.

[19] Purkayastha D., Mishra U., Biswas S. (2014) A comprehensive review on Cd(II) removal from aqueous solution. *Journal of Water Process Engineering*, 2, 105 – 128.

## 3 ORGANIC CONTAMINANTS

### 3.1 Volatile organic compounds

Hydrocarbons are organic compounds composed by carbon and hydrogen atoms, molecules with a structure given by a linear or branched chain are known as aliphatic hydrocarbons, while compounds with a cyclic chain as basic structure are known as aromatic hydrocarbons.

Among these compounds, volatile organic compounds (VOCs) have an important role regarding environmental pollution. VOCs are characterised by high vapour pressure at room temperature as consequence the low boiling point that makes them very volatile.

VOC is a class of chemical substances that includes a wide range of organic compounds with different chemical and physical properties, they are ubiquitous and are originated from both natural and anthropogenic sources.

The annual anthropogenic emissions correspond to 142 teragrams of carbon emitted as VOCs. The main sources of VOCs from human activities are from varnish and protecting films: they are used as solvents and are slowly released into the atmosphere, common solvents are aliphatic hydrocarbons, ethylacetate and acetone.

Some VOCs are dangerous for the environment and human health, so their use and emissions, especially in indoor environments, are regulated by law; their toxic effects are not caused by short time contact, but derives from long-term exposure.

In this work we selected toluene and n-hexane as representative of this class of contaminants to evaluate the use of zeolites as adsorbent materials for the removal of organic pollutants from aqueous media.

#### 3.1.1 Toluene

Toluene (Fig. 3.1) is an aromatic hydrocarbon widely used in the industry as reagent or solvent. In standard conditions toluene is stable, volatile and with a low solubility in water ( $0.52 \text{ g L}^{-1}$  at  $20^\circ\text{C}$ ), it reacts as a normal aromatic hydrocarbon in electrophilic aromatic substitution reactions resulting more reactive than benzene due to the presence of the methyl group. The methyl group allows also oxidation reactions that lead to benzoic acid which is a product of high industrial importance.

In nature, toluene is present in pine oil; generally, it is obtained from fuel production by catalytic reforming processes and the final separation is obtained by distillation or solvent extraction.

Toluene belongs to the group of chemicals known as BTEX, this group includes benzene, toluene, ethylbenzene and xylenes. BTEX are present in refined petroleum products and are used as indicators to evaluate the size, age and toxicity of petroleum fuel spills and

plumes. These compounds are characterised by relatively low adsorption to soil, so they readily partition into air and leach into groundwater [1].

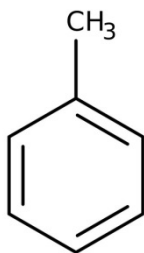


Figure 3.1 Toluene.

Toluene is employed mainly in two processes: the first one for the production of benzene by a hydrodealkylation reaction, and to obtain a mixture of benzene and xylene from a disproportionation reaction. The second use regards the production of fuels: toluene is added to petrol as an antiknock agent and to increase the number of octane.

Due to its ability to dissolve many substances (varnishes, paints, rubber, adhesives, disinfectants and many chemical reactants) it is widely used as solvent [2] in substitution of the more toxic benzene.

#### *Toluene toxicity*

Toluene is potentially less toxic than benzene, since it is less volatile; it can nonetheless cause skin irritation. Inhalation of high concentrations of toluene can cause irritation of mucous membranes of the upper respiratory tract leading to chemical pneumonia and pulmonary edema.

During acute intoxication, the prevailing symptoms are those related to the central nervous system such as altered colour vision, headache, asthenia, vertigo, drowsiness, balance and basic motor skills disorder.

Toluene is present in all the environmental compartments: it is found in air, water, soil, but mainly in superficial and ground waters, and it can reach humans through food. The diffusion of toluene in water and soil originates mainly during the extraction steps of fossil hydrocarbons from underground oilfield [3].

#### **3.1.2 n-Hexane**

n-Hexane (Fig. 3.2) is a volatile aliphatic hydrocarbon composed of a linear chain of six carbon atoms. It is a colourless liquid with a boiling point of 68.7°C and a relatively low solubility in water (0.0098 g L<sup>-1</sup>).



**Figure 3.2 Hexane.**

Hexane occurs in crude oil in small percentages and can be obtained from a number of oil fractions by refinery process. It is difficult to obtain highly pure n-hexane, to achieve it typical processes involve molecular sieve adsorption (the linear hydrocarbon is held into the cavities of the sieve, whereas the branched hydrocarbons pass straight through), batch azeotropic distillation, superfractionation and extractive distillation [4].

Hexane can be used as a solvent for the extraction of edible oils from seeds and vegetable crops with some restrictions regarding the residue content and application in preparations of different food. It is also used as a solvent for glues, varnishes and inks, and as cleaning agent in the printing industry.

#### *Hexane toxicity*

Hexane is released into the environment mainly through the combustion of fuels for heating and transportation, other sources are industrial discharges, effluents from municipal waste-treatment plants, nonpoint-source runoff, spills, sludge and other waste deposition.

The release of hexane into the atmosphere is caused by evaporation during processing of the substance, incomplete fuel combustion, or from spills in soil and water.

Hexane is classified as toxic for aquatic life with long lasting effects, it has been classified as Aquatic Chronic 2 hazard class according to the Annex VI of Regulation (EC) NO 1272/2008 (CLP Regulation).

For humans, inhalation exposure has been associated to headache, hearing deficit, dysesthesia in limbs, reduced sensation, dizziness and sleepiness, and muscle weakness. These symptoms were found consistent with neurophysiological findings in exposed individuals [4].

### *VOCs removal from water*

Water bodies contaminated with VOCs, especially BTEX, are generally treated using different technologies such as granular activated carbon (GAC), air stripping, membrane nanofiltration and carbon nanotubes.

Air stripping has the disadvantage of transferring the contaminants from liquid to gas phase, adsorption on GAC is expensive due to the replacement and disposal of the activated carbon loaded with the contaminants as hazardous waste, while other methods such as nanofiltration reverse osmosis or oxidation are poorly efficient, may not be cost-effective, or can give undesirable residuals [5].

### 3.2 Organochlorine compounds

An organochlorine compound is a compound containing at least one carbon-chlorine bond; this class of chemical compounds includes a wide structural variety with different chemical properties leading to a broad range of applications. Organochlorine compounds are very useful in many applications, but some are of serious environmental concern.

Organochlorine compounds can be found in many natural sources, in fact they are present in nearly every class of biomolecules, including alkaloids, terpenes, amino acids, flavonoids, steroids, and fatty acids [6-7]. For example, the occurrence of chloromethane in nature is mainly associated with algae growth in the aquatic environment and with the biodegradation of wood by fungi [8]. Organochlorine compounds, including toxins, are also produced in the high temperature environment caused by forest fires.

A significant source of organochlorine compounds input into the environment is represented by anthropogenic activities; especially in the last century, an important increase of these substances, including polychlorobiphenyls (PCBs), DDTs, hexachlorocyclohexanes (HCH) and hexachlorobenzene (HCB), has been reported as a consequence of their extensive use [9]. Organochlorines are widely used as pesticides, these chemicals are characterised by high persistence in the environment and high toxicity causing alteration to the food chain and the ecosystem [10]. Due to adverse effects of these compounds on the environment, the EU legislation (Regulation (EC) No 1107/2009: <https://eur-lex.europa.eu/LexUriServ/LexUriServ.do?uri=OJ:L:2009:309:0001:0050:EN:PDF>), banned the use of plant protection products containing active substances unless they have been approved for that purpose in accordance with the Regulation. Organochlorine compounds can be divided up into two classes on the basis of their boiling point: volatile organic compounds (VOCs) and semi-volatile organic compounds (SVOCs). The last one is a term used to describe a broad subgroup of VOCs that includes different classes of compounds characterised by higher molecular weight and higher boiling points (higher than water). The more common classes of SVOCs found in the environment are PCBs, polycyclic aromatic hydrocarbons (PAHs), and pesticides. Due to their lower volatility, these substances tend to persist in the water bodies for longer periods of time, this leads to possible accumulation that can reach harmful concentrations.

#### 3.2.1 Chlorobenzene

Chlorobenzene (CB) is an aromatic organic compound with chemical formula  $C_6H_5Cl$  (Fig. 3.3). It is a colourless, flammable liquid commonly used as a solvent and as an intermediate

for the production of other chemicals. It has a boiling point of 131°C and a solubility in water of 0.5 g L<sup>-1</sup>.

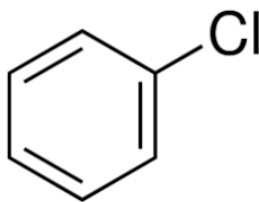


Figure 3.3 Chlorobenzene.

CB is produced by chlorination of benzene in the presence of a Lewis acid catalyst such as ferric chloride, sulfur dichloride and anhydrous aluminium chloride. It was used in the past to produce chemicals such as phenol and DDT, formerly on a large scale, but their production from chlorobenzene has been almost entirely discontinued due to the development of new processes and legislation forbidding the use of DDT [11]. Nowadays, CB is mainly used as a solvent for pesticide formulations, as a degreaser, and to produce other chemicals.

#### *Chlorobenzene toxicity*

Chlorobenzene can enter the environment from different sources including industrial and agricultural discharges, drinking water and wastewater chlorine disinfection by-products and incineration wastes. The presence of chlorinated compounds, even at low concentrations, can lead to toxic effects on not only environmental systems, but also on human health [12]. Humans may be exposed to CB mainly by occupational exposure by breathing contaminated air, but also through food or by coming in contact with contaminated soil. The negative health effects caused by CB exposure include gastrointestinal irritations, hepatotoxicity and kidney damages, for this reason, the maximum contaminant level (MCL) set by the Environmental Protection Agency (EPA) for CB is 0.1 mg L<sup>-1</sup> [13].

#### **3.2.2 Metolachlor**

The widespread use of agro-chemicals in modern agriculture leads to water pollution even though many efforts have been made to control and reduce the introduction of pollutants into the environment.

Metolachlor (2-chloro-N-(2-ethyl-6-methylphenyl)-N-(2-methoxy-1-methylethyl)acetamide, labelled MTC), with chemical formula C<sub>15</sub>H<sub>22</sub>ClNO<sub>2</sub> (Fig. 3.4) and molecular weight 283.79 g mol<sup>-1</sup>. It is an organochlorine compound that belongs to the chemical group of chloroacetanilides and it is one of the most extensively used selective herbicide for the control of annual grass weeds, yellow nutsedge and some broadleaf species around the world [14-15].

MTC was originally formulated as a racemate, a 1:1 mixture of the two enantiomers, but modern production methods lead to a higher concentration of (S)-metolachlor which is the more active enantiomer. Due to its relatively high solubility in water ( $530 \text{ mg L}^{-1}$ ), MTC is frequently detected in surface and subsurface waters and its potential to leach and migrate through the soil can lead to ground water contamination. MTC undergoes a partial degradation in agricultural soils under field conditions over a period of 15 – 50 days, usually through hydrolytic reactions and microbial transformation reactions [14].

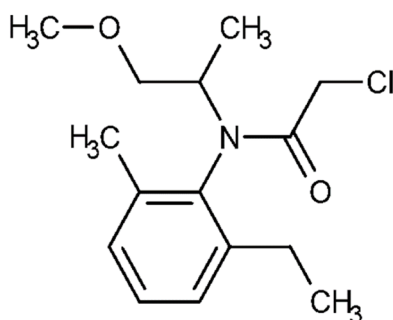


Figure 3.4 Metolachlor.

#### *2-ethyl-6-methylaniline*

Not only pesticides themselves can show negative effects on the environment and humans, but also metabolites deriving from their degradation can be equally or more toxic. This is the case of 2-ethyl-6-methylaniline (EMA), a degradation product of the herbicide metolachlor [16-20].

EMA (Fig. 3.5) has chemical formula  $\text{C}_9\text{H}_{13}\text{N}$ , molecular weight  $135.2 \text{ g mol}^{-1}$ , and is insoluble in water. Inhalation of EMA can cause weakness, reduction in respiratory rate, coma, gradual respiratory failure and mild cyanosis [21]. Osano et al. (2002) [20] found that EMA is up to 6.3 times more acutely toxic than its parent compound MTC.

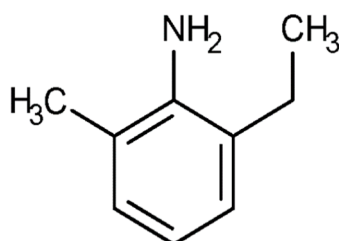


Figure 3.5 2-ethyl-6-methylaniline.

Because of the widespread use of agro-chemicals in modern agriculture, it is necessary to develop remediation technique to ensure water quality. Many methods are available for the attenuation of pesticides, including photocatalytic degradation, combined photo-Fenton and biological oxidation, aerobic degradation, nanofiltration and ozonation [22], but these

processes are usually expensive and require maintenance. Adsorption on organic or inorganic sorbent materials is the preferred way because of the high removal efficiency and reduced operational costs.

### 3.3 References

- [1] Popek E. (2018) Chapter 2 – Environmental Chemical Pollutants. In *Sampling and Analysis of Environmental Chemical Pollutants 2<sup>nd</sup> Edition*, Elsevier, 13 - 69.
- [2] US Environmental Protection Agency (2005) Toxicological Review of Toluene.
- [3] ATSDR (Agency for Toxic Substances and Disease Registry) (2015) Public Health Statement – Toluene.
- [4] Mikkelsen S. H., Warming M., Syska J., Voskian A. (2014) Survey of n-hexane. The Danish Environmental Protection Agency.
- [5] Farhadian M., Duchez D., Vachelard C., Larroche C. (2008) Monoaromatics removal from polluted water through bioreactors – A review. *Water Research*, 42, 1325 – 1341.
- [6] Wagner C., El Omari M., König G.M. (2009) Biohalogenation: Nature's Way to Synthesize Halogenated Metabolites. *Journal of Natural Products*, 72, 3, 540 – 553.
- [7] Engvild K. C. (1986) Chlorine-containing natural compounds in higher plants. *Phytochemistry*, 25, 4, 781 – 791.
- [8] World Health Organization (2000) Methyl Chloride. Concise International Chemical Assessment Document 28.
- [9] Grimalt J. O., van Drooge B. L., Ribes A., Vilanova R. M., Fernandez P., Appleby P. (2004) Persistent organochlorine compounds in soils and sediments of European high altitude mountain lakes. *Chemosphere*, 54, 1549 – 1561.
- [10] Jayaraj R., Megha P., Sreedev P. (2016) Organochlorine pesticides, their toxic effects on living organisms and their fate in the environment. *Interdisciplinary Toxicology*, 9(3-4), 90 – 100.
- [11] Rossberg M., Lendle W., Pfeleiderer G., Tögel A., Dreher E., Langer E., Rassaerts H., Kleinschmidt P., Strack H., Cook R., Beck U., Lipper K., Torkelson T. R., Löser E., Beutel K. K., Mann T. (2006) Chlorinated Hydrocarbons. In *Ullmann's Encyclopedia of Industrial Chemistry*, (Ed.).
- [12] Sennour, R.; Mimane, G.; Benghalem, A.; Taleb, S. (2009) Removal of the persistent pollutant chlorobenzene by adsorption onto activated montmorillonite. *Applied Clay Science*, 43, 503 – 506.
- [13] McClenny, W.A., Oliver, K.D., Jacumin, H.H., Jr., Daughtrey, E.H., Jr. (2002) Ambient level volatile organic compound (VOC) monitoring using solid adsorbents—Recent US EPA studies. *Journal Environmental Monitoring*, 4, 695 – 705.
- [14] Sakkas V. A., Arabatzis I. M., Konstantinou I. K., Dimou A. D., Albanis T. A., Falaras P. (2004) Metolachlor photocatalytic degradation using TiO<sub>2</sub> photocatalysts. *Applied Catalysis B: Environmental*, 49, 195 – 205.

- [15] Heydens W. F., Lamb I. C., Wilson A. G. E. (2010) Chapter 82 - Chloracetanilides. Hayes' Handbook of Pesticide Toxicology (Third Edition), 1753 – 1769.
- [16] Fava, L., Bottoni, P., Crobe, A., and Funari, E. (2000) Leaching properties of some degradation products of alachlor and metolachlor. *Chemosphere*, 41(9), 1503 – 1508.
- [17] Fava, L., Bottoni, P., Crobe, A., Barra Caracciolo, A., and Funari, E. (2001) Assessment of leaching potential of aldicarb and its metabolites using laboratory studies. *Pesticide Management Science*, 57 (12), 1135 – 1141.
- [18] Kimmel, E.C., Casida, J.C., and Ruzo, L.O. (1986) Formamidin insecticides and chloroacetanilide herbicides: disubstituted anilines and nitrosobenzenes as mammalian metabolites and bacterial mutagens. *Journal of Agricultural and Food Chemistry*, 34, 157 – 161.
- [19] Osano, O., Admiraal, W., and Otieno, D. (2002) Developmental disorders in embryos of the frog *Xenopus laevis* induced by chloroacetanilide herbicides and their degradation products. *Environmental Toxicology and Chemistry*, 21, 375 – 379.
- [20] Osano, O., Admiraal, W., Klamer, H.J.C., Pastor, D., and Bleeker, E.A.J. (2002) Comparative toxic and genotoxic effects of chloroacetanilides, formamidines and their degradation products on *Vibrio fischeri* and *Chironomus riparius*. *Environmental Pollution*, 119, 195 – 202.
- [21] U.S. Coast Guard. 1999. Chemical Hazard Response Information System (CHRIS) - Hazardous Chemical Data. Commandant Instruction 16465.12C. Washington, D.C.: U.S. Government Printing Office.
- [22] Ignatowicz K. (2009) Selection of sorbent for removing pesticides during water treatment. *Journal of Hazardous Materials*, 169, 953 – 957.

## 4 ADSORPTION

Adsorption is present in many natural (physical, chemical and biological) systems and is a phenomenon of considerable industrial importance, been a major part of many processes including chemical and bio-chemical reactions, purification and filtration. Moreover, applications of technologies involving adsorption processes for air pollution control and water treatment are well known.

Adsorption is a physico-chemical process in which substances present in liquid and/or gas phase (adsorbate) interact with a solid phase (adsorbent). Adsorption is a surface phenomenon, in the bulk of a material all the bonding requirements (ionic, covalent or metallic) of the constituent atoms of the material are filled by other atoms in the material. On the other hand, atoms localised on the surface of the adsorbent material are not completely surrounded by other atoms, so they can attract adsorbate molecules. The nature of the bonding depends on the species involved, but in general the process is classified as physical adsorption (physisorption) or chemical adsorption (chemisorption).

In physical adsorption, van der Waals interactions between the adsorbate molecules and the adsorbent surface are involved; these are weak interactions that allow the adsorbate molecules to move across the adsorbent surface (Fig. 4.1a). In chemisorption chemical bonds between adsorbate and adsorbent are formed, ionic or covalent, strong and localised, forbidding in this case any transition on the surface (Fig. 4.1b).

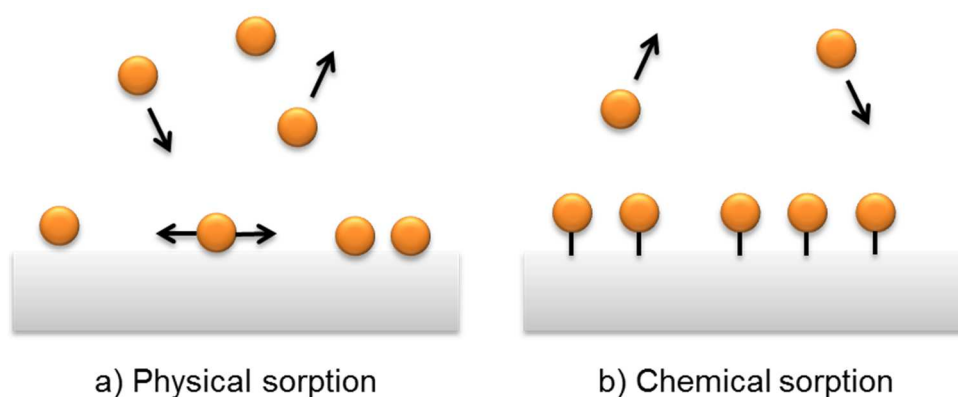


Figure 4.1 Physical and Chemical sorption of a solute onto an adsorbent material.

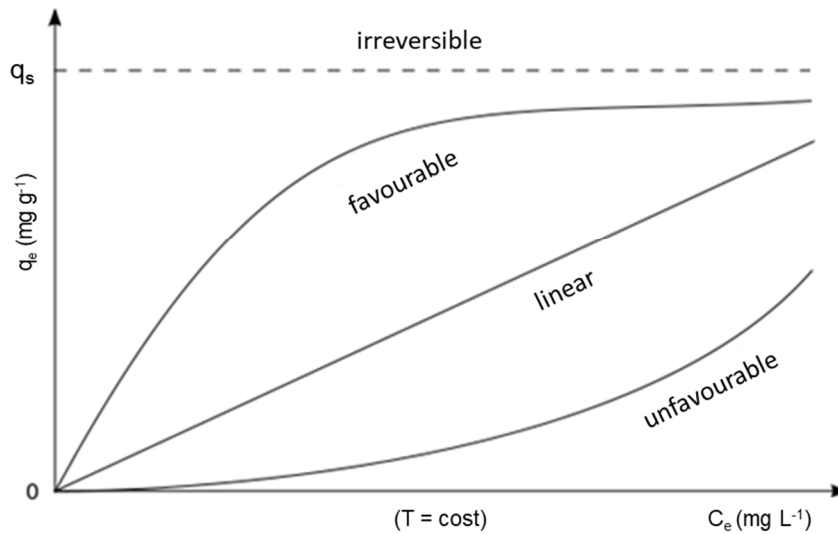
PHYSISORPTION	CHEMISORPTION
Low degree of specificity	Dependent on the reactivity of the adsorbent and adsorptive
At high relative pressure, it general occurs as a multilayer	It is usually limited to a monolayer
A physisorbed molecule keeps its identity and on desorption returns to the fluid phase in its original form	If a chemisorbed molecule undergoes reaction or dissociation, it loses its identity and cannot be recovered by desorption
It is always exothermic and the energy involved is not much larger than the energy of condensation of the adsorptive	The energy is the same order of magnitude as the energy change in a comparable chemical reaction
Physisorption systems generally attain equilibrium fairly rapidly, but equilibration may be slow if the transport process is rate-determining	An activation energy is often involved and at low temperature the system may not have sufficient thermal energy to attain thermodynamic equilibrium

Table 4.1 Differences between physisorption and chemisorption.

#### 4.1 Adsorption isotherms

Theory regarding adsorption processes has been developed, however the mechanism of the interaction between contaminants and the solid materials used for their removal is still poorly understood in many cases, thus many experiments are carried out in order to compare experimental data.

Regarding contaminants attenuation, adsorption consists in the removal of the solute from a solution resulting in its concentration onto a surface, until the amount of solute remaining in the solution is in equilibrium with that adsorbed on the surface. This equilibrium condition is described by expressing the amount of solute adsorbed per unit weight of adsorbent ( $q_e$ ) as a function of the concentration of solute remaining in the solution phase ( $C_e$ ). A representation of this type is called an adsorption isotherm (Fig. 4.2).



**Figure 4.2 Representation of adsorption isotherms.**

The adsorption isotherms represent the variation of the adsorption capacity with respect to the solute concentration in the solution. Isotherms can be favourable when they show a concavity downwards, unfavourable when they are concave upwards, or linear when the solute mass varies linearly with the adsorbent mass. Finally, when the interaction between solute and adsorbent is so strong that it is not possible to reverse the reaction, the isotherm can be considered irreversible.

Several classifications have been developed over the years, the first systematic interpretation of adsorption isotherms for solid/gas equilibria was made by Brunauer, Deming, Deming, and Teller (BDDT) in 1940. The BDDT classification has become the core of modern IUPAC classification of adsorption isotherms which are divided into five types, as illustrated in figure 4.3.

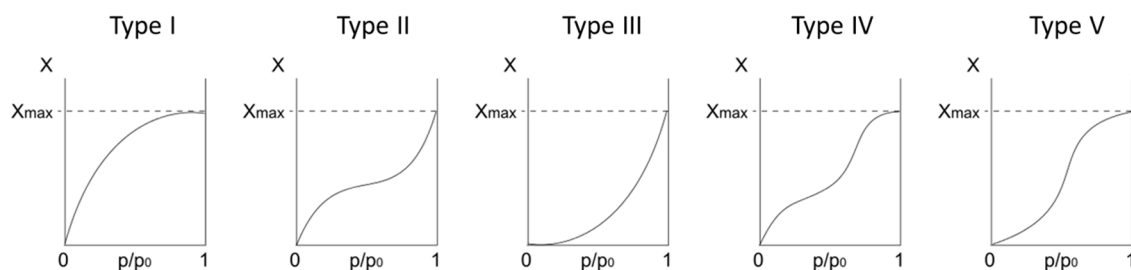


**Figure 4.3 BDDT classification of adsorption isotherms.**

Type I describes adsorption on microporous adsorbents. Types II and III are characteristic of adsorption on macroporous adsorbents with strong and weak adsorbate-adsorbent interaction respectively. Types IV and V describe adsorption isotherms with hysteresis. In

addition to the five BDDT isotherm types, IUPAC classification includes a sixth type characterised by steps [1].

Over the years, a wide variety of equilibrium isotherm models have been formulated considering physicochemical parameters and thermodynamic assumptions to provide an insight into the adsorption mechanism, surface properties and the degree of affinity of the adsorbent materials toward different adsorbates [2].

In this thesis, different adsorption isotherm models have been used to fit experimental data regarding the adsorption of organic contaminants onto zeolites and heavy metals onto waste-derived bio-adsorbents. The main adsorption isotherm models, including those applied in this work, are now discussed.

#### *Henry's adsorption isotherm*

This is the simplest adsorption isotherm model, generally used for gas – solid systems, it is expressed by the linear relationship (Eq. 4.1)

$$q = K_H \cdot C \quad (\text{Eq. 4.1})$$

Where  $q$  is the amount of solute adsorbed on the surface,  $C$  is the concentration (or pressure), and  $K_H$  is the Henry's adsorption constant. This model follows the Henry's law, it assumes that there is no interaction between the adsorbed molecules and that the degree of coverage of the adsorbate onto the adsorbent surface is low [3].

This linear model can be used to describe the initial part of many practical adsorption isotherms, including the Langmuir isotherm, when the low concentration range is considered.

#### *Langmuir isotherm model*

It was originally formulated to describe gas-solid-phase adsorption onto activated carbon, it assumes monolayer adsorption that can only occur at a finite number of definite localised sites, identical and equivalent, with no lateral interaction between the adsorbed molecules. It refers to homogeneous adsorption, and graphically is characterised by a plateau that indicates the equilibrium saturation capacity, where no further adsorption can take place.

$$q_e = \frac{q_s \cdot b \cdot C_e}{1 + b \cdot C_e} \quad (\text{Eq. 4.2})$$

Where  $q_e$  is the amount of solute adsorbed at the equilibrium ( $\text{mg g}^{-1}$ ),  $C_e$  is the equilibrium concentration ( $\text{mg L}^{-1}$ ),  $q_s$  is the saturation capacity of the adsorbent material ( $\text{mg g}^{-1}$ ) and  $b$  the adsorption constant ( $\text{L mg}^{-1}$ ).

#### *Freundlich isotherm model*

It is the earliest known relationship which describes non-ideal and reversible adsorption, not restricted to the formation of monolayer. This model can be applied to multilayer adsorption, with non-uniform distribution of adsorption heat and affinities over the heterogeneous surface.

$$q_e = K_F C_e^{1/n} \quad (\text{Eq. 4.3})$$

In the Freundlich isotherm model (Eq. 4.2),  $K_F$  is the Freundlich isotherm constant which is related to the adsorption capacity,  $q_e$  is the amount of the solute adsorbed at the equilibrium ( $\text{mg g}^{-1}$ ),  $C_e$  is the equilibrium concentration ( $\text{mg L}^{-1}$ ), and  $n$  the adsorption intensity. The slope of the isotherm ranges between 0 and 1, and it is a measure of the adsorption intensity or surface heterogeneity which becomes more heterogeneous when the value tends to zero. A value below unity implies chemisorption process where  $1/n$  above one indicates a cooperative adsorption.

This model is widely applied in heterogeneous systems, especially for organic substances on activated carbon and molecular sieves. The main limitations of this model are the lack of a fundamental thermodynamic basis and it does not approach the Henry's law at concentrations close to zero.

#### *Toth isotherm model*

Developed to improve Langmuir isotherm fittings, it is used to describe heterogeneous adsorption systems, this model assumes an asymmetrical quasi-Gaussian energy distribution with most sites having sorption energy lower than the mean value.

$$q_e = \frac{q_s K_T C_e}{(1 + (K_T \cdot C_e)^v)^{1/v}} \quad (\text{Eq. 4.4})$$

Where,  $q_e$  is the amount of solute adsorbed at the equilibrium ( $\text{mg g}^{-1}$ ),  $q_s$  is the saturation capacity,  $K_T$  the affinity constant, and  $v$  represents the heterogeneity parameter.

#### *Brunauer – Emmett – Teller (BET) isotherm model*

This theoretical model, widely used in the gas – solid equilibrium systems, was developed for multilayer adsorption, that is, solute molecules can be adsorbed either on the bare surface of the

adsorbent material or on a layer of solute already adsorbed. The BET model is expressed by the following equation:

$$q_e = \frac{q_s C_{BET} C_e}{(C_s - C_e)[1 + (C_{BET} - 1)(C_e/C_s)]} \quad (Eq. 4.5)$$

Where  $q_e$  is the amount of solute adsorbed at the equilibrium ( $\text{mg g}^{-1}$ ),  $C_e$  is the equilibrium concentration ( $\text{mg L}^{-1}$ ),  $q_s$  is the theoretical saturation capacity ( $\text{mg g}^{-1}$ ),  $C_{BET}$  the BET adsorption constant ( $\text{L mg}^{-1}$ ), and  $C_s$  the adsorbate monolayer saturation concentration ( $\text{mg L}^{-1}$ ) [2].

## 4.2 Adsorption kinetics

The adsorption of a solute onto an adsorbent material is a time-dependent process. Since the adsorption is a phenomenon important in many systems, it is necessary to evaluate the rate of this process in order to compare the performances of different adsorbents and to optimise the adsorption process itself. For these reasons, it is useful to recognise the adsorption kinetics and to determine the phenomenological coefficients which characterise the transport of the adsorbate molecules within the adsorbents [4].

The sorption mechanism can be described in four consecutive steps shown in figure 4.4:

- 1) Transport of the solute in the bulk solution towards the sorbent;
- 2) Diffusion of the solute through the liquid film that surrounds the adsorbent particles;
- 3) Diffusion of the solute into the pores of the sorbent (intraparticle diffusion);
- 4) Adsorption/desorption reaction onto the solid surface.

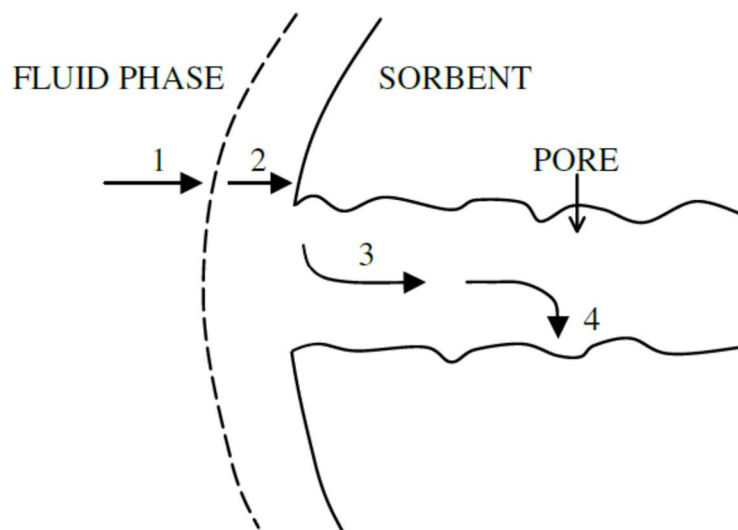


Figure 4.4 Adsorption mechanisms [5].

The rate-determining step for the sorption process can be any of those described above, or a combination of two. A wide variety of kinetic models have been used for solid/solution adsorption batch systems, the most used are Langmuir, statistical rate theory (SRT), pseudo first-order (PFO), pseudo second-order (PSO), Elovich and intraparticle diffusion model (IDM). Among these equations the latter (IDM) can be applied when the diffusion of the solute into the pores (step 3) is the rate determining step, whereas the other ones describe the adsorption kinetics when the surface reaction (step 4) controls the sorption rate [6].

The Pseudo-first and the pseudo-second order kinetic equations are empirical simplified forms of a more general kinetic equation as demonstrated by Rudzinski and Plazinski (2006) [7]. They developed a possible form of such general equation by applying the new approach to the rate of interfacial transport, called the Statistical Rate Theory.

The most widely used empirical kinetic equation is still the one proposed by Lagergren in 1898 (Eq. 4.6):

$$\frac{dN_t}{dt} = k_1(N^{(e)} - N_t) \quad (Eq. 4.6)$$

Where  $N_t$  is the amount of the solute adsorbed at a time  $t$ , and  $k_1$  and  $N^{(e)}$  are some constants.

They can be easily obtained from the following linear regression of experimental data:

$$\ln(N^{(e)} - N_t) = \ln N^{(e)} - k_1 t \quad (Eq. 4.7)$$

which represents the integral form of equation 4.6, corresponding to the boundary condition  $N_t(t=0) = 0$ . In the commonly accepted interpretation,  $k_1$  is the pseudo-first order constant and  $N^{(e)}$  should be the amount adsorbed at equilibrium. This makes equation 4.6 a “pseudo-first order” equation, by comparison with the kinetic adsorption term of the “true” first-order equation in which  $N^{(e)}$  is the maximum amount that can be adsorbed.

When compared with the adsorption term of the true first-order process, the form of equation 4.6 seemed to suggest a one-site-occupancy adsorption when the adsorbing molecule reacts with one adsorption site. Thus, it was proposed that in the case of two-site occupancy adsorption, for example when the solute molecule reacts with two adsorption sites, the rate of adsorption should be given by the following:

$$\frac{dN_t}{dt} = k_2(N^{(e)} - N_t)^2 \quad (Eq. 4.8)$$

Equation 4.8 is the so called “pseudo-second order rate equation” [4,8], and its integral form, obtained with the boundary condition  $N_i(t = 0) = 0$ , can be written as:

$$\frac{t}{N_t} = \frac{1}{N^{(e)}} t + \frac{1}{k_2(N^{(e)})^2} \quad (\text{Eq. 4.9})$$

This equation is usually employed for the analysis of experimental data.

However, it must be remembered that both equations 4.6 and 4.8 are empirical equations; in their work, Rudzinski and Plazinski (2006) [7] searched for a more general rate equation with a well-established theoretical background, applying this to the Statistical Rate Theory of Interfacial Transport (SRT).

If it is assumed that the molecules transport between two neighbouring phases through their phase boundary results primarily from single molecular events, the rate of molecular transport  $R_{12}$  between two phases 1 and 2 is expressed as:

$$R_{12} = R_e \left[ \exp\left(\frac{\mu_1 - \mu_2}{kT}\right) - \exp\left(\frac{\mu_2 - \mu_1}{kT}\right) \right] \quad (\text{Eq. 4.10})$$

where  $\mu_1$  and  $\mu_2$  are the chemical potentials of the molecules in phases 1 and 2 at non-equilibrium conditions and  $R_e$  is the exchange rate at equilibrium to which the system would evolve after being closed and equilibrated. According to Rudzinski and Plazinski (2006) [7], the new SRT approach may also explain the successful application of the empirical Lagergren equation to describe adsorption kinetics at the solid/solution interfaces. Since the Lagergren kinetic equation has always been associated with the model of one-site-occupancy adsorption, they [7] accepted the Langmuir adsorption model in their theoretical investigation. Thus, they assumed that the chemical potential of the solute molecules adsorbed on a solid surface  $\mu_s$  can be expressed as:

$$\mu_s = kT \ln \frac{\Theta}{1 - \Theta} - kT \ln q_s \quad (\text{Eq. 4.11})$$

where  $\Theta = N/N_m$  and  $q_s$  is the molecular partition function of the adsorbed solute molecule. In equation 4.11,  $N_m$  is the maximum amount that can be adsorbed, usually called the adsorption capacity. In terms of the Langmuir model, this is the total number of the adsorption sites on the surface, available for adsorption of solute molecules. For the chemical potential of the solute molecules in the bulk solution  $\mu_b$ , the following expression was assumed:

$$\mu_b = \mu_b^\circ + kT \ln c \quad (\text{Eq. 4.12})$$

where  $c$  is the bulk solution concentration. equations 4.11 and 4.12 lead to the Langmuir adsorption isotherm at equilibrium:

$$\Theta^{(e)} = \frac{K_L c^{(e)}}{1 + K_L c^{(e)}} \quad (\text{Eq. 4.13})$$

where

$$K_L = q_S \exp\left(\frac{\mu_b^\circ}{kT}\right) \quad (\text{Eq. 4.14})$$

and the superscript  $(e)$  denotes equilibrium conditions. The corresponding SRT expression for the adsorption kinetics is

$$\frac{d\Theta}{dt} = K'_{ls} \left[ \exp\left(\frac{\mu_b - \mu_s}{kT}\right) - \exp\left(\frac{\mu_s - \mu_b}{kT}\right) \right] \quad (\text{Eq. 4.15})$$

where  $K'_{ls}$  is the rate of adsorption at equilibrium. In the Langmuir model of adsorption,  $K'_{ls}$  is proportional to the frequency of the collisions of the solute molecules with the surface and to the number of the free molecules available for the adsorption sites  $(1 - \Theta^{(e)})$ . So,  $K'_{ls}$  can be written as:

$$K'_{ls} = K_{ls} c^{(e)} (1 - \Theta^{(e)}) \quad (\text{Eq. 4.16})$$

While assuming that the rate of desorption is proportional to  $\Theta^{(e)}$ , the Langmuir isotherm is again obtained (Eq. 4.13). The classical kinetic equation of the fundamental TAAD approach (Theory of Activated Adsorption/Desorption) which has been used throughout the 20<sup>th</sup> century, is:

$$\frac{d\Theta}{dt} = K_a c (1 - \Theta)^s - K_d \Theta^s \quad (\text{Eq. 4.17})$$

where  $s$  is the number of sites occupied by one adsorbed molecule,  $K_a$  and  $K_d$  are temperature-dependent constants. From equation 4.17 one can arrive either at Lagergren ( $s = 1$ ), or at pseudo-second-order equation ( $s = 2$ ) by neglecting the desorption term in that fundamental TAAD equation, and yet defining  $\Theta$  as an "efficient" surface coverage equal to  $N_i/N^{(e)}$ .

Experiments show that the coefficients  $k_1$  and  $k_2$  in the empirical equations 4.7 and 4.9 depend, for instance, on the initial concentration but there is no theoretical explanation for that. The SRT equation explains it because  $c^{(e)}$  and the total adsorption coverage  $\Theta_t^{(e)}$  depend on the amount of solid adsorbent, the volume of the solute solution, and its initial concentration.

After several calculations, Rudzinski and Plazinski (2006) [7] obtained the following equation:

$$\frac{d\Theta_t}{dt} = K_{Is}c^{(e)}(1 - \Theta_t^{(e)}c^{(e)}) \left[ \exp\left(\frac{(\Theta_t^{(e)} - \Theta_t)(\varepsilon_m - \varepsilon_l)}{kT}\right) - \exp\left(-\frac{(\Theta_t^{(e)} - \Theta_t)(\varepsilon_m - \varepsilon_l)}{kT}\right) \right] \quad (Eq. 4.18)$$

where  $\varepsilon$  is the energy of adsorption.

The applicability of the Lagergren (equation 4.6) would suggest that  $d\Theta_t/dt$  is proportional to the difference  $(\Theta_t^{(e)} - \Theta_t)$ . So, it is possible to expand the exponents within the square bracket into Taylor series around  $\Theta_t = \Theta_t^{(e)}$ . With this assumption, the terms of order  $\geq 3$  are very small and, therefore, can be neglected. In this way the pseudo-first order constant  $k_1$  is defined as:

$$k_1 = \frac{2K_{Is}c^{(e)}(1 - \Theta_t^{(e)}) (\varepsilon_m - \varepsilon_l)}{kT} \quad (Eq. 4.19)$$

The SRT approach shows that the empirical Lagergren kinetic equations should apply best in the case of “volume dominated” kinetic experiments. When noticeable changes of the bulk concentration will be observed during a kinetic experiment, then deviations from the pseudo-first-order Lagergren equation are to be expected.

In the cases where change of adsorbate concentration is noticeable, the terms of order  $\geq 3$  of Taylor expansions cannot be all neglected and other calculations leads to the pseudo-second order kinetic (equation 4.8): the pseudo-second order rate equation is just an intuitive generalisation of the Lagergren equation.

Model investigations based on the general kinetic equations show that deviations of the observed kinetics from the behaviour predicted by the pseudo-first and the pseudo-second-order kinetic equations may be due to the approximate character of these equations [7].

### 4.3 References

- [1] Aranovich G., Donohue M. (1997) Analysis of Adsorption Isotherms: Lattice Theory Predictions, Classification of Isotherms for Gas-Solid Equilibria, and Similarities in Gas and Liquid Adsorption Behavior. *Journal of Colloid and Interface Science*, 200, 273 – 290.
- [2] Foo K. Y., Hameed B.H. (2010) Insights into the modeling of adsorption isotherm systems. *Chemical Engineering Journal*, 156, 2 – 10.
- [3] Silva da Rocha M., Iha K., Faleiros A. C., Corat E. J., Vázquez Suárez-Iha M. E. (1998) Henry's Law as a Limit for an Isotherm Model Based on a Statistical Mechanics Approach. *Journal of Colloid and Interface Science*, 208, 211 – 215.
- [4] Azizian S. (2004) Kinetic models of sorption: a theoretical analysis. *Journal of Colloid and Interface Science*, 276, 47 – 52.
- [5] Noble R. D., Terry P. A. (2010) Principles of chemical separations with environmental applications. Cambridge University Press.
- [6] Haerifar M., Azizian S. (2013) Mixed Surface Reaction and Diffusion-Controlled Kinetic Model for Adsorption at the Solid/Solution Interface. *Journal of Physical Chemistry C*, 117, 16, 8310 – 8317.
- [7] Rudzinski W., Plazinski W. (2006) Kinetics of Solute Adsorption at Solid/Solution Interfaces: A Theoretical Development of the Empirical Pseudo-First and Pseudo-Second Order Kinetic Rate Equations, Based on Applying the Statistical Rate Theory of Interfacial Transport. *Journal of Physical Chemistry B*, 110, 16514 – 16525.
- [8] Blanchard G., Maunaye M., Martin G. (1984) Removal of Heavy Metals from Waters by Means of Natural Zeolites. *Water Research*, 18, 1501-1507.

# 5 ADSORBENT MATERIALS

## 5.1 Mollusc shells

Mollusca is the second larger phylum of invertebrate animals, it contains eight classes: Caudofoveata, Solenogastres, Polyplacophora, Tergomya, Bivalvia, Scaphopoda, Cephalopoda, and Gastropoda [1].

Since molluscs are soft-body animals, to protect their soft tissue from desiccation and predation they are characterised by the presence of a hard shell made of calcium carbonate which is formed by a process known as bio-mineralization.

The biologically-controlled mineralization can be summarised in the following points: i) the shell formation is strictly controlled by cascades of genes; ii) the minerals formed are not in equilibrium with the environment, in this way minerals that are thermodynamically unstable in natural conditions can still be formed; iii) the biogenic minerals are different in shape and size from their inorganic counterpart and they assemble with different levels of hierarchy; iv) the mineralization takes place in a confined space, not in direct contact with the environment; v) the entire process is modulated by an extracellular organic matrix that can be found in the calcified shell.

In general, mollusc shells are characterised by a superimposition of calcium carbonate layers (from two to five) and an organic layer known as *periostracum*.

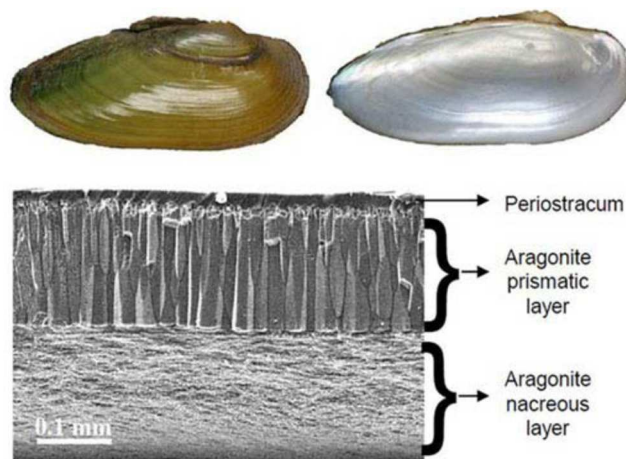


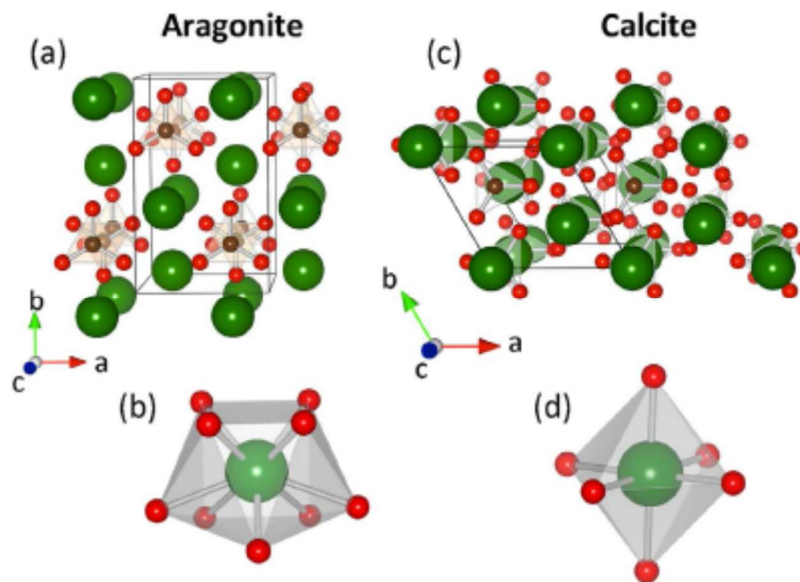
Figure 5.1 Shell structure of *Unio pictorum* (freshwater mussel) highlighting the different calcified layers and the external organic layer [2].

Figure 5.1 illustrates the typical layers that can be found in mollusc shells: the nacre, the prismatic layer and the periostracum. The nacre, also known as mother of pearl, is an organic-inorganic composite material produced by some molluscs as an inner shell layer, it is strong, resilient and iridescent. The prismatic layer is a mineralised layer composed of

elongated crystals developed perpendicularly to the shell surface, it can be composed of aragonite, calcite, or aragonite/calcite. Finally, the periostracum, a thin organic coating, is the outermost layer of the shell of many shelled organisms. It is an integral part of the shell, and it forms as the shell forms, along with the other shell layers [2].

#### *Calcite and aragonite structure*

Calcium carbonate minerals are the most widespread biogenic material found in nature [3]. According to the species, usually two calcium carbonate polymorphs are commonly found in mollusc shells: the stable form calcite and the metastable one aragonite [2].



**Figure 5.2 Aragonite and Calcite polymorphs [4].**

Calcite has a trigonal crystal structure (Fig. 5.2c) with the Ca octahedrally coordinated by oxygen atoms (Fig. 5.2d); on the other hand, the crystal structure of aragonite presents an orthorhombic symmetry with the Ca nine-fold coordinated by oxygen (Fig. 5.2a and 5.2b). Calcite and aragonite of biological origin are organic-inorganic nano-composites whose formation mechanism is not yet fully understood. It is suggested that biogenic carbonates form via transient metastable precursor phases, such as amorphous  $\text{CaCO}_3$  [4].

## *Shell formation*

The biologically controlled calcification process takes place in a confined space and involves three elements of the organism: the mantle and its outer epithelium cells, the extrapallial space, and the periostracum.

*The mantle:* a polarised tissue composed of an inner epithelium which is in contact with the environment, internal tissues, and the outer calcifying epithelium which secretes the materials needed for the shell formation.

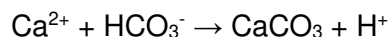
*The extrapallial space:* a narrow mucus-filled space between the mantle and the valve of the shell. The extrapallial fluid is supersaturated with respect to  $\text{CaCO}_3$ , it contains inorganic ions ( $\text{Na}^+$ ,  $\text{K}^+$ ,  $\text{Mg}^{2+}$ ,  $\text{Sr}^{2+}$ ,  $\text{Fe}^{3+}$ ,  $\text{Cl}^-$ ,  $\text{SO}_4^{2-}$ ) with a pH ranging from 7.4 to 8.3. The extrapallial fluid also contains proteins and glycosaminoglycans (GAGs) which are thought to transiently maintain the calcium in solution and allow its deposition where needed.

*The periostracum:* this protective layer is secreted by the periostracal groove at the edge of the mantle. The main roles of the periostracum are to provide the primary template for the mineralization and to delimit and enclose the extrapallial space. Moreover, it protects the shell from dissolution, fouling by microorganisms and, because of the presence of pigments, it constitutes an excellent camouflage against predators.

The  $\text{Ca}^{2+}$  and  $\text{HCO}_3^-$  ions required for the mineralisation are obtained by the water environment and through food; they are supposed to be absorbed in the inner mantle epithelium, in the gills, and in the digestive system. Two speculative ways of transport are proposed: i) the precursors are transported to the site of the mineralization in soluble form in the haemolymph (the interstitial form that circulates around the internal organs); ii) calcium stored and transported in clustered forms as amorphous granules.

Simultaneously, proteins and glycoproteins are synthesised in the outer epithelial cells and secreted in the extrapallial space by exocytosis. At this point, the inorganic ions and the organic macromolecules interact and self-assemble to form the biomineral.

The formation of calcium carbonate takes place according to the following reaction:



$\text{CaCO}_3$  precipitates with the production of one proton that decreases the pH of the fluid. To subtract the proton from the medium,  $\text{H}^+$  can be re-adsorbed in the mantle epithelium cells through transmembrane pumps such as  $\text{H}^+$ -ATPase, alternatively it can react with bicarbonate to give  $\text{CO}_2$  and  $\text{H}_2\text{O}$ . Another option is given by the reaction of  $\text{H}^+$  with ammonia ( $\text{NH}_3$ ) to form the ammonium ion ( $\text{NH}_4^+$ ), however, this possibility may be restricted to landsnails [2].

### *Shell microstructures*

Since the mineralization is a biologically controlled process, the resulting calcite and aragonite crystal are form in a wide range of microstructure, according to the species.

In table 5.1 the major groups and categories in which the microstructures can be divided, are summarised.

<b>Microstructural groups</b>
Prismatic
Spherulitic
Laminar
Crossed
Homogeneous
Isolated spicules and spikes
Isolated crystal morphotypes
<b>Microstructural categories</b>
Aragonitic prismatic
Calcitic prismatic
Nacreous, aragonitic
Porcelaneous, aragonitic
Foliated
Calcitic

**Table 5.1 Major microstructure groups and categories [5].**

### *Growth pattern*

The form of the molluscan shell depends on the organism's ecology. In molluscs whose ecology changes from the larval to adult form, the morphology of the shell also undergoes a pronounced modification at metamorphosis. The larval shell may have a completely different mineralogy to the adult conch, perhaps formed from amorphous calcite as opposed to an aragonite adult conch.

In those shelled molluscs that have indeterminate growth, the shell grows steadily over the lifetime of the mollusc by the addition of calcium carbonate to the leading edge or opening. Thus, the shell gradually becomes longer and wider and it thickens as it grows, so that it stays proportionately strong for its size.

In many cases, the rate of growth can be observed by characteristic patterns (rings) formed on the external layer of the shell.

For scallop shells, one major growth ring is formed every year (laid down in spring). This annual ring results from the build-up of small growth increments (striae) formed as successive lamellae are laid down. Each lamella is probably formed daily, but the growth rate can vary according to the conditions of the environment in which the organism grows [6].

#### *Organic components*

Even though they constitute only a small part of the shell (up to 5 wt%), organic moieties confer to the structure its characteristic mechanical properties increasing, for example, the fracture toughness of the biomaterial.

The organic fraction found in the calcium carbonate matrix is composed of: proteins, polysaccharides (mainly chitin and soluble acidic polymers), lipids, pigments, amino acids and peptides.

#### *Pigments*

The great majority of molluscs, including nearly all bivalves, are shelled and a particular characteristic is that this phylum presents a great variety of colours and patterns. The main functions of colour are thought to be for camouflage and thermoregulation, even though shell colours seem to have no utility.

Pigments, the organic molecules that are responsible of the colour of the shell, are produced by the mantle and secreted in the shell along the growing edge, usually in the outer surface layers (periostracum), but in some species they can be found also in the internal layers of the shell. The nature of every organic pigment present in the many species of the phylum Mollusca is still unknown, and only few pigments have been completely characterised. The more common classes of pigments are tetrapyrroles, carotenoids and melanins. Tetrapyrroles can be divided in two groups depending on the structure of the compounds: porphyrins with a cyclic structure, or bilins which are characterised by an overall linear main chain. These pigments are associated with a wide range of colours that can vary when complexed to proteins or by the interaction with metal ions.

Carotenoids represent the most common class of biological pigments, they are synthesised by plants and animals acquire them through food [7].

Carotenoids (fig. 5.3) can be divided in two categories according to the chemical composition: Carotenes are made up of only carbon and hydrogen, while xanthophylls contain also oxygen groups [8].

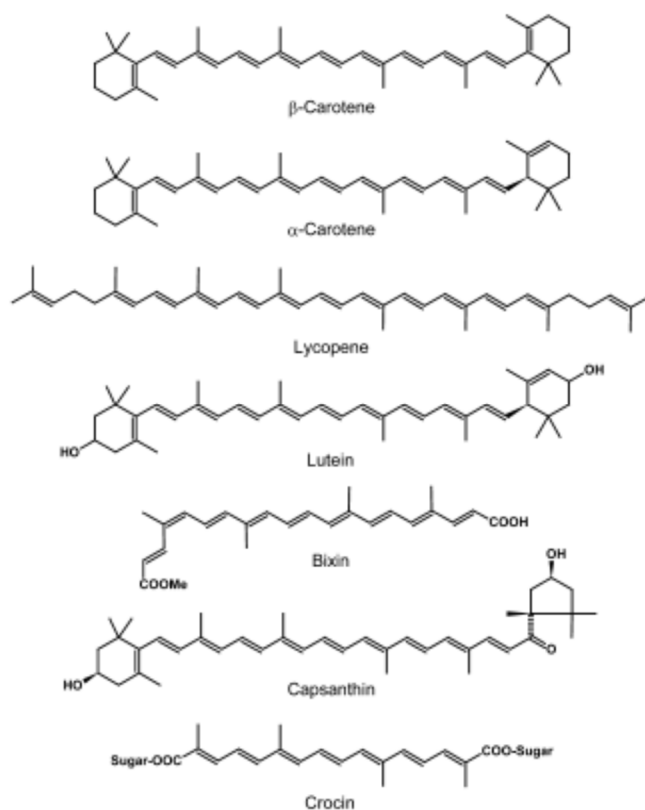


Figure 5.3 Structure of some carotenoids [8].

Results obtained with Raman microspectrometry suggest that some colours in mollusc shells are due to the presence of polyene chains supposed to be carotenoids based on comparison with spectra acquired from carotenoid standards [7].

Melanins are another group of pigments present in many organisms, they are classified as compounds of different structure and origin derived by oxidation and polymerization of tyrosine in animals and by phenolic compounds in lower organisms [7].

#### *Use of mollusc shells as bioadsorbents*

Calcium carbonate is widely used for environmental remediation because it is environmentally friendly and inexpensive. Generally, industries use calcium carbonate from geological sources (i.e. limestone, marble, aragonite, calcite), but calcium carbonate of geogenic origin is characterised by a dense bulk structure and low specific surface area that may give a low efficiency in the removal of heavy metals from wastewater. On the other hand, biogenic calcium carbonate (i.e. marine shells and eggshells) presents a different, hierarchical porous microstructure with organic components that can enhance the ability of this material to uptake heavy metals from aqueous matrices when compared to the geological counterpart [9].

For example, Tudor et al. (2006) [10] demonstrated that biogenic  $\text{CaCO}_3$  is more efficient in the uptake of lead and cadmium compared to carbonates of geologic origin.

Many studies reported the capability of molluscan and crustacean shell powder to adsorb heavy metals from water matrices considering the effect of the adsorbent grain size [11-13], different  $\text{CaCO}_3$  shell structure [14], or after the adsorbent material had been acid-pretreated [15] or calcined [16-18].

## 5.2 Microporous materials

Micro- and mesoporous materials are solids characterised by the presence of pores with diameters lower than 2 nm for microporous materials, and between 2 and 50 nm for mesoporous materials.

Ordered micro- and mesoporous materials are used in many applications as catalysts, highly selective adsorbent, but also they can be modified to create materials with additional functionality [19].

Zeolites are a class of microporous materials, widely found in nature, whose characteristics allow their use in many industrial applications.

### Zeolites

Among silicates, zeolites represent a wide class of porous materials counting more than forty natural species, plus a much larger number of synthetic types.

Zeolites were discovered in 1756 by the Swedish mineralogist A. F. Cronstedt who observed that after heating rapidly the mineral, it produced large amounts of steam from water adsorbed on the material, so he coined the term zeolite from the Greek ζέω (zéō), meaning "to boil" and λίθος (líthos), meaning "stone".

Zeolites are crystalline aluminosilicate microporous materials with chemical formula  $\text{Na}_{12}[(\text{SiO}_2)_{12}(\text{AlO}_2)_{12}] \cdot 27\text{H}_2\text{O}$ ; the three-dimensional structure is formed by tetrahedral units  $\text{TO}_4$  called primary building units (PBU) composed of  $[\text{SiO}_4]^{4-}$  and  $[\text{AlO}_4]^{5-}$  units connected to each other through oxygen atoms (fig. 5.4).

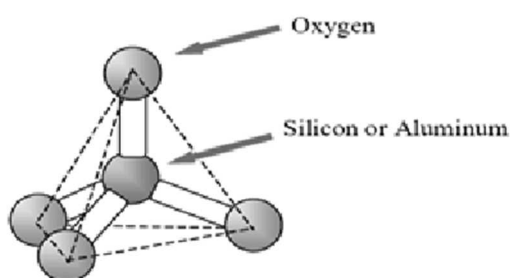


Figure 5.4  $\text{TO}_4$  unit.

The combination of  $\text{TO}_4$  units leads to the formation of different more complex structural blocks known as secondary building units (SBU). SBUs are the simplest units in which a single zeolite structure can be decomposed, there are 23 different SBU's observed which can contain up to 16 T-atoms [20]. The main SBU's are represented in figure 5.5.

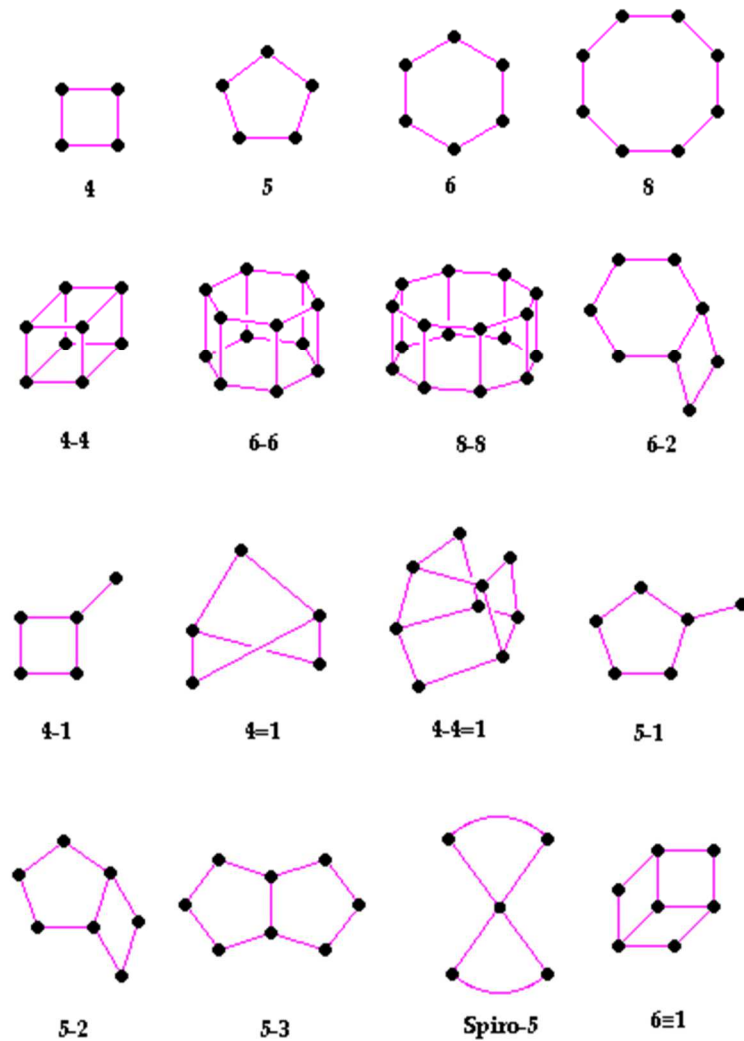


Figure 5.5 Secondary Building Units (SBU).

When secondary building units are combined together, they create complex frameworks with different structures containing regular cavities and channels with molecular dimensions. Due to the wide range of structure typologies found in zeolites, these materials are classified by the “structure commission” of the International Zeolite Association according to their crystalline structure and divided into structure types indicated by a three letters code (e.g. MFI).

In zeolites, the ratio between silicon and aluminium can vary, due to the fact that Al-O-Al bonds are not possible and only Si-O-Si or Si-O-Al bonds are allowed; according to the Si/Al ratio (SAR) zeolites can be divided into two classes:

- Zeolites with a low Si/Al (SAR < 5)
- Zeolites with a high Si/Al (SAR > 5)

A higher amount of aluminium in the structure gives to the zeolite framework a more negative overall charge giving to the material hydrophilic properties, on the other hand, zeolites with higher silicon content show hydrophobic behaviour.

### *Properties*

Zeolites belongs to a particular category of microporous materials known as molecular sieves, this classification is due to the particular characteristic of zeolites of having uniform cavities and channels interconnected with each other and with dimensions from 3 to 10 Å that results in high superficial areas and internal volumes. These features allow zeolites to host molecular or ionic species acting as molecular sieves.

The maximum dimension of the host molecule depends strictly on the dimensions of the zeolite channels defined as the diameter of the ring opening of the pore.

The substitution of  $\text{Si}^{4+}$  atoms with  $\text{Al}^{3+}$  in some  $\text{TO}_4$  units results in a net negative charge in the framework, this charge arises from the different formal valency of  $[\text{SiO}_4]^{4-}$  and  $[\text{AlO}_4]^{5-}$  tetrahedral units and is located on one of the oxygen atoms connected to the aluminium. The resulting negative charges present on the zeolite framework are balanced by counterions such as  $\text{Na}^+$ ,  $\text{Mg}^{2+}$  and  $\text{Ca}^{2+}$ . These cations are bond to the aluminosilicate framework through weak electrostatic interactions [21] and they can be exchanged with solutes present in the solution in contact with the material. This allows the use of zeolites as cations exchangers, the cation exchange capacity defines the maximum number, expressed as milliequivalent, of ions that can be substituted per gram of zeolitic material. This value depends on the Si/Al ratio and it is higher for zeolites with low SAR, since a higher amount of  $\text{Al}^{3+}$  in the structure means more negative charges on the framework and, therefore, more extra-framework species are present in the pores of the zeolite [22].

### *Applications*

Zeolites are widely used in different industrial, agricultural and medical applications as catalysts, adsorbents or ionic exchangers.

The regular porous structure and the fact that the dimensions and shape of the cavities can be modulated in synthesised zeolites, allow to employ these materials as molecular sieves in adsorption and separation technologies. The properties that make zeolites suitable materials for adsorption applications are the following:

*Stability.* Zeolites should keep their activity for long periods, the operational life is expected to be 10 to 20 years. However, experience over such period is not yet available.

The replacement or regeneration of zeolites can be easily achieved: after adsorption, the exhausted zeolites are generally subjected to a regeneration process which involves operating at high temperatures, normally from 250° and 350°C for a time ranging from 30

minutes to 1.5 hours, and in presence of an air flow (from 1.5 to 2.5 m<sup>3</sup>/hr). Under these particular conditions zeolites maintain their structural integrity, in this way they can be regenerated many times without changing their adsorption properties.

*High efficiency.* Zeolites have been used for the irreversible removal of high concentration of pharmaceuticals from water, such as erythromicine (ERY), levofloxacin (FLX), carbamazepine (CBZ) and sulphonamide antibiotics. The adsorption kinetics for the single drugs in zeolite Y showed a very fast uptake, with the complete removal of the contaminant from water achieved in less than one minute. Furthermore, it has been proved that the efficiency of zeolite is not modified when dissolved natural organic matter is present in the water stream that is been treated.

*Shape selectivity.* The ability to adsorb selectively and to separate organic molecules is one of the most important features of zeolites. The shape and dimensions of their internal pore structure strongly affects their adsorption selectivity towards host molecules. In particular, zeolites are versatile adsorbents for VOCs which are easily adsorbed even at low concentrations in indoor environment. Hydrophobic zeolites have been proven to be able to efficiently adsorb molecules against which zerovalent iron (ZVI) or granular activated carbon (GAC) are totally ineffective [23].

*Availability and cost.* Permeable reactive barrier (PRB) containing zeolites has been recognised as a cost-effective technology for water remediation. Both natural and synthetic zeolites are commercially available at low prices.

*Environmental compability.* Zeolites do not represent a source of contamination itself by solubilisation or other mobilisation mechanisms; moreover, when reacting with contaminants they do not form any by products.

Zeolites have been employed as catalysts in many industrial chemical reactions, for example petroleum cracking, isomerisation and alkylation reactions for the production of fine chemicals, dyestuffs, detergents and scents [21].

The use of zeolites as catalysts is mainly due to their 3D structure with cavities and channels that can accommodate reactive molecules with dimensions comparable with those of the zeolite channels. In this way, the reactive molecules are enclosed in a confined space and can react more efficiently.

The catalytic process is mainly due to the presence of Brønsted and Lewis acid sites on the zeolite framework, in particular catalytic reactions are influenced by:

- The presence of hydroxyl groups on the zeolite framework that act as Brønsted acid sites via reversible transfer of a proton to the adsorbed molecule;
- The existence of electrostatic field gradients that create Lewis acid sites that are able to polarise bonds of the adsorbed molecule;

- Oxygen vacancy in the framework that generate a Lewis acid site on the tetrahedral cation due to the residual positive charge on it;
- The interaction with metal ions or clusters.

The zeolitic acid sites are described with the classic models of Brønsted and Lewis: Brønsted acids are species that can donate a proton (Brønsted acid sites are present in zeolites with  $H^+$  as the extra-framework ion); Lewis acids are those that can accept an electron pair from another species, this is the case mainly for zeolites with Al tri-coordinated that can accept an electron pair and act as a Lewis acid.

### *Ga-zeolites*

Among families of catalysts, Gallium-containing zeolites are of particular interest due to their excellent performances in isomerisation, disproportionation and alkylation of aromatics and aromatisation of alkanes and/or alkenes [24-27].

In the last years, Gallium-loaded zeolites have been widely investigated and newest applications concerning the removal of  $NO_x$  from gas streams of exhaust engine and the conversion of biomass into biofuels and bio-based chemicals have been proposed [26, 28, 29].

Ga-zeolite materials can be obtained via hydrothermal crystallisation in the presence of a suitable template agent, or by post synthesis treatments, such as galliation, recrystallisation, wet impregnation, chemical vapour deposition (CVD) and ion exchange [26, 30].

Zeolites are the most important inorganic cation exchangers, nowadays they compete with cation exchange resins in water processing and in purification of wastewater and sewage. Compared to organic resins, zeolites show higher cation exchange selectivity, good thermal resistance and excellent compatibility with the environment. Since the wide use of zeolites in modern technology as selective adsorbents, molecular sieves and catalysts, ion exchange property is employed also for tailoring the structure to obtain a material with specific characteristics. Ion exchange arises because of the presence of extra-framework cations located in the zeolite channels and cages. Cations are bound to the zeolite lattice and to water molecules, when the zeolite come in contact with an electrolytic solution, the extra-framework cations can be removed from their position and replaced by other cations present in the solution [31].

The ion exchange process is suitable to introduce gallium into both tetrahedral coordinated framework and interstitial non-framework positions. Besides, the precipitation on the external surface of the zeolite crystal of a separate gallium phase, depending on the pH value during the exchange process, in aqueous solution has to be foreseen. Substitution of  $Al^{3+}$  with  $Ga^{3+}$  cations [32] into framework positions is the main source of lattice charge

defects, which give rise to Brønsted acidic Si-OH-Ga bridging hydroxyl group and, consequently, to modification of catalytic properties.

Along with the segregate gallium phase, excess gallium not incorporated in tetrahedral sites is trapped within the zeolite pores system as substituent of metal cations, ammonium ions or protons. The presence of gallium cations in extra-framework positions introduces Lewis acidity, which is also originated from oxo cations  $\text{GaO}^+$  in exchanged framework positions. Due to its size, gallium in framework positions is metastable; hence, the thermal treatment can cause the migration of  $\text{Ga}^{3+}$  to extraframework positions and its progressive aggregation in form of isolated, dimeric and polymeric species up to oxide nanoparticles [33-35]. This migration leads to the appearance of a different type of acid sites of Lewis nature [36]. As a consequence, Ga exchanged zeolites can possess both Brønsted and Lewis acid sites, working separately or in a synergistic way in acid catalysed reactions [37-38].

In this thesis, the adsorption of gallium onto zeolites, and the structural features of zeolites loaded with gallium were investigated in order to understand the nature of gallium active sites for possible industrial applications as catalysts.

## **Characterisation**

### *Thermal analysis*

Thermal analysis is a family of techniques in which the properties of materials are studied as they change with temperature. Thermal analysis includes several methods that differ from each other by the property which is measured.

Thermogravimetric analysis (TGA) is a method in which sample weight changes is monitored as a function of increasing temperature (with constant heating rate), or as a function of time (with constant temperature and/or constant mass loss). This measurement provides information about physical phenomena, such as phase transitions, absorption, adsorption and desorption; as well as chemical phenomena including chemisorption, thermal decomposition, and solid-gas reactions (e.g., oxidation or reduction). TGA can be used to determine material stability, if the material is thermally stable, there will be no observed mass change. TGA is commonly used to determine selected characteristics of materials that exhibit either mass loss or gain due to decomposition, oxidation or loss of volatiles (such as moisture). Materials characterisation can be obtained through TG analysis evaluating characteristic decomposition patterns, degradation mechanisms and reaction kinetics.

Differential thermal analysis (DTA) is a thermoanalytic technique, where the material under study and an inert reference undergo identical thermal cycles, while recording the temperature difference between sample and reference. The differential temperature is

plotted against time or temperature (DTA curve, or thermogram), in this way, changes in the sample, either exothermic or endothermic, can be detected relative to the inert reference.

A DTA curve provides information on the transformations that have occurred, such as glass transitions, crystallisation, melting and sublimation. The area under a DTA peak is the enthalpy change and it is not affected by the heat capacity of the sample.

A DTA curve can be used only as a finger print for identification purposes but usually the applications of this method are the determination of phase diagrams, heat change measurements and decomposition in various atmospheres.

### *X ray powder diffraction*

The applicability of many zeolites is linked with their long-range crystalline architecture, so it is very important to clearly understand the structure of zeolites.

The most powerful methods that allow us to obtain long-range crystalline structure are those that use the diffraction of radiation whose wavelength is of the same order of magnitude as the distances between atoms in the material structure. X rays are the most widely used radiation, but neutron and electrons can also be applied.

X ray powder diffraction (XRD) is a rapid analytical technique used for phase identification of a crystalline material and can provide information on unit cell dimensions.

XRD represent one of the basic techniques for zeolite characterisation, the XRD pattern of a zeolite is a typical fingerprint which allows to determine sample impurity, degree of crystallinity, or the size of a unit cell of the zeolite.

An XRD pattern is a plot of intensity of x rays scattered at different angles by the sample.

The features characteristic of an XRD pattern are the peak positions, their relative intensities, their widths and the background.

The peak positions, measured as  $2\theta$ , are determined by the geometry of the unit cell, which describes the 3-dimensional repeat unit of a crystal structure. The relative intensities are determined by the type and position of the various atoms within the unit cell. The width of the peaks in the pattern, give an indication of the crystalline quality of the sample. Finally, the background is an indication of whether or not an amorphous phase is present in the sample. A change in the relative intensities of the peaks indicates that a structural modification has occurred, if a variation of the positions of the peaks is observed the unit cell has been deformed, broader (or narrower) peaks indicate that the crystallinity has deteriorated (or improved). More detail can be extracted from the powder pattern if a full Rietveld (whole-profile) structure refinement is performed.

### Zeolite ZSM-5 ( $\text{NH}_4^+$ )

ZSM-5 (Zeolite Socony Mobil-5) was patented by Mobil Oil Company in 1975 and it is widely used as solid catalyst for hydrocarbon isomerisation reactions in petroleum industry. It has chemical formula  $[\text{Na}_n (\text{H}_2\text{O})_{16}] [\text{Al}_n\text{Si}_{96-n}\text{O}_{192}]$ -MFI ( $0 < n < 27$ ), framework type MFI and belongs to the pentasil family.

The pentasil chains are connected by oxygen bridges forming undulated sheets which are in turn interconnected by inversion points creating pores characterised by 10-member ring opening.

ZSM-5 present two channel systems perpendicular to each other with dimensions from 5.1 to 5.6 Å (fig. 5.6).

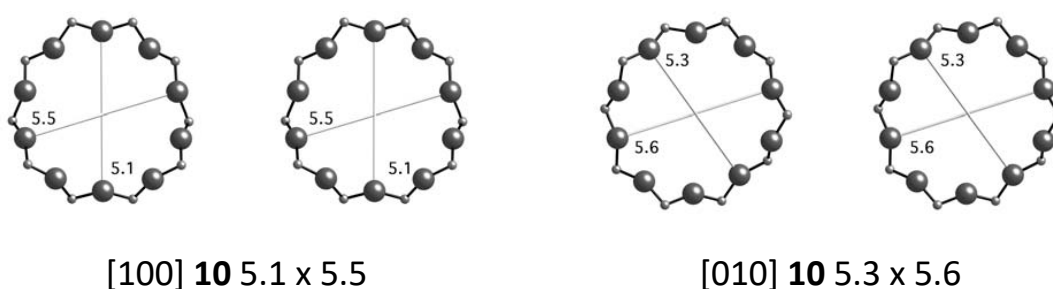


Figure 5.6 Zsm-5 ring openings of the two channel systems [20].

The crystallographic unit cell is composed of 96 T sites (Si or Al), 192 O sites, and a number of extra-framework cations which varies according to the Si/Al ratio of the material.

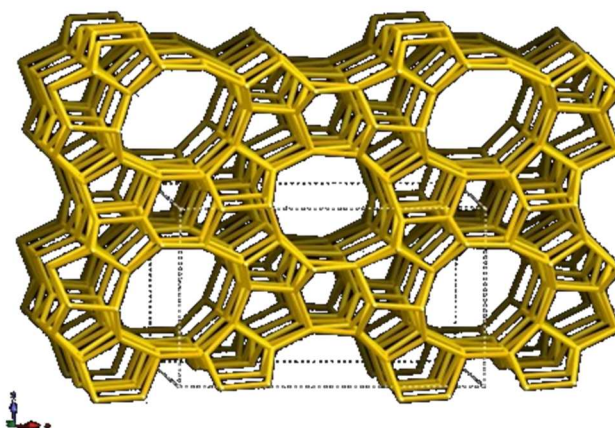


Figure 5.7 ZSM-5 framework.

### Zeolite ZSM-12

ZSM-12 (MTW topology) is a high-silica zeolite (Fig. 5.8) with chemical formula  $[\text{Na}_n (\text{H}_2\text{O})_8] [\text{Al}_n\text{Si}_{56-n}\text{O}_{112}]$ -MTW ( $n < 5$ ), it was first synthesised by Rosinski and Rubin (1983) [39], and it

is mainly used as a catalyst for the conversion of long hydrocarbon molecules such as isomerisation and alkylation of aromatic hydrocarbons [40-44].

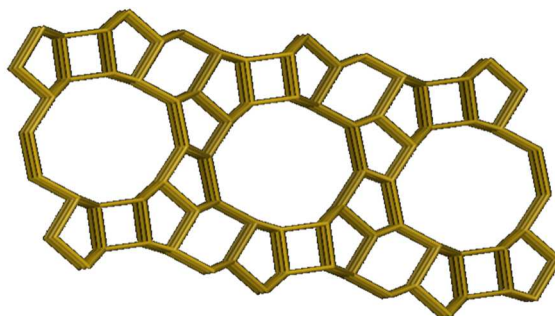
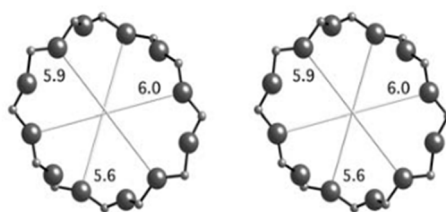


Figure 5.8 ZSM-12 framework.

ZSM-12 framework is characterised by a one-dimensional pore system delimited by 12-membered rings with 5.6 X 6.0 Å openings (Fig. 5.9).



[010] 12 5.6 x 6.0

Figure 5.9 ZSM-12 ring openings [20].

### *Zeolite Beta*

Zeolite beta was first synthesised at the Mobil Research and Development Laboratories, it has chemical formula  $[\text{Na}_7] [\text{Al}_7\text{Si}_{57}\text{O}_{128}]^{-*}\text{BEA}$  and belongs to the  $*\text{BEA}$  framework type. A particularity of this zeolite is that its structure is disordered in the c-direction, that is, well-defined layers are stacked in a more or less random way. The  $5^4$  units are linked together via 4-rings to form layers with saddle-shaped 12-rings. Contiguous layers are related to one another by a rotation of  $90^\circ$ , the disorder arises because this rotation can be in either clockwise or counter clockwise sense. Whatever the stacking sequence, zeolite beta has a 3-dimensional pore system characterised by two 12-ring channel systems perpendicular to each other, with ring openings shown in figure 5.11 [20, 45, 46].

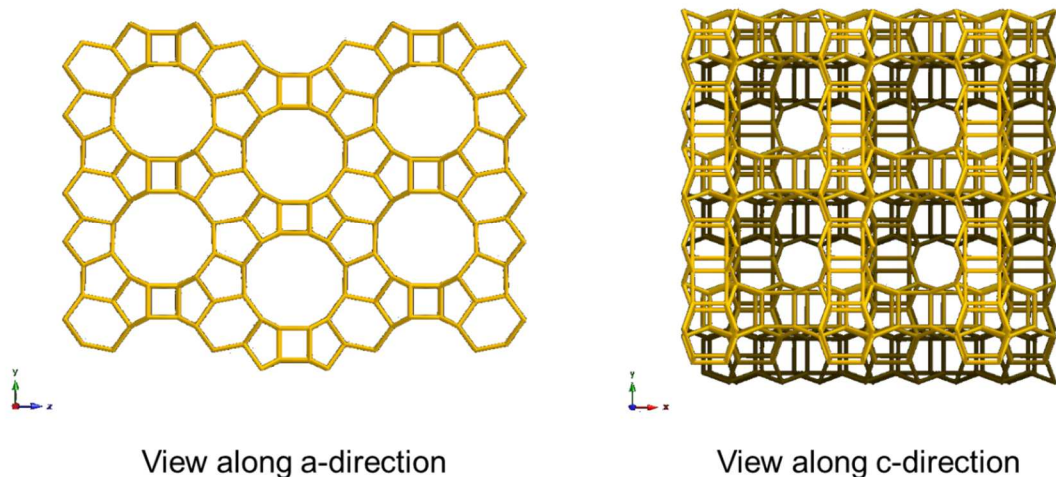


Figure 5.10 Beta framework.

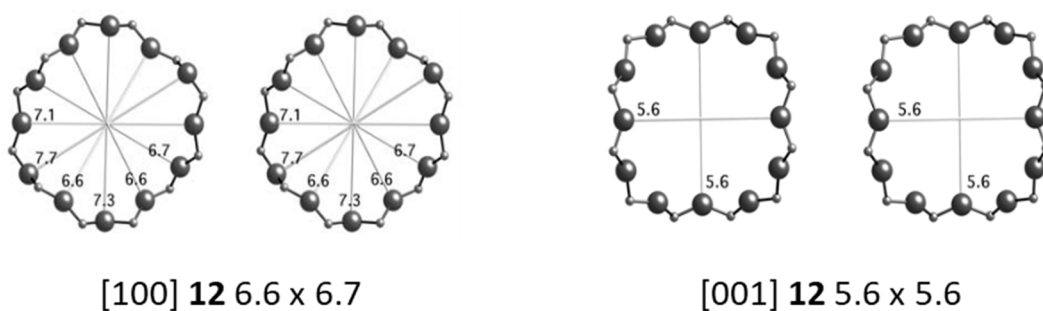


Figure 5.11 Beta ring openings of the two channel system [20].

### *Zeolite Y*

Faujasite is a mineral group in the zeolite family of silicate minerals and it was discovered in 1842 in Limberg quarries, Germany. Faujasite occurs in vesicles within basalt and phonolite lava and tuff as an alteration or authigenic mineral. It occurs with other zeolites, olivine, augite and nepheline.

Zeolite Y belongs to the faujasite group with chemical formula  $[(Ca, Mg, Na_2)_{29} (H_2O)_{240}] [Al_{58}Si_{134} O_{384}]$ -FAU and FAU framework type. The structure (Fig. 5.12) is composed of sodalite cages connected to each other through hexagonal prisms.

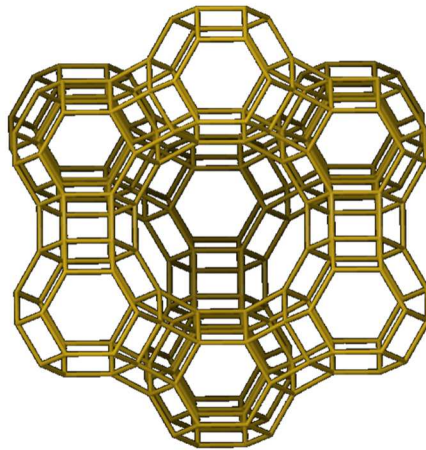
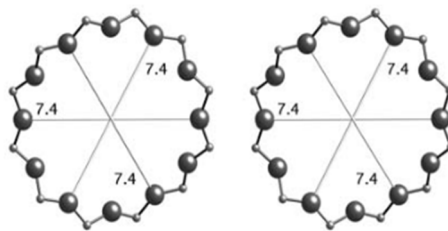


Figure 5.12 Framework of zeolite Y.

The pore system consists in 12-membered rings, shown in figure 5.13, with large openings (7.4 Å diameters) that lead to the inner cavity which has a diameter of 12 Å and is surrounded by 10 sodalite cages.



[111] 12 7.4 x 7.4

Figure 5.13 Zeolite Y ring opening [20].

The main use of Faujasite zeolites is as a catalyst in fluid catalytic cracking for the conversion of high-boiling fractions of petroleum crude to more valuable petrol, diesel and other products. Zeolite Y has replaced zeolite X in this use because it is both more active and more stable at high temperatures due to the higher Si/Al ratio. It is also used in the hydrocracking units as a platinum/palladium support to increase aromatic content of reformulated refinery products.

## Zeolite L

The first publication regarding the synthesis of zeolite L dates back to 1967 [47]. Zeolite L has chemical formula  $[K_6Na_3(H_2O)_{21}][Al_9Si_{27}O_{72}]$ -LTL and belongs to the framework type LTL (Linde Type L). The aluminosilicate framework is composed of polyhedral cages which are formed by five six-membered and six four-membered rings. These cavities are linked through the planes of their upper and lower six-membered ring, thus forming columns in which hexagonal prisms and polyhedra alternate, and which run parallel to the  $c$  axis. Each column is crosslinked to three others by single oxygen bridges which form part of planar twelve-membered rings circumscribing wide channels parallel to  $c$ . Each channel can be represented as a succession of sections, circumscribed top and bottom by twelve-membered rings shared with upper and lower adjacent sections. The rings have free diameters of 7.1 to 7.8 Å [48].

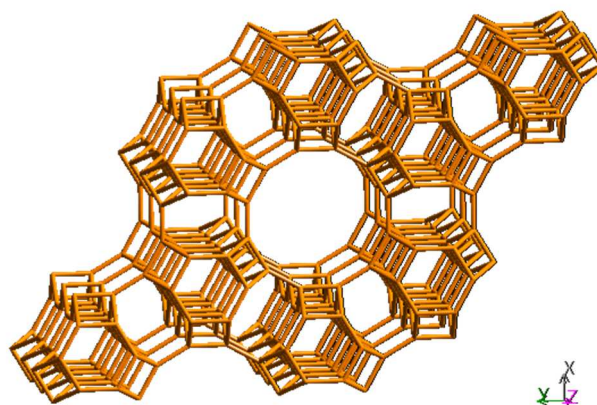
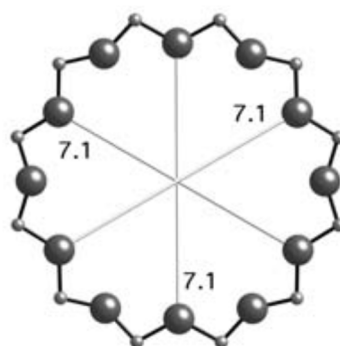


Figure 5.14 Framework of zeolite L.



[001] **12** 7.1 x 7.1

Figure 5.15 Zeolite L ring opening [20].

## Mordenite

Zeolite mordenite belongs to the MOR framework type and has chemical formula  $|\text{Na}_8(\text{H}_2\text{O})_{24}|[\text{Al}_8\text{Si}_{40}\text{O}_{96}]$ -MOR. In this framework type, units of four 5-rings are connected to one another via common edges forming chains, mirror images of these chains are joined together through oxygen atoms to form corrugated sheets. The connection of these sheets, which are displaced by half a translation in c, forms oval 12- and 8- ring openings along the corrugations. The one dimensional channel systems are displayed in figure 5.16 [46].

Zeolites with MOR structure have been widely used in chemical industry as catalysts for reactions such as hydrocracking, hydro-isomerisation, alkylation, reforming, dewaxing and for the production of dimethylamines; other applications include adsorptive separation of gas or liquid mixtures, semiconductors, chemical sensors, and nonlinear optics [49].

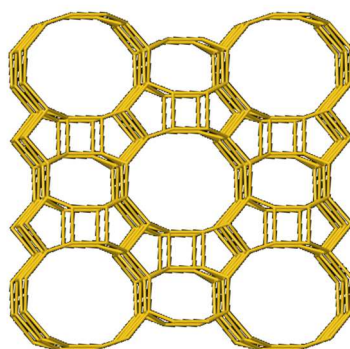


Figure 5.16 Mordenite framework.

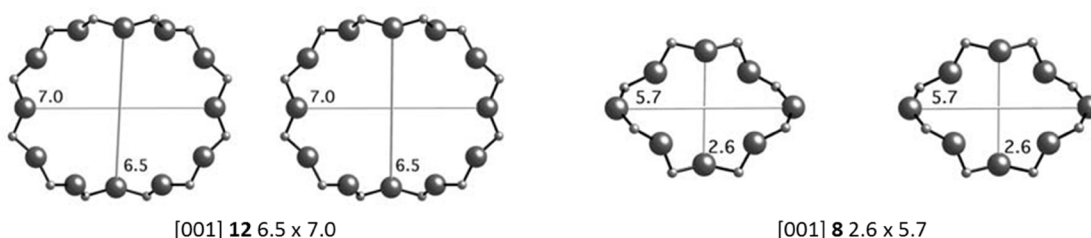


Figure 5.17 Ring openings of the two channel systems of mordenite [20].

## Ferrierite

Synthetic ferrierite, chemical formula  $|\text{Mg}_2\text{Na}_2(\text{H}_2\text{O})_{18}|[\text{Al}_6\text{Si}_{30}\text{O}_{72}]$ -FER is a medium pore type zeolite composed of chains of five membered rings, which are linked to give  $5^4$

polyhedral units from which the 3-dimensional framework is obtained. It is characterised by two dimensional networks of 10-member ring and 8-member ring channels which are perpendicular to each other [20, 50, 51, 52].

FER zeolite is used mainly for the isomerisation of 1-butene, but can also be used for the production of light olefins, such as ethylene, propylene and butenes, from naphtha cracking due to its higher selectivity toward light olefins rather than aromatic compounds when compared with zeolite ZSM-5 [53].

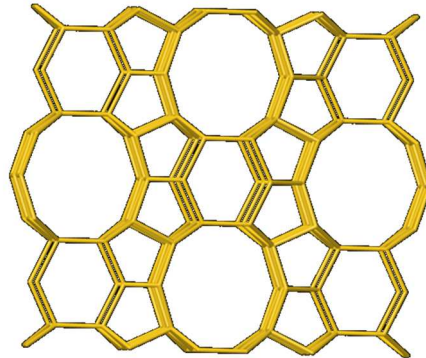


Figure 5.18 Ferrierite framework.

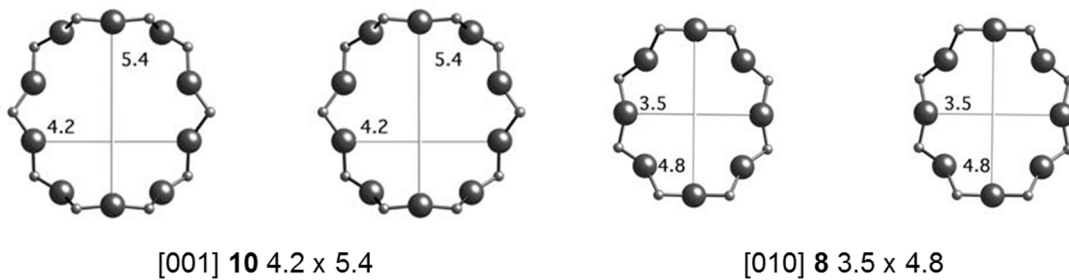


Figure 5.19 Ring openings of the two channel systems of ferrierite [20].

### 5.3 References

- [1] Furuhashi T., Schwarzinger C., Miksik I., Smrz M., Beran A. (2009) Molluscan shell evolution with review of shell calcification hypothesis. *Comparative Biochemistry and Physiology, Part B*, 154, 351 – 371.
- [2] Marin F., Le Roy N., Marie B. (2012) The formation and mineralization of mollusc shell. *Frontiers in Bioscience*, S4, 1099 – 1125.
- [3] Weiner S., Dove P. M. (2003) An Overview of Biomineralization Processes and the Problem of the Vital Effect. *Reviews in Mineralogy and Geochemistry*, 54, 1 – 30.
- [4] Soldati A. L., Jacob D. E., Glatzel P., Swarbrick J. C., Geck J. (2016) Element substitution by living organisms: the case of manganese in mollusc shell aragonite. *Scientific Reports*, 6, 22514.
- [5] de Paula S. M., Silveira M. (2009) Studies on molluscan shells: Contributions from microscopic and analytical methods. *Micron*, 40, 669 – 690.
- [6] Broom M. J., Mason J. (1978) Growth and Spawning in the Pectinid *Chlamys opercularis* in Relation to Temperature and Phytoplankton Concentration. *Marine Biology* 47, 277 – 285.
- [7] Williams S. T. (2017) Molluscan shell colour. *Biological Reviews*, 92, 1039 - 1058.
- [8] Mortensen A. (2006) Carotenoids and other pigments as natural colorants. *Pure and Applied Chemistry*, 78, n°8, 1477 – 1491.
- [9] Zhou X., Liu W., Zhang J., Wu C., Ou X., Tian C., Lin Z., Dang Z. (2017) Biogenic Calcium Carbonate with Hierarchical Organic–Inorganic Composite Structure Enhancing the Removal of Pb(II) from Wastewater. *ACS Applied Material and Interfaces*, 9, 35785 – 35793.
- [10] Tudor H. E. A., Gryte C. C., Harris C. C. (2006) Seashells: detoxifying agents for metal-contaminated waters. *Water, Air, and Soil Pollution*, 173, 209 – 242.
- [11] Köhler S. J., Cubillas P., Rodríguez – Blanco J. D., Bauer C., Prieto M. (2007) Removal of Cadmium from Wastewaters by Aragonite Shells and the Influence of Other Divalent Cations. *Environmental Science & Technology*, 41, 112 – 118.
- [12] Du Y., Zhu L., Shan G. (2012) Removal of Cd<sup>2+</sup> from contaminated water by nano-sized aragonite mollusc shell and the competition of coexisting metal ions. *Journal of Colloid and Interface Science*, 367, 378 – 382.
- [13] Ismail F. A., Aris A. Z. (2013) Experimental determination of Cd<sup>2+</sup> adsorption mechanism on low-cost biological waste. *Frontiers of Environmental Science & Engineering*, 7(3), 356 – 364.
- [14] Wu Q., Chen J., Clark M., Yu Y. (2014) Adsorption of copper to different biogenic oyster shell structures. *Applied Surface Science*, 311, 264 – 272.

- [15] Liu Y., Sun C., Xu J., Li Y. (2009) The use of raw and acid-pretreated bivalve mollusk shells to remove metals from aqueous solutions. *Journal of Hazardous Materials*, 168, 156 – 162.
- [16] Peña-Rodríguez S., Fernández-Calviño D., Nóvoa-Muñoz J. C., Arias-Estévez M., Núñez-Delgado A., Fernández-Sanjurjo M. J., Álvarez-Rodríguez E. (2010) Kinetics of Hg(II) adsorption and desorption in calcinated mussel shells. *Journal of Hazardous Materials*, 180, 622 – 627.
- [17] Alidoust D., Kawahigashi M., Yoshizawa S., Sumida H., Watanabe M. (2015) Mechanism of cadmium biosorption from aqueous solutions using calcined oyster shells. *Journal of Environmental Management*, 150, 103 – 110.
- [18] Yen H. Y., Li J. Y. (2015) Process optimization for Ni(II) removal from wastewater by calcined oyster shell powders using Taguchi method. *Journal of Environmental Management*, 161, 344 – 349.
- [19] Shüth F., Schmidt W. (2002) Microporous and Mesoporous Materials. *Advanced Engineering Materials*, 4, n°5, 269 – 279.
- [20] Baerlocher C., McCusker L. B., Olson D. H. (2007) *Atlas of Zeolite Framework Types*, 6<sup>th</sup> rev. ed., Elsevier, Amsterdam.
- [21] Moshoeshoe M., Nadiye-Tabbiruka M. S., Obuseng V. (2017) A Review of the Chemistry, Structure, Properties and Applications of Zeolites. *American Journal of Materials Science*, 7(5), 196 – 221.
- [22] Sersale R., Sand L.B. *Natural zeolites. Occurrences, properties and uses*, Pergamon Press, Elmsford, 1978.
- [23] Vignola R., Sisto R., Grillo G., Cova U., Cesti P. Process for the treatment of contaminated water by means of a bifunctional system consisting of iron and zeolites. US2009/0014390 A1 Patent (2009).
- [24] Ausavasukhi A., Sooknoi T., Resasco D. E. (2009) Catalytic deoxygenation of benzaldehyde over gallium-modified ZSM-5 zeolite. *Journal of Catalysis*, 268 (1), 68 – 78.
- [25] Kanazirev V., Mavrodinova V., Kosova L., Price G. L. (1991) Conversion of C<sub>8</sub> aromatics and n-pentane over Ga<sub>2</sub>O<sub>3</sub>/HZSM-5 mechanically mixed catalysts. *Catalysis Letters*, 9 (1-2), 35 – 42.
- [26] Fricke R., Kosslick H., Lischke G., Richter M. (2000) Incorporation of Gallium into Zeolites: Syntheses, Properties and Catalytic Application. *Chemical Reviews*, 100 (6), 2303 – 2406.
- [27] Bhan A., Delgass W. N. (2008) Propane Aromatization over HZSM-5 and Ga/HZSM-5 Catalysts. *Catalysis Reviews*, 50 (1), 19 – 151.
- [28] Yogo K., Satoru T., Michito I., Tatsuya H., Eiichi K. (1992) Selective Reduction of NO with Propane on Gallium Ion-exchange Zeolites. *Chemistry Letters*, 21 (6), 1025 – 1028.

- [29] Shamzhy M., Opanasenko M., Concepción P., Martínez A. (2019) New trends in tailoring active sites in zeolite-based catalysts. *Chemical Society Reviews*, 48, 1095 – 1149.
- [30] Uslamin E. A., Luna-Murillo B., Kosinov N., Bruijninx P. C. A., Pidko E. A., Weckhuysen B. M., Hensen E. J. M. (2019) Gallium-promoted HZSM-5 zeolites as efficient catalysts for the aromatization of biomass-derived furans. *Chemical Engineering Science*, 198, 305 – 316.
- [31] Coella C. (1996) Ion exchange equilibria in zeolite minerals. *Mineralium Deposita*, 31, 554 – 562.
- [32] Kazansky V. B., Subbotina I. R., van Santen R. A., Hensen E. J. M. (2005) DRIFTS study of the nature and chemical reactivity of gallium ions in Ga/ZSM-5: II. Oxidation of reduced Ga species in ZSM-5 by nitrous oxide or water. *Journal of Catalysis*, 233 (2), 351 – 358.
- [33] Berlier G., Spoto G., Fiscaro P., Bordiga S., Zecchina A., Giamello E., Lamberti C. (2002) Co-ordination and oxidation changes undergone by iron species in Fe-silicalite upon template removal, activation and interaction with N<sub>2</sub>O: an in situ X-ray absorption study. *Microchemical Journal*, 71 (2-3), 101 – 116.
- [34] Berlier G., Spoto G., Bordiga S., Ricchiardi G., Fiscaro P., Zecchina A., Rossetti I., Selli E., Forni L., Giamello E., Lamberti C. (2002b) Evolution of Extraframework Iron Species in Fe Silicalite: 1. Effect of Fe Content, Activation Temperature, and Interaction with Redox Agents. *Journal of Catalysis*, 208 (1), 64 – 82.
- [35] Sun K., Xia H., Hensen E., van Santen R., Li C. (2006) Chemistry of N<sub>2</sub>O decomposition on active sites with different nature: Effect of high-temperature treatment of Fe/ZSM-5. *Journal of Catalysis*, 238 (1), 186 – 195.
- [36] Rane N., Overweg A. R., Kazansky V. B., van Santen R. A., Hensen E. J. M. (2006) Characterization and reactivity of Ga<sup>+</sup> and GaO<sup>+</sup> cations in zeolite ZSM-5. *Journal of Catalysis*, 239 (2), 478 – 485.
- [37] Pidko E. A., Kazansky V. B., Hensen E. J. M., van Santen R. A. (2006) A comprehensive density functional theory study of ethane dehydrogenation over reduced extra-framework gallium species in ZSM-5 zeolite. *Journal of Catalysis*, 240 (1), 73 – 84.
- [38] Ausavasukhi A., Sooknoi T. (2009) Additional Brønsted acid sites in [Ga]HZSM-5 formed by the presence of water. *Applied Catalysis A: General*, 361 (1-2), 93 – 98.
- [39] Rosinski E. J., Rubin M. K. Preparation of ZSM-12 type zeolites. US 4391785A Patent (1983).
- [40] Perego, C., Amarilli, S., Millini, R., Bellussi, G., Girotti, G., and Terzoni, G. (1996) Experimental and computational study of beta, ZSM-12, Y, mordenite and ERB-1 in cumene synthesis. *Microporous Materials*, 6(5-6), 395–404.

- [41] Millini, R., Carluccio, L., Frigerio, F., Parker, W.O.N. Jr., and Bellussi, G. (1998) Zeolite synthesis in the presence of azonia-spiro compounds as structuredirecting agents. *Microporous and Mesoporous Materials*, 24(4-6), 199–211.
- [42] Pazzucconi, C.P.G., Millini, R., Frigerio, F., Mansani, R., and Rancati, D. (2000) U.S. Patent 6,147,270.
- [43] Yoo, K., Kashfi, R., Gopal, S., Smirniotis, P.G., Gangoda, M., and Bose, R.N. (2003) TEABr directed synthesis of ZSM-12 and its NMR characterization. *Microporous and Mesoporous Materials*, 60, 57–68.
- [44] Bortolini, O., Cavazzini, A., Giovannini, P.P., Greco, R., Marchetti, N., Massi, A., and Pasti, L. (2013) A combined kinetic and thermodynamic approach for the interpretation of continuous flow heterogeneous catalytic processes. *Chemistry–A European Journal*, 19(24), 7802–7808.
- [45] Stelzer J., Paulus M., Hunger M., Weitkamp J. (1997) Hydrophobic properties of all-silica zeolite beta. *Microporous and Mesoporous Materials*, 22, 1 – 8.
- [46] Čejka J., van Bekkum H., Corma A., Schüth F. (2007) Introduction to Zeolite Science and Practice, 3<sup>rd</sup> revised edition; Elsevier, Vol.168.
- [47] Breck D. W., Flanigen E. M. (1967) Synthesis and properties of Union Carbide zeolites L, X and Y. Conference on Molecular Sieves, Society of Chemical Industry, London.
- [48] Barrer, R., Villiger, H. (2010) The crystal structure of the synthetic zeolite L. *Zeitschrift für Kristallographie*, 128(3-6) 352 – 370.
- [49] Gao W., Amoo C. C., Zhang G., Javed M., Mazonde B., Lu C., Yang R., Xing C., Tsubaki N. (2019) Insight into solvent-free synthesis of MOR zeolite and its laboratory scale production. *Microporous and Mesoporous Materials*, 280, 187 – 194.
- [50] Vaughan P. A. (1966) The Crystal Structure of the Zeolite Ferrierite. *Acta Crystallographica*, 21, 983 – 990.
- [51] Barrer R. M., Lee J. A. (1969) Synthetic ferrierites as sorbents and molecular sieves. *Journal of Colloid and Interface Science*, 30 (1), 111 – 119.
- [52] Gramlich-Meier R., Meier W. M., Smith B. K. (1984) On faults in the framework structure of the zeolite ferrierite. *Zeitschrift für Kristallographie*, 169, 201 – 210.
- [53] Bastiani R., Lam Y. L., Assumpção Henriques C., Teixeira da Silva V. (2013) Application of ferrierite zeolite in high-olefin catalytic cracking. *Fuel*, 107, 680 – 687.

## 6 EXPERIMENTAL

### 6.1 Scallop shells as adsorbent material for the removal of heavy metals from aqueous solution

Part of the results illustrated herein are included in an article in preparation.

#### 6.1.1 Introduction

Shellfish cultivation is a well-established and still expanding activity of the food industry chain worldwide, and it is a widespread activity in several lagoons of the Adriatic Sea, such as Sacca di Goro (Fig. 6.1.1), a small and shallow lagoon located in the Southern part of the Po River delta relevant from the biological and economic point of view. Indeed, it accounts for the production of 15000 to 18000 t yr<sup>-1</sup> of clam supporting the local economy [1] and it is part of the Po Delta Park, recognised in 2015 as a Biosphere Reserve MAB UNESCO due to its biodiversity richness. On the other hand, Sacca di Goro is a fragile and highly impacted coastal system that receives effluents from the Po River which, in turn, collects sewages from the most industrialised Italian areas. Due to its position at the sea-land interface, this lagoon is considered vulnerable, and it is important to safeguard natural ecosystems and to adopt approaches to economic development that are environmentally sustainable, in particular for that which concerns waste management. Indeed, seafood processing leads to the formation of large quantities of pre-consumer and post-consumer residue, mainly composed of shells, that if not properly disposed can constitute a serious environmental issue [2].

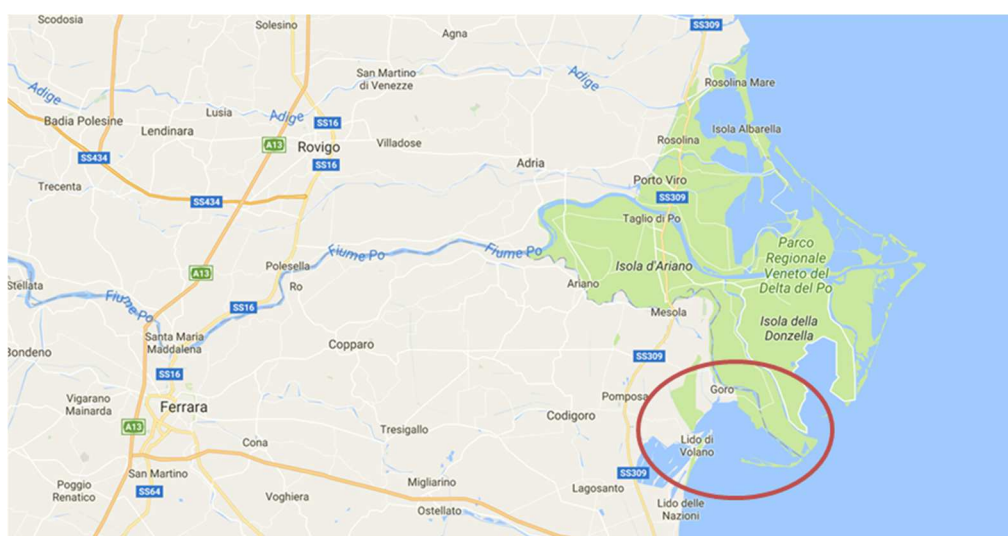


Figure 6.1.1 Sacca di Goro, Po River Delta, Italy.

In this work, scallop shells (Fig. 6.1.2), originated from the local aquaculture activities, were collected in Sacca di Goro in order to use them as bio-adsorbents for the removal of heavy metals from water.



Figure 6.1.2 White, pink and brown scallop shells.

### 6.1.2 Materials and methods

After collection, any residual organic matter was removed and the shells were thoroughly cleaned with deionised water (MilliQ, Millipore, USA) and dried in an oven at 50°C overnight. For the material characterisation and the adsorption experiments, the scallop shells were grinded to obtain a fine powder.

#### *Chemical Characterisation*

To investigate the total cation content, shell samples with different colourations, were grinded and digested in nitric acid 10%, filtered using syringe filters with PVDF membrane 0.45  $\mu\text{m}$  (ACRODISC, New York, USA). After dilution, the analyses were carried out using an Agilent 7500 ICP-QMS; the instrument operating parameters were: RF power 1450 W, sampling depth 4.2 mm, coolant gas 15 L  $\text{min}^{-1}$ , carrier gas 1.00 L  $\text{min}^{-1}$ , the isotopes measured were  $^{25}\text{Mg}$ ,  $^{39}\text{K}$ ,  $^{49}\text{Ti}$ ,  $^{51}\text{V}$ ,  $^{52}\text{Cr}$ ,  $^{55}\text{Mn}$ ,  $^{56}\text{Fe}$ ,  $^{59}\text{Co}$ ,  $^{62}\text{Ni}$ ,  $^{65}\text{Cu}$ ,  $^{66}\text{Zn}$ ,  $^{88}\text{Sr}$ ,  $^{107}\text{Ag}$ ,  $^{111}\text{Cd}$ ,  $^{113}\text{Cd}$ ,  $^{137}\text{Ba}$  and  $^{208}\text{Pb}$ .

#### *Adsorption isotherms*

Solutions containing the metals (single component solutions) were prepared by dissolving  $\text{Cd}(\text{NO}_3)_2 \cdot 4\text{H}_2\text{O}$ ,  $\text{Pb}(\text{NO}_3)_2$  or  $\text{Ni}(\text{NO}_3)_2 \cdot 6\text{H}_2\text{O}$  in deionised MilliQ water. The initial metal concentrations in the solutions were in the range of 1-350  $\text{mg L}^{-1}$ .

20 mL of metal solution was added to crimp top reaction glass flasks sealed with PTFE septa (Supelco, Bellefonte, PA, USA) with 40 mg of shell powder.

After 24h equilibration under stirring (600 rpm), the adsorbent was separated from the solution by filtration using 25 mm syringe filters with PVDF membrane 0.45  $\mu\text{m}$  (Agilent

Technologies, Santa Clara, CA, USA), the pH of the solution was recorded for each solution after equilibration.

The concentration of Ca<sup>2+</sup> and of the metal ions in the solution, before and after the contact with the adsorbent material, was determined by ICP-OES (Perkin-Elmer Optima 3100 XL) (axial view) equipped with a solid-state charge-coupled device detector (CCD), a peristaltic pump and a low-flow GemCone nebulizer coupled to a cyclonic spray chamber. Analytical lines selected for quantitative determination of calcium and the three heavy metals are reported in table 6.1.1.

Element	Analytical line (nm)
Ca	317.933
Cd	226.502
Pb	220.353
Ni	231.604

Table 6.1.1 ICP-OES Analytical lines for quantitative determination.

### 6.1.3 Results and discussion

#### *Chemical Characterisation*

The mean calcium concentration (386 mg g<sup>-1</sup>), the main element present in the shell carbonate matrix, was determined with solution based ICP-OES after mineralisation of the shell powder.

The trace elements bulk composition is reported in table 6.1.2.

	ScallopRaw a	ScallopRaw b	ScallopRaw c	ScallopRaw d	LOD
	White shell	Pink shell	Brown shell	Dark brown shell	
<sup>25</sup> Mg	93 ± 1.35	76.8 ± 0.75	106.8 ± 0.85	102.0 ± 0.21	0.167
<sup>39</sup> K	101 ± 3.62	119 ± 6.17	186 ± 4.51	129 ± 5.79	9.791
<sup>49</sup> Ti	<LOD	<LOD	0.9 ± 0.11	<LOD	0.458
<sup>51</sup> V	0.05 ± 0.04	0.05 ± 0.01	0.97 ± 0.05	0.16 ± 0.01	0.054
<sup>52</sup> Cr	0.26 ± 0.04	0.52 ± 0.05	0.49 ± 0.05	0.39 ± 0.02	0.068
<sup>55</sup> Mn	24.4 ± 0.53	24.0 ± 0.65	178 ± 4.14	123 ± 2.03	0.080
<sup>56</sup> Fe	8.2 ± 0.39	10.6 ± 0.36	476 ± 8.68	46 ± 1.33	0.219
<sup>59</sup> Co	0.16 ± 0.02	0.10 ± 0.01	1.22 ± 0.02	0.40 ± 0.01	0.003

<sup>62</sup> Ni	0.55 ± 0.09	2.2 ± 0.32	2.6 ± 0.25	3.0 ± 0.33	0.366
<sup>65</sup> Cu	1.27 ± 0.04	1.8 ± 0.10	17.4 ± 0.34	10.6 ± 0.21	0.114
<sup>66</sup> Zn	16.6 ± 0.30	16.3 ± 0.63	90 ± 2.76	33.3 ± 0.62	0.604
<sup>88</sup> Sr	1014 ± 5.81	947 ± 8.57	1068 ± 8.70	972 ± 10.36	0.012
<sup>107</sup> Ag	0.01 ± 0.02	0.01 ± 0.02	0.03 ± 0.02	0.01 ± 0.03	0.036
<sup>111</sup> Cd	<LOD	0.4 ± 0.13	0.5 ± 0.22	0.31 ± 0.09	0.298
<sup>113</sup> Cd	0.2 ± 0.11	0.30 ± 0.09	0.5 ± 0.17	0.3 ± 0.16	0.174
<sup>137</sup> Ba	1.7 ± 0.11	1.90 ± 0.07	8.4 ± 0.36	4.3 ± 0.14	0.080
<sup>208</sup> Pb	0.78 ± 0.04	0.68 ± 0.05	3.56 ± 0.08	2.1 ± 0.14	0.030

**Table 6.1.2 Trace elements bulk composition for four scallop shell specimens characterised by different colouration.**

From the results obtained it can be seen that more coloured shells present higher concentrations of many metals, in particular V, Mn, Fe, Co, Cu, Zn, Ba and Pb are higher for the sample named ScallopRaw c (brown shell), and among these elements Fe was the most abundant element in the sample. The concentration levels of Cd are close to the quantification limits of the employed technique (0.91 and 0.52  $\mu\text{g g}^{-1}$  for Cd<sup>111</sup> and Cd<sup>113</sup> respectively), thus indicating that the environmental habitat of these seashell was not severely polluted by Cd or that the replacement of Ca<sup>2+</sup> in the calcium carbonate structure during the shell formation occurs to a lesser extent.

## **Adsorption of cadmium on scallop shell powder**

### *Adsorption isotherms*

To study the adsorption mechanism of the heavy metal cadmium on scallop shell powder, the batch method was employed.

Generally, the adsorption of metal ions from aqueous solutions depends on pH, since at high pHs hydroxyl ions may complex and/or precipitate metal cations from aqueous solutions. On the other hand, carbonate dissolution can take place in acidic media. Dissolution equilibria for biogenic carbonate are complex phenomena since the heterogeneity of these materials on many different scales influence their solubility and kinetic behaviour [3]. At pH lower than 7 the aqua complex of Cd<sup>2+</sup> is the prevailing species, at this pH dissolution of biogenic carbonate is also negligible, in addition many water bodies are characterised by pHs around neutrality, recently it has been found that in Sacca di Goro pH can vary in the range 7.2-8.3 depending on season and site location [4]. Therefore, the adsorption properties of shell towards Cd<sup>2+</sup> was evaluated at pH 7.0-8.5, measured at the end of the equilibration time of the batch experiments to account for shells dissolution. The experiments were conducted at three different temperatures.

The adsorption isotherms are shown in figure 6.1.3.

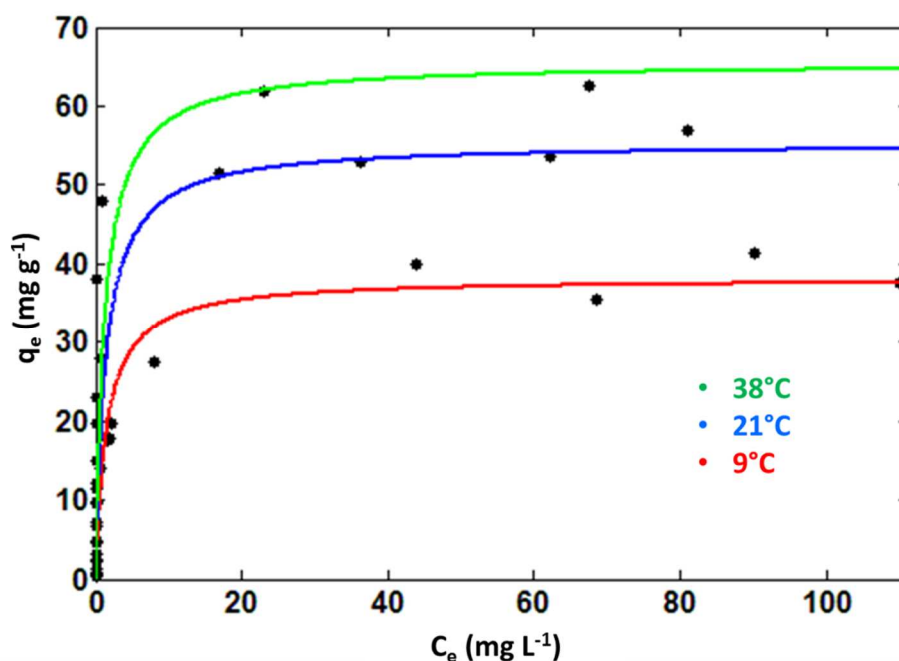


Figure 6.1.3 Cadmium adsorption isotherms at three different temperatures.

The experimental data were well fitted using the Langmuir isotherm model; the parameter obtained from the fitting are reported in table 6.1.3.

T (°C)	$q_{\max}$ (mg g <sup>-1</sup> )	b (L mg <sup>-1</sup> )	R <sup>2</sup>
9	38 ± 4.34	0.6 ± 0.37	0.9336
21	55 ± 7.40	0.7 ± 0.56	0.9371
38	65 ± 16.18	0.8 ± 0.6	0.8610

Table 6.1.3 Isotherm parameters for the adsorption of cadmium on scallop shell powder at three different temperatures.

The curves have a concave shape and they are characterised by a steep initial zone and a saturation plateau. The shape of the isotherms indicates a favourable adsorption of the metal onto the adsorbent material.

The steep initial zone of the isotherm has a linear trend (Fig. 6.1.4), and it can give information on the thermodynamics of the adsorption process.

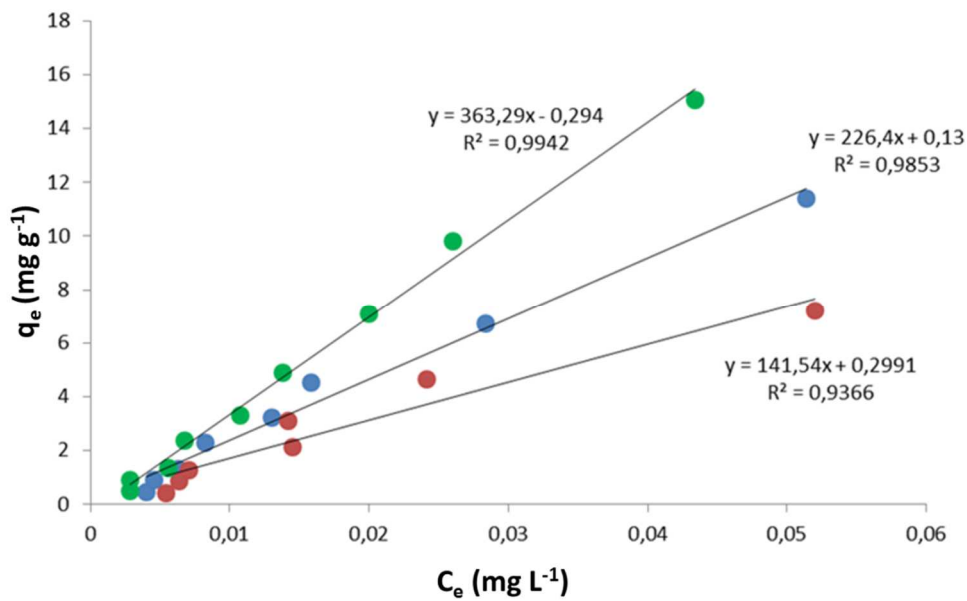


Figure 6.1.4 Initial tracts of the adsorption isotherms obtained at three different temperatures (green: 38°C, blue: 21°C, red: 9°C).

The slope of the linear tract of the isotherm is an estimation of the thermodynamic adsorption constant  $K_{ads}$  from which, through the equation 6.1.1, the Gibbs energy  $\Delta G$  can be calculated:

$$\Delta G = -RT \ln K_{ads} \quad (\text{Eq. 6.1.1})$$

Where  $\Delta G$  is the Gibbs energy expressed in  $\text{kJ mol}^{-1}$ ,  $R$  is the gas constant ( $8.314 \text{ J mol}^{-1} \text{ K}^{-1}$ ),  $T$  is the absolute temperature (K) and  $K_{ads}$  the adsorption constant expressed in  $\text{L mg}^{-1}$ .

If we use the integrated form of the Van't Hoff equation (Eq. 6.1.2) and we consider the adsorption enthalpy,  $\Delta H_{ads}$ , constant through the temperature range chosen for the experiments, we can determine the  $\Delta H_{ads}$  value which is proportional, according to the factor  $R$ , to the slope of the straight line obtained by plotting  $\ln \frac{K_{ads2}}{K_{ads1}}$  as function of  $\left(\frac{1}{T_2} - \frac{1}{T_1}\right)$ , with  $T_1 > T_2$  (Table 6.1.4 and Fig. 6.1.5).

$$\ln \frac{K_{ads2}}{K_{ads1}} = -\frac{\Delta H}{R} \left( \frac{1}{T_2} - \frac{1}{T_1} \right) \quad (\text{Eq. 6.1.2})$$

$T_2 - T_1$	$\ln K_{ads2}/K_{ads1}$	$1/T_2 - 1/T_1$
311.4 - 294	-4,73E-01	1,90E-04
311.4 - 282	-9,43E-01	3,32E-04
294 - 282	-4,70E-01	1,42E-04

Table 6.1.4 Values for the construction of the van't Hoff plot.

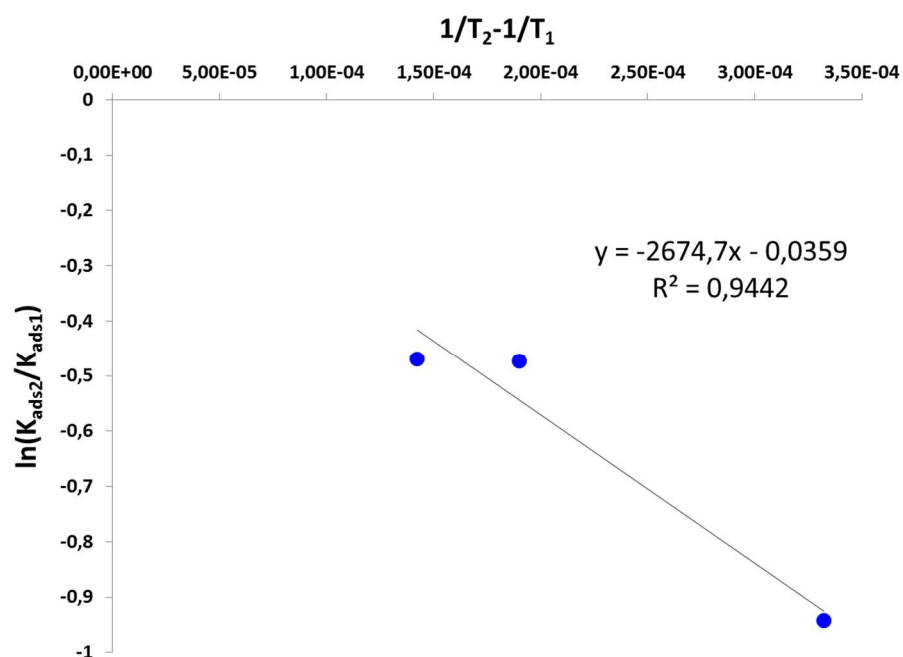


Figure 6.1.5 van't Hoff plot of the adsorption of  $Cd^{2+}$  onto scallop shell powder.

From the equation  $\Delta G = \Delta H - T\Delta S$ , the entropy of the adsorption process can be calculated for every temperature, with a resulting mean value of  $0.12 \text{ kJ mol}^{-1} \text{ K}^{-1}$ .

The thermodynamic parameters obtained are listed in table 6.1.5.

T (K)	$\Delta G$ (kJ mol <sup>-1</sup> )	$\Delta H$ (kJ mol <sup>-1</sup> )	$\Delta S$ (kJ mol <sup>-1</sup> K <sup>-1</sup> )
282	-11.62		
294	-13.25	22.23	0.12
311.4	-15.26		

Table 6.1.5 Gibbs energies ( $\Delta G$ ), enthalpy ( $\Delta H$ ) and entropy ( $\Delta S$ ) of the adsorption process for the system cadmium – scallop shell powder.

From the negative  $\Delta G$  values obtained we can conclude that the adsorption of cadmium onto scallop shell powder is a spontaneous process; moreover, the positive  $\Delta H$  found suggest the Cd uptake is an endothermic process.

#### Adsorption kinetics

The kinetic experiments were conducted at three different initial cadmium concentrations, 1 L of solution was prepared and put in contact with 5 g of shell powder. 10 mL were collected at certain time intervals, filtered with 25 mm syringe filters with PVDF membrane

0.45  $\mu\text{m}$  (Agilent Technologies, Santa Clara, CA, USA) and the cadmium residual concentration evaluated by ICP-OES.

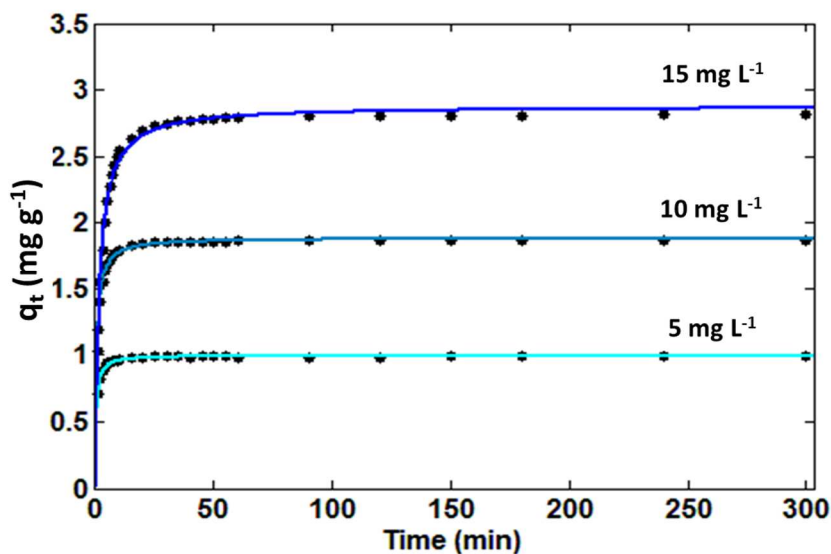


Figure 6.1.6 Effect of contact time on the adsorption of cadmium onto scallop shell powder at three different initial metal concentrations.

The experimental data were fitted using the pseudo second order (PSO) model (Eq. 6.1.3), where  $q_t$  is the amount of Cd adsorbed at time  $t$ ,  $q_e$  is the quantity adsorbed when the equilibrium is reached, and  $k_2$  the pseudo second order rate constant. The parameters obtained from the fitting are reported in table 6.1.6.

$$q_t = \frac{k_2 \cdot q_e^2 \cdot t}{1 + k_2 \cdot q_e \cdot t} \quad (\text{Eq. 6.1.3})$$

$C_0$ (mg L <sup>-1</sup> )	$k_2$ (g mg <sup>-1</sup> min <sup>-1</sup> )	$q_e$ (mg g <sup>-1</sup> )	$R^2$
5	$2.5 \pm 0.16$	$0.997 \pm 0.004$	0.9984
10	$0.87 \pm 0.05$	$1.88 \pm 0.016$	0.9984
15	$0.21 \pm 0.013$	$2.88 \pm 0.02$	0.9968

Table 6.1.6 Kinetic parameters obtained using the PSO model.

The good applicability of this model is usually associated with the situation when the rate of direct adsorption/desorption process (seen as a kind of chemical reaction further referred to as “surface reaction”) controls the overall sorption kinetics [5].

The kinetic constant  $k_2$  is a function of the initial concentration (see Fig. 6.1.7), these data were fitted by using a power law equation as suggested in Ho et al. (2001) [6], as a result the following relationship was found:  $k_2 = 93.7C_0^{-2.18}$ , which is similar to that obtained for the adsorption of Pb(II) on peat [6].

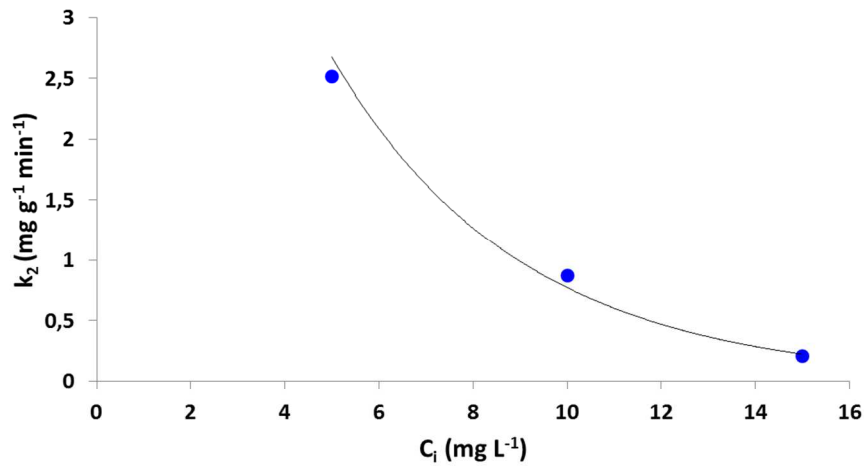


Figure 6.1.7 Kinetic constant as a function of initial cadmium concentration.

### Calcium concentration

The adsorption process is accompanied by an increase of calcium ions in solution and by an increase in pH due to dissolution of shell fragment. The concentration of calcium and carbonate species in the aqueous solution increase rapidly at the experiment beginning. The final pH depends on the initial concentration of cadmium as already observed in Köhler et al. (2007) [7]. This finding seems to be due to the formation of low soluble Cd carbonate on the surface of shell fragments.

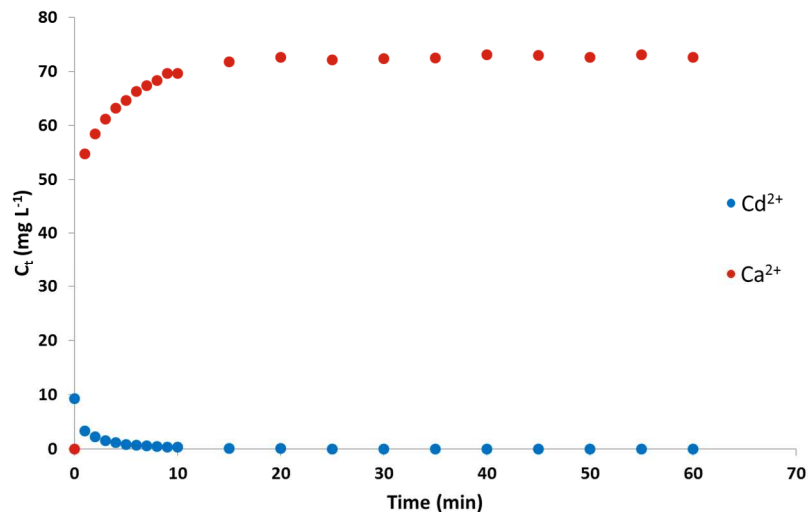


Figure 6.1.8 Variations of the concentrations of cadmium and calcium ( $\text{mg L}^{-1}$ ) during adsorption of cadmium onto scallop shell powder (kinetic data).

### Adsorption of cadmium from aqueous solutions at different salinity

To study the adsorption of cadmium from aqueous solutions that simulate conditions found in natural waters, batch adsorption experiments were performed preparing 80 mg kg<sup>-1</sup> cadmium solutions in aqueous matrix characterised by different salinity.

The adsorbed quantity was calculated and reported as a function salinity (Fig. 6.1.9).

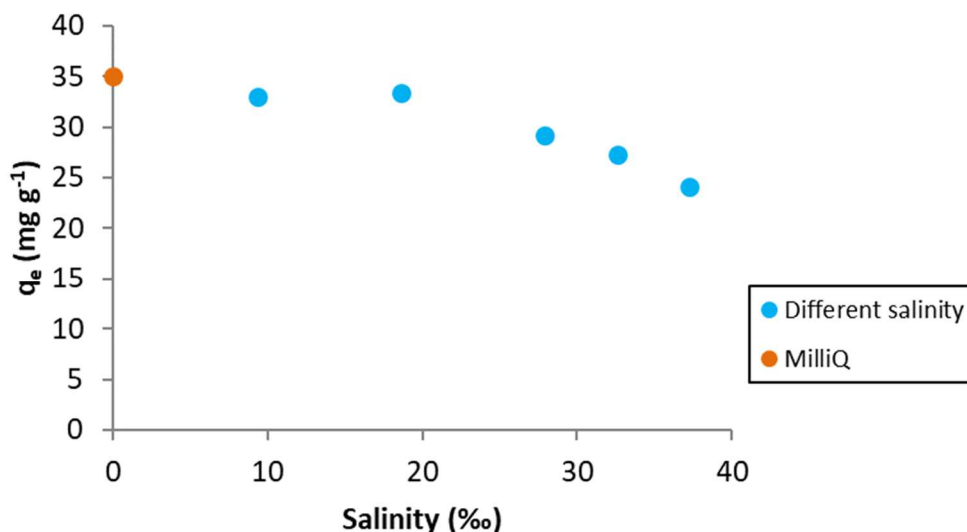


Figure 6.1.9 Uptake of cadmium onto scallop shell powder from aqueous solutions with different salinity and initial Cd concentration of 80 mg L<sup>-1</sup>.

For low salinity levels, the quantity of metal adsorbed by the scallop shell powder varies only slightly when compared to the value obtained from the adsorption performed in MilliQ water. When salinity increases, there is a decrease of the quantity of cadmium adsorbed by the bio-adsorbent up to about 27% at a salinity of 37‰. This is most probably due to the increasing concentration of Cl<sup>-</sup> ions in the aqueous matrix; Cl<sup>-</sup> is a strong complexing agent that tend to stabilise the metal ion in solution forming CdCl<sup>+</sup>, CdCl<sub>2(aq)</sub> and CdCl<sub>3</sub><sup>-</sup> species. A similar decrease in the uptake of Cd by bioadsorption onto bacteria *Bacillus jeotgali* from diluted or concentrated seawater was reported by Green-Ruiz (2008) [8].

One of the main characteristics of transitional waters, such as Sacca di Goro, is the salinity gradient. Salinity of sea waters is almost constant and around 3.5 ‰, whereas in lagoons and in transitional waters salinity can vary in a larger range between 1.5-3.5‰.

Salinity affects water chemistry and ionic strength accounting for metal mobilisation. Desorption of metals from sediments and suspended matter increases with increasing salinity due to the formation of soluble inorganic complexes with chloride and sulphate; for example, soluble cadmium has been reported to be up to 4-fold higher if the salinity varies from 0 to 10 ‰ [9].

## Adsorption of lead and nickel on scallop shell powder

The adsorption of other heavy metals, lead and nickel, were considered in this work to evaluate a possible competitive behaviour between the metal contaminants that are often present together in water bodies.

### Adsorption kinetics

Kinetic experiments for both lead and nickel were carried out in the same conditions used for cadmium.

In figure 6.1.10, the adsorbed quantity as a function of contact time with the adsorbent material are reported for the three heavy metals for the single component experiments.

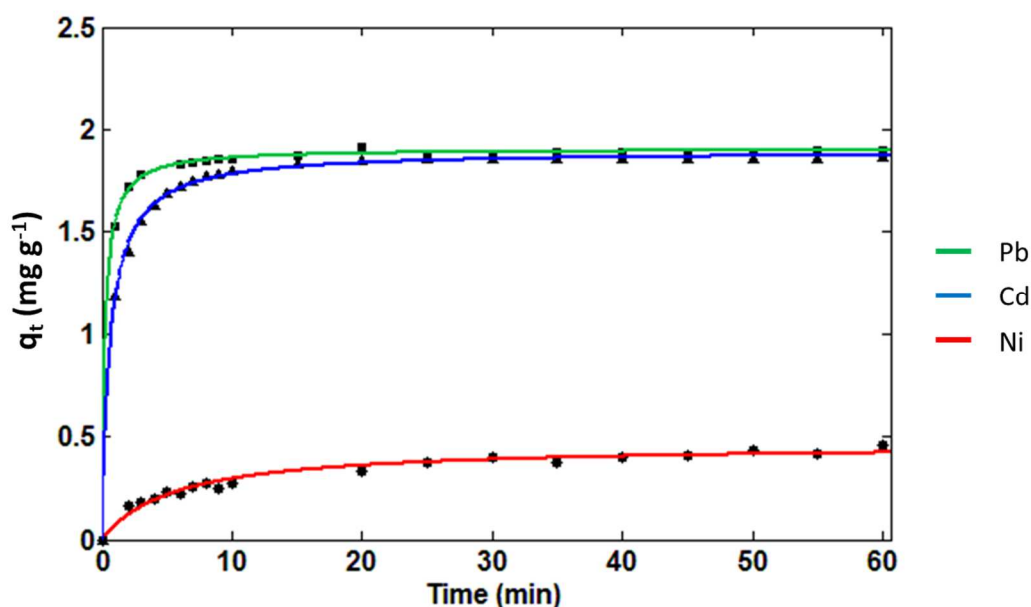


Figure 6.1.10 Adsorption kinetics for lead, cadmium and nickel obtained from single component solutions with initial concentration of  $10 \text{ mg L}^{-1}$ .

As for cadmium, also the lead and nickel experimental data were well fitted with the pseudo second order model (PSO). The parameters obtained from the fitting are reported in table 6.1.6.

	$k_2 \text{ (mg g}^{-1}\text{min}^{-1}\text{)}$	$q_e \text{ (mg g}^{-1}\text{)}$	$R^2$
<b>Ni</b>	$0.17 \pm 0.065$	$0.46 \pm 0.045$	0.9696
<b>Cd</b>	$0.87 \pm 0.047$	$1.885 \pm 0.008$	0.9989
<b>Pb</b>	$2.3 \pm 0.37$	$1.90 \pm 0.012$	0.9995

Table 6.1.6 Kinetic parameters for the three metals obtained using the PSO model.

The kinetic constant  $k_2$  is much higher for Pb, and significantly lower for Ni when compared to that of Cd; moreover, the entity of metal uptake once the equilibrium is reached is very

low for nickel, while it is about the same value for lead and cadmium. These results indicate that the adsorption on scallop shell powder is more efficient for lead and cadmium than nickel.

#### Adsorption isotherms

The investigation of the adsorption of metal species onto biogenic calcium carbonate powder was carried out for lead and nickel, especially in the low metal solution concentration range. The experiments were carried out in the same conditions used for cadmium. Figure 6.1.11 shows the uptake for each metal species in relation to the initial concentration of the solution. The adsorption of the metal contaminant increases proportionally with the increase of metal concentration in the initial solution for all three metals considered, but it is much higher for Cd and Pb than for Ni.

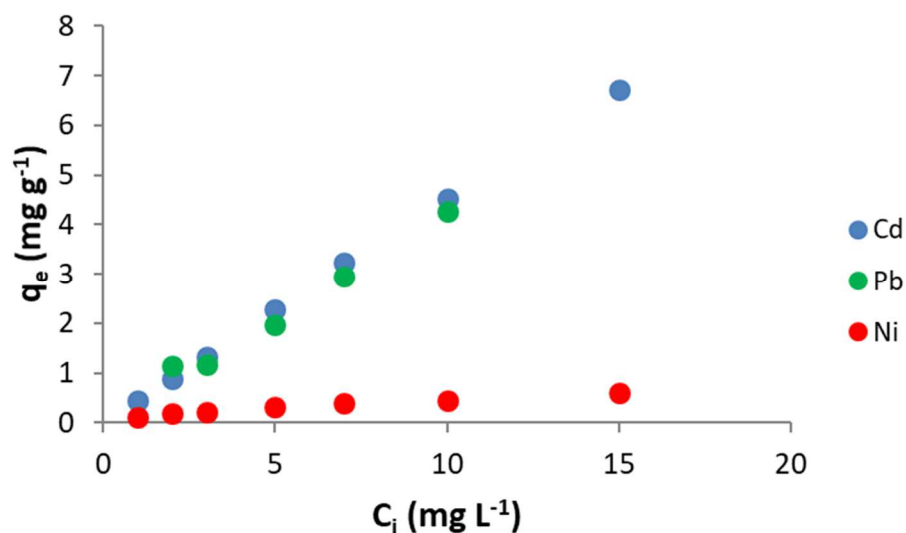


Figure 6.1.11 Metal adsorbed quantity at equilibrium ( $q_e$ ) as a function of initial metal concentration in solution ( $C_i$ ).

The different behaviour of scallop shell powder towards the adsorption of the three metals is highlighted when the initial tracts of the adsorption isotherms are compared (Fig. 6.1.12). The uptake of the metal in the low concentration range shows a linear trend for all three metals, but the slope ( $K_{ads}$ ) obtained from the linear fitting is much lower for nickel than for cadmium and lead (Table 6.1.7).

Metal	$K_{ads}$ (L g <sup>-1</sup> )	$R^2$
Cd	$257 \pm 50.25$	0.9718
Pb	$22 \pm 9.66$	0.9475
Ni	$0.034 \pm 0.0075$	0.9646

Table 6.1.7 Adsorption constant  $K_{ads}$  and coefficient of determination  $R^2$  obtained from the linear fitting for cadmium, lead and nickel.

The highest value of the adsorption constant  $K_{ads}$  was found for cadmium, for lead the value obtained is about 10 times lower, whereas for nickel  $K_{ads}$  decreases significantly.

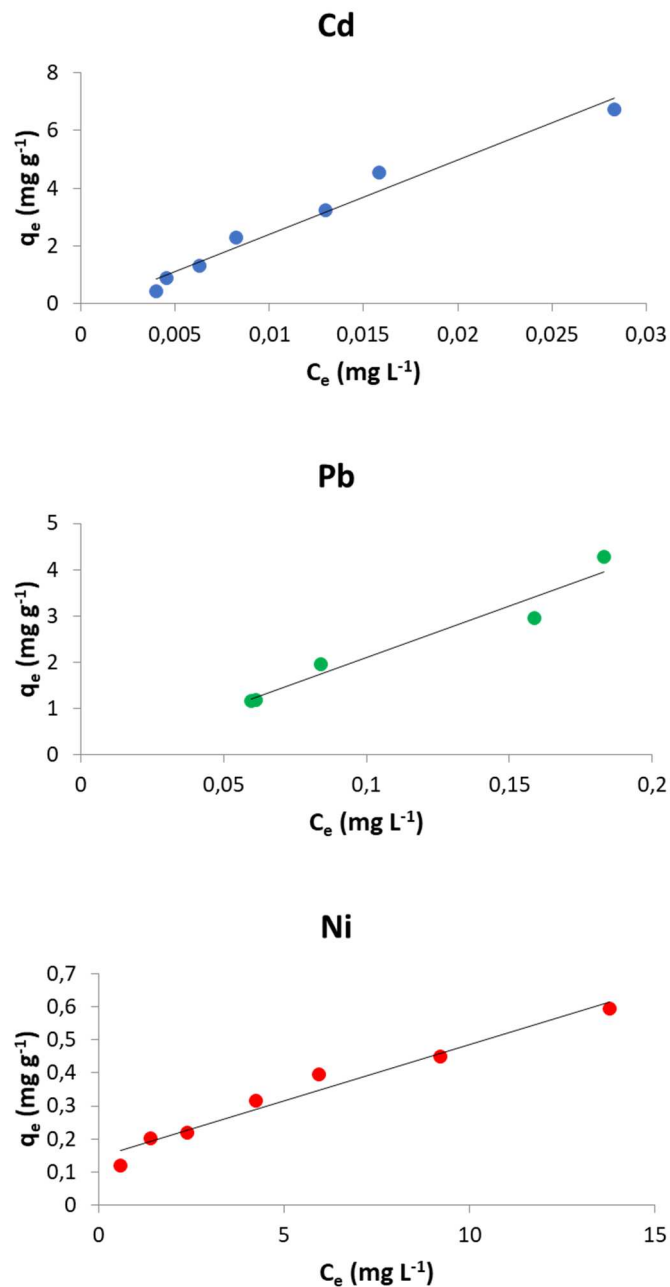


Figure 6.1.12 Initial linear tract of the adsorption isotherm for the three metals.

### Competition

Since lead showed a much higher uptake onto scallop shell powder than nickel, it was chosen to evaluate a possible effect of lead on the removal of cadmium.

Cadmium adsorption isotherms were determined from binary solutions with increasing Cd concentration and a fixed Pb concentration; in particular, cadmium adsorption experiments were carried out in presence of 10 mg L<sup>-1</sup> and 50 mg L<sup>-1</sup> of Pb.

The resulting adsorption isotherms are reported in figure 6.1.13 in comparison with the cadmium adsorption isotherm obtained from single component solutions.

The Langmuir and Toth adsorption isotherm models were used to fit the experimental data in presence of 10 mg L<sup>-1</sup> and 50 mg L<sup>-1</sup> of Pb, respectively.

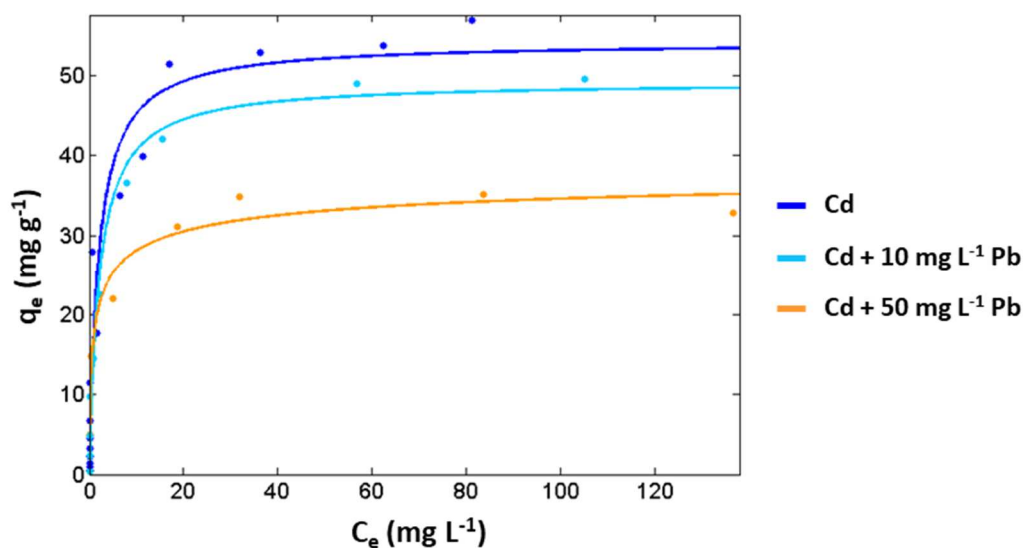


Figure 6.1.13 Cadmium adsorption isotherms obtained from solutions containing different amount of lead (0, 10 and 50 mg L<sup>-1</sup>).

When lead ions are present in the aqueous solution, the saturation capacity of scallop shell powder towards cadmium decreases, thus indicating a competitive process.

If the first tract of the cadmium adsorption isotherm is taken in consideration (Fig. 6.1.14), a different trend is observed between the adsorption from solutions containing only Cd, and solutions containing both Cd and Pb. The first tract of the cadmium isotherm obtained from the single component solutions has a linear trend, while if lead is present in the solution the cadmium uptake decreases and the trend is not linear anymore even at low concentrations. These results are consistent with those found by Köhler et al. (2007) [7] who reported that the adsorption of cadmium onto aragonite shells is influenced by the presence in solution of other divalent cations, especially lead. The selectivity of scallop shell powder towards the adsorption of lead rather than cadmium can be explained by comparing the solubility products of the carbonate phases: under the same pH and pCO<sub>2</sub> conditions, lead carbonate phases (hydrocerussite and cerussite) are less soluble than cadmium carbonate (otavite), thus, initially, the formation of PbCO<sub>3</sub> phases is preferred [7]. To better investigate on the mechanism of the adsorption process, surface and structural studies were carried out.

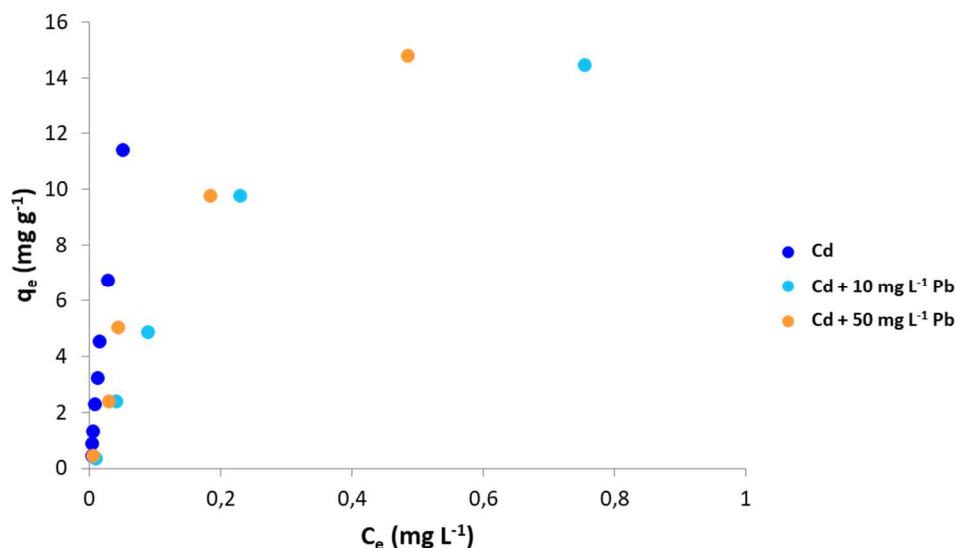


Figure 6.1.14 First tract of the cadmium adsorption isotherms in presence of lead.

### LA-ICP-MS study on the adsorption of cadmium onto scallop shells

Laser Ablation Inductively Coupled Plasma Mass Spectrometry (LA-ICP-MS) is widely used as a powerful micro analytical technique for the analysis of solid samples in a variety of scientific fields including geology, biology, and environmental and metallurgical sciences. In LA-ICP-MS, a high-energy pulsed laser beam is focused on the surface of the solid sample, in this way an aerosol is generated as a consequence of the sublimation of the superficial layers of the sample. A carrier gas flow (helium or argon) leads the aerosol into the plasma torch where the analytes are ionised, detected and quantified in the mass spectrometer.

LA-ICP-MS has been successfully applied for the analysis of the trace elemental and isotopic inventor in successively secreted carbonate layers to obtain information of past environmental conditions of seashells [10].

Compositional trace elemental variability in biogenic carbonates can be assessed by static layer by layer removal of material to obtain a depth-compositional profile. Alternatively, it can be carried out by laser ablation along a defined section oriented perpendicular to the accretionary growth direction [11].

The latter method was applied in the present study. To further investigate on the scallop shell composition and trace elements distribution, specimen of shells were analysed with this technique. Moreover, the analysis of shell samples that have been treated with cadmium containing solution allowed the investigation of the diffusion of the metal contaminant through the bio-adsorbent material.

For the study of the metal diffusion through the shell layers, the entire mollusc valves were put in contact with solutions containing  $\text{Cd}^{2+}$ , the concentrations of the metal ions were 0.1 and 1  $\text{mg L}^{-1}$ . After the equilibrium had been reached, the shells were air-dried.

To investigate the diffusion of cadmium through the sample cross section, the shells were cut along the axis of maximum growth with a low speed saw (Buehler LTD), embedded into an epoxy resin (Epofix®), ground to the desired thickness with a polishing machine equipped with a 120 grit diamond disc, then polished with 600 and 800 grit SiC powder.

LA-ICP-MS line scan analyses were conducted at ETH in Zürich (Switzerland) with an ArF Excimer laser system (GeoLas C, Lambda Physik, Göttingen, Germany) coupled to an ICP-TOFMS (icpTOF, ToFwerk, Thun, Switzerland). The instrumental operating conditions are reported in Table 6.1.8.

<b>Laser parameters</b>	
Wavelength	193 nm
Repetition rate	10 Hz
Ablation spot size	24 $\mu\text{m}$
Scan speed	3 $\mu\text{m s}^{-1}$
Carrier gas	He
Flow rate	0.6 $\text{L min}^{-1}$
<b>ICP-TOFMS</b>	
RF power	1550 W
Sampling depth	6.8 mm
Coolant gas (Ar)	16 $\text{L min}^{-1}$
Auxiliary gas (Ar)	0.80 $\text{L min}^{-1}$
Make-up gas (Ar)	0.82 $\text{L min}^{-1}$

**Table 6.1.8 LA-ICP-TOFMS operating conditions.**

The synthetic glass SRM NIST 610 was employed as external standard, while  $^{42}\text{Ca}$  was chosen as internal standard. The mean calcium concentration of the scallop shells (386  $\text{mg g}^{-1}$ ) was previously determined by solution based ICP-OES.

To assess the accuracy of the LA-ICP-TOFMS analysis, laser ablation measurements were performed on a calcium carbonate reference material (MACS-3, U.S. Geological Survey, *Box 25046, MS 963, Denver, CO 80225, USA*) containing all the metals studied in this work, and the recovery of every element was determined (see Table 6.1.9).

Element	Measured value ( $\mu\text{g g}^{-1}$ )	STD. DEV.	USGS reference values*	Recovery %
<sup>25</sup> Mg	2005.46	369.42	1756	114.21
<sup>49</sup> Ti	45.88	3.61	54.9	83.57
<sup>51</sup> V	35.36	4.72	46.3	76.37
<sup>52</sup> Cr	101.15	6.34	117	86.45
<sup>55</sup> Mn	535.38	43.67	536	99.88
<sup>56</sup> Fe	10298.64	1009.27	11200	91.95
<sup>59</sup> Co	50.38	7.44	57.1	88.24
<sup>62</sup> Ni	55.54	3.79	57.4	96.76
<sup>65</sup> Cu	112.59	20.14	120	93.82
<sup>66</sup> Zn	125.14	12.26	111	112.74
<sup>88</sup> Sr	7200.69	1809.68	6760	106.52
<sup>107</sup> Ag	61.23	19.08	53.3	114.87
<sup>111</sup> Cd	55.58	17.90	54.6	101.79
<sup>137</sup> Ba	65.85	23.74	58.7	112.18
<sup>208</sup> Pb	72.57	38.99	56.5	128.45

**Table 6.1.9** LA-ICP-TOFMS concentration data for carbonate reference material MACS-3, standard deviations, reference values and recovery obtained for each element (\*U.S. Geological Survey [12]).

In order to obtain the trace elements distribution through the shell layers, the laser ablation was conducted on the cross-section of the samples, with the line scan tracks perpendicular to the direction of growth of the shell, from the inner to the outer surface layer (Fig. 6.1.15).

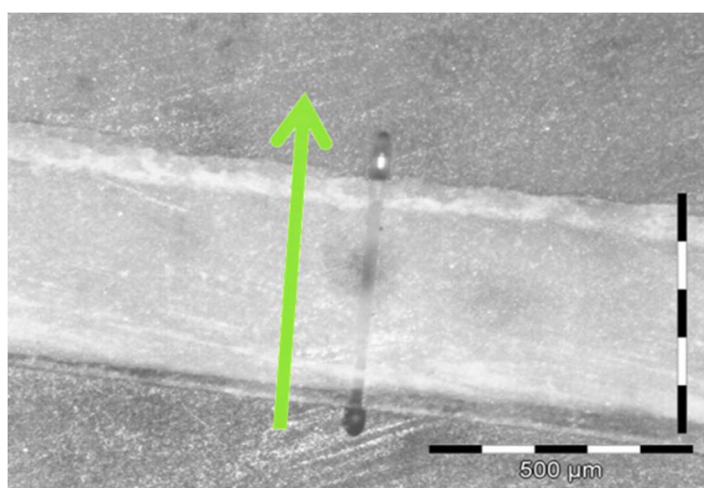


**Figure 6.1.15** Microscope image of a scallop shell cross section with the direction, perpendicular to the direction of shell growth, in which the LA-ICPTOFMS line scans were performed.

For each specimen, scans were performed in three different positions: section of the umbo region, in the middle, and on the ventral margin.

Sclerochronology is the study of physical and chemical variations in the accretionary hard tissues of invertebrates, and the temporal context in which they formed. It is particularly useful in the study of marine paleoclimatology. Sclerochronology focuses primarily upon growth patterns reflecting annual, monthly, fortnightly, tidal, daily, and sub-daily increments of time. Typical examples are the daily and sub-daily growth increments in mollusc shells as well as the annual bandings in otoliths (ear bones of fish).

Sclerochronology applied to hard parts of various organisms is now routinely used for paleoceanographic and paleoclimate reconstructions. The study includes isotopic and elemental proxies, and sometimes is termed sclerochemistry.

Sclerochronology investigation lies beyond the scope of the present work, however, some useful information can be gained from the data acquired on the sample before the contact with Cd.

In Fig. 6.1.16 the profile of the concentration ratios of Na, Mg and Sr with respect to  $^{43}\text{Ca}$  acquired on 3 different specimens is reported. Generally, for all three elements, there is variability in the concentration between the scallop shells with different colouration even though they belong to the same species. In addition, variations of the concentration can occur more or less pronounced within the same shell across the different layers (see the profiles of Na/Ca of the pink shell and Mg/Ca of the brown one). Regarding strontium, the Sr/Ca profiles show a sinusoidal trend, especially in the brown specimen, suggesting a cyclic behaviour in the incorporation of this element during the shell layers deposition, possibly related to seasonal temperature variation [13].

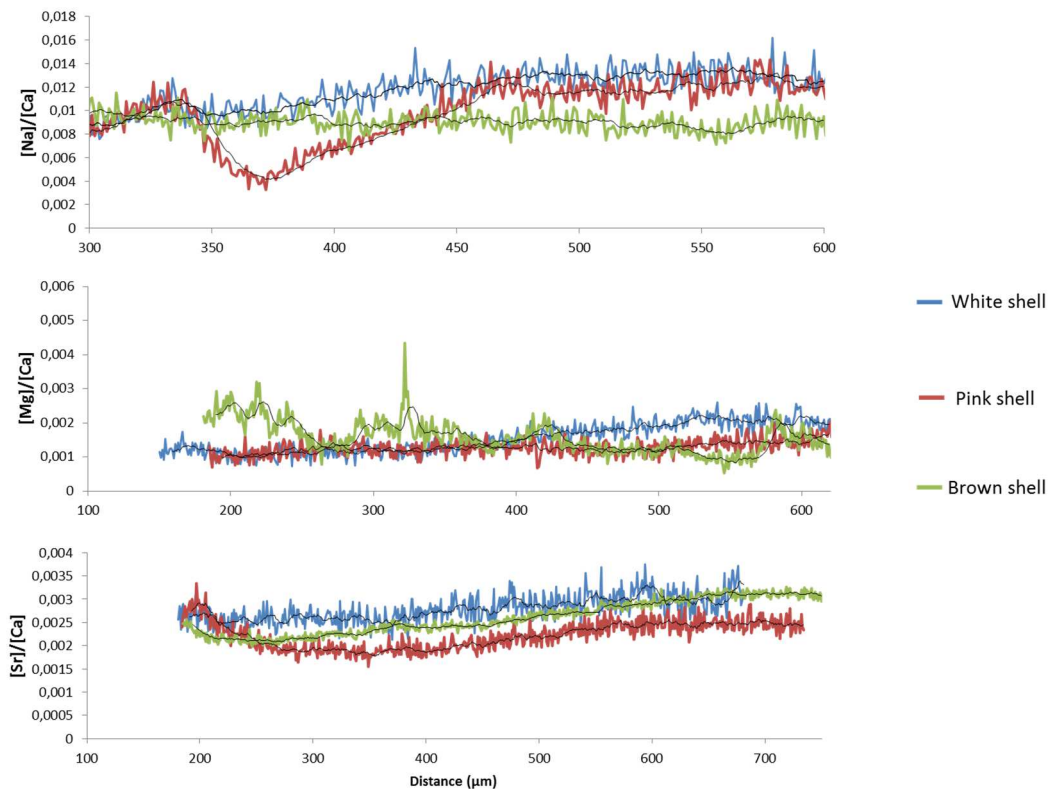


**Figure 6.1.16 Sodium, magnesium and strontium concentration profiles expressed as element/Ca ratio obtained from LA-ICP-TOFMS line scans performed on three specimens.**

In fig. 6.1.17 the Pb, V and Cd concentration profiles, reported as element/Ca ratio, performed on a scallop shell specimen of an untreated shell are shown.

Lead was detected in every shell analysed, with peak concentrations of up to  $15 \mu\text{g g}^{-1}$ . Pb shows different behaviour across the same shell, in particular the profiles obtained in the three different regions present peaks of higher concentration suggesting that during the formation of those layers the organism was surrounded by a polluted environment.

Natali and Bianchini (2018) [14] reported that the sediments of Sacca di Goro are particularly enriched regarding lead, with enrichment factors up to three with respect to the natural composition of alluvial sediments of the Padanian plain [15] taken as representative of the geogenic local background. The high Pb enrichment factor found in the lagoon sediments suggests anthropogenic contributions, possibly related to atmospheric emissions.

Vanadium is found naturally in the alluvial sediments and it was detected in shells of the Manila clam cultivated in Sacca di Goro with concentrations reaching  $9 \text{ mg kg}^{-1}$  [14].

Vanadium concentration profiles obtained from our samples (see Fig. 6.1.17) show that this trace element is always present in the carbonate matrix, with concentrations reaching  $8 \mu\text{g g}^{-1}$ , but with different trends depending on the position where the line scans were performed. To evaluate the presence and distribution of cadmium in the raw material before performing the adsorption experiments, the Cd/Ca ratio profiles were considered (see Fig. 6.1.17).

Even though cadmium was detected in almost all scans, especially in the pink and brown shells, the highest peaks did not exceed the concentration of  $2 \mu\text{g g}^{-1}$ , a value much lower than the concentrations obtained after the cadmium adsorption experiments.

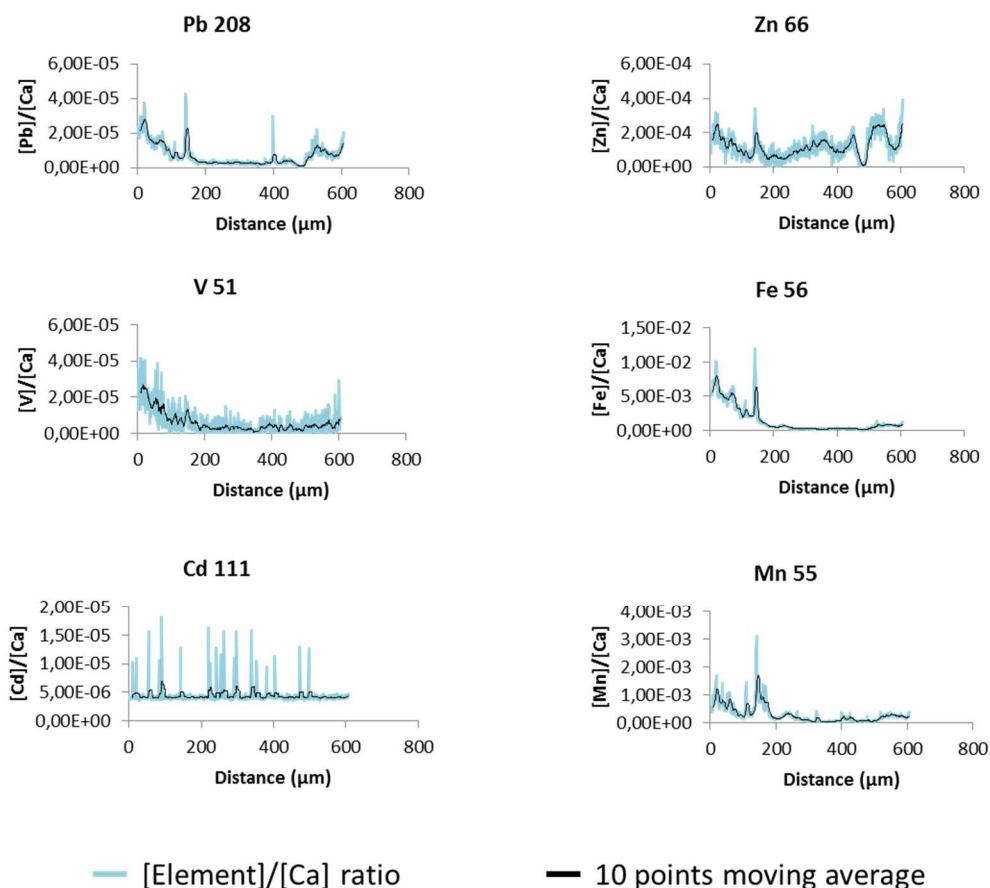


**Figure 6.1.17 Trace element concentration profiles obtained from LA-ICPTOFMS line scan carried out on a not treated brown scallop shell.**

The objective of this study was to investigate the adsorption of cadmium onto scallop shells, so to evaluate the diffusion of the metal contaminant through the shell layers LA-ICPMS was applied to obtain cadmium concentration profiles of scallop shells treated with aqueous solutions containing Cd in different concentrations. The profiles in fig. 6.1.18 show that cadmium is adsorbed mainly on the inner surface of the shell with little diffusion towards the middle. Moreover, by comparing the Cd/Ca profiles achieved from scan tracks carried out in different positions of the same specimen it can be seen that the cadmium uptake and diffusion pattern can vary across the same shell. The enrichment of cadmium mainly on the inner surface of scallop shells is in accordance with the results obtained by Sturesson (1978) [16], he found that the concentration of Cd in *Mytilus edulis* shells was higher in the nacreous layer (inner surface) when compared with the total calcium carbonate fraction. Furthermore, when considering shells of different colouration, the uptake of Cd varies, in particular, pink and brown shells show higher metal adsorption than the white ones.

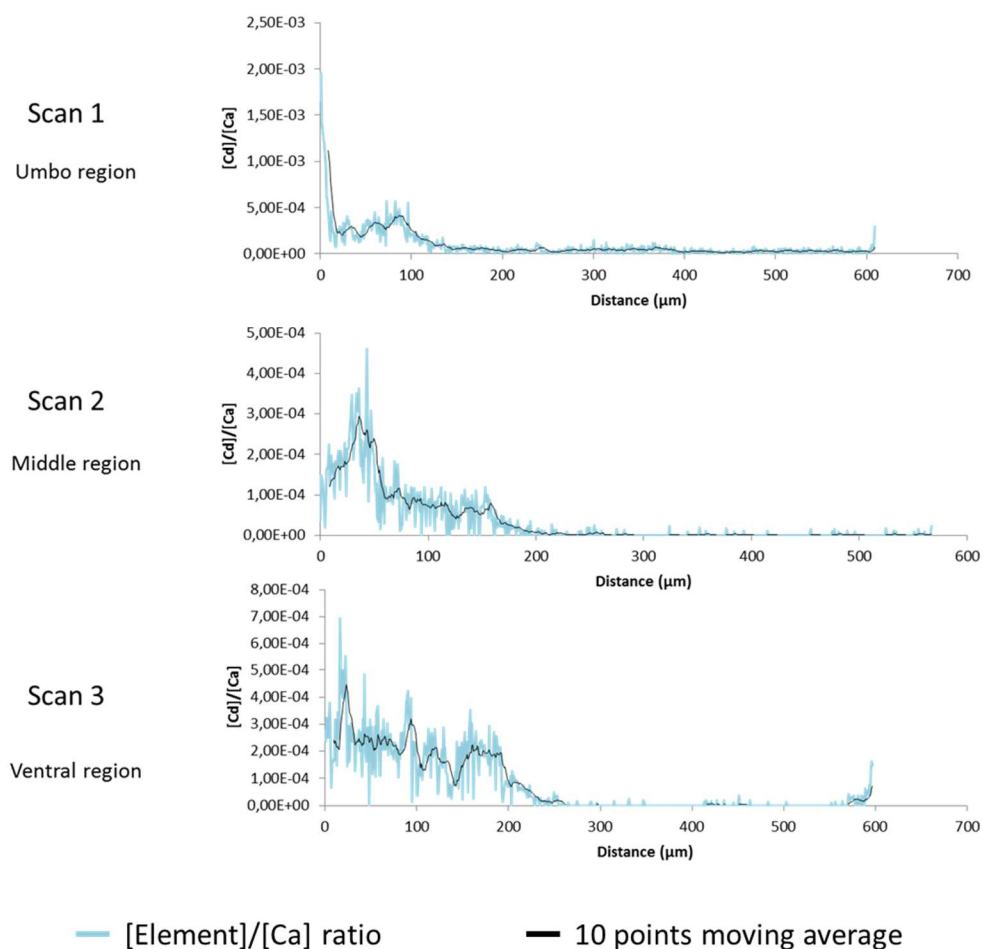


**Figure 6.1.18** Cadmium concentration profiles achieved from LA-ICP-TOFMS line scan analyses performed on three different positions of the same shell treated with cadmium solution ( $1 \text{ mg L}^{-1}$ ).

In this study we selected scallop shells presenting three different colourations (white, pink and brown).

The colouration of mollusc shells is mainly due to the presence of organic pigments, mostly tetrapyrroles, carotenoids and melanins [17]. Not only the colour and pattern of shells vary between species, but different colouration can also occur among a single species, or even a single shell can present differently coloured areas [18].

From the solution based ICP-MS analyses performed on digested shell samples, it could be concluded that darker shells adsorb the contaminant more efficiently than the white ones (Fig. 6.1.19).

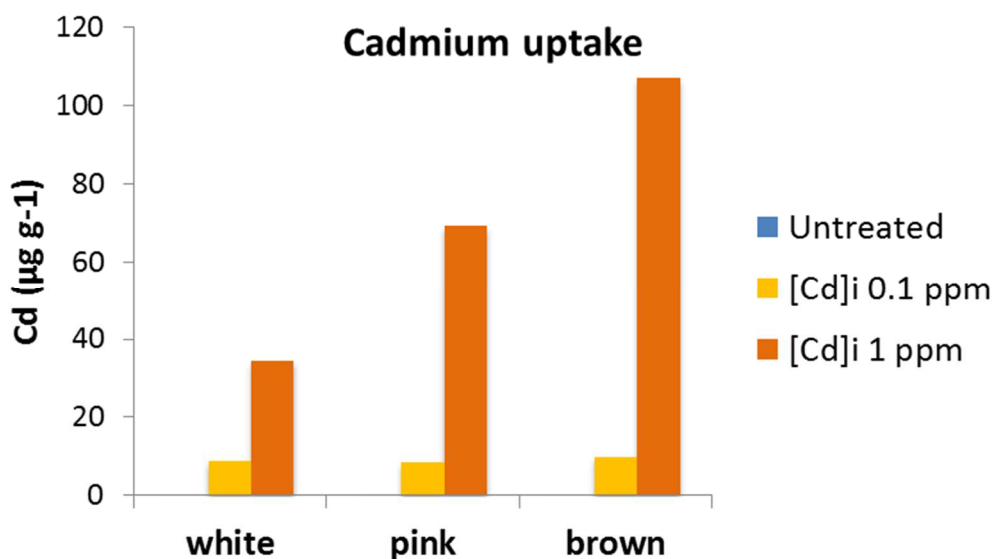


**Figure 6.1.19** Cadmium uptake onto scallop shells with different colouration treated with solutions with increasing initial Cd concentration (bulk concentration values obtained by liquid-based ICP-MS analyses).

To examine in depth this particular feature we investigated the nature of the pigments contained in our samples employing the micro-Raman technique [18-21]. Raman spectra were recorded using a Lab RAM HR Horiba spectrometer with an excitation wavelength of 632.81 nm.

In figure 6.1.20 the Raman spectra acquired on the outer surface of scallop shells presenting different colours are reported. The white shell spectrum (Fig. 6.1.20a) presents only the peaks at 1083, 707 and 274  $\text{cm}^{-1}$ , belonging to the calcite matrix, while the spectra of the pink and brown samples (Fig. 6.1.20b and 6.1.20c respectively) show two more bands, with higher intensities for the darker shells. The peaks observed at ca. 1120 and 1500  $\text{cm}^{-1}$  can be attributed to the stretching modes of the C=C double bond ( $\nu_1$ ) and the C-C single bond ( $\nu_2$ ) due to the presence of molecules characterised by a polyacetylenic chain [18, 19, 22]. In the Raman spectrum of the brown shell we observed to more bands with much lower intensity at 1010  $\text{cm}^{-1}$  and 1292  $\text{cm}^{-1}$ , the former can be attributed to the CH=CH out-of-plane wagging mode ( $\nu_4$ ) and the latter to the CH=CH in-plane rocking mode ( $\nu_3$ ) [18].

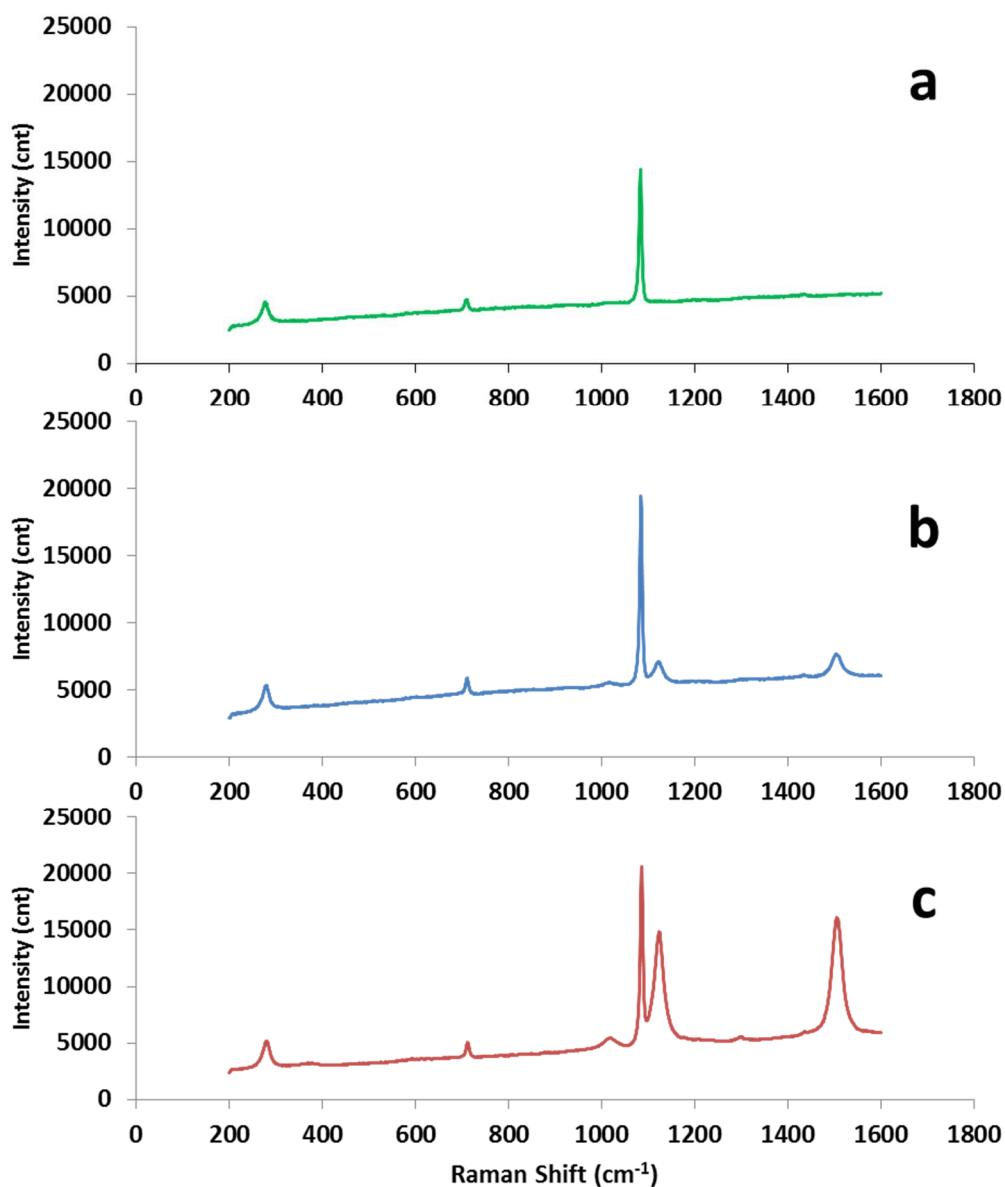


Figure 6.1.20 Micro-Raman spectra of white, pink and brown shells.

The use of micro-Raman technique allowed us to identify the nature of the scallop shell pigments as polyenes, possibly belonging to the class of carotenoids by comparison with literature [18, 21]. The presence of these organic components in the carbonate matrix results in the enhancement of the adsorption efficiency of the biogenic CaCO<sub>3</sub> towards cadmium compared to CaCO<sub>3</sub> of geologic origin [23].

### 2D Imaging

Another advantage of LA-ICP-MS technique is that it allows the acquisition of 2D elemental images of a relatively large surface providing insights into the elemental distribution across heterogeneous and multiphase samples. The elemental imaging is obtained by scanning the sample under the laser beam and acquiring the ion signals as a function of position [24].

In this work laser ablation was applied in combination with ICP-TOFMS, which allows fast and quasi-simultaneous detection of most elements of the periodic table, obtaining elemental images of small areas on the cross section of mollusc shells. In figures 6.1.21 and 6.1.22 the calcium and cadmium distribution images of two scallop shell samples, pink and brown, treated with cadmium solution are reported. From the images it can be seen that Ca intensity is constant throughout the entire section analysed for both samples.

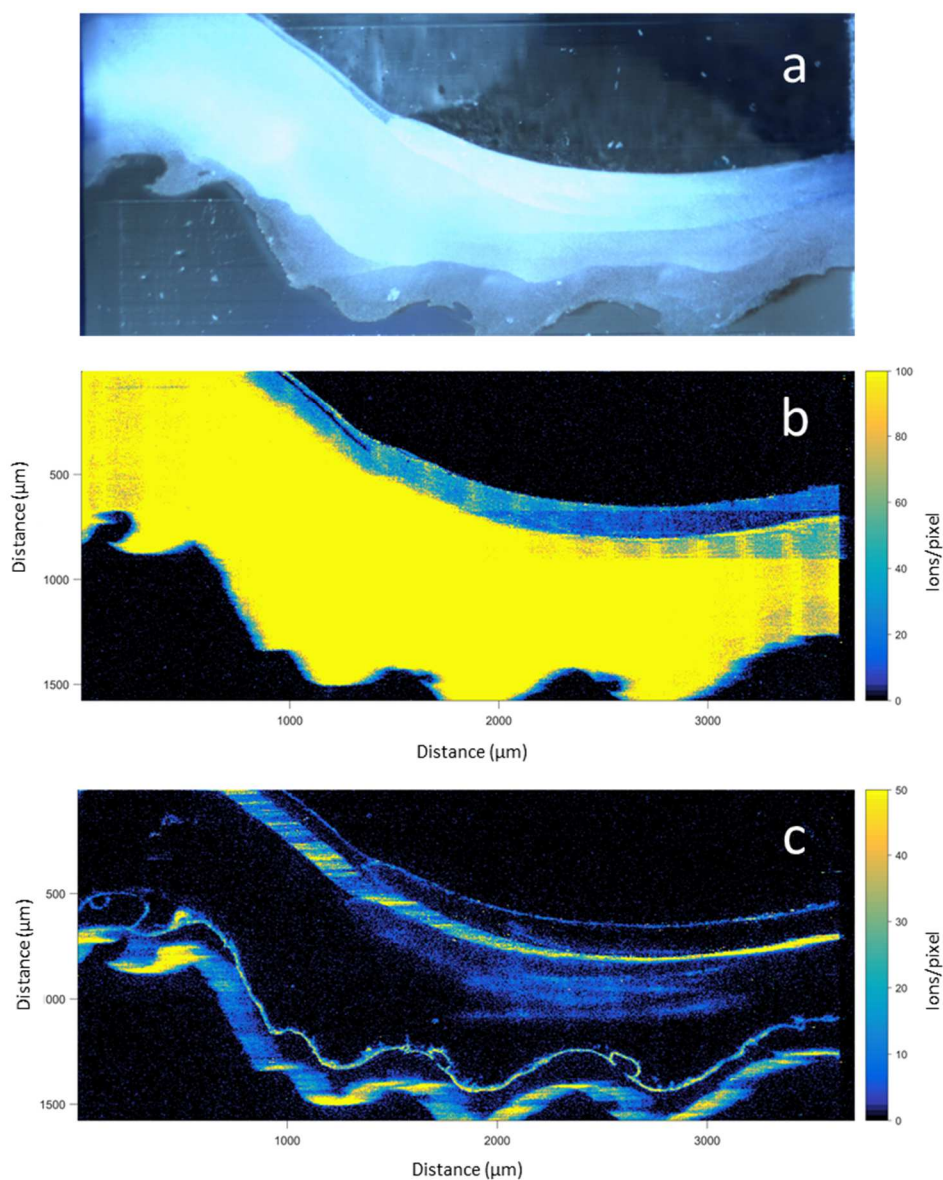
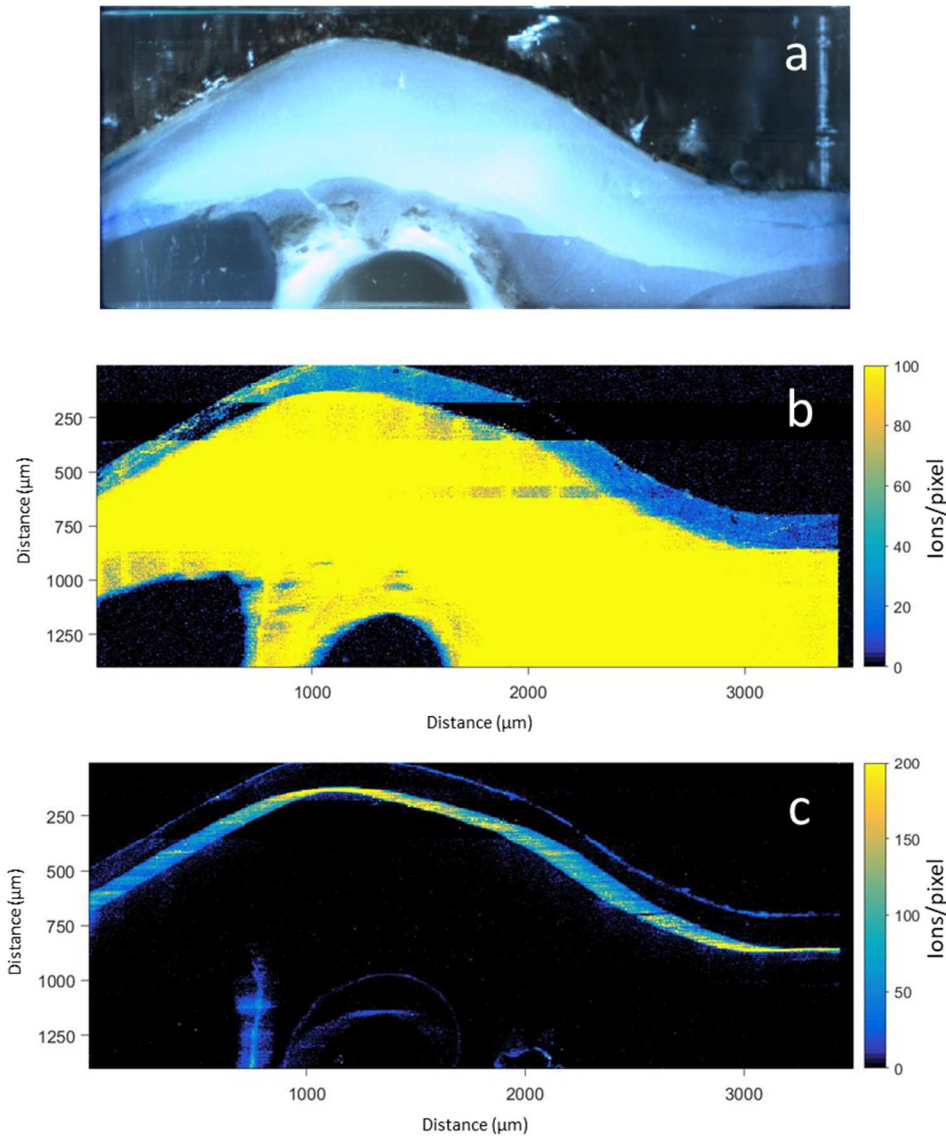


Figure 6.1.21 a) Microscope image of the section of the pink scallop shell (treated with  $1 \text{ mg kg}^{-1} \text{ Cd}$  solution) analysed in imaging mode; b)  $^{42}\text{Ca}$  distribution image; c)  $^{111}\text{Cd}$  distribution image.



**Figure 6.1.22** Microscope image of the section of the brown scallop shell (treated with  $1 \text{ mg kg}^{-1} \text{ Cd}$  solution) analysed in imaging mode; b)  $^{42}\text{Ca}$  distribution image; c)  $^{111}\text{Cd}$  distribution image.

The cadmium image of the pink scallop shell shows the metal distribution with highest ion intensities located on the inner and outer surfaces, whereas a small diffusion with lower intensity is observed in the central region of the shell section ablated. Moreover, the Cd intensity is not uniform along the surfaces, pointing out that the adsorption of the heavy metal is not homogeneous across the layer. On the other hand, the brown scallop shell presents high Cd ion intensities exclusively on the inner and outer surfaces, with no diffusion towards the internal layers. Furthermore, if we compare the intensity scales of the Cd maps of the two specimens considered, it can be seen that brown shell displays higher ion intensities than the pink one, confirming the fact that the more strongly coloured shells are

more efficient in the adsorption of the heavy metal contaminant. These observations confirm the results obtained from LA-ICPMS line scan and solution based ICPMS analyses.

### Structural analyses

To better understand the adsorption process of scallop shells towards cadmium, thermal and structural analyses were performed on the shell powders before and after Cd loading. Figure 6.1.23 reports powder diffraction patterns of both untreated (red line) and Cd-loaded (blue line) scallop shell powders, respectively, recorded under the same experimental conditions. The X-ray patterns highlighted that scallop shells are only composed of calcite, whereas in the Cd-loaded sample some additional peaks revealed the occurrence of otavite,  $\text{CdCO}_3$ .

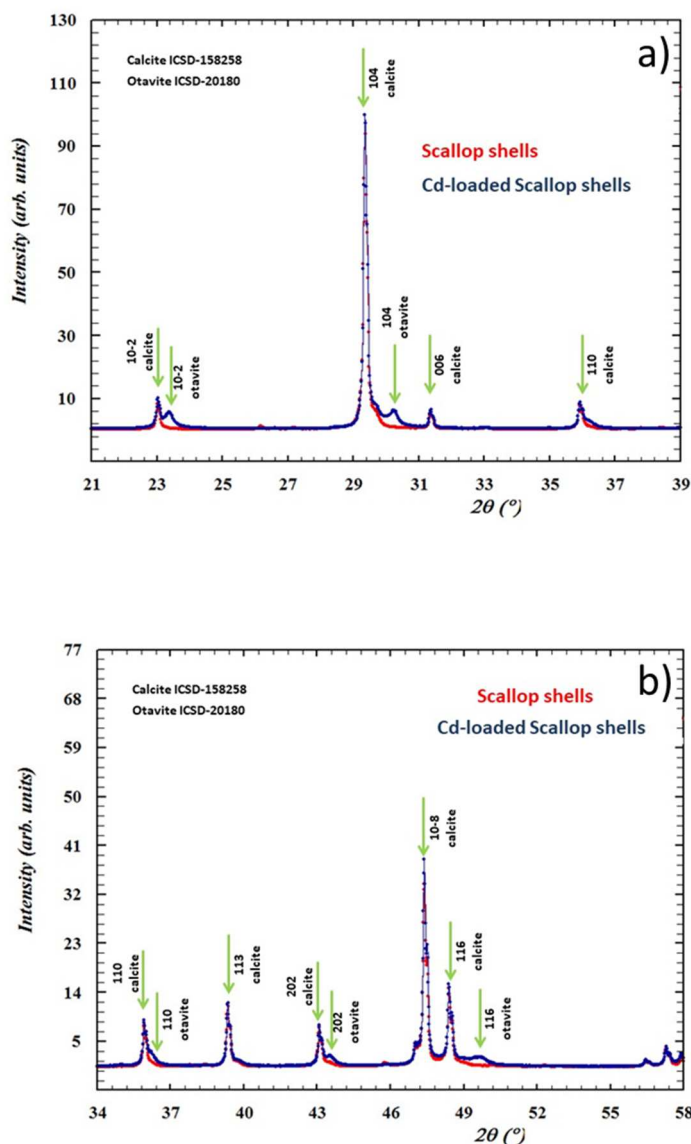


Figure 6.1.23 Comparison between XRD patterns of scallop shells (red line) and Cd- scallop shells (blue line) in the 21-39° (a) and 34-58° (b)  $2\theta$  ranges, respectively.

The Rietveld refinement was performed after identifying the crystallised minerals (ICDD cards) and finding the basic crystal structures. The refined unit cell parameters reported in Table 6.1.10 indicate that according to Stipp et al. [25] the process involved in cadmium uptake by calcite was adsorption and Cd diffusion into the outer calcite crystal, leading to the formation of  $(\text{Cd}_x\text{Ca}_{1-x})\text{CO}_3$  solid-solution. Our results indicate a distortion of the calcium octahedron, which gives rise to a contraction of both average bond length (from 2.346 Å in scallop shells to 2.327 Å in  $(\text{Cd}_x\text{Ca}_{1-x})\text{CO}_3$  Cd-loaded Scallop shells) and polyhedral volume (from = 17.151 Å<sup>3</sup> in scallop shells to 16.698 Å<sup>3</sup> in  $(\text{Cd}_x\text{Ca}_{1-x})\text{CO}_3$  Cd-loaded Scallop shells).

This finding was accompanied by a slight but significant compression of the refined unit cell volume due to the smaller ionic radius of Cadmium (0.95 Å) with respect to Calcium (1.06 Å) [26]. At the same time, the occurrence of otavite in the Cd-loaded Scallop shells sample indicated that shell calcite substrate immersed in aqueous solutions containing Cd<sup>2+</sup> acted also as passive surface, allowing the partial calcite surface dissolving and the nucleation of a minor content of otavite [27].

Scallop shells						
Calcite	Space Group	a (Å)	c (Å)	$\alpha=\beta(^{\circ})$	$\gamma(^{\circ})$	Volume(Å <sup>3</sup> )
	R -3 c	4.9987(1)	17.1099(3)	90	120	370.24(1)
Cd-loaded Scallop shells						
	Space Group	a (Å)	c (Å)	$\alpha=\beta(^{\circ})$	$\gamma(^{\circ})$	Volume(Å <sup>3</sup> )
Calcite	R -3 c	4.9981(2)	17.1109(5)	90	120	370.18(2)
Otavite	R -3 c	4.9642(2)	16.2980(8)	$\alpha,\beta$	$\gamma$	347.83(3)

Table 6.1.10 Refined unit cell parameters for scallop shells not treated and scallop shells treated with solution containing cadmium.

In order to quantify the otavite content in Cd-loaded Scallop shells, quantitative phase analysis (QPA) by use of the Rietveld method was performed. It's well known that this approach gives rise to more accurate values compared to any other single technique, such as Fourier transform infrared spectroscopy (FTIR), and electron microscopy [28-29]. In this procedure, the weight fraction  $w_i$  of each  $i^{\text{th}}$  crystalline component in the multiphase system is calculated from the corresponding refined scale parameter  $S_i$ , according to the equation:

$$w_i = \frac{S_i M_i V_i}{\sum_j S_j M_j V_j} \text{ with the normalisation condition } \sum w_i = 1.0 \quad (\text{Eq. 6.1.4})$$

with  $M_i$  and  $V_i$ , the unit cell mass and volume, respectively [30]. The final phase composition was 91% in calcite and 9% in otavite. These results are in good agreement with the data obtained from the solution-based measurements of the powdered shells.

### Thermal analyses

The nucleation of otavite was also confirmed by thermal analyses (Figure 6.1.24) showing TG/DTG curves of scallop shell (red lines) and Cd-loaded scallop shell samples (blue lines), respectively. In both samples, the weight loss at about 850°C can be attributed to the  $\text{CaCO}_3$  decomposition into calcium oxide [31], whereas the additional weigh loss in the Cd-loaded-scallop shell (temperature range 370-700°C) is ascribable to the decomposition of  $\text{CdCO}_3$  into CdO [32].

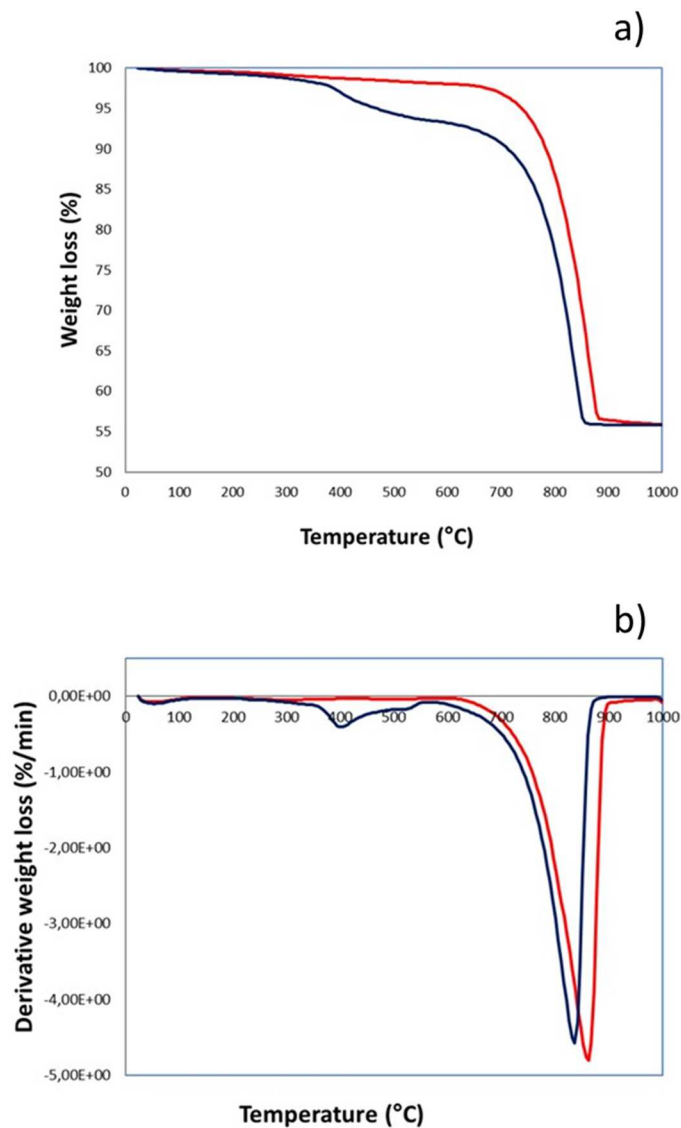


Figure 6.1.24 Comparison between TG (a) and DTG (b) curves of scallop shells (red line) and Cd- scallop shells (blue line) in the 25-1000°C temperature range.

#### 6.1.4 Conclusions

In the present work we employed scallop shells collected from Sacca di Goro to evaluate their possible use as adsorbent for the removal of metal contaminants from water bodies. As contaminant we selected cadmium because of its toxicity and environmental relevance. To study the Cd uptake and diffusion through the calcium carbonate layers of the shells we employed different analytical techniques that allowed us to evaluate the efficiency of the metal adsorption and to achieve information about the process. The shape of the adsorption isotherm combined with the relatively fast kinetics obtained from the adsorption experiments using the shell powder confirm the possible use of scallop shells as a promising adsorbent material for the removal of cadmium from water matrices.

To simulate natural water conditions, cadmium adsorption experiments were carried out from solutions with different salinity. The uptake of Cd is not significantly affected in the salinity range between 0 and 20 ‰, but for higher salinity values, the adsorption decreases due to the higher level of Cl<sup>-</sup> in solution which leads to the formation of soluble cadmium complexes.

Besides cadmium, in polluted water other metals can be present, lead and nickel were chosen due to their widespread use and adverse effects on the environment and humans. Differences in the adsorption process on scallop shell powder were observed especially between cadmium and nickel, the latter showing a slower kinetics and lower adsorption. Lead, presenting high adsorption and fast kinetics, was selected for competition experiments. The adsorption isotherm of cadmium was determined from binary aqueous solutions containing both cadmium and lead, the latter at different concentrations (0, 10 and 50 mg L<sup>-1</sup>). In the presence of lead, the saturation capacity of scallop shell powder towards cadmium decreases due to the initial preferential formation of lead carbonate phases rather than cadmium carbonate.

Concentration profiles and elemental maps acquired using LA-ICP-TOFMS on the cross section of the shells highlight the fact that cadmium is mainly adsorbed on the inner surface of the scallop shell; moreover, these results, in accordance with bulk concentration values, showed that the metal adsorption depends on the mollusc species and on the quantity of organic substances present in the calcium carbonate matrix. Indeed, we found higher cadmium uptake for scallop shells containing larger amount of organic substances. This characteristic confirms a greater adsorption efficiency of biogenic carbonates when compared to carbonates of geogenic origin.

## 6.1.5 References

- [1] Viaroli P., Giordani G., Mocenni C., Sparacino E., Lovo S., Bencivelli S. (2012) The Sacca di Goro case study. Sustainable Water Ecosystems Management in Europe, Chapter: 8, Publisher: IWA Publishing, Editors: Carlo Sessa, pp.83-95.
- [2] Yao Z., Xia M., Li H., Chen T., Ye Y., Zheng H. (2014) Bivalve Shell: Not an Abundant Useless Waste but a Functional and Versatile Biomaterial. *Critical Reviews in Environmental Science and Technology*, 44, 2502 – 2530.
- [3] Morse J. W., Arvidson R. S., Lüttge A. (2007) Calcium Carbonate Formation and Dissolution. *Chemical Reviews*, 107, 2, 342 – 381.
- [4] Pala C., Molari M., Nizzoli D., Bartoli M., Viaroli P., Manini E. (2018) Environmental Drivers Controlling Bacterial and Archaeal Abundance in the Sediments of a Mediterranean Lagoon Ecosystem. *Current Microbiology*, 75, 1147 – 1155.
- [5] Plazinski W., Dziuba J., Rudzinski W. (2013) Modeling of sorption kinetics: the pseudo-second order equation and the sorbate intraparticle diffusivity. *Adsorption*, 19, 1055 – 1064.
- [6] Ho Y. S., Ng J. C. Y., McKay G. (2001) Removal of lead(II) from effluents by sorption on peat using second-order kinetics. *Separation Science and Technology*, 36(2), 241 – 261.
- [7] Köhler S. J., Cubillas P., Rodríguez – Blanco J. D., Bauer C., Prieto M. (2007) Removal of Cadmium from Wastewaters by Aragonite Shells and the Influence of Other Divalent Cations. *Environmental Science & Technology*, 41, 112 – 118.
- [8] Green-Ruiz C., Rodriguez-Tirado V., Gomez-Gil B. (2008) Cadmium and zinc removal from aqueous solutions by *Bacillus jeotgali*: pH, salinity and temperature effects. *Bioresource Technology*, 99, 3864 – 3870.
- [9] de Souza Machado A. A., Spencer K., Kloas W., Toffolon M., Zarfl C. (2016) Metal fate and effects in estuaries: A review and conceptual model for better understanding of toxicity. *Science of the Total Environment*, 541, 268 – 281.
- [10] Ballesta-Artero I., Zhao L., Milano S., Mertz-Kraus R., Schöne B. R., van der Meer J., Witbaard R. (2018) Environmental and biological factors influencing trace elemental and microstructural properties of *Arctica islandica* shells. *Science of the Total Environment*, 645, 913 – 923.
- [11] Cariou E., Guivel C., La C., Lenta L., Elliot M. (2017) Lead accumulation in oyster shells, a potential tool for environmental monitoring. *Marine Pollution Bulletin*, 125, 19 – 29.
- [12] Jochum K. P., Scholz D., Stoll B., Weis U., Wilson S. A., Yang Q., Schwab A., Börner N., Jacob D. E., Andreae M. O. (2012) Accurate trace element analysis of speleothems and biogenic calcium carbonates by LA-ICP-MS. *Chemical Geology*, 318 – 319, 31 – 44.
- [13] Lartaud F., Chauvaud L., Richard J., Toulot A., Bollinger C., Testut L., Paulet Y. M. (2010) Experimental growth pattern calibration of Antarctic scallop shells (*Adamussium*

*colbecki*, Smith 1902) to provide a biogenic archive of high-resolution records of environmental and climatic changes. *Journal of Experimental Marine Biology and Ecology*, 393, 158 – 167.

[14] Natali C., Bianchini G. (2018) Natural vs anthropogenic components in sediments from the Po River delta coastal lagoons (NE Italy). *Environmental Science and Pollution Research*, 25, 2981 – 2991.

[15] Di Giuseppe D., Vittori Antisari L., Ferronato C., Bianchini G. (2014) New insights on mobility and bioavailability of heavy metals in soils of the Padanian alluvial plain (Ferrara Province, northern Italy). *Chemie der Erde*, 74, 615 – 623.

[16] Sturesson U. (1978) Cadmium Enrichment in Shells of *Mytilus edulis*. *Ambio*, 7(3), 122 – 125.

[17] Williams S. T. (2017) Molluscan shell colour. *Biological Reviews*, 92, 1039 - 1058.

[18] Barnard W., de Waal D. (2006) Raman investigation of pigmentary molecules in the molluscan biogenic matrix. *Journal of Raman Spectroscopy*, 37, 342 – 352.

[19] Soldati A. L., Jacob D. E., Wehrmeister U., Häger T., Hofmeister W. (2008) Micro-Raman spectroscopy of pigments contained in different calcium carbonate polymorphs from freshwater cultured pearls. *Journal of Raman Spectroscopy*, 39, 525 – 536.

[20] Thompson C. M., North E. W., White S. N., Gallager S. M. (2014) An analysis of bivalve larval shell pigments using micro-Raman spectroscopy. *Journal of Raman Spectroscopy*, 45, 349 – 358.

[21] Gaspard D., Paris C., Loubry P., Luquet G. (2019) Raman investigation of the pigment families in recent and fossil brachiopod shells. *Spectrochimica Acta Part A: Molecular and Biomolecular Spectroscopy*, 208, 73 – 84.

[22] Hedegaard C., Bardeau J. F., Chateigner D. (2005) Molluscan shell pigments: An *in situ* resonance raman study. *Journal of Molluscan Studies*, 72, 157 – 162.

[23] Tudor H. E. A., Gryte C. C., Harris C. C. (2006) Seashells: detoxifying agents for metal-contaminated waters. *Water, Air, and Soil Pollution*, 173, 209 – 242.

[24] Gundlach-Graham A., Burger M., Allner S., Schwarz G., Wang H. A. O., Gyr L., Grolimund D., Hattendorf B., Günther D. (2015) High-Speed, High-Resolution, Multielemental Laser Ablation-Inductively Coupled Plasma-Time-of-Flight Mass Spectrometry Imaging: Part I. Instrumentation and Two-Dimensional Imaging of Geological Samples. *Analytical Chemistry*, 87 (16), 8250 – 8258.

[25] Stipp S. L., Hochella Jr M. F., Parks G. A., Leckie J. O. (1992) Cd<sup>2+</sup> uptake by calcite, solid-state diffusion, and the formation of solid-solution: Interface processes observed with near-surface sensitive techniques (XPS, LEED, and AES). *Geochimica et Cosmochimica Acta*, 56(5), 1941 – 1954.

- [26] Shannon R. T., Prewitt, C. T. (1970) Revised values of effective ionic radii. *Acta Crystallographica Section B: Structural Crystallography and Crystal Chemistry*, 26(7), 1046 – 1048.
- [27] Hay M. B., Workman R. K., Manne S. (2003) Mechanisms of metal ion sorption on calcite: composition mapping by lateral force microscopy. *Langmuir*, 19(9), 3727 – 3740.
- [28] Bish D. L., Post J.E. (1993) Quantitative mineralogical analysis using the Rietveld full-pattern fitting method. *American Mineralogist.*, 78, 932 – 940.
- [29] Mumme W., Tsambourakis G., Madsen I., Hill R. (1996) Improved Petrological Modal Analyses from X-Ray Powder Diffraction Data by Use of the Rietveld Method. Part II. Selected Sedimentary Rocks. *Journal of Sedimentary Research*, 66, 132 – 138.
- [30] Gualtieri, A. F. (2003). A guided training exercise of quantitative phase analysis using EXPGUI. *GSAS Tutorials and Examples*
- [31] Halikia I., Zoumpoulakis L., Christodoulou E., Prattis D. (2001) Kinetic study of the thermal decomposition of calcium carbonate by isothermal methods of analysis. *The European Journal of Mineral Processing and Environmental Protection*, 1(2), 89 – 102.
- [32] Bultosa G., Mulokozi A. M. (1995) Kinetics of the thermal decomposition of cadmium carbonate ( $\text{CdCO}_3$ ). *Journal of Thermal Analysis*, 45, 1339 – 1348.

## 6.2 Adsorption of toluene from aqueous solutions onto zeolites

The data herein reported are part of my work of thesis and have been published in: Sarti E., Chenet T., Pasti L., Cavazzini A., Rodeghero E., Martucci A. (2017) Effects of Silica Alumina Ratio and Thermal Treatment of Beta Zeolites on the Adsorption of Toluene from Aqueous Solutions. *Minerals*, 7, 22.

### 6.2.1 Introduction

In recent years public concern has been rapidly grown regarding water pollution phenomena. Petroleum hydrocarbons represent one of the most common categories of water pollutants. Gasoline leakage from storage tank, transportation, pipelines and petrochemical wastewaters introduce these compounds into the environment, making surface waters and/or groundwaters unsuitable for many uses, including drinking [1]. BTEX (Benzene, toluene, ethylbenzene and xylene) are frequently detected in chemical and petrochemical wastewaters. These contaminants can cause adverse health effects to humans even at low concentrations [2]. Therefore, their removal from groundwater and surface waters is a problem of great importance. Among several techniques developed for BTEX removal from waters, adsorption is one of the most efficient methods, thanks to satisfactory efficiencies even at low concentrations [3], easy operation and low cost [4]. Recently, high-silica zeolites have been shown to be environmental friendly materials able to efficiently sorb several organic pollutants from water, such as pharmaceuticals [5–7], polycyclic aromatic hydrocarbons [8], phenols [9] and petrol-derived compounds [10–12]. In literature, several works have focused on the advantages of zeolites as adsorbents, such as high selectivity and capacity, rapid kinetics, reduced interference from salt and humic substances, excellent resistance to chemical, biological, mechanical and thermal stress [9,13,14]. Even if zeolites are more expensive with respect to other adsorbents, they offer the possibility to be regenerated without loss of performances at relatively low temperatures, as demonstrated in previous works [10,15].

The investigation of several synthetic zeolites such as ZSM-5 [10], mordenite [4], ferrierite [16] and Y [11] for the removal of petrol-derived compounds from aqueous solutions showed that they are a promising material for water clean-up procedures. Another adsorbent that could be employed in such treatment is zeolite beta due to its large porosity and high surface area. Zeolite beta, indeed, has a three-dimensional intersecting channels system, two mutually perpendicular straight channels each with a cross section of  $6.6 \text{ \AA} \times 6.7 \text{ \AA}$  and a sinusoidal channel with a cross section of  $5.6 \text{ \AA} \times 5.6 \text{ \AA}$  [17]. This tortuous channels system is constituted by the intersection of the two main channels. The channel intersections of zeolite beta generate cavities whose sizes are in the order of  $12\text{--}13 \text{ \AA}$  [17]. Crystallographic faults are frequently observed in beta zeolite and a structural model was proposed by

Jansen et al. [18] to explain the creation of local defects by the connection of distorted layers. The structure of zeolite beta is disordered along [00] and it is related to three ordered structures by  $a/3$  and/or  $b/3$  displacements. The three ordered polytypes are designated frameworks A, B, and C [19,20]. Polytype A is tetragonal (space group  $P4_122$  or  $P4_322$ , cell parameters  $a = b \approx 12.5 \text{ \AA}$  and  $c \approx 26.4 \text{ \AA}$ ), polytype B is monoclinic (space group  $C2/c$ , cell parameters  $a \approx b \approx 17.6 \text{ \AA}$ ,  $c \approx 14.4 \text{ \AA}$  and  $\beta \approx 114^\circ$ ), as well as Polytype C (space group  $P2/c$ , cell parameters  $a \approx b \approx 12.5 \text{ \AA}$ ,  $c \approx 27.6 \text{ \AA}$ , and  $\beta \approx 107^\circ$ ).

It has been reported that thermal and hydrothermal treatments induce chemical and structural modifications in beta zeolites, for instance Trombetta et al. [21] observed that thermal treatments can cause dealumination and formation of extraframework aluminium species. The ease of dealumination of beta may be due to the presence of defect sites close to the framework aluminium which promotes bond hydrolysis, nonetheless the microporous structure is not affected by the loss of aluminium [22]. Other zeolites, such as ZSM-5 or mordenite, do not show significant crystallinity loss or dealumination after thermal treatment [10,15,22]. The precise structural modifications of beta zeolite are still a matter of research and the global effect of calcination on beta acidity is not totally clear, because of the presence of several types of acidic sites, with different acidity degree [23,24]. However, it can be inferred that beta zeolites could undergo to greater variations in adsorption properties due to calcination with respect to other zeolites. Also the hydrophilic/hydrophobic features, controlled by varying the  $\text{SiO}_2/\text{Al}_2\text{O}_3$  ratio (SAR), can influence the behaviour of zeolites towards polar/non-polar reactants and products in adsorption and catalytic processes. In fact, the roles played both by calcination and by SAR on catalytic activity of beta zeolites received great attention [25,26]. However, there are only few works dealing with the effects of both chemical the composition and thermal treatments of beta on the adsorption properties toward solutes from water solutions. Indeed, the phenomena observed in catalytic gas phase systems could be different from those in aqueous matrix, since it has already been reported that the presence of water can strongly interfere with organic compounds adsorption [27].

Therefore, the objective of this work is to investigate the adsorptive properties of beta zeolites (notated BEAs, since they belong to BEA framework type), with different Silica/Alumina ratios (SAR) before and after calcination for the removal of toluene (TOL) from aqueous solutions. The selected adsorbents were commercial beta zeolites: the possibility to find them on the market and to use them as-received from the manufacturer was considered a strong decision point for their selection.

## 6.2.2 Materials and Methods

### *Chemicals*

Toluene (99% purity) was obtained from Sigma-Aldrich (Steinheim, Germany). High-performance liquid chromatography (HPLC) grade acetonitrile (ACN) was purchased from Merck (Darmstadt, Germany). The water was Milli-Q grade (Millipore, Billerica, MA, USA). Zeolite beta powders were obtained from Zeolyst International (Conshohocken, PA, USA) and their main characteristics are reported in Table 6.2.1.

Name	Product Code	SiO <sub>2</sub> /Al <sub>2</sub> O <sub>3</sub>	Nominal Cation	Surface Area (m <sup>2</sup> ·g <sup>-1</sup> )
Beta25	CP814E	25	Ammonium	680
Beta38	CP814C	38	Ammonium	710
Beta360	CP811C-300	360	Hydrogen	620

**Table 6.2.1 Zeolites characteristics.**

All the adsorbents were employed as-received (named Beta25, Beta38 and Beta360) and after a calcination process (referred to as Beta25c, Beta38c and Beta360c). Calcination was carried out by raising the temperature from room temperature to 600°C in 1 h, then holding at 600°C for 4 h. Finally, adsorbents were kept at room temperature for 3 h. Dry air circulation was maintained during both heating and cooling down. The calcined samples were kept in a desiccator and used within 2 days after thermal treatment.

### *Experimental*

The adsorption isotherm was determined using the batch method. Batch experiments were carried out in duplicate in 20 mL crimp top reaction glass flasks sealed with polytetrafluoroethylene (PTFE) septa (Supelco, Bellefonte, PA, USA). The flasks were filled in order to have the minimum headspace and a solid/solution ratio of 1:2 (mg mL<sup>-1</sup>) was employed. After equilibration, for 24 h at a temperature of 25.3 ± 0.5°C under stirring, the solids were separated from the aqueous solution by filtration through 0.22 µm polyvinylidene fluoride (PVDF) membrane filters purchased from Agilent Technologies (Santa Clara, CA, USA). The concentration of TOL was determined in the solutions before and after equilibration with zeolite by High Performance Liquid Chromatography/Diode Array Detection (HPLC/DAD) purchased from Waters (Waters Corporation, Milford, MA, USA).

### *Instrumentation*

The HPLC/DAD was employed under isocratic elution conditions. The column (Agilent Technologies) was 150 mm × 4.6 mm, packed with a C18 silica-based stationary phase with a particle diameter of 5 µm and thermostated at 25°C. The injection volume was 20 µL for all standards and samples. The mobile phase was a mixture ACN:H<sub>2</sub>O 70:30 and the

flow rate was 1 mL min<sup>-1</sup>. Detection wavelength was set at 215 nm. Thermogravimetric (TG), differential thermogravimetric (DTG) and differential thermal analyses (DTA) measurements of exhausted samples were performed in air up to 900°C, at 10°C min<sup>-1</sup> heating rate, using a simultaneous thermal analysis (STA) 409 PC LUX<sup>®</sup>—NETZSCH Gerätebau GmbH (Verona, Italy). X-ray powder diffraction (XRPD) patterns of zeolites after TOL adsorption were measured on a Bruker (Billerica, MA, USA) D8 Advance Diffractometer equipped with a Si (Li)SOL-X solid-state detector. Statistical elaborations were carried out through MATLAB<sup>®</sup> ver. 9.1 software (The MathWorks Inc., Natick, MA, USA).

### 6.2.3 Results and Discussion

#### *Adsorption from Aqueous Solutions*

The adsorption kinetics was studied in order to obtain some important parameters, such as the kinetic constant, which allow the estimation of the time requested for reaching the equilibrium. Moreover, from kinetics measurements, qualitative information about the steps governing the adsorption process can be gained. The uptake  $q$  (mg g<sup>-1</sup>) was calculated as follows:

$$q = \frac{(C_0 - C_e)V}{m} \quad (\text{Eq. 6.2.1})$$

where  $C_0$  is the initial concentrations in solution (mg L<sup>-1</sup>),  $C_e$  is the concentration at time  $t$  in kinetics experiments or at equilibrium (mg L<sup>-1</sup>) for isotherm modelling,  $V$  is the solution volume (L) and  $m$  is the mass of adsorbent (g).

The kinetics was very fast for all the studied materials and the time to reach equilibrium was about 10 min. As an example, the uptake data obtained for TOL on Beta360 are shown in Figure 6.2.1. The data of Figure 6.2.1 were fitted by the pseudo-second order model (Equation 6.2.2), which has been employed in many studies concerning the adsorption of organic compounds onto zeolites [28,29].

$$q_t = \frac{k_2 q^2 t}{1 + k_2 q t} \quad (\text{Eq. 6.2.2})$$

resulting high coefficients of determination ( $R^2 = 0.9915$ ). From Figure 6.2.1 it can also be seen that the surface adsorption (first part of the curve) is a faster process than the intraparticle diffusion of TOL into the zeolite micropores as already observed for ZSM-5 [10].

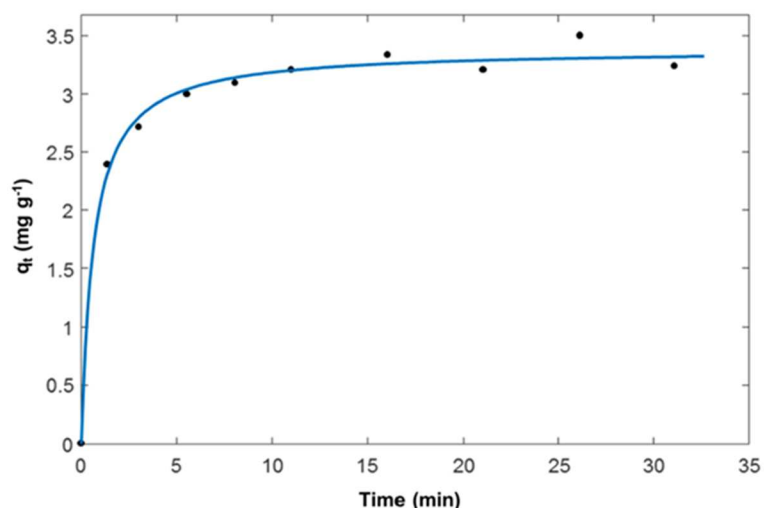


**Figure 6.2.1 Adsorption kinetics of toluene (TOL) on Beta360: TOL uptake vs. contact time.**

The relationship between the solute amount adsorbed for per unit mass of adsorbent  $q$  and its concentration at equilibrium  $C_e$  is provided by equilibrium adsorption isotherms. The Langmuir isotherm has been frequently used to describe the adsorption of organics in aqueous solutions onto hydrophobic zeolites [10,15,29]. This model considers a monolayer adsorption onto energetically equivalent adsorption sites and negligible sorbate–sorbate interactions. It can be represented by the following equation [30].

$$q = \frac{q_s b C_e}{1 + b C_e} \quad (\text{Eq. 6.2.3})$$

where  $b$  is the binding constant ( $\text{L mg}^{-1}$ ) and  $q_s$  is the saturation capacity of the adsorbent material ( $\text{mg g}^{-1}$ ). This model has already been employed for adsorption on BEAs of several classes of organic compounds, such as pharmaceuticals [6], etheramine [29], xylene isomers and ethylbenzene [31].

Freundlich isotherm is a relationship describing non-ideal and reversible adsorption, not restricted to the formation of monolayer. In fact, this empirical model can be applied to multilayer adsorption, with non-uniform distribution of adsorption heat and affinities over the heterogeneous surface [32]. The Freundlich isotherm model can be expressed as [33].

$$q = K_F C_e^{1/n} \quad (\text{Eq. 6.2.4})$$

where  $K_F$  is a constant indicative of the adsorption capacity and  $1/n$  is a measure of the surface heterogeneity, ranging between 0 and 1. The surface heterogeneity increases as  $1/n$  gets closer to zero. The Freundlich isotherm equation was found to have a better fit than the Langmuir equation for TOL adsorption on as-received BEAs (vide infra). This model was also used also by Wang et al. [28] for describing the adsorption of 1,3-propanediol on BEAs zeolites.

Another isotherm model employed to describe multiple adsorbate/adsorbent interactions is that proposed by Tóth [34].

$$q = \frac{q_s b C_e}{[1 + (b C_e)^v]^{1/v}} \quad (\text{Eq. 6.2.5})$$

where  $v$  is a parameter accounting for the heterogeneity of adsorption energies. If  $v = 1$ , the Tóth model corresponds to the Langmuir model [34].

The adsorption isotherms of TOL on both as-received and calcined BEAs are shown in Figure 6.2.2, where it can be noted that the isotherms shape of as-received and calcined beta zeolites are different from each other mainly due to modification on the adsorbate/surface interaction energy caused by calcination of the adsorbent. In particular, the thermal treatment considerably increases the adsorption efficiency of all BEAs toward TOL in the low concentration range. This finding has also been observed also for polar compounds such as pharmaceuticals [6]. It has been suggested that part of the adsorption properties of BEA zeolites originates from faults in the zeolitic structure [35]. In addition to its Brønsted acidity, beta zeolite also displays also Lewis acidity [36]. The calcination leads to the conversion of  $\text{NH}_4$ -BEA to H-BEA for Beta25 and Beta38 (see Table 6.2.1), as well as to structural and surface modifications for all the three beta zeolites [36,37]. In particular, the thermal treatment can lead to silanols condensation and, consequently, to the degradation of Brønsted acid sites by dehydroxylation. Together with the removal of water, the formation of Lewis acid sites occurs [24], as proposed by some studies [21,23] which found an increase in the ratio Lewis/Brønsted acid sites in the calcined material with respect to the as-received one. However, the global effect of calcination on beta acidity is not totally clear, because of the presence of several types of acidic sites, with different acidity degree [24,38]. It can be inferred that beta Lewis acid sites, whose formation has been promoted by thermal treatment, could interact with toluene as reported by Maretto et al. [39]. Therefore, calcination can lead to structural and compositional changes in beta zeolites, inducing to differences in adsorption properties [22,40]. The experimental data were fitted with all the three models (see Equations 6.2.3 and 6.2.5). In order to compare these models, the statistical analysis of the fitting based of the square sum of errors and the number of parameters was performed. The isotherm parameters of the best fitted model estimated by non-linear fitting of the as-received and calcined BEAs are shown in Tables 6.2.2 and 6.2.3, respectively.

As-Received Materials	$K_F(\text{mg g}^{-1}) \cdot (\text{L g}^{-1})^n$	$n$	$R^2$
Beta25	5.2 (3.5, 7.0)	0.86 (0.77, 0.95)	0.9953
Beta38	4.2 (2.5, 5.9)	0.79 (0.69, 0.89)	0.9936
Beta360	4.1 (2.8, 5.3)	0.93 (0.72, 1.1)	0.9956

**Table 6.2.2 Isotherm parameters for the adsorption of TOL on as-received BEAs estimated by non-linear fitting, according to the Freundlich model. The confidence limits at 95% of probability of the estimated parameters are reported in brackets.**

Calcined Materials	$q_s (\text{mg g}^{-1})$	$b (\text{L mg}^{-1})$	$v$	$R^2$
Beta25c	234 (193, 275)	0.073 (0.043, 0.10)	0.96 (0.70, 1.2)	0.9584
Beta38c	224 (198, 250)	0.10 (0.075, 0.13)	0.91 (0.72, 1.1)	0.9688
Beta360c	241 (201, 280)	0.55 (0.30, 0.80)	0.84 (0.62, 1.0)	0.9667

**Table 6.2.3 Isotherm parameters for the adsorption of TOL on calcined BEAs estimated by non-linear fitting, according to the Tóth model. The confidence limits at 95% of probability of the estimated parameters are reported in brackets.**

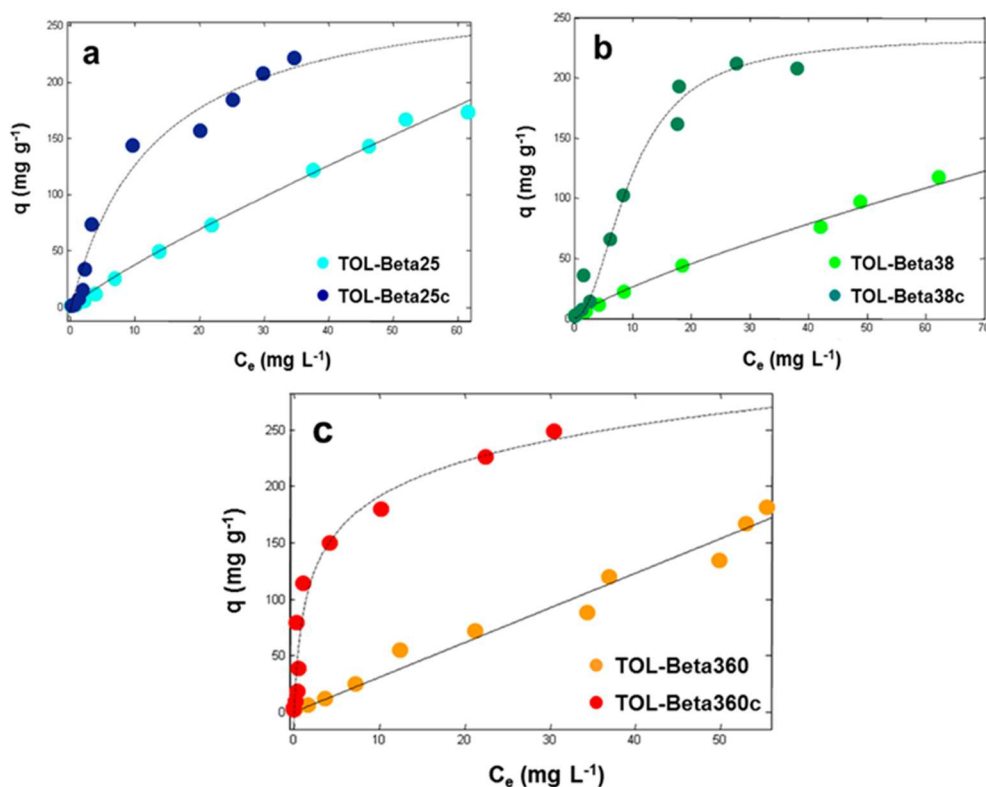


**Figure 6.2.2 Adsorption isotherms of TOL on (a) Beta25 (light blue circles: as-received, dark blue circles: calcined); (b) Beta38 (light green circles: as-received, dark green circles: calcined) and (c) Beta360 (orange circles: as-received, red circles: calcined).**

From Tables 6.2.2 and 6.2.3, it can be seen that as-received zeolites are fitted well by a Freundlich model, whereas the calcined materials are modelised by a Tóth isotherm

equation. In particular, Table 6.2.2 shows that  $n$  constant for Beta360 is not statistically different, at 95% of probability, from 1, hence TOL adsorption on this zeolite follows a linear trend. On the contrary, values of  $n$  below 1 have been observed for both Beta25 and Beta38, indicating that the adsorbent surface is heterogeneous. The values of  $K_F$  found for the three as-received BEAs are not statistically different from each other at a probability of 95%. This finding may indicate similar adsorbent/adsorbate interactions, possibly due to the effect of physisorbed water on the zeolites porosities and to the presence of structural defects in beta zeolites that make it difficult to assess the properties of the adsorption sites. By comparing calcined BEAs (Table 6.2.3), it can be seen that their saturation capacities are not statistically different at 95% of probability. High values of  $q_s$  were obtained for all the calcined adsorbents (above 20% w/w). This last finding makes calcined BEAs very promising as adsorbents in the remediation of contaminated waters at high concentration levels. Similar values of  $q_s$  were found in the adsorption of different organic contaminants on hydrophobic Y zeolite (FAU-type framework topology) [11,12]. However, the binding constants  $b$  obtained with Y zeolite were quite low, thus indicating that in the low concentrations range Y zeolite is generally less efficient than calcined BEAs. At low TOL concentrations, it has been proved that another hydrophobic zeolite, namely ZSM-5 (MFI-type framework topology) is very efficient [10]. In this case, in fact, the adsorption isotherm of TOL on ZSM-5 was characterised by a high binding constant ( $b$  was  $3.17 \pm 0.41$ ), despite the lower saturation capacity of ZSM-5 than BEAs and Y (around 8% w/w). In the light of the above findings, it can be stated that calcined BEAs represent a good compromise for that which concerning TOL adsorption from aqueous solutions in a wide concentrations range. Concerning the binding constant  $b$ , Beta360c showed a higher value than those of Beta25c and Beta38c, which are not significantly different from each other at 95% of probability. This finding could be explained by considering that adsorption onto zeolites is driven by both electrostatic and non-covalent interactions [41]. It can be supposed that electrostatic interactions have a negligible contribution to the adsorption of an organophilic solute such as TOL, characterised by  $\log K_{ow}$  of 2.73. Therefore, it can be considered that the adsorption mechanism of TOL onto BEAs is driven mainly by non-covalent interactions, which become more relevant as SAR value increases.

#### *Thermal and Structural Analyses*

Thermogravimetric analysis were carried out for the as-received materials (i.e., Beta25, Beta38 and Beta360). A total weight loss of about 17% was observed for all the three samples for temperature up to 900°C.

These weight losses can be divided up into two contributions: the first one at low temperature (i.e., lower than about 100°C) due to the loss of water molecules weakly

bonded to the zeolite surface and the second one at higher temperature mainly ascribable to the loss of ammonia from Beta25 and Beta38 as well as losses of structural water molecules and silanols condensation in all the beta samples (Figure 6.2.3).

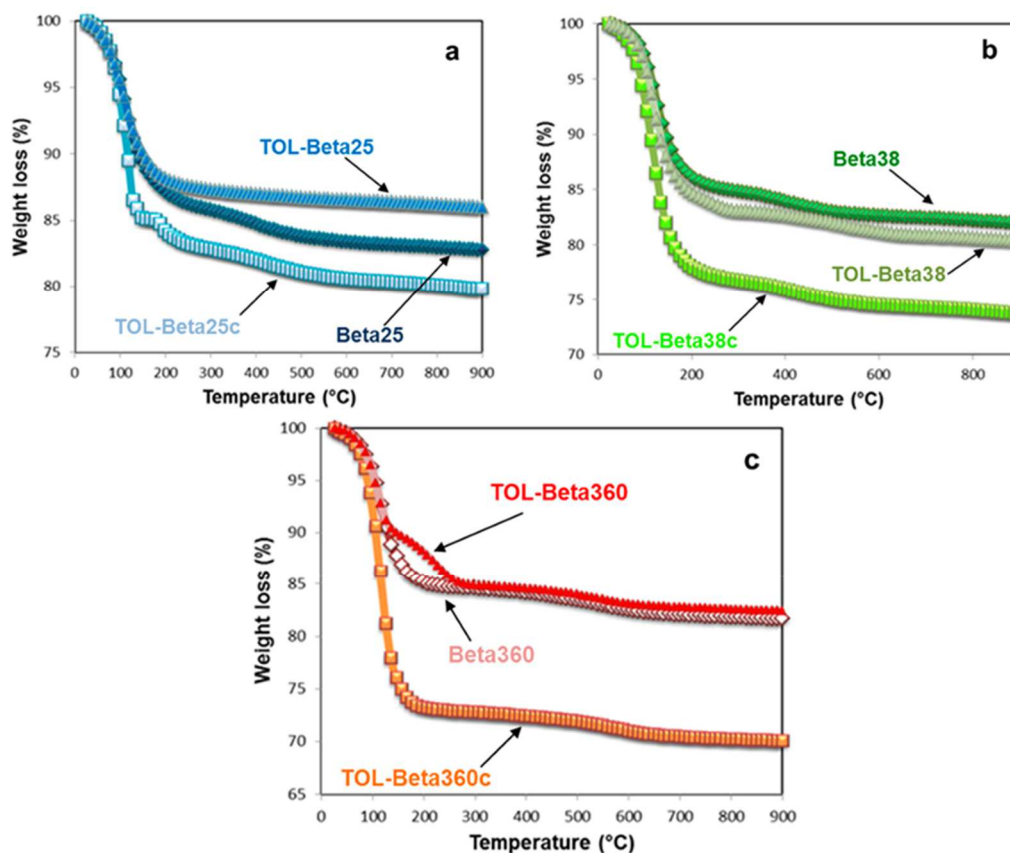


**Figure 6.2.3** Thermogravimetric curves of as-received and calcined BEAs, before and after saturation with TOL: (a) Beta25; (b) Beta38; and (c) Beta360.

The TG analyses of calcined BEAs after TOL saturation show weight losses at 900°C of 20.2%, 26.2% and 30% for Beta25c, Beta38c and Beta360c, respectively. However, these weight losses cannot be easily related to the adsorbed TOL amount since, as reported in Pasti et al. [6], the calcined zeolites can undergo to rehydration process and the temperatures at which the adsorbed water and TOL are removed from the framework are very close to each other's. This makes it difficult to ascribe the whole weight loss to water or TOL alone. However, these results are in good agreement with the saturation capacities of the materials determined by adsorption experiments (see Table 6.2.3). The X-ray powder diffraction patterns of both as-received and calcined Beta25, Beta38 and Beta360, before and after saturation with TOL are reported in Figure 6.2.4. By comparing the X-ray powder diffraction pattern of both the as-received and the calcined materials before and after TOL adsorption (see Figure 6.2.4) it can be observed that the peaks intensities in the low  $2\theta$  region change thus confirming the incorporation of molecules in the framework due to adsorption, moreover the differences in the patterns in the intermediate and high  $2\theta$  region

indicates that the process is associated with the framework flexibility (expansion or contraction of the cell volume) [42,43]. Similar behaviour is also shown when the three zeolite samples before and after thermal treatment are compared.

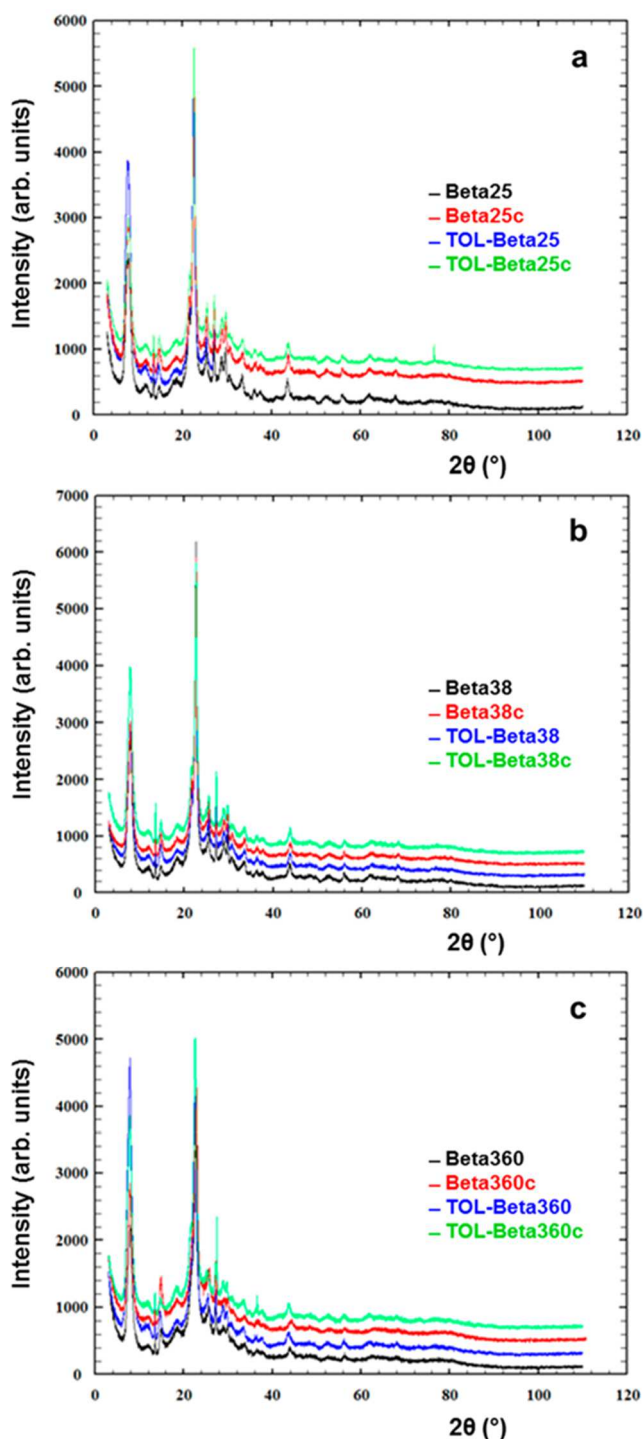


Figure 6.2.4 X-ray powder diffraction patterns of as-received and calcined BEAs before and after saturation with TOL: (a) Beta25; (b) Beta38; and (c) Beta360.

## 6.2.4 Conclusions

This work highlighted the differences in adsorption properties between as-received and calcined beta zeolites, with three different SARs, toward a water contaminant of great concern such as toluene. It has been observed that the calcination significantly improves the adsorption properties of all of the three zeolites.

The adsorption of toluene by calcined BEAs is characterised by high values of saturation capacity. The most hydrophobic calcined beta, i.e., Beta360c, showed the highest binding constant, thus indicating stronger adsorbent/adsorbate interactions than those of Beta25c and Beta38c. Consequently, Beta360 after thermal treatment is a promising adsorbent for the removal of toluene in water-containing systems. These results open new alternatives for the industrial application of this material, mainly in hydrocarbons adsorption processes in the presence of water.

## 6.2.5 References

- [1] Aivalioti M., Vamvasakis I., Gidarakos E. (2010) BTEX and MTBE adsorption onto raw and thermally modified diatomite. *J. Hazard. Mater.*, 178, 136–143.
- [2] Qu F., Zhu L., Yang K. (2009) Adsorption behaviors of volatile organic compounds (VOCs) on porous clay heterostructures (PCH). *J. Hazard. Mater.*, 170, 7–12.
- [3] Gupta V.K., Verma N. (2002) Removal of volatile organic compounds by cryogenic condensation followed by adsorption. *Chem. Eng. Sci.*, 57, 2679–2696.
- [4] Arletti R., Martucci A., Alberti A., Pasti L., Nassi M., Bagatin R. (2012) Location of MTBE and toluene in the channel system of the zeolite mordenite: Adsorption and host–guest interactions. *J. Solid State Chem.*, 194, 135–142.
- [5] Martucci A., Pasti L., Marchetti N., Cavazzini A., Dondi F., Alberti A. (2012) Adsorption of pharmaceuticals from aqueous solutions on synthetic zeolites. *Microporous Mesoporous Mater.*, 148, 174–183.
- [6] Pasti L., Sarti E., Cavazzini A., Marchetti N., Dondi F., Martucci A. (2013) Factors affecting drug adsorption on beta zeolites. *J. Sep. Sci.*, 36, 1604–1611.
- [7] Braschi I., Blasioli S., Gigli L., Gessa C.E., Alberti A., Martucci A. (2010) Removal of sulfonamide antibiotics from water: Evidence of adsorption into an organophilic zeolite Y by its structural modifications. *J. Hazard. Mater.*, 17, 218–225.
- [8] Costa A.A., Wilson W.B., Wang H., Campiglia A.D., Dias J.A., Dias S.C.L. (2012) Comparison of BEA, USY and ZSM-5 for the quantitative extraction of polycyclic aromatic hydrocarbons from water samples. *Microporous Mesoporous Mater.*, 149, 186–192.
- [9] Khalid M., Joly G., Renaud A., Magnoux P. (2004) Removal of phenol from water by adsorption using zeolites. *Ind. Eng. Chem. Res.*, 43, 5275–5280.

- [10] Rodeghero E., Martucci A., Cruciani G., Bagatin R., Sarti E., Bosi V., Pasti L. (2016) Kinetics and dynamic behaviour of toluene desorption from ZSM-5 using in situ high-temperature synchrotron powder X-ray diffraction and chromatographic techniques. *Catal. Today*, 227, 118–125.
- [11] Martucci A., Braschi I., Bisio C., Sarti E., Rodeghero E., Bagatin R., Pasti L. (2015) Influence of water on the retention of methyl tertiary-butyl ether by high silica ZSM-5 and Y zeolites: A multidisciplinary study on the adsorption from liquid and gas phase. *RSC Adv.*, 5, 86997–87006.
- [12] Pasti L., Martucci A., Nassi M., Cavazzini A., Alberti A., Bagatin R. (2012) The role of water in DCE adsorption from aqueous solutions onto hydrophobic zeolites. *Microporous Mesoporous Mater.*, 160, 182–193.
- [13] Weitkamp J. (2000) Zeolites and catalysis. *Solid State Ion.*, 131, 175–188.
- [14] Aivalioti M., Pothoulaki, D., Papoulias P., Gidaracos E. (2012) Removal of BTEX, MTBE and TAME from aqueous solutions by adsorption onto raw and thermally treated lignite. *J. Hazard. Mater.*, 207, 136–146.
- [15] Martucci A., Rodeghero E., Pasti L., Bosi V., Cruciani G. (2015) Adsorption of 1,2-dichloroethane on ZSM-5 and desorption dynamics by in situ synchrotron powder X-ray diffraction. *Microporous Mesoporous Mater.*, 215, 175–182.
- [16] Martucci A., Leardini L., Nassi M., Sarti E., Bagatin R., Pasti L. (2014) Removal of emerging organic contaminants from aqueous systems: Adsorption and location of methyl-tertiary-butylether on synthetic ferrierite. *Mineral. Mag.*, 78, 1161–1175.
- [17] Baerlocher C., Meir W.M., Olson O.H. (2001) *Atlas of Zeolite Framework Types*, 5th revised ed.; Elsevier Science: Amsterdam, The Netherlands.
- [18] Jansen J.C., Creyghton E.J., Njo S.L., van Koningsveld H., van Bekkum H. (1997) On the remarkable behaviour of zeolite Beta in acid catalysis. *Catal. Today*, 38, 205–212.
- [19] Higgins J.B., LaPierre R.B., Schlenker J.L., Rohrman A.C., Wood J.D., Kerr G.T., Rohrbaugh W.J. (1988) The framework topology of zeolite beta. *Zeolites*, 8, 446–452.
- [20] Newsam J.M., Treacy M.M.J., Koetsier W.T., De Gruyter C.B. (1988) Structural characterization of zeolite beta. *Proc. R. Soc. Lond. Ser. A*, 420, 375–405.
- [21] Trombetta M., Busca G., Storaro L., Lenarda M., Casagrande M., Zambon A. (2000) Surface acidity modifications induced by thermal treatments and acid leaching on microcrystalline H-BEA zeolite. A FTIR, XRD and MAS-NMR study. *Phys. Chem. Chem. Phys.*, 2, 3529–3537.
- [22] Beyer H.K., Nagy J.B., Karge H.G., Kiricsi I. (1995) *Catalysis by Microporous Materials*; Elsevier: Amsterdam, The Netherlands.

- [23] Otomo R., Yokoi T., Kondo J.N., Tatsumi T. (2014) Dealuminated Beta zeolite as effective bifunctional catalyst for direct transformation of glucose to 5-hydroxymethylfurfural. *Appl. Catal. A*, 470, 318–326.
- [24] Čejka J., van Bekkum H., Corma A., Schüth F. (2007) *Introduction to Zeolite Science and Practice*, 3<sup>rd</sup> revised ed., Elsevier: Amsterdam, The Netherlands.
- [25] Al-Khattaf S., Ali S.A., Aitani A.M., Žilková N., Kubička D., Čejka J. (2014) Recent advances in reactions of alkylbenzenes over novel zeolites: The effects of zeolite structure and morphology. *Catal. Rev.*, 56, 333–402.
- [26] Dědeček J., Sobalík Z., Wichterlová B. (2012) Siting and distribution of framework aluminium atoms in silicon-rich zeolites and impact on catalysis. *Catal. Rev.*, 54, 135–223.
- [27] Krishna R., van Baten J.M. (2010) Hydrogen bonding effects in adsorption of water–alcohol mixtures in zeolites and the consequences for the characteristics of the Maxwell–Stefan diffusivities. *Langmuir*, 26, 10854–10867.
- [28] Wang Z., Wu Z., Tan T. (2013) Sorption equilibrium, mechanism and thermodynamics studies of 1,3-propanediol on beta zeolite from an aqueous solution. *Bioresour. Technol.*, 145, 37–42.
- [29] Magriotis Z.M., Leal P.V.B., de Sales P.F., Papini R.M., Viana P.R.M., Augusto Arroyo P. (2014) A comparative study for the removal of mining wastewater by kaolinite, activated carbon and beta zeolite. *Appl. Clay Sci.*, 91, 55–62.
- [30] Langmuir I. (1918) The adsorption of gases on plane surfaces of glass, mica and platinum. *J. Am. Chem. Soc.*, 40, 1361–1403.
- [31] Dehkordi A.M., Khademi M. (2013) Adsorption of xylene isomers on Na-BETA zeolite: Equilibrium in batch adsorber. *Microporous Mesoporous Mater.*, 172, 136–140.
- [32] Foo K.Y., Hameed B.H. (2010) Insights into the modeling of adsorption isotherm systems. *Chem. Eng. J.*, 156, 2–10.
- [33] Freundlich H.M.F. (1906) Over the adsorption in solution. *J. Phys. Chem.*, 57, 385–471.
- [34] Tóth J. (1971) State equations of the solid gas interface layer. *Acta Chem. Acad. Sci. Hung.*, 69, 311–317.
- [35] Cambor M.A., Pérez-Pariente J. (1991) Crystallization of zeolite beta: Effect of Na and K ions. *Zeolites*, 11, 202–210.
- [36] Kunkeler P.J., Zuurdeeg B.J., van der Waal J.C., van Bokhoven J.A., Koningsberger D.C., van Bekkum H. (1998) Zeolite Beta: The relationship between calcination procedure, aluminum configuration, and lewis acidity. *J. Catal.*, 180, 234–244.
- [37] Lohse U., Altrichter B., Fricke R., Pilz W., Schreier E., Garkisch C., Jancke K. (1997) Synthesis of zeolite beta Part 2—Formation of zeolite beta and titanium-beta via an intermediate layer structure. *J. Chem. Soc. Faraday Trans.*, 93, 505–512.

- [38] Kiricsi I., Flego C., Pazzuconi G., Parker W.O., Millini R., Perego C., Bellussi G. (1994) Progress toward understanding zeolite  $\beta$  acidity: An IR and  $^{27}\text{Al}$  NMR spectroscopic study. *J. Phys. Chem.*, 98, 4627–4634.
- [39] Maretto M., Vignola R., Williams C.D., Bagatin R., Latini A., Petrangeli Papini M. (2015) Adsorption of hydrocarbons from industrial wastewater onto a silica mesoporous material: Structural and thermal study. *Microporous Mesoporous Mater.*, 203, 139–150.
- [40] Burke N.R., Trimm D.L., Howe R.F. (2003) The effect of silica:alumina ratio and hydrothermal ageing on the adsorption characteristics of BEA zeolites for cold start emission control. *Appl. Catal. B Environ.*, 46, 97–104.
- [41] Krohn J.E., Tsapatsis M. (2005) Amino acid adsorption on zeolite  $\beta$ . *Langmuir*, 21, 8743–8750.
- [42] Sánchez-Gil V., Noya E.G., Sanz A., Khatib S.J., Guil J.M., Lomba E., Marguta R., Valencia S. (2016) Experimental and simulation studies of the stepped adsorption of toluene on pure-silica MEL zeolite. *J. Phys. Chem. C*, 120, 8640–8652.
- [43] Dong J., Tian T., Ren L., Zhang Y., Xu J., Cheng X. (2015) CuO nanoparticles incorporated in hierarchical MFI zeolite as highly active electrocatalyst for non-enzymatic glucose sensing. *Colloid Surf. B*, 125, 206–212.

### **6.3 Adsorption of toluene and n-hexane onto zeolites, evaluation of competitive behaviour between aromatic and aliphatic compounds**

The data herein reported are part of my work of thesis and have been published in: – Rodeghero E., Chenet T., Martucci A., Ardit M., Sarti E., Pasti L. Selective adsorption of toluene and n-hexane binary mixture from aqueous solution on zeolite ZSM-5: Evaluation of competitive behavior between aliphatic and aromatic compounds. *Catalysis Today*, available online.

#### **6.3.1 Introduction**

It's well known that zeolites represent a benchmark in the area of porous solid-state materials, with key applications in ion exchange (ion removal and water softening), adsorption, separation and gas storage, carbon dioxide sequestration, enhanced catalysis, smart sensors and drug delivery processes [1]. These functional solid-state materials comprise pure silica which can adsorb organic components from water as well as interact with guest molecules not only at the surfaces, but throughout the bulk of the material. Hydrophobic zeolites with modular compositions and tailorable cavities are very suitable for the encapsulation of non-polar guest molecules, thus allowing for their diffusion into porosities [2–7]. Microporous aluminosilicates with uniform and ordered networks and narrow intracrystalline micropores can strongly influence selectivity in catalytic reactions as well as diffusivity through their pore channels system [6]. Their application requires that these materials have to be active not only in a wide range of operative conditions but also during prolonged periods of time. Zeolites are relatively cheap adsorbents characterised by high stability in water, effectiveness towards aggressive chemical solutions, thus representing a viable alternative to other reactive media (e.g. carbonaceous resin, activated carbon, and ion-exchange resins) [3,8,9]. Both high surface area and pore volume combined with a specific shape selectivity, ability to host guest species, and a strong stability, make these solids suitable for the removal of environmentally concerned pollutants from water such as non-methane volatile organic compounds (NMVOCs) [10–15]. Adsorption is a rapid and economical method for NMVOCs removal from water and wastewater due to the universal nature of both soluble and insoluble contaminants removal. A wide variety of NMVOCs (i.e. aliphatic/aromatic hydrocarbons and their substituted compounds, organic acids and alcohols) is present in the environment and emitted from both anthropogenic (i.e. wastewater treatment plants (WWTPs), industrial and urban wastewaters, gasoline, solvents, urban and rural run-offs) and natural (i.e. vegetation and soil microbes, geogenic, lightning, and biomass burning) sources [16,17]. Different types of zeolites are efficient in non-methane volatile organic compounds adsorption (for instance,

those with topology MFI, ITW, ERI, CHA, LTA, AFX, MOR, FER, BEA and silicalites). Their high efficiency (up to 90–99%) associated with low costs of maintenance and large functionality, make zeolites competitive towards other techniques and osmosis, ion exchange, electro-dialysis and electrolysis [10,12, 16–35,37–43]. The adsorption efficiency of zeolites could be improved or adjusted by controlling the hydrophobicity–hydrophilicity of the solid, the structure topology, the geometry of the environment of the active site and the chemical composition of the environment [6]. Due to the confinement effect, sorbate molecules in zeolites have been found to optimise van der Waals interactions with the zeolite walls by organising specific sites/microscopic cavity in order to match perfectly guest molecules size and shape to the zeolite channel/cage size and shape [44]. Consequently, the comprehension of adsorption phenomena by combining batch adsorption and X-ray powder diffraction analyses can provide a powerful tool to understand the NMVOCs selective adsorption from aqueous on zeolites as well as microscopic details for the hostguest interactions governing the competitive behaviour in complex systems. In this study we focus on the adsorption of two hydrocarbons: hexane (aliphatic) and toluene (aromatic) in order to: (i) evaluate ZSM-5 adsorption properties with respect to different type of hydrocarbons; (ii) evaluate the influence of adsorbent structure topology and NMVOCs size and shape on selectivity; (iii) gain information on location and orientation of organic compounds inside the zeolite frameworks. ZSM-5 was selected as adsorbent medium due its characteristic three dimensional micropore system whose three dimensional channel structure ensures the accessibility of host selected molecules (size of the 10-ring micropores  $\approx 5.1\text{--}5.6 \text{ \AA}$ ) (Fig. 6.3.1 a, b). Toluene (TOL) and *n*hexane (HEX) are selected as NMVOCs representative of aromatic and alkanes hydrocarbon, respectively, as well as because of their amount, emissions and toxicity [45]. This information can help with the selection of optimal adsorbent material for water remediation technology as a function of the pollutant composition.

### 6.3.2 Materials and methods

#### *Materials*

Hydrophobic ZSM-5 zeolite (code CBV 28014) supplied by Zeolyst International in its ammonium form was used as adsorbate in the present study. The characteristics reported by indicate a  $\text{SiO}_2/\text{Al}_2\text{O}_3$  molar ratio equal to 280, a  $\text{NH}_4^+$  and  $\text{Na}_2\text{O}$  contents lower than 1% and 0.05 wt.% respectively, and a surface area of  $400 \text{ m}^2 \text{ g}^{-1}$ .

### *Batch experiments*

Adsorption isotherms were determined using the batch method. Batch experiments were carried out in duplicate in 20 mL crimp top reaction glass flasks sealed with PTFE septa (Supelco, PA, USA). The flasks were filled in order to have the minimum headspace. A solid/solution ratio of 1:2 ( $\text{mg mL}^{-1}$ ) was employed, a fixed adsorbent amount was placed in contact with solution at variable composition. The samples were equilibrated for 24 h at  $20^\circ\text{C}$  ( $\pm 0.5^\circ\text{C}$ ) by keeping the flasks into jacketed glass beakers connected to a thermostated water bath (Lab Companion RW-0525G). The samples were kept under stirring by a 10-place magnetic stirrer (IKAMAG RO 10 power, IKA, Stanfer, Germany) at a stirring speed of 500 rpm. After equilibration, the solids were separated from the aqueous solution by filtration through  $0.22\ \mu\text{m}$  polyvinylidene fluoride (PVDF) membrane filters (Agilent Technologies, Santa Clara, CA, USA). To determine adsorbed quantities ( $q$ ) and equilibrium concentrations ( $C_e$ ), concentrations of TOL and/or HEX were determined in solutions after equilibration with the zeolite and in equilibrated solution not containing adsorbent. All experiments were carried out in duplicates.

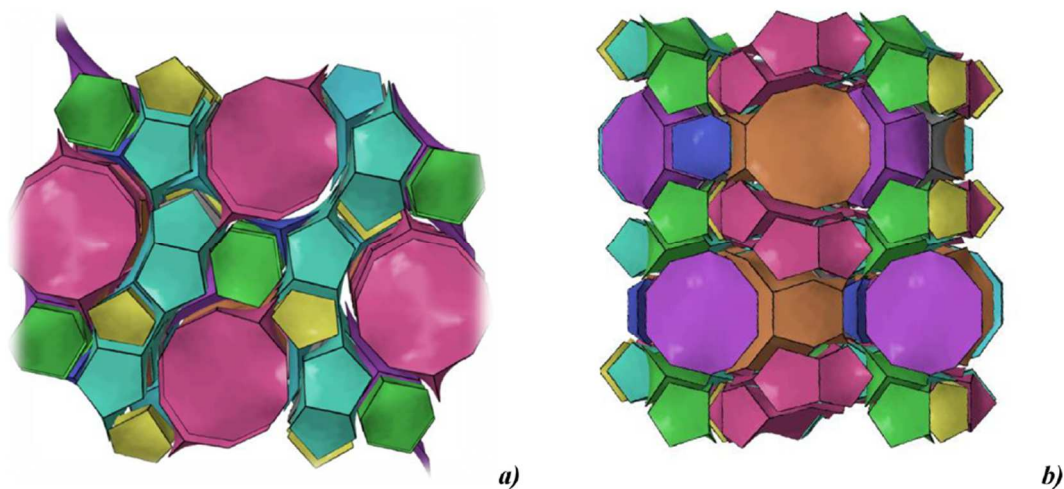


**Figure 6.3.1 Three dimensional micropore system of ZSM-5 viewed along [100] (a) and [010] (b), respectively.**

### *Gas chromatography*

The concentration of contaminants in the aqueous solution was determined by Headspace Gas Chromatography coupled to Mass Spectrometry (HS-GC-MS). The analysis was carried out using an Agilent GC-MS system (Santa Clara, CA, USA) consisting of a GC 6850 Series II Network coupled to a Pal G6500-CTC injector and a Mass Selective Detector 5973 Network. HS autosampler injector conditions are: incubation oven temperature  $80^\circ\text{C}$ , incubation time 50 min, headspace syringe temperature  $85^\circ\text{C}$ , agitation speed 250 rpm, agitation on time 30 s, agitation off time 5 s, injection volume  $500\ \mu\text{L}$ , fill speed  $30\ \mu\text{L s}^{-1}$ , syringe pull-up delay 5 s, injection speed  $250\ \mu\text{L s}^{-1}$ , pre-injection delay 0 s, post injection

delay 2 s, syringe flush 30 s with nitrogen. A DB-624 UI GC column (L=20 m, I.D.=0.18 mm,  $d_f=1.00\ \mu\text{m}$  film thickness, Agilent, Santa Clara, CA, USA) was used. High purity helium was the carrier gas with a constant flow rate of  $0.7\ \text{mL min}^{-1}$ . The oven temperature gradient started at  $40^\circ\text{C}$  for 4 min and then ramped to  $130^\circ\text{C}$  at  $15^\circ\text{C min}^{-1}$ . The injector temperature was kept at  $150^\circ\text{C}$ . All samples were injected in split mode (10:1). The mass spectrometer operated in electron impact mode (positive ion, 70 eV). The source temperature and the quadrupole temperature were set to  $230^\circ\text{C}$  and  $150^\circ\text{C}$ , respectively. The mass spectra were acquired in full scan mode. The electronic scan speed was  $1562\ \text{amu s}^{-1}$  in a mass range from 30 to 300 amu. For identification and quantification of the target analyte, the SIM (selected ion monitoring) chromatograms were extracted from the acquired signal by selecting the most abundant characteristic fragments at  $m/z$  41, 43, 57, 86 (HEX) and  $m/z=91, 92$  (TOL). Chromatographic peak of analytes was identified by comparison of the retention time and the mass spectrum with standard compound and library data; quantitative analysis was performed using calibration curves.

#### *Thermal analyses*

Thermogravimetric analysis (TGA), its derivative weight loss curve (DTG) and differential thermal analysis (DTA) on ZSM-5 before and after loading were performed using a STA 409 PC LUXX® - Netzch instrument, in order to follow pollutants mixtures release/decomposition process. The measurements were carried out at a fixed heating rate of  $10^\circ\text{C min}^{-1}$  over a temperature range of  $25\text{--}900^\circ\text{C}$  (alumina powder as reference). The degradation runs were taken under an oxidizing atmosphere (flowing dry air) for gasification at a flow rate of  $20\ \text{mL min}^{-1}$ .

#### *X-ray powder diffraction measurements and structure determination*

X-ray powder diffraction data of ZSM-5 loaded with *n*-hexane and toluene mixtures (HEX-TOL-ZSM-5) were recorded on a Bruker D8 Advance Diffractometer equipped with a Si (Li) solid-state detector, (experimental setup: Cu  $K\alpha_{1,2}$  radiation,  $3\text{--}90\ 2\theta$  range, counting time of 12 s per  $0.02\ 2\theta$  step). Structural data of ZSM-5 after only unary mixtures (i.e. one component solution) of *n*-hexane and toluene adsorption are available from the literature [11,35,46]. Nevertheless, in order to have a direct comparison by means of the same experimental setup, additional X-ray powder diffraction data collections after only *n*hexane and toluene adsorption (HEX-ZSM-5 and TOL-ZSM-5, respectively) were collected using the same strategy adopted for HEX-TOLZSM-5. All data processing was carried out by full profile Rietveld analysis using the GSAS package [47] with the EXPGUI interface [48], starting from the atomic model of Rodeghero et al. [35] in the monoclinic space group crystal system (s.g.  $P2_1/c$ ). Lattice parameters and refinement details for TOL-ZSM-5, HEX-ZSM-

5 and HEX-TOL-ZSM-5 systems are reported in Table 6.3.1. The extra-framework sites of HEX-TOL-ZSM-5 were firstly located by difference Fourier maps and then optimised using the geometry optimization tool implemented in EXPO2014 [49] (by plane wave DFT with dispersion correction, DFT-D) in order to minimise the energy of the crystal structure and to provide reasonable bond lengths and angles for HEX and TOL molecules. The positions of H atoms were also calculated. The optimised structure was then refined again with GSAS and the final structural model showed the best agreement with the experimental data. In order to secure a stable refinement, the HEX and TOL molecule coordinates were fixed in the final cycles of Rietveld refinement thus limiting the number of refined atomic displacement parameters.

	TOL-ZSM-5	HEX-ZSM-5	HEX-TOL-ZSM-5
<i>a</i> (Å)	19.9034(5)	19.9151(4)	19.8845(4)
<i>b</i> (Å)	20.1129(4)	20.1405(2)	20.1226(4)
<i>c</i> (Å)	13.3841(3)	13.4090(2)	13.4080(3)
$\alpha$	90	90	90
$\beta$	90.501(2)	90.486(1)	90.315(2)
$\gamma$	90	90	90
<i>V</i> (Å <sup>3</sup> )	5357.70(2)	5378.17(16)	5364.83(21)
Wavelength of incident radiation (Å)	1.54178	1.54178	1.54178
Refined pattern 2 $\theta$ range (°)	1-90	1-90	1-90
R <sub>wp</sub> (%)	8.8	7.7	9.5
R <sub>p</sub> (%)	6.5	5.6	6.9
R <sub>f</sub> <sup>2</sup> (%)	6.5	6.0	8.3

$$R_p = \sum [Y_{io} - Y_{ic}] / \sum Y_{io}; R_{wp} = [\sum w_i (Y_{io} - Y_{ic})^2 / \sum w_i Y_{io}^2]^{0.5}; R_{F2} = \sum |F_o^2 - F_c^2| / |F_o^2|$$

**Table 6.3.1 Lattice parameters and refinement details for TOL-ZSM-5, HEX-ZSM-5, and HEX-TOL-ZSM-5 systems.**

### 6.3.3 Results and discussion

#### *Adsorption*

The TOL–ZSM-5 system has been already investigated [35], in a wide concentration range. In Fig. 6.3.2 the adsorption isotherm of TOL on ZSM-5 in a low concentration range is reported together with that of the HEX–ZSM-5. It can be observed that the adsorbed quantity from very diluted solution is proportional to the concentration for both the systems and can be described by an adsorption isotherm type-C [36]:

$$q = KC_e \quad (\text{Eq. 6.3.1})$$

Where  $q$  is the amount of solute adsorbed for unit weight of adsorbent at the equilibrium and  $C_e$ , the concentration in the solution at equilibrium,  $K$  is the partition constant.  $K$  is roughly double for HEX, then for TOL, thus indicating a more favorable adsorption of the linear alkane with respect the aromatic compound. When a wider concentration range is considered, the TOL–ZSM-5 system is better described by a L-type isotherm, in particular a Langmuir isotherm model that has been previously employed to fit the adsorption data of various organic molecules onto zeolite. For that which concerns HEX-ZSM-5, in this case too, Langmuir isotherm model:

$$q = \frac{q_s b C_e}{1 + b C_e} \quad (\text{Eq. 6.3.2})$$

where,  $q_s$  is the saturation capacity and  $b$  the binding constant, appears to fit well the data as can be seen in Fig. 6.3.3 and from the determination coefficient in Table 6.3.2. The adsorption isotherm is characterised by a steep initial slope, which together with high  $q_s$  are desirable characteristics for adsorbent applications. In the adsorption of HEX on ZSM-5 both  $q_s$  and  $b$  are larger than those found for TOL in ref. [35], thus confirming what previously observed for the adsorption in the low concentration range. A similar behaviour has been observed in the adsorption of n-heptane and toluene onto mesoporous ZSM-5 [50]. To further investigate the selectivity of ZSM-5 with respect to HEX and TOL in aqueous solution, adsorption from equimolar binary mixtures were carried out (see Fig. 6.3.3). The effect of HEX on the competitive adsorption of TOL can be evaluated from the adsorption selectivity ( $\alpha$ ) calculated as:

$$\alpha_{TOL/HEX} = \frac{x_{z,TOL}/x_{a,TOL}}{x_{z,HEX}/x_{a,HEX}} \quad (\text{Eq. 6.3.3})$$

where  $x_z, TOL$  and  $x_z, HEX$  are the adsorbed quantity per unit mass of adsorbent material, of TOL and HEX onto ZSM-5 and  $x_a, TOL$  and  $x_a, HEX$  are the equilibrium concentration of TOL and HEX in aqueous solution, respectively. For the adsorption from equimolar binary solution the selectivity is given by the ratio of the adsorbed quantities and it approaches a value of 3.6 at saturation. Differences in the saturation capacity of ZSM-5 zeolites can be also inferred from the geometry of the channels. As a matter of fact, the analysis of shape and size of channels apertures (by means of ellipticity,  $\epsilon$ , and Crystallographic Free Area, CFA, parameters, respectively) of straight and sinusoidal channels reveals that, HEX-TOL-ZSM-5 is characterized by a CFA that in average is smaller than that of both unary mixture compounds, but a higher degree of departure from a circular shape of channel apertures ( $\epsilon$ ).

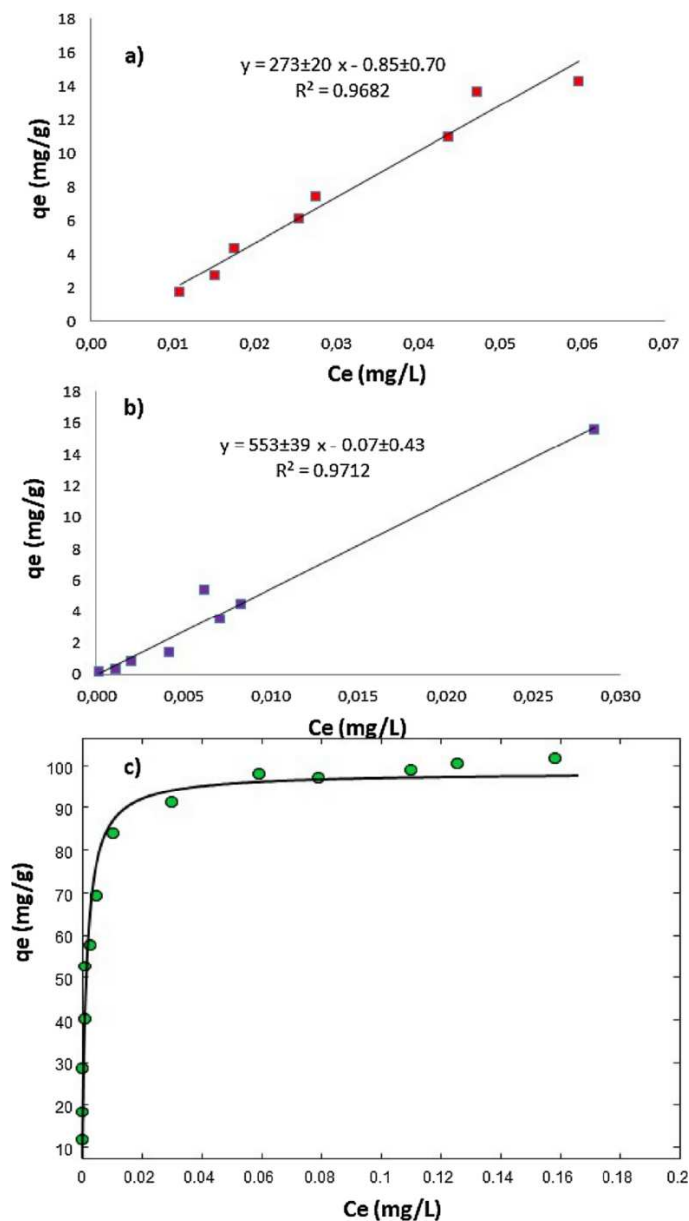


Figure 6.3.2 Adsorption isotherms (a) ZSM-5-TOL in low concentration range, ZSM-5-HEX in: (b) low concentration range, (c) wide concentration range.

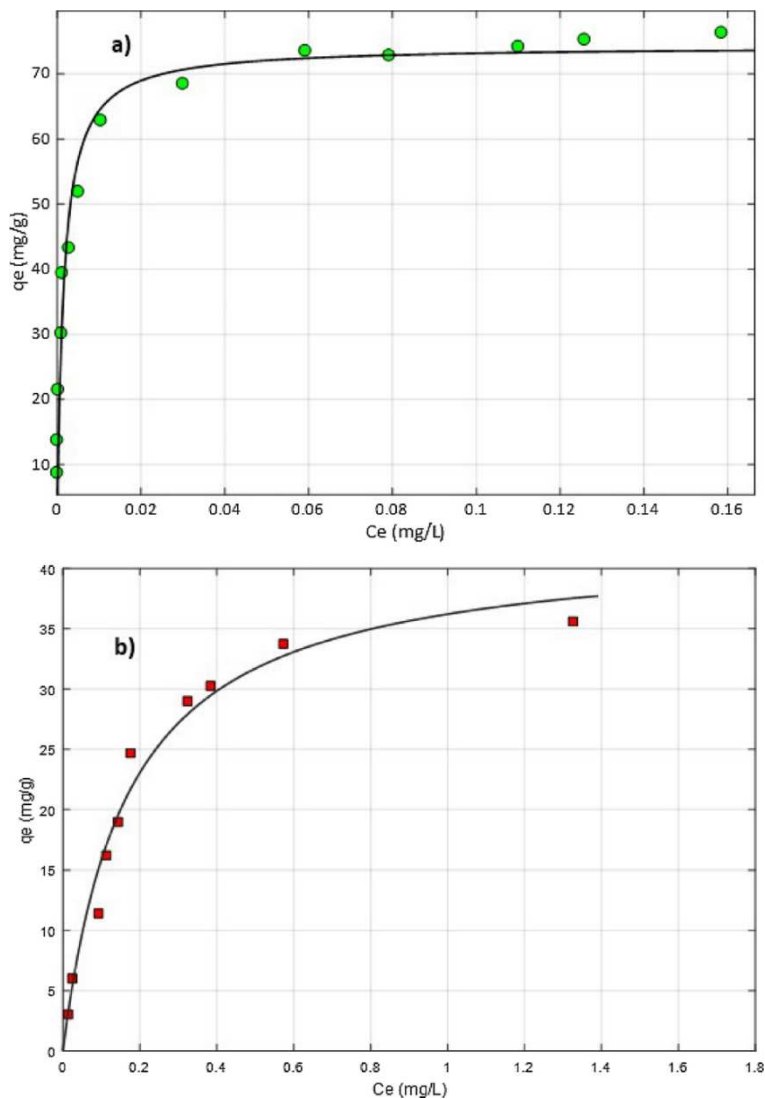


Figure 6.3.3 Adsorption isotherms of binary equimolar mixtures of HEX-TOL on ZSM-5: a) HEX; b) TOL.

			$R^2$	SSE
<b>ZSM-5-HEX</b>				
	qs	101	0.9512	595
	b	9.4		
<b>ZSM-5-HEX_TOL</b>				
HEX	qs	73.5	0.9432	384
	b	7.3		
TOL	qs	42	0.9750	38
	b	2.4		

Table 6.3.2 Isotherm parameters for the adsorption of hexane and hexane-toluene mixture on ZSM-5 (@25 °C).

### *Characterisation of TOL, HEX and HEX-TOL- loaded ZSM-5 by X-ray diffraction*

The host–guest and guest–guest interactions governing the TOL, HEX and HEX-TOL mixture adsorption were investigated by X-ray powder diffraction (XRPD). According to Rodeghero et al. [35], toluene molecules in the TOL-ZSM-5 system are spread over two crystallographic independent sites: at the straight channel (TOL1=C1, C2, C3, C4, C5, C6, C7 sites) and at the intersection between straight and sinusoidal channels (TOL2=C8, C9, C10, C11, C12, C13, C14 sites), respectively. Refinements of the atomic occupancy factors confirm the presence of 6 toluene molecules per unit cell (corresponding to about 8% in weight). Moreover, as already highlighted by Rodeghero et al. [35], the occurrence of co-adsorbed-water-toluene oligomers interacting with framework oxygens was also confirmed (Fig. 6.3.4a). Regarding the distribution of *n*-hexane molecules (Fig. 6.3.4b), the refined atomic occupancy factors indicate 8 molecules per unit cell spread over two fully occupied crystallographic independent sites: the first (i.e., HEX1) hosts 4 molecules at the intersection of straight and sinusoidal channels (in analogous way to what reported by Fujiyama et al. [51]); the second (i.e., HEX2) is occupied by 4 molecules embedded in the sinusoidal channel. The refined total *n*-hexane amount (about 10.7% in weight) well matches with the weight loss observed through the thermal analysis as shown in Fig. 6.3.5a.

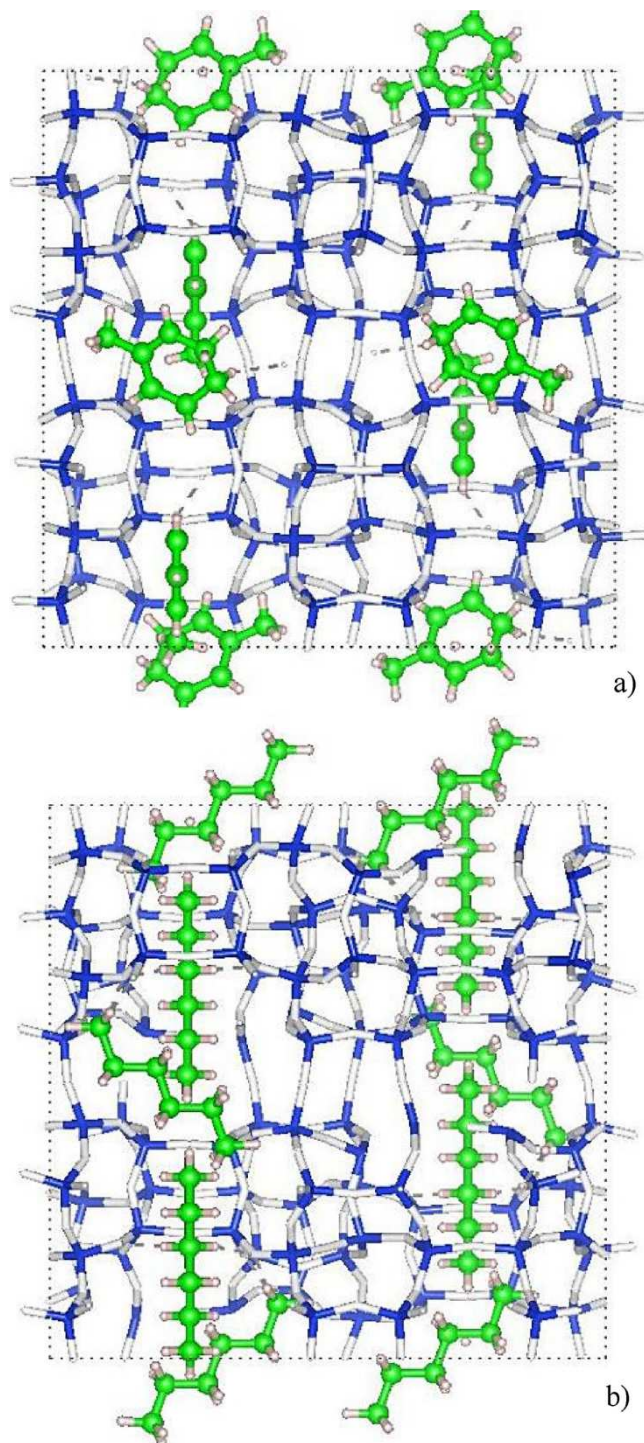


**Figure 6.3.4 Rietveld structure refinements of single component systems: a) adsorption sites of TOL in ZSM-5 structure; b) adsorption sites of HEX in ZSM-5 structure.**

The TG curve shows a gradual weight loss up to 300°C, after which the instrument recorded a plateau with 11.14% total weight loss until the end of the measurement. As regards the relation between the adsorbed organic and the ZSM-5 structure, the refined distances among the carbon sites and the framework oxygen atoms (C1-O31 2.58(1), C1-O44 2.32(1), C9-O25 2.77(1)) revealed the occurrence of host-guest interactions. No evidence of H<sub>2</sub>O molecules is recognised, but the analysis of difference Fourier maps highlights slight

disorder which could be attributed to the presence of co-adsorbed water. In both ZSM-5 loaded with unary mixtures a good correspondence with the saturation capacity estimated from the adsorption data was highlighted. After the analysis on the adsorption of samples characterised by a single organic component, attention was paid on the structural answer to organic adsorption of HEX-TOL-ZSM-5 sample, in order to test the possible competitive behaviour during the adsorption in water solution. The first evidence of effective embedding of both organics was obtained by the comparison of the collected powder diffraction patterns (Fig. 6.3.6a, b) which show slight differences in both intensity and peaks position especially at lower  $2\theta$  values. Peaks position of collected patterns scale in the following order (moving toward high  $2\theta$  values): TOL-ZSM-5 > HEX-TOL-ZSM-5 > HEX-ZSM-5, meaning that a volumetric expansion occurs from TOL-ZSM-5 to HEX-ZSM-5 samples. On the other hand, HEX-ZSM-5 show pattern very similar to that of HEX-TOL-ZSM-5 and characterised by the same peaks intensity, whereas the peaks of the TOL-ZSM-5 sample have lower intensity values. Strong similarity was also reported for lattice parameters ( $a$ ,  $b$ ,  $c$ , and  $\beta$  in Table 6.3.1) and this finding suggests a higher ZSM-5 adsorption affinity towards *n*-hexane. Rietveld structure refinements provided information about the relative position of molecules inside the structure after HEX and TOL binary mixture adsorption. Residuals of electron density calculated by mean of delta Fourier maps indicated the presence of both guest molecules but with a clear indication of preferential and differential adsorption site distribution (Fig. 6.3.7). Toluene molecules are located only in the straight channel (TOL1 site, about 0.8 molecules, corresponding to approx. 1.2% in zeolite dry weight (dw)), whereas TOL2 site (located at the channels intersections) is now empty (Fig. 6.3.7a). Molecules of *n*-hexane are always hosted at both HEX1 and HEX2 sites (7.2 HEX molecules per unit cell, corresponding to approx. 9.4% in zeolite dw) (Fig. 6.3.7b). The concentration of *n*-hexane in HEX1 site is unchanged with respect after only HEX adsorption, whereas the short distances between HEX2 and TOL1 sites prevent their simultaneous presence at the intersection of straight and sinusoidal channels; the loading of *n*-hexane in HEX2 gives rise to 3.2 molecules per unit cell. Delta Fourier maps highlight the presence of 8 co-adsorbed H<sub>2</sub>O molecules (W1 and W2 sites, respectively), corresponding to  $\approx$ 2.2% in zeolite dw. The total refined amount of adsorbed organic molecules is of about 12.5% in weight (Fig. 6.3.5a, b), in good agreement with the total weight loss (wt. %) that as estimated by means of thermal analysis as well as by adsorption methodologies. In particular, the ZSM-5-mixture DTA curve (Fig. 6.3.5c) shows a trend very similar to that obtained for HEX-ZSM-5 sample with a TOL desorption smaller contribute at the same time. The refined distances between the framework oxygen, water oxygen atoms and organic molecules suggested the occurrence of water-TOL (W1-TOL1 2.52 Å, W2-TOL2 2.96 Å) and water-HEX (W1-C3 2.94 Å, W1-C9 2.87 Å, W1-C12 2.72 Å, W2-C4 2.94 Å, W2-C9 2.83 Å, respectively) oligomers

interacting with the framework (O20-C9-HEX2 2.89 Å, O25-C12-HEX2 2.66 Å, O26-C11-HEX2 2.34 Å, O28-C9-HEX2 2.95 Å, O31-C10-HEX2 2.84 Å, O41-C11-HEX2 2.62 Å, O44-C10-HEX2 2.94 Å, respectively). In conclusion, the integration of these structural information to adsorption data allowed us to provide insights into zeolite selectivity for aromatic and alkane hydrocarbons, respectively.

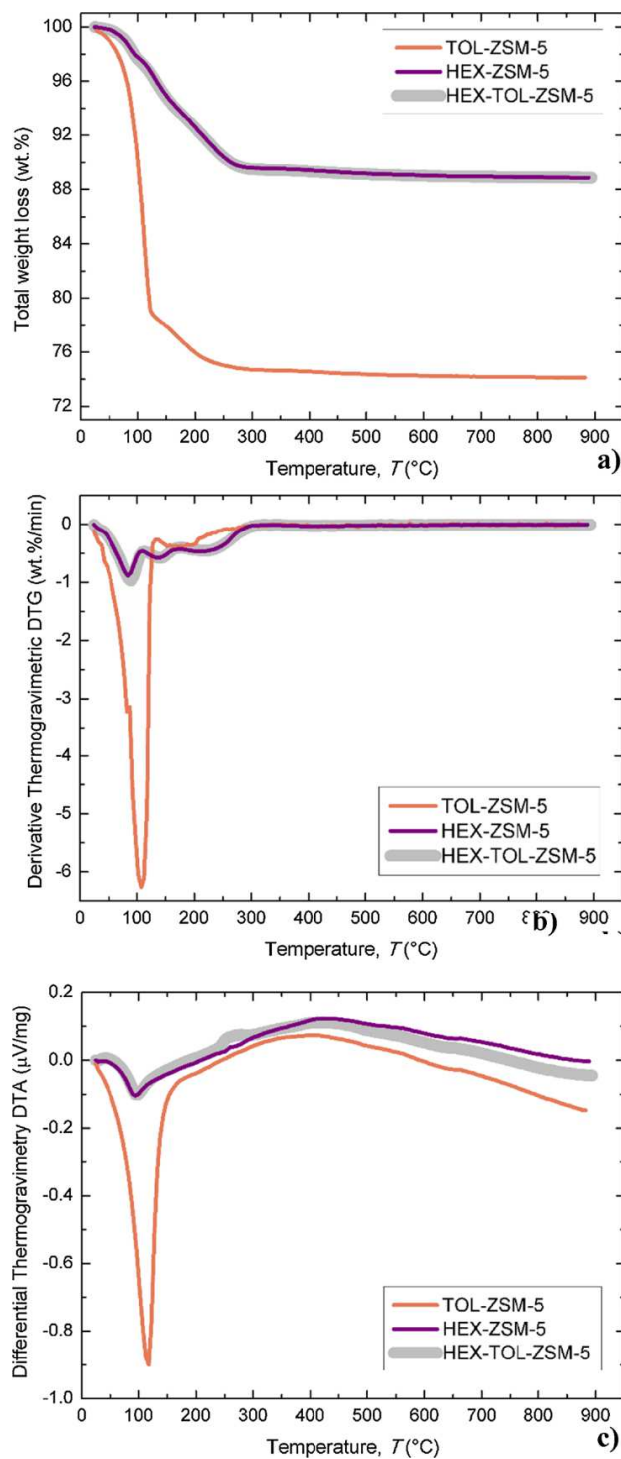


**Figure 6.3.5 Simultaneous Thermogravimetry (TG) (a); Differential Thermogravimetry (DTG) (b); Differential Thermal analyses (DTA) (c) of ZSM-5 in the temperature range 25–900 °C.**

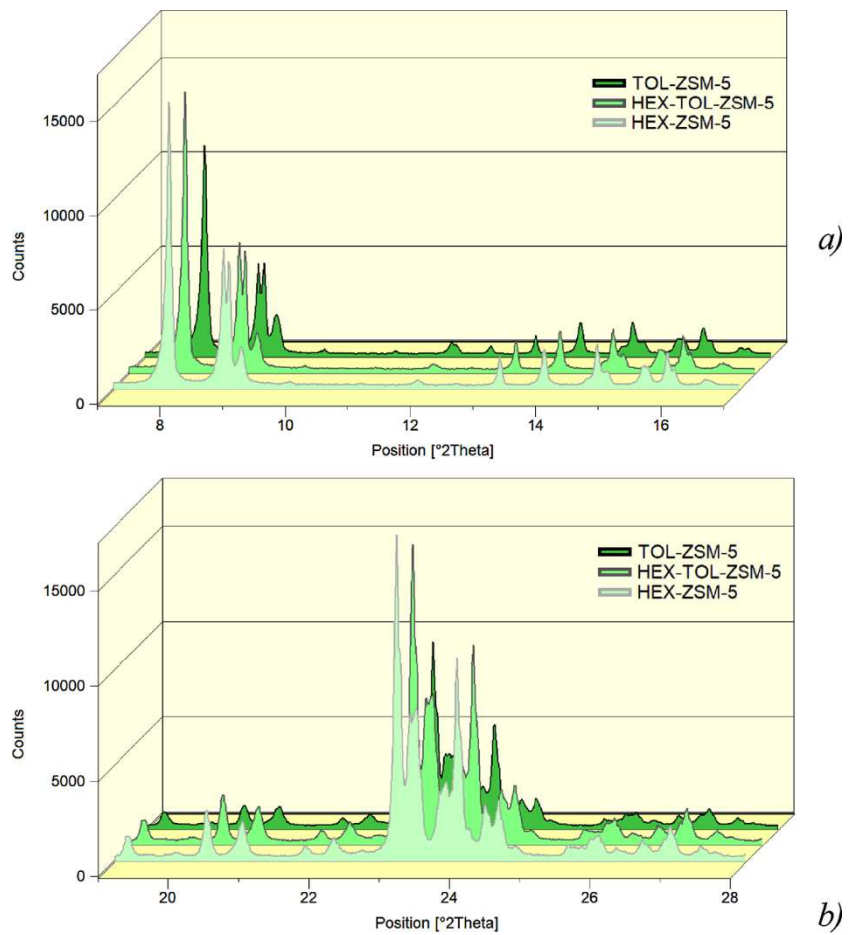


Figure 6.3.6 Cascade plot of ZSM-5 samples in selected angular ranges (7–17 °2θ, (a); and 19–28 °2θ, (b) at room temperature.

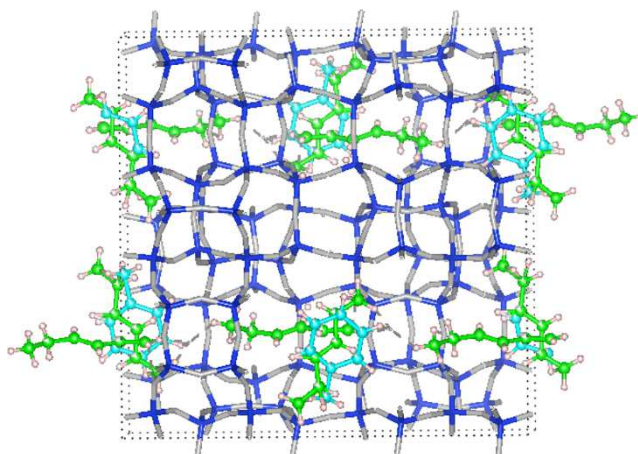


Figure 6.3.7 Adsorption sites for HEX and TOL in binary mixture along the c axis.

### 6.3.4 Conclusions

This work focused on the study of HEX and TOL absorption, in particular on the aspect of the selective behaviour of zeolite ZSM-5 regarding the adsorption of aliphatic and aromatic compounds. The evaluation of adsorption isotherm data of HEX-TOL binary mixture have suggested a higher selectivity of ZSM-5 for the alkane with respect to aromatic compound. Indeed, results pointed out that with respect to the single-component systems data (HEX-ZSM-5 and TOL-ZSM-5), the loading of both compounds in a mixture reduces the absorption of the other one. These data were resulted in a very good agreement with that was obtained both from X-ray powder diffraction and from thermal analyzes. As a matter of fact, the study of residual intensities obtained through the difference Fourier maps and the Rietveld structural investigation provided information about the relative position of HEX and TOL molecules inside the ZSM-5 adsorption sites. In particular, the refined host-guests interactions revealed a more affinity towards HEX with respect to TOL ones. This information can help with the selection of optimal adsorbent material for water remediation technology as a function of the pollutant composition.

### 6.3.5 References

- [1] Davis M. E. (2002) Ordered porous materials for emerging applications. *Nature*, 417, 813.
- [2] Braschi I., Blasioli S., Gigli L., Gessa C. E., Alberti A., Martucci A. (2010) Removal of sulfonamide antibiotics from water: evidence of adsorption into an organophilic zeolite Y by its structural modifications. *J. Hazard. Mater.* 178, 218–225.
- [3] Martucci A., Braschi I., Marchese L., Quartieri S. (2014) Recent advances in clean-up strategies of waters polluted with sulfonamide antibiotics: a review of sorbents and related properties. *Mineral. Mag.*, 78, 1115–1140.
- [4] Martucci A., Pasti L., Marchetti N., Cavazzini A., Dondi F., Alberti A. (2012) Adsorption of pharmaceuticals from aqueous solutions on synthetic zeolites. *Microporous Mesoporous Mater.*, 148, 174–183.
- [5] Stein B. A. (2003) Advanced materials progress report on advances in microporous and mesoporous solids—highlights of recent progress. *Adv. Mater.*, 763–775.
- [6] Corma A. (2003) State of the art and future challenges of zeolites as catalysts. *J. Catal.*, 216, 298–312.
- [7] Pérez-Ramírez J., Christensen C. H., Egeblad K., Christensen C. H., Groen J. C. (2008) Hierarchical zeolites: enhanced utilisation of microporous crystals in catalysis by advances in materials design. *Chem. Soc. Rev.*, 37, 2530–2542.

- [8] Ali I., Asim M., Khan T. A. (2012) Low cost adsorbents for the removal of organic pollutants from wastewater. *J. Environ. Manage.*, 113, 170–183.
- [9] Rossner A., Snyder S. A., Knappe D. R. (2009) State of the art and future challenges of zeolites as catalysts. *Water Res.*, 43, 3787–3796.
- [10] Pasti L., Rodeghero E., Sarti E., Bosi V., Cavazzini A., Bagatin R., Martucci A. (2016) Competitive adsorption of VOCs from binary aqueous mixtures on zeolite ZSM-5. *RSC Adv.*, 6 (59), 54544–54552.
- [11] Nishi K., Hidaka A., Yokomori Y. (2005) Structure of toluene6.4-ZSM-5 and the toluene disproportionation reaction on ZSM-5, *Acta Crystallogr. Sect. B: Struct. Sci.*, 61, 160–163.
- [12] Sarti E., Chenet T., Pasti L., Cavazzini A., Rodeghero E., Martucci A. (2017) Effect of silica alumina ratio and thermal treatment of beta zeolites on the adsorption of toluene from aqueous solutions. *Minerals*, 7.
- [13] Costa A. A., Wilson W. B., Wang H., Campiglia A. D., Dias J. A., Dias S. C. L. (2012) Comparison of BEA, USY and ZSM-5 for the quantitative extraction of polycyclic aromatic hydrocarbons from water samples. *Microporous Mesoporous Mater.*, 149, 186–192.
- [14] Khalid M., Joly G., Renaud A., Magnoux P. (2004) State of the art and future challenges of zeolites as catalysts. *Ind. Eng. Chem. Res.*, 43, 5275–5280.
- [15] Perego C., Bagatin R., Tagliabue M., Vignola R. (2013) Zeolites and related mesoporous materials for multi-talented environmental solutions. *Microporous Mesoporous Mater.*, 166, 37–49.
- [16] Atasoy E., Döğeroğlu T., Kara S. (2004) State of the art and future challenges of zeolites as catalysts. *Water Res.*, 38, 3265–3274.
- [17] Chary N. S., Fernandez-Alba A. R. (2012) Determination of volatile organic compounds in drinking and environmental waters. *TrAC –Trends Anal. Chem.*, 32, 60–75.
- [18] Makowski W., Majda D. (2005) Equilibrated thermodesorption studies of adsorption of n-hexane and n-heptane on zeolites Y, ZSM-5 and ZSM-11. *Appl. Surf. Sci.*, 252, 707–715.
- [19] Sun X. Y., Li J. W., Li Y. X., Yang S. C., Chen B. H. (2009) Adsorption of benzene and propylene in zeolite ZSM-5: grand canonical Monte Carlo simulations. *Chem. Res. Chin. Univ.*, 25, 377–382.
- [20] Floquet N., Coulomb J. P., Bellat J. P., Simon J. M., Weber G., Andre G. (2007) Heptane adsorption in silicalite-1: neutron scattering investigation. *J. Phys. Chem. C*, 111, 18182–18188.
- [21] Floquet N., Simon J. M., Coulomb J. P., Bellat J. P., Weber G., Andre G. (2009) Heptane adsorption in silicalite-1: molecular dynamics simulation. *Microporous Mesoporous Mater.*, 122, 61–71.
- [22] Krishna R., Calero S., Smit B. (2002) Investigation of entropy effects during sorption of mixtures of alkanes in MFI zeolite. *Chem. Eng. J.*, 88, 81–94.

- [23] Song L., Sun Z. L., Ban H. Y., Dai M., Rees L. V. C. (2005) Benzene adsorption in microporous materials. *Adsorption*, 11, 325–339.
- [24] Calero S., Schenk M., Dubbeldam D., Maesen T. L. M., Smit B. (2004) The selectivity of n-hexane hydroconversion on MOR-, MAZ-, and FAU-type zeolites. *J. Catal.*, 228, 121–129.
- [25] Denayer J. F. M., Devriese L. I., Couck S., Martens J., Singh R., Webley P. A., Baron G. V. (2008) Cage and window effects in the adsorption of n-alkanes on chabazite and SAPO-34. *J. Phys. Chem. C*, 112, 16593–16599.
- [26] Hibbe F., Chmelik C., Heinke L., Pramanik S., Li J., Ruthven D. M., et al. (2011) The nature of surface barriers on nanoporous solids explored by microimaging of transient guest distributions. *J. Am. Chem. Soc.*, 133, 2804–2807.
- [27] Krishna R., Smit B., Calero S. (2002) Entropy effects during sorption of alkanes in zeolites. *Chem. Soc. Rev.*, 31, 185–194.
- [28] Martucci A., Pasti L., Nassi M., Alberti A., Arletti R., Bagatin R., Vignola R., Sticca R. (2012) Adsorption mechanism of 1,2-dichloroethane into an organophilic zeolite mordenite: a combined diffractometric and gas chromatographic study. *Microporous Mesoporous Mater.*, 151, 358–367.
- [29] Arletti R., Martucci A., Alberti A., Pasti L., Nassi M. (2019) Location of MTBE and toluene in the channel system of the zeolite mordenite: adsorption and host–guest interactions. *J. Solid State Chem.*
- [30] Pasti L., Martucci A., Nassi M., Cavazzini A., Alberti A., Bagatin R. (2012) The role of water in DCE adsorption from aqueous solutions onto hydrophobic zeolites. *Microporous Mesoporous Mater.*, 160, 182–193.
- [31] Martucci A., Leardini L., Nassi M., Sarti E., Bagatin R., Pasti L. (2014) Removal of emerging organic contaminants from aqueous systems: adsorption and location of methyl-tertiary-butylether on synthetic ferrierite. *Mineral. Mag.*, 78, 1161–1176.
- [32] Kamiya N., Oshiro T., Tan S., Nishi K., Yokomori Y. (2013) Adsorption process of phenol on silicalite-1 and crystal structure of phenol@silicalite-1 using a single crystal X-ray diffraction method. *Microporous Mesoporous Mater.*, 169, 168–175.
- [33] Martucci A., Rodeghero E., Pasti L., Bosi V., Cruciani G. (2015) Adsorption of 1,2-dichloroethane on ZSM-5 and desorption dynamics by in situ synchrotron powder X-ray diffraction. *Microporous Mesoporous Mater.*, 215.
- [34] Kamiya N., Iwama W., Kudo T., Nasuno T., Fujiyama S., Nishi K., Yokomori Y. (2011) Determining the structure of a benzene@silicalite-1 zeolite using a single-crystal X-ray method. *Acta Crystallogr. Sect. B: Struct. Sci.*, 67, 508–515.
- [35] Rodeghero E., Martucci A., Cruciani G., Bagatin R., Sarti E., Bosi V., Pasti L. (2016) Kinetics and dynamic behaviour of toluene desorption from ZSM-5 using in situ high-

temperature synchrotron powder X-ray diffraction and chromatographic techniques. *Catal. Today*, 277.

[36] Giles C. H., Smith D., Huitson A. (1974) A general treatment and classification of the solute adsorption isotherm. I. Theoretical. *J. Colloid Interface Sci.*, 47 (3), 755–765.

[37] Gomez I. J., Arnaiz B., Cacioppo M., Arcudi F., Prato M. (2018) Nitrogen-doped Carbon Nanodots for bioimaging and delivery of paclitaxel. *J. Mater. Chem. B*, 6.

[38] Ali I., Gupta V. K. (2007) Advances in water treatment by adsorption technology. *Nat. Protoc.*, 1, 2661–2667.

[39] Gupta V. K., Ali I., Saleh T. A., Nayak A., Agarwal S. (2012) State of the art and future challenges of zeolites as catalysts. *RSC Adv.*, 2, 6380–6388.

[40] Laurencin C. T., El-Amin S. F., Ibim S. E., Willoughby D. A., Attawia M., Allcock H. R., Ambrosio A. A. (1996) A highly porous 3-dimensional polyphosphazene polymer matrix for skeletal tissue regeneration. *J. Biomed. Mater. Res.*, 30, 133–138.

[41] Ali I. (2014) Water treatment by adsorption columns: evaluation at ground level. *Sep. Purif. Rev.*, 43, 175–205.

[42] Gupta V. K., Carrott P. J. M., Ribeiro Carrott M. M. L., Suhas. (2009) Low-cost adsorbents: growing approach to wastewater treatment—a review. *Crit. Rev. Environ. Sci. Technol.*, 39, 783–842.

[43] Smith B., Maesen T. L. M. (1995) Commensurate freezing of alkanes in channels of zeolite. *Nature*.

[44] Derouane E. G. (1987) The energetics of sorption by molecular sieves: surface curvature effects. *Chem. Phys. Lett.*, 142, 200–204.

[45] Dollard G. J., Dumitrescu P., Telling S., Dixon J., Derwent R. G. (2007) Observed trends in ambient concentrations of C<sub>2</sub>–C<sub>8</sub> hydrocarbons in the United Kingdom over the period from 1993 to 2004. *Atmos. Environ.*, 41, 2559–2569.

[46] Morell H., Angermund K., Lewis A. R., Brouwer D. H., Fyfe C.A., Gies H. (2002) Structural investigation of silicalite-I loaded with n-hexane by X-ray diffraction, <sup>29</sup>Si MAS NMR, and molecular modelling. *Chem. Mater.*, 14, 2192–2198.

[47] Larson A. C., Von Dreele R. B., Alamos L. (2000) *Laur 86-748 ©*, Structure.

[48] Toby B. H. (2001) EXPGUI, a graphical user interface for GSAS. *J. Appl. Crystallogr.*, 34, 210–213.

[49] Altomare A., Cuocci C., Giacovazzo C., Moliterni A., Rizzi R., Corriero N., Falcicchio A. (2013) EXPO2013: a kit of tools for phasing crystal structures from powder data. *J. Appl. Crystallogr.*, 46, 1231–1235.

[50] Zhao H., Ma J., Zhang Q., Liu Z., Li R. (2014) Adsorption and diffusion of n-heptane and toluene over mesoporous ZSM-5 zeolites. *Ind. Eng. Chem. Res.*, 53, 13810–13819.

[51] Fujiyama Y., Seino S., Kamiya S., Nishi N., Yoza K., Yokomori Y. (2014) Adsorption structures of non-aromatic hydrocarbons on silicalite-1 using the single-crystal X-ray diffraction method. *Phys. Chem. Chem. Phys.*, 16, 15839–15845.

## 6.4 Adsorption of chlorobenzene onto zeolites

The data herein reported are part of my work of thesis and have been published in: Pasti L., Rodeghero E., Beltrami G., Ardit M., Sarti E., Chenet T., Stevanin C., Martucci A. (2018) Insights into Adsorption of Chlorobenzene in High Silica MFI and FAU Zeolites Gained from Chromatographic and Diffractometric Techniques. *Minerals*, 8, 80.

### 6.4.1 Introduction

Industrial and agricultural discharges, chlorine disinfection by-products (DBPs) of drinking water and wastewater, and incineration of wastes are the main sources of chlorine and organochlorine compounds (OCICs), such as chlorobenzene (CB). These compounds can cause toxic effects on both human health and environmental systems, even at low concentration [1]. In particular, the Environmental Protection Agency (EPA) fixed the maximum contaminant level (MCL) of CB at  $0.1 \text{ mg L}^{-1}$ ; above this threshold value CB can cause negative health effects, such as gastrointestinal irritations, hepatotoxicity and kidney damages [2]. Therefore, it is important to remove this pollutant from the environment and different methodologies have been proposed.

Actually, the physical method based on adsorption processes is a recuperative method exploited for in situ water treatments which combines high flexibility of the system, efficiency even at low concentration levels, low energy, cheap operating costs, and possible waste reductions [3]. Different adsorbent materials can be employed, and their efficiency depends on the host-guest interactions between sorbent and sorbate [4–13]. In general, carbonaceous adsorbents are low cost materials, widely employed in remediation technology. However, their applicability can be limited by fouling that cause a pore blocking (i.e., to the presence of dissolved organic matter), to low adsorption capacity, sharp rise of bed temperature and difficulty of regeneration [14–17]. In recent years, organic contaminants removal by single-walled carbon nanotubes (SWCNTs) has attracted great interest due to their chemical, electronic and mechanical properties [18]. However, the saturation capacity of these adsorbents for OCICs is moderate and functional groups on the surface of carbonaceous adsorbents can further reduce the adsorption features [19–21]. In the past few decades, surfactant modified clays have been proposed as a potential alternative to carbonaceous adsorbents for removing OCIC pollutants. Indeed, it has been proved that these materials are efficient and they can be easily regenerated. One of the main disadvantages is their limited stability due to a progressive release of surfactant which can have a negative impact on biota [22–25]. Synthetic and hydrophobic zeolites offer an attractive and efficient option for the removal of chlorine, and organochlorine compounds from water. The main advantages are related to their high surface area and porous structure, high specific capacity and organic pollutants selectivity. Additionally, fast kinetics,

mechanical, biological and chemical stability make them promising and efficient adsorbents [4,6–8,26–28]. Furthermore, their high thermal stability guarantees the possibility of regeneration through thermal treatments in order to reintroduce them in new adsorption processes [5,29–33].

This work is part of a wider study aimed at systematically evaluating the adsorptive capacity of high silica zeolites (HSZ) (e.g., mordenite, ZSM-5, faujasite, beta, ferrierite [4,7,10,29,30]) for fuel-based compounds differing in chemical properties (e.g., polarity, functional groups, size, host-guest interactions, etc.), which can provide useful information to accurately predict the behaviour of HSZs as well as improve their individual performance.

The objective of this study is to evaluate the capability of two commercial HSZs, ZSM-5 (MFI topology), and Y zeolite (FAU topology) [34], for removal of chlorobenzene (CB) from water. For that purpose, the adsorption process from water was investigated in order to gain information on the interactions between the selected organic contaminant and hydrophobic zeolites. The information gathered from this work provides a tool for the selection of adsorbent materials for environmental remediation. Additionally, the investigation of host-guest interactions can provide information on the fate and transport of OCICs in the environment, and in particular for the partition of those contaminants in the mineral fraction of soils, normally constituted by aluminosilicate.

#### **6.4.2 Materials and Methods**

High-silica Y (code HSZ-390HUA, 200 SiO<sub>2</sub>/Al<sub>2</sub>O<sub>3</sub> molar ratio, 750 m<sup>2</sup> g<sup>-1</sup> surface area, 0.05 wt % Na<sub>2</sub>O content) and ZSM-5 (code CBV 28014, 280 SiO<sub>2</sub>/Al<sub>2</sub>O<sub>3</sub> molar ratio, 400 m<sup>2</sup> g<sup>-1</sup> surface area, 0.01 wt % Na<sub>2</sub>O content) hydrophobic zeolites were purchased in their as-synthesised form by Tosoh Corporation (Tokyo, Japan) and Zeolyst International (Conshohocken, PA, USA) respectively. Chlorobenzene (CB) in its anhydrous form (purity of 99.8%) was provided by Sigma-Aldrich (Steinheim, Germany) and used as received.

##### *Batch Adsorption*

The adsorption isotherm was determined using the batch method. Batch experiments were carried out in duplicate in 20 mL crimp top reaction glass flasks sealed with PTFE septa (Supelco, Bellefonte, PA, USA). The flasks were filled in order to have the minimum headspace and a solid:solution ratio of 1:2 (mg mL<sup>-1</sup>) was employed. After equilibration, for 24 h at a temperature of 25.3 ± 0.5°C under stirring, the solids were separated from the aqueous solution using centrifugation (14,000 rpm for 30 min).

The concentration of contaminants in the aqueous solution, before and after the contact with the adsorbent was determined by Headspace Gas Chromatography coupled to Mass Spectrometry (HS-GC-MS). The analysis was carried out using an Agilent GC-MS system

(Santa Clara, CA, USA) consisting of a GC 6850 Series II Network coupled to a Pal G6500-CTC injector and a Mass Selective Detector 5973 Network. HS autosampler injector conditions are: incubation oven temperature 80°C, incubation time 50 min, headspace syringe temperature 85°C, agitation speed 250 rpm, agitation on time 30 s, agitation off time 5 s, injection volume 500  $\mu\text{L}$ , fill speed 30  $\mu\text{L s}^{-1}$ , syringe pull-up delay 5 s, injection speed 250  $\mu\text{L s}^{-1}$ , pre-injection delay 0 s, post injection delay 2 s, syringe flush 30 s with nitrogen. A DB-624 UI GC column (L = 20 m, I.D. = 0.18 mm, df = 1.00  $\mu\text{m}$  film thickness, Agilent, Santa Clara, CA, USA) was used. High purity helium was the carrier gas with a constant flow rate of 0.7  $\text{mL min}^{-1}$ . The oven temperature gradient started at 40°C for 4 min and then ramped to 130°C at 15  $^{\circ}\text{C min}^{-1}$ . The injector temperature was kept at 150°C. All samples were injected in split mode (10:1). The mass spectrometer operated in electron impact mode (positive ion, 70 eV). The source temperature and the quadrupole temperature were set to 230°C and 150°C, respectively. The mass spectra were acquired in full scan mode. The electronic scan speed was 1562  $\text{amu s}^{-1}$  in a mass range from 30 to 300  $\text{amu}$ . For identification and quantification of the target analyte the SIM (selected ion monitoring) chromatograms were extracted from the acquired signal by selecting the most abundant characteristic fragments at  $m/z = 112$ . Chromatographic peak of analytes was identified by comparison of the retention time and the mass spectrum with standard compound and library data; quantitative analysis was performed using calibration curves.

### *Thermal Analyses*

The Netzsch STA 409 PC LUXX® (Gerätebau, Germany) simultaneous TG/DTA thermogravimetric balance was employed in order to carry out both thermogravimetric (TG) and differential thermal analyses (DTA) on Y and ZSM-5 zeolites before and after CB loading. The measurements were performed in constant air flux conditions using a heating rate of 10 $^{\circ}\text{C min}^{-1}$ , from room temperature (RT) to 900°C.

### *X-ray Powder Diffraction Data Collection and Refinement Strategy*

X-ray diffraction patterns on powders of Y and ZSM-5 zeolites loaded with CB were carried out on a Bruker D8 Advance (Karlsruhe, Germany) diffractometer (Cu  $\text{K}\alpha_{1,2}$  radiation) equipped with a Sol-X detector. Diffraction data were collected at RT, in 3 $^{\circ}$ –110 $^{\circ}$  2 $\theta$  (for ZSM-5) and 3 $^{\circ}$ –100 $^{\circ}$  2 $\theta$  (for Y zeolite) 2 $\theta$  ranges respectively, with a counting time of 12 s each 0.02 $^{\circ}$  2 $\theta$ . GSAS software [35] and the EXPGUI graphical interface [36] were employed for Y–CB and ZSM-5–CB structural refinements through a full profile Rietveld analysis. Unit-cell and structural parameters were determined starting from the monoclinic  $\text{P}2_1/n$  (for ZSM-5) and the cubic  $\text{Fd-3}$  (for Y) space groups of Martucci et al. [10], and Braschi et al. [11] structural models, respectively. The Bragg peak profiles were modelled by a Pseudo-Voigt

function with 0.001% cut-off peak intensity. Refined coefficients were: two Gaussian terms (i.e., the  $\tan^2\theta$  dependent GU and the  $\theta$  independent GW), and two Lorentzian terms (i.e.,  $\cos\theta^{-1}$  dependent LX,  $\tan\theta$  dependent LY), respectively. A Chebyshev polynomial function with 24 and 22 coefficients was used in order to empirically fit the instrumental background for Y and ZSM-5, respectively. In both structural refinements, scale factor,  $2\theta$ -zero shift and unit-cell parameters were also refined. Soft constraints were initially imposed on Si–O, O–O, C–C and C–Cl bond distances (tolerance ( $\sigma$ ) value of 0.04 Å) and completely removed in the final cycles. Finally, atomic coordinates, site occupancy and isotropic atomic displacement parameters were refined. Furthermore, the displacement parameters for a given atom type were constrained to be equivalent (i.e., Si and O sites), thus limiting the number of refined atomic displacement parameters to two. Additionally, in Y–CB  $x/a$  and  $y/b$  parameters of the chlorobenzene molecule were constrained to be equal in order to maintain the planarity. Table 6.4.1 reports the details of the data collection and Rietveld refinements.

Parameter	ZSM-5	ZSM-5-CB	Y	Y-CB
	[Si <sub>96</sub> O <sub>192</sub> ]	[Si <sub>96</sub> O <sub>192</sub> ]-6(C <sub>6</sub> H <sub>5</sub> Cl)-8(H <sub>2</sub> O)	[Si <sub>192</sub> O <sub>384</sub> ]	[Si <sub>192</sub> O <sub>384</sub> ]-32(C <sub>6</sub> H <sub>5</sub> Cl)-70(H <sub>2</sub> O)
Space group	<i>P2<sub>1</sub>/n</i>	<i>P2<sub>1</sub>/n</i>	<i>Fd-3m</i>	<i>Fd-3</i>
<i>a</i> (Å)	19.899(5)	19.919(1)	24.259(1)	24.263(1)
<i>b</i> (Å)	20.117(6)	20.107(1)	24.259(1)	24.263(1)
<i>c</i> (Å)	13.389(4)	13.3967(1)	24.259(1)	24.263(1)
$\alpha$ (°)	90	90	90	90
$\beta$ (°)	90.546(3)	90.528(3)	90	90
$\gamma$ (°)	90	90	90	90
<i>V</i> (Å <sup>3</sup> )	5359.9(3)	5365.7(5)	14,277.1(1)	14,284.4(6)
Wavelength (Å): Cu K $\alpha_1$	1.540593	1.540593	1.540593	1.540593
Cu K $\alpha_2$	1.544427	1.544427	1.544427	1.544427
Refined $2\theta$ (°) range	3°–110°	3°–110°	3°–100°	3°–100°
Contributing reflections	5861	6362	620	620
<i>N</i> <sub>obs</sub>	5350	5350	4850	4850
<i>N</i> <sub>var</sub>	289	301	40	40
<i>R</i> <sub>wp</sub> (%)	10.3	13.3	12.8	12.9
<i>R</i> <sub>p</sub> (%)	9.4	10.4	12.5	12.6
<i>R</i> <sub>F</sub> <sup>2</sup> (%)	7.00	7.25	9.95	10.0

$$R_p = \Sigma[Y_{io} - Y_{ic}]/\Sigma Y_{io}; R_{wp} = [\Sigma w_i(Y_{io} - Y_{ic})^2/\Sigma w_i Y_{io}^2]^{0.5}; R_F^2 = \Sigma|F_o^2 - F_c^2|/|F_o^2|$$

**Table 6.4.1** Details of the data collection and Rietveld refinements.

### 6.4.3 Results and Discussion

#### Adsorption Isotherms from Aqueous Solutions

The uptake  $q$  ( $\text{mg g}^{-1}$ ) was calculated as follows:

$$q = \frac{(C_0 - C)V}{m} \quad (\text{Eq. 6.4.1})$$

where  $C_0$  is the initial concentrations in solution ( $\text{mg L}^{-1}$ ),  $C$  is the concentration at time  $t$  in kinetics experiments ( $\text{mg L}^{-1}$ ),  $V$  is the solution volume (L) and  $m$  is the mass of sorbent (g). In Figure 6.4.1 the uptake data for CB on Y and ZSM-5 are reported.

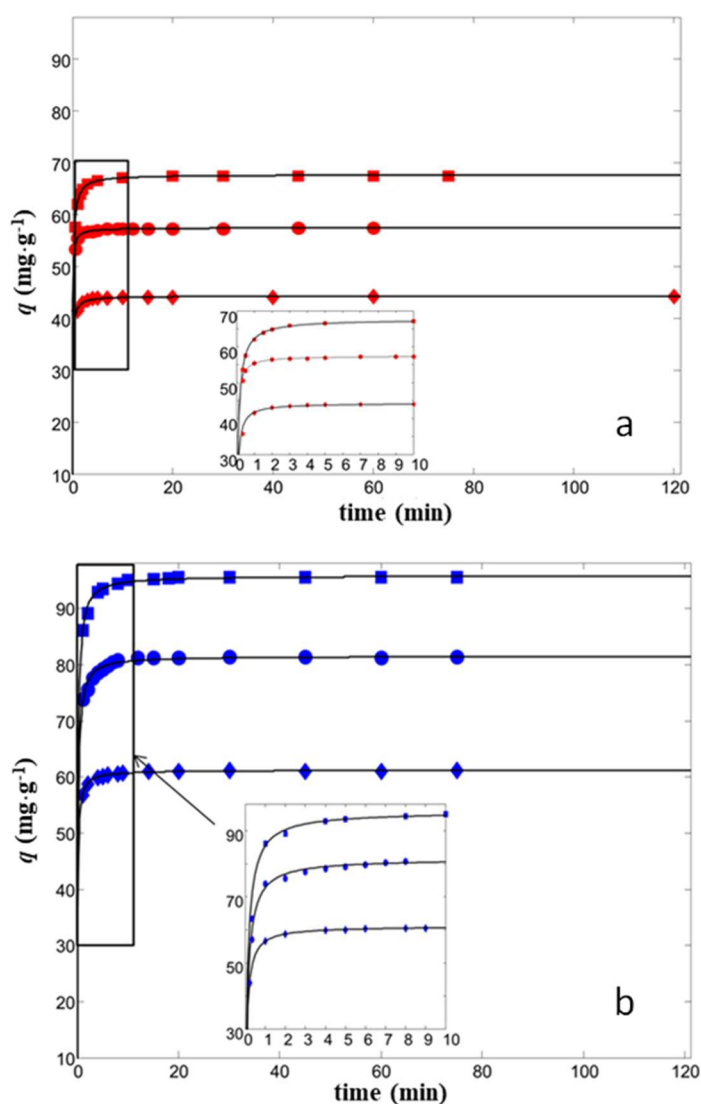


Figure 6.4.1 Chlorobenzene (CB) uptake vs. contact time for ZSM-5 (a) and Y (b) for initial concentration of 35, 25, 15  $\text{mg/L}$ . The insets: enlarged image of the boxed regions.

It can be seen that the kinetics of the adsorption process was very fast; the equilibrium was reached in about 10 min. Similar behaviours were also observed for the adsorption of other

aqueous contaminants, such as dichloroethane and toluene onto ZSM-5 and Y zeolites [5–10,13]. We have previously verified [5–10,13] that uptake data of the investigated zeolites can be fitted by the pseudo-second order model as:

$$q_t = \frac{k_2 q_e^2 t}{1 + k_2 q_e t} \quad (\text{Eq. 6.4.2})$$

where  $q_t$  and  $q_e$  are the amounts of solute adsorbed per mass of sorbent at time  $t$  and at equilibrium, respectively, and  $k_2$  is the second-order adsorption rate constant. The values of equilibrium uptake  $q_e$  and the adsorption rate constant  $k_2$  were obtained from non-linear fit of  $q_t$  vs.  $t$  (see Table 6.4.2). Analogous to what was observed for the adsorption of other aqueous contaminants, the uptake data of CB can be modelled by a pseudo-second order kinetic model, as indicated from the high coefficient of determination.

	$C_0$ (mg L <sup>-1</sup> )	$q_t$ (mg g <sup>-1</sup> )	$k_2$ (g L <sup>-1</sup> mg <sup>-1</sup> )	$R^2$
ZSM-5	15	23.4 (23.3, 23.5)	0.44 (0.41, 0.47)	0.9845
	25	44.3 (44.2, 44.3)	0.37 (0.33, 0.41)	0.9803
	35	67.6 (67.5, 67.6)	0.21 (0.19, 0.23)	0.9985
Y	25	39.3 (39.2, 39.4)	0.14 (0.11, 0.17)	0.9822
	35	70.3 (70.2, 70.3)	0.13 (0.11, 0.15)	0.9969
	45	82.3 (82.4, 82.5)	0.10 (0.085, 0.12)	0.9935

**Table 6.4.2 Estimated kinetics parameters (see Equation (6.4.2)). The confidence limits at 95% of probability of the estimated parameters are reported in brackets.**

Furthermore, for the adsorption of CB it can be noted that the kinetic constant decreases by increasing the initial concentration [37], and that the adsorption onto Y zeolites is characterised by a lower kinetic constant than that found for ZSM-5. These findings allow us to generalise the difference observed in the adsorption kinetics of these two zeolites. In particular, the adsorption kinetics of neutral organic molecules (namely, toluene, dichloroethane, methyl tert-butylether and CB), which differ from each other in physicochemical properties and molecular dimensions, is faster on ZSM-5 than on Y zeolite.

It has been already shown that adsorption of organics in aqueous solutions onto ZSM-5 hydrophobic zeolites are well fitted by the Langmuir equation [5,6,8,13], that assumes monolayer adsorption onto energetically equivalent adsorption sites and negligible sorbate–sorbate interactions. The relationships describing the Langmuir isotherm is [38]:

$$q = \frac{q_s b C_e}{1 + b C_e} \quad (\text{Eq. 6.4.3})$$

where  $b$  is the binding constant ( $\text{L mg}^{-1}$ ) and  $q_s$  is the saturation capacity of the adsorbent material ( $\text{mg g}^{-1}$ ). The experimental data obtained for the adsorption of CB on both ZSM-5 and Y are shown in Figure 6.4.2. It can be observed that the isotherms are shaped differently from each other; they can be classified as concave (Type I) and sigmoidal (Type V) isotherms, respectively.

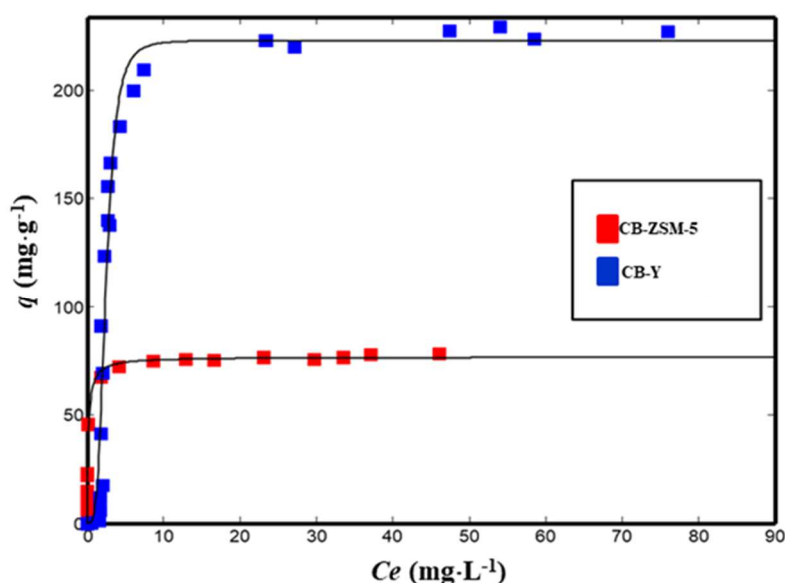


Figure 6.4.2 Adsorption isotherms of CB for ZSM-5 (red squares) and Y (blue squares).

Similar differences in the adsorption of polar organic compound from aqueous solution onto ZSM-5 and Y were also observed for methyl tert-butylether and toluene. In such cases, a Hill isotherm model was employed:

$$q_e = q_s \frac{c_e^n}{K_H + c_e^n} \quad (\text{Eq. 6.4.4})$$

where  $K_H$  is the Hill constant, and  $n$  is the Hill coefficient which is related to the degree of cooperativity. The Hill isotherm is often employed to describe cooperative adsorption in biological systems, and it has also been used to model adsorption data on zeolites due to evidence of the presence of water-organic compound clusters [39] inside the zeolite frameworks. Since the tendency to form clusters increases by increasing the porosity

dimensions, the clusters are more probably formed in the large cage of Y than in the channel system of ZSM-5 [40]. To evaluate if clusters can be formed for CB, a structural investigation was carried out (vide infra). In Table 6.4.3, the isotherm parameters for ZSM-5 and Y estimated by non linear fitting of Equations 6.4.3 and 6.4.4 respectively, are reported. It can be seen that the saturation capacity of these zeolites are higher than those obtained with graphite materials (i.e., 28.3 mg g<sup>-1</sup> for dichlorobenzene) [41], and in particular Y zeolite has a saturation value higher than adsorbents single-walled carbon nanotubes, especially if they are partially oxidized [42]. In addition, HSZs can be regenerated without significant loss of their adsorption properties [5,6,29,30]. Therefore, hydrophobic zeolites are very promising adsorbents for the removal of chlorinated aromatic compounds from water.

			<i>R</i> <sup>2</sup>	SSE*
Langmuir				
CB-ZSM-5	<i>q</i> <sub>s</sub>	76.6 (74.8, 79.5)	0.9874	198
	<i>b</i>	5.0 (3.7, 6.6)		
Hill				
CB-Y	<i>q</i> <sub>s</sub>	227 (218, 245)	0.9654	2135
	<i>K</i> <sub>H</sub>	9.2 (6.6, 12.1)		
	<i>n</i>	5.5 (4.3, 6.7)		

**Table 6.4.3 Isotherm parameters for the adsorption of CB on ZSM-5 and Y. (\*SSE: sum of squared errors)**

### *Structural Modifications upon Chlorobenzene Adsorption on High Silica Zeolites*

#### Y-CB

Y zeolite (FAU framework topology [34]) is built up of large cavities ( $\alpha$  cages or supercages) with a diameter of 12 Å linked to four other supercages through 12 membered-ring windows (diameter of 7.4 Å) and cuboctahedral  $\beta$  cages connected each other through double hexagonal rings (D6R). Topological symmetry of the unloaded material is cubic Fd-3m, but it has been highlighted that the embedding of organic compounds can decrease the symmetry to Fd-3 [10–13,43]. A careful examination of powder diffraction patterns after chlorobenzene adsorption highlights that Y-CB peak positions are quite similar to those of the as-synthesised material in all the 2 $\theta$  range investigated. Contrariwise, peak intensities strongly decrease after pollutant incorporation, especially at low 2 $\theta$  angles (Figure 6.4.3).

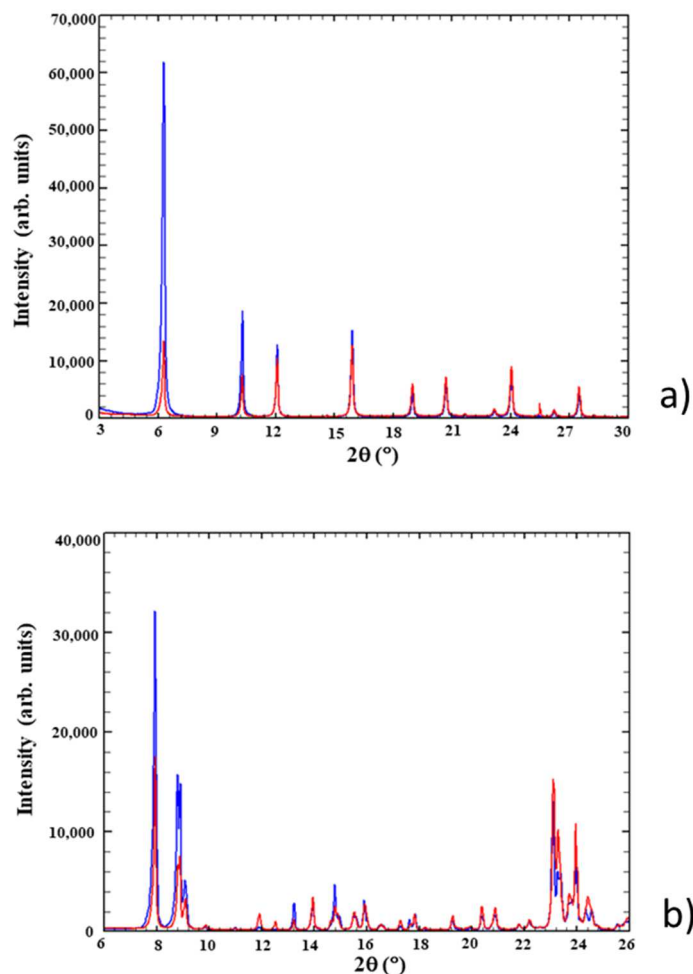


**Figure 6.4.3** Observed powder diffraction patterns of Y–CB (a) and ZSM-5–CB (b), respectively, showing differences both in intensity and position of the diffraction peaks in the low and intermediate  $2\theta$  regions. Blue lines represent the unloaded samples, red lines the loaded ones.

These differences suggest variations in the extraframework species content as well as in the lattice parameters (Table 6.4.1), thus attesting to CB adsorption into the porous structure of the zeolite. After adsorption, the T1–O and T2–O mean distances are 1.621 and 1.620 Å, respectively, the O–T–O angles range from 103.3° to 112.3°. The T–O–T bond angles adopt a wide range of values from 125° to 171° (mean value = 142°). The T–O, T–O–T and O–T–O grand mean values are in high agreement with those reported for other pure silica zeolites (PSZ) [44]. Furthermore, after adsorption the channel ellipticity  $\epsilon$  (defined as the ratio between the smaller and larger O–O “free diameters” of the 12-rings) changed ( $\epsilon = 1.02$  in Y,  $\epsilon = 1.21$  in Y–CB) and at the same time, the openings reached a wider Crystallographic Free Area (C.F.A., sensu Baerlocher [34]) when compared with the as-synthesised material (Table 6.4.4), thus confirming the high flexibility of FAU-type materials [45,46].

Parameter	Y-CB	Y [11]
O4–O4 distance (Å)	11.16	9.81
O1–O1 distance (Å)	9.68	9.70
Free diameter O4–O4 (Å)	8.46	7.11
Free diameter O1–O1 (Å)	6.98	7.00
Mean diameter (Å)	7.72	7.06
Mean radius (Å)	3.86	3.53
C.F.A. (Å <sup>2</sup> )	46.81	39.07
$\epsilon$	1.21	1.01

**Table 6.4.4 Crystallographic Free Area and ellipticity ( $\epsilon$ ) comparison between unloaded Y [11] and Y–CB systems. C.F.A. =  $\pi(\text{mean radius})^2$  (Å<sup>2</sup>);  $\epsilon$  = ratio between the longest and the shortest pore dimensions.**

Rietveld structural refinement allows us to detect 32 CB molecules per unit cell (corresponding to ~ 22.0% dry weight, dw %) located within the Y supercage (Figure 6.4.4a). Chlorobenzene molecules occupy one crystallographic independent and partially occupied site, and statistically can assume six different orientations (Figure 6.4.4a).

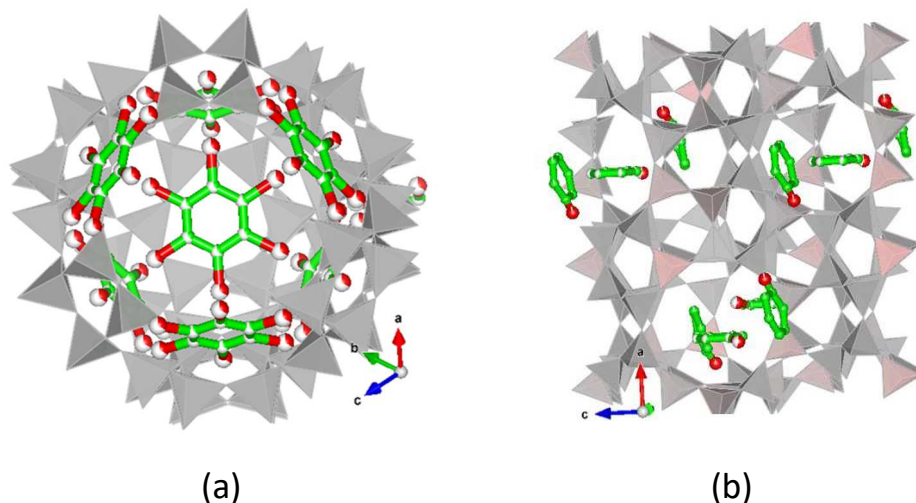


**Figure 6.4.4 Distribution of CB molecules in Y (a) and ZSM-5 (b) zeolites, respectively. Chlorine (red circle) and carbon (green circle) are shown. Drawings produced by VESTA 3 [47].**

Moreover, the evidence of relatively short Cl–O1 bond distances (i.e., Cl–O1 = 2.723(1) Å and 2.680 Å, respectively) proves that chlorobenzene directly interacts with framework oxygens. Furthermore, difference-Fourier maps of the electron density analysis revealed the presence of co-adsorbed H<sub>2</sub>O molecules hosted in three additional extraframework sites. Additionally, based on the W sites refined distance these sites interact with both each

other and chlorine atoms forming oligomers ( $W2-W2 = 2.93 \text{ \AA}$ ,  $W3-Cl = 3.21 \text{ \AA}$  and  $W1-W2 = 2.93$  and  $2.74 \text{ \AA}$ , respectively) that strongly interact with the framework oxygen atoms via chlorine (Figure 6.4.4a). According to the recent literature [5–8,10–13,29,44], the strong interactions among organic molecules–H<sub>2</sub>O short chain-frameworks play a relevant role in stabilising the guest structures within the zeolite porosity. On a whole, on the basis of Rietveld refinement 70 H<sub>2</sub>O molecules (~ 8% dw %) were detected in good agreement with the TG curve (Figure 6.4.5a), which shows two main weight losses: the first one (about 7.3 dw % zeolite, 25–110°C) is related to desorption of species retained on the surface, the second one (23.5 dw % zeolite, 110–900°C) to the removal from the structure of loaded CB and H<sub>2</sub>O molecules.

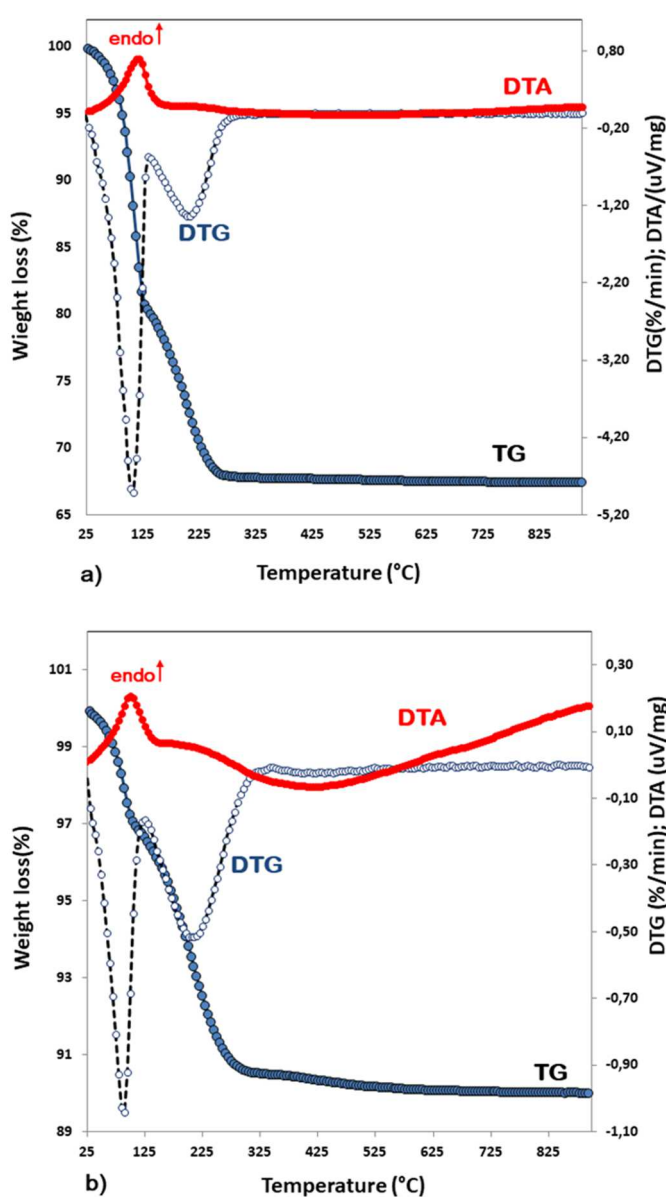


Figure 6.4.5 Thermal analysis of Y (a) and ZSM-5 (b) loaded with chlorobenzene from room temperature to 900 °C. In blue and gray circles, the total weight loss curve (TG) and the derivative of it (DTG); in red the differential thermal analysis (DTA) curve.

## ZSM-5–CB

The ZSM-5 zeolite framework consists of two intersecting channel systems: a straight channel parallel to [010] direction and a sinusoidal one parallel to [100] direction [34]. Both channels are limited by 10MR of  $\text{TO}_4$  tetrahedra with free diameters of 5.4–5.6 Å and 5.1–5.5 Å for sinusoidal and straight channel, respectively. After CB adsorption, the evolution of the powder diffraction pattern indicates that ZSM-5 maintains its crystallinity as well as the monoclinic  $\text{P}2_1/n$  symmetry. In Table 6.4.1, the comparison between refined lattice parameters of starting material and of the ZSM-5–CB system highlights the occurrence of chlorobenzene adsorption in the ZSM-5 micropores. The structural characterisation was carried out starting with the model proposed by Rodeghero et al. [6] and an examination of the difference Fourier maps of the electron density suggested the presence of extraframework content. In detail, some of recognised maxima were reasonably attributed to chlorobenzene adsorption sites in both the sinusoidal channel (CB2 sites) and the intersection between sinusoidal and straight channels (CB1 sites) (Figure 6.4.4b). On the whole, a total amount of about 6 molecules per unit cell (p.u.c.) of organics were detected. Besides, residual maxima of difference Fourier maps also indicate the presence of co-adsorbed  $\text{H}_2\text{O}$  molecules ( $\sim 1.5$  dw %) hosted at W1 and W2 sites. In particular, based on the refined distances between the extraframework content and framework oxygen atoms strong interactions among chlorobenzene molecules hosted in both adsorption sites (CB1 and CB2),  $\text{H}_2\text{O}$  molecules (W1 and W2 sites), and framework oxygen atoms occur (i.e.,  $\text{O}4\text{--C}10 = 3.01(1)$  Å,  $\text{O}18\text{--C}9 = 2.61(1)$  Å,  $\text{O}31\text{--C}11 = 2.69(1)$  Å,  $\text{O}47\text{--C}11 = 2.99(1)$  Å,  $\text{W}2\text{--W}2 = 3.15(1)$  Å,  $\text{O}26\text{--C}12 = 3.03(3)$  Å,  $\text{W}1\text{--C}1 = 3.16(3)$  Å) (Figure 6.4.4b). Additionally, thermogravimetric analysis (Figure 6.4.5b) indicated that relevant weight loss, occurring at temperatures higher than 100°C (7% in weight), is due to the expulsion from the structure of extraframework ions embedded in the ZSM-5 channels. The residual one at lower temperature can be ascribed to the expulsion of water and/or CB molecules bonded to the surface (3% in weight below  $\sim 100$  °C). These results are quite well supported by the total amount of adsorbed molecules detected through both saturation capacity determined by the adsorption isotherm and the results obtained by Rietveld analysis. After adsorption, the T–O bond length ranges from 1.602 to 1.608 Å, the O–T–O angles varies from 96° to 125°, with a mean value of 109.4°. According to Wragg et al. [44] the T–O–T bond angles adopt a wide range of values from 124° to 178°. Regarding the channel geometry, after organics adsorption, any changes in both shape and channel dimension were also evaluated. Specifically, both straight and sinusoidal channels hosting the organic molecules change their shape and become more elliptical (Table 6.4.5).

<u>Straight Channel</u>									
O-O distance (Å)	O7-O1	O8-O2	O31-O37	O44-O46	O47-O48				$\epsilon$
ZSM-5-CB	8.22	8.20	8.02	8.22	7.97				1.03
ZSM-5	7.90	7.94	8.04	8.41	7.80				1.08
Free diameter (Å)	O7-O1	O8-O2	O31-O37	O44-O46	O47-O48				
ZSM-5-CB	5.52	5.50	5.32	5.52	5.27				-
ZSM-5	5.20	5.24	5.34	5.71	5.10				-
<u>Mean diameter (Å)</u>	<u>Mean diameter (Å)</u>	<u>Mean radius (Å)</u>	<u>C.F.A. (Å<sup>2</sup>)</u>						
ZSM-5-CB	5.43	2.71	23.12						-
ZSM-5	5.32	2.66	22.20						-
O-O distance (Å)	O11-O5	O20-O18	O21-O22	O27-O33	O28-O34				$\epsilon$
ZSM-5-CB	8.08	7.89	8.11	8.22	8.08				1.04
ZSM-5	8.19	8.35	7.98	8.13	7.76				1.08
Free diameter (Å)	O11-O5	O20-O18	O21-O22	O27-O33	O28-O34				
ZSM-5-CB	5.38	5.19	5.41	5.52	5.38				
ZSM-5	5.49	5.65	5.28	5.43	5.06				
<u>Mean diameter (Å)</u>	<u>Mean diameter (Å)</u>	<u>Mean radius (Å)</u>	<u>C.F.A. (Å<sup>2</sup>)</u>						
ZSM-5-CB	5.37	2.69	22.67						
ZSM-5	5.38	2.69	22.74						
<u>Sinusoidal Channel</u>									
O-O distance (Å)	O20-O15	O24-O26	O27-O2	O28-O1	O41-O46				$\epsilon$
ZSM-5-CB	8.08	7.87	7.76	8.16	8.69				1.12
ZSM-5	8.15	8.07	7.97	7.76	8.51				1.10
Free diameter (Å)	O20-O15	O24-O26	O27-O2	O28-O1	O41-O46				
ZSM-5-CB	5.38	5.17	5.06	5.46	5.99				
ZSM-5	5.45	5.37	5.27	5.06	5.81				
<u>Mean diameter (Å)</u>	<u>Mean diameter (Å)</u>	<u>Mean radius (Å)</u>	<u>C.F.A. (Å<sup>2</sup>)</u>						
ZSM-5-CB	5.41	2.71	23.01						
ZSM-5	5.39	2.70	22.82						$\epsilon$
O-O distance (Å)	O17-O18	O23-O25	O30-O5	O31-O4	O44-O43				$\epsilon$
ZSM-5-CB	7.50	8.58	8.20	7.89	7.75				1.14
ZSM-5	7.30	8.31	8.32	8.05	7.95				1.14
Free diameter (Å)	O17-O18	O23-O25	O30-O5	O31-O4	O44-O43				
ZSM-5-CB	4.80	5.88	5.50	5.19	5.05				
ZSM-5	4.60	5.61	5.62	5.35	5.25				
<u>Mean diameter (Å)</u>	<u>Mean diameter (Å)</u>	<u>Mean radius (Å)</u>	<u>C.F.A. (Å<sup>2</sup>)</u>						
ZSM-5-CB	5.28	2.64	21.92						
ZSM-5	5.29	2.64	21.93						

Table 6.4.5 C.F.A. and ellipticity ( $\epsilon$ ) comparison between unloaded ZSM-5 [13] and ZSM-5-CB systems.

C.F.A. =  $\pi(\text{mean radius})^2$  (Å<sup>2</sup>);  $\epsilon$  = ratio between the longest and the shortest pore dimensions.

#### 6.4.4 Conclusions

This work aims to highlight the adsorptive capacity of commercial high silica zeolites ZSM-5 (MFI topology), and Y zeolite (FAU topology), for removal of chlorobenzene (CB) from water. Both high silica ZSM-5 and Y zeolites are characterised by fast kinetics, that combined with good adsorption capacity, suggest they can be efficiently used as a sorbent media to control the concentration of chlorobenzene in water systems. In particular, ZSM-5 is more efficient in the removal of CB at low concentration level, while Y shows higher saturation capacity than ZSM-5. Difference Fourier maps of the electron density provide insight into the preferred zeolite adsorption sites in both microporous materials. The refined framework–extraframework bond distances highlight the existence of CB, and hydrophobic zeolites interactions mediated via co-adsorbed H<sub>2</sub>O molecules. Adsorption of CB on ZSM-5 and Y zeolites is accompanied by structural changes, i.e. variations in both unit-cell parameters and channel shape when compared to the as-synthesised microporous materials, clearly confirming the very relevant role of H<sub>2</sub>O molecules in both the diffusion and adsorption processes in hydrophobic zeolites. After adsorption, the channels become more distorted, thus indicating remarkable framework flexibility for both ZSM-5 and Y zeolites.

#### 6.4.5 Refereces

- [1] Sennour R., Mimane G., Benghalem A., Taleb S. (2009) Removal of the persistent pollutant chlorobenzene by adsorption onto activated montmorillonite. *Appl. Clay Sci.*, 43, 503–506.
- [2] McClenny W. A., Oliver K. D., Jacumin H. H. Jr., Daughtrey E. H. Jr. (2002) Ambient level volatile organic compound (VOC) monitoring using solid adsorbents—Recent US EPA studies. *J. Environ. Monitor.*, 4, 695–705.
- [3] Khan F. I., Ghoshal A. K. (2000) Removal of Volatile Organic Compounds from polluted air. *J. Prevent. Proc.*, 13, 527–545.
- [4] Sarti E., Chenet T., Pasti L., Cavazzini A., Rodeghero E., Martucci A. (2017) Effect of silica alumina ratio and thermal treatment of beta zeolites on the adsorption of toluene from aqueous solutions. *Minerals*, 7, 22.
- [5] Rodeghero E., Pasti L., Sarti E., Cruciani G., Bagatin R., Martucci A. (2017) Temperature-induced desorption of methyl tert-butyl ether confined on ZSM-5: An in situ synchrotron XRD powder diffraction study. *Minerals*, 7, 34.
- [6] Rodeghero E., Martucci A., Cruciani G., Bagatin R., Sarti E., Bosi V., Pasti L. (2016) Kinetics and dynamic behaviour of toluene desorption from ZSM-5 using in situ high-temperature synchrotron powder X-ray diffraction and chromatographic techniques. *Catal. Today*, 227, 118–125.

- [7] Arletti R., Martucci A., Alberti A., Pasti L., Nassi M., Bagatin R. (2012) Location of MTBE and toluene in the channel system of the zeolite mordenite: Adsorption and host–guest interactions. *J. Solid State Chem.*, 194, 135–142.
- [8] Pasti L., Rodeghero E., Sarti E., Bosi V., Cavazzini A., Bagatin R., Martucci A. (2016) Competitive adsorption of VOCs from binary aqueous mixtures on zeolite ZSM-5. *RSC Adv.*, 6, 54544–54552.
- [9] Pasti L., Sarti E., Cavazzini A., Marchetti N., Dondi F., Martucci A. (2013) Factors affecting drug adsorption on beta zeolites. *J. Sep. Sci.*, 36, 1604–1611.
- [10] Martucci A., Pasti L., Marchetti N., Cavazzini A., Dondi F., Alberti A. (2012) Adsorption of pharmaceuticals from aqueous solutions on synthetic zeolites. *Micropor. Mesopor. Mat.*, 148, 174–183.
- [11] Braschi I., Blasioli S., Gigli L., Gessa C.E., Alberti A., Martucci A. (2010) Removal of sulfonamide antibiotics from water: Evidence of adsorption into an organophilic zeolite Y by its structural modifications. *J. Hazard. Mater.*, 17, 218–225.
- [12] Blasioli S., Martucci A., Paul G., Gigli L., Cossi M., Johnston C.T., Marchese L., Braschi I. (2014) Removal of sulfamethoxazole sulfonamide antibiotic from water by high silica zeolites: A study of the involved host–guest interactions by a combined structural, spectroscopic, and computational approach. *J. Colloid. Interf. Sci.*, 419, 148–159.
- [13] Pasti L., Martucci A., Nassi M., Cavazzini A., Alberti A., Bagatin R. (2012) The role of water in DCE adsorption from aqueous solutions onto hydrophobic zeolites. *Micropor. Mesopor. Mat.*, 160, 182–193.
- [14] Guo Y., Li Y., Zhu T., Ye M., Wang X. (2013) Adsorption of SO<sub>2</sub> and chlorobenzene on activated carbon. *Adsorpt.*, 19, 1109–1116.
- [15] Crisafulli R., Milhome M. A. L., Cavalcante R. M., Silveira E. R., De Keukeleire D., Nascimento R. F. (2008) Removal of some polycyclic aromatic hydrocarbons from petrochemical wastewater using low-cost adsorbents of natural origin. *Bioresource Technol.*, 99, 4515–4519.
- [16] Kim B. K., Ryu S. K., Kim B. J., Park S. J. (2006) Roles of Acid-Base Interactions in Hydrogen Chloride Removal by Activated Carbon Fibers. *J. Ind. Eng. Chem.*, 12, 121–126.
- [17] Park S. J., Kim B. J. (2004) Influence of oxygen plasma treatment on hydrogen chloride removal of activated carbon fibers. *J. Colloid Interf. Sci.*, 275, 590–595.
- [18] Chin C. J. M., Shih M. W., Tsai H. J. (2010) Adsorption of nonpolar benzene derivatives on single-walled carbon nanotubes. *Appl. Surf. Sci.*, 256, 6035–6039.
- [19] Long C., Li Q., Li Y., Liu Y., Li A., Zhang Q. (2010) Adsorption characteristics of benzene–chlorobenzene vapor on hypercrosslinked polystyrene adsorbent and a pilot-scale application study. *Chem. Eng. J.*, 160, 723–728.

- [20] Chen W., Duan L., Zhu D. (2007) Adsorption of polar and nonpolar organic chemicals to carbon nanotubes. *Environ. Sci. Technol.*, 41, 8295–8300.
- [21] Balamurugan K., Subramanian V. (2013) Adsorption of chlorobenzene onto (5,5) armchair single-walled Carbon nanotube and graphene sheet: Toxicity versus adsorption strength. *J. Phys. Chem. C*, 117, 21217–21227.
- [22] Lee J. J., Choi J., Park J. W. (2002) Simultaneous sorption of lead and chlorobenzene by organobentonite. *Chemosphere*, 49, 1309–1315.
- [23] Witthuhn B., Klauth P., Pernyeszi T., Vereecken H., Klumpp E. (2006) Organoclays for Aquifer Bioremediation: Adsorption of Chlorobenzene on Organoclays and its Degradation by RHODOCOCCLUS B528. *Water Air Soil Poll. Focus*, 6, 317–329.
- [24] Jarraya I., Fourmentin S., Benzina M., Bouaziz S. (2010) VOC adsorption on raw and modified clay materials. *Chem. Geol.*, 275, 1–8.
- [25] Altare C. R., Bowman R. S., Katz L. E., Kinney K. A., Sullivan E. J. (2007) Regeneration and long-term stability of surfactant-modified zeolite for removal of volatile organic compounds from produced water. *Micropor. Mesopor. Mat.*, 105, 305–316.
- [26] Anderson M. A. (2000) Removal of MTBE and Other Organic Contaminants from Water by Sorption to High Silica Zeolites. *Environ. Sci. Technol.*, 34, 725–727.
- [27] Damjanović L., Rakić V., Rac V., Stošić D., Auroux A. (2010) The investigation of phenol removal from aqueous solutions by zeolites as solid adsorbents. *J. Hazard. Mat.*, 184, 477–484.
- [28] Perego C., Bagatin R., Tagliabue M., Vignola R. (2013) Zeolites and related mesoporous materials for multi-talented environmental solutions. *Micropor. Mesopor. Mat.*, 166, 37–49.
- [29] Leardini L., Martucci A., Braschi I., Blasioli S., Quartieri S. (2014) Regeneration of high-silica zeolites after sulfamethoxazole antibiotic adsorption: A combined in situ high-temperature synchrotron X-ray powder diffraction and thermal degradation study. *Mineral. Mag.*, 78, 1141–1160.
- [30] Braschi I., Blasioli S., Buscaroli E., Montecchio D., Martucci A. (2016) Physicochemical regeneration of high silica zeolite Y used to clean-up water polluted with sulfonamide antibiotics. *J. Environ. Sci.*, 43, 302–312.
- [31] Vignola R., Cova U., Fabiani F., Sbardellati T., Sisto R., Vignola R. Process for the regeneration of nonpolar adsorbing zeolites used for the treatment of contaminated water. Patent WO/2009/000429, 31 December 2008.
- [32] Alberti A., Martucci A. (2005) Phase transformations and structural modifications induced by heating in microporous materials. *Stud. Surf. Sci. Catal.*, 155, 19–43.
- [33] Alberti A., Martucci A. (2011) Reconstructive phase transitions in microporous materials: Rules and factors affecting them. *Micropor. Mesopor. Mat.*, 141, 192–198.

- [34] Baerlocher C., McCusker L. B., Olson D. H. (2007) *Atlas of Zeolite Framework Types*, 6th ed.; Elsevier: Amsterdam, The Netherlands.
- [35] Larson A. C., Von Dreele R. B. (1994) *GSAS General Structure Analysis System*, LANSCE, MS-H805; Los Alamos National Laboratory: Los Alamos, NM, USA.
- [36] Toby B. H. (2001) EXPGUI, a graphical user interface for GSAS. *J. Appl. Crystallogr.*, 34, 210–213.
- [37] Azizian S., Haerifar M., Bashiri H. (2009) Adsorption of methyl violet onto granular activated carbon: Equilibrium, kinetics and modeling. *Chem. Eng. J.*, 146, 36–41.
- [38] De Moor B. A., Reyniers M. F., Gobin O. C., Lercher J. A., Marin G. B. (2011) Adsorption of C<sub>2</sub>-C<sub>8</sub> n-Alkanes in Zeolites. *J. Phys. Chem. C*, 115, 1204–1219.
- [39] Martucci A., Braschi I., Bisio C., Sarti E., Rodeghero E., Bagatin R., Pasti L. (2015) Influence of water on the retention of methyl tertiary-butyl ether by high silica ZSM-5 and Y zeolites: A multidisciplinary study on the adsorption from liquid and gas phase. *RSC Advances*, 5, 86997–87006.
- [40] Martucci A., Braschi I., Marchese L., Quartieri S. (2014) Recent advances in clean-up strategies of waters polluted with sulfonamide antibiotics: A review of sorbents and related properties. *Mineral. Mag.*, 78, 1115–1140.
- [41] Li X., Chen G. H. (2009) Surface modified graphite nanosheets used as adsorbent to remove 1,2-dichlorobenzene from water. *Mater. Lett.*, 63, 930–932.
- [42] Yu F., Ma J., Wu Y. (2011) Adsorption of toluene, ethylbenzene and m-xylene on multi-walled carbon nanotubes with different oxygen contents from aqueous solutions. *J. Hazard. Mater.*, 192, 1370–1379.
- [43] Krishna R., van Baten J. M. (2010) Highlighting a Variety of Unusual Characteristics of Adsorption and Diffusion in Microporous Materials Induced by Clustering of Guest Molecules. *Langmuir*, 26, 8450–8463.
- [44] Wragg D. S., Morris R. E., Burton A. W. (2008) Pure silica zeolite-type frameworks: A structural analysis. *Chem. Mater.*, 20, 1561–1570.
- [45] Leardini L., Martucci A., Alberti A., Cruciani G. (2013) Template burning effects on stability and boron coordination in boron lewyne studied by in situ time resolved synchrotron powder diffraction. *Micropor. Mesopor. Mater.*, 167, 117–126.
- [46] Baur W. H. (1992) Self-limiting distortion by antirotating hinges is the principle of flexible but noncollapsible frameworks. *J. Solid State Chem.*, 97, 243–247.
- [47] Momma K., Izumi F. (2011) VESTA 3 for three-dimensional visualization of crystal, volumetric and morphology data. *J. Appl. Crystallogr.*, 44, 1272–1276.

## 6.5 Adsorption of the Metolachlor metabolite EMA onto zeolite ZSM-12 from aqueous solutions

The data herein reported are part of my work of thesis and have been published in: Rodeghero E., Pasti L., Nunziante G., Chenet T., Gigli L., Plaisier J. R., Martucci A. (2019) Highlighting the capability of zeolites for agro-chemicals contaminants removal from aqueous matrix: Evidence of 2-ethyl-6-methylaniline adsorption on ZSM-12. *American Mineralogist*, 104, 317 – 324.

### 6.5.1 Introduction

The degradation of water resources is an increasing problem world-wide, and many efforts have been done to control point source pollution from homes and industry. However, water pollution from agriculture is becoming a major concern due to the widespread use of agro-chemicals in modern agriculture. Indeed, many of these substances have [1] harmful effect on aquatic organisms, insects and mammals and they persist in the aquatic systems for many years after their application [2]. In Europe, pesticides are considered hazardous substances in accordance with current directives regarding water [3]. The World Health Organization reported that ~3,000,000 cases of pesticide poisoning and 220,000 deaths occur in developing countries [4].

Drinking water quality standard should not exceed 0.1 g L<sup>-1</sup> for an individual pesticide concentration and 0.5 g L<sup>-1</sup> for all pesticide concentration [5]. Due to the diffuse nature of contamination from agro-chemicals, and to the mobility of these compounds into the environmental compartments, their presence it is more difficult to control.

The pesticides are transferred from soil to water through various pathways (e.g. surface runoff, subsurface and groundwater flows) either in solution or sorbed onto particles [6]. Among the agro-chemicals category above mentioned, Metolachlor (C<sub>15</sub>H<sub>22</sub>ClNO<sub>2</sub>, 2-Chloro-N-(2-ethyl-6-methylphenyl)-N-(2-methoxy-1-methylethyl)acetamide, labelled MTC) and their metabolites are frequently detected in surface and subsurface water (from 0.1 g L<sup>-1</sup> to more than 100 mg L<sup>-1</sup> U. [7,8]) due to the relatively high water solubility (530 mg L<sup>-1</sup>) that impart to it high potential to leach and migrate through the soil and contaminate ground water [9]. Moreover, chloroacetanilide degradation products such as 2-ethyl-6-methylaniline (C<sub>2</sub>H<sub>5</sub>C<sub>6</sub>H<sub>3</sub>(CH<sub>3</sub>)NH<sub>2</sub>, labelled EMA) are more or equally toxic compared to their parent pesticide compound [10-14] and are promutagens in the Ames test [12]. The rate and the extent of chloroacetanilide degradation is strongly dependent on environmental conditions such as temperature [15], moisture content [16], concentration of hydroxyl radical (OH) [17], and microbial activity [18-20]. In consequence, it is mandatory to develop

mitigation measures able to prevent pollutants diffusion into environment and therefore to reduce their impact [21]. Many treatment strategies have been proposed for the removal of these pollutants, including biological, chemical and/or physical methods [22-27].

Despite the availability of various clean up methods, adsorption by organic or inorganic sorbent media is still preferred due the high removal efficiency and reduced operational cost. Activated charcoal, mesoporous phenolic resin and mesoporous carbon exhibited good properties as adsorbents in virtue of their high surface area and narrow mesopore distribution [28-30]. Organoclays and organo/layered double hydroxides have also been proven to be suitable in reducing and even prevent the environmental impact caused by some pesticides and in particular metolachlor [1, 9, 31-36].

Additionally, zeolites have been investigated for the removal of pesticides from waters [37]. These microporous materials represent a promising candidate as an environmentally friendly alternative in the removal of agro-chemicals compounds from water. The main advantages of zeolites are related to the structural and chemical features of their framework, which can be modulated by varying the pore opening and the  $\text{SiO}_2/\text{Al}_2\text{O}_3$  ratio (SAR). Typically, these materials show high surface area, high specific capacity, mechanical, biological and chemical stability and adsorption selectivity. In particular, it has been demonstrated that High Silica Zeolites (HSZs) show strong selectivity [38-47], very fast kinetics in the adsorption of organic species. Moreover, their high stability in water, resistance to aggressive chemical solutions make these materials promising and efficient alternative to other reactive adsorbent media [43, 48-62].

In the present work we explore for the first time the capability of ZSM-12 to remove contaminants metabolites from aqueous matrix. For this purpose, EMA was chosen as target metabolite and we selected ZSM-12 zeolite (MTW topology) whose channel system could be an attractive host to incorporate EMA. The structure of the ZSM-12 host is reported in Figure 6.5.1. The framework has one-dimensional pore system delimited by 12 membered-rings (12MRs) [63]  $\{[010] 5.6 \times 6.0\text{\AA}\}$ , which is slightly larger than that of MFI zeolites  $\{[100] 5.1 \times 5.5 \leftrightarrow [010] 5.3 \times 5.6\}$ . The regular one-dimensional nanochannel system is ideal to prevent inserted molecules from escaping as well as the entering of other competitive molecules [64-67].

To date, this zeolite is an efficient catalyst for the shape selective conversion of long hydrocarbon molecules such as isomerisation and alkylation of aromatic hydrocarbons [68-72] and it has not yet been used as sorbent.

To assess the capability of ZSM-12 for removal the of EMA from aqueous solution, chromatographic, thermogravimetric and synchrotron X-ray powder diffractometric techniques were applied. In particular, to evaluate the structural basis for the EMA sorption X-ray powder diffraction characterisation was carried out on the as-synthesised, the

calcined and the EMA loaded – ZSM-12, respectively. The complexity of this host-guest system highlights the importance of understanding and controlling not only the interactions of guests with the host but also the interactions between guests and the influence of coadsorbed molecules. This information provides also a basis on the fate and transport of EMA in the environment and in particular in zeolite soil and water applications.

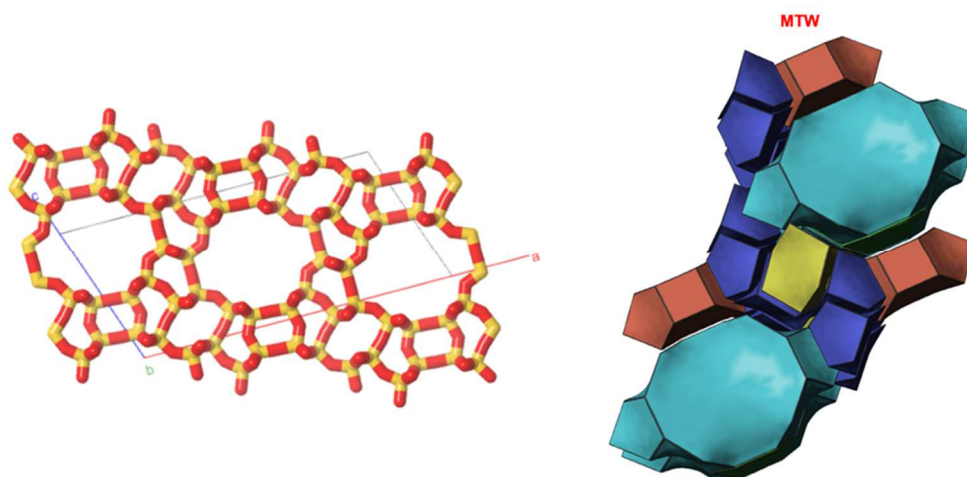


Figure 6.5.1 ZSM-12 (MTW topology) one-dimensional pore system view along [010].

## 6.5.2 Materials and Methods

### *Synthesis*

The hydrothermal ZSM-12 synthesis (SAR=200) was carried out following the protocol proposed by Millini et al. (2004) [72] using NaOH, aluminium source  $[Al_2(SO_4)_3 \cdot 16H_2O]$  and 6-azonia-spiro-[5,5]-undecane as structure directing agent (SDA). The bromide salt of SDA was dissolved in demineralised water and then exchanged into the hydroxide form by electrodialysis. The resulting solution was heated at 353 K and tetraethylortosilicate (TEOS, Aerosil 200) was gradually dropped into above solution under stirring. After aging at room temperature for 4 h, the mixture was filtered and washed with deionised water and dried overnight at 423 K. The solid product was then calcined by raising the temperature from room temperature to 600°C in 1 hour, then holding at 600°C for 4 hours. Finally, adsorbents were kept at room temperature for 3 hours. Air circulation was maintained during heating. The samples were kept in a desiccator and used within 2 days after thermal treatment.

### *Batch Adsorption*

The adsorption isotherm was determined using the batch method. Batch experiments were carried out in duplicate in 20 mL crimp top reaction glass flasks sealed with PTFE septa (Supelco, Bellefonte, PA, USA). The flasks were filled in order to have the minimum

headspace and a solid/solution ratio of 1:2 (mg mL<sup>-1</sup>) was employed. After equilibration, for 24 hours at a temperature of 25.3 ± 0.5°C under stirring, the solids were separated from the aqueous solution using centrifugation (14000 rpm for 30 min).

Chromatographic determinations of EMA before and after the contact with ZSM-12 were made on a Waters HPLC system (Waters Associates, Milford, Mass) equipped with a binary pump and a DAD UV–VIS detector. The column was a Kromasil Eternity 0.46 x 15 cm C18-packed, particle diameter 5 µm, (Eka Nobel). An injector (7725i, Rheodyne, Cotati, CA, USA) with a 20 µL loop was employed. The mobile phase was a mixture of water and ACN, 50:50% v/v. Solvents were filtered before use (Nylon 66 membranes, 0.45 µm, Supelco, Bellefonte, PA, USA). The concentration of EMA was determined by measuring UV absorbance and by interpolating values against previously constructed calibration curves.

#### *Thermal analyses*

Thermal analyses (TG and DTA) of both calcined (ZSM-12-C) and EMA loaded – ZSM-12 (ZSM-12-EMA) were performed on a STA 409 PC LUXX® - Netzsch. The measurements were carried out in air flow with a heating rate using a 10°C min<sup>-1</sup> heating rate up to 900°C.

#### *X-ray Powder Diffraction Data Collection and Refinement Strategy*

The XRD patterns of calcined ZSM-12 before and after EMA loading were collected at the MCX beamline of Elettra-Sincrotrone (Trieste, Italy) using a fixed wavelength of 0.827Å (Figure 6.5.2).

The powders were loaded and packed in a 0.5 mm boron capillary, mounted on a standard goniometric head, and spun during data collection. The diffraction patterns were recorded through a crystal analyser scintillation detector in the 3–50 2θ range. Structural refinements were performed by full profile Rietveld analysis using the GSAS package [74] with the EXPGUI interface [75]. The refinements of both ZSM-12-C and ZSM-12-EMA samples were performed in the C2/c space group using the starting framework model reported in Fyfe et al. (1990) [76]. The background profiles were firstly edited manually and further empirically fitted using a Chebyshev polynomial with 26 variable coefficients. The Bragg peak profile was modeled using a pseudo-Voigt function with 0.01% cut-off peak intensity. The scale factor, 2θ-zero shift, and unit-cell parameters were accurately refined. Table 6.5.1 reports the refinement parameters for all samples investigated. The extra-framework sites were located by difference Fourier maps and H-atoms were not considered within the structure refinement due to their low scattering factors. The thermal displacement parameters were constrained in the following way: the same value for all the tetrahedral atoms, a second value for all the framework oxygen atoms, a third one for the extraframework atoms. Soft restraints were applied on the tetrahedral cations and coordinated framework oxygen atom

distances during the first stages of refinement, and left free in the last cycles. The final atomic positions, thermal parameters and occupancies of ZSM-12-C and ZSM-12-EMA atoms are reported in Tables 6.5.2 and 6.5.3, respectively. Selected bond distances and angles are listed in Tables 6.5.4 and 6.5.5, respectively. The detailed structural refinements both calcined and EMA loaded ZSM-12 are described separately in the following section.

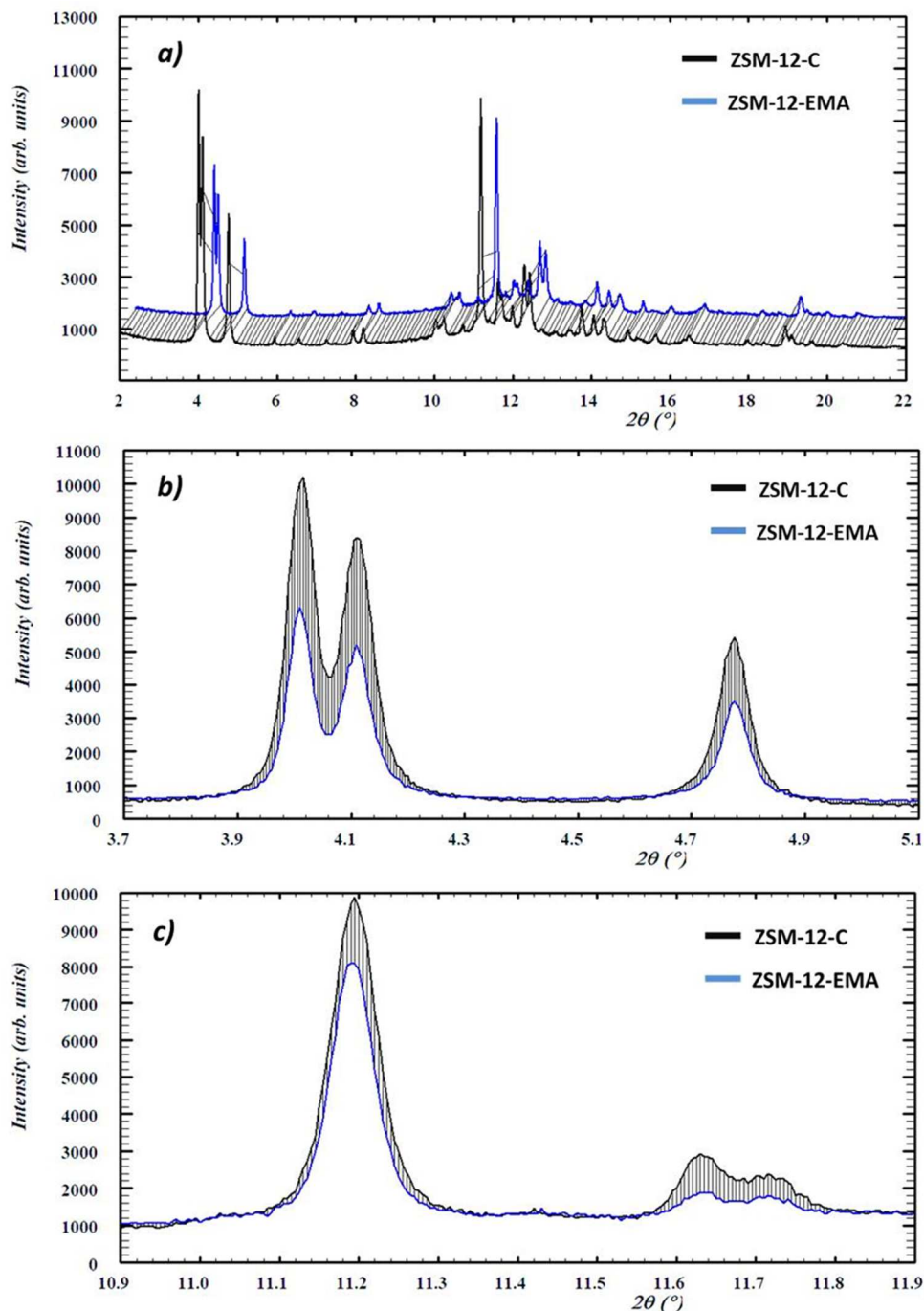


**Figure 6.5.2 Comparison between the XRPD spectra collected on ZSM-12 before and after EMA adsorption in the 2.0-23° (a), 3.7-5.1° (b) and 10.9-11.9° (c) 2theta ranges, respectively. Black lines represent the unloaded sample, blue lines the loaded one.**

	ZSM-12-C	ZSM-12-EMA
Space group	<i>C2/c</i>	<i>C2/c</i>
<i>a</i> (Å)	24.9984(11)	29.993(7)
<i>b</i> (Å)	5.0336(1)	5.0341(9)
<i>c</i> (Å)	24.3844(8)	24.377(5)
$\beta$	107.9(1)	107.9(2)
<i>V</i> (Å <sup>3</sup> )	2919.1(2)	2918.9(2)
Incident radiation wavelength (Å)	0.82700	0.82700
Refined pattern 2 $\theta$ range (°)	2.45-50.00	2.45-50.00
<i>R</i> <sub>wp</sub> (%)	7.40	7.71
<i>R</i> <sub>p</sub> (%)	6.00	6.05
<i>R</i> <sup>2</sup> (%)	9.10	11.30
N. of contributing reflections	1889	1797
<i>N</i> <sub>obs</sub>	9312	9357
<i>N</i> <sub>var</sub>	101	152

**Table 6.5.1 Crystal data and refinement parameters for ZSM-12-C and ZSM-12-EMA, respectively.**

Atoms	x/a	y/b	z/c	U <sub>i</sub> /U <sub>e</sub> *100	Occupancy
T1	0.4356(4)	0.5950(2)	0.4149(3)	1.25(2)	1.00
T2	0.0640(4)	-0.0420(2)	0.4587(4)	1.25(2)	1.00
T3	0.3722(4)	0.1012(2)	0.3592(4)	1.25(2)	1.00
T4	0.1407(3)	0.4708(2)	0.4513(4)	1.25(2)	1.00
T5	0.2741(4)	-0.0010(2)	0.4178(4)	1.25(2)	1.00
T6	0.2089(3)	0.4704(2)	0.3755(4)	1.25(2)	1.00
T7	0.2890(3)	0.0739(2)	0.2526(4)	1.25(2)	1.00
O1	0.4207(7)	0.6480(3)	0.4744(5)	2.50(3)	1.00
O2	0.5007(5)	0.5384(4)	0.4180(6)	2.50(3)	1.00
O3	0.4195(6)	0.8734(2)	0.3810(7)	2.50(3)	1.00
O4	0.3245(7)	0.0490(4)	0.3906(8)	2.50(3)	1.00
O5	0.0898(6)	-0.3163(3)	0.4423(8)	2.50(3)	1.00
O6	0.3551(4)	0.0951(4)	0.2884(4)	2.50(3)	1.00
O7	0.2546(8)	0.3257(2)	0.2658(8)	2.50(3)	1.00
O8	0.2375(7)	0.2528(3)	0.4247(6)	2.50(3)	1.00
O9	0.1504(5)	0.5306(4)	0.3892(5)	2.50(3)	1.00
O10	0.1881(6)	0.4864(4)	0.5149(4)	2.50(3)	1.00

O11	0.3046(6)	0.0510(3)	0.1924(4)	2.50(3)	1.00
O12	0.4013(7)	0.3922(3)	0.3657(6)	2.50(3)	1.00
O13	0.1063(6)	0.1859(3)	0.4453(8)	2.50(3)	1.00
O14	0.2557(6)	0.6848(2)	0.4079(8)	2.50(3)	1.00

**Table 6.5.2 Atomic coordinates, thermal parameters and occupancies of ZSM-12-C framework atoms.**

Atoms	x/a	y/b	z/c	U <sub>i</sub> /U <sub>e</sub> *100	Occupancy
T1	0.0618(32)	0.0280(16)	0.0859(32)	2.04(3)	1.00
T2	0.0697(31)	0.0491(16)	0.9625(36)	2.34(3)	1.00
T3	0.3706(29)	0.0192(17)	0.3605(30)	2.34(3)	1.00
T4	0.3598(26)	0.0441(15)	0.5512(34)	2.34(3)	1.00
T5	0.2816(31)	0.0790(16)	0.4247(30)	2.34(3)	1.00
T6	0.2791(34)	0.0500(16)	0.1137(28)	2.34(3)	1.00
T7	0.2813(28)	0.0250(20)	0.2450(34)	2.34(3)	1.00
O1	0.0869(45)	0.0410(39)	0.0321(37)	2.75(4)	1.00
O2	0.0031(32)	0.0560(29)	0.9301(51)	2.75(4)	1.00
O3	0.4225(46)	0.1822(19)	0.8860(58)	2.75(4)	1.00
O4	0.3274(49)	0.0240(27)	0.8964(57)	2.75(4)	1.00
O5	0.4081(44)	0.1670(19)	0.0508(56)	2.75(4)	1.00
O6	0.3410(38)	-0.0710(31)	0.7931(33)	2.75(4)	1.00
O7	0.2477(56)	0.2461(21)	0.2705(47)	2.75(4)	1.00
O8	0.2273(43)	0.1082(16)	0.5711(50)	2.75(4)	1.00
O9	0.3403(41)	0.0312(33)	0.1062(41)	2.75(4)	1.00
O10	0.3084(41)	0.0871(31)	0.4931(31)	2.75(4)	1.00
O11	0.2916(51)	0.0752(33)	0.1818(30)	2.75(4)	1.00
O12	0.0944(53)	0.2051(20)	0.6282(53)	2.75(4)	1.00
O13	0.1095(51)	0.1711(18)	0.4460(58)	2.75(4)	1.00
O14	0.2328(45)	0.1392(18)	0.9007(58)	2.75(4)	1.00
C1	0.056000	0.067108	0.274428	9.84(5)	0.50(1)
C2	-0.020980	0.069070	0.191410	9.84(5)	0.50(1)
C3	0.0350(55)	0.0671(53)	0.2163(55)	9.84(5)	0.50(1)
C6	0.0408(44)	0.0691(43)	0.3663(43)	9.84(5)	0.50(1)
C7	0.0647(50)	0.2122(53)	0.1932(53)	9.84(5)	0.50(1)
C8	0.1060(40)	0.1426(43)	0.1995(43)	9.84(5)	0.50(1)

N	0.1008(50)	0.2074(50)	0.2888(50)	9.84(5)	0.50(1)
W	0.4022(28)	0.1481(33)	0.2064(28)	6.57(9)	0.55(4)

**Table 6.5.3 Atomic coordinates, thermal parameters and occupancies of ZSM-12-EMA atoms.**

Distance (Å)	ZSM-12-C	Distance (Å)	ZSM-12-EMA
T1-O1	1.629(6)	T1-O1	1.618(27)
T1-O2	1.630(6)	T1-O2	1.604(27)
T1-O3	1.614(6)	T1-O3	1.607(28)
T1-O12	1.607(6)	T1-O12	1.611(28)
<T1-O>	1.620	<T1-O>	1.610
T2-O1	1.645(6)	T2-O1	1.619(27)
T2-O2	1.638(6)	T2-O2	1.610(27)
T2-O5	1.624(6)	T2-O5	1.602(28)
T2-O13	1.658(6)	T2-O13	1.616(27)
<T2-O>	1.641	<T2-O>	1.612
T3-O3	1.614(6)	T3-O3	1.614(28)
T3-O4	1.625(6)	T3-O4	1.600(27)
T3-O6	1.645(6)	T3-O6	1.602(28)
T3-O12	1.622(6)	T3-O12	1.617(27)
<T3-O>	1.627	<T3-O>	1.608
T4-O5	1.627(6)	T4-O5	1.612(27)
T4-O9	1.635(6)	T4-O9	1.606
T4-O10	1.638(6)	T4-O10	1.609(27)
T4-O13	1.655(6)	T4-O13	1.619
<T4-O>	1.639	<T4-O>	1.612
T5-O4	1.614	T5-O4	1.594(27)
T5-O8	1.611	T5-O8	1.598(28)
T5-O10	1.622	T5-O10	1.596(27)
T5-O14	1.644	T5-O14	1.609(28)
<T5-O>	1.623	<T5-O>	1.599
T6-O8	1.620	T6-O8	1.601(28)
T6-O9	1.625	T6-O9	1.596(28)
T6-O11	1.637	T6-O11	1.598(28)
T6-O14	1.608	T6-O14	1.613(28)

<T6-O>	1.622	<T6-O>	1.602
T7-O6	1.617	T7-O6	1.605(27)
T7-O7	1.619	T7-O7	1.630(28)
T7-O7	1.627	T7-O7	1.572(27)
T7-O11	1.635	T7-O11	1.656(28)
<T7-O>	1.625	<T7-O>	1.616

**Table 6.5.4 Selected bond distances of ZSM-12-C and ZSM-12-EMA, respectively.**

Angle (°)	ZSM-12-C	Angle (°)	ZSM-12-EMA
T1-O1-T2	141.5(11)	T1-O1-T2	144.1(18)
T1-O2-T2	146.7(11)	T1-O2-T2	158.0(17)
T1-O3-T3	145.8(12)	T1-O3-T3	143.0(17)
T1-O12-T3	140.1(13)	T1-O12-T3	151.0(17)
T2-O5-T4	151.6(13)	T2-O5-T4	154.0(17)
T2-O13-T4	158.0(14)	T2-O13-T4	156.1(18)
T3-O4-T5	176.3(17)	T3-O4-T5	153.1(18)
T3-O6-T7	117.4(8)	T3-O6-T7	139.1(18)
T4-O9-T6	123.8(9)	T4-O9-T6	131.2(18)
T4-O10-T5	170.1(13)	T4-O10-T5	152.0(14)
T5-O8-T6	126.5(11)	T5-O8-T6	123.0(12)
T5-O14-T6	147.8(12)	T5-O14-T6	144.0(14)
T6-O11-T7	153.5(12)	T6-O11-T7	157.0(14)
T7-O7-T7	153.8(13)	T7-O7-T7	141.0(13)

**Table 6.5.5 Selected tetrahedral angles of ZSM-12-C and ZSM-12-EMA, respectively.**

### 6.5.3 Results and discussion

#### *Adsorption from aqueous solutions*

The data obtained from batch experiments at room temperature were fitted to the Langmuir isotherm model [77]. Figure 6.5.3 shows the adsorption isotherm of EMA on zeolite ZSM-

12: it can be observed that adsorption isotherm is concave, and it is characterised by a steep initial zone and a saturation zone (plateau adsorbed concentration). The concave shape of the adsorption isotherm indicates a favorable adsorption and therefore a practical applicability of ZSM-12 in adsorption based technologies. The Langmuir model describes an adsorption process on a homogenous surface, and it does not take into account of adsorbate-adsorbate interactions, and adsorbate-solvent interactions. Additionally, the model represents an adsorbent characterised by energetically equivalent sites. This hypothesis can, at least in first approximation, be satisfied by considering that the interaction energies of different sites are close to each other enough to be equivalent to a single site characterised by adsorption energy and adsorption constant corresponding to the average values of those of all the adsorption sites on the adsorbent material [78]. This model has been applied to describe the adsorption on different zeolites of many organic compounds both from gas and liquid phases [58, 61, 62, 79, 80].

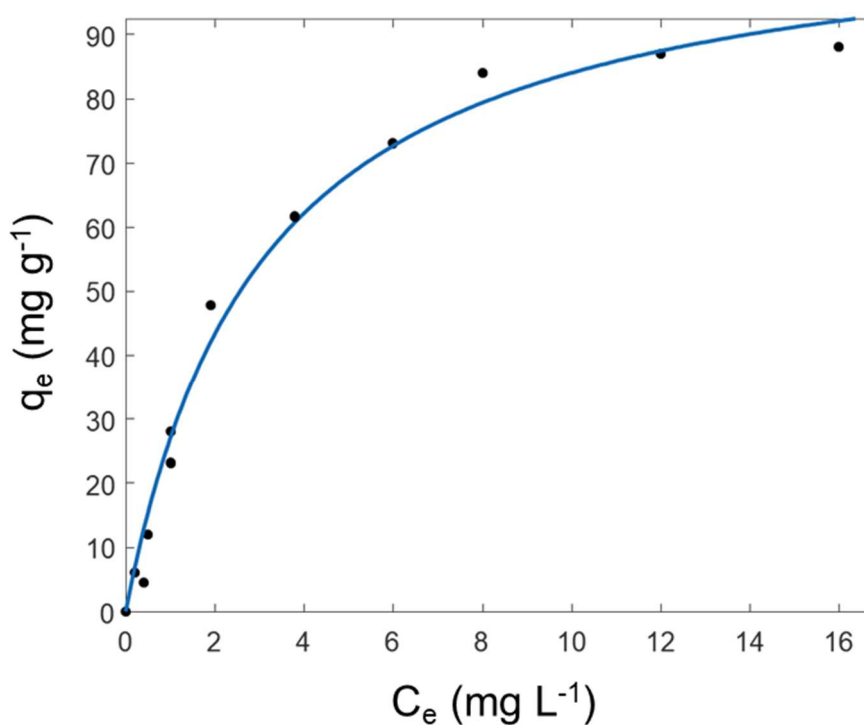


**Figure 6.5.3 Adsorption isotherms of EMA on ZSM-12 at 298.5 K.**

Table 6.5.6 summarizes the adsorption values obtained from the adsorption of EMA on ZSM-12. The high determination coefficient confirms that Langmuir model well represent the data, and therefore that EMA molecules adsorb on sites of zeolite having similar energy values. This finding, however, it is not sufficient to assess which sites of the framework are participating to the adsorption process. The estimated saturation capacity of ZSM-12 is

lower than that found for S-Metolachlor on organosilicas, however the adsorption onto ZSM-12 seems to be more favorable than that on organosilica in low concentration range, which are more similar to environmental conditions [81]. Additionally, the saturation capacity ( $q_s$ , see Table 6.5.6) of EMA on ZSM-12 is higher than that reported for Metolachlor onto activated carbons [82]. Therefore, ZSM-12 seems to be a promising adsorbent material for the removal of pesticides metabolites from aqueous matrix. To gain more information on the ZSM-12 sites involved in the adsorption process, a structural analysis was performed.

$q_s$ (mg/g)	$b$ (g/L)	$R^2$
109.7 (97.65, 121.8)	0.326 (0.2179, 0.4341)	0.9869

**Table 6.5.6 Estimated parameter for Langmuir model ( $q = \frac{q_s b c}{1 + b c}$ ); in parenthesis are reported the confidence bonds at 95% of probability.**

### 3.2 Thermal and structural analyses

To better understand the ZSM-12 finding, the structure of the sample after calcination (ZSM-12-C) was refined starting from the structural model reported by Fyfe et al. (1990) [76] taken from the International Zeolite Association (IZA) website (calcined ZSM-12, MTW framework). The monoclinic unit cell with the space group C 2/c was used along with the initial unit cell dimensions of  $a = 24.8633 \text{ \AA}$ ,  $b = 5.01238 \text{ \AA}$ ,  $c = 24.3275 \text{ \AA}$ ,  $\beta = 107.7215^\circ$ , cell formula units  $Z=1$  (Figure 6.5.4a). Our refinements are in good agreement with others [83-85]. Figure 6.5.4b shows TG/DTG/DTA curves of the title compound. The first weight loss (as well as endothermic peak in DTA) from room temperature to about  $105^\circ\text{C}$  can be related to the desorption of physically adsorbed water from the surface ( $\sim 1.8\%$  dry wet/wet). The residual one ( $\sim 3.0\%$  dry wet/wet) comprises the desorption of carbonaceous residue from SDA calcination escaping from the micropores.

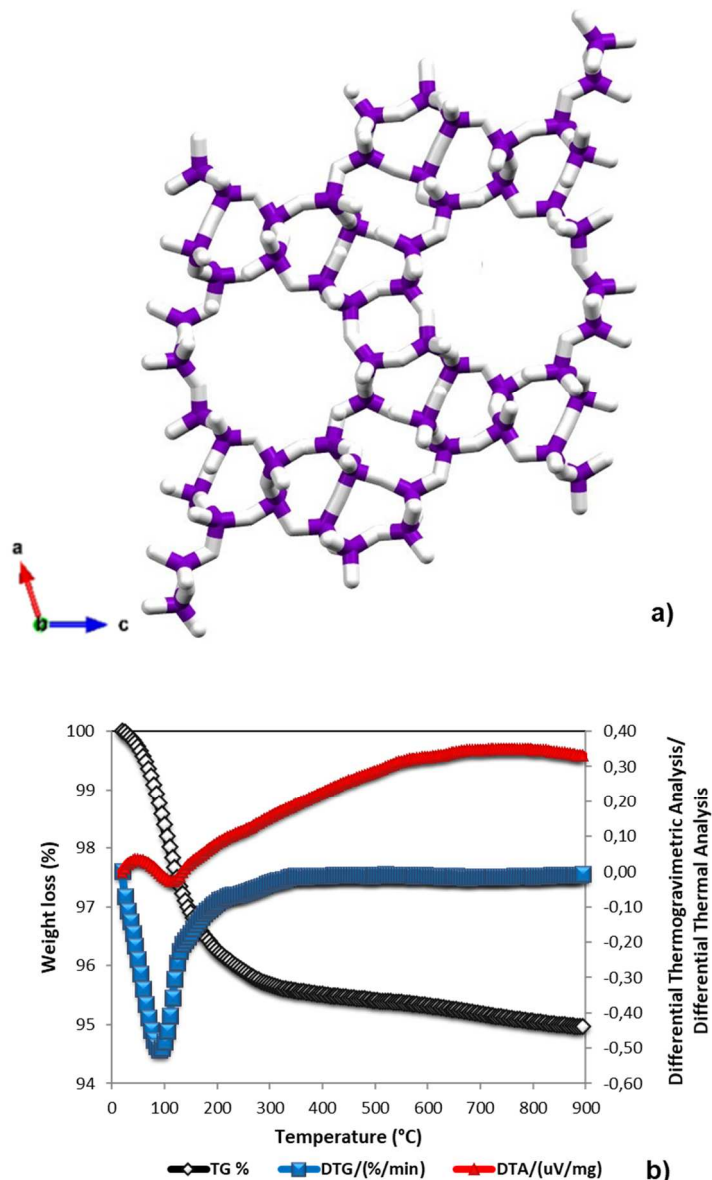


Figure 6.5.4 ZSM-12-C structure view along [010] (a) and TG/DTG/DTA curves (b).

Tables 6.5.2 and 6.5.3 reports refinement details of calcined ZSM-12 and EMA loaded ZSM-12 and Figure 6.5.2 highlights their normalised powder patterns in the range between  $2 - 20^\circ$  (Figure 6.5.2a) and  $3.3-5.7^\circ 2\theta$ , respectively.

The powder patterns of both samples possess different intensity diffraction peaks, especially in the low  $2\theta$  region (Figure 6.5.2b), which is strongly related to extraframework content and, consequently, could be connected with the presence of adsorbed EMA molecules. Additionally, the absence of additional diffraction peaks as well as of C-centering forbidden peaks indicates that the space group does not change after adsorption. The  $C2/c$  space group was maintained in ZSM-12-EMA structure refinement, which was performed starting from the framework atomic coordinates obtained for ZSM12-C. Notwithstanding this, the position of diffraction peaks (and consequently, the unit cell parameters values) in

the two patterns are not remarkably modified (and then the unit cell parameters):  $a = 24.9984(11)$   $b = 5.03362(14)$   $c = 24.3844(8)$   $\beta = 107.9428(26)$  Cell volume = 2919.12(19) in ZSM-12-C;  $a = 24.993(7)$   $b = 5.0341(9)$   $c = 24.377(5)$   $\beta = 107.879(18)$  Cell volume = 2918.9(12) in ZSM-12-EMA, respectively). The difference electron density map revealed an electron cloud in the ZSM-12 channels whose molecular geometry is very near to EMA ideal one. It reveals the presence of seven partially occupied extraframework sites (C1, C2, C3, C4, C5, C6 and N, respectively), localised inside the 12MR (Figure 6.5.5a) fitting the 12-ring aperture very well (Figure 6.5.5a). Reasonable values for C–C, N–C and C–O bond distances and related angles were obtained without to use the rigid model approach (Table 6.5.4).

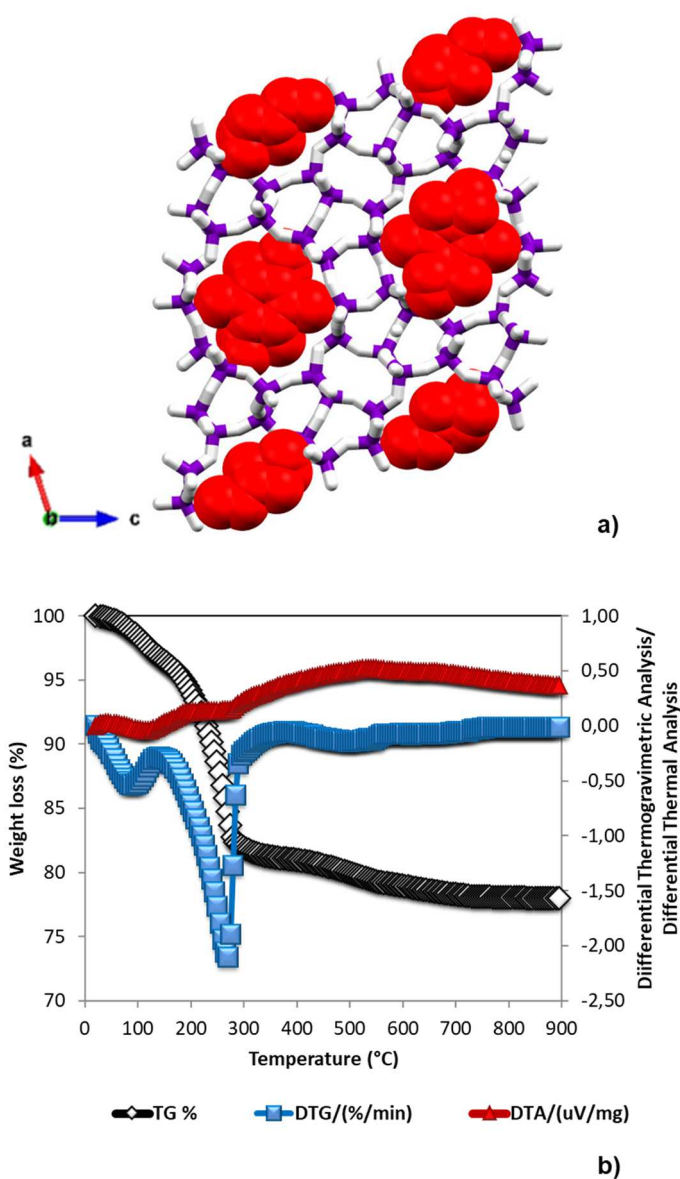


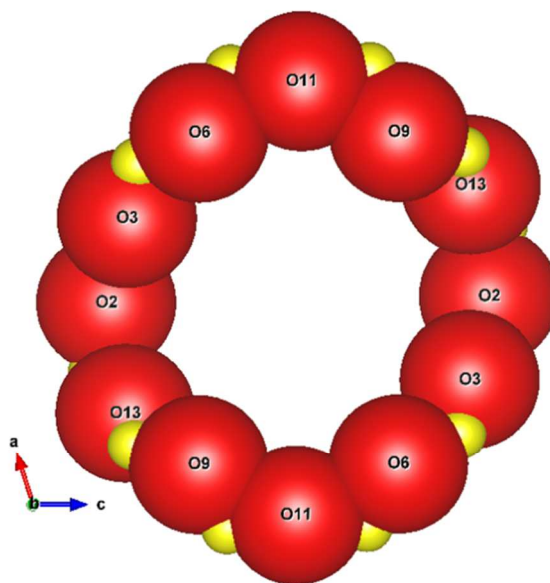
Figure 6.5.5 ZSM-12-EMA structure view along [010] (a) and TG/DTG/DTA curves (b).

The refined distances of EMA from the framework oxygen atoms (i.e. C1-W 3.09 Å; C2-W 2.96 Å, C3-W 2.94 Å, N-W 2.82 Å, N-O9 3.01 Å, N-O11 3.16 Å, C6-O6 2.87 Å, C8-O6 3.15 and 2.51 Å respectively) suggest that the organic molecules interact with the framework and this interactions are mediated by another extraframework site detected by Difference Fourier map. This last was assigned to co-adsorbed water. Furthermore, the occupancy of EMA and water atoms refined to 4.0 (14% in dry weight) and 4.5 molecules (2% in dry weight) per unit cell, which correlates well with the weight loss accounted by thermogravimetric analysis. Figure 6.5.5b shows TG/DTG/DTA curves of the loaded sample. Also in this case the first weight loss (as well as endothermic peak in DTA) from room temperature to about 105°C can be related to the desorption of physically adsorbed water/EMA from the surface (~3.0% dry wet/wet). The residual one (~17.0% dry wet/wet) comprises the desorption of extraframework species (EMA and water molecules) from within the channels.

Water molecules interact with both the NH<sub>2</sub>- and methyl groups of EMA thus forming oligomers bonded to framework oxygens. The occurrence of such molecular complexes was also detected in hydrophobic zeolites loaded with non-polar species [38, 40, 41, 57, 58, 61, 62]. They “immobilise” the pollutants in the cages thus preventing inserted molecules from desorbing as well as the entering of other competitive molecules.

After EMA adsorption, the analysis of rings was useful to calculate pore diameters variations in ZSM-12. As reported by Bermúdez and Sastre (2017) [86] “Pores differ from rings in that pores are those rings which define channels; thus, ‘pores’ are a subgroup of ‘rings’”. In this work the ring diameters have been calculated considering the distance between two opposite oxygen atoms and then subtracting twice the IZA recommended value of the oxygen radius (1.35 Å). These information are crucial for a deep knowledge of both transport properties as well as zeolite–adsorbate and adsorbate–adsorbate interactions [86-90].

The ZSM-12-EMA diameters of 12-rings become larger and circular with respect to the ZSM-12-C ones and the Crystallographic Free Areas (C.F.A.) of the rings undergoes a marked increase to best fitting the organic in 12-ring aperture (Figure 6.5.6).



ZSM-12-C	Distance (Å)	Free Diameter (Å)
O11-O11	9.297	6.597
O6-O6	8.022	5.322
O3-O3	8.534	5.834
O2-O2	8.134	5.434
O9-O9	8.863	5.737
CFA (Å <sup>2</sup> )= $\pi r^2$	r=mean radius=2.892	26.269
ELLIPTICITY ( $\epsilon$ )	$\epsilon=(O11-O11)/(O2-O2)$	1.159

ZSM-12-EMA	Distance (Å)	Free Diameter (Å)
O11-O11	9.915	7.215
O6-O6	8.822	6.122
O3-O3	8.645	5.945
O2-O2	8.733	6.033
O9-O9	8.863	6.163
CFA (Å <sup>2</sup> )= $\pi r^2$	r=mean radius=3.147	31.113
ELLIPTICITY ( $\epsilon$ )	$\epsilon=(O11-O11)/(O3-O3)$	1.147

Figure 6.5.6 Experimental diameters of 12-rings in four ZSM-12-C and ZSM-12-EMA, respectively.

## 6.5.4 Conclusions

The increased awareness of soils, water and ground water contamination by chloroacetanilide herbicides has pushed the research towards economically feasible and environmentally friendly remediation technologies. Adsorption is a simple and economic procedure involved in the water treatment which is able to control the mobility, fate, bioavailability and reactivity of emerging organic pollutants in the environment. Zeolites

show high surface area, high specific capacity, mechanical, biological/chemical stability and high adsorption selectivity thus representing economically feasible and environmentally friendly adsorbents media capable of removing these pollutants from water. In this work the efficiency of ZSM-12 zeolite for agro-chemicals contaminant (2-ethyl-6-methylaniline, EMA) removal from aqueous matrix was highlighted by chromatographic, thermogravimetric and synchrotron X-ray powder diffractometric techniques. We have herein demonstrated that synthetic ZSM-12 is a good candidate for pesticide metabolite EMA removal. Indeed, its adsorption isotherm follows a Langmuir model, and shows a favourable adsorption. In addition, the saturation capacity of ZSM-12 is higher than that of other widely employed adsorbent materials such as activated carbon and mesoporous organosilica. Indeed, the saturation capacity of granular activated was found equal to  $3.3 \text{ mg g}^{-1}$  [82]. On the other hand, mesoporous organosilicas, shown very high saturation capacity ( $500 \text{ mg g}^{-1}$ ) at pH=4, however, the adsorption quantities at pH=4 on these materials do not exceed  $50 \text{ mg g}^{-1}$  with solution concentration lower than  $30 \text{ mg L}^{-1}$ , thus indicating lower adsorption efficiency in concentration range similar to natural conditions [81]. The organic molecules are effectively embedded in the zeolite framework as demonstrated from structural analysis. EMA interacts with water molecule to form oligomers which, in turn, interact with framework atoms. The formation of these supramolecular complexes confers stability to the pollutants in the zeolite cages thus preventing adsorbed molecules from desorbing as well as the entering of other competitive molecules. All these findings contribute to assess that ZSM-12 could be a promising materials to control and minimize water pollution from EMA as well as other agro-chemicals contaminants.

### 6.5.5 References

- [1] Otero R., Esquivel D., Ulibarri M. A. Jiménez-Sanchidrián C., Romero-Salguero F. J., Fernandez J. M. (2013) Adsorption of the herbicide S-Metolachlor on periodic mesoporous Organosilicas. *Chemical Engineering Journal*, 228, 205– 213.
- [2] Shukla G., Kumar A., Bhanti M., Joseph P. E., Taneja A., (2006) Organochlorine pesticide contamination of ground water in the city of Hyderabad. *Environmental International* 32, 244–247.
- [3] Levitan L. (2000) “How to” and “why”: assessing the enviro–social impacts of pesticides. *Crop Protection*, 19(8-10), 629-636.
- [4] World Health Organization (2010) International code of conduct on the distribution and use of pesticides: Guidelines for the Registration of Pesticides.
- [5] Commission Directive 98/83/EC, (1998) Council Directive 98/83/EC of 3 Nov 1998 on the quality of water intended for human consumption - Drinking Water Directive (DWD) Revision of Annex II and Annex III. Meeting of the Drinking Water Committee.

- [6] Boithias L., Sauvage S., Taghavi L., Merlina G., Probst J. L., Pérez J. M. S. (2011) Occurrence of metolachlor and trifluralin losses in the Save river agricultural catchment during floods. *Journal of Hazardous Materials*, 196, 210-219.
- [7] Traub-Eberhard U., Hensche K. P., Kordel W., Klein W. (1995) Influence of different field sites on pesticide movement into subsurface drain, *Pesticide Science*, 43, 121–129.
- [8] Gaynor J. D., Mactavish D. C., Findlay W. I. (1995) Atrazine and metolachlor loss in surface and subsurface runoff from three tillage treatments in corn. *Journal of Environmental Quality*, 24, 246–256.
- [9] Nennemann A. Mishael Y., Nir S., Rubin B., Polubesova T., Bergaya F., van Damme H., Lagaly G. (2001) Clay-based formulations of metolachlor with reduced leaching, *Applied Clay Science*, 18(5), 265–275.
- [10] Fava L., Bottoni P., Crobe A., Funari E. (2000) Leaching properties of some degradation products of alachlor and metolachlor. *Chemosphere* 41 (9), 1503–1508.
- [11] Fava L., Bottoni P., Crobe A., Barra Caracciolo A., Funari E. (2001) Assessment of leaching potential of aldicarb and its metabolites using laboratory studies. *Pesticide Management Science* 57 (12), 1135–1141.
- [12] Kimmel E. C., Casida J. C., Ruzo L. O. (1986) Formamidin insecticides and chloroacetanilide herbicides: disubstituted anilines and nitrosobenzenes as mammalian metabolites and bacterial mutagens. *Journal of Agricultural and Food Chemistry* 34, 157–161.
- [13] Osano O., Admiraal W., Otieno D. (2002) Developmental disorders in embryos of the frog *Xenopus laevis* induced by chloroacetanilide herbicides and their degradation products. *Environmental Toxicology and Chemistry*, 21, 375-379.
- [14] Osano O., Admiraal W., Klamer H. J. C., Pastor D., Bleeker E. A. J. (2002) Comparative toxic and genotoxic effects of chloroacetanilides, formamidines and their degradation products on *Vibrio fischeri* and *Chironomus riparius*. *Environmental Pollution*, 119, 195-202.
- [15] Osano O., Nzyuko D., Tole M., Admiraal W. (2003) The fate of chloroacetanilide herbicides and their degradation products in the Nzoia Basin, Kenya. *AMBIO: A Journal of the Human Environment*, 32(6), 424-427.
- [16] Gerstl Z., Nasser A., Mingelgrin U. (1998) Controlled release of pesticides into soils from clay– polymer formulations. *Journal of Agricultural and Food Chemistry*, 46(9), 3797-3802.
- [17] Webster E., Mackay D., Wania F. (1998) Evaluating environmental persistence. *Environmental Toxicology Chemistry* 17, 2148-2158.
- [18] Bollag J. M., McGahen L. L., Minard R. D., Liu S. Y. (1986) Bioconversion of alachlor in an anaerobic stream sediment. *Chemosphere* 15, 153-162.

- [19] Liu D., Maguire R. J., Pacepavicius G. J., Aoyama I., Okamura H. (1995) Microbial transformation of metolachlor. *Environmental Toxicology and Water Quality*, 10, 249-258.
- [20] Stamper D. M., Tuovinen O. H. (1998) Biodegradation of the acetanilide herbicides alachlor, metolachlor, and propachlor. *Critical Reviews in Microbiology*, 24, 1-22.
- [21] Zhang X., Zhang, M. (2011) Modeling effectiveness of agricultural BMPs to reduce sediment load and organophosphate pesticides in surface runoff. *Science of the Total Environment*, 409(10) 1949-1958.
- [22] Kovaivos I. D., Paraskeva C. A., Koutsoukos P. G. (2011) Adsorption of atrazine from aqueous electrolyte solutions on humic acid and silica. *Journal of colloid and interface science*, 356(1), 277-285.
- [23] Bezbaruah A. N., Thompson J. M., Chisholm B. J. (2009) Remediation of alachlor and atrazine contaminated water with zero-valent iron nanoparticles. *Journal of Environmental Science and Health, Part B* 44(6) 518-524.
- [24] Zadaka D., Nir S., Radian A., Mishael Y. G. (2009) Atrazine removal from water by polycation–clay composites: effect of dissolved organic matter and comparison to activated carbon. *Water Research*, 43(3), 677-683.
- [25] Liu Y., Zhang J., Sheng C., Zhang Y., Zhao L. (2010) Preliminary study on a new technique for wet removal of nitric oxide from simulated flue gas with an ultraviolet (UV)/H<sub>2</sub>O<sub>2</sub> process. *Energy and Fuels*, 24(9), 4925-4930.
- [26] Coffinet S., Rifai A., Genty C., Souissi Y., Bourcier S., Sablier M., Bouchonnet S. (2012) Characterization of the photodegradation products of metolachlor: structural elucidation, potential toxicity and persistence. *Journal of Mass Spectrometry*, 47(12), 1582-1593.
- [27] Elsayed O. F., Maillard E., Vuilleumier S., Imfeld G. (2014) Bacterial communities in batch and continuous-flow wetlands treating the herbicide S-metolachlor. *Science of the Total Environment*, 499, 327-335.
- [28] Jiang H., Adams C., Graziano N., Roberson A., McGuire M., Khiari D. (2006) Occurrence and removal of chloro-s-triazines in water treatment plants. *Environmental science and technology*, 40(11), 3609-3616.
- [29] Lopez-Ramon M. V., Fontecha-Camara M. A., Alvarez-Merino M. A., MorenoCastilla C. (2007) Removal of diuron and amitrol from water under static and dynamic conditions using activated carbon in form of fiber, cloth and grains. *Water Research*, 41, 2865–2870.
- [30] Bakouri H. E., Morillo J., Usero J., Quassini A. (2009) Natural attenuation of pesticide water contamination by using ecological adsorbents: application for chlorinated pesticides included in European water framework directives, *Journal of Hydrology*, 364 175–181.
- [31] Reichle W.T. (1986) Synthesis of anionic clay minerals (mixed metal hydroxides, hydrotalcite). *Solid State Ionics* 22, 135–141.

- [32] Rives V. (2001) Layered Double Hydroxides: Present and Future. Nova Science Publishers, Inc., New York.
- [33] Wang B., Zhang H., Evans D., Duan X. (2005) Surface modification of layered double hydroxides and incorporation of hydrophobic organic compounds. *Materials Chemistry and Physics* 92, 190–196.
- [34] Chaara D., Bruna F., Ulibarri M. A., Draoui K., Barriga C., Pavlovic I. (2011) Organo/layered double hydroxide nanohybrids used to remove non ionic pesticides, *Journal of Hazardous Materials*, 196, 350–359.
- [35] Si Y. B., Takagi K., Iwasaki A., Zhou D. M. (2009) Adsorption, desorption and dissipation of metolachlor in surface and subsurface soils, *Pest Management Science*, 65, 956–962.
- [36] Mastrocicco M., Colombani N., Cavazzini A., Pasti L. (2009) A green and fast chromatographic method for determining organic compound mobility in soils, *Journal of Chromatography A*, 1216(40), 6802-6809.
- [37] De Smedt C., Ferrer F., Leus K., Spanoghe P. (2015) Removal of Pesticides from Aqueous Solutions by Adsorption on Zeolites as Solid Adsorbents. *Adsorption Science and Technology*, 33(5), 457 – 485.
- [38] Martucci A., Pasti L., Marchetti N., Cavazzini A., Dondi F., Alberti A. (2012) Adsorption of pharmaceuticals from aqueous solutions on synthetic zeolites. *Microporous and Mesoporous Materials*, 148(1), 174-183.
- [39] Martucci A., Pasti L., Nassi M., Alberti A., Arletti R., Bagatin R., Vignola R., Sticca R. (2012). Adsorption mechanism of 1, 2-dichloroethane into an organophilic zeolite mordenite: a combined diffractometric and gas chromatographic study. *Microporous and Mesoporous Materials*, 151, 358-367.
- [40] Pasti L., Martucci A., Nassi M., Cavazzini A., Alberti A., Bagatin R. (2012) The role of water in DCE adsorption from aqueous solutions onto hydrophobic zeolites. *Microporous and Mesoporous Materials*, 160, 182-193.
- [41] Arletti R., Martucci A., Alberti A., Pasti L., Nassi M., Bagatin R. (2012) Location of MTBE and toluene in the channel system of the zeolite mordenite: Adsorption and host–guest interactions. *Journal of Solid State Chemistry*, 194, 135-142.
- [42] Blasioli S., Martucci A., Paul G., Gigli L., Cossi M., Johnston C. T., Marchese L., Braschi I. (2014) Removal of sulfamethoxazole sulfonamide antibiotic from water by high silica zeolites: a study of the involved host–guest interactions by a combined structural, spectroscopic, and computational approach. *Journal of colloid and interface science*, 419, 148-159.
- [43] Martucci A., Cremonini M. A., Blasioli S., Gigli L., Gatti G., Marchese L., Braschi I. (2013) Adsorption and reaction of sulfachloropyridazine sulfonamide antibiotic on a high

silica mordenite: A structural and spectroscopic combined study. *Microporous and Mesoporous Materials*, 170, 274-286.

[44] Kyzas G. Z., Kostoglou M., Lazaridis N. K., Lambropoulou D. A., Bikiaris D. N. (2013) Environmental friendly technology for the removal of pharmaceutical contaminants from wastewaters using modified chitosan adsorbents. *Chemical Engineering Journal*, 222, 248-258.

[45] Vilaça N., Amorim R., Martinho O., Reis R. M., Baltazar F., Fonseca A. M., Neves I. C. (2011) Encapsulation of  $\alpha$ -cyano-4-hydroxycinnamic acid into a NaY zeolite. *Journal of materials science*, 46(23), 7511.

[46] Rakić V., Rajić N., Daković A., Auroux A. (2013) The adsorption of salicylic acid, acetylsalicylic acid and atenolol from aqueous solutions onto natural zeolites and clays: Clinoptilolite, bentonite and kaolin. *Microporous and Mesoporous Materials*, 166, 185-194.

[47] Datt A., Fields D., Larsen S. C. (2012) An experimental and computational study of the loading and release of aspirin from zeolite HY. *Journal of Physical Chemistry C*, 116(40), 21382-21390.

[48] Rossner A., Snyder S. A., Knappe D. R. (2009) Removal of emerging contaminants of concern by alternative adsorbents. *Water Research*, 43(15), 3787-3796.

[49] Damjanović L., Rakić V., Rac V., Stošić D., Auroux A. (2010) The investigation of phenol removal from aqueous solutions by zeolites as solid adsorbents. *Journal of hazardous materials*, 184(1-3), 477-484.

[50] Amorim R., Vilaça N., Martinho O., Reis R. M., Sardo M., Rocha J., Fonseca A. M., Baltazar F., Neves I. C. (2012) Zeolite structures loading with an anticancer compound as drug delivery systems. *The Journal of Physical Chemistry C*, 116(48), 25642-25650.

[51] Braschi I., Gatti G., Bisio C., Berlier G., Sacchetto V., Cossi M., Marchese L. (2012) The role of silanols in the interactions between methyl tert-butyl ether and high-silica faujasite Y: an infrared spectroscopy and computational model study. *The Journal of Physical Chemistry C*, 116(12), 6943-6952.

[52] Sacchetto V., Gatti G., Paul G., Braschi I., Berlier G., Cossi M., Marchese L., Bagatin R., Bisio C. (2013) The interactions of methyl tert-butyl ether on high silica zeolites: a combined experimental and computational study. *Physical Chemistry Chemical Physics*, 15(32), 13275-13287.

[53] Datt A., Burns E. A., Dhuna N. A., Larsen, S. C. (2013) Loading and release of 5-fluorouracil from HY zeolites with varying  $\text{SiO}_2/\text{Al}_2\text{O}_3$  ratios. *Microporous and Mesoporous Materials*, 167, 182-187.

[54] Pasti L., Sarti E., Cavazzini A., Marchetti N., Dondi F., Martucci A. (2013) Factors affecting drug adsorption on beta zeolites. *Journal of Separation Science*, 36(9-10), 1604-1611.

- [55] Martucci A., Pasti L., Sarti E., Bagatin R. (2013). Emerging organic pollutants removal from water using high silica zeolites. *Mineralogical Magazine*, 77(5), 1699-1699.
- [56] Martucci A., Leardini L., Nassi M., Sarti E., Bagatin R., Pasti L. (2014) Removal of emerging organic contaminants from aqueous systems: Adsorption and location of methyl-tertiary-butylether on synthetic ferrierite. *Mineralogical Magazine*, 78(5), 1161-1176.
- [57] Martucci A., Rodeghero E., Pasti L., Bosi V., Cruciani G. (2015) Adsorption of 1, 2-dichloroethane on ZSM-5 and desorption dynamics by in situ synchrotron powder X-ray diffraction. *Microporous and Mesoporous Materials*, 215, 175-182.
- [58] Leardini L., Martucci A., Braschi I., Blasioli S., Quartieri S. (2014) Regeneration of high-silica zeolites after sulfamethoxazole antibiotic adsorption: a combined in situ high-temperature synchrotron X-ray powder diffraction and thermal degradation study. *Mineralogical Magazine*, 78(5), 1141-1159.
- [59] Genç N., Dogan E. C. (2015) Adsorption kinetics of the antibiotic ciprofloxacin on bentonite, activated carbon, zeolite, and pumice. *Desalination and Water Treatment*, 53(3), 785-793.
- [60] Pasti L., Rodeghero E., Sarti E., Bosi V., Cavazzini A., Bagatin R., Martucci A. (2016). Competitive adsorption of VOCs from binary aqueous mixtures on zeolite ZSM-5. *RSC Advances*, 6(59), 54544-54552.
- [61] Rodeghero E., Pasti L., Sarti E., Cruciani G., Bagatin R., Martucci A. (2017) Temperature-induced desorption of methyl tert-butyl ether confined on ZSM-5: An in situ synchrotron XRD powder diffraction study. *Minerals*, 7(3), 34.
- [62] Rodeghero E., Martucci A., Cruciani G., Sarti E., Cavazzini A., Costa V., Bagatin R., Pasti L. (2017) Detailed investigation of thermal regeneration of high-silica ZSM-5 zeolite through in situ synchrotron X-ray powder diffraction and adsorption studies. *The Journal of Physical Chemistry C*, 121(33), 17958-17968.
- [63] Baerlocher C., McCusker L. B., Olson D. H. (2007) *Atlas of Zeolite Framework Types*, 6<sup>th</sup> rev. ed., Elsevier, Amsterdam.
- [64] Corma A. (1997). From microporous to mesoporous molecular sieve materials and their use in catalysis. *Chemical reviews*, 97(6), 2373-2420.
- [65] Rosinski E J., Rubin M. K. (1983) Preparation of ZSM-12 type zeolites. U.S. Patent No 4, 391, 785.
- [66] Trewella J. C., Schlenker J. L., Woessner D. E., Higgins J. B. (1985) The silicon-29 MAS-n.m.r. spectrum of ZSM—12, *Zeolites*, 5 130– 131.
- [67] Fyfe C. A., Strobl H., Kokotailo G. T., Pasztor C. T., Barlow G. E., Bradley S. (1988) Correlations between lattice structures of zeolites and their <sup>29</sup>Si MAS NMR spectra: zeolites KZ-2, ZSM-12, and Beta. *Z. Zeolites*, 8, 132–136.

- [68] Perego C., Amarilli S., Millini R., Bellussi G., Girotti G., Terzoni G. (1996) Experimental and computational study of beta, ZSM-12, Y, mordenite and ERB-1 in cumene synthesis. *Microporous materials*, 6(5-6), 395-404.
- [69] Millini R., Carluccio L., Frigerio F., Parker W. O. N. Jr, Bellussi G. (1998) Zeolite synthesis in the presence of azonia-spiro compounds as structure-directing agents<sup>1</sup>. *Microporous and mesoporous materials*, 24(4-6), 199-211.
- [70] Yoo K., Kashfi R., Gopal S., Smirniotis P. G., Gangoda M., Bose R. N. (2003) TEABr directed synthesis of ZSM-12 and its NMR characterization. *Microporous and Mesoporous Materials*, 60, 57–68.
- [71] Pazzucconi C. P. G., Millini R., Frigerio F., Mansani R., Rancati D. (2000) US Patent 6, 147, 270.
- [72] Bortolini O., Cavazzini A., Giovannini P. P., Greco R., Marchetti N., Massi A., Pasti L. (2013) A Combined Kinetic and Thermodynamic Approach for the Interpretation of Continuous-Flow Heterogeneous Catalytic Processes. *Chemistry—A European Journal*, 19(24), 7802-7808.
- [73] Millini R., Perego C., Frigerio F., Carluccio L. C., Bellussi G. (2004) Azonia-spiro compounds as structure directing agents: A computational study. In *Recent advances in the science and technology of zeolites and related materials: proceedings of the 14th International Zeolite Conference, Cape Town, South Africa, 25-30th April 2004* Vol. 154, p. 275. Elsevier.
- [74] Larson A. C., Von Dreele R. B. (2000) General Structure Analysis System "GSAS"; Los Alamos National Laboratory Report, Los Alamos, LAUR 86-748.
- [75] Toby B. H. J. (2001) EXPGUI, a Graphical User Interface for GSAS. *Journal of Applied Crystallography*, 34, 210–213.
- [76] Fyfe C. A., Gies H., Kokotailo G. T., Marler B., Cox D. E. (1990) *Journal of Physical Chemistry*, 94, 3718-3721.
- [77] Foo K. Y., Hameed B. H. (2010) Insights into the modeling of adsorption isotherm systems. *Chemical engineering journal*, 156(1), 2-10.
- [78] Ruthven D. M. (1984) *Principles of adsorption and adsorption processes*. John Wiley and Sons.
- [79] Rodeghero E., Martucci A., Cruciani G., Bagatin R., Sarti E., Bosi V., Pasti L. (2016) Kinetics and dynamic behaviour of toluene desorption from ZSM-5 using in situ high-temperature synchrotron powder X-ray diffraction and chromatographic techniques. *Catalysis Today*, 277, 118–125.
- [80] Perego C., Bagatin R., Tagliabue M., Vignola R. (2013) Zeolites and related mesoporous materials for multi-talented environmental solutions. *Microporous and Mesoporous Materials*, 166, 37–49.

- [81] Otero R., Esquivel D., Ulibarri M. A., Jiménez-Sanchidrián C., Romero-Salguero F. J., Fernandez J. M. (2013) Adsorption of the herbicide S-Metolachlor on periodic mesoporous Organosilicas. *Chemical Engineering Journal*, 228, 205– 213.
- [82] Kumar Y. B., Singh N., Singh, S. B. (2013) Removal of Atrazine, Metribuzin, Metolachlor and Alachlor by Granular Carbon, *Journal of Environmental and Analytical toxicology*, 3(7), 1-5.
- [83] Brouwer D. H. (2008) A structure refinement strategy for NMR crystallography: An improved crystal structure of silica-ZSM-12 zeolite from <sup>29</sup>Si chemical shift tensors. *Journal of Magnetic Resonance*, 194(1), 136-146.
- [84] Fyfe C. A., Brouwer D. H. (2006) Optimization, Standardization, and Testing of a New NMR Method for the Determination of Zeolite Host– Organic Guest Crystal Structures. *Journal of the American Chemical Society*, 128(36), 11860-11871.
- [85] Kasunič M., Legiša J., Meden A., Logar N. Z., Beale A. M., Golobič A. (2009) Crystal structure of pure-silica ZSM-12 with tetraethylammonium cations from X-ray powder diffraction data. *Microporous and Mesoporous Materials*, 122, 255-263.
- [86] Bermúdez D., Sastre G. (2017) Calculation of pore diameters in zeolites. *Theoretical Chemistry Accounts*, 136(10), 116.
- [87] Foster M. D., Rivin I., Treacy M. M. J., Delgado-Friedrichs O. (2006) A geometric solution to the largest-free-sphere problem in zeolite frameworks. *Microporous and Mesoporous Materials*, 90, 32–38.
- [88] Curtis R. A., Deem M. W. (2003) A statistical mechanics study of ring size, ring shape, and the relation to pores found in zeolites. *Journal of Physical Chemistry B*, 107, 8612–8620.
- [89] Haldoupis E., Nair S., Sholl D. S. (2011) Pore size analysis of > 250000 hypothetical zeolites. *Physical Chemistry Chemical Physics*, 13(11), 5053-5060.
- [90] Krishna R., van Baten J. M. (2012) Investigating the relative influences of molecular dimensions and binding energies on diffusivities of guest species inside nanoporous crystalline materials. *The Journal of Physical Chemistry C*, 116(44), 23556-23568.

## 6.6 Gallium-exchanged zeolites

The data herein reported are part of my work of thesis and have been published in: Beltrami G., Chenet T., Pasti L., Gigli L., Pollastri S., Martucci A. Insights on Ga-zeolite catalysts: X-ray powder diffraction and absorption spectroscopy characterization at ambient conditions. *Catalysis Today*, available online.

### 6.6.1 Introduction

Zeolite are crystalline microporous materials whose framework is build up by corner-sharing  $\text{TO}_4$  tetrahedra, where T usually contain  $\text{Si}^{4+}$  or  $\text{Al}^{3+}$ . The insertion of other tetrahedral coordinated heteroatoms (*e.g.*, Fe, Ga, Ge, B, Ti, *etc*) provides a means to modify their physicochemical properties as well as to increase their catalytic activity [1]. In addition, zeolite properties can be also modified by cation exchange process, in such a case, the type and localisation of extraframework cations control and influence their selectivity and catalytic activity [2]. An interesting family of catalysts is that of Ga-loaded zeolites due to their excellent performances in isomerisation, disproportionation and alkylation of aromatics and aromatisation of alkanes and/or alkenes [3–6]. Gallium-containing zeolites have been widely investigated in the last decades and newest applications concerning the removal of  $\text{NO}_x$  from gas streams of exhaust engine and the conversion of biomass into biofuels and bio-based chemicals have been proposed [5,7,8]. Ga-zeolite catalysts can be obtained through hydrothermal crystallisation in presence of the suitable template agent or post synthesis treatments, such as galliation, recrystallisation, wet impregnation, chemical vapour deposition (CVD) and ion exchange [5,9].

The ion exchange process is suitable to introduce gallium into both tetrahedral coordinated framework and interstitial non-framework positions. Besides, the precipitation on the external surface of the zeolite crystal of a separate gallium phase in aqueous solution, depending on the pH value during the exchange process, has to be foreseen. Substitution of  $\text{Al}^{3+}$  with  $\text{Ga}^{3+}$  cations [10] into framework positions is the main source of lattice charge defects, which give rise to Brønsted acidic Si–OH–Ga bridging hydroxyl group and, consequently, to modification of catalytic properties. To understand the precise nature and functioning of the active sites in working zeolites, incorporation of  $\text{Ga}^{3+}$  into the zeolite framework has been highlighted by means of solid-state NMR, EXAFS, *in situ* X-ray photoelectron spectroscopy, IR spectroscopy and DFT calculations [11–17]. Along with the segregate gallium phase, excess gallium not incorporated in tetrahedral sites is trapped within the zeolite pores system as substituent of metal cations, ammonium ions or protons. The presence of gallium cations in extraframework positions introduces Lewis acidity, which is also originated from oxo cations  $\text{GaO}^+$  in exchanged framework positions. Due to its size, gallium in framework positions is metastable; hence, the thermal treatment can cause the

migration of Ga<sup>3+</sup> to extraframework positions and its progressive aggregation in form of isolated, dimeric and polymeric species up to oxide nanoparticles [18–20]. This migration leads to the appearance of a different type of acid sites of Lewis nature [21]. As a consequence, Ga exchanged zeolites can possess both Brønsted and Lewis acid sites, working separately or in a synergistic way in acid catalysed reactions [22,23]. To our knowledge, in spite of the large number of both spectroscopic and computational studies, very few detailed structural investigations have been conducted so far to explore the gallium centres using X-ray diffraction methods. With this aim, in this work we intend to investigate the structural features of Ga-loaded zeolites in order to elucidate the nature of the gallium active sites combining X-ray powder diffraction (XRPD), X-ray absorption spectroscopy (XAS) and adsorption study.

Among zeolites, gallium modified L (LTL), mordenite (MOR) and ferrierite (FER), have been employed as catalysts [24]. Consequently, these large and medium pore materials were selected in this work to: 1) investigate the adsorptive properties of hydrophobic synthetic zeolites; 2) characterise zeolites structure at ambient conditions, 3) locate and quantify Ga<sup>3+</sup> cations in framework and non-framework positions, 4) determine the presence of water molecules completing the extraframework Ga<sup>3+</sup> coordination, 5) determine unit cell dimensions as well as host-guest interactions by the analysis of bond length distances. All these information are essential not only for their characterisation but also for their industrial applications.

## 6.6.2 Materials and methods

### *Zeolites*

The synthetic zeolite L sample (HSZ-500KOA code) was purchased by Tosoh Corporation in the K form, with a SiO<sub>2</sub>/Al<sub>2</sub>O<sub>3</sub> (SAR) ratio of 6.1, an Na<sub>2</sub>O content of 0.25 wt % and a surface area of about 290 m<sup>2</sup>/g. MOR (CBV10A code) and FER (CP914C code) samples were supplied by Zeolyst International in Na<sup>+</sup> and ammonium forms, respectively. The first is characterised by a SAR equal to 13, a Na<sub>2</sub>O content of 6.5 wt % and a surface area of 425 m<sup>2</sup> g<sup>-1</sup>, whereas the second by a SAR equal to 20, Na<sub>2</sub>O content lower than 0.05 wt % and surface area of 400 m<sup>2</sup> g<sup>-1</sup>.

Parameter	Ga-L	Ga-MOR	Ga-FERR
	$\text{Ga}_{2.57}\text{K}_2((\text{GaAlSi})_{36}\text{O}_{72})\cdot 14\text{H}_2\text{O}$	$\text{Ga}_{1.16}\text{Na}_2((\text{GaAlSi})_{48}\text{O}_{96})\cdot 13\text{H}_2\text{O}$	$\text{Ga}_{1.3}((\text{GaAlSi})_{36}\text{O}_{72})\cdot 5\text{H}_2\text{O}$
Wavelength (Å)	1.54059	1.54059	1.54059
2θ (°) range	5.5-100	5.5-100	5.5-100
N <sub>obs</sub>	1339	1482	1564
N <sub>var</sub>	56	76	64
R <sub>wp</sub> (%)	14.45	13.35	14.59
R <sub>p</sub> (%)	10.83	10.17	11.34
R <sub>F</sub> <sup>2</sup> (%)	16.85	11.32	12.29

$$R_p = \frac{\sum |Y_{io} - Y_{ic}|}{\sum Y_{io}}; R_{wp} = \left[ \frac{\sum w_i (Y_{io} - Y_{ic})^2}{\sum w_i Y_{io}^2} \right]^{0.5}; R_F^2 = \frac{\sum |F_o^2 - F_c^2|}{|F_o^2|}$$

**Table 6.6.1 Crystallographic data obtained from the Rietveld refinements of Ga-L, Ga-MOR and Ga-FER systems.**

#### *Cation exchange*

As-received L and MOR zeolites were exchanged with ammonium by the following procedure: 1 g of zeolite was stirred in 200 mL of 0.5 M solution of ammonium nitrate (> 99%, Sigma Aldrich) in MilliQ water at 343 K for 24 h. The suspension was then filtered, by using a Nylon filter 0.22 μm (Sigma Aldrich) at room temperature and rinsed with 300 mL of MilliQ water. This procedure was repeated twice. The ammonium form of L and MOR and the as-received FER were heated in a furnace for five hours at ~ 600°C in order to obtain the calcined-form.

#### *Wet impregnation*

Cation exchange capacity was determined by using aqueous solutions of gallium nitrate ( $\text{Ga}(\text{NO}_3)_3 \cdot x\text{H}_2\text{O}$ , Aldrich 99.9%) at different initial concentrations (5, 10, 20, 50, 70, 100, 150 and 200 mg L<sup>-1</sup>), placed in contact with zeolites (L, FER and MOR) with a solid/liquid ratio of 1:1 (mg mL<sup>-1</sup>). The suspensions were kept at 343 K under stirring during the contact time at pH 4.3, the pH was monitored during the contact and variation of 0.3 pH unit occur from the beginning to the end of the contact. All batch experiments were carried out in duplicate. The concentrations of Ga<sup>3+</sup> in the solutions after the contact with zeolites and in the reference solutions obtained by keeping solutions in the same conditions of the adsorption experiments but without the addition of zeolites, were quantified by ICP-OES (Perkin-Elmer Optima 3100 XL) (axial view) equipped with a solid-state charge-coupled device detector (CCD), a peristaltic pump and a low-flow GemCone nebuliser coupled to a

cyclonic spray chamber. Background correction was carried out using a two-points method. Analytical line 294.364 nm was selected for quantitative determination. The amount of exchanged cations at equilibrium,  $q_e$  ( $\text{mg g}^{-1}$ ), was calculated from the mass balance equation, Eq. (6.6.1):

$$q_e = \frac{(C_i - C_e)V}{M} \quad (\text{Eq. 6.6.1})$$

where  $C_i$  and  $C_e$  ( $\text{mg L}^{-1}$ ) are the liquid-phase concentrations of Ga in the reference solution and at equilibrium respectively;  $V$  (L) is the volume of the solution and  $M$  (g) is the mass of dry zeolite used. Samples of saturated zeolite exchanged with Ga were used for structural and spectroscopic investigations. Calcined Mordenite, Ferrierite and L zeolites (0.5 g) were suspended with stirring in 500 mL of an aqueous solution of gallium nitrate ( $\text{Ga}(\text{NO}_3)_3 \cdot x\text{H}_2\text{O}$ , Aldrich 99.9%) at pH 4.2, 343 K for 24 h. The zeolites were recovered by filtration, washed with 200 mL of MilliQ water and dried in oven at 383 K overnight.

#### *X-ray powder diffraction and Rietveld refinements*

Powder patterns of the Ga-exchanged zeolites, here after called Ga-L, Ga-MOR and Ga-FER were collected on a Bruker D8 Advance diffractometer equipped with a Si/Li solid state detector (Sol-X). Measurements were performed at Room Temperature, using the  $\text{CuK}\alpha_{1,2}$  wavelength, in a  $3\text{--}100^\circ 2\theta$  range. Full profile Rietveld refinements were performed through the GSAS software [25] and the EXPGUI graphical interface [26], using the hexagonal  $P6/mmm$  and the orthorhombic  $Cmcm$  and  $Immm$  space groups for Ga-L, Ga-MOR and Ga-FER systems, respectively. Details on the refined parameters are reported in Table 6.6.1 and below:

**Ga-L.** Peak profiles were modelled through the Pseudo-Voigt function with 0.1% cut-off peak intensity. The profile function selected was the number 2 and the coefficients refined were: Gaussian  $\theta$ -independent  $GW$ , Lorentian  $\cos\theta^{-1}$   $LX$  and  $\tan\theta$ -dependent  $LY$  terms, peak asymmetry and  $ptec$  parameters. The empirical background was fitted through the Chebyshev polynomial function and 18 coefficients.

**Ga-MOR.** Peak profiles were modelled through the Pseudo-Voigt function with 0.5% cut-off peak intensity. The profile function selected was the number 2 and the coefficients refined were: Gaussian  $\theta$ -independent  $GW$ ,  $\tan^2\theta$ -dependent  $GU$ ,  $\tan\theta$ -dependent  $GV$  and Lorentian  $\cos\theta^{-1}$  dependent  $LX$  terms, peak asymmetry and  $ptec$  parameters. The empirical background was fitted through the Chebyshev polynomial function and 26 coefficients.

**Ga-FER.** Peak profiles were modelled through the Pseudo-Voigt function with 0.1% cut-off peak intensity. The profile function selected was the number 2 and the coefficients refined were: Gaussian  $\theta$ -independent  $GW$ , Lorentian  $\cos\theta^{-1}LX$  and  $\tan\theta$ -dependent  $LY$  terms, peak asymmetry,  $ptec$  and  $stec$  parameters. The empirical background was fitted through the Chebyshev polynomial function and 15 coefficients. Scale factor and  $2\theta$  zero shift were also accurately refined for all the systems. Besides, in all the structural refinements soft constraints were initially imposed on tetrahedral distances ( $\sigma=0.04$  Å) and completely removed in the last refinement cycles. Whereas, atomic coordinates, site occupancies and isotropic atomic displacement parameters (UIISO) were refined, constraining equivalent UIISO for framework oxygen atoms of each system.

#### *X-ray absorption spectroscopy*

Ga K-edge XAS spectra were collected at the XAFS beamline (ELETTRA, Trieste, Italy) [27] in transmission mode using fixed exit double crystal Si(111) monochromator. For all the samples, energy calibration was accomplished by collecting simultaneously a reference spectrum of a GaAs pellet placed in a second experimental chamber after the sample and after the I1 ionisation chamber, with the position of the first inflection point taken at 10,369.0 eV. All spectra were collected at room temperature and in vacuum conditions, with a variable energy step as a function of the energy: large step (5 eV) in the first 200 eV of the spectrum, smaller step (0.2 eV) in the XANES region and a  $k$ -constant step of  $0.03 \text{ \AA}^{-1}$  (up to 1.8 eV) in the EXAFS region. For each sample, 4 spectra have been collected and merged in order to increase the signal to noise ratio; merged spectra were then normalised with respect to the high-energy side of the curve and EXAFS signals have been extracted using the Athena software [28]. The extracted EXAFS signals were then Fourier transformed using a Hanning window in the  $k$  range  $3\text{--}15 \text{ \AA}^{-1}$  and quantitative analysis were carried out using the Artemis software (Demeter 0.9.25 package) [28,29]. Structural model for the calculation of the theoretical paths were retrieved by Rietveld refinements of the XRPD data of Ga-FER, Ga-MOR, Ga-L. Along with the samples, the compound  $\text{Ga}(\text{NO}_3)_3 \cdot x\text{H}_2\text{O}$  used for the sample preparation was also measured as reference for octahedral coordinated gallium.

### 6.6.3 Results and discussion

#### *Adsorption of gallium on calcined zeolites*

The gallium exchanged zeolites were obtained by wet impregnation by placing in contact aqueous solution of gallium nitrate with zeolites. During this process, the solution pH can affect the adsorption, since in very acidic media ( $\text{pH} < 2$ ) the stability of zeolite diminished, and dissolution phenomena occur with change in crystallinity and in composition (dealumination) of the adsorbent material [30]. On the other hand, Gallium undergoes hydrolysis and polymerisation in aqueous solution, with increasing pH. Starting from  $\text{pH} > 2$ , a progressive formation of hydroxylated monomeric specie occurs and at slightly acid pH polymeric polycations are the dominant species. Therefore, a compromise pH value equal to 4 was selected for the experiments. The total quantity of gallium adsorbed from the solution at different concentrations were evaluated by atomic spectroscopy. In Fig. 6.6.1(a–c) the adsorption isotherms are reported, it can be seen that all the three zeolites show an L-Type isotherm, and zeolite L is characterised by a higher saturation capacity. The data were fitted by Langmuir and Toth isotherm models given respectively by the equations. 6.6.2 and 6.6.3:

$$q_e = \frac{q_s K_L C_e}{1 + b C_e} \quad (\text{Eq. 6.6.2})$$

$$q_e = \frac{q_s K_T C_e}{(1 + (b C_e)^v)^{1/v}} \quad (\text{Eq. 6.6.3})$$

where,  $q_s$  is the saturation capacity and  $K_L$  and  $K_T$  the affinity constant for the Langmuir and the Toth models, respectively, in Eq. 6.6.3  $v$  represent the heterogeneity parameter. The fitting results are reported in Table 6.6.2, the values in parenthesis indicate the confidence limits at 95 % of probability. As can be seen from the coefficient of determination listed in this table, both the Langmuir and the Toth models fit quite well the experimental data. In particular, for both L and FER, the heterogeneity parameter  $v$  appearing in the Toth isotherm (see Table 6.6.2) is not significantly different from 1 and for  $v = 1$ , the Toth isotherm corresponds to the Langmuir one. On the contrary, for MOR a  $v$  value lower than 1 was found. The heterogeneity parameter is related to the width of the energy distribution function, and lower value correspond to larger distribution and, therefore, to energetically heterogeneous sites on the surface. From the adsorption data therefore it seems that the adsorption onto MOR could involve sites of different energies. However, it should be mentioned that Langmuir isotherm has also been employed to describe the adsorption on multiple sites [31], in such cases it is supposed that their interactions energies are similar

and they can be averaged to give a single averaged energy for all the sites. To gain more information on the involved site, a structural investigation on the Ga-exchanged zeolites were carried out.

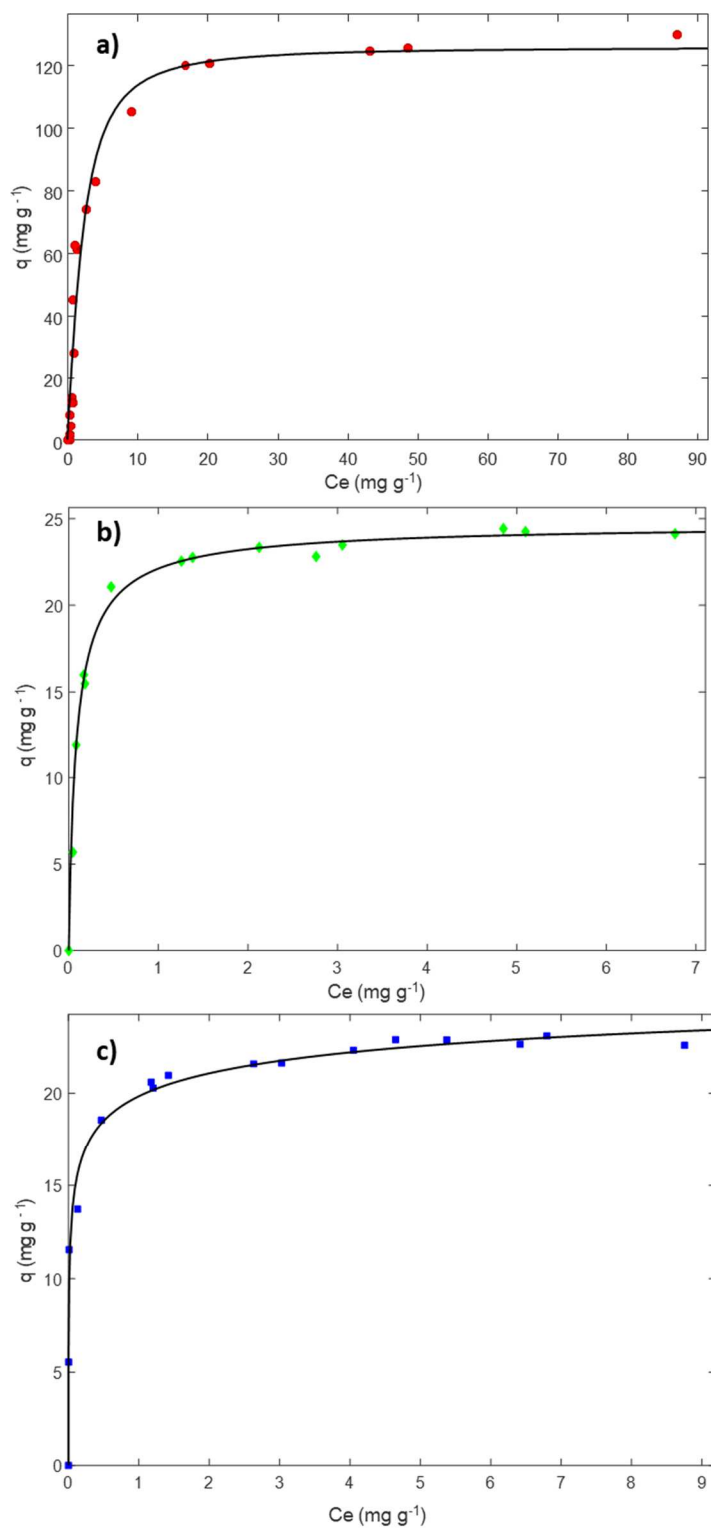


Figure 6.6.1 Adsorption of gallium on a) L zeolite, b) Ferrierite and c) Mordenite.

Parameters	L	FER	MOR
$q_s$	78.02	24.52	21.36
(mg g <sup>-1</sup> )	(70.71, 85.33)	(23.86, 25.17)	(20.07, 22.65)
$K_L$	0.3841	9.946	34.9
(dm <sup>3</sup> mg <sup>-1</sup> )	(0.2723, 0.4959)	(8.329, 11.56)	(17.87, 51.9)
R <sup>2</sup>	0.9505	0.9913	0.9328
$q_s$	71.16	24.76	30.47
(mg g <sup>-1</sup> )	(65.61, 76.71)	(23.72, 25.8)	(21.88, 39.07)
$K_T$	0.2788	14.14	38.4
(dm <sup>3</sup> mg <sup>-1</sup> )	(0.2191, 0.3385)	(7.92, 20.36)	(25.7 52.3)
$\nu$	0.83	0.86	0.2291
R <sup>2</sup>	(0.42, 1.24)	(0.64, 1.08)	(0.1135, 0.3447)
	0.9696	0.9954	0.9874

**Table 6.6.2 Gallium cation exchange isotherm parameters.  $q_e$  (mg g<sup>-1</sup>): exchanged concentration at equilibrium;  $C_e$  (mg dm<sup>-3</sup>): concentration in the solution at equilibrium;  $K_L$ ,  $K_T$  (dm<sup>3</sup> mg<sup>-1</sup>): affinity constants for the Langmuir and the Tóth models, respectively;  $q_s$  (mg g<sup>-1</sup>) cation exchange capacity;  $\nu$  heterogeneity parameter in the Tóth model (see text for further details). Confidence bounds at 95% of probability are reported in parenthesis.**

### X-ray powder diffraction results

#### Ga-L system

Zeolite L (ideal formula  $K_6Na_3Al_9Si_{27}O_{72} \cdot 21H_2O$ , framework-type LTL) is a large pore material whose framework is built from columns of cancrinite cages stacked with double six membered rings (D6R) along the *c* axis [32]. The 4-rings in these columns are cross-linked to form continuous 12-ring channels along the *c*-direction with a maximum diameter of 12.6 Å [33]. The Ga-L crystal structure was refined in the *P6/mmm* space group, starting from the atomic coordinates reported by Barrer and Villiger, H. (1969) [33]. The refined Ga-L lattice parameters are the following:  $a=b=18.2177(24)$  Å,  $c=7.5538(15)$  Å and  $V=2171.1(6)$  Å<sup>3</sup>. According to Newsam [34] the framework bond distances confirm the not random distribution of Al (and/or Ga) in the tetrahedral sites. The T1-O bond lengths range from 1.630(4) and 1.668(3) Å (mean distance of 1.650 Å); whereas the T2-O ranges from 1.639(6), Å and 1.846(1) Å (mean distance 1.722 Å). Compared with the mean < T-O > bond lengths refined for the L-LTL precursor (< T1-O > =1.640 Å and < T2-O > =1.654 Å, *in preparation*), a lightening of both tetrahedral distances is observed. This result suggests the incorporation of gallium in both tetrahedral sites and a Ga-enrichment in the T2 one due to the longer average < T2-O > bond length. From the structural point of view, noteworthy are the very narrow T-O-T angles centred on the O1 and O5 framework oxygen atoms (T1-O1-

$T1=112.6(5)$  and  $T2-O5-T2=115.4(3)^\circ$ , even if they are not the narrowest found in zeolites [35–38]. The difference Fourier map generated using the GSAS package [25,26] highlights the presence of six extraframework sites, which were distributed among  $K^+$  and  $Ga^{3+}$  cations, and water molecules (Fig. 6.6.2). The notexchanged  $K^+$  was localised at the centre of the 6MR (corresponding to the KB site in the L-LTL zeolite [33]), within the cancrinite cage. Two extraframework sites were assigned to  $Ga^{3+}$  ions (*i.e.*, labelled Ga1 and Ga2, respectively) and were located not far from the centre of the 8MR (Ga1) and close to the edge of the 12MR channel (Ga2), respectively. The remaining three partially occupied sites were all positioned within the 12MR channel and were attributed to  $H_2O$  molecules (*i.e.*, W1, W2 and W3 sites, respectively).  $K^+$  is six-fold coordinated to six framework oxygens, as suggested by the  $K1-O3=2.92[x6]$  Å distance. Ga1 is sixfold coordinated to O4 and O6 framework oxygen atoms ( $Ga1-O4=2.85[x4]$  Å and  $Ga1-O6=2.21[x2]$  Å). The refined bond distances ( $Ga2-W1=2.67[x2]$  Å,  $Ga2-W2=2.23[x2]$  Å and  $Ga2-W3=2.56[x4]$  Å) and occupancies of W1, W2 and/or W3 water molecules indicate that Ga2 is four (with W1 and W2, or only W3) or sixfold coordinated (with W1 or W2 and W3) to water. Indeed, bond distances suggest also the presence of short W1-W3-W3 water oligomers developing along the  $[001]$  direction, as testified by the  $W1-W3=2.26$  and  $W3-W3=2.98$  Å distances. On the whole, Rietveld refinement reveals the presence of  $\sim 14$  water molecules, 2  $K^+$  and 2.57 atoms of  $Ga^{3+}$  per unit cell, respectively. The K and Ga values are consistently lower than the theoretical concentration, which can be calculated on the basis of the aluminium content of the L precursor. This discrepancy cannot be attributed to an underestimation of the cations sites found in our refinements, neither to an incomplete  $NH_4^+$  ion exchange or dihydroxylation and/or dealumination during calcination, as well as residual  $NH_4^+$  after calcination. Moreover, difference Fourier (DF) map does not show any indication of extraframework sites, attributable to  $NH_4^+$  groups. The hypothesis of extraframework  $Al^{3+}$  atoms is also disregarded by the DF synthesis that does not show any maximum that can be interpreted as oxygen atoms coordinated to  $Al^{3+}$ . We suggest that the lattice charge defects give rise to Brønsted acidic Si–OH–Ga bridging hydroxyl group, whose occurrence is confirmed by the lengthening of the T–O distance after gallium incorporation. Recently, Beltrami et al. [personal communication] demonstrated the presence of Brønsted acid sites through neutron powder diffraction on the acidic form of zeolite L. The first site (D1) was located on the framework oxygen O5, not far from the centre of the 8-ring of the cancrinite cage. The second (D2 site) on the framework oxygen O1, heading towards the centre of the 12MR channel. On the whole, 7.6 Brønsted sites were recognised, in consistence with the tetrahedral aluminium content determined starting from the Si/Al ratio. In our refinement, the T–O distances involving the O5 and O1 framework oxygens were always among the largest of the tetrahedra. At the same time, the attractive force of Brønsted acid sites could

reasonably be responsible of the very narrow T-O-T angles centred on the O1 and O5 framework oxygen atoms (T1-O1-T1=112.7(5) and T2-O5-T2=115.4(3)°). As reported by Fricke et al. (2000) [5], the excess of gallium determines the formation of a segregate phase coexisting with the main zeolitic one. In this case, a phase of gallium hydroxide (GaO(OH)) was recognised through the qualitative analysis, which highlights the presence of some extra peaks (*i.e.*, [101], [200] and [201] *hkl* reflections at the 21.41 and 18.06 and 26.68° 2 $\theta$  angles, respectively) not attributable to the L zeolite (Fig. 6.6.3). The semi-quantitative analysis reveals the presence of 83 and 17 wt % of L zeolite and GaO(OH), respectively.

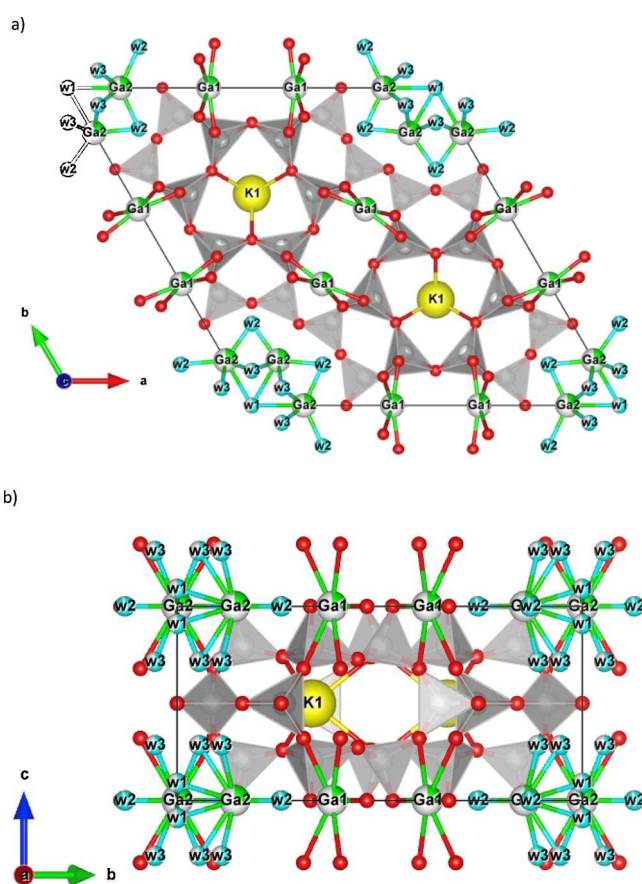


Figure 6.6.2 Extraframework content distribution of Ga-L system. Projection along c (a) and a (b) axis.

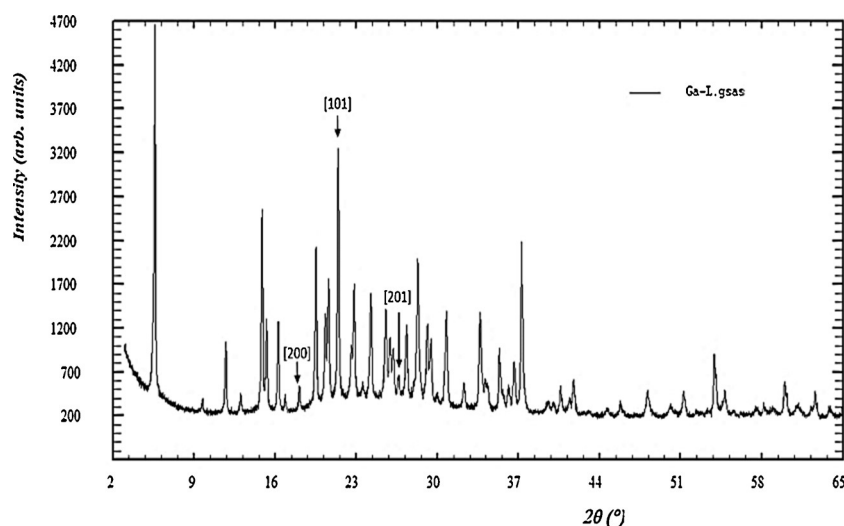


Figure 6.6.3 Powder diffraction pattern of Ga-L system.

### Ga-MOR system

Mordenite (ideal formula  $[\text{Na}_8^+][\text{Al}_8\text{Si}_{40}\text{O}_{96}]\cdot 24\text{H}_2\text{O}$ , framework type MOR) is a medium pore zeolite characterised by a monodimensional channel system, which consists of 12-membered rings running parallel to the  $[001]$  direction interconnected along the  $[010]$  direction through 8MR side pockets [32]. The crystal structure of the gallium-exchanged mordenite was refined using the topological orthorhombic  $Cmcm$  symmetry starting from the structural model of Alberti et al. (1986) [39]. After the Ga-exchange, lattice parameters highlight a slight reduction of the unit cell volume (Ga-MOR=2766.35(25) Å<sup>3</sup>, Na-MOR=2781.58(25) Å<sup>3</sup>) compared to the ones of the starting Na-MOR sample, due to the decrease of  $b$  and  $c$  parameters (Ga-MOR:  $b=20.3510(9)$  Å,  $c=7.4940(4)$  Å; Na-MOR:  $b=20.4447(10)$  Å,  $c=7.5152(4)$  Å). On the contrary, along  $a$  direction, a small increase is observed (18.1387(9) and 18.1038(10) for Ga-MOR and Na-MOR, respectively). The comparison of the mean tetrahedral distances between the exchanged ( $\langle \text{T1-O} \rangle = 1.662$  Å,  $\langle \text{T2-O} \rangle = 1.654$  Å,  $\langle \text{T3-O} \rangle = 1.658$  Å,  $\langle \text{T4-O} \rangle = 1.657$  Å) and the Na-form ( $\langle \text{T1-O} \rangle = 1.654$  Å,  $\langle \text{T2-O} \rangle = 1.650$  Å,  $\langle \text{T3-O} \rangle = 1.657$  Å,  $\langle \text{T4-O} \rangle = 1.656$  Å) does not show any indication about a preferential siting of gallium in framework positions. On the contrary, intertetrahedral angles of the Ga-MOR are narrower than those of the starting material. Among them, noteworthy is the shrinkage of the T3-O9-T3 angle, which moves from 165.5° in the Na-MOR to 151.9° in the Ga-MOR. The analysis of the difference Fourier map allows to detect the presence of extraframework sites assigned to residual  $\text{Na}^+$  cation,  $\text{Ga}^{3+}$  and water molecules, respectively (Fig. 6.6.4). Not exchanged  $\text{Na}^+$  (labelled Na2) is located within the 8MR in a six-fold coordination with O1 (Na2-O1=3.06 Å [x4]) and O6 (Na2-O6=3.01 Å [x2]) framework oxygen atoms. Gallium site (labelled Ga1) is positioned within the 12MR

channel, along with all the three sites attributed to water molecules (W1, W2 and W3), which have a fundamental role in the completion of the gallium cation coordination. In this case, gallium is five-fold coordinated, as testified by the following bond distances: Ga1-W1=2.10 Å, Ga1-W2=2.09 Å [x2] and Ga1-W3=2.00 Å [x2]. Furthermore, W2 and W3 show to be hydrogen bonded each other (W2-W3=2.56 Å [x4]), thus forming short W2-W3 water oligomers running along the 12MR. No further residual electron density, attributable to NH<sub>4</sub><sup>+</sup> groups, were detected through the DF map, thus indicating that all the ammonium content has been substituted by Ga<sup>3+</sup> and that the extraframework gallium quantified is the maximum exchangeable for our mordenite. Concerning the amount of the extraframework content, refined occupancies indicate the presence of 2 and 1.16 a.u.c of Na<sup>+</sup> and Ga<sup>3+</sup> cations, respectively, along with 13 water molecules per unit cell. Na<sup>+</sup> and Ga<sup>3+</sup> values obtained are lower than the theoretical concentration, hence also in this case the presence of Brønsted acidic Si-OH-Ga bridging hydroxyl group has to be supposed to counterbalance the framework charge defect. Martucci et al. (2000) [40] reports that the position of Brønsted acid sites does not strictly depends on the nature of the zeolite (natural or synthetic) and on its Si/Al ratio. Indeed, in all the three samples considered in that work (with Si/Al ratio equal to 5.5, 5.6 and 10, respectively), the four Brønsted acid sites detected were constantly located on the same framework oxygen atoms. The first, D1, was on framework oxygen O10 and headed towards the center of the 12-ring; the second, D2, was on the framework oxygen O6 and headed towards the side pocket; the third, D3, was on O5 and headed towards the center of the 12-ring; the last, D4, was on O9 and headed toward the center of the eight-ring. Hence, it is reasonable to assume the presence of charge compensator protons in these sites. The comparison of powder patterns before and after gallium exchange shows the occurrence of [301] and [200] *hkl* reflections at the 33.64 and 18.09° 2θ angles, respectively. This testifies the presence of the segregate gallium hydroxide phase arising from the gallium-exchange process (Fig. 6.6.5). The semi-quantitative analysis reveals the presence of 74 and 26 wt % of mordenite and GaO(OH), respectively.

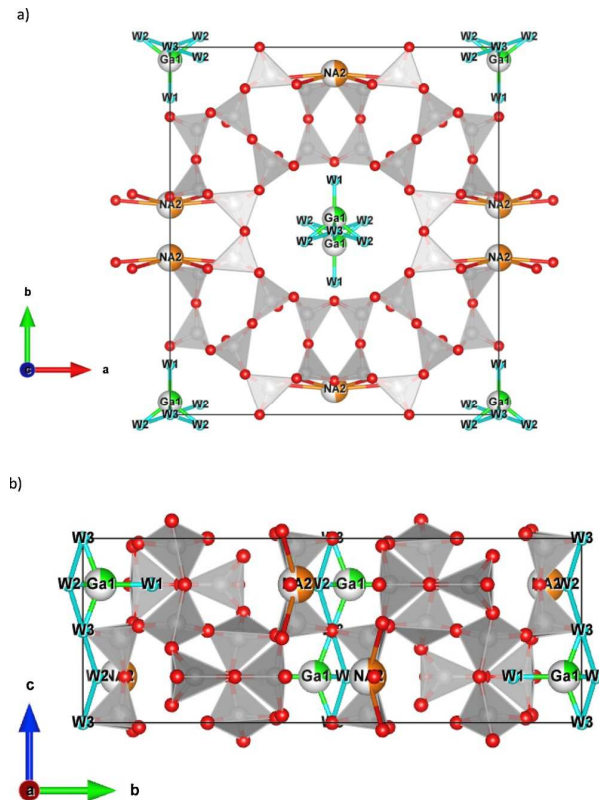


Figure 6.6.4 Extraframework content distribution of Ga-MOR system. Projection along *c* (a) and *a* (b) axis.

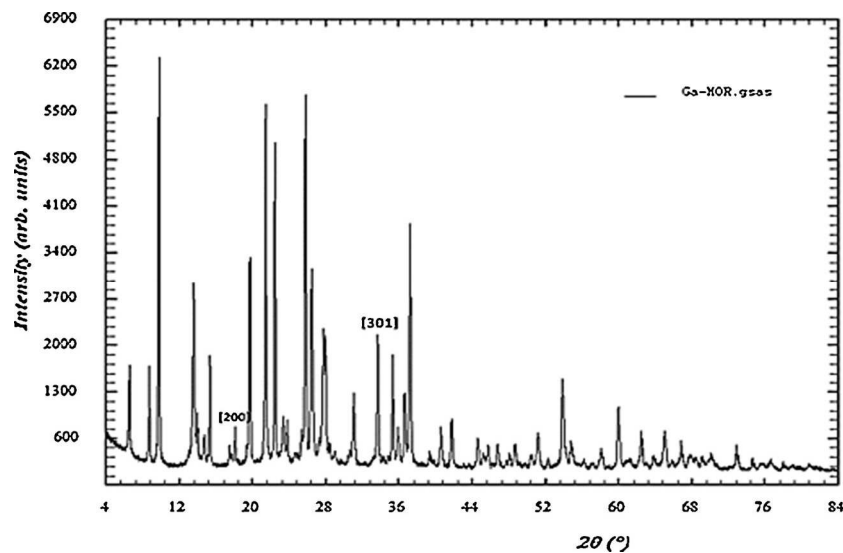


Figure 6.6.5 Powder pattern of Ga-MOR system.

### Ga-FER system

Ferrierite (ideal formula  $[Mg_2^{2+}Na_2^+][Al_6Si_{30}O_{72}] \cdot 18H_2O$ , framework type FER) is a medium pore pentasil zeolite, characterised by a two dimensional channel system built on the intersection of 10-membered and 8-membered ring (10 and 8MR) channels running parallel

to the  $[001]$  and  $[010]$  crystallographic directions, respectively. 10MR alternating along the  $b$  direction with the so-called ferrierite cages, structural units originated by the intersection of 8MR and 6MR channels [32]. In this work, due to the absence of  $I$ -centering forbidden peaks ( $h + k + l = 2n + 1$  reflections), the Ga-FER crystal structure was refined in the  $Immm$  space group, starting from the atomic coordinates reported by Dalconi et al. (2003) [41]. From the analysis of the lattice parameters obtained through the Rietveld refinement, not noteworthy differences can be detected between the starting  $\text{NH}_4$ -ferrierite [42] and Ga-exchanged sample. Indeed, it is highlighted a very small reduction of the unit cell volume ( $\text{NH}_4\text{-FER}=1978.6(1) \text{ \AA}^3$ ,  $\text{Ga-FER}=1977.20(15) \text{ \AA}^3$ ) principally attributable to the slight decrease of  $a$  and  $b$  parameters, whereas  $c$  remains almost unchanged ( $\text{NH}_4\text{-FER}$ :  $a=18.8477(8) \text{ \AA}$ ,  $b=14.1049(5) \text{ \AA}$ ,  $c=7.4425(2) \text{ \AA}$ ;  $\text{Ga-FER}$ :  $a=18.8394(10) \text{ \AA}$ ,  $b=14.0885(6) \text{ \AA}$ ,  $c=7.4494(2) \text{ \AA}$ ). On the contrary, the comparison of framework bond distances and angles between them, suggests that the metal-exchange process has led to the incorporation of gallium within tetrahedral sites. After the Ga-exchange,  $\langle \text{T-O} \rangle$  distances of the four tetrahedral sites appear homogeneously longer ( $\text{Ga-FER}$ :  $\langle \text{T1-O} \rangle = 1.651 \text{ \AA}$ ,  $\langle \text{T2-O} \rangle = 1.654 \text{ \AA}$ ,  $\langle \text{T3-O} \rangle = 1.653 \text{ \AA}$  and  $\langle \text{T4-O} \rangle = 1.635 \text{ \AA}$ ;  $\text{NH}_4\text{-FER}$ :  $\langle \text{T1-O} \rangle = 1.607 \text{ \AA}$ ,  $\langle \text{T2-O} \rangle = 1.607 \text{ \AA}$ ,  $\langle \text{T3-O} \rangle = 1.609 \text{ \AA}$  and  $\langle \text{T4-O} \rangle = 1.607 \text{ \AA}$ ), whereas T-O-T angles result narrower than that of the precursor, thus suggesting the presence of tetrahedral  $\text{Ga}^{3+}$  cations. Indeed, according to Fricke et al. (2000) [5], structural modifications strongly depend on the concentration of gallium and on the degree of substitution achieved. The analysis of the difference Fourier map reveals the presence of five partially occupied extraframework sites: three of them are occupied by water molecules (sites labelled W1, W2 and W3), the remaining by gallium cations (sites labelled Ga1 and Ga2). W1, W2 and Ga1 are located within the 10-membered ring, whereas W3 and Ga2 close to the edges of the 8-membered ring window, which defines the limits of the ferrierite cage (Fig. 6.6.6). As already observed in Ga-L system, no evidences of ammonium are highlighted by the DF analysis, thus indicating that all the  $\text{NH}_4$  content has been replaced by gallium after the exchange. Along with the  $\sim 5$  water molecules per unit cell, the refinement of the extraframework  $\text{Ga}^{3+}$  occupancies highlighted the presence of 1.3 ions per unit cell, in good agreement with the amount of ammonium calculated in the precursor sample ( $\sim 1.2$  ions per unit cell; [42]). The analysis of the extraframework bond lengths reveals the existence of strong interactions among water molecules and  $\text{Ga}^{3+}$  cations. Distances refined indicate that Ga1 site is four-fold coordinated exclusively to water molecules ( $\text{Ga1-W1}=2.09 \text{ \AA}$  [x2] and  $\text{Ga1-W2}=2.09 \text{ \AA}$  [x2]). Besides, W1 and W2 interact between, them thus creating W1-W2-W1 short oligomers ( $\text{W1-W2}=2.96 \text{ \AA}$  [x2] oriented parallel to the 10MR channel and hydrogen bonded to the O8 framework oxygen atom ( $\text{O8-W1}=2.53 \text{ \AA}$  [x4]). Ga2 site is coordinated by the W3 site, as testified by the  $\text{Ga2 W3}=2.06 \text{ \AA}$  [x2] distance. No other

interactions between Ga2 and H<sub>2</sub>O were detected and no additional reasonable electronic density residues to be attributed to water were recognised. Considering that, the four-fold coordination is the lowest for Ga<sup>3+</sup> cations, the presence of some not detectable protons completing the gallium coordination has to be assumed [43]. Also in this case, the segregate phase of gallium hydroxide was recognised through the qualitative analysis. It has been highlighted by the occurrence of two extra reflections (*i.e.*, [101] and [301] *hkl* at the 21.41 and 33.61° 2θ angles, respectively) not attributable to the ferrierite and not present in the NH<sub>4</sub>-FER powder pattern (Fig. 6.6.7).

The semi-quantitative analysis reveals the 96 and 4 wt% of ferrierite and GaO(OH), respectively.

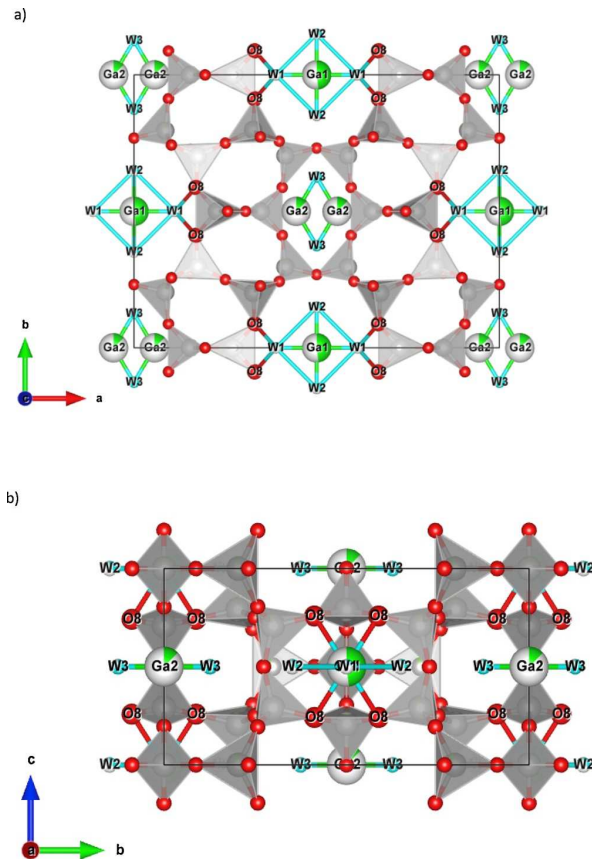


Figure 6.6.6 Extraframework content distribution of Ga-FER system: projection along c (a) and a (b) axis.

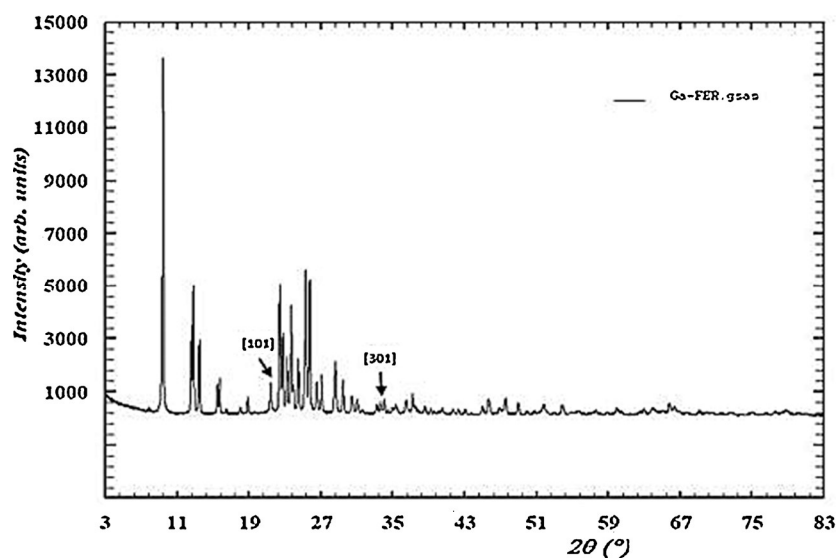


Figure 6.6.7 Powder pattern of Ga-FER system.

### XAS

Fig. 6.6.8 shows the normalised spectra of all samples and  $\text{Ga}(\text{NO}_3)_3 \cdot x\text{H}_2\text{O}$  whereas the corresponding  $k^2\chi(k)$  experimental data are reported in Fig. 6.6.9. As can be seen in the zoom area of Fig. 6.6.8, the two peaks in the white line of Ga-exchanged zeolites (at energies of 10,375 and 10,379 eV) are a preliminary indication of the fact that Ga is present in both tetrahedral and octahedral geometry, according to previous studies [44,45]. The presence of Ga atoms in non-equivalent crystallographic sites, due to the symmetry of the zeolites, together with the secondary phase  $\text{GaO}(\text{OH})$  in various amount in all the samples (as evidenced by the XRPD data) complicated the EXAFS refinements, so we focused only on the first shell. First-shell contribution has been modelled using Ga–O bond distances coming from the Ga in tetrahedral sites of the zeolite (as the Ga atoms in extraframework sites have longer bond distances) and the octahedral Ga in  $\text{GaO}(\text{OH})$  impurity (structural model taken from [46]). This strategy has been adopted as Ga–O bond distances in tetrahedral and octahedral coordination are quite similar and partially overlapping [47], confirmed also by our quantitative EXAFS results on the first-shell, summarised in Table 6.6.3 (fits are shown in Fig. 6.6.10a–c).

The obtained average bond lengths are of  $1.928 \pm 0.01 \text{ \AA}$ ,  $1.937 \pm 0.02 \text{ \AA}$ ,  $1.925 \pm 0.02 \text{ \AA}$  for Ga-Ferr, Ga-Mor and Ga-L respectively; the refined value (1.04) of the amplitude factor  $S_0^2$  on the  $\text{Ga}(\text{NO}_3)_3 \cdot x\text{H}_2\text{O}$  reference compound is almost identical to that obtained for the zeolite samples. As can be seen in Table 6.6.3, the major contribution to the EXAFS signal is due to Ga in  $\text{GaO}(\text{OH})$  impurity, being about 80% in all the samples; nevertheless, a good fit cannot be achieved without introducing also tetrahedral Ga contribution. This fact, together with the XANES information of the splitted peak of the white line (zoom area in Fig.

6.6.8), allows us to confirm the presence of tetrahedral Ga and consequent incorporation into the zeolite framework.

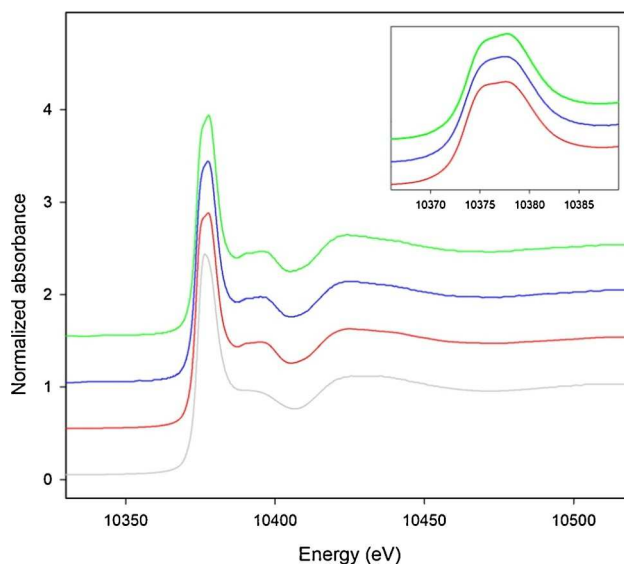


**Figure 6.6.8** Normalised spectra (from the top to the bottom) of: Ga-MOR (green), Ga-FER (blue), Ga-L (red) and Ga(NO<sub>3</sub>)<sub>3</sub> reference (grey). Small box on the top right is a zoom around the edge area of Ga-exchanged zeolite samples.

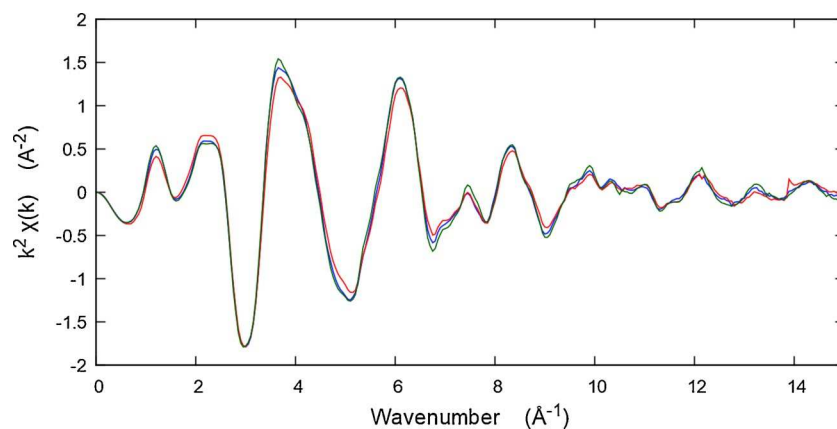


**Figure 6.6.9**  $k^2\chi(k)$  experimental data of Ga-MOR (green), Ga-FER (blue) and Ga-L (red).

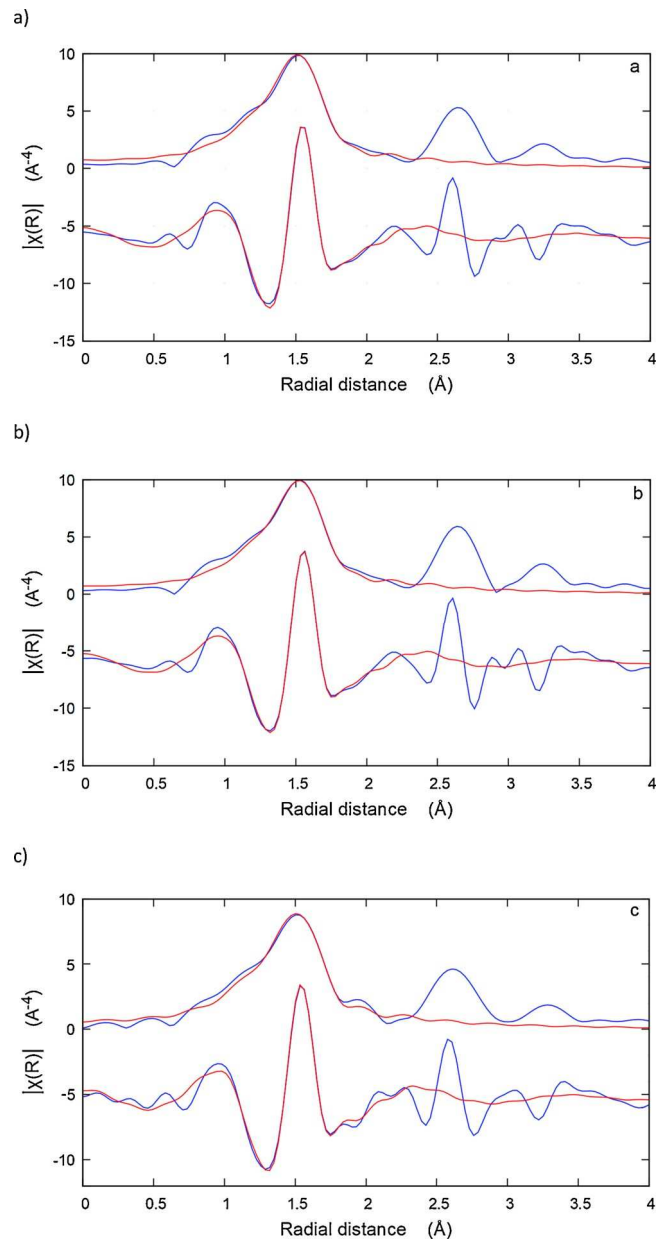


**Figure 6.6.10** The obtained EXAFS fit on the three samples: a) Ga-FER; b) Ga-MOR; c) Ga-L.

Sample	Shells	%	Ref.	N	$R(\text{\AA})^a$	$S_0^2$	R-factor	$\sigma^2(\text{\AA}^2)$	$\Delta E_0(\text{eV})$
Ga(NO <sub>3</sub> ) <sub>3</sub> ·xH <sub>2</sub> O			[48]			1.04 (8)	0.012	0.007 (1)	6 (1)
	Site1 - Ga - O <sub>1</sub>	0.5		6	1.939 (4)				
	Site2 - Ga - O <sub>4</sub>	0.5		4	1.935 (4)				
	Site2 - Ga - O <sub>5</sub>			2	1.961 (4)				
Fer						1.05 (5)	0.003	0.002 (2)	2 (2)
	Site1 <sup>b</sup> - Ga - O	0.2 (1)*0.5		4	1.93 (1)				
	Site2 <sup>b</sup> - Ga - O	0.2 (1)*0.5		3	1.91 (1)				
	Site2 <sup>b</sup> - Ga - O			1	1.94 (1)				
	GaO(OH) contamination:		[46]					0.005 (1)	
	Ga - O <sub>1</sub>	0.8 (1)		3	1.904 (6)				
Ga - O <sub>2</sub>			3	2.031 (6)					
Mor						1.05 (4)	0.003	0.001 (3)	3 (1)
	Site1 <sup>b</sup> - Ga - O	0.15 (8)*0.5		4	1.96 (2)				
	Site2 <sup>b</sup> - Ga - O	0.15 (8)*0.5		4	1.92 (2)				
	GaO(OH) contamination:		[46]					0.005 (2)	
	Ga - O <sub>1</sub>	0.85 (8)		3	1.912 (8)				
Ga - O <sub>2</sub>			3	2.040 (8)					
L						1.05 (9)	0.004	0.001 (3)	3 (1)
	T1 - Ga - O <sub>4</sub>	0.16 (4)*0.5		4	1.93 (2)				
	T2 - Ga - O <sub>5</sub>	0.16 (4)*0.5		2	1.91 (2)				
	T2 - Ga - O <sub>6</sub>			2	1.94 (2)				
	GaO(OH) contamination:		[46]					0.007 (2)	
	Ga - O <sub>1</sub>	0.84 (4)		3	1.900 (3)				
Ga - O <sub>2</sub>			3	2.026 (3)					

**Table 6.6.3 Crystallographic data and structural parameters as obtained from the R-space fit by using the theoretical references [46, 48].**

<sup>a</sup>All the bond lengths values are in excellent agreement with the mean values reported by Gagné and Hawthorne (2018) [47] for Ga<sup>3+</sup> ion in both tetrahedral and octahedral coordination. <sup>b</sup>These sites represent an average of the Ga atoms in tetrahedral coordination and did not refer to the real crystallographic sites.

## 6.6.4 Conclusions

In this work the investigation of the structural features of Gallium substituted L, mordenite and ferrierite zeolites allowed us to elucidate the nature of the gallium active sites combining X-ray powder diffraction (XRPD), X-ray absorption spectroscopy (XAS) and adsorption study. Rietveld structure refinements allowed us to locate and quantify Ga<sup>3+</sup> cations in framework and non-framework positions as well as determine the presence of water molecules completing the extraframework Ga<sup>3+</sup> coordination. The lightening of tetrahedral bond distances and narrowing of intertetrahedral angles suggest that the metal cation was incorporated in tetrahedral sites. This is corroborated by EXAFS results, which show that the average bond lengths of the first shell are longer than the <T-O> distances expected in presence of Si<sup>4+</sup> and Al<sup>3+</sup> as framework cations. All these information are essential not only for their characterisation but also for their industrial applications.

## 6.6.5 References

- [1] Szostak R. (1992) Handbook of Molecular Sieves. Van Nostrand Reinhold, New York.
- [2] Guzzinati R., Sarti E., Catani M., Costa V., Pagnoni A., Martucci A., Rodeghero E., Capitani D., Pietrantonio M., Cavazzini A., Pasti L. (2018) Formation of Supramolecular Clusters at the Interface of Zeolite X Following the Adsorption of Rare-Earth Cations and Their Impact on the Macroscopic Properties of the Zeolite ChemPhysChem 19 (17) ,2208–2217.
- [3] Ausavasukhi A., Sooknoi T., Resasco D. E. (2009) Catalytic deoxygenation of benzaldehyde over gallium-modified ZSM-5 zeolite. J. Catal. 268 (1), 68–78.
- [4] Kanazirev V., Mavrodinova V., Kosova L., Price G. L. (1991) Conversion of C<sub>8</sub> aromatics and n-pentane over Ga<sub>2</sub>O<sub>3</sub>/HZSM-5 mechanically mixed catalysts. Catal. Lett. 9 (1-2), 35–42.
- [5] Fricke R., Kosslick H., Lischke G., Richter M. (2000) Incorporation of Gallium into Zeolites: Syntheses, Properties and Catalytic Application. Chem. Rev. 100 (6), 2303–2406.
- [6] Bhan A., Nicholas Delgass W. (2008) Propane Aromatization over HZSM-5 and Ga/HZSM-5 Catalysts. Catal. Rev. 50 (1), 19–151.
- [7] Yogo K., Tanaka S., Ihara M., Hishiki T., Kikuchi E. (1992) Selective Reduction of NO with Propane on Gallium Ion-exchanged Zeolites. Chem. Lett. 21 (6), 1025–1028.
- [8] Shamzhy M., Opanasenko M., Concepción P., Martínez A. (2019) New trends in tailoring active sites in zeolite-based catalysts. Chem. Soc. Rev. 48, 1095–1149.
- [9] Uslamin E. A., Luna-Murillo B., Kosinov N., Bruijninx P. C., Pidko E. A., Weckhuysen B. M., Hensen E. J. M. (2019) Gallium-promoted HZSM-5 zeolites as efficient catalysts for the aromatization of biomass-derived furans. Chem. Eng. Sci. 198, 305–316.
- [10] Kazansky V. B., Subbotina I. R., Van Santen R. A., Hensen E. J. M. (2005) DRIFTS study of the nature and chemical reactivity of gallium ions in Ga/ZSM-5: II. Oxidation of reduced Ga species in ZSM-5 by nitrous oxide or water. J. Catal. 233 (2), 351–358.
- [11] Szostak R., Nair V., Simmons D. K., Thomas T. L., Kuvadia R., Dunson B., Shieh D. C. (1988) Framework and Nonframework Ion Contribution to Molecular Sieve Catalytic Activity. Stud. Surf. Sci. Catal. 37, 403–411.
- [12] Otero Areán C., Turnes Palomino G., Geobaldo F., Zecchina A. (1996) Characterization of gallosilicate MFI-type zeolites by IR spectroscopy of adsorbed probe molecules. J. Phys. Chem. 100 (16), 6678–6690.
- [13] Bayense C. R., Kentgens A. P., De Haan J. W., Van de Ven L. J., Van Hooff J. H. (1992) Determination of gallium in H(Ga)ZSM5 zeolites by gallium-71 MAS NMR spectroscopy. J. Phys. Chem. 96 (2), 775–782.

- [14] Lamberti C., Turnes Palomino G., Bordiga S., Arduino D., Zecchina A., Vlais G. (1999) EXAFS Study of Ti, Fe and Ga Substituted Silicalites. *Jpn. J. Appl. Phys.* 38 (S1), 55–58.
- [15] Rodrigues V. D. O., Júnior A. C. F. (2012) On catalyst activation and reaction mechanisms in propane aromatization on Ga/HZSM5 catalysts. *Appl. Catal. A-Gen.*, 435, 68–77.
- [16] Serykh A. I., Amiridis M. D. (2009) In situ X-ray photoelectron spectroscopy study of gallium-modified MFI zeolite. *Surf. Sci.* 603 (13), 2037–2041.
- [17] Pidko E. A., van Santen R. A. (2009) Structure–Reactivity Relationship for Catalytic Activity of Gallium Oxide and Sulfide Clusters in Zeolite. *J Phys. Chem. C* 113 (11), 4246–4249.
- [18] Berlier G., Spoto G., Fiscaro P., Bordiga S., Zecchina A., Giamello E., Lamberti C. (2002) Co-ordination and oxidation changes undergone by iron species in Fe-silicalite upon template removal, activation and interaction with N<sub>2</sub>O: an in situ X-ray absorption study. *Microchem. J.* 71 (2-3), 101–116.
- [19] Berlier G., Spoto G., Bordiga S., Ricchiardi G., Fiscaro P., Zecchina A., Rossetti I., Selli E., Forni L., Giamello E., Lamberti C. (2002) Evolution of Extraframework Iron Species in Fe Silicalite: 1. Effect of Fe Content, Activation Temperature, and Interaction with Redox Agents. *J. Catal.* 208 (1), 64–82.
- [20] Sun K., Xia H., Hensen E. J. M., van Santen R. A., Li C. (2006) Chemistry of N<sub>2</sub>O decomposition on active sites with different nature: Effect of high-temperature treatment of Fe/ZSM-5. *J. Catal.* 238 (1), 186–195.
- [21] Rane N., Overweg A. R., Kazansky V. B., Van Santen R. A., Hensen E. J. M. (2006) Characterization and reactivity of Ga<sup>+</sup> and GaO<sup>+</sup> cations in zeolite ZSM-5. *J. Catal.* 239 (2), 478–485.
- [22] Pidko E. A., Kazansky V. B., Hensen E. J. M., van Santen R. A. (2006) A comprehensive density functional theory study of ethane dehydrogenation over reduced extra-framework gallium species in ZSM-5 zeolite. *J. Catal.* 240 (1), 73–84.
- [23] Ausavasukhi A., Sooknoi T. (2009) Additional Brønsted acid sites in [Ga]HZSM-5 formed by the presence of water. *Appl. Catal. A-Gen.*, 361 (1-2), 93–98.
- [24] Přeč J., Pizarro P., Serrano D. P., Čejka J. (2018) From 3D to 2D zeolite catalytic materials. *Chem. Soc. Rev.* 47, 8263–8306.
- [25] Larson A. C. (2000) General structure analysis system (GSAS), Los Alamos Nat. Lab. Rep. LAUR, 86–748.
- [26] Toby B. H. (2001) EXPGUI, a graphical user interface for GSAS. *J. Appl. Cryst.* 34, 210–213.

- [27] Di Cicco A., Aquilanti G., Minicucci M., Principi E., Novello N., Cognigni A., Olivi L. (2009) Novel XAFS capabilities at ELETTRA synchrotron light source. *J. Phys. Conf. Ser.* 190 (1), 012043.
- [28] Ravel B., Newville M. (2005) ATHENA, ARTEMIS, HEPHAESTUS: data analysis for X-ray absorption spectroscopy using IFEFFIT. *J. Synchrotron Rad.* 12, 537–541.
- [29] Newville M. (2001) IFEFFIT: interactive XAFS analysis and FEFF fitting. *J. Synchrotron Rad.* 8, 322–324.
- [30] Petushkov A., Freeman J., Larsen S. C. (2010) Framework Stability of Nanocrystalline NaY in Aqueous Solution at Varying pH. *Langmuir* 26 (9), 6695–6701.
- [31] Ardit M., Martucci A., Pasti L., Rodeghero E., Beltrami G., Cruciani G. (2018) Organic Guests within a Ferroelastic Host: The Case of High Silica Zeolite ZSM-5. *J. Phys. Chem. C.* 122 (13), 7249–7259.
- [32] Baerlocher C., McCusker L. B., Olson D. H. (2007) *Atlas of Zeolite Framework Types*, 6<sup>th</sup> rev. ed., Elsevier, Amsterdam.
- [33] Barrer R. M., Villiger H. (1969) The crystal structure of the synthetic zeolite L. *Z. Krist - Cryst Mater.* 128 (1-6), 352–370.
- [34] Newsam J. M. (1987) Aluminium partitioning in zeolite L. *J. Chem. Soc. Chem. Commun.* 2, 123–124.
- [35] Stuckenschmidt E., Joswig W., Baur W. H. (1996) Flexibility and distortion of the collapsible framework of NAT topology: the crystal structure of H<sub>3</sub>O-natrolite. *Eur. J. Miner.* 8, 85–92.
- [36] Cannillo E., Coda A., Fagnani G. (1966) The crystal structure of bavenite. *Acta Cryst.* 20 (2), 301–309.
- [37] Sani A., Cruciani G., Gualtieri A. F. (2002) Dehydration dynamics of Ba-phillipsite: an in situ synchrotron powder diffraction study. *Phys. Chem. Miner.* 29 (5), 351–361.
- [38] Cruciani G., Martucci A., Meneghini C. (2003) Dehydration dynamics of epistilbite by in situ time resolved synchrotron powder diffraction. *Eur. J. Miner.* 15 (2), 257–266.
- [39] Alberti A., Davoli P., Vezzalini G. (1986) The crystal structure refinement of a natural mordenite. *Z. Krist - Cryst Mater.* 175 (1-4), 249–256.
- [40] Martucci A., Cruciani G., Alberti A., Ritter C., Ciambelli P., Rapacciuolo M. (2000) Location of Brønsted sites in D-mordenites by neutron powder diffraction. *Microporous Mesoporous Mater.* 35, 405–412.
- [41] Dalconi M. C., Alberti A., Cruciani G., Ciambelli P., Fonda E. (2003) Siting and coordination of cobalt in ferrierite: XRD and EXAFS studies at different Co loadings. *Microporous Mesoporous Mater.* 62 (3), 191–200.

- [42] Martucci A., Leardini L., Nassi M., Sarti E., Bagatin R., Pasti L. (2014) Removal of emerging organic contaminants from aqueous systems: adsorption and location of methyl-tertiary-butylether on synthetic ferrierite. *Miner. Mag.* 78 (5), 1161–1175.
- [43] Joshi Y. V., Thomson K. T. (2005) The roles of gallium hydride and Brønsted acidity in light alkane dehydrogenation mechanisms using Ga-exchanged HZSM-5 catalysts: A DFT pathway analysis. *Catal. Today* 105 (1), 106–121.
- [44] Nishi K., Shimizu K., Takamatsu M., Yoshida H., Satsuma A., Tanaka T., Yoshida S., Hattori T. (1998) Deconvolution analysis of Ga K-Edge XANES for quantification of gallium coordinations in oxide environments. *J. Phys. Chem. B* 102 (50), 10190–10195.
- [45] Akatsuka M., Yoshida T., Yamamoto N., Yamamoto M., Ogawa S., Yagi S. (2016) XAFS analysis for quantification of the gallium coordinations in Al<sub>2</sub>O<sub>3</sub>-supported Ga<sub>2</sub>O<sub>3</sub> photocatalysts. *J. Phys. Conf. Ser.* 712 (1), 012056.
- [46] Li S. J., Zheng C., Lobringn K. C. (2003) Refinement of the crystal structure of gallium oxide hydroxide, GaO(OH). *Z. Krist -New Cryst. St.* 218 (JG), 11–12.
- [47] Gagné O. C., Hawthorne F. C. (2018) Bond-length distributions for ions bonded to oxygen: metalloids and post-transition metals. *Acta Crystallogr. B* 74 (1), 63–78.
- [48] Hendsbee A. D., Pye C. C., Masuda J. D. (2009) Hexa-aqua-gallium(III) trinitrate trihydrate. *Acta Crystallogr.* E65 (8), i65.

## 7 MICROPLASTICS

One of the major marine water quality problems recognised nowadays is the accumulation of plastics. Plastic materials are contaminants of great concern due to their resistance to degradation. In this chapter, a work on the presence of plastics in a marine species of the Mediterranean Sea and its effects on the health status of the fish is presented. The work here reported, which is part of my work of thesis, was recently submitted as article to the journal Marine Environmental Research.

### **Adverse Effects of Plastic Ingestion on the Mediterranean Small-Spotted Catshark (*Scyliorhinus canicula*).**

#### **7.1 Introduction**

The abundance of plastic debris floating in Mediterranean waters was first reported in 1980 [1]. Later studies confirmed the distribution, abundance and characteristics of plastic debris in the basin thanks to visual counts supported by surface nets tows allowing detection and quantification of microplastics, (MP from 1  $\mu\text{m}$  to  $<1$  mm) [2-6]. Plastic particles are in fact typically grouped into categories from macro (MaP  $>1$  cm) to nano (from 1 to  $<1000$  nm) depending on their size (as measured by their diameter or by considering the larger dimension as classifier for irregular or fiber debris) according to the classification proposed by Hartmann N et al., 2019 [7].

In the Mediterranean Sea, MP concentrations is ranging from tens to hundreds of thousands of items per square kilometer; this abundant presence of buoyant plastic debris is likely related to the high human pressure and the hydrodynamics of this semi-enclosed basin [8-9] which is also one of world's busiest shipping routes, receiving waters from densely populated river shorelines (e.g., Nile, Ebro, Rhone and Po) while being connected to the Atlantic Ocean only by the Strait of Gibraltar. For its characteristics, the Mediterranean basin has a water residence time as long as a century [10] and its shores house 10% of the global coastal population (ca. 100 million people within the 10-km coastal strip) [11].

MP are divided in two types: 1) primary, found in most commonly utilised products (e.g. cosmetic and personal care products, insect repellents, sunscreens, products for children), and 2) secondary, originating from the fragmentation of larger plastic debris through biological degradation, photo-degradation, chemical deposition and physical fragmentation [12]. Both primary and secondary MP are present in sea water where the most represented synthetic polymers are polypropylene (PP), polyethylene (PE), polystyrene (PS), polyvinylchloride (PVC) and polyethylene terephthalate (PET) [13].

MP in the marine environment are dispersed via oceanic currents and wind patterns throughout the water column [14], in a variety of colours, shapes, sizes and densities [15].

Their persistence, availability and the biomagnification of the associated harmful chemicals, represent a potential hazard to marine life throughout the food web also if there is very few studies in field [16-17]. MP interaction with marine organisms has been described for zooplankton [18], invertebrates [19-20], fish [20-22], turtles [23], birds [24] and mammals [25], including endangered species [26].

Fish may accidentally ingest particulate while they are feeding on their prey or ingest plastic debris because of their resemblance to prey: the first report of MP ingestion in fish was in 1972 [27]. Depending on plastic size and species, particles may be expelled or accumulate in the gastrointestinal tract (GIT), where could cause physical damage (e.g. block of feeding appendages or filters, and obstruction of GIT), and in some cases inflammation leading to death [28-29].

In the last few years, the presence of plastics debris in fish has been described in species captured in the oceans, seas and freshwater raising concerns on their potential negative effects [30-33]. In addition, several authors have studied in controlled conditions the effects of virgin MP intake or as vehicles of other toxic compounds. Potential damage is related to the physical properties, regarding the interaction of the particles with the organism tissues and to the chemical properties, concerning the transfer of contaminants or leaching of plastic additives [34-36]. Indeed, plastics, due to their lipophilic nature, have the potential to adsorb many hydrophobic persistent organic pollutants which may increase their harmful effect on biota. Up to now, it has not been completely elucidated the contribution of chemicals to plastic toxicity. Recent studies suggest that the two main routes of uptake in fish are represented by the ingestion and inhalation, since MP were found to accumulate and cause tissue damage in GIT and gills [28, 35]. Histological observations on exposed fish confirmed that MP were able to induce a strong inflammatory response in the target tissues [36]. The transcriptomic profiling of zebrafish larvae exposed to PS also suggested the activation of immune response, with the up-regulation of genes related to the complement system [37-38]. Lu et al. (2016) [39] reported how the accumulation of PE in gills, gut and liver of zebrafish causes oxidative stress, inflammation in fish liver and a disturbed lipid and energy metabolism [39].

Besides inflammation and metabolic disorders, MP absorption and distribution in different tissues and cells can result in several types of effects, such as behaviour alterations, predatory performance reduction, neurotoxicity, decreased growth [34, 35, 40-43]. Moreover, given the chemical properties, the MP uptake by aquatic organisms with other contaminants is a route to harmful chemicals including styrene, metals, phthalates, bisphenol A, polycyclic aromatic hydrocarbons (PAHs), polychlorinated biphenyls (PCBs) or polybrominated diphenyl ethers (PBDEs) [44-45]. For example, the japanese medaka (*Oryzias latipes*), exposed for short-time to both virgin and marine PE fragments,

showed bioaccumulation of PAHs, PCBs and PBDEs, with signs of liver stress and early tumor formation [34, 40].

The small-spotted catshark (*Scyliorhinus canicula*, Linnaeus, 1758, SC) is a species of the family Scyliorhinidae. It is one of the most abundant cartilaginous fish in the central Mediterranean Sea [46] and inhabits the continental shelves off the coasts of Norway and the British Isles up to Senegal. It is a small, shallow-water shark inhabiting waters of depths ranging from a few meters (mt) down to 400 mt [47,48]. SC feeds opportunistically on a wide range of macrobenthic fauna, with Crustacea, Mollusca, Annelida, and Echinodermata as preferred prey. Feeding preference may depend on SC age and feeding intensity is highest during the summer due to the higher availability of living preys [48].

Given their low commercial value and abundance in the Mediterranean Sea (this species is currently listed as "Least Concern" on the IUCN Red List of Threatened Species), SC has been chosen as model in this study, as representative sample of the potential hazard fish in the southern waters of Italy are subject.

Here we present the description and analysis of effects of plastics (MP and MaP) in SC from two different geographic locations in the southern region of the central Mediterranean Sea, near: 1) Mazara del Vallo (MDV), SW Sicily and 2) Lampedusa (LMP), Italy's southernmost island. Plastics have been isolated from the GIT of SC, quantified and analysed with Raman spectroscopy to identify the polymer category. *S. canicula* was further investigated through the analysis of spleen transcripts of key genes involved in adaptive and innate immunity to evaluate the potential of future research hypothesis linking plastic presence to health status.

## **7.2 Material and methods**

### *Samples collection*

One hundred specimens of SC were collected on March 16, 2018 near Mazara del Vallo (N=48, N=25 females, F, and N=23 males, M), SW Sicily, Italy and on May 7<sup>th</sup>, 2018, near Lampedusa island (N=52, N=14 females, F, and N=38 males, M), Italy's southernmost island, in the FAO General Fisheries Commission for the Mediterranean (GFCM) areas marked as Geographical Sub-Area (GSA) 16 and GSA13 in Figure 7.1, respectively (Figure 7.1; Supplementary Table 1).

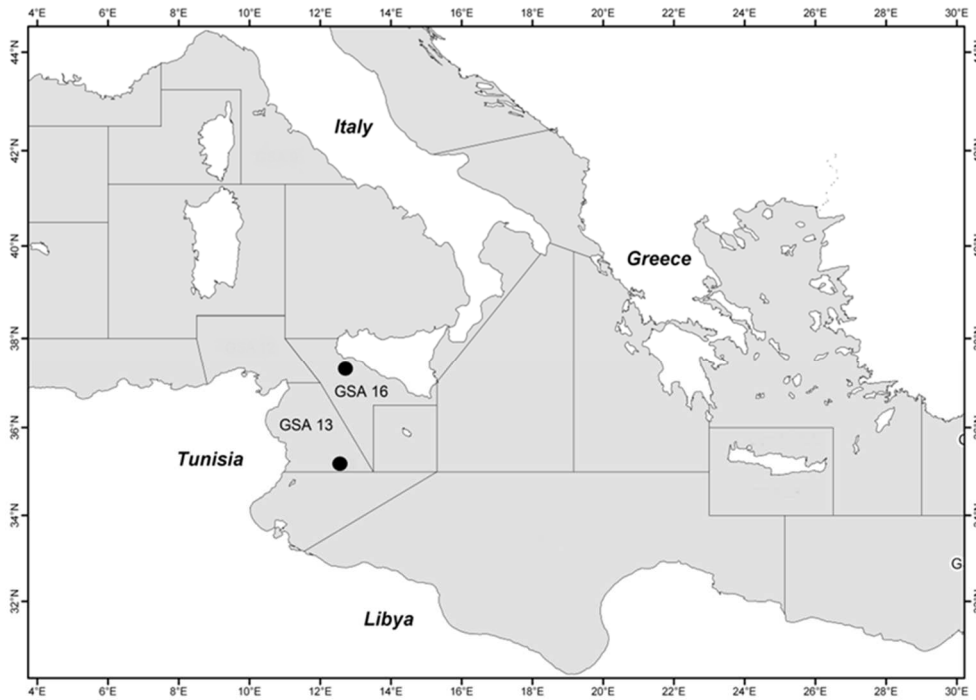


**Figure 7.1** Sampling sites, located within FAO GFCM GSAs.

Dots represent the 2 locations of sampling, south of Mazara del Vallo, GSA 16 and south of Lampedusa, GSA 13. Lampedusa samples were collected in deep water. GFCM, General Fisheries Commission for the Mediterranean; GSA, Geographical Sub-Area.

### *Morphometric indices*

Fish total length (TL), body weight (BW), spleen weight (SPL W), liver weight (LIV W) and GIT weight (GIT W), gender and maturity stage were recorded. Visceral weight (VW) was calculated subtracting the carcass weight (CW) to the using BW. Fish were weighed after sampling, then spleen, liver and GIT were removed by dissection and weighted after evisceration. All the weights were measured using Sartorius balance (model: MSEE6202P-000-D0) to an accuracy of 0.01 grams.

Sexual maturity was defined by 6 stages of gonadic development according to the Medits (International Bottom Trawl Survey in the Mediterranean) scale [49].

Condition factor (CF) was calculated as follows:  $(BW \times 100) / TL^3$ . The hepato-somatic index (HSI), the spleno-somatic index (SSI) and the GIT somatic index (GSI) were calculated as follows:  $HSI = \text{liver weight (g)} \times 100 / \text{body weight (g)}$ ,  $SSI = \text{spleen weight (g)} \times 100 / \text{body weight (g)}$ ,  $GSI = \text{GIT weight (g)} \times 100 / \text{body weight (g)}$  (Supplementary Table 1).

Sample ID	Gender	MAT	TL	BW	CW	VW	CF	SPL W	SSI	LIV W	HIS	GIT W	GSI (g)	Date 2018	LS
SC1	M	1	42,00	245,10	200,62	44,48	0,33	0,66	0,27	17,17	7,01	16,78	6,85	16-mar	MDV
SC2	M	2	39,00	186,11	157,77	28,34	0,31	0,75	0,40	10,34	5,56	11,01	5,92	16-mar	MDV
SC3	F	4	45,00	294,11	230,23	63,88	0,32	0,79	0,27	14,39	4,89	20,60	7,00	16-mar	MDV
SC4	F	5	43,00	254,05	198,29	55,76	0,32	0,98	0,39	26,66	10,49	19,43	7,65	16-mar	MDV
SC5	M	2	39,50	182,92	155,00	27,92	0,30	0,66	0,36	10,58	5,78	10,50	5,74	16-mar	MDV
SC6	M	1	33,50	104,68	91,01	13,67	0,28	0,37	0,35	4,76	4,55	7,72	7,37	16-mar	MDV
SC7	F	3	40,50	245,02	187,62	57,40	0,37	0,88	0,36	24,58	10,03	14,43	5,89	16-mar	MDV
SC8	F	2	33,50	118,53	99,08	19,45	0,32	0,78	0,66	6,08	5,13	11,09	9,36	16-mar	MDV
SC9	M	4	45,00	303,99	248,30	55,69	0,33	0,67	0,22	14,10	4,64	13,57	4,46	16-mar	MDV
SC10	M	1	39,50	209,30	166,67	42,63	0,34	0,79	0,38	13,16	6,29	15,38	7,35	16-mar	MDV
SC11	F	3	41,00	260,30	205,87	54,43	0,38	0,78	0,30	21,25	8,16	17,17	6,60	16-mar	MDV
SC12	F	1	34,50	127,30	110,60	16,70	0,31	0,51	0,40	6,03	4,74	8,87	6,97	16-mar	MDV
SC13	F	1	35,50	137,50	118,32	19,18	0,31	0,57	0,41	10,01	7,28	8,23	5,99	16-mar	MDV
SC14	M	4	40,50	197,58	159,56	38,02	0,30	0,60	0,30	10,95	5,54	10,36	5,24	16-mar	MDV
SC15	F	4	41,00	267,70	186,99	80,71	0,39	0,43	0,16	14,07	5,26	24,32	9,08	16-mar	MDV
SC49	M	4	36,50	151,80	127,41	24,39	0,31	0,36	0,24	5,14	3,39	7,97	5,25	7-mag	LMP
SC50	F	3	35,00	151,82	118,48	33,34	0,35	0,54	0,36	15,59	10,27	10,66	7,02	7-mag	LMP
SC51	F	2	32,00	121,80	98,75	23,05	0,37	0,45	0,37	10,85	8,91	8,87	7,28	7-mag	LMP
SC52	M	2	36,00	155,08	130,58	24,50	0,33	0,68	0,44	7,03	4,53	9,13	5,89	7-mag	LMP
SC53	F	2	37,00	157,90	131,39	26,51	0,31	0,67	0,42	10,87	6,88	11,62	7,36	7-mag	LMP
SC54	M	2	38,00	173,59	138,99	34,60	0,32	0,51	0,29	9,66	5,56	11,92	6,87	7-mag	LMP
SC55	M	4	35,50	129,70	105,39	24,31	0,29	0,29	0,22	6,76	5,21	9,87	7,61	7-mag	LMP
SC56	M	2	36,00	144,72	115,63	29,09	0,31	0,57	0,39	9,42	6,51	13,71	9,47	7-mag	LMP
SC57	F	4	36,50	161,30	122,43	38,87	0,33	0,56	0,35	13,03	8,08	8,64	5,36	7-mag	LMP
SC58	M	2	35,50	147,88	126,27	21,61	0,33	0,40	0,27	7,39	5,00	6,83	4,62	7-mag	LMP
SC59	M	5	38,50	206,30	167,04	39,26	0,36	0,62	0,30	10,38	5,03	12,78	6,19	7-mag	LMP
SC60	F	5	35,50	155,94	123,01	32,93	0,35	0,63	0,40	15,95	10,23	10,13	6,50	7-mag	LMP
SC61	F	3	36,50	174,00	131,86	42,14	0,36	0,53	0,30	20,13	11,57	8,77	5,04	7-mag	LMP
SC62	M	2	35,50	120,46	102,45	18,01	0,27	0,62	0,51	6,21	5,16	6,62	5,50	7-mag	LMP
SC63	M	4	38,50	171,80	145,30	26,50	0,30	0,55	0,32	10,25	5,97	6,59	3,84	7-mag	LMP

**Table 7.1 Sample subset of *S. canicula* used in the chemistry and gene expression analyses.**

SC, *S. canicula*. Gender: M, male sample, F, female sample. MAT, stage of gonadal maturity (1-5). L, total length; W, total weight. CW, carcass weight. VW, viscera weight. SPL W, spleen weight. LIV W, liver weight. GIT W, gastro-intestinal tract weight. SSI, spleno-somatic index. HIS, hepato-somatic index. GSI, GIT somatic index. Length is measured in centimeters (cm); weight is measured in grams (g). LS, location of sampling. MDV, Mazara del Vallo; LMP, Lampedusa.

#### *Chemistry: plastic isolation and identification in the GIT*

After sampling, fish were quickly frozen and stored at -20°C. Successively, they were processed in the laboratory, where they were washed with MilliQ water, sectioned and the entire GIT (esophagus to vent), liver and spleen were removed. Liver and spleen were fixed

in RNeasy® and stored in separated closed container at -20°C for subsequent isolation of RNA, whereas GIT was wrapped in aluminum foil and then frozen at -20°C in a closed container.

GIT samples were digested at 60°C for 24 h in 10% KOH (Merck) in MilliQ® water, filtered with 0.45 µm nitrocellulose filter before use, according to the protocol published by Dehaut A et al. (2016) [50]. Following digestion, samples were filtered on 8 µm cellulose nitrate filters (Whatman). In the case of the presence of debris in the digestate, a density-based separation step using an isopropyl solution of NaCl (Sigma Aldrich) was performed. The solution was added to the digestate (2:1, v/v) and stirred for 10 min before being left to settle for 1 h. The supernatant, containing the floating plastic particles was collected and filtered, as previously described. Plastic debris of big size that could not be digested nor filtered were isolated and analysed as undigested MaP. The filters that by visual inspection contained plastic debris contaminated with undigested organic residues or minerals were subject to a further basic digestion step according to the procedure reported in Roch et al. (2017) [51] and washed by a dilute acid aqueous solution (HCl 0.1M), it was observed that after this treatment plastic debris were not broken into smaller fragments. Blank samples were prepared and analysed in parallel as controls to account for microplastic contamination from the digestion and filtering processes (i.e., 'digestion control'). In details, digestion solutions were placed into a clean beaker, heated at 60 °C for 24 h, and vacuum filtered onto a nitrocellulose filter 0.45 µm, (the procedure was repeated ten times; n = 10). Microplastic was quantified and characterised as reported for fish samples (vide infra). The blank samples contamination (mean No. filter<sup>-1</sup>) consisted only of fibers with average values of 4.2 (± 0.5).

Measures to avoid contamination were adopted during all the extraction procedure, cotton lab coat and nitrile gloves were used and glassware equipment were thoroughly washed and rinsed with MilliQ water before use, all materials were covered between use with aluminum foils, and filters were stored in glass petri dishes.

Filters were first examined and sorted by visual inspection with a stereo microscope following protocol [50]. Microscopic analysis of the filters was performed with a Nikon SMZ745T stereomicroscope, equipped with a Nikon Digital Sight DS-F12 camera.

All the MaP, fragments and filaments were analysed with Raman spectroscopy. The size of the analysed subset should insure a representative view of the particle size distribution and chemical nature as suggested by Kedzierski M et al. 2019 [52]. Spectra were generated with a LabRam HR800 micro-Raman instrument from Horiba Scientific equipped with an air-cooled CCD detector at -70 °C, an Olympus BXF microscope, a 600 lines/mm grating and a 50× objective were used to collect the Raman scattering signals. The excitation source was a He-Ne laser (632.8 nm line) with a maximum laser power of 20 mW.

A minimal spectral accumulation of 10 times 1 s was used; if a high background was recorded the accumulations were increased to a maximum of 100 times 1 s to improve the signal-to-noise ratio.

### *Gene expression analysis*

*RNA Extraction.* Total RNA from spleen samples of thirty selected samples (Table 7.1) was extracted using RNeasy Plus Mini Kit (Qiagen, Hilden, Germany) following the manufacturer's instructions. Tissue (about 30 mg) lysis and homogenisation was performed with T 10 basic ULTRA-TURRAX® (IKA, Staufen, Germany). Genomic DNA was removed through an in-column DNase I digestion (Qiagen). The RNA concentration and the quality of the extractions were assessed with a BioSpec-nano UV-Vis spectrophotometer (Shimadzu Italia S.r.l., Milan, Italy). The RNA samples that did not meet the absorbance ratio cutoff (1.8-2.0 for the 280/260; 2.0-2.2 for the 260/230) were extracted more than once.

*Quantitative real time PCR (q-PCR).* A panel of immunity genes [*T cell receptor beta (TCRB)*, *T cell receptor delta (TCRD)* and *immunoglobulin M (IgM)*], and housekeeping genes [*ribosomal protein 13 (RPL13)*, *actin beta 1 (ACTb)* and *ribosomal protein L29 (RPL29)*] was selected from the literature.

Primers for the selected genes were obtained from literature or designed with Primer 3 on different exons to exclude any genomic DNA co-amplification: ncbi accession numbers of the sequences used were KY434203 (TCRB); KY434205 (TCRD); JX555996 ( $\mu$  heavy chain IgM) [53-55] (Table 7.2). Reverse transcription was performed using iScript™ cDNA synthesis kit (Bio-Rad, California, USA) according to the manufacturer's instructions using 1  $\mu$ g total RNA. The qPCR reaction was performed in triplicates in 96 wells plates, using the EvaGreen Dye Master mix (Bio-Rad) on CFX Connect Real-Time Detection system (Bio-Rad). qPCR efficiencies were calculated using the equation from Dhar et al. (2009) [56]. The amplification efficiency of each primer couple was checked through the creation of a five points standard curve with serially diluted 1:5 cDNA from 5 samples (MDV: SC7, SC9, SC11 and LMP: SC56, SC57) (Table 2). cDNA was reverse transcribed from 1  $\mu$ g of total RNA using SsoFast™ EvaGreen® Supermix (Bio-Rad) in a total volume of 10  $\mu$ L of a reaction mix containing 10 ng cDNA, 0.3  $\mu$ M of each primer, 2 $\times$  Evagreen enzyme and DNase-free sterile water. qPCR reactions were run as follows: 1 cycle of 98 °C for 30 min, 49 cycles of 95 °C for 5 s, 60 °C for 10 s; melting curve 65 °C–95 °C: increment 0.5 °C every 5 min. Each reaction was run in triplicate, together with a tri- plicate of no-template controls. The average Ct values were normalised to the values of the housekeeping genes RPL13. RPL13 was the most stable house-keeping gene amongst those tested (e.g RPL13, ACTb, RPL29). Comparative Ct method of analysis ( $2^{-\Delta\Delta Ct}$ ) was used to determined changes of expression between control and treated samples on CFX connect manager

software 3.1 (Bio-Rad). Fold differences were calculated accounting for differences in primer efficiencies using the Pfaffl method [57].

Label	Gene Description	Sequence (5' -> 3')	Acc. n.	Slope	R <sup>2</sup>	Eff	Amp
RPL13	Large Ribosomal Subunit Protein 13	F: GCTCCAAGTTAATCATCTTCCCA R: GCCTTGAAATTCTTCTCATCCTC	AY130423	-3,2	0,91	104	2,0
ACTb	Actin beta	F: CGAGACCTTCAATACCCCTGC R: CATAACCTTCGTAGATGGGCACAG	AJ312004	-3,1	0,95	110	2,1
RPS29	Large Ribosomal Subunit Protein 29	F: CATCAGCAGCTTTACTGGTCTCATC R: GAAGCCGATGTCTTTAGCGTATTG	n/a	-3,0	0,95	114	2,1
TCRB	T cell receptor beta, B (TCRbB)	F: CGTCAATGGCGAAGAAATGC R: TGTCATGTTGCGTGCTCTTGG	KY434203	-3,1	0,9	110	2,1
IgM	Immunoglobulin M heavy chain	F: CGATGGACTACTCCCGAGAA R: CACAGCTGATTTTGCTGCAT	JX555996	-3,1	0,97	110	2,1
TCRD	T cell receptor delta (TCRD)	F: TGCTTGGCATCAGACTTCTACCC R: TTACCCAGGTGAGATTTTCGG	KY434205	-3,2	0,98	100	2,0

**Table 7.2 Sequences and amplification efficiency of primers used in q-PCR analysis.**

Slopes (-3.1, -3.6), R<sup>2</sup>, efficiencies (Eff, 90-110) and amplification (Amp) for each primer couple was checked through the creation of a five points standard curve with serially diluted 1:5 cDNA from 5 samples (MDV: SC7, SC9, SC11 and LMP: SC56, SC57). Amplification and efficiency were calculated using the equation from Dhar et al. (2009) [56].

### *Statistical analysis*

Data were analysed within and between locations. Morphometric data were analysed within MDV and LMP, related to gender (male and females) and/or presence or absence of MaP in the GIT. Student t-test and ANOVA were used in comparison to detect significant differences between groups compared, for morphometric data and for gene expression analysis.

## **7.3 Results and discussion**

### *Morphometric data analysis*

All the morphometric data for the 100 samples were analysed to examine if significant differences exist between the samples from the two locations studied. Variation in TL and BW did not account for a difference in CF between MDV and LMP while the gonadal maturity and liver size had interesting dissimilarities (Table 7.3, Supplementary Table 2).

Diff	Md	MAT	CF	HSI
F		- 34%	0%	- 24%
M		- 34%	- 3%	+ 20%

**Table 7.3 Percentage of change in MDV samples compared to LMP samples.**

Md, Morphometric data. Diff, % of change in MDV vs LMP. F, females; M, males. MAT, gonadal maturity. CF, condition factor. HIS, hepato-somatic index.

In detail: MDV, both females and males SC have smaller (< 34%) index of gonadal maturity when compared to samples from LMP. Moreover, MDV males have bigger liver (HSI > 20%), while females have smaller liver (HSI < 24%) compared to LMP specimens.

The smaller gonadal maturity in MDV specimens may be linked to the great difference in the existing anthropogenic activities in the two locations of sampling. MDV sampling site is close to a port with the largest fishing fleet in Italy, while LMP sampling site is in a pristine area, near Lampedusa, the Italian southernmost island inhabited by only 6.000 people in an area of 20.2 square kilometers. The difference in human activity, contamination and consequently greater stress conditions in MDV, may have an effect on the appropriate development of the MDV fish and may correlated to the overall differences we observed amongst the two shark's populations. The translation of stress to the organismal/population level and higher is not straightforward. In teleosts, acute and chronic stressors can stimulate physiological changes at the organismal level, impacting growth rate, reproductive output or investments, and disease resistance [58-60]. In contrast, very little is known about the physiological changes linked to stress in elasmobranchs. Indeed, the extent to which elasmobranchs are affected by pervasive anthropogenic threats, such as habitat degradation, climate change and pollution and its transient or prolonged impacts on health and fitness (e.g., somatic growth and reproduction) remains poorly understood [61]. We could assume that they respond to threats in a similar way teleosts do, but the nature and magnitude of the response could be highly species-specific and related to ecological factors and the type and duration of the stressors. Plastic contamination and the ingestion by aquatic organisms, including species of commercial importance for fisheries, are well documented in the Mediterranean Sea [16] and we can reasonably assume that it will continue to increase in the foreseeable future; filling the knowledge gaps on the occurrence and adverse effects caused by (of the) polymers actually present in the environment is necessary to assess / understand the impact of these contaminants on biota (degree of the biological impact).

### *Effects and composition of plastics in the GIT of S. canicula*

The GIT of 50 selected specimens was analysed for plastic presence, quantity and type. Plastic were either grouped as fibers, MP fragments or MaP (Figure 7.2 and Figure 7.3) following the proposed by Hartmann N et al., 2019 [7].

We found debris in the shape of fibers (filaments and lines) and fragments in about 80% of the samples analysed (86.3 % of the MDV samples, and 75.7 % from LMP samples), both coloured and clear (Figure 7.3; Table 7.4). Artificially dyed debris and filaments and debris identified by Raman spectroscopy where referred as plastic particles. A total number of 138 particles were counted by visual inspection: 115 fibers shape (83.3%), which were classified based on the diameter size in 56 fibers and 59 filaments and 23 fragments (16.7%). According to size classes, the plastic debris were divided up as follows: 17 were in the range 1-10  $\mu\text{m}$ , 72 were in the range 20  $\mu\text{m}$  e 100  $\mu\text{m}$ , 38 the range 20  $\mu\text{m}$  e 100  $\mu\text{m}$  and 11 were in the range 1cm – 5cm (MaP). Considering the colour, 88 debris were dark coloured (63.8%), 30 were light coloured (21.7%) and 20 were transparent (14.5%).

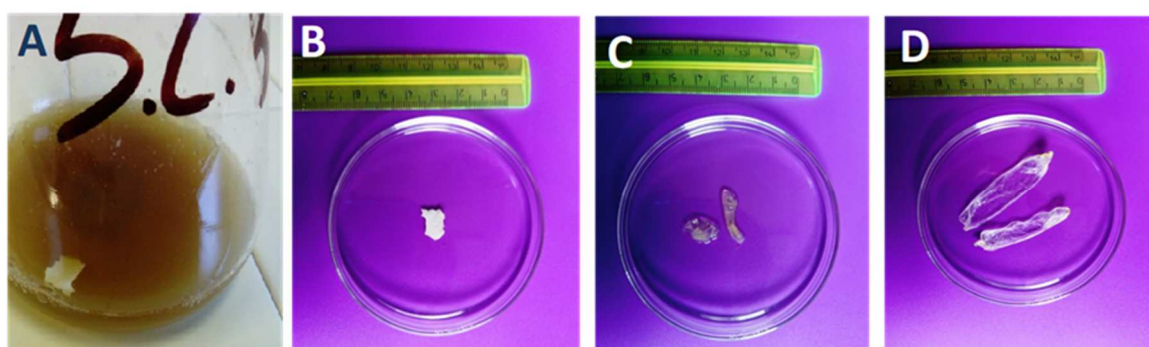


**Figure 7.2 Images of undigested plastics MaP from 3 different samples.**

A, Digested GIT tissue with undigested plastic; same specimen is shown in B. C- D MaP found in the GIT of two other specimens. MaP were identified by Raman spectroscopy: B (polypropylene), C (Polyethylene terephthalate), D (polyethylene).

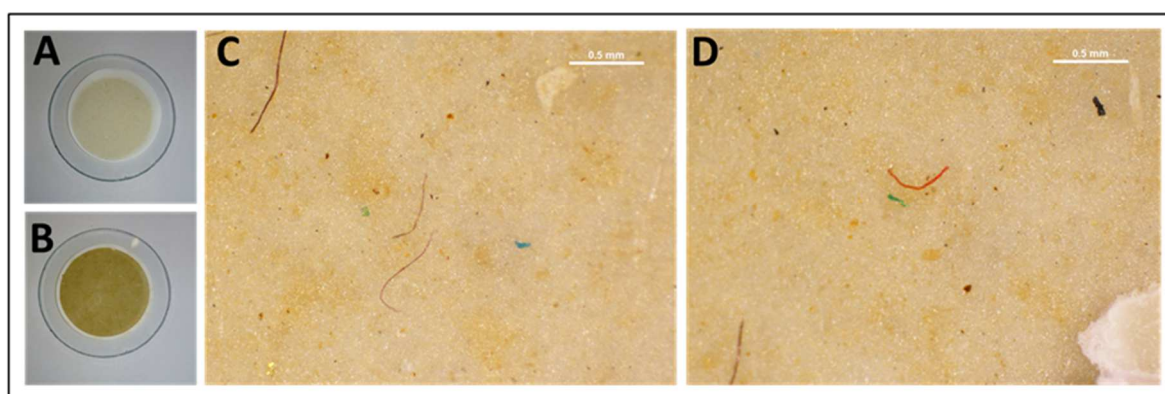


**Figure 7.3 Microscope images of MP debris found on filters in 2 different samples.**

A, B. Filters after digestion of SC6 and SC7. C, D. Microscope image of plastic debris on filters.

All fragments and filaments were analysed with Raman microspectroscopy, fibers identification resulted in many cases problematic possibly due to additive/pigments contained in the fibers or to adhesion of organic residues. The uncertainty in identification of fibers constituents and therefore the bias induced by a partial identification of the samples, combined with the fact that fibers can also derive from contamination during the sample preparation procedure suggest us to limit the data only to MaP, fragments and filaments.

In addition, in the present work we aim to investigate possible MaP effects on the inflammatory system of *S. Canicula*. MP filaments and fragments accounted for a similar number in the two location with an ingested average by individual of 1.32 items in MDV vs 1.04 items in LMP (Table 7.4).

Catch area	N. specimens	Total number MP	Filaments	Fragments	Average / fish
GSA 16 MDV	25	33	24	9	1.32
GSA 13 LMP	25	26	19	7	1.04

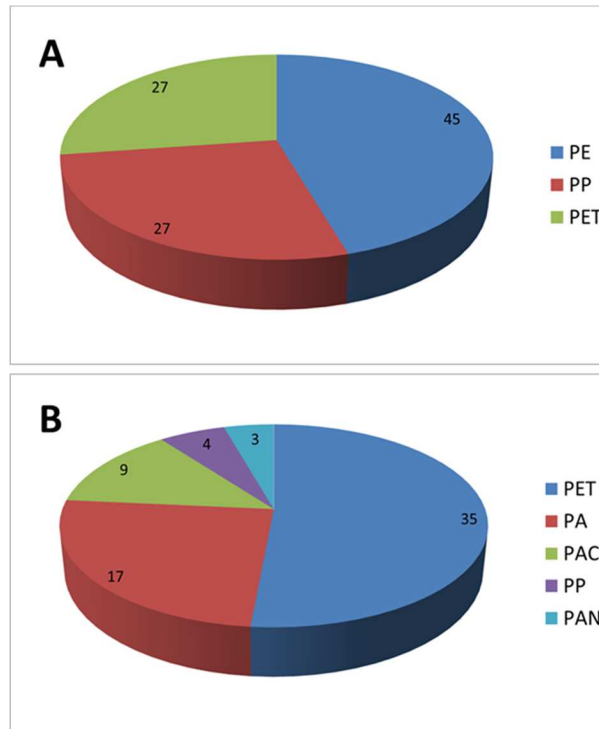
  

Catch area	N. specimens	Total number MP	Filaments	Fragments	Average / fish
GSA 16 MDV	25	6	-	6	
GSA 13 LMP	25	5	-	5	

**Table 7.4 Microplastic (MP) and Macroplastic (MaP) total number, particles, fibers, and average ingested by individual fish.**

Differently, MaP were detected in 18% of the samples analysed. Specifically, in 20% of the MDV samples, and 16% from LMP samples. All specimens with MaP from MDV were females, while those with MaP from LMP were 50% males and 50% females (Supplementary Table 3).

MaP were composed of the polymers polypropylene, polyethylene and polyethylenterephthalate whereas MP were mainly identified as polyester, acrylic, nylon 6, and colourant (Figure 7.4). Average values of MP composition were not significantly different in the two sites.



**Figure 7.4 Plastic debris composition.**

*A, B.* MaP and MP composition: PE polyethylene, PP polypropylene, PET Polyethylene terephthalate, PA Polyamide, PAC Polyacrylate, PAN Polyacrylonitrile. The numbers refer to percentage values.

The analysis of morphological data associated to the presence of MaP in samples from both locations showed no correlation to CF and VW. However, a significant increase in liver weight (49%,  $p < 0.05$ ) and HIS (26%,  $p < 0.01$ ) was observed (Supplementary Table 4A). In the correlation to MaP, MDV specimens showed an increase in the weight of all organs, although only the liver and HSI returned a significant increase of 67% and 34%, respectively of the total weight ( $p < 0.005$ ) (Figure 7.5, Supplementary Table 4B). In LMP, the MaP specimens showed an increase of VW but the variation was non-significant; nevertheless, the liver was still subject to the highest increase (Figure 7.5, Supplementary Table 4C). In general, females from both locations have higher VW probably due to higher structural and functional demands linked to vitellogenesis and maternal immunity (LIV W is 25% and 44% higher in females than males in MDV and LMP, respectively) (Supplementary Table 4D and 4E).

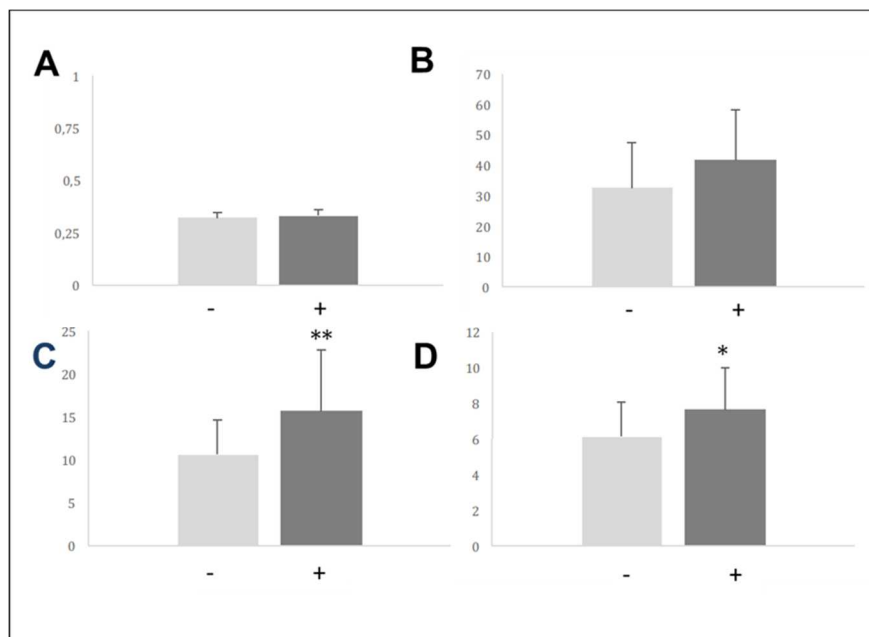


**Figure 7.5 Morphometric changes correlated to the presence of MaP in GIT samples from both locations.**

A, Condition factor, CF. B, Viscera weight. C, liver weight, LIV W. D, Hepato-somatic index, HSI. (+), MaP isolated; (-), no MaP detected. \*  $p < 0.05$ , \*\*  $p < 0.01$ . 30. Samples/individuals: MDV, N = 15; LMP, N = 15. MDV: N = 10 MaP (+), N = 5 MaP (-); LMP: N = 4 MaP (+), N = 11 MaP (-).

The analysis of morphometric data of specimens sampled at MDV and LMP related to both MaP detection and gender, resulted in non-significant differences although it is evident that MDV females have an increase of BW that is only in part related to the increase in VW (Supplementary Table 5A). In LMP the increase of VW is more evident in females than males (Supplementary Table 5B). The females have VW that is 31% ( $p < 0.05$ ) than males (Supplementary Table 5C). BW and VW were higher in samples with MaP females and lower in males (Supplementary Table 5D and 5E). The correlation analysis is clearly showing that females in MDV have smaller liver activity than those in LMP, while the males in MDV have higher liver activity, almost as the males in MDV are stimulated to invest more in liver functions, which is usually a female feature (e.g. vitellogenesis) rather than in male characters (in males the body weight should be higher because is correlated to bones and muscles, for examples). The feminisation-like evidence and the smaller gonadal maturity overall observed could severely impact the reproduction rate and fitness of the SC population in MDV. It has been previously observed that the exposure to endocrine disrupting chemicals (additives of plastics) can strongly influence the course of sex differentiation and unbalance the sex ratio in zebrafish populations; in other freshwater species vitellogenin concentration in male fish have been described in correlation to the exposure to estrogenic contaminants [62-63]. Decreased growth rate, decreased fecundity and negative impacts on subsequent generations have also been linked to plastic exposure in both marine and terrestrial species [64-65].

### *Gene Expression*

In order to move beyond simply studying the presence and type of plastics, the effects on the underlying physiological mechanisms should be investigated. A first step in this direction was to identify if significant genes involved in the organism immune response were changing and if there was any correlation with the presence of plastic (and specifically MaP) described. There are two main layers of immune responses: innate immune responses and adaptive immune responses. The innate immune system creates a fast, non-specific reaction to the pathogen infecting the host organism. If the pathogen persists despite innate defenses, then the adaptive immune system will engage the microbe with specificity and memory. The adaptive (or acquired) immune system mounts to a discriminating long lasting immune response directed by two types of lymphocytes, T cells (cell-mediated immunity) and B cells producing immunoglobulins (Ig) (humoral immune response) [66]. Cartilaginous fish and elasmobranchs (sharks, skates and rays), in particular, are the first jawed vertebrate group to emerge in evolution and are the oldest group relative to mammals having an immune system grounded upon Ig, T cell receptors (TCR), the major histocompatibility complex (MHC), as well as RAG-mediated rearrangement, somatic hypermutation and the presence of primary and secondary lymphoid tissues [67]. Immunoglobulins (IgM) were discovered in sharks almost 40 years ago and while some features of the immune system are simple and primordial, other features, including the Ig system, can be quite complex (e.g. the presence of two non-IgM isotypes, IgW and IgNAR) [67-68]. It is highly probable that each of these isotypes evolved to mediate a particular type of defense mechanism, although there are no functional data as yet for the non-IgM isotypes. The genes that were analysed in this study were those related to canonical immune response pathways, *IgM*, *TCRB* and *TCRD* [55, 68].

RNA extraction from spleen of the 30 specimens was successful and all samples were retrotranscribed and used as template in the real time qPCR of *TCRB* and *IgM*, specifically related to adaptive immunity activity and *TCRD*, linked to innate immunity activity. Samples analysed within location group (MDV and LMP separately), considering the presence (MaP +) or absence (MaP -) of plastics, showed differences in the immune response activation.

In MDV (5 MaP + and 8 MaP -) specimens, MaP + spleens showed a significant increase in the expression of all immune-related genes: fold increases were: 1.2 for *TCRB* ( $p < 0.02$ ), 2.1 for *TCRD* ( $p < 0.01$ ) and 3.1 for *IgM* ( $p < 0.01$ ) (Figure 7.6). When the analysis was restricted to only females (5 MaP + and MaP -), fold increases were: 3.5 for *TCRB* (not significant), 6.3 for *TCRD* ( $p < 0.02$ ), and 16.4 for *IgM* ( $p < 0.02$ ) (Figure 7.6).

In LMP specimens (4 MaP + and 11 MaP -), MaP + spleens showed minimal and not significant variations of immune-related gene transcripts: fold increases were 0.13 (*TCRB*),

0.23 (TCRD) and 0.18 (IgM). Data analysed separating males and females gave the same outcome (data not shown).

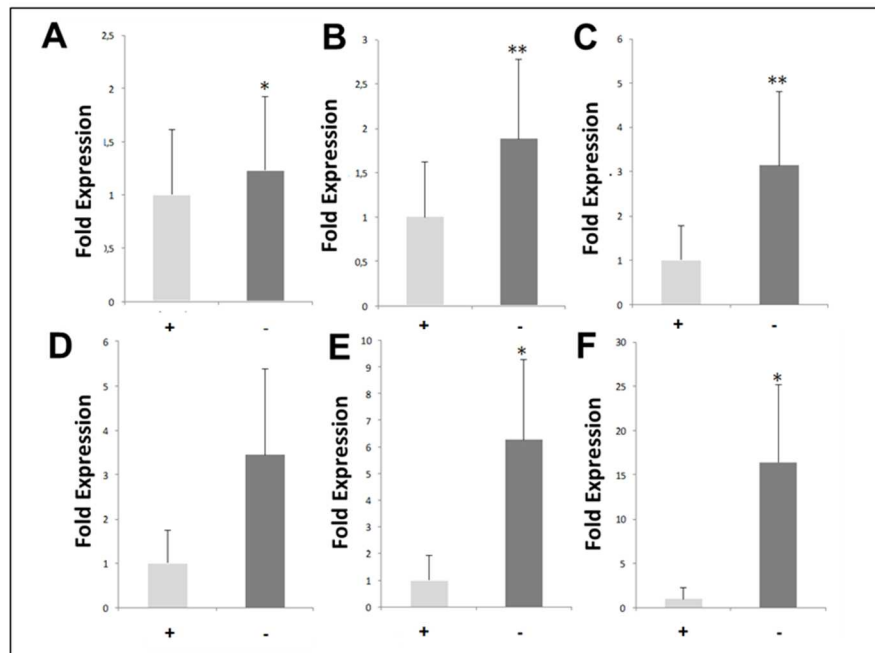


**Figure 7.6 Expression of immune-related genes in *S. canicula* spleen samples from MDV.**

A, D, TCRB; B, E, TCRD; C, F, IgM. Normalized fold expression relative to HK gene (RPL13) in spleen of specimens with macroplastic MaP (+) vs specimens without MaP (-) in the digested GIT of all MDV samples (A-C) or only female MDV samples (D-F). Statistically different comparison are represented by asterisks: \*,  $p < 0.02$ ; \*\*,  $p < 0.01$ . MDV, 1, Mazara del Vallo.

Results from spleen gene expression were somewhat correlated with what we observed in the previous analyses. The changes observed in the expression of the three immune-related genes in spleen were greater in MDV samples than in LMP samples, consistently with the hypothesis that the adverse effects observed may be correlated to the highest degree of MDV anthropogenic pollution, in which MaP, co-present with MP (detected in on nearly all samples) are most likely additive for chemical co-contaminants.

#### 7.4 Conclusion

The present study reports high frequencies of microplastic consumption as well as the presence of macroplastic ingestion in the small spotted shark, *S. canicula*, sampled in two different locations of the Mediterranean Sea. From a first examination, it may be hypothesised that sharks could be less susceptible to microplastic ingestion than macroplastics, given the potential correlation of macroplastic presence to changes in expression of immune-related genes. But the link between plastics and the unavoidable absorbed chemicals, differently distributed in the locations examined, needs to be specifically addressed, given the estrogenic effects hereby reported on maturity and gender

development that could be caused, for example, by endocrine disruptors present in the most contaminated site.

To our knowledge, this is the first study to explore the influence of plastic ingestion by a shark species in the Mediterranean Sea. The occurrence and high frequency of ingested plastic debris hereby reported highlights the ubiquitous nature of this pollutant throughout the Mediterranean Sea and the importance of targeting plastics and their co-contaminants in future pollution control efforts.

## 7.5 References

- [1] Morris R. J. (1980) Floating debris in the Mediterranean. *Mar Pollut Bull.*; 11: 125.
- [2] Aliani S., Griffa A., Molcard A. (2003) Floating debris in the Ligurian Sea, north-western Mediterranean. *Mar Pollut Bull.*, 46(9), 1142-1149.
- [3] Suaria G., Aliani S. (2014) Floating debris in the Mediterranean Sea. *Mar Pollut Bull.*, 86(1-2), 494-504.
- [4] Faure F., Saini C., Potter G., Galgani F., de Alencastro L. F., Hagmann P. (2015) An evaluation of surface micro- and mesoplastic pollution in pelagic ecosystems of the Western Mediterranean Sea. *Environ Sci Pollut Res Int.*, 22(16), 12190-12197.
- [5] Ruiz-Orejón L. F., Sardá R., Ramis-Pujol J. (2016) Floating plastic debris in the Central and Western Mediterranean Sea. *Mar Environ Res.*, 120, 136-144.
- [6] Zeri C., Adamopoulou A., Bojanić Varezić D., Fortibuoni T., Kovač Viršek M., Kržan A., Mandić M., Mazziotti C., Palatinus A., Peterlin M., Prvan M., Ronchi F., Siljic J., Tutman P., Vlachogianni T. (2018) Floating plastics in Adriatic waters (Mediterranean Sea): From the macro- to the micro-scale. *Mar Pollut Bull.*, 136, 341-350.
- [7] Hartmann N. B., Hu T., Thompson R. C., Hassello M., Verschoor A., Daugaard A. E., et al. (2019) Are we speaking the same language? Recommendations for a definition and categorization framework for plastic debris. *Environ. Sci. Technol.*, 53(3), 1039-1047.
- [8] Eriksen M., Lebreton L. C., Carson H. S., Thiel M., Moore C. J., Borerro J. C., Galgani F., Ryan P. G., Reisser J. (2014) Plastic Pollution in the World's Oceans: More than 5 Trillion Plastic Pieces Weighing over 250,000 Tons Afloat at Sea. *PLoS One*, 9(12), e111913.
- [9] Cózar A., Sanz-Martín M., Martí E., González-Gordillo J. I., Ubeda B., Gálvez J. Á., Irigoien X., Duarte C. M. (2015) Plastic accumulation in the Mediterranean Sea. *PLoS One*, 10(4), e0121762.
- [10] Lacombe H., Gascard J. C., Gonella J., Bethoux J. P. (1981) Response of the Mediterranean to the water and energy fluxes across its surface, on seasonal and interannual scales. *Oceanologica Acta*, 4(2), 247–255.
- [11] CIESIN, Center for International Earth Science Information Network. National Aggregates of Geospatial Data: Population, Landscape and Climate Estimates Version 3.

National Aeronautics and Space Administration Socioeconomic Data and Applications Center, Palisades, NY). Available: <http://sedac.ciesin.columbia.edu/data/set/nagdc-population-landscape-climate-estimates-v3>. Accessed 2012 Oct 16.

[12] Auta H. S., Emenike C. U., Fauziah S. H. (2017) Distribution and importance of microplastics in the marine environment: A review of the sources, fate, effects, and potential solutions. *Environ Int.*, 102, 165-176.

[13] Rocha-Santos and Duarte. (2015) A critical overview of the analytical approaches to the occurrence, the fate and the behavior of microplastics in the environment. *Trends Analyt Chem.*, 65, pp. 47-53.

[14] Lebreton L. C., Greer S. D., Borrero J. C. (2012) Numerical modelling of floating debris in the world's oceans. *Mar Pollut Bull.*, 64(3), 653-661.

[15] Reisser J., Slat B., Noble K., du Plessis K., Epp M., Proietti M., de Sonnevile J., Becker T., Pattiaratchi C. (2014) The vertical distribution of buoyant plastics at sea. *Biogeosci Discuss.*, 11, 16207-16226.

[16] Lusher A. L., Hollman P. C. H., Mendoza-Hill J. J. (2017) Microplastics in fisheries and aquaculture: status of knowledge on their occurrence and implications for aquatic organisms and food safety. *FAO Fisheries and Aquaculture Technical Paper*. No. 615. Rome, Italy.

[17] Romeo T., Pietro B., Pedà C., Consoli P., Andaloro F., Fossi M. C. (2015) First evidence of presence of plastic debris in stomach of large pelagic fish in the Mediterranean Sea. *Mar Pollut Bull.*, 95(1), 358-361.

[18] Bessa F., Barría P., Neto J. M., Frias J. P. G. L., Otero V., Sobral P., Marques J. C. (2018) Occurrence of microplastics in commercial fish from a natural estuarine environment. *Mar Pollut Bull.*, 128, 575-584.

[19] Avio C. G., Gorbi S., Milan M., Benedetti M., Fattorini D., d'Errico G., Pauletto M., Bargelloni L., Regoli F. (2015) Pollutants bioavailability and toxicological risk from microplastics to marine mussels. *Environ Pollut.*, 198, 211-222.

[20] Digka N., Tsangaris C., Torre M., Anastasopoulou A., Zeri C. (2018) Microplastics in mussels and fish from the Northern Ionian Sea. *Mar Pollut Bull.*, 135, 30-40.

[21] Compa M., Ventero A., Iglesias M., Deudero S. (2018) Ingestion of microplastics and natural fibres in *Sardina pilchardus* (Walbaum, 1792) and *Engraulis encrasicolus* (Linnaeus, 1758) along the Spanish Mediterranean coast. *Mar Pollut Bull.*, 128, 89-96.

[22] Renzi M., Specchiulli A., Blašković A., Manzo C., Mancinelli G., Cilenti L. (2019) Marine litter in stomach content of small pelagic fishes from the Adriatic Sea: sardines (*Sardina pilchardus*) and anchovies (*Engraulis encrasicolus*). *Environ Sci Pollut Res Int.*, 26(3), 2771-2781.

- [23] Domènech F., Aznar F. J., Raga J. A., Tomás J. (2019) Two decades of monitoring in marine debris ingestion in loggerhead sea turtle, *Caretta caretta*, from the western Mediterranean. *Environ Pollut.*, 244, 367-378.
- [24] Wilcox C., Van Sebille E., Hardesty B. D. (2015) Threat of plastic pollution to seabirds is global, pervasive, and increasing. *Proc Natl Acad Sci U S A.*, 112(38), 11899-11904.
- [25] Fossi M. C., Marsili L., Bainsi M., Giannetti M., Coppola D., Guerranti C., Caliani I., Minutoli R., Lauriano G., Finoia M. G., Rubegni F., Panigada S., Bérubé M., Urbán Ramírez J., Panti C. (2016) Fin whales and microplastics: The Mediterranean Sea and the Sea of Cortez scenarios. *Environ Pollut.*, 209, 68-78.
- [26] Deudero S., Alomar C. (2015) Mediterranean marine biodiversity under threat: Reviewing influence of marine litter on species. *Mar Pollut Bull.*, 98(1-2), 58-68.
- [27] Carpenter E. J., Anderson S. J., Harvey G. R., Miklas H. P., Peck B. B. (1972) Polystyrene spherules in coastal waters. *Science.*, 178(4062), 749-750.
- [28] Li W. C., Tse H. F., Fok L. (2016) Plastic waste in the marine environment: A review of sources, occurrence and effects. *Sci Total Environ.*, 566-567, 333-349.
- [29] Werner S., Budziak A., Franeker J., van Galgani F., Hanke G., Maes T., Matiddi M., Nilsson P., Oosterbaan L., Priestland E., Thompson R., Veiga J., Vlachogianni T. (2016) Harm Caused by Marine Litter: MSFD GES TG Marine Litter - Thematic Report.
- [30] Ory N., Chagnon C., Felix F., Fernández C., Ferreira J. L., Gallardo C., Garcés Ordóñez O., Henostroza A., Laaz E., Mizraji R., Mojica H., Murillo Haro V., Ossa Medina L., Preciado M., Sobral P., Urbina M. A., Thiel M. (2018) Low prevalence of microplastic contamination in planktivorous fish species from the southeast Pacific Ocean. *Mar Pollut Bull.*, 127, 211-216.
- [31] Bessa F., Barría P., Neto J. M., Frias J. P. G. L, Otero V., Sobral P., Marques J. C. (2018) Occurrence of microplastics in commercial fish from a natural estuarine environment. *Mar Pollut Bull.*, 128, 575-584.
- [32] Pellini G., Gomiero A., Fortibuoni T., Ferrà C., Grati F., Tasseti A. N., Polidori P., Fabi G., Scarcella G. (2018) Characterization of microplastic litter in the gastrointestinal tract of *Solea solea* from the Adriatic Sea. *Environ Pollut.*, 234, 943-952.
- [33] Silva-Cavalcanti J. S., Silva J. D. B., França E. J., Araújo M. C. B., Gusmão F. (2017) Microplastics ingestion by a common tropical freshwater fishing resource. *Environ Pollut.*, 221, 218-226.
- [34] Rochman C. M., Hoh E., Kurobe T., Teh S. J. (2013) Ingested plastic transfers hazardous chemicals to fish and induces hepatic stress. *Sci Rep.*, 3, 3263.
- [35] Pedà C., Caccamo L., Fossi M. C., Gai F., Andaloro F., Genovese L., Perdichizzi A., Romeo T., Maricchiolo G. (2016) Intestinal alterations in European sea bass *Dicentrarchus*

labrax (Linnaeus, 1758) exposed to microplastics: Preliminary results. *Environ Pollut.*, 212, 251-256.

[36] Limonta G., Mancia A., Benkhalqui A., Bertolucci C., Abelli L., Fossi M. C., Panti C. Microplastics induce transcriptional changes, immune response and behavioral alterations in adult zebrafish. In review.

[37] Veneman W. J., Spaik H. P., Brun N. R., Bosker T., Vijver M. G. (2017) Pathway analysis of systemic transcriptome responses to injected polystyrene particles in zebrafish larvae. *Aquat Toxicol.*, 190, 112-120.

[38] Pitt J. A., Kozal J. S., Jayasundara N., Massarsky A., Trevisan R., Geitner N., Wiesner M., Levin E. D., Di Giulio R. T. (2018) Uptake, tissue distribution, and toxicity of polystyrene nanoparticles in developing zebrafish (*Danio rerio*). *Aquat Toxicol.*, 194, 185-194.

[39] Lu Y., Zhang Y., Deng Y., Jiang W., Zhao Y., Geng J., Ding L., Ren H. (2016) Uptake and Accumulation of Polystyrene Microplastics in Zebrafish (*Danio rerio*) and Toxic Effects in Liver. *Environ Sci Technol.*, 50(7), 4054-4060.

[40] Rochman C. M., Kurobe T., Flores I., Teh S. J. (2014) Early warning signs of endocrine disruption in adult fish from the ingestion of polyethylene with and without sorbed chemical pollutants from the marine environment. *Sci Total Environ.*, 493, 656-661.

[41] Ferreira P., Fonte E., Soares M. E., Carvalho F., Guilhermino L. (2016) Effects of multi-stressors on juveniles of the marine fish *Pomatoschistus microps*: Gold nanoparticles, microplastics and temperature. *Aquat Toxicol.*, 170, 89-103.

[42] Barboza L. G. A., Vieira L. R., Branco V., Figueiredo N., Carvalho F., Carvalho C., Guilhermino L. (2018) Microplastics cause neurotoxicity, oxidative damage and energy-related changes and interact with the bioaccumulation of mercury in the European seabass, *Dicentrarchus labrax* (Linnaeus, 1758). *Aquat Toxicol.*, 95, 49-57.

[43] Barboza L. G. A., Vieira L. R., Guilhermino L. (2018) Single and combined effects of microplastics and mercury on juveniles of the European seabass (*Dicentrarchus labrax*): Changes in behavioural responses and reduction of swimming velocity and resistance time. *Environ Pollut.*, 236, 1014-1019.

[44] Koelmans A. A., Besseling E., Foekema E. M. (2014) Leaching of plastic additives to marine organisms. *Environ Pollut.*, 187, 49-54.

[45] Barboza L. G. A., Vieira L. R., Branco V., Carvalho C., Guilhermino L. (2018) Microplastics increase mercury bioconcentration in gills and bioaccumulation in the liver, and cause oxidative stress and damage in *Dicentrarchus labrax* juveniles. *Sci Rep.*, 8(1), 15655.

[46] Ragonese S., Vitale S., Dimech M., Mazzola S. (2013) Abundances of demersal sharks and chimaera from 1994-2009 scientific surveys in the central Mediterranean Sea. *PLoS One*, 8(9), e74865.

- [47] Geraci M. L., Ragonese S., Norrito G., Scannella D., Falsone F., Vitale S. (2017) [Chapter 2] A tale on the demersal and bottom dwelling Chondrichthyes in the south of Sicily through 20 years of scientific survey. Pp. 13–37. In: Rodrigues-Filho L. F., de Luna Sales J. B. (eds.) Chondrichthyes—Multidisciplinary approach. IntechOpen, London, UK.
- [48] Rodriguez-Cabello C., Sanchez F., Olaso I. (2007) Distribution patterns and sexual segregations of *Scyliorhinus canicula* (L.) in the Cantabrian Sea. *Journal of Fish Biology*, 70, 1568–1586.
- [49] Anonymous (2016) International bottom trawl survey in the Mediterranean. Instruction manual. Version 8. [MEDITS—handbook. Version n. 8.] MEDITS Working Group.
- [50] Dehaut A., Cassone A. L., Frère L., Hermabessiere L., Himber C., Rinnert E., Rivière G., Lambert C., Soudant P., Huvet A., Duflos G., Paul-Pont I. (2016) Microplastics in seafood: Benchmark protocol for their extraction and characterization. *Environ Pollut.*, 215, 223-233.
- [51] Roch S., Brinker A. (2017) Rapid and efficient method for the detection of microplastic in the gastrointestinal tract of fishes. *Environ Sci Technol.*, 51(8), 4522-4530.
- [52] Kedzierski M., Villain J., Falcou-Préfol M., Kerros M. E., Henry M., et al. (2019) Microplastics in Mediterranean Sea: A protocol to robustly assess contamination characteristics. *PLoS One*, 14(2), e0212088.
- [53] Crouch K., Smith L. E., Williams R., Cao W., Lee M., Jensen A., Dooley H. (2013) Humoral immune response of the small-spotted catshark, *Scyliorhinus canicula*. *Fish Shellfish Immunol.*, 34(5), 1158-1169.
- [54] Li R., Redmond A. K., Wang T., Bird S., Dooley H., Secombes C. J. (2015) Characterisation of the TNF superfamily members CD40L and BAFF in the small-spotted catshark (*Scyliorhinus canicula*). *Fish Shellfish Immunol.*, 47(1), 381-389.
- [55] Pettinello R., Redmond A. K., Secombes C. J., Macqueen D. J., Dooley H. (2017) Evolutionary history of the T cell receptor complex as revealed by small-spotted catshark (*Scyliorhinus canicula*). *Dev Comp Immunol.*, 74, 125-135.
- [56] Dhar A. K., Bowers R. M., Licon K. S., Veazey G., Read B. (2009) Validation of reference genes for quantitative measurement of immune gene expression in shrimp. *Mol Immunol.*, 46(8-9), 1688-1695.
- [57] Pfaffl M. W. (2001) A new mathematical model for relative quantification in real-time RT-PCR. *Nucleic Acids Res.*, 29(9), e45.
- [58] Davis M. W. (2002) Key principles for understanding fish bycatch discard mortality. *Can J Fish Aquat Sci.*, 59, 1834-1843.
- [59] Iwama G. K., Afonso L. O. B., Vijayan M. M. (2006) Stress in fish. D.E. Evans, J.B. Claiborne (Eds.), *The Physiology of Fishes* (3 ed.), CRC Press, Boca Raton, FL, pp. 319-342.

- [60] Ramsay J. M., Watral V., Schreck C. B., Kent M. L. (2009) Pseudoloma neurophilia infections in zebrafish *Danio rerio*: effects of stress on survival, growth, and reproduction. *Dis Aquat Organ.*, 88(1), 69-84.
- [61] Skomal G. B., Mandelman J. W. (2012) The physiological response to anthropogenic stressors in marine elasmobranch fishes: a review with a focus on the secondary response. *Comp Biochem Physiol A Mol Integr Physiol.*, 162(2), 146-155.
- [62] Von Hippel F. A., Miller P. K., Carpenter D. O., Dillon D., Smayda L., Katsiadaki I., Titus T. A., Batzel P., Postlethwait J. H., Buck C. L. (2018) Endocrine disruption and differential gene expression in sentinel fish on St. Lawrence Island, Alaska: Health implications for indigenous residents. *Environ Pollut.*, 234, 279-287.
- [63] Santos D., Luzio A., Coimbra A. M. (2017) Zebrafish sex differentiation and gonad development: A review on the impact of environmental factors. *Aquat Toxicol.*, 191, 141-163.
- [64] Huerta Lwanga E., Gertsen H., Gooren H., Peters P., Salánki T., van der Ploeg M., Besseling E., Koelmans A. A., Geissen V. (2016) Microplastics in the Terrestrial Ecosystem: Implications for *Lumbricus terrestris* (Oligochaeta, Lumbricidae). *Environ Sci Technol.*, 50(5), 2685-2691.
- [65] Sussarellu R., Suquet M., Thomas Y., Lambert C., Fabioux C., Pernet M. E., Le Goïc N., Quillien V., Mingant C., Epelboin Y., Corporeau C., Guyomarch J., Robbins J., Paul-Pont I., Soudant P., Huvet A. (2016) Oyster reproduction is affected by exposure to polystyrene microplastics. *Proc Natl Acad Sci U S A.*, 113(9), 2430-2435.
- [66] Rauta P. R., Nayak B., Das S. (2012) Immune system and immune responses in fish and their role in comparative immunity study: a model for higher organisms. *Immunol Lett.*, 148(1), 23-33.
- [67] Flajnik M. F. (2002) Comparative analyses of immunoglobulin genes: surprises and portents. *Nat Rev Immunol.*, 2(9), 688-698.
- [68] Dooley H., Flajnik M. F. (2006) Antibody repertoire development in cartilaginous fish. *Dev Comp Immunol.*, 30(1-2), 43-56.

## 7.6 Supplementary Tables

### Supplementary Table 1

ID	Gender	Maturity	TL (cm)	BW (g)	VW (g)	SPL W (g)	LIV W (g)	GIT W (g)	Date	Location
SC1	M	1	42	245.1	200.62	0.66	17.17	16.78	16/3/18	South Mazara
SC2	M	2	39	186.11	157.77	0.75	10.34	11.01	16/3/18	South Mazara
SC5	M	2	39.5	182.92	155	0.66	10.58	10.5	16/3/18	South Mazara
SC6	M	1	33.5	104.68	91.01	0.37	4.76	7.72	16/3/18	South Mazara
SC9	M	4	45	303.99	248.3	0.67	14.1	13.57	16/3/18	South Mazara
SC10	M	1	39.5	209.3	166.67	0.79	13.16	15.38	16/3/18	South Mazara
SC14	M	4	40.5	197.58	159.56	0.6	10.95	10.36	16/3/18	South Mazara
SC16	M	1	34.5	130.75	109.03	0.44	6.94	11.17	16/3/18	South Mazara
SC17	M	1	34	122.13	103	0.54	6.65	9.36	16/3/18	South Mazara
SC19	M	4	44.5	279.32	225.32	1.08	18.38	18.25	16/3/18	South Mazara
SC21	M	1	32	101.22	83.79	0.32	6.57	9.33	16/3/18	South Mazara
SC22	M	2	43	254.54	212.88	0.59	10.52	11.35	16/3/18	South Mazara
SC23	M	1	32.5	100.68	86.86	0.52	4.54	6.64	16/3/18	South Mazara
SC24	M	4	45.5	315.09	258.65	0.67	14.27	12.91	16/3/18	South Mazara
SC27	M	2	40.5	214.7	178.89	0.61	15.17	10.04	16/3/18	South Mazara
SC29	M	2	38	160.4	131.75	0.56	10.44	11.77	16/3/18	South Mazara
SC33	M	1	37.5	143.2	122.15	0.69	7.22	11.36	16/3/18	South Mazara
SC37	M	2	44.5	288.2	243.43	0.68	13.28	12.45	16/3/18	South Mazara
SC38	M	4	42.5	238.1	205.8	1.08	13	6.75	16/3/18	South Mazara
SC39	M	4	44.5	267.2	224.9	0.7	16.5	10.45	16/3/18	South Mazara
SC41	M	4	43	256	216.7	0.71	12.07	9.89	16/3/18	South Mazara
SC42	M	2	37.5	159.4	137.1	0.69	8.53	9.18	16/3/18	South Mazara
SC45	M	4	46.5	302.2	258.7	0.63	10.34	11.98	16/3/18	South Mazara
SC3	F	4	45	294.11	230.23	0.79	14.39	20.6	16/3/18	South Mazara
SC4	F	5	43	254.05	198.29	0.98	26.66	19.43	16/3/18	South Mazara
SC7	F	3	40.5	245.02	187.62	0.88	24.58	14.43	16/3/18	South Mazara
SC8	F	2	33.5	118.53	99.08	0.78	6.08	11.09	16/3/18	South Mazara
SC11	F	3	41	260.3	205.87	0.78	21.25	17.17	16/3/18	South Mazara
SC12	F	1	34.5	127.3	110.6	0.51	6.03	8.87	16/3/18	South Mazara
SC13	F	1	35.5	137.5	118.32	0.57	10.01	8.23	16/3/18	South Mazara
SC15	F	4	41	267.7	186.99	0.43	14.07	24.32	16/3/18	South Mazara
SC18	F	1	35	143.7	119.9	0.58	7.35	13.84	16/3/18	South Mazara
SC20	F	5	40.5	231.62	187.84	1.08	17.48	15.86	16/3/18	South Mazara
SC25	F	2	41	228.55	183.11	0.58	21.93	15.64	16/3/18	South Mazara
SC26	F	2	43.5	231.5	196.01	0.6	16.02	11.38	16/3/18	South Mazara
SC28	F	2	35.5	124.6	104.31	0.44	6.84	11.31	16/3/18	South Mazara
SC30	F	4	42	275.4	202.41	0.84	20.27	21.44	16/3/18	South Mazara

SC31	F	4	45	321.8	240.83	0.58	13.4	29.31	16/3/18	South Mazara
SC32	F	4	46	317	240.21	0.7	18.22	25.17	16/3/18	South Mazara
SC34	F	2	41	225.5	177.92	0.5	17.55	10.8	16/3/18	South Mazara
SC35	F	4	44.5	287.1	214.82	0.62	14.61	21.27	16/3/18	South Mazara
SC36	F	1	32	103.1	87.61	0.42	6.67	6.72	16/3/18	South Mazara
SC40	F	3	43	336.4	254	1.03	27.4	26.32	16/3/18	South Mazara
SC43	F	2	40.5	225.3	176.6	0.7	19.12	21.03	16/3/18	South Mazara
SC44	F	4	45	330	251.4	0.75	16.3	23.3	16/3/18	South Mazara
SC46	F	1	37	168	139.4	0.53	12.45	11.27	16/3/18	South Mazara
SC47	F	4	42.5	256.8	188.2	0.81	12.15	20.41	16/3/18	South Mazara
SC48	F	1	35	136	116.63	0.86	5.71	11.16	16/3/18	South Mazara
SC49	M	4	36.5	151.8	127.41	0.36	5.14	7.97	7/5/18	South Lampedusa
SC52	M	2	36	155.08	130.58	0.68	7.03	9.13	7/5/18	South Lampedusa
SC54	M	2	38	173.59	138.99	0.51	9.66	11.92	7/5/18	South Lampedusa
SC55	M	4	35.5	129.7	105.39	0.29	6.76	9.87	7/5/18	South Lampedusa
SC56	M	2	36	144.72	115.63	0.57	9.42	13.71	7/5/18	South Lampedusa
SC58	M	2	35.5	147.88	126.27	0.4	7.39	6.83	7/5/18	South Lampedusa
SC59	M	5	38.5	206.3	167.04	0.62	10.38	12.78	7/5/18	South Lampedusa
SC62	M	2	35.5	120.46	102.45	0.62	6.21	6.62	7/5/18	South Lampedusa
SC63	M	4	38.5	171.8	145.3	0.55	10.25	6.59	7/5/18	South Lampedusa
SC65	M	3	39.5	180.4	155.9	0.68	5.89	8.61	7/5/18	South Lampedusa
SC68	M	2	35.5	142.38	119.59	0.27	6.18	6.02	7/5/18	South Lampedusa
SC69	M	4	38.5	169.5	138	0.68	5.8	14.52	7/5/18	South Lampedusa
SC70	M	4	35.5	156.99	131.56	0.43	7.16	8.46	7/5/18	South Lampedusa
SC71	M	4	36.5	167.2	138.9	0.42	5.12	12.7	7/5/18	South Lampedusa
SC72	M	4	32.5	117.86	93.08	0.51	7.55	13.91	7/5/18	South Lampedusa
SC73	M	4	36.5	139.4	111.71	0.47	5.26	12.42	7/5/18	South Lampedusa
SC74	M	4	36	142.93	119.48	0.67	5.76	9.42	7/5/18	South Lampedusa
SC75	M	5	32.5	127.7	105.8	0.68	7.78	7.59	7/5/18	South Lampedusa
SC77	M	2	33	115.8	95.78	0.56	6.99	7.45	7/5/18	South Lampedusa
SC78	M	4	39.5	200.3	164.53	0.33	8.43	12.6	7/5/18	South Lampedusa
SC79	M	4	37.5	170.3	145.65	0.42	7.59	9.44	7/5/18	South Lampedusa
SC80	M	3	35	127.1	103.17	3.34	4.51	8.87	7/5/18	South Lampedusa
SC81	M	5	37.5	198.7	150.14	0.32	6.63	25.64	7/5/18	South Lampedusa
SC82	M	3	38	187.5	147.07	0.51	6.85	14.66	7/5/18	South Lampedusa
SC83	M	4	40.5	220.2	177.3	0.37	10.88	21.29	7/5/18	South Lampedusa
SC84	M	4	39.5	197.2	150.3	0.59	9.27	26.1	7/5/18	South Lampedusa
SC86	M	4	39.5	194.4	156.66	0.27	7.04	20.91	7/5/18	South Lampedusa
SC87	M	3	36.5	142.2	120.03	0.36	6.15	8.02	7/5/18	South Lampedusa
SC88	M	3	35.5	155.7	116.07	0.34	6.95	26.25	7/5/18	South Lampedusa
SC89	M	3	39.5	185.1	155.19	0.49	6.97	7.42	7/5/18	South Lampedusa
SC90	M	3	38	186.7	148.59	0.32	7.04	19.2	7/5/18	South Lampedusa
SC91	M	5	37.5	170.5	140.32	0.41	6.23	9.58	7/5/18	South Lampedusa

SC92	M	4	42	245.4	201.87	0.23	12.36	15.96	7/5/18	South Lampedusa
SC93	M	4	38.5	199.1	149.15	0.22	6.82	23.14	7/5/18	South Lampedusa
SC94	M	5	41	199.1	168.5	0.37	6.81	13.02	7/5/18	South Lampedusa
SC96	M	3	37	167.8	142.76	0.33	5.65	7.97	7/5/18	South Lampedusa
SC97	M	3	40	197.9	158.5	0.3	10.47	12.31	7/5/18	South Lampedusa
SC99	M	5	35.5	148.6	123.74	0.33	7.28	6.65	7/5/18	South Lampedusa
SC50	F	3	35	151.82	118.48	0.54	15.59	10.66	7/5/18	South Lampedusa
SC51	F	2	32	121.8	98.75	0.45	10.85	8.87	7/5/18	South Lampedusa
SC53	F	2	37	157.9	131.39	0.67	10.87	11.62	7/5/18	South Lampedusa
SC57	F	4	36.5	161.3	122.43	0.56	13.03	8.64	7/5/18	South Lampedusa
SC60	F	5	35.5	155.94	123.01	0.63	15.95	10.13	7/5/18	South Lampedusa
SC61	F	3	36.5	174	131.86	0.53	20.13	8.77	7/5/18	South Lampedusa
SC64	F	1	31.5	107.2	89.99	0.52	7.34	9.37	7/5/18	South Lampedusa
SC66	F	6	35.5	156.99	127.66	0.6	16.23	11.38	7/5/18	South Lampedusa
SC67	F	6	34	129.3	107.8	0.46	10.56	8.41	7/5/18	South Lampedusa
SC76	F	6	34.5	127.6	100.72	0.38	12.91	8.94	7/5/18	South Lampedusa
SC85	F	6	36.5	154.9	120.84	0.53	10.05	18.91	7/5/18	South Lampedusa
SC95	F	5	39	198.43	158.1	0.79	18.1	9.98	7/5/18	South Lampedusa
SC98	F	5	37.5	199.9	149.3	0.37	11.97	16.69	7/5/18	South Lampedusa
SC100	F	5	35.5	152.3	118.92	0.28	13.93	10.1	7/5/18	South Lampedusa

## Supplementary Table 2

### Males

ID	Gender	TL (cm)	BW (g)	CF	CW (g)	CSI	VW (g)	VSI	Maturity	SPL W (g)	SSI	LIV W (g)	HSI	GIT W (g)	GITI	Location
SC1	M	42	245.1	0.3308	200.62	0.8185	44.48	0.1815	1	0.66	0.0027	17.17	0.0701	16.78	0.0685	MDV
SC2	M	39	186.11	0.3137	157.77	0.8477	28.34	0.1523	2	0.75	0.0040	10.34	0.0556	11.01	0.0592	MDV
SC5	M	39.5	182.92	0.2968	155	0.8474	27.92	0.1526	2	0.66	0.0036	10.58	0.0578	10.5	0.0574	MDV
SC6	M	33.5	104.68	0.2784	91.01	0.8694	13.67	0.1306	1	0.37	0.0035	4.76	0.0455	7.72	0.0737	MDV
SC9	M	45	303.99	0.3336	248.3	0.8168	55.69	0.1832	4	0.67	0.0022	14.1	0.0464	13.57	0.0446	MDV
SC10	M	39.5	209.3	0.3396	166.67	0.7963	42.63	0.2037	1	0.79	0.0038	13.16	0.0629	15.38	0.0735	MDV
SC14	M	40.5	197.58	0.2974	159.56	0.8076	38.02	0.1924	4	0.6	0.0030	10.95	0.0554	10.36	0.0524	MDV
SC16	M	34.5	130.75	0.3184	109.03	0.8339	21.72	0.1661	1	0.44	0.0034	6.94	0.0531	11.17	0.0854	MDV
SC17	M	34	122.13	0.3107	103	0.8434	19.13	0.1566	1	0.54	0.0044	6.65	0.0545	9.36	0.0766	MDV
SC19	M	44.5	279.32	0.3170	225.32	0.8067	54	0.1933	4	1.08	0.0039	18.38	0.0658	18.25	0.0653	MDV
SC21	M	32	101.22	0.3089	83.79	0.8278	17.43	0.1722	1	0.32	0.0032	6.57	0.0649	9.33	0.0922	MDV
SC22	M	43	254.54	0.3201	212.88	0.8363	41.66	0.1637	2	0.59	0.0023	10.52	0.0413	11.35	0.0446	MDV
SC23	M	32.5	100.68	0.2933	86.86	0.8627	13.82	0.1373	1	0.52	0.0052	4.54	0.0451	6.64	0.0660	MDV
SC24	M	45.5	315.09	0.3345	258.65	0.8209	56.44	0.1791	4	0.67	0.0021	14.27	0.0453	12.91	0.0410	MDV
SC27	M	40.5	214.7	0.3232	178.89	0.8332	35.81	0.1668	2	0.61	0.0028	15.17	0.0707	10.04	0.0468	MDV
SC29	M	38	160.4	0.2923	131.75	0.8214	28.65	0.1786	2	0.56	0.0035	10.44	0.0651	11.77	0.0734	MDV
SC33	M	37.5	143.2	0.2715	122.15	0.8530	21.05	0.1470	1	0.69	0.0048	7.22	0.0504	11.36	0.0793	MDV
SC37	M	44.5	288.2	0.3270	243.43	0.8447	44.77	0.1553	2	0.68	0.0024	13.28	0.0461	12.45	0.0432	MDV

SC38	M	42.5	238.1	0.3102	205.8	0.8643	32.3	0.1357	4	1.08	0.0045	13	0.0546	6.75	0.0283	MDV
SC39	M	44.5	267.2	0.3032	224.9	0.8417	42.3	0.1583	4	0.7	0.0026	16.5	0.0618	10.45	0.0391	MDV
SC41	M	43	256	0.3220	216.7	0.8465	39.3	0.1535	4	0.71	0.0028	12.07	0.0471	9.89	0.0386	MDV
SC42	M	37.5	159.4	0.3023	137.1	0.8601	22.3	0.1399	2	0.69	0.0043	8.53	0.0535	9.18	0.0576	MDV
SC45	M	46.5	302.2	0.3006	258.7	0.8561	43.5	0.1439	4	0.63	0.0021	10.34	0.0342	11.98	0.0396	MDV
SC49	M	36.5	151.8	0.3122	127.41	0.8393	24.39	0.1607	4	0.36	0.0024	5.14	0.0339	7.97	0.0525	LMP
SC52	M	36	155.08	0.3324	130.58	0.8420	24.5	0.1580	2	0.68	0.0044	7.03	0.0453	9.13	0.0589	LMP
SC54	M	38	173.59	0.3164	138.99	0.8007	34.6	0.1993	2	0.51	0.0029	9.66	0.0556	11.92	0.0687	LMP
SC55	M	35.5	129.7	0.2899	105.39	0.8126	24.31	0.1874	4	0.29	0.0022	6.76	0.0521	9.87	0.0761	LMP
SC56	M	36	144.72	0.3102	115.63	0.7990	29.09	0.2010	2	0.57	0.0039	9.42	0.0651	13.71	0.0947	LMP
SC58	M	35.5	147.88	0.3305	126.27	0.8539	21.61	0.1461	2	0.4	0.0027	7.39	0.0500	6.83	0.0462	LMP
SC59	M	38.5	206.3	0.3615	167.04	0.8097	39.26	0.1903	5	0.62	0.0030	10.38	0.0503	12.78	0.0619	LMP
SC62	M	35.5	120.46	0.2693	102.45	0.8505	18.01	0.1495	2	0.62	0.0051	6.21	0.0516	6.62	0.0550	LMP
SC63	M	38.5	171.8	0.3011	145.3	0.8458	26.5	0.1542	4	0.55	0.0032	10.25	0.0597	6.59	0.0384	LMP
SC65	M	39.5	180.4	0.2927	155.9	0.8642	24.5	0.1358	3	0.68	0.0038	5.89	0.0326	8.61	0.0477	LMP
SC68	M	35.5	142.38	0.3182	119.59	0.8399	22.79	0.1601	2	0.27	0.0019	6.18	0.0434	6.02	0.0423	LMP
SC69	M	38.5	169.5	0.2970	138	0.8142	31.5	0.1858	4	0.68	0.0040	5.8	0.0342	14.52	0.0857	LMP
SC70	M	35.5	156.99	0.3509	131.56	0.8380	25.43	0.1620	4	0.43	0.0027	7.16	0.0456	8.46	0.0539	LMP
SC71	M	36.5	167.2	0.3438	138.9	0.8307	28.3	0.1693	4	0.42	0.0025	5.12	0.0306	12.7	0.0760	LMP
SC72	M	32.5	117.86	0.3433	93.08	0.7898	24.78	0.2102	4	0.51	0.0043	7.55	0.0641	13.91	0.1180	LMP
SC73	M	36.5	139.4	0.2867	111.71	0.8014	27.69	0.1986	4	0.47	0.0034	5.26	0.0377	12.42	0.0891	LMP
SC74	M	36	142.93	0.3063	119.48	0.8359	23.45	0.1641	4	0.67	0.0047	5.76	0.0403	9.42	0.0659	LMP
SC75	M	32.5	127.7	0.3720	105.8	0.8285	21.9	0.1715	5	0.68	0.0053	7.78	0.0609	7.59	0.0594	LMP
SC77	M	33	115.8	0.3222	95.78	0.8271	20.02	0.1729	2	0.56	0.0048	6.99	0.0604	7.45	0.0643	LMP
SC78	M	39.5	200.3	0.3250	164.53	0.8214	35.77	0.1786	4	0.33	0.0016	8.43	0.0421	12.6	0.0629	LMP
SC79	M	37.5	170.3	0.3229	145.65	0.8553	24.65	0.1447	4	0.42	0.0025	7.59	0.0446	9.44	0.0554	LMP
SC80	M	35	127.1	0.2964	103.17	0.8117	23.93	0.1883	3	3.34	0.0263	4.51	0.0355	8.87	0.0698	LMP
SC81	M	37.5	198.7	0.3768	150.14	0.7556	48.56	0.2444	5	0.32	0.0016	6.63	0.0334	25.64	0.1290	LMP
SC82	M	38	187.5	0.3417	147.07	0.7844	40.43	0.2156	3	0.51	0.0027	6.85	0.0365	14.66	0.0782	LMP
SC83	M	40.5	220.2	0.3315	177.3	0.8052	42.9	0.1948	4	0.37	0.0017	10.88	0.0494	21.29	0.0967	LMP
SC84	M	39.5	197.2	0.3200	150.3	0.7622	46.9	0.2378	4	0.59	0.0030	9.27	0.0470	26.1	0.1324	LMP
SC86	M	39.5	194.4	0.3154	156.66	0.8059	37.74	0.1941	4	0.27	0.0014	7.04	0.0362	20.91	0.1076	LMP
SC87	M	36.5	142.2	0.2924	120.03	0.8441	22.17	0.1559	3	0.36	0.0025	6.15	0.0432	8.02	0.0564	LMP
SC88	M	35.5	155.7	0.3480	116.07	0.7455	39.63	0.2545	3	0.34	0.0022	6.95	0.0446	26.25	0.1686	LMP
SC89	M	39.5	185.1	0.3003	155.19	0.8384	29.91	0.1616	3	0.49	0.0026	6.97	0.0377	7.42	0.0401	LMP
SC90	M	38	186.7	0.3402	148.59	0.7959	38.11	0.2041	3	0.32	0.0017	7.04	0.0377	19.2	0.1028	LMP
SC91	M	37.5	170.5	0.3233	140.32	0.8230	30.18	0.1770	5	0.41	0.0024	6.23	0.0365	9.58	0.0562	LMP
SC92	M	42	245.4	0.3312	201.87	0.8226	43.53	0.1774	4	0.23	0.0009	12.36	0.0504	15.96	0.0650	LMP
SC93	M	38.5	199.1	0.3489	149.15	0.7491	49.95	0.2509	4	0.22	0.0011	6.82	0.0343	23.14	0.1162	LMP
SC94	M	41	199.1	0.2889	168.5	0.8463	30.6	0.1537	5	0.37	0.0019	6.81	0.0342	13.02	0.0654	LMP
SC96	M	37	167.8	0.3313	142.76	0.8508	25.04	0.1492	3	0.33	0.0020	5.65	0.0337	7.97	0.0475	LMP
SC97	M	40	197.9	0.3092	158.5	0.8009	39.4	0.1991	3	0.3	0.0015	10.47	0.0529	12.31	0.0622	LMP
SC99	M	35.5	148.6	0.3321	123.74	0.8327	24.86	0.1673	5	0.33	0.0022	7.28	0.0490	6.65	0.0448	LMP

	N	TL (cm)	BW (g)	CF	CW (g)	CSI	VW (g)	VSI	Maturity	SPL W (g)	SSI	LIV W (g)	HSI	GIT W (g)	GITI	
MDV	23	39.98	207.08	0.31	172.95	0.837	34.13	0.163	2.35	0.65	0.0034	11.11	0.054	11.23	0.059	
LMP	38	37.21	167.24	0.32	136.54	0.818	30.71	0.182	3.55	0.52	0.0034	7.36	0.045	12.51	0.074	
Δ		7%	24%	-3%	27%	2%	11%	-10%	-34%	25%	0%	51%	20%	-10%	25%	
F test		0.0002	0.0000	0.1066	0.0000	0.0461	0.0231	0.0461	0.1228	0.0000	0.0000	0.0000	0.9946	0.0006	0.0104	
T (1,3)		0.0047	0.0078	0.0217	0.0040	0.0018	0.1375	0.0018	0.0002	0.0705	0.4722	0.0001	0.0002	0.1283	0.0063	
T (2,2)		0.0020	0.1707	0.0369	0.0746	0.0013	0.5069	0.0013	0.0069	0.6004	0.8141	0.0060	0.0176	0.0063	0.0013	

## Females

ID	Gender	TL (cm)	BW (g)	CF	CW (g)	CSI	VW (g)	VSI	Maturity	SPL W (g)	SSI	LIV W (g)	HSI	GIT W (g)	GITI	Location
SC3	F	45	294.11	0.3228	230.23	0.7828	63.88	0.2172	4	0.79	0.0027	14.39	0.0489	20.6	0.0700	MDV
SC4	F	43	254.05	0.3195	198.29	0.7805	55.76	0.2195	5	0.98	0.0039	26.66	0.1049	19.43	0.0765	MDV
SC7	F	40.5	245.02	0.3688	187.62	0.7657	57.4	0.2343	3	0.88	0.0036	24.58	0.1003	14.43	0.0589	MDV
SC8	F	33.5	118.53	0.3153	99.08	0.8359	19.45	0.1641	2	0.78	0.0066	6.08	0.0513	11.09	0.0936	MDV
SC11	F	41	260.3	0.3777	205.87	0.7909	54.43	0.2091	3	0.78	0.0030	21.25	0.0816	17.17	0.0660	MDV
SC12	F	34.5	127.3	0.3100	110.6	0.8688	16.7	0.1312	1	0.51	0.0040	6.03	0.0474	8.87	0.0697	MDV
SC13	F	35.5	137.5	0.3073	118.32	0.8605	19.18	0.1395	1	0.57	0.0041	10.01	0.0728	8.23	0.0599	MDV
SC15	F	41	267.7	0.3884	186.99	0.6985	80.71	0.3015	4	0.43	0.0016	14.07	0.0526	24.32	0.0908	MDV
SC18	F	35	143.7	0.3352	119.9	0.8344	23.8	0.1656	1	0.58	0.0040	7.35	0.0511	13.84	0.0963	MDV
SC20	F	40.5	231.62	0.3487	187.84	0.8110	43.78	0.1890	5	1.08	0.0047	17.48	0.0755	15.86	0.0685	MDV
SC25	F	41	228.55	0.3316	183.11	0.8012	45.44	0.1988	2	0.58	0.0025	21.93	0.0960	15.64	0.0684	MDV
SC26	F	43.5	231.5	0.2812	196.01	0.8467	35.49	0.1533	2	0.6	0.0026	16.02	0.0692	11.38	0.0492	MDV
SC28	F	35.5	124.6	0.2785	104.31	0.8372	20.29	0.1628	2	0.44	0.0035	6.84	0.0549	11.31	0.0908	MDV
SC30	F	42	275.4	0.3717	202.41	0.7350	72.99	0.2650	4	0.84	0.0031	20.27	0.0736	21.44	0.0779	MDV
SC31	F	45	321.8	0.3531	240.83	0.7484	80.97	0.2516	4	0.58	0.0018	13.4	0.0416	29.31	0.0911	MDV
SC32	F	46	317	0.3257	240.21	0.7578	76.79	0.2422	4	0.7	0.0022	18.22	0.0575	25.17	0.0794	MDV
SC34	F	41	225.5	0.3272	177.92	0.7890	47.58	0.2110	2	0.5	0.0022	17.55	0.0778	10.8	0.0479	MDV
SC35	F	44.5	287.1	0.3258	214.82	0.7482	72.28	0.2518	4	0.62	0.0022	14.61	0.0509	21.27	0.0741	MDV
SC36	F	32	103.1	0.3146	87.61	0.8498	15.49	0.1502	1	0.42	0.0041	6.67	0.0647	6.72	0.0652	MDV
SC40	F	43	336.4	0.4231	254	0.7551	82.4	0.2449	3	1.03	0.0031	27.4	0.0815	26.32	0.0782	MDV
SC43	F	40.5	225.3	0.3392	176.6	0.7838	48.7	0.2162	2	0.7	0.0031	19.12	0.0849	21.03	0.0933	MDV
SC44	F	45	330	0.3621	251.4	0.7618	78.6	0.2382	4	0.75	0.0023	16.3	0.0494	23.3	0.0706	MDV
SC46	F	37	168	0.3317	139.4	0.8298	28.6	0.1702	1	0.53	0.0032	12.45	0.0741	11.27	0.0671	MDV
SC47	F	42.5	256.8	0.3345	188.2	0.7329	68.6	0.2671	4	0.81	0.0032	12.15	0.0473	20.41	0.0795	MDV
SC48	F	35	136	0.3172	116.63	0.8576	19.37	0.1424	1	0.86	0.0063	5.71	0.0420	11.16	0.0821	MDV
SC50	F	35	151.82	0.3541	118.48	0.7804	33.34	0.2196	3	0.54	0.0036	15.59	0.1027	10.66	0.0702	LMP
SC51	F	32	121.8	0.3717	98.75	0.8108	23.05	0.1892	2	0.45	0.0037	10.85	0.0891	8.87	0.0728	LMP
SC53	F	37	157.9	0.3117	131.39	0.8321	26.51	0.1679	2	0.67	0.0042	10.87	0.0688	11.62	0.0736	LMP
SC57	F	36.5	161.3	0.3317	122.43	0.7590	38.87	0.2410	4	0.56	0.0035	13.03	0.0808	8.64	0.0536	LMP
SC60	F	35.5	155.94	0.3486	123.01	0.7888	32.93	0.2112	5	0.63	0.0040	15.95	0.1023	10.13	0.0650	LMP
SC61	F	36.5	174	0.3578	131.86	0.7578	42.14	0.2422	3	0.53	0.0030	20.13	0.1157	8.77	0.0504	LMP
SC64	F	31.5	107.2	0.3430	89.99	0.8395	17.21	0.1605	1	0.52	0.0049	7.34	0.0685	9.37	0.0874	LMP
SC66	F	35.5	156.99	0.3509	127.66	0.8132	29.33	0.1868	6	0.6	0.0038	16.23	0.1034	11.38	0.0725	LMP

SC67	F	34	129.3	0.3290	107.8	0.8337	21.5	0.1663	6	0.46	0.0036	10.56	0.0817	8.41	0.0650	LMP
SC76	F	34.5	127.6	0.3107	100.72	0.7893	26.88	0.2107	6	0.38	0.0030	12.91	0.1012	8.94	0.0701	LMP
SC85	F	36.5	154.9	0.3185	120.84	0.7801	34.06	0.2199	6	0.53	0.0034	10.05	0.0649	18.91	0.1221	LMP
SC95	F	39	198.43	0.3345	158.1	0.7968	40.33	0.2032	5	0.79	0.0040	18.1	0.0912	9.98	0.0503	LMP
SC98	F	37.5	199.9	0.3791	149.3	0.7469	50.6	0.2531	5	0.37	0.0019	11.97	0.0599	16.69	0.0835	LMP
SC100	F	35.5	152.3	0.3404	118.92	0.7808	33.38	0.2192	5	0.28	0.0018	13.93	0.0915	10.1	0.0663	LMP
	<b>N</b>	<b>TL (cm)</b>	<b>BW (g)</b>	<b>CF</b>	<b>CW (g)</b>	<b>CSI</b>	<b>VW (g)</b>	<b>VSI</b>	<b>Maturity</b>	<b>SPL W (g)</b>	<b>SSI</b>	<b>LIV W (g)</b>	<b>HSI</b>	<b>GIT W (g)</b>	<b>GITI</b>	
MDV	25	40.12	225.88	0.34	176.73	0.795	49.15	0.21	2.76	0.69	0.0033	15.06	0.0661	16.81	0.0746	
LMP	14	35.46	153.53	0.34	121.38	0.794	32.15	0.21	4.21	0.52	0.0035	13.39	0.0873	10.89	0.0716	
$\Delta$		13%	47%	0%	46%	0%	53%	0%	-34%	33%	-6%	12%	-24%	54%	4%	
F test		0.0098	0.0004	0.0918	0.0005	0.0812	0.0007	0.0812	0.3152	0.1824	0.1460	0.0223	0.7609	0.0111	0.1867	
T (1,3)		0.0000	0.0000	0.2763	0.0000	0.4672	0.0015	0.4672	0.0062	0.0010	0.3627	0.1527	0.0006	0.0002	0.2991	
T (2,2)		0.0004	0.0011	0.5993	0.0004	0.9422	0.0146	0.9422	0.0061	0.0045	0.7523	0.3823	0.0012	0.0023	0.5631	

**Supplementary Table 3:** Occurrence of UMaP in *S. canicula* GIT samples.

<b>Sample ID</b>	<b>Sex</b>	<b>Location</b>	<b>MaP</b>
SC1	M	MDV	N
SC2	M	MDV	N
SC3	F	MDV	Y
SC4	F	MDV	Y
SC5	M	MDV	N
SC6	M	MDV	N
SC7	F	MDV	Y
SC8	F	MDV	N
SC9	M	MDV	N
SC10	M	MDV	N
SC11	F	MDV	Y
SC12	F	MDV	Y
SC13	F	MDV	N
SC14	M	MDV	N
SC15	F	MDV	N
SC49	M	LMP	N
SC50	F	LMP	Y
SC51	F	LMP	N
SC52	M	LMP	N
SC53	F	LMP	N
SC54	M	LMP	N
SC55	M	LMP	N
SC56	M	LMP	Y
SC57	F	LMP	Y
SC58	M	LMP	N
SC59	M	LMP	N
SC60	F	LMP	N
SC61	F	LMP	N
SC62	M	LMP	N
SC63	M	LMP	Y

**Supplementary Table 4A:** Morphometric data of all specimens sampled related to UMaP detection.

4A	N	TL (cm)	BW (g)	CW	VW (g)	CF	W SPL (g)	SSI (g)	W LIV (g)	HSI (g)	W GIT (g)	GSI (g)
UMa P-	2 1	37,40 ± 3,13	173,71 ± 51,33	141,26 ± 38,51	32,45 ± 15,29	0,32 ± 0,03	0,57 ± 0,14	0,35 ± 0,11	10,55 ± 4,10	6,12 ± 1,98	11,12 ± 4,00	6,45 ± 1,32
UMa P+	9	38,89 ± 3,71	201,16 ± 61,63	159,38 ± 46,13	41,77 ± 16,55	0,33 ± 0,03	0,68 ± 0,17	0,35 ± 0,04	15,69 ± 7,08	7,68 ± 2,27	13,34 ± 5,01	6,64 ± 1,56
<i>p</i>		n/s	n/s	n/s	n/s	n/s	n/s	0.0117	0.018	0.0477	n/s	n/s
$\Delta$		4%	16%	13%	29%	3%	19%	0%	49%	26%	20%	3%

**Supplementary Table 4B:** Morphometric data of specimens sampled at MDV related to UMaP detection.

4B	F	M	TL (cm)	BW (g)	CW (g)	VW (g)	CF	W SPL (g)	SSI (g)	W LIV (g)	HSI (g)	W GIT (g)	GSI (g)
MDV UMaP-	3	7	38,90 ± 3,72	195,34 ± 64,48	186,52 ± 45,25	49,63 ± 18,76	0,32 ± 0,03	0,63 ± 0,14	0,35 ± 0,14	11,12 ± 3,75	5,70 ± 0,92	12,90 ± 4,94	6,74 ± 1,59
MDV UMaP+	5	0	40,80 ± 3,95	236,16 ± 63,62	158,33 ± 47,64	37,01 ± 20,21	0,34 ± 0,03	0,79 ± 0,18	0,34 ± 0,06	18,58 ± 8,42	7,66 ± 2,74	16,10 ± 4,68	6,82 ± 0,64
<i>p</i>			n/s	n/s	n/s	n/s	n/s	n/s	n/s	0.0039	n/s	n/s	n/s
$\Delta$			5%	21%	18%	34%	6%	25%	-3%	67%	34%	25%	1%

**Supplementary Table 4C:** Morphometric data of specimens sampled at LMP related to UMaP detection.

4C	F	M	TL (cm)	BW (g)	CW (g)	VW (g)	CF	W SPL (g)	SSI (g)	W LIV (g)	HSI (g)	W GIT (g)	GSI (g)
LMP UMaP-	4	7	36,05 ± 1,69	154,04 ± 25,17	125,74 ± 19,16	28,30 ± 7,74	0,33 ± 0,03	0,52 ± 0,13	0,34 ± 0,09	10,03 ± 4,52	6,50 ± 2,61	9,50 ± 2,01	6,19 ± 1,02
LMP UMaP+	2	2	36,50 ± 1,47	157,41 ± 11,75	125,46 ± 13,52	31,95 ± 5,41	0,32 ± 0,02	0,56 ± 0,01	0,35 ± 0,03	12,07 ± 2,81	7,71 ± 1,93	9,90 ± 3,04	6,42 ± 2,41
<i>p</i>			n/s	n/s	n/s	n/s	n/s	0.0027	n/s	n/s	n/s	n/s	0.0321
$\Delta$			1%	2%	0%	13%	-1%	6%	3%	20%	19%	4%	4%

**Supplementary Table 4D:** Morphometric data of specimens sampled at MDV, related to gender.

4D	N	TL (cm)	BW (g)	CW (g)	VW (g)	CF	W SPL (g)	SSI (g)	W LIV (g)	HSI (g)	W GIT (g)	GSI (g)
MDV F	8	39,25 ± 4,22	213,06 ± 72,70	167,13 ± 49,97	45,94 ± 24,21	0,34 ± 0,03	0,72 ± 0,19	0,37 ± 0,14	15,38 ± 8,03	7 ± 2,36	9,78 ± 2,17	7,32 ± 1,31
MDV M	7	39,86 ± 3,48	204,24 ± 61,08	168,42 ± 47,93	35,82 ± 13,72	0,31 ± 0,02	0,64 ± 0,14	0,33 ± 0,07	11,58 ± 3,86	5,62 ± 0,87	12,19 ± 3,18	6,13 ± 1,10
<i>p</i>		n/s	n/s	n/s	n/s	n/s	n/s	n/s	n/s	n/s	n/s	0.0265
$\Delta$		2%	-4%	1%	-22%	-8%	-10%	-11%	-25%	-20%	-21%	-16%

**Supplementary Table 4E:** Morphometric data of specimens sampled at LMP, related to gender.

4E	N	TL (cm)	BW (g)	CW (g)	VW (g)	CF	W SPL (g)	SSI (g)	W LIV (g)	HSI (g)	W GIT (g)	GSI (g)
LMP F	6	35,42 ± 1,83	153,79 ± 17,40	120,99 ± 12,11	32,81 ± 7,20	0,35 ± 0,03	0,56 ± 0,07	0,37 ± 0,04	14,40 ± 3,69	9,32 ± 2,03	9,78 ± 2,17	6,43 ± 1,73
LMP M	9	36,67 ± 1,30	155,70 ± 19,28	128,78 ± 20,20	26,92 ± 6,55	0,31 ± 0,03	0,50 ± 0,15	0,33 ± 0,11	7,51 ± 1,87	4,84 ± 0,71	9,30 ± 2,39	5,99 ± 1,01
<i>p</i>		n/s	n/s	n/s	n/s	n/s	n/s	0.0113	n/s	n/s	0.0006	0.00003
$\Delta$		4%	1%	6%	-18%	-9%	-9%	-10%	-44%	-45%	-3%	-4%

**Supplementary Table 5A:** Morphometric data of specimens sampled at MDV related to UMaP detection and gender.

5A	Females	TL (cm)	BW (g)	CW (g)	VW (g)	CF	W SPL (g)	SSI (g)	W LIV (g)	HSI (g)	W GIT (g)	GSI (g)
MDV F UMaP +	3	40,80 ± 3,95	236,16 ± 63,62	186,52 ± 45,25	49,63 ± 18,76	0,34 ± 0,03	0,79 ± 0,18	0,34 ± 0,06	18,58 ± 8,42	7,66 ± 2,74	16,10 ± 4,68	6,82 ± 0,64
MDV F UMaP -	5	36,67 ± 3,88	174,58 ± 81,20	134,80 ± 46,21	39,78 ± 35,45	0,34 ± 0,04	0,59 ± 0,18	0,41 ± 0,25	10,05 ± 4,00	5,89 ± 1,21	14,55 ± 8,58	8,14 ± 1,87
<i>p</i>		n/s	n/s	n/s	n/s	n/s	n/s	n/s	n/s	n/s	n/s	n/s
$\Delta$		11%	35%	38%	25%	1%	33%	-17%	85%	30%	11%	-16%

**Supplementary Table 5B:** Morphometric data of specimens sampled at LMP related to UMaP detection and female gender.

5B	Females	TL (cm)	BW (g)	CW (g)	VW (g)	CF	W SPL (g)	SSI (g)	W LIV (g)	HSI (g)	W GIT (g)	GSI (g)
LMP F UMaP +	2	35,25 ± 3,54	152,41 ± 21,95	121,25 ± 23,08	31,16 ± 8,39	0,35 ± 0,04	0,57 ± 0,10	0,38 ± 0,05	14,45 ± 4,48	9,40 ± 2,00	9,85 ± 1,33	6,54 ± 1,08
LMP F UMaP -	2	35,75 ± 1,06	156,56 ± 6,70	120,46 ± 2,79	36,11 ± 3,91	0,34 ± 0,02	0,55 ± 0,01	0,35 ± 0,01	14,31 ± 1,81	9,17 ± 1,55	9,65 ± 1,43	6,19 ± 1,18
<i>p</i>		n/s	n/s	n/s	n/s	n/s	n/s	n/s	n/s	n/s	n/s	n/s
$\Delta$		1%	3%	-1%	16%	-1%	-4%	-6%	-1%	-2%	-2%	-5%

**Supplementary Table 5C:** Morphometric data of specimens sampled at LMP related to UMaP detection and male gender.

5C	Males	TL (cm)	BW (g)	CW (g)	VW (g)	CF	W SPL (g)	SSI (g)	W LIV (g)	HSI (g)	W GIT (g)	GSI (g)
LMP M UMaP +	2	36,50 ± 1,26	154,97 ± 28,49	128,3 ± 23,08	26,67 ± 7,50	0,32 ± 0,03	0,50 ± 0,15	0,33 ± 0,11	7,51 ± 1,87	4,84 ± 0,71	9,30 ± 2,39	5,99 ± 1,01
LMP M UMaP -	7	37,25 ± 1,77	158,26 ± 19,15	120,46 ± 2,79	27,80 ± 1,83	0,31 ± 0,01	0,56 ± 0,01	0,36 ± 0,05	9,84 ± 0,59	6,24 ± 0,38	10,15 ± 5,03	6,65 ± 3,99
<i>p</i>		n/s	n/s	n/s	n/s	n/s	n/s	n/s	0.014	0.0014	n/s	0.0151
$\Delta$		2%	2%	2%	4%	-3%	13%	10%	31%	29%	9%	11%

**Supplementary Table 5D:** Morphometric data of only female specimens related to UMaP detection.

<b>5D</b>	<b>N</b>	<b>TL (cm)</b>	<b>BW (g)</b>	<b>CW (g)</b>	<b>VW (g)</b>	<b>CF</b>	<b>W SPL (g)</b>	<b>SSI (g)</b>	<b>W LIV (g)</b>	<b>HSI (g)</b>	<b>W GIT (g)</b>	<b>GSI (g)</b>
<b>UMaP -</b>	7	35,86 ± 2,85	161,91 ± 50,79	127,06 ± 29,75	34,85 ± 21,80	0,34 ± 0,03	0,58 ± 0,12	0,39 ± 0,15	12,57 ± 4,57	7,89 ± 2,45	11,86 ± 5,64	7,23 ± 1,57
<b>UMaP +</b>	7	39,36 ± 4,08	213,41 ± 64,92	167,65 ± 49,04	45,77 ± 16,76	0,34 ± 0,03	0,72 ± 0,18	0,35 ± 0,15	17,36 ± 7,22	8,10 ± 2,44	14,26 ± 4,98	6,64 ± 0,78
<b>p</b>		0.0452	n/s	0.0455	n/s	n/s	n/s	0.0119	n/s	n/s	n/s	n/s
<b>Δ</b>		10%	32%	32%	31%	-1%	24%	-12%	38%	3%	20%	-8%

**Supplementary Table 5E:** Morphometric data of only male specimens related to UMaP detection.

<b>5E</b>	<b>N</b>	<b>TL (cm)</b>	<b>BW (g)</b>	<b>CW (g)</b>	<b>VW (g)</b>	<b>CF</b>	<b>W SPL (g)</b>	<b>SSI (g)</b>	<b>W LIV (g)</b>	<b>HSI (g)</b>	<b>W GIT (g)</b>	<b>GSI (g)</b>
<b>UMaP -</b>	14	38,18 ± 3,06	179,61 ± 52,44	148,36 ± 41,36	31,25 ± 11,64	0,31 ± 0,03	0,57 ± 0,16	0,33 ± 0,09	9,55 ± 3,60	5,23 ± 0,86	10,75 ± 3,09	6,06 ± 1,02
<b>UMaP +</b>	2	37,25 ± 11,77	19,15	130,47 ± 20,98	27,80 ± 1,83	0,31 ± 0,03	0,56 ± 0,01	0,36 ± 0,05	9,84 ± 0,59	6,24 ± 0,38	10,15 ± 5,03	6,65 ± 3,99
<b>p</b>		0.02316	0.04289	0.03799	n/s	n/s	0.03711	n/s	0.02764	n/s	n/s	0.00357
<b>Δ</b>		-2%	-12%	-12%	-11%	-3%	-2%	9%	3%	19%	-6%	10%

## 8 CONCLUSIONS

In this work of thesis, different adsorbent materials were employed for the removal of some classes of contaminants from aqueous solutions. The adsorption process was thoroughly studied in all cases through adsorption experiments and structural investigation.

- Scallop shells, which constitute a waste generated by seafood processing, were selected to study the adsorption of heavy metals (cadmium, lead and nickel) from aqueous matrices. In particular, the cadmium adsorption mechanism and diffusion through the carbonate shell layers was evaluated employing different analytical techniques. This investigation allowed to define a superficial adsorption mechanism. In addition, the heavy metal adsorption causes a structural modification of the shell layers, and this phenomenon can be employed for assessing contamination using shellfish as bioindicator. Moreover, experiments were conducted at different salinities in order to simulate natural conditions, the uptake of cadmium resulted significantly affected only at salinities higher than 20‰, due to the formation of soluble cadmium chloride complexes.

Differences in the adsorption process on scallop shell powder were observed especially between cadmium and nickel, the latter showing a slower kinetics and lower adsorption. Lead, showing high adsorption and fast kinetics, was selected for the competition experiments: in presence of lead, the saturation capacity of scallop shell powder towards cadmium decreases due to the initial preferential formation of lead carbonate phases rather than cadmium carbonate. The results obtained demonstrate that scallop shells represent a valid material for the removal of heavy metals from waters.

- Zeolites were employed for the adsorption of some organic contaminants (toluene, n-hexane, chlorobenzene and 2-ethyl-6-methylaniline which is a metabolite of the pesticide metolachlor). Zeolites with different structure and SARs were selected to determine the influence of this characteristics on the adsorption process. In all cases, zeolites showed fast kinetics and high saturation capacities towards the contaminants selected, sometimes higher than those of other widely employed adsorbent materials (i.e. activated carbon and mesoporous organosilica). Competitive behaviour was observed between toluene and n-hexane in the adsorption onto zeolite ZSM-5; in particular, the zeolite showed higher selectivity towards the aliphatic rather than the aromatic compound.

In each case, zeolites proved to be excellent adsorbent materials for the adsorption of organic contaminants of great concern from water matrices.

In this work of thesis, zeolites were studied not only for the removal of contaminants, but also for the adsorption of gallium to generate new materials with different catalytic properties. In particular, zeolite L, MOR and FER were selected, and the adsorption of gallium was obtained through wet impregnation. Structural characterisation allowed to determine the nature of gallium active sites: in specific, Ga was found to be incorporated in the tetrahedral sites of the zeolites. The gallium-exchanged zeolites obtained could represent promising materials for industrial applications.

The final part of this work of thesis includes a study on the presence of macro and microplastics in the gastrointestinal tract of the Mediterranean Small-Spotted Catshark (*Scyliorhinus canicula*) and their adverse effects on the organism. The results obtained showed high frequency of plastic material into the organisms; moreover, from a first examination it seems that sharks could be more susceptible to macroplastics rather than microplastics, given the potential correlation between macroplastics presence and the changes in the expression of immune-related genes. It should be underlined that it is not clear if the negative effects on the fish health is due to the plastics themselves, to their additives or to substances adsorbed on their surface. Indeed, the investigation herein reported is the initial part of a larger project. To elucidate the plastic toxic components the future steps would be the evaluation of the adsorption of organic contaminants, such as polycyclic aromatic hydrocarbons (PAHs), onto microplastics that could lead to the release of harmful substances in aquatic species.

## 9 PAPERS

1 – Sarti E., Chenet T., Pasti L., Cavazzini A., Rodeghero E., Martucci A. (2017) Effects of Silica Alumina Ratio and Thermal Treatment of Beta Zeolites on the Adsorption of Toluene from Aqueous Solutions. *Minerals*, 7, 22.

2 – Pasti L., Rodeghero E., Beltrami G., Ardit M., Sarti E., Chenet T., Stevanin C., Martucci A. (2018) Insights into Adsorption of Chlorobenzene in High Silica MFI and FAU Zeolites Gained from Chromatographic and Diffractometric Techniques. *Minerals*, 8, 80.

3 – Rodeghero E., Pasti L., Nunziante G., Chenet T., Gigli L., Plaisier J. R., Martucci A. (2019) Highlighting the capability of zeolites for agro-chemicals contaminants removal from aqueous matrix: Evidence of 2-ethyl-6-methylaniline adsorption on ZSM-12. *American Mineralogist*, 104, 317 – 324.

4 – Rodeghero E., Chenet T., Martucci A., Ardit M., Sarti E., Pasti L. Selective adsorption of toluene and n-hexane binary mixture from aqueous solution on zeolite ZSM-5: Evaluation of competitive behavior between aliphatic and aromatic compounds. *Catalysis Today*, available online.

5 – Beltrami G., Chenet T., Pasti L., Gigli L., Pollastri S., Martucci A. Insights on Ga-zeolite catalysts: X-ray powder diffraction and absorption spectroscopy characterization at ambient conditions. *Catalysis Today*, available online.

6 – Mancia A., Chenet T., Bono G., Geraci M. L., Vaccaro C., Munari C., Mistri M., Cavazzini A., Pasti L. (2020) Adverse effects of plastic ingestion on the Mediterranean small-spotted catshark (*Scyliorhinus canicula*). *Marine Environmental Research*, 155, 104876.

Article

# Effect of Silica Alumina Ratio and Thermal Treatment of Beta Zeolites on the Adsorption of Toluene from Aqueous Solutions

Elena Sarti <sup>1</sup>, Tatiana Chenet <sup>1</sup>, Luisa Pasti <sup>1,\*</sup>, Alberto Cavazzini <sup>1</sup>, Elisa Rodeghero <sup>2</sup> and Annalisa Martucci <sup>2</sup>

<sup>1</sup> Department of Chemical and Pharmaceutical Sciences, University of Ferrara, Via Fossato di Mortara 17, 44121 Ferrara, Italy; elena.sarti@unife.it (E.S.); tatiana.chenet@unife.it (T.C.); alberto.cavazzini@unife.it (A.C.)

<sup>2</sup> Department of Physics and Earth Sciences, University of Ferrara, Via Saragat 1, 44122 Ferrara, Italy; elisa.rodeghero@unife.it (E.R.); annalisa.martucci@unife.it (A.M.)

\* Correspondence: luisa.pasti@unife.it; Tel.: +39-0532-455-346

Academic Editor: Huifang Xu

Received: 23 December 2016; Accepted: 10 February 2017; Published: 15 February 2017

**Abstract:** The adsorption of toluene from aqueous solutions onto hydrophobic zeolites was studied by combining chromatographic, thermal and structural techniques. Three beta zeolites (notated BEAs, since they belong to BEA framework type), with different SiO<sub>2</sub>/Al<sub>2</sub>O<sub>3</sub> ratios (i.e., 25, 38 and 360), before and after calcination, were tested as adsorbents of toluene from aqueous media. This was performed by measuring the adsorbed quantities of toluene onto zeolites in a wide concentration range of solute. The adsorption data were fitted with isotherms whose models are based on surface heterogeneity of the adsorbent, according to the defective structure of beta zeolites. The thermal treatment considerably increases the adsorption of toluene, in the low concentration range, on all BEAs, probably due to surface and structural modifications induced by calcination. Among the calcined BEAs, the most hydrophobic zeolite (i.e., that with SiO<sub>2</sub>/Al<sub>2</sub>O<sub>3</sub> ratio of 360) showed the highest binding constant, probably due to its high affinity for an organophilic solute such as toluene. The high sorption capacity was confirmed by thermogravimetric analyses on BEAs, before and after saturation with toluene.

**Keywords:** adsorption; zeolites; beta; toluene

## 1. Introduction

In recent years public concern has been rapidly grown regarding water pollution phenomena. Petroleum hydrocarbons represent one of the most common categories of water pollutants. Gasoline leakage from storage tank, transportation, pipelines and petrochemical wastewaters introduce these compounds into the environment, making surface waters and/or groundwaters unsuitable for many uses, including drinking [1]. BTEX (Benzene, toluene, ethylbenzene and xylene) are frequently detected in chemical and petrochemical wastewaters. These contaminants can cause adverse health effects to humans even at low concentrations [2]. Therefore their removal from groundwater and surface waters is a problem of great importance. Among several techniques developed for BTEX removal from waters, adsorption is one of the most efficient methods, thanks to satisfactory efficiencies even at low concentrations [3], easy operation and low cost [4]. Recently, high-silica zeolites have been shown to be environmental friendly materials able to efficiently sorb several organic pollutants from water, such as pharmaceuticals [5–7], polycyclic aromatic hydrocarbons [8], phenols [9] and petrol-derived compounds [10–12].

In literature, several works have focused on the advantages of zeolites as adsorbents, such as high selectivity and capacity, rapid kinetics, reduced interference from salt and humic substances, excellent

resistance to chemical, biological, mechanical and thermal stress [9,13,14]. Even if zeolites are more expensive with respect to other adsorbents, they offer the possibility to be regenerated without loss of performances at relatively low temperatures, as demonstrated in previous works [10,15].

The investigation of several synthetic zeolites such as ZSM-5 [10], mordenite [4], ferrierite [16] and Y [11] for the removal of petrol-derived compounds from aqueous solutions showed that they are a promising material for water clean-up procedures. Another adsorbent that could be employed in such treatment is zeolite beta due to its large porosity and high surface area. Zeolite beta, indeed, has a three-dimensional intersecting channels system, two mutually perpendicular straight channels each with a cross section of  $6.6 \text{ \AA} \times 6.7 \text{ \AA}$  and a sinusoidal channel with a cross section of  $5.6 \text{ \AA} \times 5.6 \text{ \AA}$  [17]. This tortuous channels system is constituted by the intersection of the two main channels. The channel intersections of zeolite beta generate cavities whose sizes are in the order of  $12\text{--}13 \text{ \AA}$  [17]. Crystallographic faults are frequently observed in beta zeolite and a structural model was proposed by Jansen et al. [18] to explain the creation of local defects by the connection of distorted layers. The structure of zeolite beta is disordered along [001] and it is related to three ordered structures by  $a/3$  and/or  $b/3$  displacements. The three ordered polytypes are designated frameworks A, B, and C [19,20]. Polytype A is tetragonal (space group  $P4_122$  or  $P4_322$ , cell parameters  $a = b \approx 12.5 \text{ \AA}$  and  $c \approx 26.4 \text{ \AA}$ ), polytype B is monoclinic (space group  $C2/c$ , cell parameters  $a \approx b \approx 17.6 \text{ \AA}$ ,  $c \approx 14.4 \text{ \AA}$  and  $\beta \approx 114^\circ$ ), as well as Polytype C (space group  $P2/c$ , cell parameters  $a \approx b \approx 12.5 \text{ \AA}$ ,  $c \approx 27.6 \text{ \AA}$ , and  $\beta \approx 107^\circ$ ).

It has been reported that thermal and hydrothermal treatments induce chemical and structural modifications in beta zeolites, for instance Trombetta et al. [21] observed that thermal treatments can cause dealumination and formation of extraframework aluminium species. The ease of dealumination of beta may be due to the presence of defect sites close to the framework aluminium which promotes bond hydrolysis, nonetheless the microporous structure is not affected by the loss of aluminium [22]. Other zeolites, such as ZSM-5 or mordenite, do not show significant crystallinity loss or dealumination after thermal treatment [10,15,22]. The precise structural modifications of beta zeolite are still a matter of research and the global effect of calcination on beta acidity is not totally clear, because of the presence of several types of acidic sites, with different acidity degree [23,24]. However, it can be inferred that beta zeolites could undergo to greater variations in adsorption properties due to calcination with respect to other zeolites. Also the hydrophilic/hydrophobic features, controlled by varying the  $\text{SiO}_2/\text{Al}_2\text{O}_3$  ratio (SAR), can influence the behaviour of zeolites towards polar/non-polar reactants and products in adsorption and catalytic processes. In fact, the roles played both by calcination and by SAR on catalytic activity of beta zeolites received great attention [25,26]. However there are only few works dealing with the effects of both chemical the composition and thermal treatments of beta on the adsorption properties toward solutes from water solutions. Indeed, the phenomena observed in catalytic gas phase systems could be different from those in aqueous matrix, since it has already been reported that the presence of water can strongly interfere with organic compounds adsorption [27].

Therefore, the objective of this work is to investigate the adsorptive properties of beta zeolites (notated BEAs, since they belong to BEA framework type), with different Silica/Alumina ratios (SAR) before and after calcination for the removal of toluene (TOL) from aqueous solutions. The selected adsorbents were commercial beta zeolites: the possibility to find them on the market and to use them as-received from the manufacturer was considered a strong decision point for their selection.

## 2. Materials and Methods

### 2.1. Chemicals

Toluene (99% purity) was obtained from Sigma-Aldrich (Steinheim, Germany). High-performance liquid chromatography (HPLC) grade acetonitrile (ACN) was purchased from Merck (Darmstadt, Germany). The water was Milli-Q grade (Millipore, Billerica, MA, USA). Zeolite beta powders were obtained from Zeolyst International (Conshohocken, PA, USA) and their main characteristics are reported in Table 1.

**Table 1.** Zeolites characteristics.

Name	Product Code	SiO <sub>2</sub> /Al <sub>2</sub> O <sub>3</sub>	Nominal Cation	Surface Area (m <sup>2</sup> ·g <sup>-1</sup> )
Beta25	CP814E	25	Ammonium	680
Beta38	CP814C	38	Ammonium	710
Beta360	CP811C-300	360	Hydrogen	620

All the adsorbents were employed as-received (named Beta25, Beta38 and Beta360) and after a calcination process (referred to as Beta25c, Beta38c and Beta360c). Calcination was carried out by raising the temperature from room temperature to 600 °C in 1 h, then holding at 600 °C for 4 h. Finally, adsorbents were kept at room temperature for 3 h. Dry air circulation was maintained during both heating and cooling down. The calcined samples were kept in a desiccator and used within 2 days after thermal treatment.

## 2.2. Experimental

The adsorption isotherm was determined using the batch method. Batch experiments were carried out in duplicate in 20 mL crimp top reaction glass flasks sealed with polytetrafluoroethylene (PTFE) septa (Supelco, Bellefonte, PA, USA). The flasks were filled in order to have the minimum headspace and a solid/solution ratio of 1:2 (mg·mL<sup>-1</sup>) was employed. After equilibration, for 24 h at a temperature of 25.3 ± 0.5 °C under stirring, the solids were separated from the aqueous solution by filtration through 0.22 µm polyvinylidene fluoride (PVDF) membrane filters purchased from Agilent Technologies (Santa Clara, CA, USA). The concentration of TOL was determined in the solutions before and after equilibration with zeolite by High Performance Liquid Chromatography/Diode Array Detection (HPLC/DAD) purchased from Waters (Waters Corporation, Milford, MA, USA).

## 2.3. Instrumentation

The HPLC/DAD was employed under isocratic elution conditions. The column (Agilent Technologies) was 150 mm × 4.6 mm, packed with a C18 silica-based stationary phase with a particle diameter of 5 µm and thermostated at 25 °C. The injection volume was 20 µL for all standards and samples. The mobile phase was a mixture ACN:H<sub>2</sub>O 70:30 and the flow rate was 1 mL/min. Detection wavelength was set at 215 nm. Thermogravimetric (TG), differential thermogravimetric (DTG) and differential thermal analyses (DTA) measurements of exhausted samples were performed in air up to 900 °C, at 10 °C·min<sup>-1</sup> heating rate, using a simultaneous thermal analysis (STA) 409 PC LUX<sup>®</sup>—NETZSCH Gerätebau GmbH (Verona, Italy). X-ray powder diffraction (XRPD) patterns of zeolites after TOL adsorption were measured on a Bruker (Billerica, MA, USA) D8 Advance Diffractometer equipped with a Si (Li)SOL-X solid-state detector. Statistical elaborations were carried out through MATLAB<sup>®</sup> ver. 9.1 software (The MathWorks Inc., Natick, MA, USA).

## 3. Results and Discussion

### 3.1. Adsorption from Aqueous Solutions

The adsorption kinetics was studied in order to obtain some important parameters, such as the kinetic constant, which allow the estimation of the time requested for reaching the equilibrium. Moreover, from kinetics measurements, qualitative information about the steps governing the adsorption process can be gained. The uptake  $q$  (mg·g<sup>-1</sup>) was calculated as follows:

$$q = \frac{(C_0 - C_e)V}{m} \quad (1)$$

where  $C_0$  is the initial concentrations in solution (mg·L<sup>-1</sup>),  $C_e$  is the concentration at time  $t$  in kinetics experiments or at equilibrium (mg·L<sup>-1</sup>) for isotherm modelling,  $V$  is the solution volume (L) and  $m$  is the mass of adsorbent (g).

The kinetics was very fast for all the studied materials and the time to reach equilibrium was about 10 min. As an example, the uptake data obtained for TOL on Beta360 are shown in Figure 1. The data of Figure 1 were fitted by the pseudo-second order model (Equation (2)), which has been employed in many studies concerning the adsorption of organic compounds onto zeolites [28,29].

$$q_t = \frac{k_2 q^2 t}{1 + k_2 q t} \quad (2)$$

where  $q_t$  and  $q$  are the amounts of solute sorbed per mass of adsorbent at time  $t$  and at equilibrium, respectively, and  $k_2$  is the second-order adsorption rate constant. The equilibrium uptake  $q$  and the adsorption rate constant  $k_2$  were obtained from non-linear fit of  $q_t$  vs.  $t$ . Values of 3.39 (3.28, 3.50) and 0.46 (0.31, 0.62) were obtained for  $q_e$  and  $k_2$ , respectively: the confidence limits at 95% of probability are reported in brackets. The pseudo-second-order model fitted well all the sorption data as demonstrated by the resulting high coefficients of determination ( $R^2 = 0.9915$ ). From Figure 1 it can also be seen that the surface adsorption (first part of the curve) is a faster process than the intraparticle diffusion of TOL into the zeolite micropores as already observed for ZSM-5 [10].

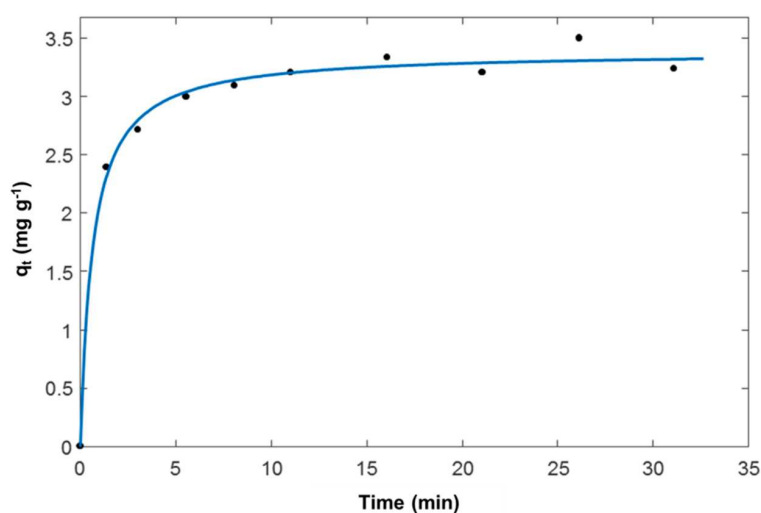


Figure 1. Adsorption kinetics of toluene (TOL) on Beta360: TOL uptake vs. contact time.

The relationship between the solute amount adsorbed for per unit mass of adsorbent  $q$  and its concentration at equilibrium  $C_e$  is provided by equilibrium adsorption isotherms. The Langmuir isotherm has been frequently used to describe the adsorption of organics in aqueous solutions onto hydrophobic zeolites [10,15,29]. This model considers a monolayer adsorption onto energetically equivalent adsorption sites and negligible sorbate–sorbate interactions. It can be represented by the following equation [30].

$$q = \frac{q_s b C_e}{1 + b C_e} \quad (3)$$

where  $b$  is the binding constant ( $L \cdot mg^{-1}$ ) and  $q_s$  is the saturation capacity of the adsorbent material ( $mg \cdot g^{-1}$ ). This model has already been employed for adsorption on BEAs of several classes of organic compounds, such as pharmaceuticals [6], etheramine [29], xylene isomers and ethylbenzene [31].

Freundlich isotherm is a relationship describing non-ideal and reversible adsorption, not restricted to the formation of monolayer. In fact, this empirical model can be applied to multilayer adsorption, with non-uniform distribution of adsorption heat and affinities over the heterogeneous surface [32]. The Freundlich isotherm model can be expressed as [33].

$$q = K_F C_e^{1/n} \quad (4)$$

where  $K_F$  is a constant indicative of the adsorption capacity and  $1/n$  is a measure of the surface heterogeneity, ranging between 0 and 1. The surface heterogeneity increases as  $1/n$  gets closer to zero. The Freundlich isotherm equation was found to have a better fit than the Langmuir equation for TOL adsorption on as-received BEAs (vide infra). This model was also used also by Wang et al. [28] for describing the adsorption of 1,3-propanediol on BEAs zeolites.

Another isotherm model employed to describe multiple adsorbate/adsorbent interactions is that proposed by Tóth [34].

$$q = \frac{q_s b C_e}{[1 + (b C_e)^v]^{1/v}} \quad (5)$$

where  $v$  is a parameter accounting for the heterogeneity of adsorption energies. If  $v = 1$ , the Tóth model corresponds to the Langmuir model [34].

The adsorption isotherms of TOL on both as-received and calcined BEAs are shown in Figure 2, where it can be noted that the isotherms shape of as-received and calcined beta zeolites are different from each other mainly due to modification on the adsorbate/surface interaction energy caused by calcination of the adsorbent. In particular, the thermal treatment considerably increases the adsorption efficiency of all BEAs toward TOL in the low concentration range. This finding has also been observed also for polar compounds such as pharmaceuticals [6]. It has been suggested that part of the adsorption properties of BEA zeolites originates from faults in the zeolitic structure [35]. In addition to its Brønsted acidity, beta zeolite also displays also Lewis acidity [36]. The calcination leads to the conversion of  $\text{NH}_4$ -BEA to H-BEA for Beta25 and Beta38 (see Table 1), as well as to structural and surface modifications for all the three beta zeolites [36,37]. In particular, the thermal treatment can lead to silanols condensation and, consequently, to the degradation of Brønsted acid sites by dehydroxylation. Together with the removal of water, the formation of Lewis acid sites occurs [24], as proposed by some studies [21,23] which found an increase in the ratio Lewis/Brønsted acid sites in the calcined material with respect to the as-received one. However, the global effect of calcination on beta acidity is not totally clear, because of the presence of several types of acidic sites, with different acidity degree [24,38]. It can be inferred that beta Lewis acid sites, whose formation has been promoted by thermal treatment, could interact with toluene as reported by Maretto et al. [39]. Therefore, calcination can lead to structural and compositional changes in beta zeolites, inducing to differences in adsorption properties [22,40]. The experimental data were fitted with all the three models (see Equations (3)–(5)). In order to compare these models, the statistical analysis of the fitting based of the square sum of errors and the number of parameters was performed. The isotherm parameters of the best fitted model estimated by non-linear fitting of the as-received and calcined BEAs are shown in Tables 2 and 3, respectively.

**Table 2.** Isotherm parameters for the adsorption of TOL on as-received BEAs estimated by non-linear fitting, according to the Freundlich model. The confidence limits at 95% of probability of the estimated parameters are reported in brackets.

As-Received Materials	$K_F$ ( $\text{mg}\cdot\text{g}^{-1}$ ) $\cdot$ ( $\text{L}\cdot\text{g}^{-1}$ ) $^n$	$n$	$R^2$
Beta25	5.2 (3.5, 7.0)	0.86 (0.77, 0.95)	0.9953
Beta38	4.2 (2.5, 5.9)	0.79 (0.69, 0.89)	0.9936
Beta360	4.1 (2.8, 5.3)	0.93 (0.72, 1.1)	0.9956

**Table 3.** Isotherm parameters for the adsorption of TOL on calcined BEAs estimated by non-linear fitting, according to the Tóth model. The confidence limits at 95% of probability of the estimated parameters are reported in brackets.

Calcined Materials	$q_s$ ( $\text{mg}\cdot\text{g}^{-1}$ )	$b$ ( $\text{L}\cdot\text{mg}^{-1}$ )	$v$	$R^2$
Beta25c	234 (193, 275)	0.073 (0.043, 0.10)	0.96 (0.70, 1.2)	0.9584
Beta38c	224 (198, 250)	0.10 (0.075, 0.13)	0.91 (0.72, 1.1)	0.9688
Beta360c	241 (201, 280)	0.55 (0.30, 0.80)	0.84 (0.62, 1.0)	0.9667

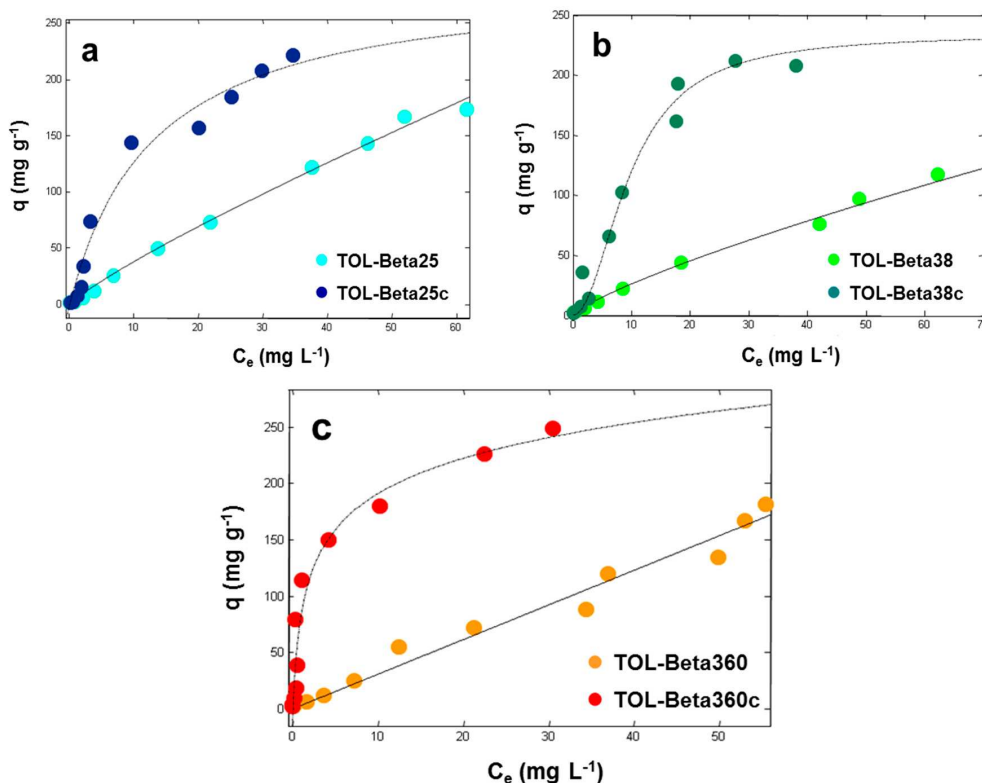


**Figure 2.** Adsorption isotherms of TOL on (a) Beta25 (light blue circles: as-received, dark blue circles: calcined); (b) Beta38 (light green circles: as-received, dark green circles: calcined) and (c) Beta360 (orange circles: as-received, red circles: calcined).

From Tables 2 and 3, it can be seen that as-received zeolites are fitted well by a Freundlich model, whereas the calcined materials are modeled by a Tóth isotherm equation. In particular, Table 2 shows that  $n$  constant for Beta360 is not statistically different, at 95% of probability, from 1, hence TOL adsorption on this zeolite follows a linear trend. On the contrary, values of  $n$  below 1 have been observed for both Beta25 and Beta38, indicating that the adsorbent surface is heterogeneous. The values of  $K_F$  found for the three as-received BEAs are not statistically different from each other at a probability of 95%. This finding may indicate similar adsorbent/adsorbate interactions, possibly due to the effect of physisorbed water on the zeolites porosities (see Section 3.2) and to the presence of structural defects in beta zeolites that make it difficult to assess the properties of the adsorption sites. By comparing calcined BEAs (Table 3), it can be seen that their saturation capacities are not statistically different at 95% of probability. High values of  $q_s$  were obtained for all the calcined adsorbents (above 20%  $w/w$ ). This last finding makes calcined BEAs very promising as adsorbents in the remediation of contaminated waters at high concentration levels. Similar values of  $q_s$  were found in the adsorption of different organic contaminants on hydrophobic Y zeolite (FAU-type framework topology) [11,12]. However, the binding constants  $b$  obtained with Y zeolite were quite low, thus indicating that in the low concentrations range Y zeolite is generally less efficient than calcined BEAs. At low TOL concentrations, it has been proved that another hydrophobic zeolite, namely ZSM-5 (MFI-type framework topology) is very efficient [10]. In this case, in fact, the adsorption isotherm of TOL on ZSM-5 was characterized by a high binding constant ( $b$  was  $3.17 \pm 0.41$ ), despite the lower saturation capacity of ZSM-5 than BEAs and Y (around 8%  $w/w$ ). In the light of the above findings, it can be stated that calcined BEAs represent a good compromise for that which concerning TOL adsorption from aqueous solutions in a wide concentrations range. Concerning the binding constant  $b$ , Beta360c showed a higher value than those of Beta25c and Beta38c, which are not significantly different from each other at 95% of probability. This finding could be explained by considering that adsorption onto zeolites is driven by

both electrostatic and non-covalent interactions [41]. It can be supposed that electrostatic interactions have a negligible contribution to the adsorption of an organophilic solute such as TOL, characterized by  $\log K_{ow}$  of 2.73. Therefore, it can be considered that the adsorption mechanism of TOL onto BEAs is driven mainly by non-covalent interactions, which become more relevant as SAR value increases.

### 3.2. Thermal and Structural Analyses

Thermogravimetric analysis were carried out for the as-received materials (i.e., Beta25, Beta38 and Beta360). A total weight loss of about 17% was observed for all the three samples for temperature up to 900 °C.

These weight losses can be divided up into two contributions: the first one at low temperature (i.e., lower than about 100 °C) due to the loss of water molecules weakly bonded to the zeolite surface and the second one at higher temperature mainly ascribable to the loss of ammonia from Beta25 and Beta38 as well as losses of structural water molecules and silanols condensation in all the beta samples (Figure 3).

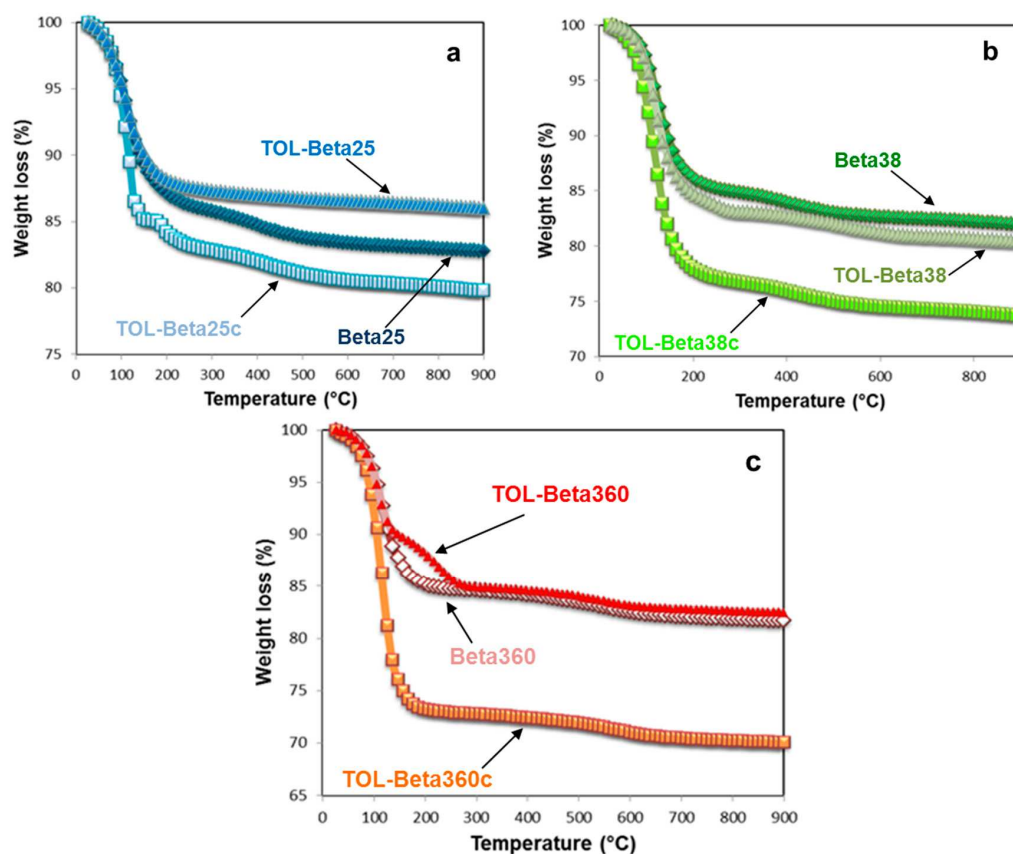


**Figure 3.** Thermogravimetric curves of as-received and calcined BEAs, before and after saturation with TOL: (a) Beta25; (b) Beta38; and (c) Beta360.

The TG analyses of calcined BEAs after TOL saturation show weight losses at 900 °C of 20.2%, 26.2% and 30% for Beta25c, Beta38c and Beta360c, respectively. However, these weight losses cannot be easily related to the adsorbed TOL amount since, as reported in Pasti et al. [6], the calcined zeolites can undergo to rehydration process and the temperatures at which the adsorbed water and TOL are removed from the framework are very close to each other's. This makes it difficult to ascribe the whole weight loss to water or TOL alone. However, these results are in good agreement with the saturation capacities of the materials determined by adsorption experiments (see Table 3). The X-ray powder diffraction patterns of both as-received and calcined Beta25, Beta38 and Beta360, before and

after saturation with TOL are reported in Figure 4. By comparing the X-ray powder diffraction pattern of both the as-received and the calcined materials before and after TOL adsorption (see Figure 4) it can be observed that the peaks intensities in the low  $2\theta$  region change thus confirming the incorporation of molecules in the framework due to adsorption, moreover the differences in the patterns in the intermediate and high  $2\theta$  region indicates that the process is associated with the framework flexibility (expansion or contraction of the cell volume) [42,43]. Similar behaviour is also shown when the three zeolite samples before and after thermal treatment are compared.

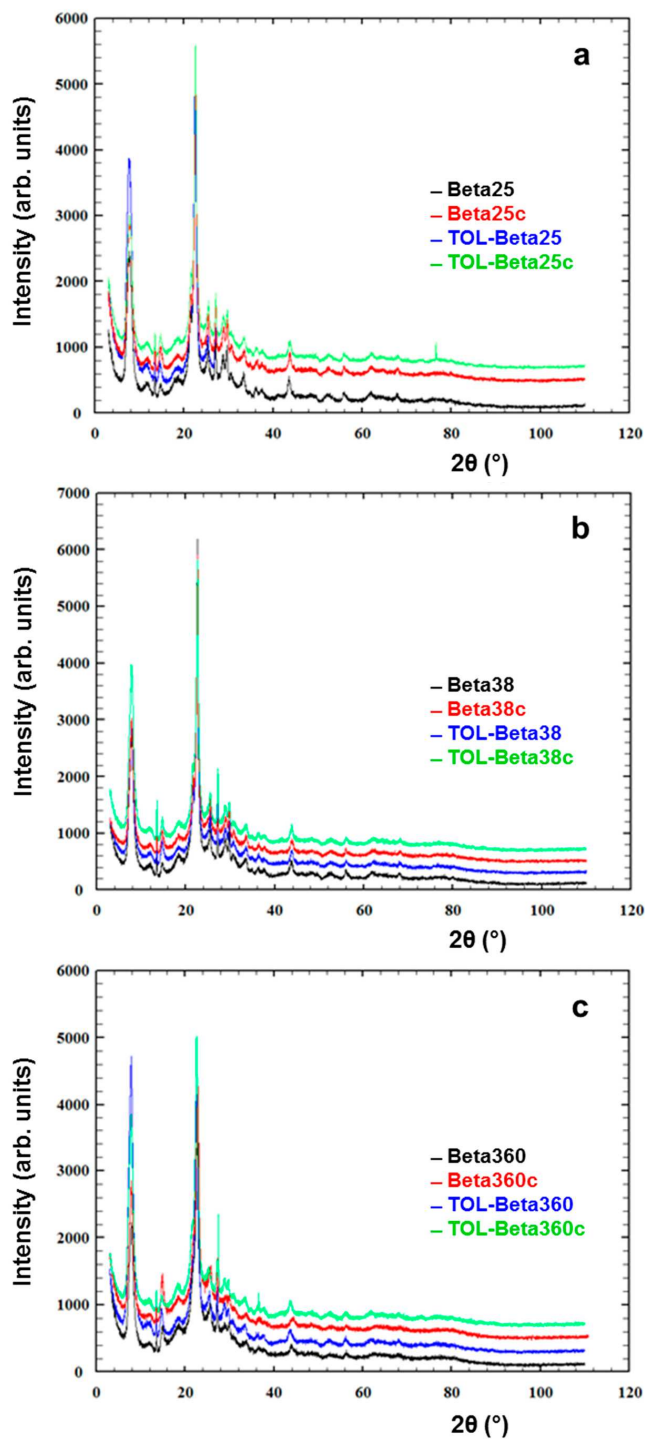


**Figure 4.** X-ray powder diffraction patterns of as-received and calcined BEAs before and after saturation with TOL: (a) Beta25; (b) Beta38; and (c) Beta360.

#### 4. Conclusions

This work highlighted the differences in adsorption properties between as-received and calcined beta zeolites, with three different SARs, toward a water contaminant of great concern such as toluene. It has been observed that the calcination significantly improves the adsorption properties of all of the three zeolites.

The adsorption of toluene by calcined BEAs is characterized by high values of saturation capacity. The most hydrophobic calcined beta, i.e., Beta360c, showed the highest binding constant, thus indicating stronger adsorbent/adsorbate interactions than those of Beta25c and Beta38c. Consequently, Beta360 after thermal treatment is a promising adsorbent for the removal of toluene in water-containing systems. These results open new alternatives for the industrial application of this material, mainly in hydrocarbons adsorption processes in the presence of water.

**Acknowledgments:** Federico Giacometti is acknowledged for performing some of the experiments.

**Author Contributions:** Elena Sarti wrote the paper and performed some of the adsorption experiments with Tatiana Chenet; Luisa Pasti, Alberto Cavazzini and Annalisa Martucci conceived and designed the experiments and analyzed the data; Elisa Rodeghero performed thermogravimetric and X-ray data analysis.

**Conflicts of Interest:** The authors declare no conflicts of interest.

#### References

1. Aivalioti, M.; Vamvasakis, I.; Gidakos, E. BTEX and MTBE adsorption onto raw and thermally modified diatomite. *J. Hazard. Mater.* **2010**, *178*, 136–143. [[CrossRef](#)] [[PubMed](#)]
2. Qu, F.; Zhu, L.; Yang, K. Adsorption behaviors of volatile organic compounds (VOCs) on porous clay heterostructures (PCH). *J. Hazard. Mater.* **2009**, *170*, 7–12. [[CrossRef](#)] [[PubMed](#)]
3. Gupta, V.K.; Verma, N. Removal of volatile organic compounds by cryogenic condensation followed by adsorption. *Chem. Eng. Sci.* **2002**, *57*, 2679–2696. [[CrossRef](#)]
4. Arletti, R.; Martucci, A.; Alberti, A.; Pasti, L.; Nassi, M.; Bagatin, R. Location of MTBE and toluene in the channel system of the zeolite mordenite: Adsorption and host–guest interactions. *J. Solid State Chem.* **2012**, *194*, 135–142. [[CrossRef](#)]
5. Martucci, A.; Pasti, L.; Marchetti, N.; Cavazzini, A.; Dondi, F.; Alberti, A. Adsorption of pharmaceuticals from aqueous solutions on synthetic zeolites. *Microporous Mesoporous Mater.* **2012**, *148*, 174–183. [[CrossRef](#)]
6. Pasti, L.; Sarti, E.; Cavazzini, A.; Marchetti, N.; Dondi, F.; Martucci, A. Factors affecting drug adsorption on beta zeolites. *J. Sep. Sci.* **2013**, *36*, 1604–1611. [[CrossRef](#)] [[PubMed](#)]
7. Braschi, I.; Blasioli, S.; Gigli, L.; Gessa, C.E.; Alberti, A.; Martucci, A. Removal of sulfonamide antibiotics from water: Evidence of adsorption into an organophilic zeolite Y by its structural modifications. *J. Hazard. Mater.* **2010**, *17*, 218–225. [[CrossRef](#)] [[PubMed](#)]
8. Costa, A.A.; Wilson, W.B.; Wang, H.; Campiglia, A.D.; Dias, J.A.; Dias, S.C.L. Comparison of BEA, USY and ZSM-5 for the quantitative extraction of polycyclic aromatic hydrocarbons from water samples. *Microporous Mesoporous Mater.* **2012**, *149*, 186–192. [[CrossRef](#)]
9. Khalid, M.; Joly, G.; Renaud, A.; Magnoux, P. Removal of phenol from water by adsorption using zeolites. *Ind. Eng. Chem. Res.* **2004**, *43*, 5275–5280. [[CrossRef](#)]
10. Rodeghero, E.; Martucci, A.; Cruciani, G.; Bagatin, R.; Sarti, E.; Bosi, V.; Pasti, L. Kinetics and dynamic behaviour of toluene desorption from ZSM-5 using in situ high-temperature synchrotron powder X-ray diffraction and chromatographic techniques. *Catal. Today* **2016**, *227*, 118–125. [[CrossRef](#)]
11. Martucci, A.; Braschi, I.; Bisio, C.; Sarti, E.; Rodeghero, E.; Bagatin, R.; Pasti, L. Influence of water on the retention of methyl tertiary-butyl ether by high silica ZSM-5 and Y zeolites: A multidisciplinary study on the adsorption from liquid and gas phase. *RSC Adv.* **2015**, *5*, 86997–87006. [[CrossRef](#)]
12. Pasti, L.; Martucci, A.; Nassi, M.; Cavazzini, A.; Alberti, A.; Bagatin, R. The role of water in DCE adsorption from aqueous solutions onto hydrophobic zeolites. *Microporous Mesoporous Mater.* **2012**, *160*, 182–193. [[CrossRef](#)]
13. Weitkamp, J. Zeolites and catalysis. *Solid State Ion.* **2000**, *131*, 175–188. [[CrossRef](#)]

14. Aivalioti, M.; Pothoulaki, D.; Papoulias, P.; Gidakos, E. Removal of BTEX, MTBE and TAME from aqueous solutions by adsorption onto raw and thermally treated lignite. *J. Hazard. Mater.* **2012**, *207*, 136–146. [[CrossRef](#)] [[PubMed](#)]
15. Martucci, A.; Rodeghero, E.; Pasti, L.; Bosi, V.; Cruciani, G. Adsorption of 1,2-dichloroethane on ZSM-5 and desorption dynamics by in situ synchrotron powder X-ray diffraction. *Microporous Mesoporous Mater.* **2015**, *215*, 175–182. [[CrossRef](#)]
16. Martucci, A.; Leardini, L.; Nassi, M.; Sarti, E.; Bagatin, R.; Pasti, L. Removal of emerging organic contaminants from aqueous systems: Adsorption and location of methyl-tertiary-butylether on synthetic ferrierite. *Mineral. Mag.* **2014**, *78*, 1161–1175. [[CrossRef](#)]
17. Baerlocher, C.; Meir, W.M.; Olson, O.H. *Atlas of Zeolite Framework Types*, 5th revised ed.; Elsevier Science: Amsterdam, The Netherlands, 2001.
18. Jansen, J.C.; Creighton, E.J.; Njo, S.L.; van Koningsveld, H.; van Bekkum, H. On the remarkable behaviour of zeolite Beta in acid catalysis. *Catal. Today* **1997**, *38*, 205–212. [[CrossRef](#)]
19. Higgins, J.B.; LaPierre, R.B.; Schlenker, J.L.; Rohrman, A.C.; Wood, J.D.; Kerr, G.T.; Rohrbaugh, W.J. The framework topology of zeolite beta. *Zeolites* **1988**, *8*, 446–452. [[CrossRef](#)]
20. Newsam, J.M.; Treacy, M.M.J.; Koetsier, W.T.; De Gruyter, C.B. Structural characterization of zeolite beta. *Proc. R. Soc. Lond. Ser. A* **1988**, *420*, 375–405. [[CrossRef](#)]
21. Trombetta, M.; Busca, G.; Storaro, L.; Lenarda, M.; Casagrande, M.; Zambon, A. Surface acidity modifications induced by thermal treatments and acid leaching on microcrystalline H-BEA zeolite. A FTIR, XRD and MAS-NMR study. *Phys. Chem. Chem. Phys.* **2000**, *2*, 3529–3537. [[CrossRef](#)]
22. Beyer, H.K.; Nagy, J.B.; Karge, H.G.; Kiricsi, I. *Catalysis by Microporous Materials*; Elsevier: Amsterdam, The Netherlands, 1995.
23. Otomo, R.; Yokoi, T.; Kondo, J.N.; Tatsumi, T. Dealuminated Beta zeolite as effective bifunctional catalyst for direct transformation of glucose to 5-hydroxymethylfurfural. *Appl. Catal. A Gen.* **2014**, *470*, 318–326. [[CrossRef](#)]
24. Čejka, J.; van Bekkum, H.; Corma, A.; Schüth, F. *Introduction to Zeolite Science and Practice*, 3rd revised ed.; Elsevier: Amsterdam, The Netherlands, 2007.
25. Al-Khattaf, S.; Ali, S.A.; Aitani, A.M.; Žilková, N.; Kubička, D.; Čejka, J. Recent advances in reactions of alkylbenzenes over novel zeolites: The effects of zeolite structure and morphology. *Catal. Rev.* **2014**, *56*, 333–402. [[CrossRef](#)]
26. Dědeček, J.; Sobalík, Z.; Wichterlová, B. Siting and distribution of framework aluminium atoms in silicon-rich zeolites and impact on catalysis. *Catal. Rev.* **2012**, *54*, 135–223. [[CrossRef](#)]
27. Krishna, R.; van Baten, J.M. Hydrogen bonding effects in adsorption of water–alcohol mixtures in zeolites and the consequences for the characteristics of the Maxwell–Stefan diffusivities. *Langmuir* **2010**, *26*, 10854–10867. [[CrossRef](#)] [[PubMed](#)]
28. Wang, Z.; Wu, Z.; Tan, T. Sorption equilibrium, mechanism and thermodynamics studies of 1,3-propanediol on beta zeolite from an aqueous solution. *Bioresour. Technol.* **2013**, *145*, 37–42. [[CrossRef](#)] [[PubMed](#)]
29. Magriotis, Z.M.; Leal, P.V.B.; de Sales, P.F.; Papini, R.M.; Viana, P.R.M.; Augusto Arroyo, P. A comparative study for the removal of mining wastewater by kaolinite, activated carbon and beta zeolite. *Appl. Clay Sci.* **2014**, *91*, 55–62. [[CrossRef](#)]
30. Langmuir, I. The adsorption of gases on plane surfaces of glass, mica and platinum. *J. Am. Chem. Soc.* **1918**, *40*, 1361–1403. [[CrossRef](#)]
31. Dehkordi, A.M.; Khademi, M. Adsorption of xylene isomers on Na-BETA zeolite: Equilibrium in batch adsorber. *Microporous Mesoporous Mater.* **2013**, *172*, 136–140. [[CrossRef](#)]
32. Foo, K.Y.; Hameed, B.H. Insights into the modeling of adsorption isotherm systems. *Chem. Eng. J.* **2010**, *156*, 2–10. [[CrossRef](#)]
33. Freundlich, H.M.F. Over the adsorption in solution. *J. Phys. Chem.* **1906**, *57*, 385–471.
34. Tóth, J. State equations of the solid gas interface layer. *Acta Chem. Acad. Sci. Hung.* **1971**, *69*, 311–317.
35. Cambor, M.A.; Pérez-Pariente, J. Crystallization of zeolite beta: Effect of Na and K ions. *Zeolites* **1991**, *11*, 202–210. [[CrossRef](#)]
36. Kunkeler, P.J.; Zuurdeeg, B.J.; van der Waal, J.C.; van Bokhoven, J.A.; Koningsberger, D.C.; van Bekkum, H. Zeolite Beta: The relationship between calcination procedure, aluminum configuration, and lewis acidity. *J. Catal.* **1998**, *180*, 234–244. [[CrossRef](#)]

37. Lohse, U.; Altrichter, B.; Fricke, R.; Pilz, W.; Schreier, E.; Garkisch, C.; Jancke, K. Synthesis of zeolite beta Part 2—Formation of zeolite beta and titanium-beta via an intermediate layer structure. *J. Chem. Soc. Faraday Trans.* **1997**, *93*, 505–512. [[CrossRef](#)]
38. Kiricsi, I.; Flego, C.; Pazzuconi, G.; Parker, W.O.; Millini, R.; Perego, C.; Bellussi, G. Progress toward understanding zeolite  $\beta$  acidity: An IR and  $^{27}\text{Al}$  NMR spectroscopic study. *J. Phys. Chem.* **1994**, *98*, 4627–4634. [[CrossRef](#)]
39. Maretto, M.; Vignola, R.; Williams, C.D.; Bagatin, R.; Latini, A.; Petrangeli Papini, M. Adsorption of hydrocarbons from industrial wastewater onto a silica mesoporous material: Structural and thermal study. *Microporous Mesoporous Mater.* **2015**, *203*, 139–150. [[CrossRef](#)]
40. Burke, N.R.; Trimm, D.L.; Howe, R.F. The effect of silica:alumina ratio and hydrothermal ageing on the adsorption characteristics of BEA zeolites for cold start emission control. *Appl. Catal. B Environ.* **2003**, *46*, 97–104. [[CrossRef](#)]
41. Krohn, J.E.; Tsapatsis, M. Amino acid adsorption on zeolite  $\beta$ . *Langmuir* **2005**, *21*, 8743–8750. [[CrossRef](#)] [[PubMed](#)]
42. Sánchez-Gil, V.; Noya, E.G.; Sanz, A.; Khatib, S.J.; Guil, J.M.; Lomba, E.; Marguta, R.; Valencia, S. Experimental and simulation studies of the stepped adsorption of toluene on pure-silica MEL zeolite. *J. Phys. Chem. C* **2016**, *120*, 8640–8652. [[CrossRef](#)]
43. Dong, J.; Tian, T.; Ren, L.; Zhang, Y.; Xu, J.; Cheng, X. CuO nanoparticles incorporated in hierarchical MFI zeolite as highly active electrocatalyst for non-enzymatic glucose sensing. *Colloid Surf. B* **2015**, *125*, 206–212. [[CrossRef](#)] [[PubMed](#)]



© 2017 by the authors; licensee MDPI, Basel, Switzerland. This article is an open access article distributed under the terms and conditions of the Creative Commons Attribution (CC BY) license (<http://creativecommons.org/licenses/by/4.0/>).

Article

# Insights into Adsorption of Chlorobenzene in High Silica MFI and FAU Zeolites Gained from Chromatographic and Diffractometric Techniques

Luisa Pasti <sup>1,\*</sup>, Elisa Rodeghero <sup>2</sup>, Giada Beltrami <sup>2</sup>, Matteo Ardit <sup>2</sup>, Elena Sarti <sup>1</sup>, Tatiana Chenet <sup>1</sup>, Claudia Stevanin <sup>1</sup> and Annalisa Martucci <sup>2,\*</sup> 

<sup>1</sup> Department of Chemistry and Pharmaceutical Sciences, University of Ferrara, Via L. Borsari 46, 44121 Ferrara, Italy; elena.sarti@unife.it (E.S.); tatiana.chenet@unife.it (T.C.); claudia.stevanin@unife.it (C.S.)

<sup>2</sup> Department of Physics and Earth Sciences, University of Ferrara, Via Saragat 1, 44122 Ferrara, Italy; elisa.rodeghero@unife.it (E.R.); giada.beltrami@unife.it (G.B.); rdtmtt@unife.it (M.A.)

\* Correspondence: psu@unife.it (L.P.); mrs@unife.it (A.M.); Tel.: +39-0532-455346 (L.P.); +39-0532-974730 (A.M.)

Received: 9 January 2018; Accepted: 19 February 2018; Published: 26 February 2018

**Abstract:** In this work, the capability of two commercial high silica zeolites (HSZs), namely ZSM-5 and Y, for the removal of chlorobenzene (CB) from water was investigated by combining chromatographic and diffractometric techniques. The adsorption isotherms and kinetics of CB on ZSM-5 and Y zeolites were determined from batch tests. The adsorption kinetics were very fast; the time to reach equilibrium was less than 10 min. The equilibrium data of CB on the two HSZs showed dissimilarities that are particularly evident in the adsorption data concerning the low concentration range, where Y zeolite is characterized by low adsorption. On the contrary, at higher solution concentrations the adsorption capacity of Y is higher than that of ZSM-5. The crystalline structures of Y and ZSM-5 saturated with CB were investigated by X-ray diffraction (XRD) techniques. Rietveld refinement analyses of XRD data allowed for quantitative probing of the structural modifications of both zeolites after CB adsorption and provided insight into the preferred zeolite adsorption sites in both microporous materials. The refined framework–extraframework bond distances confirm that interactions between the selected organic contaminant and hydrophobic zeolites are mediated via co-adsorbed H<sub>2</sub>O. The occurrence of H<sub>2</sub>O–CB–framework oxygen oligomers explains variations in both the unit cell parameters and the shape of the channels, clearly confirming that water plays a very relevant role in controlling the diffusion and adsorption processes in hydrophobic zeolites.

**Keywords:** chlorobenzene; sorption; ZSM-5; X-ray powder diffraction; Rietveld structure refinement; chromatography

## 1. Introduction

Industrial and agricultural discharges, chlorine disinfection by-products (DBPs) of drinking water and wastewater, and incineration of wastes are the main sources of chlorine and organochlorine compounds (OCICs), such as chlorobenzene (CB). These compounds can cause toxic effects on both human health and environmental systems, even at low concentration [1]. In particular, the Environmental Protection Agency (EPA) fixed the maximum contaminant level (MCL) of CB at 0.1 mg/L; above this threshold value CB can cause negative health effects, such as gastrointestinal irritations, hepatotoxicity and kidney damages [2]. Therefore, it is important to remove this pollutant from the environment and different methodologies have been proposed.

Actually, the physical method based on adsorption processes is a recuperative method exploited for in situ water treatments which combines high flexibility of the system, efficiency even at low

concentration levels, low energy, cheap operating costs, and possible waste reductions [3]. Different adsorbent materials can be employed, and their efficiency depends on the host-guest interactions between sorbent and sorbate [4–13]. In general, carbonaceous adsorbents are low cost materials, widely employed in remediation technology. However, their applicability can be limited by fouling that cause a pore blocking (i.e., to the presence of dissolved organic matter), to low adsorption capacity, sharp rise of bed temperature and difficulty of regeneration [14–17]. In recent years, organic contaminants removal by single-walled carbon nanotubes (SWCNTs) has attracted great interest due to their chemical, electronic and mechanical properties [18]. However, the saturation capacity of these adsorbents for OCICs is moderate and functional groups on the surface of carbonaceous adsorbents can further reduce the adsorption features [19–21]. In the past few decades, surfactant modified clays have been proposed as a potential alternative to carbonaceous adsorbents for removing OCIC pollutants. Indeed, it has been proved that these materials are efficient and they can be easily regenerated. One of the main disadvantages is their limited stability due to a progressive release of surfactant which can have a negative impact on biota [22–25]. Synthetic and hydrophobic zeolites offer an attractive and efficient option for the removal of chlorine, and organochlorine compounds from water. The main advantages are related to their high surface area and porous structure, high specific capacity and organic pollutants selectivity. Additionally, fast kinetics, mechanical, biological and chemical stability make them promising and efficient adsorbents [4,6–8,26–28]. Furthermore, their high thermal stability guarantees the possibility of regeneration through thermal treatments in order to reintroduce them in new adsorption processes [5,29–33].

This work is part of a wider study aimed at systematically evaluating the adsorptive capacity of high silica zeolites (HSZ) (e.g., mordenite, ZSM-5, faujasite, beta, ferrierite [4,7,10,29,30]) for fuel-based compounds differing in chemical properties (e.g., polarity, functional groups, size, host-guest interactions, etc.), which can provide useful information to accurately predict the behavior of HSZs as well as improve their individual performance.

The objective of this study is to evaluate the capability of two commercial HSZs, ZSM-5 (MFI topology), and Y zeolite (FAU topology) [34], for removal of chlorobenzene (CB) from water. For that purpose, the adsorption process from water was investigated in order to gain information on the interactions between the selected organic contaminant and hydrophobic zeolites. The information gathered from this work provides a tool for the selection of adsorbent materials for environmental remediation. Additionally, the investigation of host-guest interactions can provide information on the fate and transport of OCICs in the environment, and in particular for the partition of those contaminants in the mineral fraction of soils, normally constituted by aluminosilicate.

## 2. Experimental Methods

### 2.1. Materials and Methods

High-silica Y (code HSZ-390HUA, 200 SiO<sub>2</sub>/Al<sub>2</sub>O<sub>3</sub> molar ratio, 750 m<sup>2</sup>/g surface area, 0.05 wt % Na<sub>2</sub>O content) and ZSM-5 (code CBV 28014, 280 SiO<sub>2</sub>/Al<sub>2</sub>O<sub>3</sub> molar ratio, 400 m<sup>2</sup>/g surface area, 0.01 wt % Na<sub>2</sub>O content) hydrophobic zeolites were purchased in their as-synthesized form by Tosoh Corporation (Tokyo, Japan) and Zeolyst International (Conshohocken, PA, USA) respectively.

Chlorobenzene (CB) in its anhydrous form (purity of 99.8%) was provided by Sigma-Aldrich (Steinheim, Germany) and used as received.

### 2.2. Batch Adsorption

The adsorption isotherm was determined using the batch method. Batch experiments were carried out in duplicate in 20 mL crimp top reaction glass flasks sealed with PTFE septa (Supelco, Bellefonte, PA, USA). The flasks were filled in order to have the minimum headspace and a solid:solution ratio of 1:2 (mg·mL<sup>-1</sup>) was employed. After equilibration, for 24 h at a temperature of 25.3 ± 0.5 °C under

stirring, the solids were separated from the aqueous solution using centrifugation (14,000 rpm for 30 min).

The concentration of contaminants in the aqueous solution, before and after the contact with the adsorbent was determined by Headspace Gas Chromatography coupled to Mass Spectrometry (HS-GC-MS). The analysis was carried out using an Agilent GC-MS system (Santa Clara, CA, USA) consisting of a GC 6850 Series II Network coupled to a Pal G6500-CTC injector and a Mass Selective Detector 5973 Network.

HS autosampler injector conditions are: incubation oven temperature 80 °C, incubation time 50 min, headspace syringe temperature 85 °C, agitation speed 250 rpm, agitation on time 30 s, agitation off time 5 s, injection volume 500 µL, fill speed 30 µL·s<sup>-1</sup>, syringe pull-up delay 5 s, injection speed 250 µL·s<sup>-1</sup>, pre-injection delay 0 s, post injection delay 2 s, syringe flush 30 s with nitrogen. A DB-624 UI GC column (L = 20 m, I.D. = 0.18 mm, df = 1.00 µm film thickness, Agilent, Santa Clara, CA, USA) was used. High purity helium was the carrier gas with a constant flow rate of 0.7 mL·min<sup>-1</sup>. The oven temperature gradient started at 40 °C for 4 min and then ramped to 130 °C at 15 °C·min<sup>-1</sup>. The injector temperature was kept at 150 °C. All samples were injected in split mode (10:1). The mass spectrometer operated in electron impact mode (positive ion, 70 eV). The source temperature and the quadrupole temperature were set to 230 °C and 150 °C, respectively. The mass spectra were acquired in full scan mode. The electronic scan speed was 1562 amu·s<sup>-1</sup> in a mass range from 30 to 300 amu. For identification and quantification of the target analyte the SIM (selected ion monitoring) chromatograms were extracted from the acquired signal by selecting the most abundant characteristic fragments at  $m/z = 112$ . Chromatographic peak of analytes was identified by comparison of the retention time and the mass spectrum with standard compound and library data; quantitative analysis was performed using calibration curves.

### 2.3. Thermal Analyses

The Netzsch STA 409 PC LUXX<sup>®</sup> (Gerätebau, Germany) simultaneous TG/DTA thermogravimetric balance was employed in order to carry out both thermogravimetric (TG) and differential thermal analyses (DTA) on Y and ZSM-5 zeolites before and after CB loading. The measurements were performed in constant air flux conditions using a heating rate of 10 °C/min, from room temperature (RT) to 900 °C.

### 2.4. X-ray Powder Diffraction Data Collection and Refinement Strategy

X-ray diffraction patterns on powders of Y and ZSM-5 zeolites loaded with CB were carried out on a Bruker D8 Advance (Karlsruhe, Germany) diffractometer (Cu K $\alpha_{1,2}$  radiation) equipped with a Sol-X detector. Diffraction data were collected at RT, in 3°–110° 2 $\theta$  (for ZSM-5) and 3°–100° 2 $\theta$  (for Y zeolite) 2 $\theta$  ranges respectively, with a counting time of 12 s each 0.02° 2 $\theta$ . Figure S1 reported observed, calculated and difference X-ray powder diffraction patterns of Y–CB (a) and ZSM-5–CB (b), respectively.

GSAS software [35] and the EXPGUI graphical interface [36] were employed for Y–CB and ZSM-5–CB structural refinements through a full profile Rietveld analysis. Unit-cell and structural parameters were determined starting from the monoclinic  $P2_1/n$  (for ZSM-5) and the cubic  $Fd-3$  (for Y) space groups of Martucci et al. [10], and Braschi et al. [11] structural models, respectively. The Bragg peak profiles were modelled by a Pseudo-Voigt function with 0.001% cut-off peak intensity. Refined coefficients were: two Gaussian terms (i.e., the  $\tan^2\theta$  dependent GU and the  $\theta$  independent GW), and two Lorentzian terms (i.e.,  $\cos\theta^{-1}$  dependent LX,  $\tan\theta$  dependent LY), respectively. A Chebyshev polynomial function with 24 and 22 coefficients was used in order to empirically fit the instrumental background for Y and ZSM-5, respectively. In both structural refinements, scale factor, 2 $\theta$ -zero shift and unit-cell parameters were also refined. Soft constraints were initially imposed on Si–O, O–O, C–C and C–Cl bond distances (tolerance ( $\sigma$ ) value of 0.04 Å) and completely removed in the final cycles. Finally, atomic coordinates, site occupancy and isotropic atomic displacement parameters were

refined. Furthermore, the displacement parameters for a given atom type were constrained to be equivalent (i.e., Si and O sites), thus limiting the number of refined atomic displacement parameters to two. Additionally, in Y-CB  $x/a$  and  $y/b$  parameters of the chlorobenzene molecule were constrained to be equal in order to maintain the planarity. Table 1 reports the details of the data collection and Rietveld refinements. In Supplementary Materials (Tables S1 and S2, respectively) the refined atomic coordinates, occupancies and isotropic thermal parameters of Y and ZSM-5 loaded structures are reported. Extraframework atomic fractional coordinates, thermal isotropic displacement factor and occupancy of Y-CB and ZSM-5-CB are in Tables S3 and S4, respectively. Selected bond distances (Å) and angles (°) within both the Y-CB and ZSM-5-CB framework and extraframework atoms are listed in Tables S5 and S6, respectively. CIFs for all reported crystal structures are added in Supplementary Materials as supplementary information.

**Table 1.** Details of the data collection and Rietveld refinements.

Parameter	ZSM-5	ZSM-5-CB	Y	Y-CB
	[Si <sub>96</sub> O <sub>192</sub> ]	[Si <sub>96</sub> O <sub>192</sub> ]·6(C <sub>6</sub> H <sub>5</sub> Cl)·8(H <sub>2</sub> O)	[Si <sub>192</sub> O <sub>384</sub> ]	[Si <sub>192</sub> O <sub>384</sub> ]·32(C <sub>6</sub> H <sub>5</sub> Cl)·70(H <sub>2</sub> O)
Space group	<i>P</i> 2 <sub>1</sub> / <i>n</i>	<i>P</i> 2 <sub>1</sub> / <i>n</i>	<i>Fd</i> -3 <i>m</i>	<i>Fd</i> -3
<i>a</i> (Å)	19.899(5)	19.919(1)	24.259(1)	24.263(1)
<i>b</i> (Å)	20.117(6)	20.107(1)	24.259(1)	24.263(1)
<i>c</i> (Å)	13.389(4)	13.3967(1)	24.259(1)	24.263(1)
$\alpha$ (°)	90	90	90	90
$\beta$ (°)	90.546(3)	90.528(3)	90	90
$\gamma$ (°)	90	90	90	90
<i>V</i> (Å <sup>3</sup> )	5359.9(3)	5365.7(5)	14,277.1(1)	14,284.4(6)
Wavelength (Å): Cu K $\alpha$ <sub>1</sub>	1.540593	1.540593	1.540593	1.540593
Cu K $\alpha$ <sub>2</sub>	1.544427	1.544427	1.544427	1.544427
Refined 2 $\theta$ (°) range	3°–110°	3°–110°	3°–100°	3°–100°
Contributing reflections	5861	6362	620	620
<i>N</i> <sub>obs</sub>	5350	5350	4850	4850
<i>N</i> <sub>var</sub>	289	301	40	40
<i>R</i> <sub>wp</sub> (%)	10.3	13.3	12.8	12.9
<i>R</i> <sub>p</sub> (%)	9.4	10.4	12.5	12.6
<i>R</i> <sub>F</sub> <sup>2</sup> (%)	7.00	7.25	9.95	10.0

$R_p = \sum |Y_{io} - Y_{ic}| / \sum Y_{io}$ ;  $R_{wp} = [\sum w_i (Y_{io} - Y_{ic})^2 / \sum w_i Y_{io}^2]^{0.5}$ ;  $R_F^2 = \sum |F_o^2 - F_c^2| / |F_o^2|$

### 3. Results and Discussion

#### 3.1. Adsorption Isotherms from Aqueous Solutions

The uptake  $q$  (mg·g<sup>−1</sup>) was calculated as follows:

$$q = \frac{(C_0 - C)V}{m} \quad (1)$$

where  $C_0$  is the initial concentrations in solution (mg·L<sup>−1</sup>),  $C$  is the concentration at time  $t$  in kinetics experiments (mg·L<sup>−1</sup>),  $V$  is the solution volume (L) and  $m$  is the mass of sorbent (g). In Figure 1 the uptake data for CB on Y and ZSM-5 are reported.

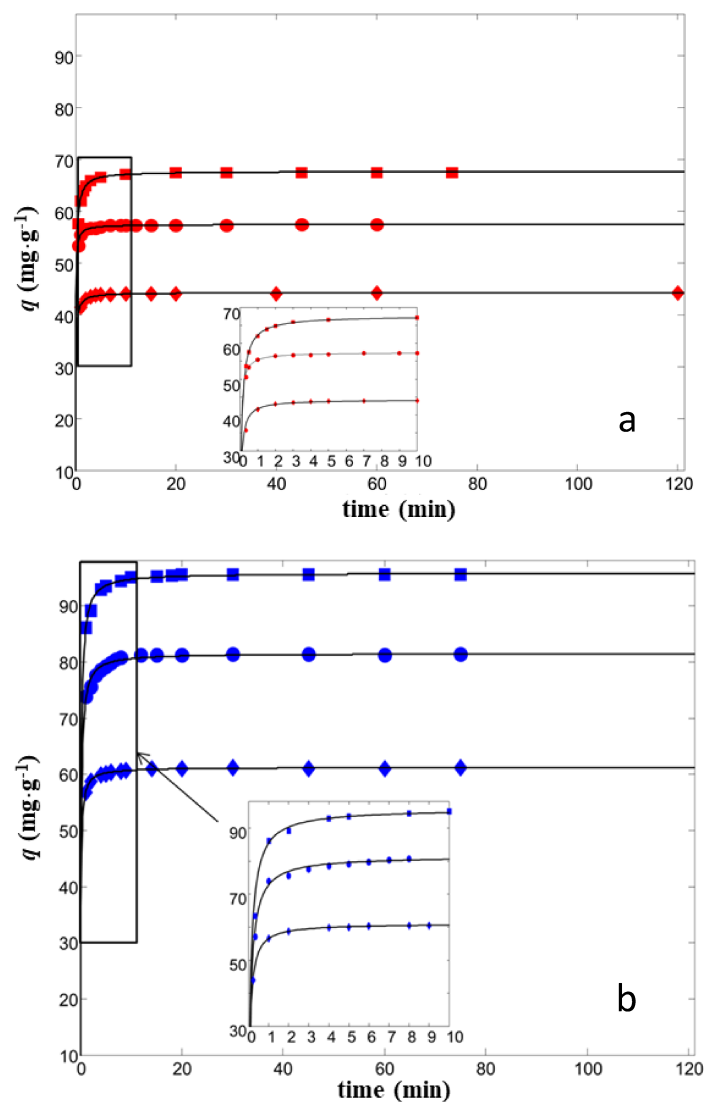


**Figure 1.** Chlorobenzene (CB) uptake vs. contact time for ZSM-5 (a) and Y (b) for initial concentration of 35, 25, 15 mg/L. The insets: enlarged image of the boxed regions.

It can be seen that the kinetics of the adsorption process was very fast; the equilibrium was reached in about 10 min. Similar behaviors were also observed for the adsorption of other aqueous contaminants, such as dichloroethane and toluene onto ZSM-5 and Y zeolites [5–10,13].

We have previously verified [5–10,13] that uptake data of the investigated zeolites can be fitted by the pseudo-second order model as:

$$q_t = \frac{k_2 q_e^2 t}{1 + k_2 q_e t} \quad (2)$$

where  $q_t$  and  $q_e$  are the amounts of solute adsorbed per mass of sorbent at time  $t$  and at equilibrium, respectively, and  $k_2$  is the second-order adsorption rate constant. The values of equilibrium uptake  $q_e$  and the adsorption rate constant  $k_2$  were obtained from non-linear fit of  $q_t$  vs.  $t$  (see Table 2). Analogous to what was observed for the adsorption of other aqueous contaminants, the uptake data of CB can be modelled by a pseudo-second order kinetic model, as indicated from the high coefficient of determination.

**Table 2.** Estimated kinetics parameters (see Equation (2)). The confidence limits at 95% of probability of the estimated parameters are reported in brackets.

	$C_0$ (mg·L <sup>-1</sup> )	$q_t$ (mg·g <sup>-1</sup> )	$k_2$ (g·L <sup>-1</sup> ·mg <sup>-1</sup> )	$R^2$
ZSM-5	15	23.4 (23.3, 23.5)	0.44 (0.41, 0.47)	0.9845
	25	44.3 (44.2, 44.3)	0.37 (0.33, 0.41)	0.9803
	35	67.6 (67.5, 67.6)	0.21 (0.19, 0.23)	0.9985
Y	25	39.3 (39.2, 39.4)	0.14 (0.11, 0.17)	0.9822
	35	70.3 (70.2, 70.3)	0.13 (0.11, 0.15)	0.9969
	45	82.3 (82.4, 82.5)	0.10 (0.085, 0.12)	0.9935

Furthermore, for the adsorption of CB it can be noted that the kinetic constant decreases by increasing the initial concentration [37], and that the adsorption onto Y zeolites is characterized by a lower kinetic constant than that found for ZSM-5. These findings allow us to generalize the difference observed in the adsorption kinetics of these two zeolites. In particular, the adsorption kinetics of neutral organic molecules (namely, toluene, dichloroethane, methyl tert-butylether and CB), which differ from each other in physicochemical properties and molecular dimensions, is faster on ZSM-5 than on Y zeolite.

It has been already shown that adsorption of organics in aqueous solutions onto ZSM-5 hydrophobic zeolites are well fitted by the Langmuir equation [5,6,8,13], that assumes monolayer adsorption onto energetically equivalent adsorption sites and negligible sorbate–sorbate interactions. The relationships describing the Langmuir isotherm is [38]:

$$q = \frac{q_s b C_e}{1 + b C_e} \quad (3)$$

where  $b$  is the binding constant (L·mg<sup>-1</sup>) and  $q_s$  is the saturation capacity of the adsorbent material (mg·g<sup>-1</sup>). The experimental data obtained for the adsorption of CB on both ZSM-5 and Y are shown in Figure 2. It can be observed that the isotherms are shaped differently from each other; they can be classified as concave (Type I) and sigmoidal (Type V) isotherms, respectively.

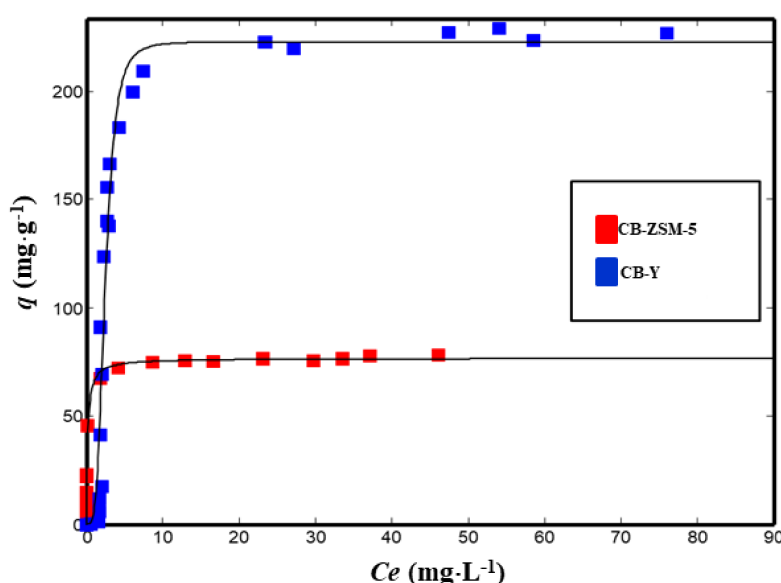


**Figure 2.** Adsorption isotherms of CB for ZSM-5 (red squares) and Y (blue squares).

Similar differences in the adsorption of polar organic compound from aqueous solution onto ZSM-5 and Y were also observed for methyl tert-butylether and toluene. In such cases, a Hill isotherm model was employed:

$$q_e = q_s \frac{c_e^n}{K_H + c_e^n} \quad (4)$$

where  $K_H$  is the Hill constant, and  $n$  is the Hill coefficient which is related to the degree of cooperativity. The Hill isotherm is often employed to describe cooperative adsorption in biological systems, and it has also been used to model adsorption data on zeolites due to evidence of the presence of water-organic compound clusters [39] inside the zeolite frameworks. Since the tendency to form clusters increases by increasing the porosity dimensions, the clusters are more probably formed in the large cage of Y than in the channel system of ZSM-5 [40]. To evaluate if clusters can be formed for CB, a structural investigation was carried out (vide infra).

In Table 3, the isotherm parameters for ZSM-5 and Y estimated by non linear fitting of Equations (3) and (4) respectively, are reported. It can be seen that the saturation capacity of these zeolites are higher than those obtained with graphite materials (i.e., 28.3 mg/g for dichlorobenzene) [41], and in particular Y zeolite has a saturation value higher than adsorbents single-walled carbon nanotubes, especially if they are partially oxidized [42]. In addition HSZs can be regenerated without significant loss of their adsorption properties [5,6,29,30]. Therefore hydrophobic zeolites are very promising adsorbents for the removal of chlorinated aromatic compounds from water.

**Table 3.** Isotherm parameters for the adsorption of CB on ZSM-5 and Y. SSE: sum of squared errors.

			$R^2$	SSE
Langmuir				
CB-ZSM-5	$q_s$	76.6 (74.8, 79.5)	0.9874	198
	$b$	5.0 (3.7, 6.6)		
Hill				
CB-Y	$q_s$	227 (218, 245)	0.9654	2135
	$K_H$	9.2 (6.6, 12.1)		
	$n$	5.5 (4.3, 6.7)		

### 3.2. Structural Modifications upon Chlorobenzene Adsorption on High Silica Zeolites

#### 3.2.1. Y-CB

Y zeolite (FAU framework topology [34]) is built up of large cavities ( $\alpha$  cages or supercages) with a diameter of 12 Å linked to four other supercages through 12 membered-ring windows (diameter of 7.4 Å) and cuboctahedral  $\beta$  cages connected each other through double hexagonal rings (D6R). Topological symmetry of the unloaded material is cubic  $Fd-3m$ , but it has been highlighted that the embedding of organic compounds can decrease the symmetry to  $Fd-3$  [10–13,43]. A careful examination of powder diffraction patterns after chlorobenzene adsorption highlights that Y-CB peak positions are quite similar to those of the as-synthesized material in all the  $2\theta$  range investigated. Contrariwise, peak intensities strongly decrease after pollutant incorporation, especially at low  $2\theta$  angles (Figure 3).

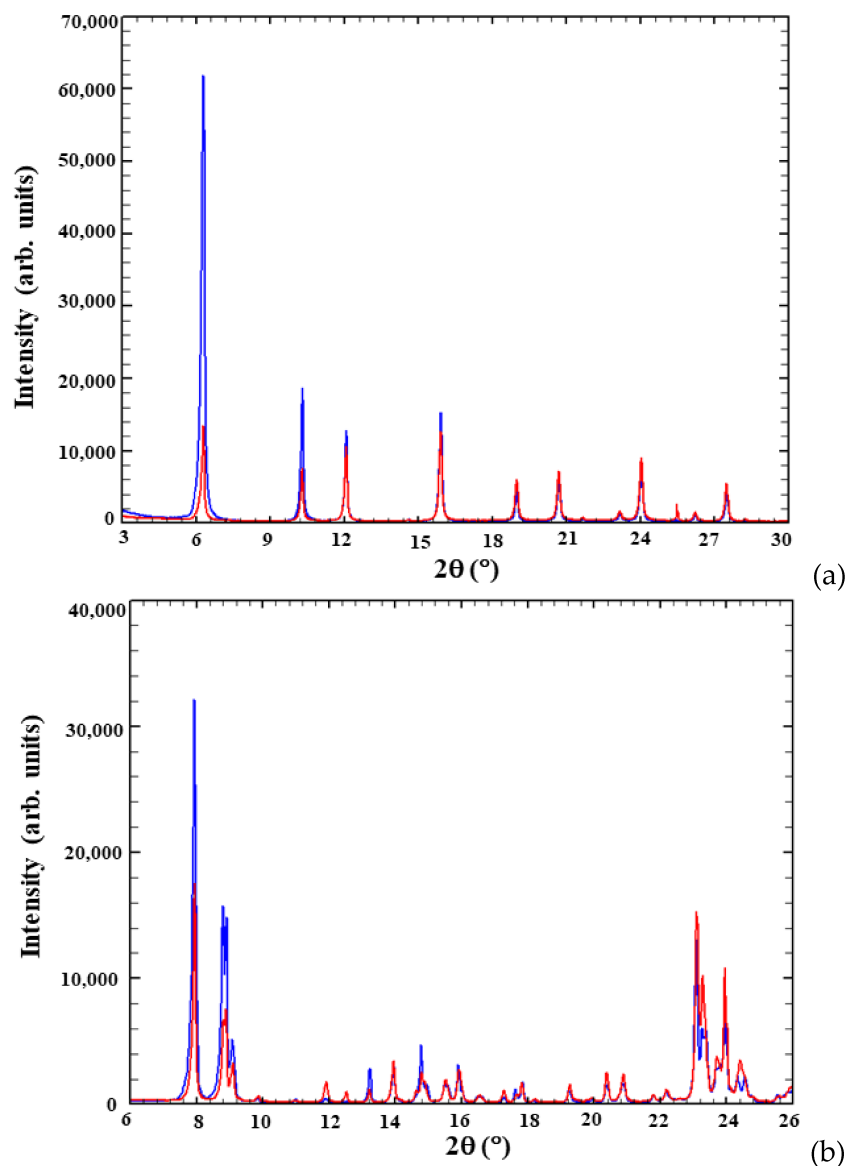


**Figure 3.** Observed powder diffraction patterns of Y-CB (a) and ZSM-5-CB (b), respectively, showing differences both in intensity and position of the diffraction peaks in the low and intermediate  $2\theta$  regions. Blue lines represent the unloaded samples, red lines the loaded ones.

These differences suggest variations in the extraframework species content as well as in the lattice parameters (Table 1), thus attesting to CB adsorption into the porous structure of the zeolite. After adsorption, the T1–O and T2–O mean distances are 1.621 and 1.620 Å, respectively, the O–T–O angles range from 103.3° to 112.3° (Table S5). The T–O–T bond angles adopt a wide range of values from 125° to 171° (mean value = 142°). The T–O, T–O–T and O–T–O grand mean values (Table S5) are in high agreement with those reported for other pure silica zeolites (PSZ) [44]. Furthermore, after adsorption the channel ellipticity  $\varepsilon$  (defined as the ratio between the smaller and larger O–O “free diameters” of the 12-rings) changed ( $\varepsilon = 1.02$  in Y,  $\varepsilon = 1.21$  in Y-CB) and at the same time, the openings reached a wider Crystallographic Free Area (C.F.A., sensu Baerlocher [34]) when compared with the as-synthesised material (Table 4), thus confirming the high flexibility of FAU-type materials [45,46].

**Table 4.** Crystallographic Free Area and ellipticity ( $\epsilon$ ) comparison between unloaded Y [11] and Y-CB systems. C.F.A. =  $\pi \cdot (\text{mean radius})^2$  ( $\text{\AA}^2$ );  $\epsilon$  = ratio between the longest and the shortest pore dimensions.

Parameter	Y-CB	Y [11]
O4–O4 distance ( $\text{\AA}$ )	11.16	9.81
O1–O1 distance ( $\text{\AA}$ )	9.68	9.70
Free diameter O4–O4 ( $\text{\AA}$ )	8.46	7.11
Free diameter O1–O1 ( $\text{\AA}$ )	6.98	7.00
Mean diameter ( $\text{\AA}$ )	7.72	7.06
Mean radius ( $\text{\AA}$ )	3.86	3.53
C.F.A. ( $\text{\AA}^2$ )	46.81	39.07
$\epsilon$	1.21	1.01

Rietveld structural refinement allows us to detect 32 CB molecules per unit cell (corresponding to ~22.0% dry weight, dw %) located within the Y supercage (Figure 4a). Chlorobenzene molecules occupy one crystallographic independent and partially occupied site (C and Cl atoms in Table S3), and statistically can assume six different orientations (Figure 4a).

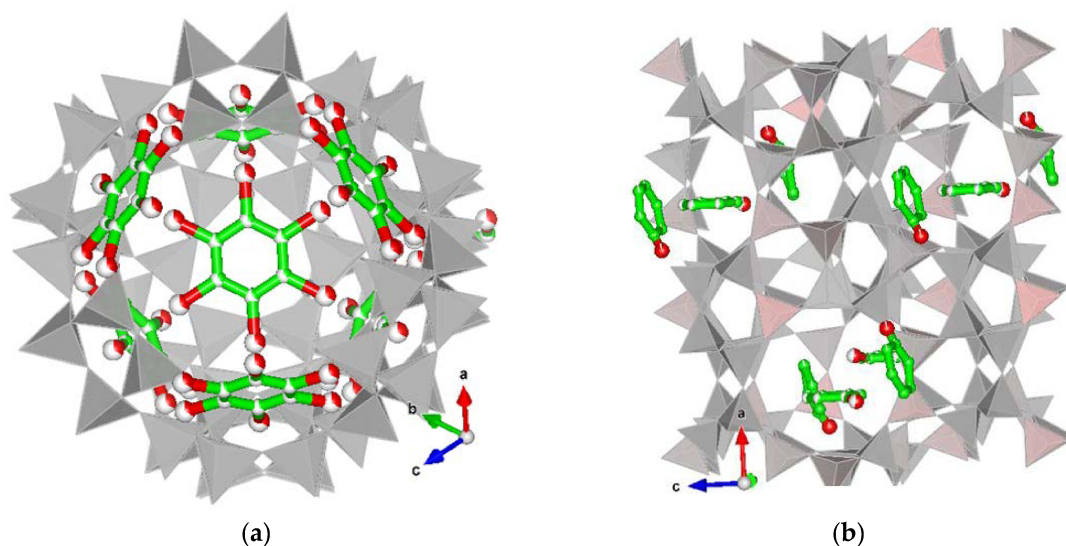


**Figure 4.** Distribution of CB molecules in Y (a) and ZSM-5 (b) zeolites, respectively. Chlorine (red circle) and carbon (green circle) are shown. Drawings produced by VESTA 3 [47].

Moreover, the evidence of relatively short Cl–O1 bond distances (i.e., Cl–O1 = 2.723(1)  $\text{\AA}$  and 2.680  $\text{\AA}$ , respectively) proves that chlorobenzene directly interacts with framework oxygens.

Furthermore, difference-Fourier maps of the electron density analysis revealed the presence of co-adsorbed  $\text{H}_2\text{O}$  molecules hosted in three additional extraframework sites (W1, W2 and W3 sites, respectively, Table S3). Additionally, based on the W sites refined distance these sites interact with both each other and chlorine atoms forming oligomers (W2–W2 = 2.93  $\text{\AA}$ , W3–Cl = 3.21  $\text{\AA}$  and W1–W2 = 2.93 and 2.74  $\text{\AA}$ , respectively) that strongly interact with the framework oxygen atoms via chlorine (Figure 4a). According to the recent literature [5–8,10–13,29,44], the strong interactions among organic molecules– $\text{H}_2\text{O}$  short chain-frameworks play a relevant role in stabilizing the guest structures within the zeolite porosity.

On a whole, on the basis of Rietveld refinement 70  $\text{H}_2\text{O}$  molecules (~8% dw %) were detected in good agreement with the TG curve (Figure 5a), which shows two main weight losses: the first one (about 7.3 dw % zeolite, 25–110  $^\circ\text{C}$ ) is related to desorption of species retained on the surface, the second one (23.5 dw % zeolite, 110–900  $^\circ\text{C}$ ) to the removal from the structure of loaded CB and  $\text{H}_2\text{O}$  molecules.

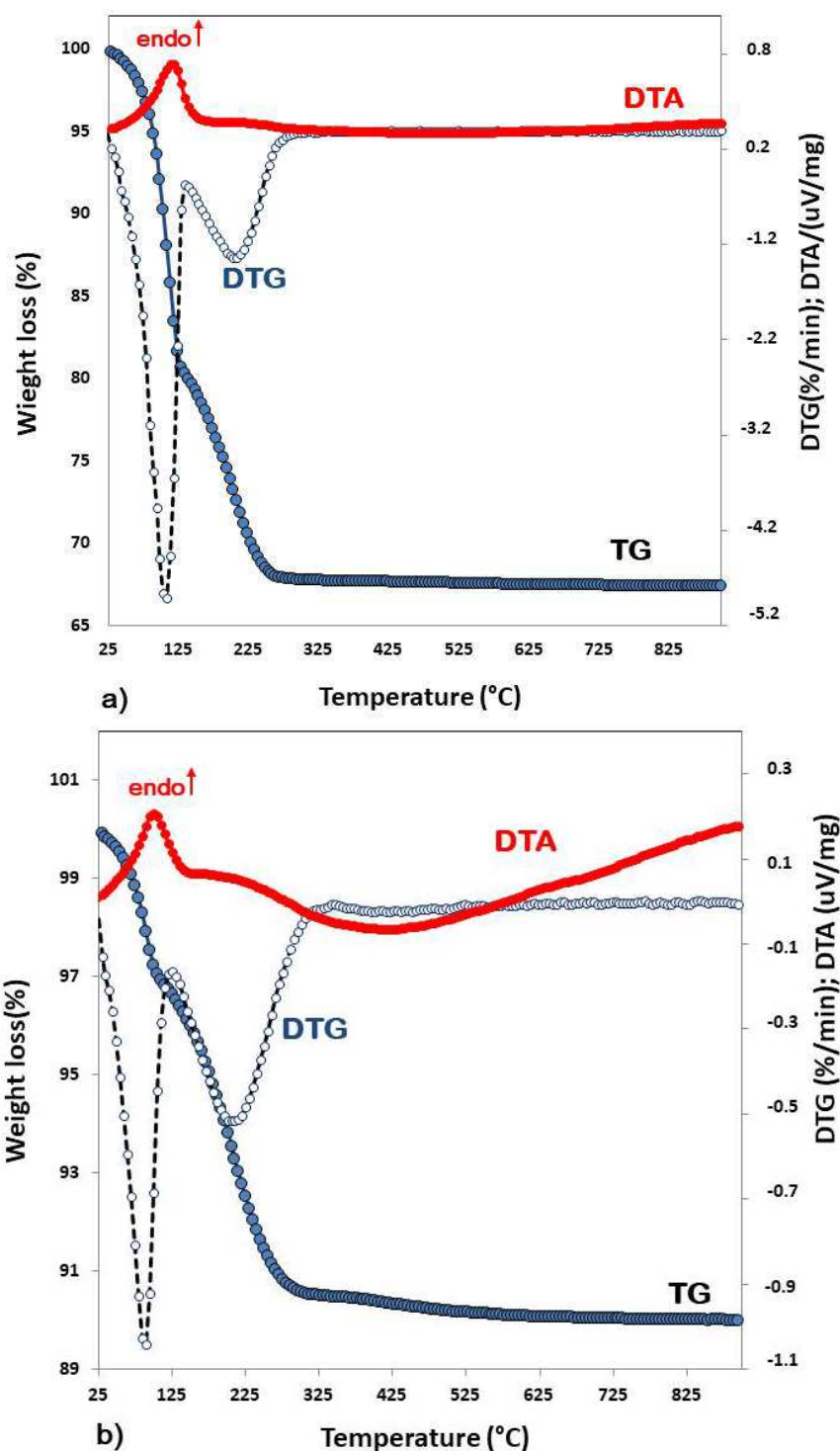


**Figure 5.** Thermal analysis of Y (a) and ZSM-5 (b) loaded with chlorobenzene from room temperature to 900 °C. In blue and gray circles, the total weight loss curve (TG) and the derivative of it (DTG); in red the differential thermal analysis (DTA) curve.

### 3.2.2. ZSM-5-CB

The ZSM-5 zeolite framework consists of two intersecting channel systems: a straight channel parallel to [010] direction and a sinusoidal one parallel to [100] direction [34]. Both channels are limited by 10MR of  $\text{TO}_4$  tetrahedra with free diameters of 5.4–5.6 Å and 5.1–5.5 Å for sinusoidal and straight channel, respectively. After CB adsorption, the evolution of the powder diffraction pattern

indicates that ZSM-5 maintains its crystallinity as well as the monoclinic  $P2_1/n$  symmetry. In Table 1, the comparison between refined lattice parameters of starting material and of the ZSM-5–CB system highlights the occurrence of chlorobenzene adsorption in the ZSM-5 micropores. The structural characterization was carried out starting with the model proposed by Rodeghero et al. [6] and an examination of the difference Fourier maps of the electron density suggested the presence of extraframework content. In detail, some of recognized maxima were reasonably attributed to chlorobenzene adsorption sites in both the sinusoidal channel (CB2 sites) and the intersection between sinusoidal and straight channels (CB1 sites) (Table S4, Figure 4b). On the whole, a total amount of about 6 molecules per unit cell (p.u.c.) of organics were detected. Besides, residual maxima of difference Fourier maps also indicate the presence of co-adsorbed H<sub>2</sub>O molecules (~1.5 dw %) hosted at W1 and W2 sites. In particular, based on the refined distances between the extraframework content and framework oxygen atoms strong interactions among chlorobenzene molecules hosted in both adsorption sites (CB1 and CB2), H<sub>2</sub>O molecules (W1 and W2 sites), and framework oxygen atoms occur (i.e., O4–C10 = 3.01(1) Å, O18–C9 = 2.61(1) Å, O31–C11 = 2.69(1) Å, O47–C11 = 2.99(1) Å, W2–W2 = 3.15(1) Å, O26–C12 = 3.03(3) Å, W1–C1 = 3.16(3) Å) (Figure 4b and Table S6). Additionally, thermogravimetric analysis (Figure 5b) indicated that relevant weight loss, occurring at temperatures higher than 100 °C (7% in weight), is due to the expulsion from the structure of extraframework ions embedded in the ZSM-5 channels. The residual one at lower temperature can be ascribed to the expulsion of water and/or CB molecules bonded to the surface (3% in weight below ~100 °C).

These results are quite well supported by the total amount of adsorbed molecules detected through both saturation capacity determined by the adsorption isotherm and the results obtained by Rietveld analysis. After adsorption, the T–O bond length ranges from 1.602 to 1.608 Å, the O–T–O angles varies from 96° to 125°, with a mean value of 109.4° (Table S6). According to Wragg et al. [44] the T–O–T bond angles adopt a wide range of values from 124° to 178° (Table S6). Regarding the channel geometry, after organics adsorption, any changes in both shape and channel dimension were also evaluated. Specifically, both straight and sinusoidal channels hosting the organic molecules change their shape and become more elliptical (Table 5).

**Table 5.** C.F.A. and ellipticity ( $\epsilon$ ) comparison between unloaded ZSM-5 [13] and ZSM-5–CB systems. C.F.A. =  $\pi \cdot (\text{mean radius})^2$  ( $\text{\AA}^2$ );  $\epsilon$  = ratio between the longest and the shortest pore dimensions.

Straight Channel						
O–O distance ( $\text{\AA}$ )	O7–O1	O8–O2	O31–O37	O44–O46	O47–O48	$\epsilon$
ZSM-5–CB	8.22	8.20	8.02	8.22	7.97	1.03
ZSM-5	7.90	7.94	8.04	8.41	7.80	1.08
Free diameter ( $\text{\AA}$ )	O7–O1	O8–O2	O31–O37	O44–O46	O47–O48	
ZSM-5–CB	5.52	5.50	5.32	5.52	5.27	-
ZSM-5	5.20	5.24	5.34	5.71	5.10	-
	Mean diameter ( $\text{\AA}$ )	Mean radius ( $\text{\AA}$ )	C.F.A. ( $\text{\AA}^2$ )			
ZSM-5–CB	5.43	2.71	23.12			-
ZSM-5	5.32	2.66	22.20			-
O–O distance ( $\text{\AA}$ )	O11–O5	O20–O18	O21–O22	O27–O33	O28–O34	$\epsilon$
ZSM-5–CB	8.08	7.89	8.11	8.22	8.08	1.04
ZSM-5	8.19	8.35	7.98	8.13	7.76	1.08
Free diameter ( $\text{\AA}$ )	O11–O5	O20–O18	O21–O22	O27–O33	O28–O34	
ZSM-5–CB	5.38	5.19	5.41	5.52	5.38	
ZSM-5	5.49	5.65	5.28	5.43	5.06	
	Mean diameter ( $\text{\AA}$ )	Mean radius ( $\text{\AA}$ )	C.F.A. ( $\text{\AA}^2$ )			
ZSM-5–CB	5.37	2.69	22.67			
ZSM-5	5.38	2.69	22.74			
Sinusoidal Channel						
O–O distance ( $\text{\AA}$ )	O20–O15	O24–O26	O27–O2	O28–O1	O41–O46	$\epsilon$
ZSM-5–CB	8.08	7.87	7.76	8.16	8.69	1.12
ZSM-5	8.15	8.07	7.97	7.76	8.51	1.10
Free diameter ( $\text{\AA}$ )	O20–O15	O24–O26	O27–O2	O28–O1	O41–O46	
ZSM-5–CB	5.38	5.17	5.06	5.46	5.99	
ZSM-5	5.45	5.37	5.27	5.06	5.81	
	Mean diameter ( $\text{\AA}$ )	Mean radius ( $\text{\AA}$ )	C.F.A. ( $\text{\AA}^2$ )			
ZSM-5–CB	5.41	2.71	23.01			
ZSM-5	5.39	2.70	22.82			
O–O distance ( $\text{\AA}$ )	O17–O18	O23–O25	O30–O5	O31–O4	O44–O43	$\epsilon$
ZSM-5–CB	7.50	8.58	8.20	7.89	7.75	1.14
ZSM-5	7.30	8.31	8.32	8.05	7.95	1.14
Free diameter ( $\text{\AA}$ )	O17–O18	O23–O25	O30–O5	O31–O4	O44–O43	
ZSM-5–CB	4.80	5.88	5.50	5.19	5.05	
ZSM-5	4.60	5.61	5.62	5.35	5.25	
	Mean diameter ( $\text{\AA}$ )	Mean radius ( $\text{\AA}$ )	C.F.A. ( $\text{\AA}^2$ )			
ZSM-5–CB	5.28	2.64	21.92			
ZSM-5	5.29	2.64	21.93			

#### 4. Conclusions

This work aims to highlight the adsorptive capacity of commercial high silica zeolites ZSM-5 (MFI topology), and Y zeolite (FAU topology), for removal of chlorobenzene (CB) from water. Both high silica ZSM-5 and Y zeolites are characterized by fast kinetics, that combined with good adsorption capacity, suggest they can be efficiently used as a sorbent media to control the concentration of chlorobenzene in water systems. In particular, ZSM-5 is more efficient in the removal of CB at low concentration level, while Y shows higher saturation capacity than ZSM-5. Difference Fourier maps of the electron density provide insight into the preferred zeolite adsorption sites in both microporous materials. The refined framework–extraframework bond distances highlight the existence of CB, and hydrophobic zeolites interactions mediated via co-adsorbed H<sub>2</sub>O molecules. Adsorption of CB on ZSM-5 and Y zeolites is accompanied by structural changes, i.e. variations in both unit-cell parameters and channel shape when compared to the as-synthesized microporous materials, clearly confirming the very relevant role of H<sub>2</sub>O molecules in both the diffusion and adsorption processes in hydrophobic zeolites. After adsorption, the channels become more distorted, thus indicating remarkable framework flexibility for both ZSM-5 and Y zeolites.

**Supplementary Materials:** The following are available online at [www.mdpi.com/2075-163x/8/3/80/s1](http://www.mdpi.com/2075-163x/8/3/80/s1), Figure S1: Observed (dotted line), calculated (solid line) and difference (bottom) X-ray powder diffraction patterns of Y–CB (a) and ZSM-5–CB (b), respectively, Table S1: Framework atomic fractional coordinates and thermal isotropic displacement factor of Y–CB, Table S2: Framework atomic fractional coordinates and thermal isotropic displacement factor of ZSM-5–CB, Table S3: Extraframework atomic fractional coordinates, thermal isotropic displacement factor and occupancy of Y–CB, Table S4: Extraframework atomic fractional coordinates, thermal isotropic displacement factor and occupancy of ZSM-5–CB;  $x/a$  atomic fractional coordinates of CB<sub>2</sub> molecule atoms have exactly the same values, in order to maintain the molecule planarity, Table S5: Selected bond distances (Å) and angles (°) within both the Y–CB framework and extraframework atoms at  $T_{amb}$ , Table S6: Selected bond distances (Å) and angles (°) within both the ZSM-5–CB framework and extraframework atoms at  $T_{amb}$ . CIFs for all reported crystal structures are added as Supplementary Information.

**Acknowledgments:** The authors thank the Italian University and Scientific Research Ministry (Grant PRIN Prot. 2015HK93L7), the Istituto ENI Donegani-Environmental Technologies (Novara, Italy) and the Laboratory Terra&Acqua Tech, Technopole of Ferrara of Emilia-Romagna High Technology Network for their financial support.

**Author Contributions:** The manuscript was written with contributions from all authors. All authors have given approval to the final version of the manuscript. Annalisa Martucci wrote the paper and performed the X-ray and chromatographic experiments with Luisa Pasti; Elisa Rodeghero, Giada Beltrami and Matteo Ardit conceived and designed the XRD experiments and analyzed the data; Elena Sarti, Tatiana Chenet and Claudia Stevanin conceived and designed the adsorption experiments and analyzed the data.

**Conflicts of Interest:** The authors declare no conflict of interest.

#### References

1. Sennour, R.; Mimane, G.; Benghalem, A.; Taleb, S. Removal of the persistent pollutant chlorobenzene by adsorption onto activated montmorillonite. *Appl. Clay Sci.* **2009**, *43*, 503–506. [[CrossRef](#)]
2. McClenny, W.A.; Oliver, K.D.; Jacumin, H.H., Jr.; Daughtrey, E.H., Jr. Ambient level volatile organic compound (VOC) monitoring using solid adsorbents—Recent US EPA studies. *J. Environ. Monitor.* **2002**, *4*, 695–705. [[CrossRef](#)]
3. Khan, F.I.; Ghoshal, A.K. Removal of Volatile Organic Compounds from polluted air. *J. Prevent. Proc.* **2000**, *13*, 527–545. [[CrossRef](#)]
4. Sarti, E.; Chenet, T.; Pasti, L.; Cavazzini, A.; Rodeghero, E.; Martucci, A. Effect of silica alumina ratio and thermal treatment of beta zeolites on the adsorption of toluene from aqueous solutions. *Minerals* **2017**, *7*, 22. [[CrossRef](#)]
5. Rodeghero, E.; Pasti, L.; Sarti, E.; Cruciani, G.; Bagatin, R.; Martucci, A. Temperature-induced desorption of methyl tert-butyl ether confined on ZSM-5: An in situ synchrotron XRD powder diffraction study. *Minerals* **2017**, *7*, 34. [[CrossRef](#)]

6. Rodeghero, E.; Martucci, A.; Cruciani, G.; Bagatin, R.; Sarti, E.; Bosi, V.; Pasti, L. Kinetics and dynamic behaviour of toluene desorption from ZSM-5 using in situ high-temperature synchrotron powder X-ray diffraction and chromatographic techniques. *Catal. Today* **2016**, *227*, 118–125. [[CrossRef](#)]
7. Arletti, R.; Martucci, A.; Alberti, A.; Pasti, L.; Nassi, M.; Bagatin, R. Location of MTBE and toluene in the channel system of the zeolite mordenite: Adsorption and host–guest interactions. *J. Solid State Chem.* **2012**, *194*, 135–142. [[CrossRef](#)]
8. Pasti, L.; Rodeghero, E.; Sarti, E.; Bosi, V.; Cavazzini, A.; Bagatin, R.; Martucci, A. Competitive adsorption of VOCs from binary aqueous mixtures on zeolite ZSM-5. *RSC Adv.* **2016**, *6*, 54544–54552. [[CrossRef](#)]
9. Pasti, L.; Sarti, E.; Cavazzini, A.; Marchetti, N.; Dondi, F.; Martucci, A. Factors affecting drug adsorption on beta zeolites. *J. Sep. Sci.* **2013**, *36*, 1604–1611. [[CrossRef](#)] [[PubMed](#)]
10. Martucci, A.; Pasti, L.; Marchetti, N.; Cavazzini, A.; Dondi, F.; Alberti, A. Adsorption of pharmaceuticals from aqueous solutions on synthetic zeolites. *Micropor. Mesopor. Mat.* **2012**, *148*, 174–183. [[CrossRef](#)]
11. Braschi, I.; Blasioli, S.; Gigli, L.; Gessa, C.E.; Alberti, A.; Martucci, A. Removal of sulfonamide antibiotics from water: Evidence of adsorption into an organophilic zeolite Y by its structural modifications. *J. Hazard. Mater.* **2010**, *17*, 218–225. [[CrossRef](#)] [[PubMed](#)]
12. Blasioli, S.; Martucci, A.; Paul, G.; Gigli, L.; Cossi, M.; Johnston, C.T.; Marchese, L.; Braschi, I. Removal of sulfamethoxazole sulfonamide antibiotic from water by high silica zeolites: A study of the involved host–guest interactions by a combined structural, spectroscopic, and computational approach. *J. Colloid Interf. Sci.* **2014**, *419*, 148–159. [[CrossRef](#)] [[PubMed](#)]
13. Pasti, L.; Martucci, A.; Nassi, M.; Cavazzini, A.; Alberti, A.; Bagatin, R. The role of water in DCE adsorption from aqueous solutions onto hydrophobic zeolites. *Micropor. Mesopor. Mat.* **2012**, *160*, 182–193. [[CrossRef](#)]
14. Guo, Y.; Li, Y.; Zhu, T.; Ye, M.; Wang, X. Adsorption of SO<sub>2</sub> and chlorobenzene on activated carbon. *Adsorpt.* **2013**, *19*, 1109–1116. [[CrossRef](#)]
15. Crisafulli, R.; Milhome, M.A.L.; Cavalcante, R.M.; Silveira, E.R.; De Keukeleire, D.; Nascimento, R.F. Removal of some polycyclic aromatic hydrocarbons from petrochemical wastewater using low-cost adsorbents of natural origin. *Bioresource Technol.* **2008**, *99*, 4515–4519. [[CrossRef](#)] [[PubMed](#)]
16. Kim, B.K.; Ryu, S.K.; Kim, B.J.; Park, S.J. Roles of Acid-Base Interactions in Hydrogen Chloride Removal by Activated Carbon Fibers. *J. Ind. Eng. Chem.* **2006**, *12*, 121–126.
17. Park, S.J.; Kim, B.J. Influence of oxygen plasma treatment on hydrogen chloride removal of activated carbon fibers. *J. Colloid Interf. Sci.* **2004**, *275*, 590–595. [[CrossRef](#)] [[PubMed](#)]
18. Chin, C.J.M.; Shih, M.W.; Tsai, H.J. Adsorption of nonpolar benzene derivatives on single-walled carbon nanotubes. *Appl. Surf. Sci.* **2010**, *256*, 6035–6039. [[CrossRef](#)]
19. Long, C.; Li, Q.; Li, Y.; Liu, Y.; Li, A.; Zhang, Q. Adsorption characteristics of benzene–chlorobenzene vapor on hypercrosslinked polystyrene adsorbent and a pilot-scale application study. *Chem. Eng. J.* **2010**, *160*, 723–728. [[CrossRef](#)]
20. Chen, W.; Duan, L.; Zhu, D. Adsorption of polar and nonpolar organic chemicals to carbon nanotubes. *Environ. Sci. Technol.* **2007**, *41*, 8295–8300. [[CrossRef](#)] [[PubMed](#)]
21. Balamurugan, K.; Subramanian, V. Adsorption of chlorobenzene onto (5,5) armchair single-walled Carbon nanotube and graphene sheet: Toxicity versus adsorption strength. *J. Phys. Chem. C* **2013**, *117*, 21217–21227. [[CrossRef](#)]
22. Lee, J.J.; Choi, J.; Park, J.W. Simultaneous sorption of lead and chlorobenzene by organobentonite. *Chemosphere* **2002**, *49*, 1309–1315. [[CrossRef](#)]
23. Witthuhn, B.; Klauth, P.; Pernyeszi, T.; Vereecken, H.; Klumpp, E. Organoclays for Aquifer Bioremediation: Adsorption of Chlorobenzene on Organoclays and its Degradation by RHODOCOCOCUS B528. *Water Air Soil Poll. Focus* **2006**, *6*, 317–329. [[CrossRef](#)]
24. Jarraya, I.; Fourmentin, S.; Benzina, M.; Bouaziz, S. VOC adsorption on raw and modified clay materials. *Chem. Geol.* **2010**, *275*, 1–8. [[CrossRef](#)]
25. Altare, C.R.; Bowman, R.S.; Katz, L.E.; Kinney, K.A.; Sullivan, E.J. Regeneration and long-term stability of surfactant-modified zeolite for removal of volatile organic compounds from produced water. *Micropor. Mesopor. Mat.* **2007**, *105*, 305–316. [[CrossRef](#)]
26. Anderson, M.A. Removal of MTBE and Other Organic Contaminants from Water by Sorption to High Silica Zeolites. *Environ. Sci. Technol.* **2000**, *34*, 725–727. [[CrossRef](#)]

27. Damjanović, L.; Rakić, V.; Rac, V.; Stošić, D.; Auroux, A. The investigation of phenol removal from aqueous solutions by zeolites as solid adsorbents. *J. Hazard. Mat.* **2010**, *184*, 477–484. [[CrossRef](#)] [[PubMed](#)]
28. Perego, C.; Bagatin, R.; Tagliabue, M.; Vignola, R. Zeolites and related mesoporous materials for multi-talented environmental solutions. *Micropor. Mesopor. Mat.* **2013**, *166*, 37–49. [[CrossRef](#)]
29. Leardini, L.; Martucci, A.; Braschi, I.; Blasioli, S.; Quartieri, S. Regeneration of high-silica zeolites after sulfamethoxazole antibiotic adsorption: A combined in situ high-temperature synchrotron X-ray powder diffraction and thermal degradation study. *Mineral. Mag.* **2014**, *78*, 1141–1160. [[CrossRef](#)]
30. Braschi, I.; Blasioli, S.; Buscaroli, E.; Montecchio, D.; Martucci, A. Physicochemical regeneration of high silica zeolite Y used to clean-up water polluted with sulfonamide antibiotics. *J. Environ. Sci.* **2016**, *43*, 302–312. [[CrossRef](#)] [[PubMed](#)]
31. Vignola, R.; Cova, U.; Fabiani, F.; Sbardellati, T.; Sisto, R.; Vignola, R. Process for the regeneration of nonpolar adsorbing zeolites used for the treatment of contaminated water. Patent WO/2009/000429, 31 December 2008.
32. Alberti, A.; Martucci, A. Phase transformations and structural modifications induced by heating in microporous materials. *Stud. Surf. Sci. Catal.* **2005**, *155*, 19–43. [[CrossRef](#)]
33. Alberti, A.; Martucci, A. Reconstructive phase transitions in microporous materials: Rules and factors affecting them. *Micropor. Mesopor. Mat.* **2011**, *141*, 192–198. [[CrossRef](#)]
34. Baerlocher, C.; McCusker, L.B.; Olson, D.H. *Atlas of Zeolite Framework Types*, 6th ed.; Elsevier: Amsterdam, The Netherlands, 2007.
35. Larson, A.C.; Von Dreele, R.B. *GSAS General Structure Analysis System, LANSCE, MS-H805*; Los Alamos National Laboratory: Los Alamos, NM, USA, 1994.
36. Toby, B.H. EXPGUI, a graphical user interface for GSAS. *J. Appl. Crystallogr.* **2001**, *34*, 210–213. [[CrossRef](#)]
37. Azizian, S.; Haerifar, M.; Bashiri, H. Adsorption of methyl violet onto granular activated carbon: Equilibrium, kinetics and modeling. *Chem. Eng. J.* **2009**, *146*, 36–41. [[CrossRef](#)]
38. De Moor, B.A.; Reyniers, M.F.; Gobin, O.C.; Lercher, J.A.; Marin, G.B. Adsorption of C2–C8 *n*-Alkanes in Zeolites. *J. Phys. Chem. C* **2011**, *115*, 1204–1219. [[CrossRef](#)]
39. Martucci, A.; Braschi, I.; Bisio, C.; Sarti, E.; Rodeghero, E.; Bagatin, R.; Pasti, L. Influence of water on the retention of methyl tertiary-butyl ether by high silica ZSM-5 and Y zeolites: A multidisciplinary study on the adsorption from liquid and gas phase. *RSC Advances* **2015**, *5*, 86997–87006. [[CrossRef](#)]
40. Martucci, A.; Braschi, I.; Marchese, L.; Quartieri, S. Recent advances in clean-up strategies of waters polluted with sulfonamide antibiotics: A review of sorbents and related properties. *Mineral. Mag.* **2014**, *78*, 1115–1140. [[CrossRef](#)]
41. Li, X.; Chen, G.H. Surface modified graphite nanosheets used as adsorbent to remove 1,2-dichlorobenzene from water. *Mater. Lett.* **2009**, *63*, 930–932. [[CrossRef](#)]
42. Yu, F.; Ma, J.; Wu, Y. Adsorption of toluene, ethylbenzene and *m*-xylene on multi-walled carbon nanotubes with different oxygen contents from aqueous solutions. *J. Hazard. Mater.* **2011**, *192*, 1370–1379. [[CrossRef](#)] [[PubMed](#)]
43. Krishna, R.; van Baten, J.M. Highlighting a Variety of Unusual Characteristics of Adsorption and Diffusion in Microporous Materials Induced by Clustering of Guest Molecules. *Langmuir* **2010**, *26*, 8450–8463. [[CrossRef](#)] [[PubMed](#)]
44. Wragg, D.S.; Morris, R.E.; Burton, A.W. Pure silica zeolite-type frameworks: A structural analysis. *Chem. Mater.* **2008**, *20*, 1561–1570. [[CrossRef](#)]
45. Leardini, L.; Martucci, A.; Alberti, A.; Cruciani, G. Template burning effects on stability and boron coordination in boron levynite studied by in situ time resolved synchrotron powder diffraction. *Micropor. Mesopor. Mater.* **2013**, *167*, 117–126. [[CrossRef](#)]
46. Baur, W.H. Self-limiting distortion by antirotating hinges is the principle of flexible but noncollapsible frameworks. *J. Solid State Chem.* **1992**, *97*, 243–247. [[CrossRef](#)]
47. Momma, K.; Izumi, F. VESTA 3 for three-dimensional visualization of crystal, volumetric and morphology data. *J. Appl. Crystallogr.* **2011**, *44*, 1272–1276. [[CrossRef](#)]



# Supplementary Materials: Insights into Adsorption of Chlorobenzene in High Silica MFI and FAU Zeolites Gained from Chromatographic and Diffractometric Techniques

Luisa Pasti, Elisa Rodeghero, Giada Beltrami, Matteo Ardit, Elena Sarti, Tatiana Chenet, Claudia Stevanin and Annalisa Martucci

**Figure S1.** Observed (dotted line), calculated (solid line) and difference (bottom) X-ray powder diffraction patterns of Y-CB (a) and ZSM-5-CB (b), respectively.

**Table S1.** Framework atomic fractional coordinates and thermal isotropic displacement factor of Y-CB.

**Table S2.** Framework atomic fractional coordinates and thermal isotropic displacement factor of ZSM-5-CB.

**Table S3.** Extraframework atomic fractional coordinates, thermal isotropic displacement factor and occupancy of Y-CB.

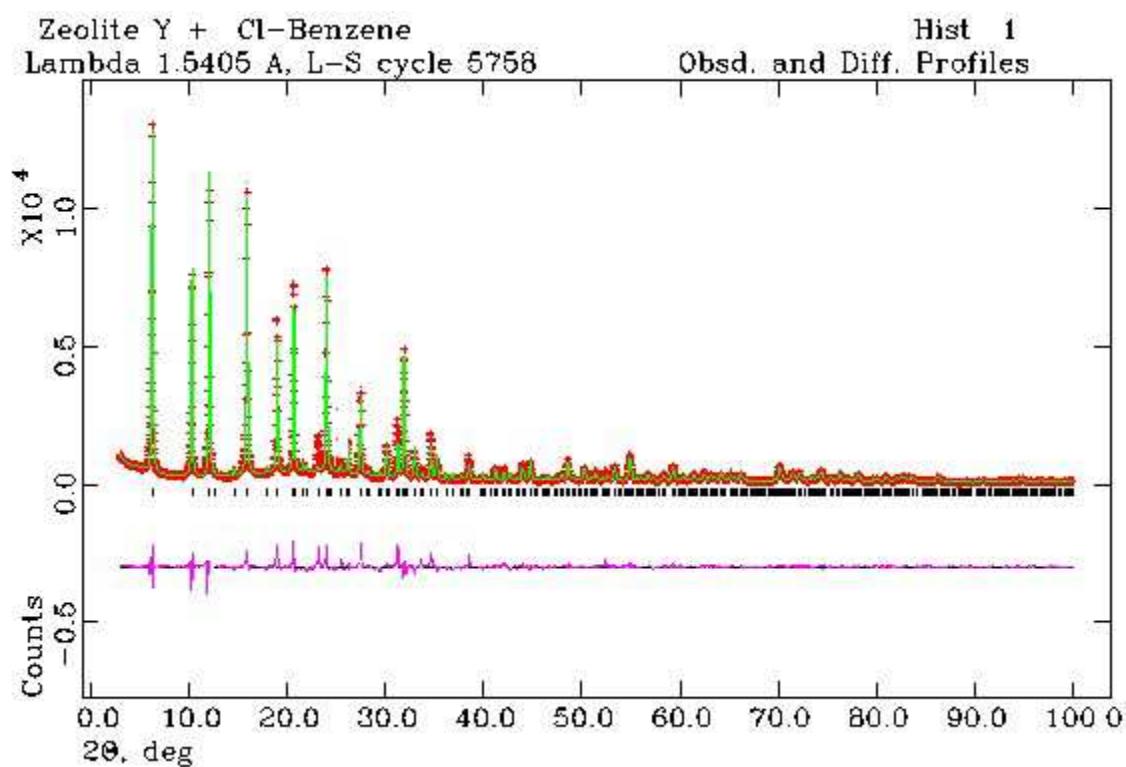
**Table S4.** Extraframework atomic fractional coordinates, thermal isotropic displacement factor and occupancy of ZSM-5-CB;  $x/a$  atomic fractional coordinates of CB2 molecule atoms have exactly the same values, in order to maintain the molecule planarity.

**Table S5.** Selected bond distances (Å) and angles (°) within both the Y-CB framework and extraframework atoms at  $T_{amb}$ .

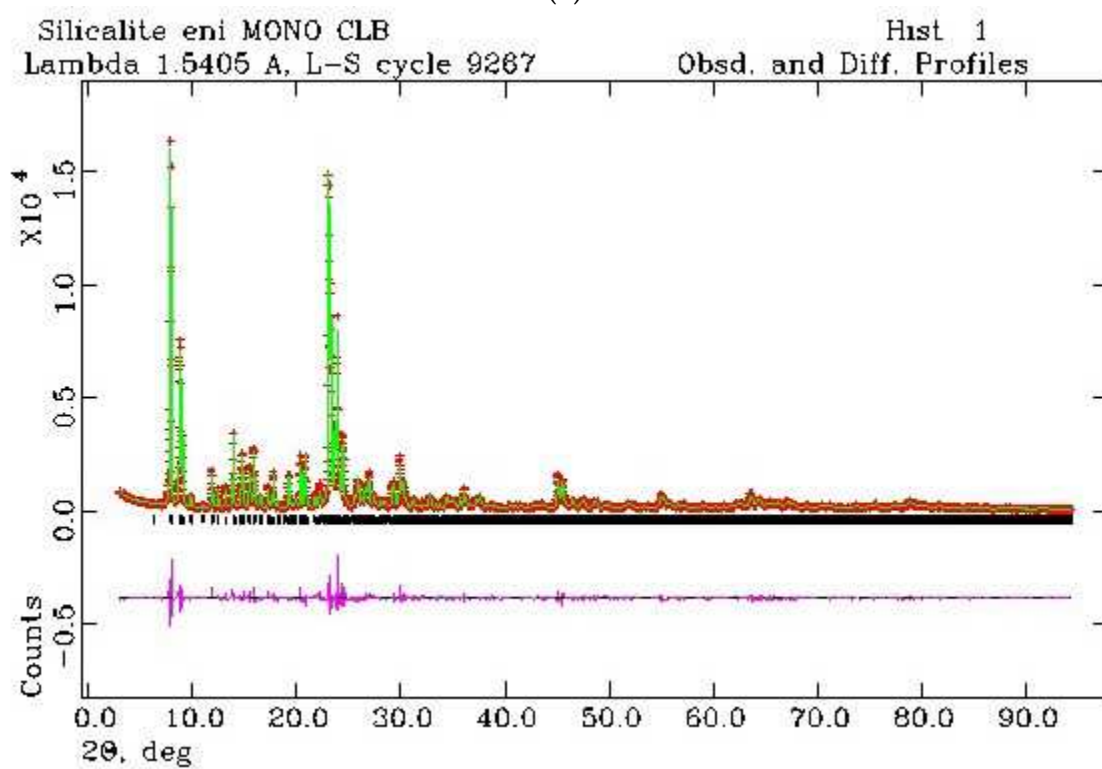
**Table S6.** Selected bond distances (Å) and angles (°) within both the ZSM-5-CB framework and extraframework atoms at  $T_{amb}$ .

Crystallographic Information File (CIF) of Y-CB

Crystallographic Information File (CIF) of ZSM-5-CB



(a)



(b)

**Figure S1.** Observed (dotted line), calculated (solid line) and difference (bottom) X-ray powder diffraction patterns of Y-CB (a) and ZSM-5-CB (b), respectively.

**Table S1.** Framework atomic fractional coordinates and thermal isotropic displacement factor of Y-CB.

Sites	$x/a$	$y/b$	$z/c$	$U_{iso}$ (Å <sup>2</sup> )	Fraction
T1	-0.0536(1)	0.1178(2)	0.0380(1)	0.002(1)	1.00
T2	-0.0534(1)	0.0330(1)	0.1234(1)	0.002(1)	1.00
O1	-0.1080(3)	-0.0029(1)	0.1099(1)	0.005(1)	1.00
O2	-0.0053(7)	-0.0094(1)	0.1417(2)	0.005(1)	1.00
O3	-0.0333(1)	0.0607(1)	0.0660(1)	0.005(1)	1.00
O4	-0.0546(2)	0.0858(1)	0.1640(1)	0.005(1)	1.00

**Table S2.** Framework atomic fractional coordinates and thermal isotropic displacement factor of ZSM-5-CB.

Sites	$x/a$	$y/b$	$z/c$	$U_{iso}$ (Å <sup>2</sup> )	Fraction
T1	0.0501(4)	0.4255(4)	-0.3339(5)	0.52(1)	1.00
T2	0.0303(4)	0.3159(4)	-0.1760(8)	0.52(1)	1.00
T3	0.0632(4)	0.2806(2)	0.0325(3)	0.52(1)	1.00
T4	0.0658(4)	0.1215(2)	0.0359(2)	0.52(1)	1.00
T5	0.0275(1)	0.0727(4)	-0.1785(5)	0.52(1)	1.00
T6	0.0590(4)	0.1914(4)	-0.3193(3)	0.52(1)	1.00
T7	-0.1748(3)	0.4261(1)	-0.3355(4)	0.52(1)	1.00
T8	-0.1296(3)	0.3149(1)	-0.1827(6)	0.52(1)	1.00
T9	-0.1757(3)	0.2712(1)	0.0337(6)	0.52(1)	1.00
T10	-0.1829(3)	0.1191(1)	0.0346(3)	0.52(1)	1.00
T11	-0.1309(2)	0.0698(4)	-0.1786(4)	0.52(1)	1.00
T12	-0.1638(5)	0.1882(2)	-0.3172(5)	0.52(1)	1.00
T13	0.4411(3)	0.4281(4)	-0.3370(4)	0.52(1)	1.00
T14	0.4721(2)	0.3179(4)	-0.1879(4)	0.52(1)	1.00
T15	0.4354(2)	0.2828(2)	0.0313(2)	0.52(1)	1.00
T16	0.4335(3)	0.1235(2)	0.0193(2)	0.52(1)	1.00
T17	0.4717(4)	0.0729(2)	-0.1960(2)	0.52(1)	1.00
T18	0.4361(4)	0.1930(4)	-0.3274(4)	0.52(1)	1.00
T19	0.6657(1)	0.4225(1)	-0.3232(2)	0.52(1)	1.00
T20	0.6305(2)	0.3069(4)	-0.1734(4)	0.52(1)	1.00
T21	0.6653(2)	0.2756(3)	0.0500(2)	0.52(1)	1.00
T22	0.6717(3)	0.1191(3)	0.0376(2)	0.52(1)	1.00
T23	0.6324(2)	0.0732(6)	-0.1837(4)	0.52(1)	1.00
T24	0.6815(4)	0.1911(4)	-0.3163(4)	0.52(1)	1.00
O1	0.0484(5)	0.3843(6)	-0.2314(4)	0.71(2)	1.00
O2	0.0738(3)	0.3144(2)	-0.0749(3)	0.71(2)	1.00
O3	0.0620(3)	0.2009(4)	0.0264(4)	0.71(2)	1.00
O4	0.0634(2)	0.1021(2)	-0.0803(3)	0.71(2)	1.00
O5	0.0453(6)	0.1197(4)	-0.2713(4)	0.71(2)	1.00
O6	0.0433(3)	0.2516(6)	-0.2444(4)	0.71(2)	1.00
O7	-0.1567(4)	0.3785(4)	-0.2429(3)	0.71(2)	1.00
O8	-0.1634(3)	0.3002(3)	-0.0765(4)	0.71(2)	1.00
O9	-0.1554(4)	0.1940(4)	0.0356(4)	0.71(2)	1.00
O10	-0.1594(3)	0.0884(4)	-0.0702(4)	0.71(2)	1.00

O11	-0.1567(5)	0.1152(4)	-0.2696(4)	0.71(2)	1.00
O12	-0.1385(4)	0.2480(3)	-0.2470(4)	0.71(2)	1.00
O13	-0.0498(5)	0.3216(4)	-0.1675(4)	0.71(2)	1.00
O14	-0.0516(3)	0.0682(4)	-0.1568(3)	0.71(2)	1.00
O15	0.1222(3)	0.4169(4)	-0.3852(4)	0.71(2)	1.00
O16	-0.0138(4)	0.4025(4)	-0.3986(4)	0.71(2)	1.00
O17	-0.1357(4)	0.4017(4)	-0.4332(4)	0.71(2)	1.00
O18	0.1338(4)	0.1817(4)	-0.3605(4)	0.71(2)	1.00
O19	-0.0011(3)	0.2057(4)	-0.3964(4)	0.71(2)	1.00
O20	-0.1322(3)	0.1841(4)	-0.4268(4)	0.71(2)	1.00
O21	0.0599(4)	0.0022(4)	-0.2069(4)	0.71(2)	1.00
O22	-0.1630(3)	-0.0006(3)	-0.2087(4)	0.71(2)	1.00
O23	-0.2552(4)	0.4281(3)	-0.3435(3)	0.71(2)	1.00
O24	-0.2411(3)	0.2009(3)	-0.3454(4)	0.71(2)	1.00
O25	-0.2543(3)	0.2769(3)	0.0577(3)	0.71(2)	1.00
O26	-0.2550(4)	0.1077(3)	0.0843(3)	0.71(2)	1.00
O27	0.4406(3)	0.3835(4)	-0.2378(4)	0.71(2)	1.00
O28	0.4396(3)	0.3142(3)	-0.0787(3)	0.71(2)	1.00
O29	0.4356(3)	0.2031(3)	0.0258(5)	0.71(2)	1.00
O30	0.4389(4)	0.0929(4)	-0.0910(3)	0.71(2)	1.00
O31	0.4357(3)	0.1213	-0.2750(3)	0.71(2)	1.00
O32	0.4574(3)	0.2530(4)	-0.2546(4)	0.71(2)	1.00
O33	0.6554(4)	0.3721(3)	-0.2317(3)	0.71(2)	1.00
O34	0.6562(3)	0.3066(4)	-0.0597(3)	0.71(2)	1.00
O35	0.6591(4)	0.1975(3)	0.0277(3)	0.71(2)	1.00
O36	0.6605(4)	0.0963(3)	-0.0764	0.71(2)	1.00
O37	0.6613(3)	0.1204(3)	-0.2698(3)	0.71(2)	1.00
O38	0.6620(4)	0.2454(4)	-0.2334	0.71(2)	1.00
O39	0.5503(4)	0.2996(3)	-0.1794(4)	0.71(2)	1.00
O40	0.5522(4)	0.0783(3)	-0.1942(3)	0.71(2)	1.00
O41	0.3779(4)	0.4188(4)	-0.4104(3)	0.71(2)	1.00
O42	0.5051(3)	0.4133(4)	-0.4057(3)	0.71(2)	1.00
O43	0.6415(3)	0.3911(3)	-0.4275(3)	0.71(2)	1.00
O44	0.3651(3)	0.1872(3)	-0.3836(3)	0.71(2)	1.00
O45	0.5017(3)	0.2017(3)	-0.3951(3)	0.71(2)	1.00
O46	0.6299(3)	0.1972(3)	-0.4084(3)	0.71(2)	1.00
O47	0.4484(3)	-0.0023(4)	-0.2169(3)	0.71(2)	1.00
O48	0.6539(4)	-0.0021(3)	-0.2070(4)	0.71(2)	1.00

---

**Table S3.** Extraframework atomic fractional coordinates, thermal isotropic displacement factor and occupancy of Y–CB.

Sites	<i>x/a</i>	<i>y/b</i>	<i>z/c</i>	<i>U</i> <sub>iso</sub> (Å <sup>2</sup> )	Fraction
C	0.4768(1)	0.4768(1)	0.5463(3)	0.161(3)	0.34(6)
Cl	0.4496(1)	0.4496(1)	0.6008(1)	0.161(3)	0.34(6)
W1	0.3096(4)	0.3096(4)	0.3096(4)	0.113(1)	0.82(1)
W2	0.4176(2)	0.4176(2)	0.4176(2)	0.113(1)	0.80(8)
W3	0.6277(1)	0.2209(1)	0.0081(1)	0.113(1)	0.18(1)

**Table S4.** Extraframework atomic fractional coordinates, thermal isotropic displacement factor and occupancy of ZSM-5–CB; *x/a* atomic fractional coordinates of CB2 molecule atoms have exactly the same values, in order to maintain the molecule planarity.

Sites	<i>x/a</i>	<i>y/b</i>	<i>z/c</i>	<i>U</i> <sub>iso</sub> (Å <sup>2</sup> )	Fraction
C1	0.7547(4)	0.5975(9)	0.0273(7)	0.211(7)	0.93(5)
C2	0.3017(5)	0.4444(9)	0.008(5)	0.211(7)	0.93(5)
C3	0.8151(8)	0.5686(7)	0.0564(6)	0.211(7)	0.93(5)
C4	0.8237(4)	0.5008(8)	0.0502(8)	0.211(7)	0.93(5)
C5	0.7110(7)	0.4899(6)	−0.0129(7)	0.211(7)	0.93(5)
C6	0.2285(7)	0.5386(9)	−0.0175(5)	0.211(7)	0.93(5)
Cl1	0.0991(2)	0.5357(2)	0.921(2)	0.211(7)	0.93(5)
C8	0.213(4)	0.1474(7)	0.7608(3)	0.285(2)	0.54(6)
C9	0.213(6)	0.0885(8)	0.7066(3)	0.285(2)	0.54(6)
C10	0.213(4)	0.0834(7)	0.9116(3)	0.285(2)	0.54(6)
C11	0.213(3)	0.1444(7)	0.8632(3)	0.285(2)	0.54(6)
C12	0.213(7)	0.0274(7)	0.8573(3)	0.285(2)	0.54(6)
C13	0.213(8)	0.0275(7)	0.7553(3)	0.285(2)	0.54(6)
Cl2	0.213(9)	−0.0544(7)	0.7127(3)	0.285(2)	0.54(6)
W1	0.7170(9)	0.7343(5)	0.1285(5)	0.193(3)	1.00(2)
W2	0.4209(7)	0.5034(5)	−0.0025(8)	0.193(3)	1.00(3)

**Table S5.** Selected bond distances (Å) and angles (°) within both the Y–CB framework and extraframework atoms at *T*<sub>amb</sub>.

Distance	Value (Å)	Distance	Value (Å)
T1–O1	1.629	T2–O1	1.619
T1–O2	1.612	T2–O2	1.620
T1–O3	1.622	T2–O3	1.621
T1–O4	1.620	T2–O4	1.619
Mean Value	1.621	Mean Value	1.620
Angle	Value (°)	Angle	Value (°)
O1–T1–O2	105.6	O1–T2–O2	107.7
O1–T1–O3	110.5	O1–T2–O3	107.3
O1–T1–O4	117.7	O1–T2–O4	122.3
O2–T1–O3	112.3	O2–T2–O3	106.4
O2–T1–O4	103.3	O2–T2–O4	110.4
O3–T1–O4	107.3	O3–T2–O4	101.6
Mean value	109.45	Mean value	109.3
Angle	Value (°)	Angle	Value (°)
T1–O1–T2	124.7	O1–Cl	2.680
T1–O2–T2	142.7	O1–Cl	2.723
T1–O3–T2	128.6	O4–Cl	2.599

T1–O4–T2	171.4	C–C	1.379
Mean value	141.8	Mean value	1.620
<b>Distance</b>	<b>Value (Å)</b>	<b>Distance</b>	<b>Value (Å)</b>
W2–W2	2.926	W1–W3	2.201
W2–W1	2.737	W3–CL	2.454
W2–W3	2.421	W3–CL	3.211

**Table S6.** Selected bond distances (Å) and angles (°) within both the ZSM-5–CB framework and extraframework atoms at  $T_{amb}$ .

<b>Distance</b>	<b>Value (Å)</b>
T1–O1	1.604
T1–O15	1.606
T1–O16	1.602
T1–O47	1.604
Mean value	1.604
T2–O1	1.604
T2–O2	1.604
T2–O6	1.606
T2–O13	1.605
Mean value	1.605
T3–O2	1.606
T3–O3	1.605
T3–O45	1.607
T3–O46	1.606
Mean value	1.606
T4–O3	1.604
T4–O4	1.605
T4–O42	1.605
T4–O43	1.602
Mean value	1.604
T5–O4	1.606
T5–O5	1.603
T5–O14	1.606
T5–O21	1.604
Mean value	1.605
T6–O5	1.603
T6–O6	1.605
T6–O18	1.604
T6–O19	1.603
Mean value	1.604
T7–O7	1.605
T7–O17	1.605
T7–O23	1.604
T7–O48	1.605
Mean value	1.605
T8–O7	1.604
T8–O8	1.606
T8–O12	1.606
T8–O13	1.605
Mean value	1.605
T9–O8	1.609

T9-O9	1.603
T9-O25	1.605
T9-O44	1.604
Mean value	1.605
<hr/>	
T10-O9	1.603
T10-O10	1.607
T10-O26	1.604
T10-O41	1.605
Mean value	1.605
<hr/>	
T11-O10	1.606
T11-O11	1.605
T11-O14	1.606
T11-O22	1.604
Mean value	1.605
<hr/>	
T12-O11	1.605
T12-O12	1.607
T12-O20	1.604
T12-O24	1.604
Mean value	1.605
<hr/>	
T13-O21	1.603
T13-O27	1.604
T13-O41	1.603
T13-O42	1.605
Mean value	1.604
<hr/>	
T14-O27	1.605
T14-O28	1.606
T14-O32	1.608
T14-O39	1.605
Mean value	1.606
<hr/>	
T15-O19	1.605
T15-O20	1.605
T15-O28	1.606
T15-O29	1.604
Mean value	1.605
<hr/>	
T16-O16	1.603
T16-O17	1.605
T16-O29	1.603
T16-O30	1.605
Mean value	1.604
<hr/>	
T17-O30	1.606
T17-O31	1.604
T17-O40	1.607
Mean value	1.605
<hr/>	
T18-O31	1.603
T18-O32	1.606
T18-O44	1.603
T18-O45	1.605
Mean value	1.604
<hr/>	
T19-O22	1.605
T19-O23	1.604
T19-O33	1.605
T19-O43	1.604

Mean value	1.605
T20-O33	1.605
T20-O34	1.603
T20-O38	1.607
T20-O39	1.605
Mean value	1.605
T21-O18	1.605
T21-O25	1.606
T21-O34	1.605
T21-O35	1.603
Mean value	1.605
T22-O15	1.606
T22-O26	1.602
T22-O35	1.602
T22-O36	1.608
Mean value	1.605
T23-O36	1.607
T23-O37	1.605
T23-O40	1.607
T23-O48	1.605
Mean value	1.606
T24-O24	1.605
T24-O37	1.605
T24-O38	1.606
T24-O46	1.605
Mean value	1.605
<b>Angle</b>	<b>Value (°)</b>
O1-T1-O15	109.6
O1-T1-O16	107
O1-T1-O47	96.1
O15-T1-O16	116.6
O15-T1-O47	105.3
O16-T1-O47	120.2
Mean value	109.1
O1-T2-O2	106.6
O1-T2-O6	112.8
O1-T2-O13	101.5
O2-T2-O6	112.2
O2-T2-O13	118.2
O6-T2-O13	105.1
Mean value	109.4
O2-T3-O3	112.3
O2-T3-O45	123.5
O2-T3-O46	102.1
O3-T3-O45	103.9
O3-T3-O46	108.3
O45-T3-O46	105.8
Mean value	109.3
O3-T4-O4	99.5
O3-T4-O42	116
O3-T4-O43	103.1
O4-T4-O42	110.4

O4-T4-O43	106.2
O42-T4-O43	119.5
Mean value	109.1
<hr/>	
O4-T5-O5	108.6
O4-T5-O14	107.7
O4-T5-O21	109.9
O5-T5-O14	113.4
O5-T5-O21	104.2
O14-T5-O21	113
Mean value	109.5
<hr/>	
O5-T6-O6	113.2
O5-T6-O18	100.9
O5-T6-O19	107
O6-T6-O18	119.6
O6-T6-O19	96.8
O18-T6-O19	119.4
Mean value	109.5
<hr/>	
O7-T7-O17	109.9
O7-T7-O23	106.5
O7-T7-O48	101.8
O17-T7-O23	116.3
O17-T7-O48	115.9
O23-T7-O48	105
Mean value	109.3
<hr/>	
O7-T8-O8	116.7
O7-T8-O12	111.3
O7-T8-O13	109.1
O8-T8-O12	105.9
O8-T8-O13	108.9
O12-T8-O13	104.1
Mean value	109.3
<hr/>	
O8-T9-O9	109
O8-T9-O25	108.2
O8-T9-O44	111.4
O9-T9-O25	108.2
O9-T9-O44	111.6
O25-T9-O44	108.3
Mean value	109.5
<hr/>	
O9-T10-O10	105.5
O9-T10-O26	115.9
O9-T10-O41	100.8
O10-T10-O26	125.1
O10-T10-O41	89.7
O26-T10-O41	114.6
Mean value	108.6
<hr/>	
O10-T11-O11	116.2
O10-T11-O14	101.2
O10-T11-O22	106.9
O11-T11-O14	117.3
O11-T11-O22	100.7
O14-T11-O22	114.7
Mean value	109.5

O11-T12-O12	115.2
O11-T12-O20	106.5
O11-T12-O24	108.7
O12-T12-O20	116.8
O12-T12-O24	108.3
O20-T12-O24	100.1
Mean value	109.3
O21-T13-O27	102.5
O21-T13-O41	108.8
O21-T13-O42	113.2
O27-T13-O41	115.7
O27-T13-O42	112.4
O41-T13-O42	104.5
Mean value	109.5
O27-T14-O28	104.9
O27-T14-O32	111.5
O27-T14-O39	126.5
O28-T14-O32	113.4
O28-T14-O39	108.8
O32-T14-O39	91.6
Mean value	109.4
O19-T15-O20	112.9
O19-T15-O28	116.8
O19-T15-O29	99.7
O20-T15-O28	101.9
O20-T15-O29	115.6
O28-T15-O29	110.5
Mean value	109.6
O16-T16-O17	100.6
O16-T16-O29	105.8
O16-T16-O30	117.3
O17-T16-O29	108.4
O17-T16-O30	107.9
O29-T16-O30	115.6
Mean value	109.3
O30-T17-O31	104
O30-T17-O40	112.4
O30-T17-O47	105.6
O31-T17-O40	114.3
O31-T17-O47	109.1
O40-T17-O47	110.8
Mean value	109.4
O31-T18-O32	114.3
O31-T18-O44	97.6
O31-T18-O45	110.7
O32-T18-O44	124.6
O32-T18-O45	92.8
O44-T18-O45	117.6
Mean value	109.6
O22-T19-O23	90.7
O22-T19-O33	113.6
O22-T19-O43	126.9

O23-T19-O33	107.7
O23-T19-O43	99.9
O33-T19-O43	112.2
Mean value	108.5
<hr/>	
O33-T20-O34	111.5
O33-T20-O38	105.2
O33-T20-O39	111.2
O34-T20-O38	110.4
O34-T20-O39	111
O38-T20-O39	107.2
Mean value	109.4
<hr/>	
O18-T21-O25	109.7
O18-T21-O34	115.7
O18-T21-O35	129.3
O25-T21-O34	99.1
O25-T21-O35	95.9
O34-T21-O35	101.6
Mean value	108.6
<hr/>	
O15-T22-O26	104.2
O15-T22-O35	113.7
O15-T22-O36	113.7
O26-T22-O35	108.3
O26-T22-O36	116.8
O35-T22-O36	100.4
Mean value	109.5
<hr/>	
O36-T23-O37	110.3
O36-T23-O40	113.5
O36-T23-O48	110.9
O37-T23-O40	105.1
O37-T23-O48	108.7
O40-T23-O48	108.1
Mean value	109.4
<hr/>	
O24-T24-O37	116.5
O24-T24-O38	108.8
O24-T24-O46	114.5
O37-T24-O38	105.7
O37-T24-O46	101.9
O38-T24-O46	108.9
Mean value	109.4
<hr/>	
T1-O1-T2	147.7
T2-O2-T3	133.7
T3-O3-T4	171.7
T4-O4-T5	153.4
T5-O5-T6	151.7
T2-O6-T6	175.3
T7-O7-T8	159.5
T8-O8-T9	161.3
T9-O9-T10	145.5
T10-O10-T11	170.5
T11-O11-T12	148.0
T8-O12-T12	167.0
T2-O13-T8	165.6

T5–O14–T11	158.6
T1–O15–T22	151.5
T1–O16–T16	168.2
T7–O17–T16	147.6
T6–O18–T21	124.0
T6–O19–T15	176.0
T12–O20–T15	129.3
T5–O21–T13	136.7
T11–O22–T19	142.9
T7–O23–T19	165.4
T12–O24–T24	147.8
T9–O25–T21	163.9
T10–O26–T22	129.4
T13–O27–T14	143.2
T14–O28–T15	151.4
T15–O29–T16	178.3
T16–O30–T17	158.8
T17–O31–T18	146.1
T14–O32–T18	173.5
T19–O33–T20	158.2
T20–O34–T21	154.7
T21–O35–T22	159.6
T22–O36–T23	167.5
T23–O37–T24	153.6
T20–O38–T24	165.2
T14–O39–T20	161.5
T17–O40–T23	171.3
T10–O41–T13	157.4
T4–O42–T13	164.6
T4–O43–T19	127.3
T9–O44–T18	136.6
T3–O45–T18	172.6
T3–O46–T24	157.5
T1–O47–T17	140.7
T7–O48–T23	148.0
<hr/>	
<b>Distance</b>	<b>Value (Å)</b>
C5–C6	1.39
C5–C4	2.40
C5–C2	1.35
C5–C3	2.76
C5–C1	2.39
C5–W2	2.64
C6–C5	1.39
C6–C4	1.38
C6–C2	2.41
C6–C3	2.38
C6–C1	2.76
C6–Cl1	2.70
C4–C5	2.40
C4–C6	1.38
C4–C2	2.83
C4–C3	1.38

---

C4-C1	2.40
C4-C11	1.75
C2-O20	3.03
C2-C5	1.35
C2-C6	2.41
C2-C4	2.83
C2-C3	2.49
C2-C1	1.48
C2-W2	2.66
C2-C14	2.97
C3-C5	2.76
C3-C6	2.38
C3-C4	1.38
C3-C2	2.49
C3-C1	1.39
C3-C12	2.94
C3-C7	2.72
C1-O24	3.21
C1-C5	2.39
C1-C6	2.76
C1-C4	2.40
C1-C2	1.48
C1-C3	1.39
C1-W1	3.16
C1-C14	2.76
C8-O18	2.36
C8-O25	3.19
C8-C9	1.39
C8-C10	2.40
C8-C11	1.37
C8-C12	2.74
C8-C13	2.41
C8-W1	3.13
C9-O18	2.61
C9-C8	1.39
C9-C10	2.75
C9-C11	2.38
C9-C12	2.36
C9-C13	1.39
C9-C12	2.87
C10-O4	3.01
C10-O43	2.64
C10-C8	2.40
C10-C9	2.75
C10-C11	1.39
C10-C12	1.34
C10-C13	2.38
C11-O4	3.19
C11-C8	1.37
C11-C9	2.38
C11-C10	1.39
C11-C12	2.35

---

C11–C13	2.76
C11–W1	2.81
C12–O21	3.20
C12–O26	2.95
C12–O41	2.93
C12–C8	2.74
C12–C9	2.36
C12–C10	1.34
C12–C11	2.35
C12–C13	1.37
C12–C14	2.54
C13–O21	3.14
C13–C8	2.41
C13–C9	1.39
C13–C10	2.38
C13–C11	2.76
C13–C12	1.37
C13–C12	1.74
W1–O20	3.33
W1–O28	3.33
W1–C1	3.16
W1–C8	3.13
W1–C11	2.81
W2–C5	2.64
W2–C2	2.66
W2–W2	3.15
CL2–O21	3.44
CL2–O26	3.03
CL2–O27	3.32
CL2–O41	3.26
CL2–C2	2.97
CL2–C3	2.94
CL2–C1	2.76
CL2–C9	2.87
CL2–C12	2.54
CL2–C13	1.74
Cl1–O31	2.69
Cl1–O44	3.17
Cl1–O47	2.99
Cl1–C6	2.70
Cl1–C4	1.75
Cl1–C3	2.72

---

**Crystallographic Information File (CIF) of Y-CBY-CB**

```
_symmetry_space_group_name_H-M   'Fd-3'  
_cell_length_a    24.263506  
_cell_length_b    24.263506  
_cell_length_c    24.263506  
_cell_angle_alpha  90.0000  
_cell_angle_beta  90.0000  
_cell_angle_gamma  90.0000  
loop_  
_atom_site_label  
_atom_site_type_symbol  
_atom_site_fract_x  
_atom_site_fract_y  
_atom_site_fract_z  
_atom_site_B_iso_or_equiv  
_atom_site_occupancy  
SI1 SI -0.05360 0.11780 0.03802 0.197391754562 1.00000  
SI2 SI -0.05346 0.03299 0.12335 0.197391754562 1.00000  
O1 O -0.10804 -0.00289 0.10993 0.394783509124 1.00000  
O2 O -0.00534 -0.00939 0.14171 0.394783509124 1.00000  
O3 O -0.03333 0.06065 0.06604 0.394783509124 1.00000  
O4 O -0.05463 0.08582 0.16401 0.394783509124 1.00000  
w2 O 0.41760 0.41760 0.41760 9.04496393424 0.80392  
w1 O 0.30959 0.30959 0.30959 9.04496393424 0.82154  
C1 C 0.47678 0.47678 0.54634 12.7041333236 0.33590  
w3 O 0.62774 0.22086 0.00814 9.04496393424 0.18780  
CL1 CL 0.44958 0.44958 0.60084 12.7041333236 0.33590
```

**Crystallographic Information File (CIF) of ZSM-5-CB**

```
_symmetry_space_group_name_H-M 'P21/n'  
_cell_length_a 19.919321  
_cell_length_b 20.109558  
_cell_length_c 13.395503  
_cell_angle_alpha 90.0000  
_cell_angle_beta 90.3905  
_cell_angle_gamma 90.0000  
loop_  
_atom_site_label  
_atom_site_type_symbol  
_atom_site_fract_x  
_atom_site_fract_y  
_atom_site_fract_z  
_atom_site_B_iso_or_equiv  
_atom_site_occupancy  
SI1 SI 0.05010 0.42550 -0.33391 0.41452268458 1.00000  
SI2 SI 0.03031 0.31594 -0.17604 0.41452268458 1.00000  
SI3 SI 0.06317 0.28059 0.03250 0.41452268458 1.00000  
SI4 SI 0.06578 0.12149 0.03589 0.41452268458 1.00000  
SI5 SI 0.02748 0.07270 -0.17852 0.41452268458 1.00000  
SI6 SI 0.05904 0.19140 -0.31926 0.41452268458 1.00000  
SI7 SI -0.17483 0.42614 -0.33549 0.41452268458 1.00000  
SI8 SI -0.12956 0.31494 -0.18272 0.41452268458 1.00000  
SI9 SI -0.17567 0.27118 0.03375 0.41452268458 1.00000  
SI10 SI -0.18289 0.11913 0.03461 0.41452268458 1.00000  
SI11 SI -0.13091 0.06979 -0.17856 0.41452268458 1.00000  
SI12 SI -0.16376 0.18816 -0.31719 0.41452268458 1.00000  
SI13 SI 0.44109 0.42809 -0.33705 0.41452268458 1.00000  
SI14 SI 0.47207 0.31785 -0.18791 0.41452268458 1.00000  
SI15 SI 0.43537 0.28278 0.03134 0.41452268458 1.00000  
SI16 SI 0.43351 0.12352 0.01930 0.41452268458 1.00000  
SI17 SI 0.47173 0.07287 -0.19599 0.41452268458 1.00000  
SI18 SI 0.43613 0.19295 -0.32742 0.41452268458 1.00000  
SI19 SI 0.66574 0.42249 -0.32322 0.41452268458 1.00000  
SI20 SI 0.63048 0.30694 -0.17338 0.41452268458 1.00000  
SI21 SI 0.66526 0.27562 0.04999 0.41452268458 1.00000  
SI22 SI 0.67166 0.11910 0.03762 0.41452268458 1.00000  
SI23 SI 0.63244 0.07315 -0.18366 0.41452268458 1.00000  
SI24 SI 0.68150 0.19112 -0.31632 0.41452268458 1.00000  
O1 O 0.04839 0.38426 -0.23144 0.557829098392 1.00000  
O2 O 0.07378 0.31442 -0.07487 0.557829098392 1.00000  
O3 O 0.06198 0.20090 0.02639 0.557829098392 1.00000  
O4 O 0.06341 0.10206 -0.08032 0.557829098392 1.00000  
O5 O 0.04533 0.11968 -0.27131 0.557829098392 1.00000  
O6 O 0.04327 0.25164 -0.24440 0.557829098392 1.00000  
O7 O -0.15674 0.37854 -0.24294 0.557829098392 1.00000  
O8 O -0.16344 0.30023 -0.07652 0.557829098392 1.00000  
O9 O -0.15544 0.19405 0.03559 0.557829098392 1.00000  
O10 O -0.15936 0.08842 -0.07025 0.557829098392 1.00000  
O11 O -0.15669 0.11520 -0.26963 0.557829098392 1.00000  
O12 O -0.13849 0.24803 -0.24695 0.557829098392 1.00000
```

O13 O -0.04984 0.32159 -0.16754 0.557829098392 1.00000  
O14 O -0.05156 0.06816 -0.15675 0.557829098392 1.00000  
O15 O 0.12220 0.41693 -0.38520 0.557829098392 1.00000  
O16 O -0.01379 0.40255 -0.39858 0.557829098392 1.00000  
O17 O -0.13567 0.40174 -0.43317 0.557829098392 1.00000  
O18 O 0.13382 0.18167 -0.36052 0.557829098392 1.00000  
O19 O -0.00109 0.20575 -0.39644 0.557829098392 1.00000  
O20 O -0.13217 0.18413 -0.42684 0.557829098392 1.00000  
O21 O 0.05992 0.00224 -0.20693 0.557829098392 1.00000  
O22 O -0.16296 -0.00064 -0.20872 0.557829098392 1.00000  
O23 O -0.25518 0.42810 -0.34345 0.557829098392 1.00000  
O24 O -0.24111 0.20091 -0.34537 0.557829098392 1.00000  
O25 O -0.25429 0.27687 0.05773 0.557829098392 1.00000  
O26 O -0.25498 0.10772 0.08435 0.557829098392 1.00000  
O27 O 0.44055 0.38346 -0.23782 0.557829098392 1.00000  
O28 O 0.43955 0.31423 -0.07868 0.557829098392 1.00000  
O29 O 0.43557 0.20310 0.02584 0.557829098392 1.00000  
O30 O 0.43888 0.09287 -0.09101 0.557829098392 1.00000  
O31 O 0.43565 0.12127 -0.27501 0.557829098392 1.00000  
O32 O 0.45736 0.25295 -0.25464 0.557829098392 1.00000  
O33 O 0.65543 0.37206 -0.23169 0.557829098392 1.00000  
O34 O 0.65621 0.30662 -0.05970 0.557829098392 1.00000  
O35 O 0.65912 0.19754 0.02769 0.557829098392 1.00000  
O36 O 0.66048 0.09635 -0.07639 0.557829098392 1.00000  
O37 O 0.66132 0.12040 -0.26983 0.557829098392 1.00000  
O38 O 0.66202 0.24538 -0.23343 0.557829098392 1.00000  
O39 O 0.55034 0.29961 -0.17937 0.557829098392 1.00000  
O40 O 0.55219 0.07833 -0.19416 0.557829098392 1.00000  
O41 O 0.37786 0.41880 -0.41044 0.557829098392 1.00000  
O42 O 0.50509 0.41334 -0.40569 0.557829098392 1.00000  
O43 O 0.64147 0.39114 -0.42750 0.557829098392 1.00000  
O44 O 0.36506 0.18718 -0.38359 0.557829098392 1.00000  
O45 O 0.50172 0.20171 -0.39509 0.557829098392 1.00000  
O46 O 0.62994 0.19723 -0.40843 0.557829098392 1.00000  
O47 O 0.44837 -0.00226 -0.21689 0.557829098392 1.00000  
O48 O 0.65387 -0.00214 -0.20702 0.557829098392 1.00000  
C5 C 0.71101 0.48992 -0.01282 16.5809073832 0.93337  
C6 C 0.22847 0.53856 -0.01752 16.5809073832 0.93337  
C4 C 0.82371 0.50085 0.05021 16.5809073832 0.93337  
C2 C 0.30172 0.44442 0.00800 16.5809073832 0.93337  
C3 C 0.81510 0.56856 0.05637 16.5809073832 0.93337  
C1 C 0.75470 0.59747 0.02726 16.5809073832 0.93337  
C8 C 0.21303 0.14737 0.76076 22.5394538431 0.54944  
C9 C 0.21303 0.08846 0.70666 22.5394538431 0.54944  
C10 C 0.21303 0.08337 0.91158 22.5394538431 0.54944  
C11 C 0.21303 0.14436 0.86321 22.5394538431 0.54944  
C12 C 0.21303 0.02742 0.85731 22.5394538431 0.54944  
C13 C 0.21303 0.02742 0.75525 22.5394538431 0.54944  
W1 O 0.71704 0.73433 0.12855 15.3066251725 1.00000  
W2 O 0.42098 0.50336 -0.00245 15.2497763471 1.00000  
CL-2 CL 0.21303 -0.05442 0.71269 22.5394538431 0.54947  
CL-1 CL 0.09900 0.53573 0.92100 16.5809073832 0.93333

OUTLOOKS IN EARTH AND PLANETARY MATERIALS

Highlighting the capability of zeolites for agro-chemicals contaminants removal from aqueous matrix: Evidence of 2-ethyl-6-methylaniline adsorption on ZSM-12

ELISA RODEGHERO<sup>1</sup>, LUISA PASTI<sup>2,\*</sup>†, GIUSEPPE NUNZIANTE<sup>1</sup>, TATIANA CHENET<sup>2</sup>, LARA GIGLI<sup>3</sup>, JASPER R. PLAISIER<sup>3</sup>, AND ANNALISA MARTUCCI<sup>4,\*</sup>

<sup>1</sup>Department of Physics and Earth Sciences, University of Ferrara, via Saragat 1, I-44100 Ferrara, Italy

<sup>2</sup>Department of Chemistry and Pharmaceutical Sciences, University of Ferrara, I-44100 Ferrara, Italy

<sup>3</sup>Elettra-Sincrotrone Trieste, I-34149, Basovizza Trieste, Italy

<sup>4</sup>Department of Physics and Earth Sciences, University of Ferrara, via Saragat 1, I-44100 Ferrara, Italy; Orcid 0000-0002-6467-881X

ABSTRACT

Chloroacetanilides and their degradation products are frequently detected in surface and subsurface water due to their relatively high water solubility and their high potential to leach and migrate through the soil and contaminate groundwater.

In this study, we explored for the first time the capability of ZSM-12 zeolite for 2-ethyl-6-methylaniline [C<sub>2</sub>H<sub>5</sub>C<sub>6</sub>H<sub>3</sub>(CH<sub>3</sub>)NH<sub>2</sub>, labeled EMA] removal from water by combining chromatographic, thermogravimetric, and synchrotron X-ray powder diffractometric techniques. Rietveld refinement revealed the incorporation of about 4 EMA molecules per unit cell, in very good agreement with the weight loss given by TG analyses and with the saturation capacity determined by the adsorption isotherms.

The formation of supramolecular complexes mediated by co-adsorbed water and their strong interaction to framework O atoms confers stability to the pollutants in the zeolite cages. This prevents adsorbed molecules from desorbing as well as the entering of other competitive molecules. The rapid kinetics combined with the good adsorption capacity makes ZSM-12 a promising material to control and minimize water pollution from acetanilide compounds as well as other agro-chemicals contaminants.

**Keywords:** 2-ethyl-6-methylaniline adsorption, water pollution, ZSM-12, chromatography, thermogravimetry, synchrotron X-ray powder diffraction; Microporous Materials: Crystal-chemistry, properties, and utilizations

INTRODUCTION

The degradation of water resources is an increasing problem worldwide, and many efforts have been made to control point source pollution from homes and industry. However, water pollution from agriculture is becoming a major concern due to the widespread use of agro-chemicals in modern agriculture. Indeed, many of these substances have (Otero et al. 2013, 2014) harmful effects on aquatic organisms, insects, and mammals, and they persist in the aquatic systems for many years after their application (Shukla et al. 2006). In Europe, pesticides are considered hazardous substances as specified in current directives regarding water (Levitan 2000). The World Health Organization reported that ~3 000 000 cases of pesticide poisoning and 220 000 deaths occur in developing countries (World Health Organization 2010).

Drinking water quality standard should not exceed 1×10<sup>6</sup> µg/L for an individual pesticide concentration and 5×10<sup>6</sup> µg/L for the total pesticide concentration (Commission Directive 98/83/EC 1998). Due to the diffuse nature of contamination from agro-chemicals and the mobility of these compounds in the environment, their presence is difficult to control.

The pesticides are transferred from soil to water through vari-

ous pathways (e.g., surface runoff, subsurface, and groundwater flows) either in solution or adsorbed onto particles. (Boithias et al. 2011). Among the agro-chemicals mentioned above, Metolachlor [C<sub>15</sub>H<sub>22</sub>ClNO<sub>2</sub>, 2-chloro-N-(2-ethyl-6-methylphenyl)-N-(2-methoxy-1-methylethyl)acetamide, labeled MTC] and its metabolites are frequently detected in surface and subsurface water (from 1×10<sup>6</sup> µg/L to more than 1×10<sup>9</sup> µg/L) (Traub-Eberhard et al. 1995; Gaynor et al. 1995) due to its relatively high water solubility (530 mg/L) that facilitates leaching, migrating through the soil, and contaminating groundwater (Nennemann et al. 2001). Moreover, chloroacetanilide degradation products such as 2-ethyl-6-methylaniline [C<sub>2</sub>H<sub>5</sub>C<sub>6</sub>H<sub>3</sub>(CH<sub>3</sub>)NH<sub>2</sub>, labeled EMA] are more or equally toxic compared to their parent pesticide compound (Fava et al. 2000, 2001; Kimmel et al. 1986; Osano et al. 2002a, 2002b) and are promutagens in the Ames test (Kimmel et al. 1986). The rate and the extent of chloroacetanilide degradation strongly depend on environmental conditions such as temperature (Osano et al. 2003), moisture content (Gerstl et al. 1998), concentration of hydroxyl radicals (OH) (Webster et al. 1998), and microbial activity (Bollag et al. 1986; Liu et al. 1995; Stamper and Tuovinen 1998). Therefore, it is mandatory to develop mitigation measures able to prevent diffusion of pollutants into environment to reduce their impact (Zhang and Zhang 2011). Many treatment strategies have been proposed for the removal of these pollutants, including biological, chemical,

\* E-mail: mrs@unife.it and psu@unife.it

† Special collection papers can be found online at <http://www.minsocam.org/MSA/AmMin/special-collections.html>.

and/or physical methods (Bezbaruah et al. 2009; Zadaka et al. 2009; Liu et al. 2010; Kovaivos et al. 2011; Coffinet et al. 2012; Elsayed et al. 2014).

Despite the availability of various clean up methods, adsorption by organic or inorganic sorbent media is still preferred due the high removal efficiency and reduced operational cost. Activated charcoal, mesoporous phenolic resin, and mesoporous carbon are characterized by high surface area and narrow mesopore distribution thus exhibiting good properties as adsorbents depending on their particle size, porosity, degree of carbonization, and method of activation (Jiang et al. 2006; López-Ramon et al. 2007; Bakouri et al. 2009). Organoclay and organo/layered double hydroxides have also been proven to be suitable in reducing and even preventing the environmental impact caused by some pesticides, particularly metolachlor (Reichle 1986; Rives 2001; Wang et al. 2005; Otero et al. 2012; Chaara et al. 2011; Si et al. 2009; Nennemann et al. 2001; Mastroicco et al. 2009; Singh 2009).

As an alternative, zeolites have been investigated for the removal of pesticides from water (De Smedt et al. 2015). These microporous materials represent a promising candidate for the environmentally friendly removal of agro-chemicals from the water. The main advantages of zeolites are related to the structural and chemical features of their framework, which can be modulated by varying the pore opening and the  $\text{SiO}_2/\text{Al}_2\text{O}_3$  ratio (SAR). Typically, these materials have a large surface area, high specific capacity, and are characterized by high mechanical, biological, and chemical stability and strong adsorption selectivity. In particular, it has been demonstrated that high-silica zeolites (HSZs) show strong selectivity (Vilaça et al. 2011; Martucci et al. 2012a, 2012b; Pasti et al. 2012; Arletti et al. 2012; Datt et al. 2012; Martucci et al. 2013a, 2013b; Kyzas et al. 2013; Rakić et al. 2013; Blasioli et al. 2014) and very fast kinetics in the adsorption of organic species. Moreover, their high stability in water and their resistance to aggressive chemical solutions make these materials a promising and efficient alternative to other reactive adsorbent media (Rossner et al. 2009; Damjanović et al. 2010; Amorim et al. 2012; Braschi et al. 2012; Sacchetto et al. 2013; Datt et al. 2013; Pasti et al. 2013; Martucci et al. 2013a, 2013b, 2014, 2015; Leardini et al. 2014; Genç and Dogan 2015; Pasti et al. 2016; Rodeghero et al. 2017a, 2017b). Exhausted zeolites can be easily regenerated and reused thus preventing the disposal of contaminated materials. The most common regeneration techniques include thermal (Wang et al. 2006; Leardini et al. 2014; Rodeghero et al. 2017a, 2017b), chemical and extraction (Jung et al. 2004; Wang et al. 2006; Braschi et al. 2016), electric/electrochemical (Zhang et al. 2013), photochemical treatments (Litter and Quici 2010; Braschi et al. 2016), as well as microwave (Polaert et al. 2010; Zendehdel et al. 2014) and ultrasound methods (Wang and Yang 2007). Recently, the adsorption capacity of thermally regenerated zeolites was demonstrated to be very close to the initial loading capacity. This shows that the heating process does not affect the adsorption properties of regenerated samples (Leardini et al. 2014; Martucci et al. 2015b; Braschi et al. 2016). In the present work, we explore for the first time the capability of ZSM-12 to remove contaminant metabolites from an aqueous matrix. For this purpose, EMA was chosen as target metabolite. ZSM-12 zeolite (MTW topology) was chosen as its

channel system could be an attractive host to incorporate EMA. The structure of the ZSM-12 host is reported in Figure 1. The framework has a one-dimensional pore system delimited by 12-membered rings (12MRs) (Baerlocher et al. 2007)  $\{[010] 5.6 \times 6.0 \text{ \AA}\}$ , which is slightly larger than that of MFI zeolites  $\{[100] 5.1 \times 5.5 \leftrightarrow [010] 5.3 \times 5.6\}$ . The regular one-dimensional nanochannel system imposes severe space restrictions and geometrical constraints on the guest species thus preventing inserted molecules from escaping and other competitive molecules from entering (Rosinski and Rubin 1983; Trewella et al. 1985; Fyfe et al. 1988; Corma 1997).

To date, this zeolite is used as an efficient catalyst for the shape selective conversion of long hydrocarbon molecules such as the isomerization and alkylation of aromatic hydrocarbons (Perego et al. 1996; Millini et al. 1998; Pazzucconi et al. 2000; Yoo et al. 2003; Bortolini et al. 2013). It has not yet been used as a sorbent.

To assess the capability of ZSM-12 for removal of EMA from the aqueous matrix, chromatographic, thermogravimetric, and synchrotron X-ray powder diffractometric techniques were applied. In particular, to evaluate the structural basis for the EMA sorption, characterization by X-ray powder diffraction was carried out on the as-synthesized, the calcined and the EMA-loaded ZSM-12, respectively. The complexity of this host-guest system highlights the importance of understanding and controlling not only the interactions of guests with the host but also the interactions between guests and the influence of co-adsorbed molecules. The results described here provide the basis for understanding the fate and transport mechanisms of EMA in the environment and in particular in zeolite soil and water applications.

## EXPERIMENTAL METHODS

### Materials and methods

**Synthesis.** The hydrothermal ZSM-12 synthesis (SAR = 38) was carried out following the protocol proposed by Millini et al. (2004) using NaOH, aluminum source  $[\text{Al}_2(\text{SO}_4)_3 \cdot 16\text{H}_2\text{O}]$  and 6-azonia-spiro-[5,5]-undecane as structure directing agent (SDA). The bromide salt of SDA was dissolved in demineralized water and then exchanged into the hydroxide form by electro dialysis. The resulting solution was heated at 353 K and tetraethylortosilicate (TEOS, Aerosil 200) was gradually dropped into the solution under stirring. After aging at room temperature for 4 h,

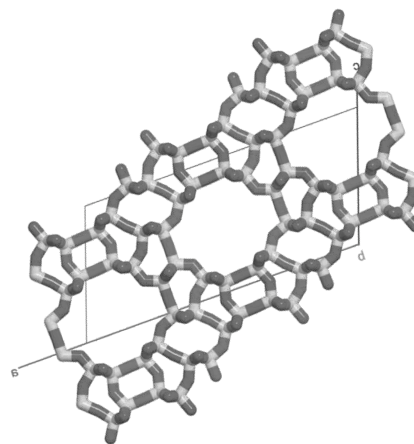


FIGURE 1. ZSM-12 (MTW topology) one-dimensional pore system view along [010].

the mixture was filtered and washed with deionized water and dried overnight at 423 K. The solid product was then calcined by raising the temperature from room temperature to 600 °C in 1 h, then holding at 600 °C for 4 h. Finally, adsorbents were kept at room temperature for 3 h. Air circulation was maintained during heating. The samples were kept in a desiccator and used within 2 days after thermal treatment.

**Batch adsorption.** The adsorption isotherm was determined using the batch method. Batch experiments were carried out in duplicate in 20 mL crimp top reaction glass flasks sealed with PTFE septa (Supelco, Bellefonte, Pennsylvania, U.S.A.). The flasks were filled to have the minimum headspace and a solid/solution ratio of 1:2 (mg:mL<sup>-1</sup>) was employed. After equilibration, for 24 h at a temperature of 25.3 ± 0.5 °C under stirring, the solids were separated from the aqueous solution using centrifugation (14 000 rpm for 30 min).

Chromatographic determinations of EMA before and after the contact with ZSM-12 were made on a Waters HPLC system (Waters Associates, Milford, Massachusetts) equipped with a binary pump and a DAD UV-VIS detector. The column was a Kromasil Eternity 0.46 × 15 cm C18-packed, particle diameter 5 μm, (Eka Nobel). An injector (7725i, Rheodyne, Cotati, California, U.S.A.) with a 20 μL loop was employed. The mobile phase was a mixture of water and ACN, 50:50% v/v. Solvents were filtered before use (Nylon 66 membranes, 0.45 μm, Supelco, Bellefonte, Pennsylvania, U.S.A.). The concentration of EMA was determined by measuring UV absorbance and by interpolating values against previously constructed calibration curves.

**Thermal analyses.** Thermal analyses (TG and DTA) of both calcined (ZSM-12-C) and EMA loaded ZSM-12 (ZSM-12-EMA) were performed on a STA 409 PC LUX-X-Netzsch. The measurements were carried out in air flow with a heating rate using a 10 °C/min heating rate up to 900 °C.

### X-ray powder diffraction data collection and refinement strategy

The XRD patterns of calcined ZSM-12 before and after EMA loading were collected at the MCX beamline of Elettra-Sincrotrone Trieste, (Italy) using a fixed wavelength of 0.827 Å (Rebuffi et al. 2014) (Fig. 2).

The powders were loaded and packed in a 0.5 mm boron capillary, mounted on a standard goniometric head, and spun during data collection. The diffraction patterns were recorded through a scintillation detector in the 3–50 °2θ range. Structural refinements were performed by full profile Rietveld analysis using the GSAS package (Larson and Von Dreele 2000) with the EXPGUI interface (Toby 2001). The refinements of both ZSM-12-C and ZSM-12-EMA samples were performed in the *C2/c* space group using the starting framework model reported in Fyfe et al. (1990). The background profiles were first edited manually and further empirically fitted using a Chebyshev polynomial with 26 variable coefficients. The Bragg peak profile was modeled using a pseudo-Voigt function with 0.01% cut-off peak intensity. The scale factor, 2θ-zero shift, and unit-cell parameters were accurately refined. Table 1 reports the refinement parameters for all samples investigated. The extra-framework sites were located by difference Fourier maps and H-atoms were not considered within the structure refinement due to their low scattering factors. The thermal displacement parameters were constrained in the following way: the same value for all the tetrahedral atoms, a second value for all the framework oxygen atoms, and a third one for the extraframework atoms. Soft restraints were applied on the tetrahedral cations and coordinated framework oxygen atom distances during the first stages of refinement and left free in the last cycles. Selected bond angles are listed in Table 2. The detailed structural refinements of both calcined and EMA loaded ZSM-12 are described separately in the following section.

## RESULTS AND DISCUSSION

### Adsorption from aqueous solutions

The data obtained from batch experiments at room temperature were fitted to the Langmuir isotherm model (Foo and Hameed 2010). Figure 3 shows the adsorption isotherm of EMA on zeolite ZSM-12: it can be observed that the adsorption isotherm is concave, and it is characterized by a steep initial zone and a saturation zone (plateau adsorbed concentration). The concave shape of the adsorption isotherm indicates a favorable adsorption and therefore a practical applicability of ZSM-12 in adsorption-based technologies. The Langmuir model describes an adsorption process on a homogenous surface, and it does not

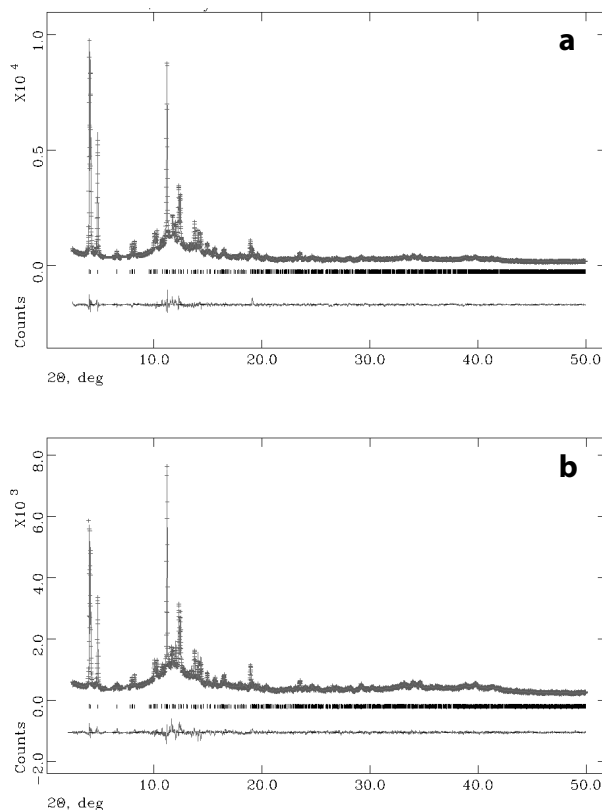


**FIGURE 2.** Representative Rietveld refined pattern for ZSM-12-c (a) and ZSM-12-EMA (b), respectively. Observed (crosses), calculated (green line), Bragg diffraction peaks (vertical bars), and the difference profile (violet line) obtained by GSAS evaluation program.

**TABLE 1.** Crystal data and refinement parameters for ZSM-12-C and ZSM-12-EMA, respectively

	ZSM-12-C <i>C2/c</i>	ZSM-12-EMA <i>C2/c</i>
Space group	<i>C2/c</i>	<i>C2/c</i>
<i>a</i> (Å)	24.9984(11)	29.993(7)
<i>b</i> (Å)	5.0336(1)	5.0341(9)
<i>c</i> (Å)	24.3844(8)	24.377(5)
$\beta$	107.9(1)	107.9(2)
<i>V</i> (Å <sup>3</sup> )	2919.1(2)	2918.9(2)
Incident radiation wavelength (Å)	0.82700	0.82700
Refined pattern 2θ range (°)	3.00–50.00	3.00–50.00
<i>R</i> <sub>wp</sub> (%)	7.40	7.71
<i>R</i> <sub>p</sub> (%)	6.00	6.05
<i>R</i> <sub>f</sub> <sup>2</sup> (%)	9.10	11.30
No. of contributing reflections	1889	1797
<i>N</i> <sub>obs</sub>	9312	9357
<i>N</i> <sub>var</sub>	101	152

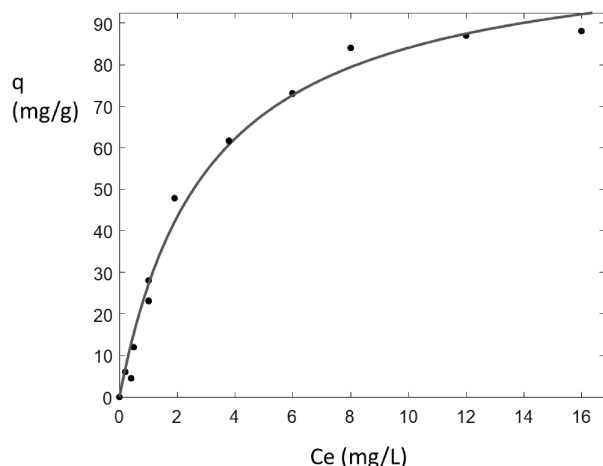
take into account adsorbate-adsorbate interactions and adsorbate-solvent interactions. Furthermore, the model represents an adsorbent characterized by energetically equivalent sites. This hypothesis can, at least in first approximation, be satisfied by considering that the interaction energies of different sites are close enough to each other to be equivalent to a single site characterized by an adsorption energy and an adsorption constant corresponding to the average values of those of all adsorption sites on the adsorbent material (Ruthven 1984). This model has been applied to describe the adsorption on different zeolites

**TABLE 2.** Selected angles (°) of 2-ethyl-6-methylaniline in ZSM-12-EMA

ZSM-12-EMA	Angle (°)
C2-C1-C3	121.2(1)
C2-C1-N	119.7(1)
C3-C1-N	108.2(1)
C1-C2-C3	119.5(1)
C1-C2-C4	122.3(1)
C3-C2-C4	118.2(1)
C1-C3-C2	119.3(1)
C1-C3-C5	111.6(1)
C2-C3-C5	117.2(1)
C3-C5-C6	114.7(1)

**TABLE 3.** Estimated parameter for Langmuir model [ $q = (q_b b) / (1 + b)$ ]; the confidence bonds at 95% of probability are in parentheses

$q_b$ (mg/g)	$b$ (g/L)	$R^2$
109.7 (97.65, 121.8)	0.326 (0.2179, 0.4341)	0.9869

**FIGURE 3.** Adsorption isotherms of EMA on ZSM-12 at 298.5 K.

of many organic compounds both from gas and liquid phases (Rodeghero et al. 2017a, 2017b; Rodeghero et al. 2016; Perego et al. 2013; Leardini et al. 2014).

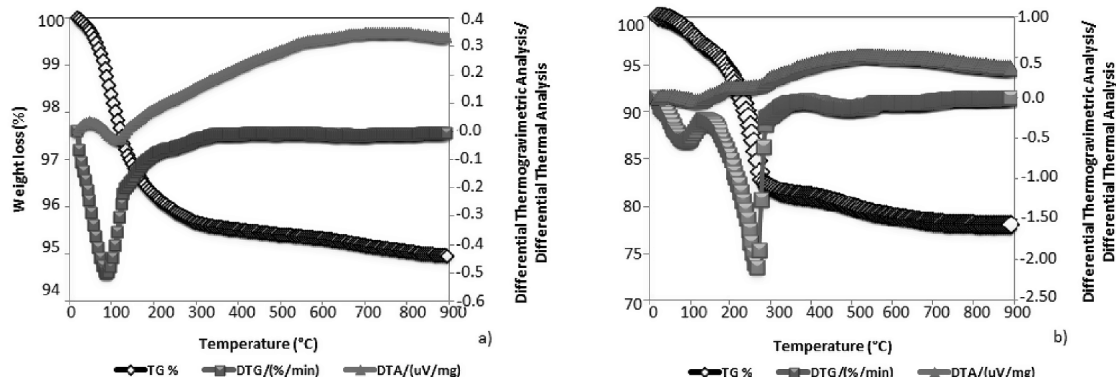
Table 3 summarizes the adsorption values obtained from the adsorption of EMA on ZSM-12. The high determination coefficient confirms that the Langmuir model represents the data well, and, therefore, that EMA molecules adsorb on sites of zeolite having similar energy values. This finding, however, is not sufficient to assess which sites of the framework are participating in the adsorption process. The estimated saturation capacity of ZSM-12 is lower than that found for S-Metolachlor

on organosilicas, (Kumar et al. 2013; Otero et al. 2014; López et al. 2015). However, the adsorption onto ZSM-12 seems to be more favorable than that on organosilica in the low concentration range, which is more similar to environmental conditions. (Otero et al. 2013). Additionally, the saturation capacity (see Table 3) of EMA on ZSM-12 is higher than that reported for Metolachlor onto activated carbons (Kumar et al. 2013). Therefore, ZSM-12 seems to be a promising adsorbent material for the removal of pesticide metabolites from an aqueous matrix. To gain more information on the ZSM-12 sites involved in the adsorption process, a structural analysis was performed.

### Thermal and structural analyses

To better understand the ZSM-12 finding, the structure of the sample after calcination (ZSM-12-C) was refined starting from the structural model reported by Fyfe et al. (1990) taken from the International Zeolite Association (IZA) website (calcined ZSM-12, MTW framework). A monoclinic unit cell with space group  $C2/c$  was used with the initial unit-cell dimensions of  $a = 24.8633(3)$  Å,  $b = 5.01238(7)$  Å,  $c = 24.3275(7)$  Å,  $\beta = 107.7215(6)^\circ$ , cell formula units  $Z = 1$  (Fig. 4a). Our refinement is in good agreement with others (Fyfe and Brouwer 2006; Brouwer 2008; Kasunič et al. 2009). Figure 4b shows TG/DTG/DTA curves of the title compound. The first weight loss (as well as endothermic peak in DTA) from room temperature to about 105 °C can be related to the desorption of physically adsorbed water from the surface (~1.8% dry wet/wet). The residual one (~3.0% dry wet/wet) comprises the desorption of carbonaceous residue from SDA calcination escaping from the micropores.

In both calcined ZSM-12 and EMA loaded ZSM-12, the absence of additional diffraction peaks as well as of  $C$ -centering forbidden peaks indicates that the space group does not change after adsorption. The  $C2/c$  space group was maintained in ZSM-12-EMA structure refinement, which was performed starting from the framework atomic coordinates obtained for ZSM12-C (all coordinates are available in the CIF<sup>1</sup> file). Notwithstanding this, the position of diffraction peaks (and consequently,

**FIGURE 4.** ZSM-12-C (a) and ZSM-12-EMA (b) TG/DTG/DTA curves.

the unit-cell parameters) in the two patterns are not remarkably modified [ $a = 24.9984(11)$ ,  $b = 5.03362(14)$ ,  $c = 24.3844(8)$ ,  $\beta = 107.9428(26)$ , Cell volume = 2919.12(19) in ZSM-12-C;  $a = 24.993(7)$ ,  $b = 5.0341(9)$ ,  $c = 24.377(5)$ ,  $\beta = 107.879(18)$ , cell volume = 2918.9(12) in ZSM-12-EMA, respectively]. The difference electron density map revealed an electron cloud in the ZSM-12 channels whose molecular geometry is very close to the EMA ideal one. It reveals the presence of seven partially occupied extra-framework sites (C1, C2, C3, C4, C5, C6, and N, respectively), localized inside the 12MR (Fig. 5a) fitting the 12-ring aperture very well. Reasonable values for C-C-C, N-C-C angles were obtained without using the rigid model approach (Table 2).

The refined distances of EMA from the framework oxygen atoms suggest that the organic molecules interact with the framework [i.e., N-O9 3.01(1) Å, N-O11 3.16(1) Å, C4-O6 2.87(1) Å, C6-O6 3.15(1), and 2.51(1) Å, respectively], and these interactions are mediated by another extraframework site detected in the difference Fourier map that was assigned to co-adsorbed water [W-O9 2.53(1) Å, W-O11(1) 2.67 Å, W-O6 2.99(1) Å, W-N 2.82(1) Å]. Furthermore, the occupancy of EMA and water atoms refined to 4.0 (14% in dry weight) and 4.5 molecules (2% in dry weight) per unit cell, which correlates well with the weight loss observed by thermogravimetric analysis. Figure 5b shows the TG/DTG/DTA curves of the loaded sample. Also, in this case, the first weight loss (as well as an endothermic peak in DTA) from room temperature to about 105 °C can be related to the desorption of physically adsorbed water/EMA from the surface (~3.0% dry wet/wet). The residual one (~17.0.0% dry wet/wet) comprises the desorption of extraframework species (EMA and water molecules) from within the channels.

Water molecules interact with both the NH<sub>2</sub>- and methyl groups of EMA thus forming oligomers bonded to framework O atoms (Fig. 6). The occurrence of such molecular complexes

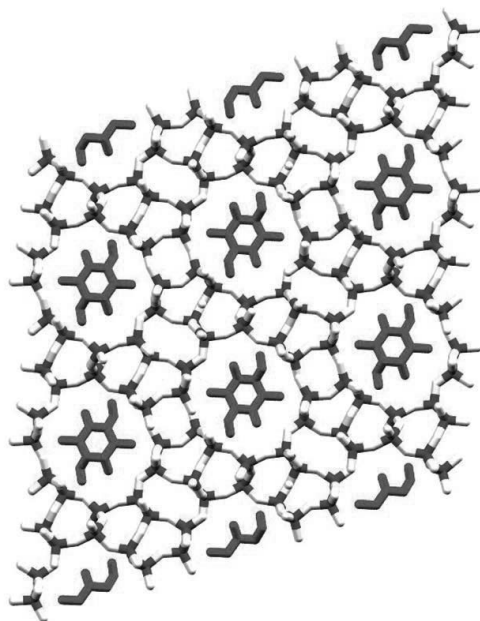


FIGURE 5. ZSM-12-EMA structure view along [010].

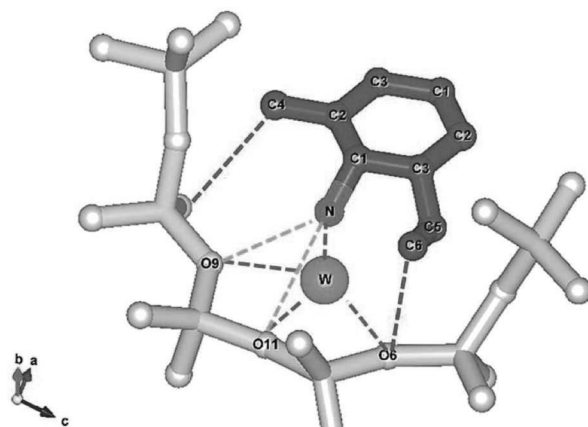


FIGURE 6. Interactions of water molecules-EMA oligomers with framework O atoms.

was also detected in hydrophobic zeolites loaded with non-polar species (Pasti et al. 2012; Martucci et al. 2012, 2015; Arletti et al. 2012; Leardini et al. 2014; Rodeghero et al. 2017a, 2017b). They “immobilize” the pollutants in the cages thus preventing inserted molecules from desorbing as well as the entering of other competitive molecules.

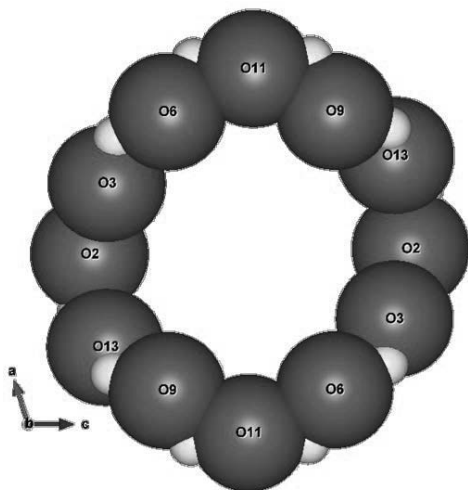
After EMA adsorption, the analysis of rings was useful to calculate pore diameter variations in ZSM-12. As reported by Bermúdez and Sastre (2017) “Pores differ from rings in that pores are those rings which define channels; thus, ‘pores’ are a subgroup of ‘rings’.” In this work the ring diameters have been calculated considering the distance between two opposite oxygen atoms and then subtracting twice the IZA recommended value of the oxygen radius (1.35 Å). This information is crucial for a deep knowledge of both transport properties as well as zeolite-adsorbate and adsorbate-adsorbate interactions (Bermúdez and Sastre 2017; Foster et al. 2006; Curtis and Deem 2003; Haldoupis et al. 2011; Krishna and van Baten 2012).

The ZSM-12-EMA diameters of 12-rings become larger and circular with respect to the ZSM-12-C ones and the Crystallographic Free Areas (C.F.A.) of the rings undergo a marked increase to best fit the organic molecule in the 12-ring aperture (Fig. 7).

## IMPLICATIONS

The increased awareness of soils, water, and groundwater contamination by chloroacetanilide herbicides has pushed research toward economically feasible and environmentally friendly remediation technologies. Adsorption is a simple and economical procedure involved in the water treatment that is able to control the mobility, fate, bioavailability, and reactivity of emerging organic pollutants in the environment. Zeolites show high surface area, high specific capacity, mechanical, biological/chemical stability, and high adsorption selectivity thus representing economically feasible and environmentally friendly adsorbent media capable of removing these pollutants from water.

In this work, the efficiency of ZSM-12 zeolite for agro-chemicals contaminant (2-ethyl-6-methylaniline, EMA) removal from aqueous matrix was highlighted by chromatographic, thermogravimetric, and synchrotron X-ray powder diffractometric techniques.



ZSM-12-C	Distance (Å)	Free Diameter (Å)
O11-O11	9.297	6.597
O6-O6	8.022	5.322
O3-O3	8.534	5.834
O2-O2	8.134	5.434
O9-O9	8.863	5.737
CFA (Å <sup>2</sup> )=πr <sup>2</sup>	r=mean radius=2.892	26.269
ELLIPTICITY (ε)	ε=(O11-O11)/(O2-O2)	1.159

ZSM-12-EMA	Distance (Å)	Free Diameter (Å)
O11-O11	9.915	7.215
O6-O6	8.822	6.122
O3-O3	8.645	5.945
O2-O2	8.733	6.033
O9-O9	8.863	6.163
CFA (Å <sup>2</sup> )=πr <sup>2</sup>	r=mean radius=3.147	31.113
ELLIPTICITY (ε)	ε=(O11-O11)/(O3-O3)	1.147

FIGURE 7. Experimental diameters of 12-rings in four ZSM-12-C and ZSM-12-EMA, respectively.

We have herein demonstrated that synthetic ZSM-12 is a good candidate for pesticide metabolite EMA removal. Indeed, its adsorption isotherm follows a Langmuir model and shows a favorable adsorption. In addition, the saturation capacity of ZSM-12 is higher than that of other widely employed adsorbent materials such as activated carbon and mesoporous organosilica. Indeed, the saturation capacity of granular activated was found to be equal to 3.3 mg/g (Kumar et al. 2013). On the other hand, in mesoporous organosilicas, which show very high saturation capacity (500 mg/g) the adsorption quantities on these materials do not exceed 50 mg/g with solution concentration lower than 30 mg/L<sup>1</sup>. Thus indicates a lower adsorption efficiency in concentration ranges similar to natural conditions (Otero et al. 2013). The organic molecules are effectively embedded in the zeolite framework as demonstrated from structural analysis. EMA interacts with water molecules to form oligomers that,

in turn, interact with framework atoms. The formation of these supramolecular complexes stabilizes the pollutants in the zeolite cages thus preventing adsorbed molecules from desorbing as well as the entering of other competitive molecules. All these findings contribute to an evaluation that ZSM-12 could be a promising material to control and minimize water pollution from EMA as well as other agro-chemicals contaminants.

## FUNDING

This work was supported by the Italian MIUR (PRIN2015 “ZAPPING” High-pressure nano-confinement in Zeolites: the Mineral Science know-how APPLIED to engineering of innovative materials for technological and environmental applications” (2015HK93L7)).

## REFERENCES CITED

- Amorim, R., Vilaça, N., Martinho, O., Reis, R.M., Sardo, M., Rocha, J., Fonseca, A.M., Baltazar, F., and Neves, I.C. (2012) Zeolite structures loading with an anticancer compound as drug delivery systems. *The Journal of Physical Chemistry C*, 116(48), 25642–25650.
- Arelt, R., Martucci, A., Alberti, A., Pasti, L., Nassi, M., and Bagatin, R. (2012) Location of MTBE and toluene in the channel system of the zeolite mordenite: Adsorption and host-guest interactions. *Journal of Solid State Chemistry*, 194, 135–142.
- Baerlocher, C., McCusker, L.B., and Olson, D.H. (2007) *Atlas of Zeolite Framework Types*. Elsevier.
- Bakouri, H.E., Morillo, J., Usero, J., and Quassini, A. (2009) Natural attenuation of pesticide water contamination by using ecological adsorbents: application for chlorinated pesticides included in European water framework directives. *Journal of Hydrology*, 364, 175–181.
- Bermúdez, D., and Sastre, G. (2017) Calculation of pore diameters in zeolites. *Theoretical Chemistry Accounts*, 136(10), 116.
- Bezbaruah, A.N., Thompson, J.M., and Chisholm, B.J. (2009) Remediation of alachlor and atrazine contaminated water with zero-valent iron nanoparticles. *Journal of Environmental Science and Health, Part B* 44(6), 518–524.
- Blasioli, S., Martucci, A., Paul, G., Gigli, L., Cossi, M., Johnston, C.T., Marchese, L., and Braschi, I. (2014) Removal of sulfamethoxazole sulfonamide antibiotic from water by high silica zeolites: a study of the involved host-guest interactions by a combined structural, spectroscopic, and computational approach. *Journal of Colloid and Interface Science*, 419, 148–159.
- Boithias, L., Sauvage, S., Taghavi, L., Merlina, G., Probst, J.L., and Pérez, J.M.S. (2011) Occurrence of metolachlor and trifluralin losses in the Save river agricultural catchment during floods. *Journal of Hazardous Materials*, 196, 210–219.
- Bollag, J.M., McGahen, L.L., Minard, R.D., and Liu, S.Y. (1986) Bioconversion of alachlor in an anaerobic stream sediment. *Chemosphere*, 15, 153–162.
- Bortolini, O., Cavazzini, A., Giovannini, P.P., Greco, R., Marchetti, N., Massi, A., and Pasti, L. (2013) A combined kinetic and thermodynamic approach for the interpretation of continuous flow heterogeneous catalytic processes. *Chemistry—A European Journal*, 19(24), 7802–7808.
- Braschi, I., Gatti, G., Bisio, C., Berlier, G., Sacchetto, V., Cossi, M., and Marchese, L. (2012) The role of silanols in the interactions between methyl tert-butyl ether and high-silica faujasite Y: an infrared spectroscopy and computational model study. *The Journal of Physical Chemistry C*, 116(12), 6943–6952.
- Braschi, I., Blasioli, S., Buscaroli, E., Montecchio, D., and Martucci, A. (2016) Physicochemical regeneration of high silica zeolite Y used to clean-up water polluted with sulfonamide antibiotics. *Journal of Environmental Sciences*, 43, 302–312.
- Brouwer, D.H. (2008) A structure refinement strategy for NMR crystallography: An improved crystal structure of silica-ZSM-12 zeolite from <sup>29</sup>Si chemical shift tensors. *Journal of Magnetic Resonance*, 194(1), 136–146.
- Chaara, D., Bruna, F., Ulibarri, M.A., Draoui, K., Barriga, C., and Pavlovic I. (2011) Organo/layered double hydroxide nanohybrids used to remove non ionic pesticides. *Journal of Hazardous Materials*, 196, 350–359.
- Coffinet, S., Rifai, A., Genty, C., Souissi, Y., Bourcier, S., Sablier, M., and Bouchonnet, S. (2012) Characterization of the photodegradation products of metolachlor: Structural elucidation, potential toxicity and persistence. *Journal of Mass Spectrometry*, 47(12), 1582–1593.
- Directive, C. (1998) On the quality of water intended for human consumption. *Official Journal of the European Communities*, 330, 32–54.
- Corma, A. (1997) From microporous to mesoporous molecular sieve materials and their use in catalysis. *Chemical Reviews*, 97(6), 2373–2420.
- Curtis, R.A., and Deem, M.W. (2003) A statistical mechanics study of ring size, ring shape, and the relation to pores found in zeolites. *Journal of Physical Chemistry B*, 107, 8612–8620.
- Damjanović, L., Rakić, V., Rac, V., Stošić, D., and Auroux, A. (2010) The investigation of phenol removal from aqueous solutions by zeolites as solid adsorbents.

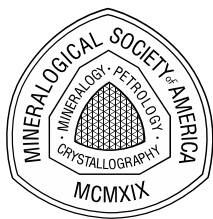
- Journal of Hazardous Materials, 184(1-3), 477–484.
- Datt, A., Fields, D., and Larsen, S.C. (2012) An experimental and computational study of the loading and release of aspirin from zeolite HY. *Journal of Physical Chemistry C*, 116(40), 21,382–21,390.
- Datt, A., Burns, E.A., Dhuna, N.A., and Larsen, S.C. (2013) Loading and release of 5-fluorouracil from HY zeolites with varying SiO<sub>2</sub>/Al<sub>2</sub>O<sub>3</sub> ratios. *Microporous and Mesoporous Materials*, 167, 182–187.
- De Smedt, C., Ferrer, F., Leus, K., and Spanoghe, P. (2015) Removal of pesticides from aqueous solutions by adsorption on zeolites as solid adsorbents. *Adsorption Science and Technology*, 33(5), 457–485.
- Elsayed, O.F., Maillard, E., Vuilleumier, S., and Imfeld, G. (2014) Bacterial communities in batch and continuous-flow wetlands treating the herbicide S-metolachlor. *Science of the Total Environment*, 499, 327–335.
- Fava, L., Bottoni, P., Crobe, A., and Funari, E. (2000) Leaching properties of some degradation products of alachlor and metolachlor. *Chemosphere*, 41(9), 1503–1508.
- Fava, L., Bottoni, P., Crobe, A., Barra Caracciolo, A., and Funari, E. (2001) Assessment of leaching potential of aldicarb and its metabolites using laboratory studies. *Pesticide Management Science*, 57(12), 1135–1141.
- Foo, K.Y., and Hameed, B.H. (2010) Insights into the modeling of adsorption isotherm systems. *Chemical Engineering Journal*, 156(1), 2–10.
- Foster, M.D., Rivin, I., Treacy, M.M.J., and Delgado-Friedrichs, O. (2006) A geometric solution to the largest-free-sphere problem in zeolite frameworks. *Microporous and Mesoporous Materials*, 90, 32–38.
- Fyfe, C.A., and Brouwer, D.H. (2006) Optimization, standardization, and testing of a new NMR method for the determination of zeolite host—organic guest crystal structures. *Journal of the American Chemical Society*, 128(36), 11,860–11,871.
- Fyfe, C.A., Strobl, H., Kokotailo, G.T., Pasztor, C.T., Barlow, G.E., and Bradley, S. (1988) Correlations between lattice structures of zeolites and their <sup>29</sup>Si MAS NMR spectra: zeolites KZ-2, ZSM-12, and beta. *Zeolites*, 8, 132–136.
- Fyfe, C.A., Gies, H., Kokotailo, G.T., Marler, B., and Cox, D.E. (1990) Crystal structure of silica-ZSM-12 by the combined use of high-resolution solid-state MAS NMR spectroscopy and synchrotron X-ray powder diffraction. *Journal of Physical Chemistry*, 94, 3718–3721.
- Gaynor, J.D., Mactavish, D.C., and Findlay, W.I. (1995) Atrazine and metolachlor loss in surface and subsurface runoff from three tillage treatments in corn. *Journal of Environmental Quality*, 24, 246–256.
- Genç, N., and Dogan, E.C. (2015) Adsorption kinetics of the antibiotic ciprofloxacin on bentonite, activated carbon, zeolite, and pumice. *Desalination and Water Treatment*, 53(3), 785–793.
- Gerstl, Z., Nasser, A., and Mingelgrin, U. (1998) Controlled release of pesticides into soils from clay-polymer formulations. *Journal of Agricultural and Food Chemistry*, 46(9), 3797–3802.
- Haldoupis, E., Nair, S., and Sholl, D.S. (2011) Pore size analysis of >250,000 hypothetical zeolites. *Physical Chemistry Chemical Physics*, 13(11), 5053–5060.
- Jiang, H., Adams, C., Graziano, N., Roberson, A., McGuire, M., and Khari, D. (2006) Occurrence and removal of chloro-s-triazines in water treatment plants. *Environmental Science and Technology*, 40(11), 3609–3616.
- Jung, J.Y., Chung, Y.C., Shin, H.S., and Son, D.H. (2004) Enhanced ammonia nitrogen removal using consistent biological regeneration and ammonium exchange of zeolite in modified SBR process. *Water Research*, 38(2), 347–354.
- Kasunić, M., Legiša, J., Meden, A., Logar, N.Z., Beale, A.M., and Golobić, A. (2009) Crystal structure of pure-silica ZSM-12 with tetraethylammonium cations from X-ray powder diffraction data. *Microporous and Mesoporous Materials*, 122, 255–263.
- Kimmel, E.C., Casida, J.C., and Ruzo, L.O. (1986) Formamide insecticides and chloroacetanilide herbicides: disubstituted anilines and nitrosobenzenes as mammalian metabolites and bacterial mutagens. *Journal of Agricultural and Food Chemistry*, 34, 157–161.
- Kovaios, I.D., Paraskeva, C.A., and Koutsoukos, P.G. (2011) Adsorption of atrazine from aqueous electrolyte solutions on humic acid and silica. *Journal of Colloid and Interface Science*, 356(1), 277–285.
- Krishna, R., and van Baten, J.M. (2012) Investigating the relative influences of molecular dimensions and binding energies on diffusivities of guest species inside nanoporous crystalline materials. *The Journal of Physical Chemistry C*, 116(44), 23556–23568.
- Kumar, Y.B., Singh, N., and Singh, S.B. (2013) Removal of atrazine, metribuzin, metolachlor and alachlor by granular carbon. *Journal of Environmental and Analytical Toxicology*, 3(7), 1–5.
- Kyzas, G.Z., Kostoglou, M., Lazaridis, N.K., Lambropoulou, D.A., and Bikiaris, D.N. (2013) Environmental friendly technology for the removal of pharmaceutical contaminants from wastewaters using modified chitosan adsorbents. *Chemical Engineering Journal*, 222, 248–258.
- Larson, A.C., and Von Dreele, R.B. (2000) General Structure Analysis System (GSAS). Los Alamos National Laboratory Report LAUR 86-748.
- Leardini, L., Martucci, A., Braschi, I., Blasioli, S., and Quartieri, S. (2014) Regeneration of high-silica zeolites after sulfamethoxazole antibiotic adsorption: a combined in situ high-temperature synchrotron X-ray powder diffraction and thermal degradation study. *Mineralogical Magazine*, 78(5), 1141–1159.
- Levitani, L. (2000) “How to” and “why”: assessing the enviro-social impacts of pesticides. *Crop Protection*, 19(8-10), 629–636.
- Litter, M., and Quici, N. (2010) Photochemical advanced oxidation processes for water and wastewater treatment. *Recent Patents on Engineering*, 4(3), 217–241.
- Liu, D., Maguire, R.J., Pacepavicius, G.J., Aoyama, I., and Okamura, H. (1995) Microbial transformation of metolachlor. *Environmental Toxicology and Water Quality*, 10, 249–258.
- Liu, Y., Zhang, J., Sheng, C., Zhang, Y., and Zhao, L. (2010) Preliminary study on a new technique for wet removal of nitric oxide from simulated flue gas with an ultraviolet (UV)/H<sub>2</sub>O<sub>2</sub> process. *Energy and Fuels*, 24(9), 4925–4930.
- López, M.I., Otero, R., Esquivel, D., Jiménez-Sanchidrián, C., Fernández, J.M., and Romero-Salguero, F.J. (2015) Evaluation of different bridged organosilicas as efficient adsorbents for the herbicide S-metolachlor. *RSC Advances*, 5(31), 24,158–24,166.
- López-Ramon, M.V., Fontecha-Cámara, M.A., Alvarez-Merino, M.A., and Moreno-Castilla, C. (2007) Removal of diuron and amitrol from water under static and dynamic conditions using activated carbon in form of fiber, cloth and grains. *Water Research*, 41, 2865–2870.
- Martucci, A., Pasti, L., Marchetti, N., Cavazzini, A., Dondi, F., and Alberti, A. (2012a) Adsorption of pharmaceuticals from aqueous solutions on synthetic zeolites. *Microporous and Mesoporous Materials*, 148(1), 174–183.
- Martucci, A., Pasti, L., Nassi, M., Alberti, A., Arletti, R., Bagatin, R., Vignola, R., and Sticca, R. (2012b) Adsorption mechanism of 1,2-dichloroethane into an organophilic zeolite mordenite: a combined diffractometric and gas chromatographic study. *Microporous and Mesoporous Materials*, 151, 358–367.
- Martucci, A., Cremonini, M.A., Blasioli, S., Gigli, L., Gatti, G., Marchese, L., and Braschi, I. (2013a) Adsorption and reaction of sulfachloropyridazine sulfonamide antibiotic on a high silica mordenite: A structural and spectroscopic combined study. *Microporous and Mesoporous Materials*, 170, 274–286.
- Martucci, A., Pasti, L., Sarti, E., and Bagatin, R. (2013b) Emerging organic pollutants removal from water using high silica zeolites. *Mineralogical Magazine*, 77(5), 1699 (abstract).
- Martucci, A., Leardini, L., Nassi, M., Sarti, E., Bagatin, R., and Pasti, L. (2014) Removal of emerging organic contaminants from aqueous systems: Adsorption and location of methyl-tertiary-butylether on synthetic ferrierite. *Mineralogical Magazine*, 78(5), 1161–1176.
- Martucci, A., Braschi, I., Bisio, C., Sarti, E., Rodeghero, E., Bagatin, R., and Pasti, L. (2015a) Influence of water on the retention of methyl tertiary-butyl ether by high silica ZSM-5 and Y zeolites: A multidisciplinary study on the adsorption from liquid and gas phase. *RSC Advances*, 5(106), 86997–87006.
- Martucci, A., Rodeghero, E., Pasti, L., Bosi, V., and Cruciani, G. (2015b) Adsorption of 1,2-dichloroethane on ZSM-5 and desorption dynamics by in situ synchrotron powder X-ray diffraction. *Microporous and Mesoporous Materials*, 215, 175–182.
- Mastrociccio, M., Colombani, N., Cavazzini, A., and Pasti, L. (2009) A green and fast chromatographic method for determining organic compound mobility in soils. *Journal of Chromatography A*, 1216(40), 6802–6809.
- Millini, R., Carluccio, L., Frigerio, F., Parker, W.O.N. Jr., and Bellussi, G. (1998) Zeolite synthesis in the presence of azonia-spiro compounds as structure-directing agents. *Microporous and Mesoporous Materials*, 24(4-6), 199–211.
- Millini, R., Perego, C., Frigerio, F., Carluccio, L.C., and Bellussi, G. (2004) Azonia-spiro compounds as structure directing agents: A computational study. In Recent advances in the science and technology of zeolites and related materials: proceedings of the 14th International Zeolite Conference, Cape Town, South Africa, 25–30th April 2004, vol. 154, 275. Elsevier.
- Nennemann, A., Mishaal, Y., Nir, S., Rubin, B., Polubesova, T., Bergaya, F., van Damme, H., and Lagaly, G. (2001) Clay-based formulations of metolachlor with reduced leaching. *Applied Clay Science*, 18(5), 265–275.
- Osano, O., Admiraal, W., and Otieno, D. (2002a) Developmental disorders in embryos of the frog *Xenopus laevis* induced by chloroacetanilide herbicides and their degradation products. *Environmental Toxicology and Chemistry*, 21, 375–379.
- Osano, O., Admiraal, W., Klamer, H.J.C., Pastor, D., and Bleeker, E.A.J. (2002b) Comparative toxic and genotoxic effects of chloroacetanilides, formamidines and their degradation products on *Vibrio fischeri* and *Chironomus riparius*. *Environmental Pollution*, 119, 195–202.
- Osano, O., Nzyuko, D., Tole, M., and Admiraal, W. (2003) The fate of chloroacetanilide herbicides and their degradation products in the Nzoia Basin, Kenya. *AMBIO: A Journal of the Human Environment*, 32(6), 424–427.
- Otero, R., Esquivel, D., Ulibarri, M.A., Jiménez-Sanchidrián, C., Romero-Salguero, F.J., and Fernández, J.M. (2013) Adsorption of the herbicide S-Metolachlor on periodic mesoporous organosilicas. *Chemical Engineering Journal*, 228, 205–213.
- Otero, R., Esquivel, D., Ulibarri, M.A., Romero-Salguero, F.J., Van Der Voort, P., and Fernández, J.M. (2014) Mesoporous phenolic resin and mesoporous carbon for the removal of S-Metolachlor and Bentazon herbicides. *Chemical Engineering Journal*, 251, 92–101.
- Pasti, L., Martucci, A., Nassi, M., Cavazzini, A., Alberti, A., and Bagatin, R. (2012) The role of water in DCE adsorption from aqueous solutions onto hydrophobic

- zeolites. *Microporous and Mesoporous Materials*, 160, 182–193.
- Pasti, L., Sarti, E., Cavazzini, A., Marchetti, N., Dondi, F., and Martucci, A. (2013) Factors affecting drug adsorption on beta zeolites. *Journal of Separation Science*, 36(9–10), 1604–1611.
- Pasti, L., Rodeghero, E., Sarti, E., Bosi, V., Cavazzini, A., Bagatin, R., and Martucci, A. (2016) Competitive adsorption of VOCs from binary aqueous mixtures on zeolite. *ZSM-5*. *RSC Advances*, 6(59), 54,544–54,552.
- Pazzucconi, C.P.G., Millini, R., Frigerio, F., Mansani, R., and Rancati, D. (2000) U.S. Patent 6,147,270.
- Perego, C., Amarilli, S., Millini, R., Bellussi, G., Girotti, G., and Terzoni, G. (1996) Experimental and computational study of beta, ZSM-12, Y, mordenite and ERB-1 in cumene synthesis. *Microporous Materials*, 6(5–6), 395–404.
- Perego, C., Bagatin, R., Tagliabue, M., and Vignola, R. (2013) Zeolites and related mesoporous materials for multi-talented environmental solutions. *Microporous and Mesoporous Materials*, 166, 37–49.
- Polaert, I., Estel, L., Huyghe, R., and Thomas, M. (2010) Adsorbents regeneration under microwave irradiation for dehydration and volatile organic compounds gas treatment. *Chemical Engineering Journal*, 162(3), 941–948.
- Rakić, V., Rajić, N., Daković, A., and Auroux, A. (2013) The adsorption of salicylic acid, acetylsalicylic acid and atenolol from aqueous solutions onto natural zeolites and clays: Clinoptilolite, bentonite and kaolin. *Microporous and Mesoporous Materials*, 166, 185–194.
- Rebuffi, L., Plaisier, J.R., Abdellatif, M., Lausi, A., and Scardi, P. (2014) MCX: A synchrotron radiation beamline for X-ray diffraction line profile analysis. *Zeitschrift für Anorganische und Allgemeine Chemie*, 640 (15), 3100–3106.
- Reichle, W.T. (1986) Synthesis of anionic clay minerals (mixed metal hydroxides, hydrotalcite). *Solid State Ionics*, 22, 135–141.
- Rives, V. (2001) *Layered Double Hydroxides: Present and Future*. Nova Science, New York.
- Rodeghero, E., Martucci, A., Cruciani, G., Bagatin, R., Sarti, E., Bosi, V., and Pasti, L. (2016) Kinetics and dynamic behaviour of toluene desorption from ZSM-5 using in situ high-temperature synchrotron powder X-ray diffraction and chromatographic techniques. *Catalysis Today*, 277, 118–125.
- Rodeghero, E., Pasti, L., Sarti, E., Cruciani, G., Bagatin, R., and Martucci, A. (2017a) Temperature-induced desorption of methyl tert-butyl ether confined on ZSM-5: An in situ synchrotron XRD powder diffraction study. *Minerals*, 7(3), 34.
- Rodeghero, E., Martucci, A., Cruciani, G., Sarti, E., Cavazzini, A., Costa, V., Bagatin, R., and Pasti, L. (2017b) Detailed investigation of thermal regeneration of high-silica ZSM-5 zeolite through in situ synchrotron X-ray powder diffraction and adsorption studies. *The Journal of Physical Chemistry C*, 121(33), 17,958–17,968.
- Rosinski, E.J., and Rubin, M.K. (1983) Preparation of ZSM-12 type zeolites. U.S. Patent 4,391,785.
- Rossner, A., Snyder, S.A., and Knappe, D.R. (2009) Removal of emerging contaminants of concern by alternative adsorbents. *Water Research*, 43(15), 3787–3796.
- Ruthven, D.M. (1984) *Principles of Adsorption and Adsorption Processes*. Wiley.
- Sacchetto, V., Gatti, G., Paul, G., Braschi, I., Berlier, G., Cossi, M., Marchese, L., Bagatin, R., and Bisio, C. (2013) The interactions of methyl tert-butyl ether on high silica zeolites: a combined experimental and computational study. *Physical Chemistry Chemical Physics*, 15(32), 13275–13287.
- Shukla, G., Kumar, A., Bhanti, M., Joseph, P.E., and Taneja, A. (2006) Organochlorine pesticide contamination of ground water in the city of Hyderabad. *Environmental International*, 32, 244–247.
- Si, Y.B., Takagi, K., Iwasaki, A., and Zhou, D.M. (2009) Adsorption, desorption and dissipation of metolachlor in surface and subsurface soils. *Pest Management Science*, 65, 956–962.
- Singh, N. (2009) Adsorption of herbicides on coal fly ash from aqueous solutions. *Journal of Hazardous Materials*, 168(1), 233–237.
- Stamper, D.M., and Tuovinen, O.H. (1998) Biodegradation of the acetanilide herbicides alachlor, metolachlor, and propachlor. *Critical Reviews in Microbiology*, 24, 1–22.
- Toby, B.H.J. (2001) EXPGUI, a Graphical User Interface for GSAS. *Journal of Applied Crystallography*, 34, 210–213.
- Traub-Eberhard, U., Hensche, K.P., Kordel, W., and Klein, W. (1995) Influence of different field sites on pesticide movement into subsurface drain. *Pesticide Science*, 43, 121–129.
- Trewella, J.C., Schlenker, J.L., Woessner, D., E., and Higgins, J., B. (1985) The silicon-29 MAS-n.m.r. spectrum of ZSM-12, Zeolites, 5, 130–131.
- Vilaça, N., Amorim, R., Martinho, O., Reis, R.M., Baltazar, F., Fonseca, A.M., and Neves, I.C. (2011) Encapsulation of  $\alpha$ -cyano-4-hydroxycinnamic acid into a NaY zeolite. *Journal of materials science*, 46(23), 7511.
- Wang, Y., and Yang, R.T. (2007) Desulfurization of liquid fuels by adsorption on carbon-based sorbents and ultrasound-assisted sorbent regeneration. *Langmuir*, 23(7), 3825–3831.
- Wang, B., Zhang, H., Evans, D., and Duan, X. (2005) Surface modification of layered double hydroxides and incorporation of hydrophobic organic compounds. *Materials Chemistry and Physics*, 92, 190–196.
- Wang, S., Li, H., Xie, S., Liu, S., and Xu, L. (2006) Physical and chemical regeneration of zeolitic adsorbents for dye removal in wastewater treatment. *Chemosphere*, 65(1), 82–87.
- Webster, E., Mackay, D., and Wania, F. (1998) Evaluating environmental persistence. *Environmental Toxicology Chemistry*, 17, 2148–2158.
- World Health Organization (2010) International code of conduct on the distribution and use of pesticides: Guidelines for the Registration of Pesticides. [http://apps.who.int/iris/bitstream/handle/10665/70293/WHO\\_HTM\\_NTD\\_WHOPEP\\_2010.7\\_eng.pdf](http://apps.who.int/iris/bitstream/handle/10665/70293/WHO_HTM_NTD_WHOPEP_2010.7_eng.pdf)
- Yoo, K., Kashfi, R., Gopal, S., Smirniotis, P.G., Gangoda, M., and Bose, R.N. (2003) TEABr directed synthesis of ZSM-12 and its NMR characterization. *Microporous and Mesoporous Materials*, 60, 57–68.
- Zadaka, D., Nir, S., Radian, A., and Mishaal, Y.G. (2009) Atrazine removal from water by polycation–clay composites: effect of dissolved organic matter and comparison to activated carbon. *Water Research*, 43(3), 677–683.
- Zendehdel, M., Kalateh, Z., and Mortezaei, Z. (2014) Photocatalytic activity of the nano-sized TiO<sub>2</sub>/NaY zeolite for removal of methylene blue. *The Journal of Novel Applied Sciences*, 3, 135–141.
- Zhang, X., and Zhang, M. (2011) Modeling effectiveness of agricultural BMPs to reduce sediment load and organophosphate pesticides in surface runoff. *Science of the Total Environment*, 409(10), 1949–1958.
- Zhang, C., Jiang, Y., Li, Y., Hu, Z., Zhou, L., and Zhou, M. (2013) Three-dimensional electrochemical process for wastewater treatment: a general review. *Chemical Engineering Journal*, 228, 455–467.

MANUSCRIPT RECEIVED JULY 23, 2018  
 MANUSCRIPT ACCEPTED DECEMBER 4, 2018  
 MANUSCRIPT HANDLED BY G. DIEGO GATTA

### Endnote:

<sup>1</sup>Deposit item AM-19-36754, CIF. Deposit items are free to all readers and found on the MSA website, via the specific issue's Table of Contents (go to [http://www.minsocam.org/MSA/AmMin/TOC/2019/Mar2019\\_data/Mar2019\\_data.html](http://www.minsocam.org/MSA/AmMin/TOC/2019/Mar2019_data/Mar2019_data.html)).



MINERALOGICAL SOCIETY OF AMERICA  
3635 Concorde Pkwy Ste 500 • Chantilly VA 20151-1110 • USA  
Tel: 1 (703) 652-9950 • Fax: 1 (703) 652-9951 • Internet:  
www.minsocam.org

18 November 2019

Tatiana Chenet  
University of Ferrara  
Via Borsari 46  
Ferrara (FE) I-44100  
Italy

Email [tatiana.chenet@unife.it](mailto:tatiana.chenet@unife.it)

Dear Ms. Chenet:

I received your e-mail message of 2019-11-14 requesting permission to reproduce the following article in its entirety in your thesis:

- Rodeghero E., Pasti L., Nunziante G., Chenet T., Gigli L., Plaisier J. R., Martucci A. (2019). Highlighting the capability of zeolites for agro-chemicals contaminants removal from aqueous matrix: Evidence of 2-ethyl-6-methylaniline adsorption on ZSM-12. *American Mineralogist*, Volume 104, 317-324.

It is with pleasure that we grant you permission to reproduce this article for inclusion without cost and all subsequent editions of the work, its ancillaries, and other derivative works, in any form or medium, whether now known or hereafter developed, in all languages, for distribution throughout the world on the conditions that reference is given to the original publication of the Mineralogical Society of America.

Sincerely,

J. Alexander Speer  
Executive Director, MSA



# Selective adsorption of toluene and *n*-hexane binary mixture from aqueous solution on zeolite ZSM-5: Evaluation of competitive behavior between aliphatic and aromatic compounds

E. Rodeghero<sup>a</sup>, T. Chenet<sup>b</sup>, A. Martucci<sup>a,\*</sup>, M. Ardit<sup>a</sup>, E. Sarti<sup>b</sup>, L. Pasti<sup>b,\*</sup>

<sup>a</sup> Department of Physics and Earth Sciences, University of Ferrara, Via Saragat, 1, I-44123 Ferrara, Italy

<sup>b</sup> Department of Chemistry and Pharmaceutical Sciences, University of Ferrara, Via L. Borsari, 46, I-44123 Ferrara, Italy

## ARTICLE INFO

### Keywords:

ZSM-5  
Toluene  
*n*-Hexane  
Binary mixture adsorption  
Competitive behavior

## ABSTRACT

In this study, high silica ZSM-5 was selected as an adsorbent for the removal of toluene (TOL) and *n*-hexane (HEX) binary mixtures from aqueous solution over a wide range of concentrations. In comparison with the single component systems, the binary mixture induced to a selective adsorption by the ZSM-5 zeolite. As a matter of fact, a selective adsorption, described by a competitive dual site Langmuir adsorption isotherm, is revealed where alkane compound is preferred to the aromatic one. Results from adsorption isotherm were related to the structural answer of the ZSM-5 framework as a function of a HEX-TOL equimolar binary mixture adsorption. Rietveld refinements provided information about the relative position of both molecules within the ZSM-5, and on the intermolecular distances between the adsorption sites of HEX and TOL. Residuals of electron density calculated by mean of delta Fourier maps indicated the presence of both guest molecules but with a clear indication of preferential towards *n*-hexane, and a clear differential adsorption site distribution. The occurrence of host-guest interactions in the narrow intracrystalline micropores between the solid catalyst and embedded molecules have been revealed.

## 1. Introduction

It's well known that zeolites represent a benchmark in the area of porous solid-state materials, with key applications in ion exchange (ion removal and water softening), adsorption, separation and gas storage, carbon dioxide sequestration, enhanced catalysis, smart sensors and drug delivery processes [1]. These functional solid-state materials comprise pure silica which can adsorb organic components from water as well as interact with guest molecules not only at the surfaces, but throughout the bulk of the material. Hydrophobic zeolites with modular compositions and tailorable cavities are very suitable for the encapsulation of non-polar guest molecules, thus allowing for their diffusion into porosities [2–7]. Microporous aluminosilicates with uniform and ordered networks and narrow intracrystalline micropores can strongly influence selectivity in catalytic reactions as well as diffusivity through their pore channels system [6]. Their application requires that these materials have to be active not only in a wide range of operative conditions but also during prolonged periods of time. Zeolites are relatively cheap adsorbents characterized by high stability in water, effectiveness towards aggressive chemical solutions, thus representing a

viable alternative to other reactive media (e.g. carbonaceous resin, activated carbon, and ion-exchange resins) [3,8,9]. Both high surface area and pore volume combined with a specific shape selectivity, ability to host guest species, and a strong stability, make these solids suitable for the removal of environmentally concerned pollutants from water such as non-methane volatile organic compounds (NMVOCs) [10–15]. Adsorption is a rapid and economical method for NMVOCs removal from water and wastewater due to the universal nature of both soluble and insoluble contaminants removal. A wide variety of NMVOCs (i.e. aliphatic/aromatic hydrocarbons and their substituted compounds, organic acids and alcohols) is present in the environment and emitted from both anthropogenic (i.e. wastewater treatment plants (WWTPs), industrial and urban wastewaters, gasoline, solvents, urban and rural run-offs) and natural (i.e. vegetation and soil microbes, geogenic, lightning, and biomass burning) sources [16,17]. Different types of zeolites are efficient in non-methane volatile organic compounds adsorption (for instance, those with topology MFI, ITW, ERI, CHA, LTA, AFX, MOR, FER, BEA and silicalites). Their high efficiency (up to 90–99%) associated with low costs of maintenance and large functionality, make zeolites competitive towards other techniques and

\* Corresponding authors.

E-mail addresses: [mrs@unife.it](mailto:mrs@unife.it) (A. Martucci), [psu@unife.it](mailto:psu@unife.it) (L. Pasti).

<https://doi.org/10.1016/j.cattod.2019.09.015>

Received 13 July 2019; Received in revised form 20 August 2019; Accepted 11 September 2019

0920-5861/© 2019 Elsevier B.V. All rights reserved.

methodologies for NMVOCs removal from water bodies, such as reverse osmosis, ion exchange, electro-dialysis and electrolysis [10,12,16–35,37–43]. The adsorption efficiency of zeolites could be improved or adjusted by controlling the hydrophobicity–hydrophilicity of the solid, the structure topology, the geometry of the environment of the active site and the chemical composition of the environment [6]. Due to the confinement effect, sorbate molecules in zeolites have been found to optimize van der Waals interactions with the zeolite walls by organising specific sites/microscopic cavity in order to match perfectly guests molecules size and shape to the zeolite channel/cage size and shape [44]. Consequently, the comprehension of adsorption phenomena by combining batch adsorption and X-ray powder diffraction analyses can provide a powerful tool to understand the NMVOCs selective adsorption from aqueous on zeolites as well as microscopic details for the host-guest interactions governing the competitive behaviour in complex systems.

In this study we focus on the adsorption of two hydrocarbons: hexane (aliphatic) and toluene (aromatic) in order to: (i) evaluate ZSM-5 adsorption properties with respect to different type of hydrocarbons; (ii) evaluate the influence of adsorbent structure topology and NMVOCs size and shape on selectivity; (iii) gain information on location and orientation of organic compounds inside the zeolite frameworks.

ZSM-5 was selected as adsorbent medium due its characteristic three dimensional micropore system whose three dimensional channel structure ensures the accessibility of host selected molecules (size of the 10-ring micropores  $\approx 5.1\text{--}5.6 \text{ \AA}$ ) (Fig. 1 a, b). Toluene (TOL) and *n*-hexane (HEX) are selected as NMVOCs representative of aromatic and alkanes hydrocarbon, respectively, as well as because of their amount, emissions and toxicity [45]. This information can help with the selection of optimal adsorbent material for water remediation technology as a function of the pollutants composition.

## 2. Material and methods

### 2.1. Materials

Hydrophobic ZSM-5 zeolite (code CBV 28014) supplied by Zeolyst International in its ammonium form was used as adsorbate in the present study. The characteristics reported by indicate a  $\text{SiO}_2/\text{Al}_2\text{O}_3$  molar ratio equal to 280, a  $\text{NH}_4^+$  and  $\text{Na}_2\text{O}$  contents lower than 1% and 0.05 wt.% respectively, and a surface area of  $400 \text{ m}^2 \text{ g}^{-1}$ .

### 2.2. Batch experiments

Adsorption isotherms were determined using the batch method. Batch experiments were carried out in duplicate in 20 ml crimp top

reaction glass flasks sealed with PTFE septa (Supelco, PA, USA). The flasks were filled in order to have the minimum headspace. A solid/solution ratio of 1:2 ( $\text{mg mL}^{-1}$ ) was employed, a fixed adsorbent amount was placed in contact with solution at variable composition. The samples were equilibrated for 24 h at  $20 \text{ }^\circ\text{C}$  ( $\pm 0.5 \text{ }^\circ\text{C}$ ) by keeping the flasks into jacketed glass beakers connected to a thermostated water bath (Lab Companion RW-0525G). The samples were kept under stirring by a 10-place magnetic stirrer (IKAMAG RO 10 power, IKA, Stanfer, Germany) at a stirring speed of 500 rpm. After equilibration, the solids were separated from the aqueous solution by filtration through  $0.22 \mu\text{m}$  polyvinylidene fluoride (PVDF) membrane filters (Agilent Technologies, Santa Clara, CA, USA). To determine adsorbed quantities (*q*) and equilibrium concentrations (*C<sub>e</sub>*), concentrations of TOL and/or HEX were determined in solutions after equilibration with the zeolite and in equilibrated solution not containing adsorbent. All experiments were carried out in duplicates.

### 2.3. Gas chromatography

The concentration of contaminants in the aqueous solution was determined by Headspace Gas Chromatography coupled to Mass Spectrometry (HS-GC-MS).

The analysis was carried out using an Agilent GC-MS system (Santa Clara, CA, USA) consisting of a GC 6850 Series II Network coupled to a Pal G6500-CTC injector and a Mass Selective Detector 5973 Network.

HS autosampler injector conditions are: incubation oven temperature  $80 \text{ }^\circ\text{C}$ , incubation time 50 min, headspace syringe temperature  $85 \text{ }^\circ\text{C}$ , agitation speed 250 rpm, agitation on time 30 s, agitation off time 5 s, injection volume  $500 \mu\text{L}$ , fill speed  $30 \mu\text{L s}^{-1}$ , syringe pull-up delay 5 s, injection speed  $250 \mu\text{L s}^{-1}$ , pre-injection delay 0 s, post injection delay 2 s, syringe flush 30 s with nitrogen.

A DB-624 UI GC column ( $L = 20 \text{ m}$ ,  $\text{I.D.} = 0.18 \text{ mm}$ ,  $df = 1.00 \mu\text{m}$  film thickness, Agilent, Santa Clara, CA, USA) was used. High purity helium was the carrier gas with a constant flow rate of  $0.7 \text{ mL min}^{-1}$ . The oven temperature gradient started at  $40 \text{ }^\circ\text{C}$  for 4 min and then ramped to  $130 \text{ }^\circ\text{C}$  at  $15 \text{ }^\circ\text{C min}^{-1}$ . The injector temperature was kept at  $150 \text{ }^\circ\text{C}$ . All samples were injected in split mode (10:1).

The mass spectrometer operated in electron impact mode (positive ion, 70 eV). The source temperature and the quadrupole temperature were set to  $230 \text{ }^\circ\text{C}$  and  $150 \text{ }^\circ\text{C}$ , respectively.

The mass spectra were acquired in full scan mode. The electronic scan speed was  $1562 \text{ amu s}^{-1}$  in a mass range from 30 to 300 amu. For identification and quantification of the target analyte, the SIM (selected ion monitoring) chromatograms were extracted from the acquired signal by selecting the most abundant characteristic fragments at  $m/z$  41, 43, 57, 86 (HEX) and  $m/z = 91, 92$  (TOL). Chromatographic peak of

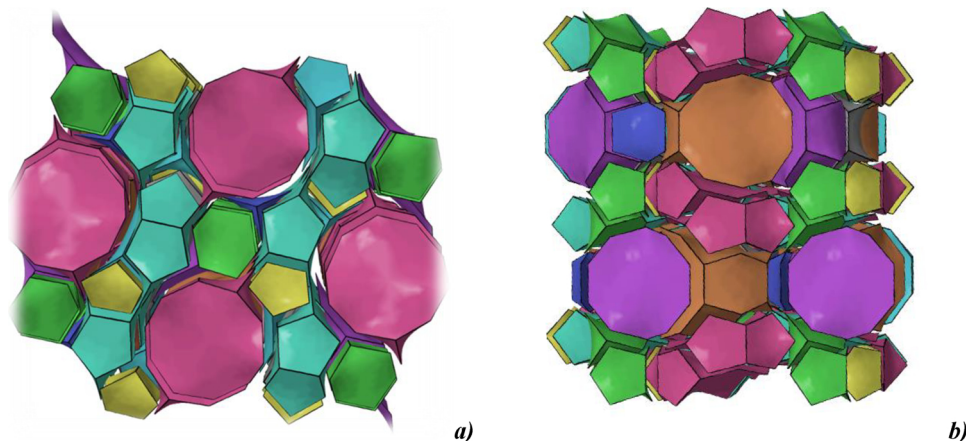


Fig. 1. Three dimensional micropore system of ZSM-5 viewed along [100] (a) and [010] (b), respectively.

analytes was identified by comparison of the retention time and the mass spectrum with standard compound and library data; quantitative analysis was performed using calibration curves.

#### 2.4. Thermal analyses

Thermogravimetric analysis (TGA), its derivative weight loss curve (DTG) and differential thermal analysis (DTA) on ZSM-5 before and after loading were performed using a STA 409 PC LUX<sup>®</sup> - Netzsch instrument, in order to follow pollutants mixtures release/decomposition process. The measurements were carried out at a fixed heating rate of 10 °C/min over a temperature range of 25–900 °C (alumina powder as reference). The degradation runs were taken under an oxidizing atmosphere (flowing dry air) for gasification at a flow rate of 20 ml/min.

#### 2.5. X-ray powder diffraction measurements and structure determination

X-ray powder diffraction data of ZSM-5 loaded with *n*-hexane and toluene mixtures (HEX-TOL-ZSM-5) were recorded on a Bruker D8 Advance Diffractometer equipped with a Si (Li) solid-state detector, (experimental setup: Cu K $\alpha$ 1,2 radiation, 3–90 2 $\theta$  range, counting time of 12 s per 0.02 2 $\theta$  step). Structural data of ZSM-5 after only unary mixtures (i.e. one component solution) of *n*-hexane and toluene adsorption are available from the literature [11,35,46]. Nevertheless, in order to have a direct comparison by means of the same experimental setup, additional X-ray powder diffraction data collections after only *n*-hexane and toluene adsorption (HEX-ZSM-5 and TOL-ZSM-5, respectively) were collected using the same strategy adopted for HEX-TOL-ZSM-5. All data processing was carried out by full profile Rietveld analysis using the GSAS package [47] with the EXPGUI interface [48], starting from the atomic model of Rodeghero et al. [35] in the monoclinic space group crystal system (s.g. P2<sub>1</sub>/c). Lattice parameters and refinement details for TOL-ZSM-5, HEX-ZSM-5 and HEX-TOL-ZSM-5 systems are reported in Table 1.

The extra-framework sites of HEX-TOL-ZSM-5 were firstly located by difference Fourier maps and then optimized using the geometry optimization tool implemented in EXPO2014 [49] (by plane wave DFT with dispersion correction, DFT-D) in order to minimize the energy of the crystal structure and to provide reasonable bond lengths and angles for HEX and TOL molecules. The positions of H atoms were also calculated. The optimized structure was then refined again with GSAS and the final structural model showed the best agreement with the experimental data. In order to secure a stable refinement, the HEX and TOL molecule coordinates were fixed in the final cycles of Rietveld refinement thus limiting the number of refined atomic displacement parameters.

**Table 1**

Lattice parameters and refinement details for TOL-ZSM-5, HEX-ZSM-5, and HEX-TOL-ZSM-5 systems.

	TOL-ZSM-5	HEX-ZSM-5	HEX-TOL-ZSM-5
<i>a</i> (Å)	19.9034(5)	19.9151(4)	19.8845(4)
<i>b</i> (Å)	20.1129(4)	20.1405(2)	20.1226(4)
<i>c</i> (Å)	13.3841(3)	13.4090(2)	13.4080(3)
$\alpha$	90	90	90
$\beta$	90.501(2)	90.486(1)	90.315(2)
$\gamma$	90	90	90
<i>V</i> (Å <sup>3</sup> )	5357.70(2)	5378.17(16)	5364.83(21)
Wavelength of incident radiation (Å)	1.54178	1.54178	1.54178
Refined pattern 2 $\theta$ range (°)	1–90	1–90	1–90
<i>R</i> <sub>wp</sub> (%)	8.8	7.7	9.5
<i>R</i> <sub>p</sub> (%)	6.5	5.6	6.9
<i>R</i> <sub>F2</sub> (%)	6.5	6.0	8.3

$$R_p = \frac{\sum |Y_{io} - Y_{ic}|}{\sum Y_{io}}; \quad R_{wp} = \frac{[\sum w_i(Y_{io} - Y_{ic})^2 / \sum w_i Y_{io}^2]^{0.5}}{\sum F_o^2}; \quad R_{F2} = \frac{\sum |F_o^2 - F_c^2|}{\sum F_o^2}$$

The fractional final coordinates with the hydrogens calculated as well as the main bond distances are listed in Tables 1–6 SI as Supplementary information.

### 3. Results and discussion

#### 3.1. Adsorption

The TOL-ZSM-5 system has been already investigated [35], in a wide concentration range. In Fig. 2 the adsorption isotherm of TOL on ZSM-5 in a low concentration range is reported together with that of the HEX-ZSM-5. It can be observed that the adsorbed quantity from very diluted solution is proportional to the concentration for both the systems and can be described by an adsorption isotherm type-C [36]:

$$q = K C_e \quad (1)$$

Where *q* is the amount of solute adsorbed for unit weight of adsorbent at the equilibrium and *C<sub>e</sub>*, the concentration in the solution at equilibrium, *K* is the partition constant. *K* is roughly double for HEX, then for TOL, thus indicating a more favorable adsorption of the linear alkane with respect the aromatic compound.

When a wider concentration range is considered, the TOL-ZSM-5 system is better described by a L-type isotherm, in particular a Langmuir isotherm model that has been previously employed to fit the adsorption data of various organic molecules onto zeolite.

For that which concerns HEX-ZSM-5, in this case too, Langmuir isotherm model:

$$q = \frac{q_s b C_e}{1 + b C_e} \quad (2)$$

where, *q<sub>s</sub>*, is the saturation capacity and *b* the binding constant, appears to fit well the data as can be seen in Fig. 3 and from the determination coefficient in Table 2. The adsorption isotherm is characterized by a steep initial slope, which together with high *q<sub>s</sub>* are desirable characteristics for adsorbent applications. In the adsorption of HEX on ZSM-5 both *q<sub>s</sub>* and *b* are larger than those found for TOL in ref. [35], thus confirming what previously observed for the adsorption in the low concentration range. A similar behavior has been observed in the adsorption of *n*-heptane and toluene onto mesoporous ZSM-5 [50]. To further investigate the selectivity of ZSM-5 with respect to HEX and TOL in aqueous solution, adsorption from equimolar binary mixtures were carried out (see Fig. 3). The effect of HEX on the competitive adsorption of TOL can be evaluated from the adsorption selectivity ( $\alpha$ ) calculated as:

$$\alpha_{TOL/HEX} = \frac{x_{z,TOL}/x_{a,TOL}}{x_{z,HEX}/x_{a,HEX}} \quad (3)$$

where *x<sub>z,TOL</sub>* and *x<sub>z,HEX</sub>* are the adsorbed quantity per unit mass of adsorbent material, of TOL and HEX onto ZSM-5 and *x<sub>a,TOL</sub>* and *x<sub>a,HEX</sub>* are the equilibrium concentration of TOL and HEX in aqueous solution, respectively. For the adsorption from equimolar binary solution the selectivity is given by the ratio of the adsorbed quantities and it approaches a value of 3.6 at saturation. Differences in the saturation capacity of ZSM-5 zeolites can be also inferred from the geometry of the channels. As a matter of fact, the analysis of shape and size of channels apertures (by means of ellipticity,  $\epsilon$ , and Crystallographic Free Area, CFA, parameters, respectively) of straight and sinusoidal channels reveals that, HEX-TOL-ZSM-5 is characterized by a CFA that in average is smaller than that of both unary mixture compounds, but a higher degree of departure from a circular shape of channel apertures ( $\epsilon$ ) (see Table 7 SI).

#### 3.2. Characterization of TOL, HEX and HEX-TOL- loaded ZSM-5 by X-ray diffraction

The host-guest and guest-guest interactions governing the TOL,

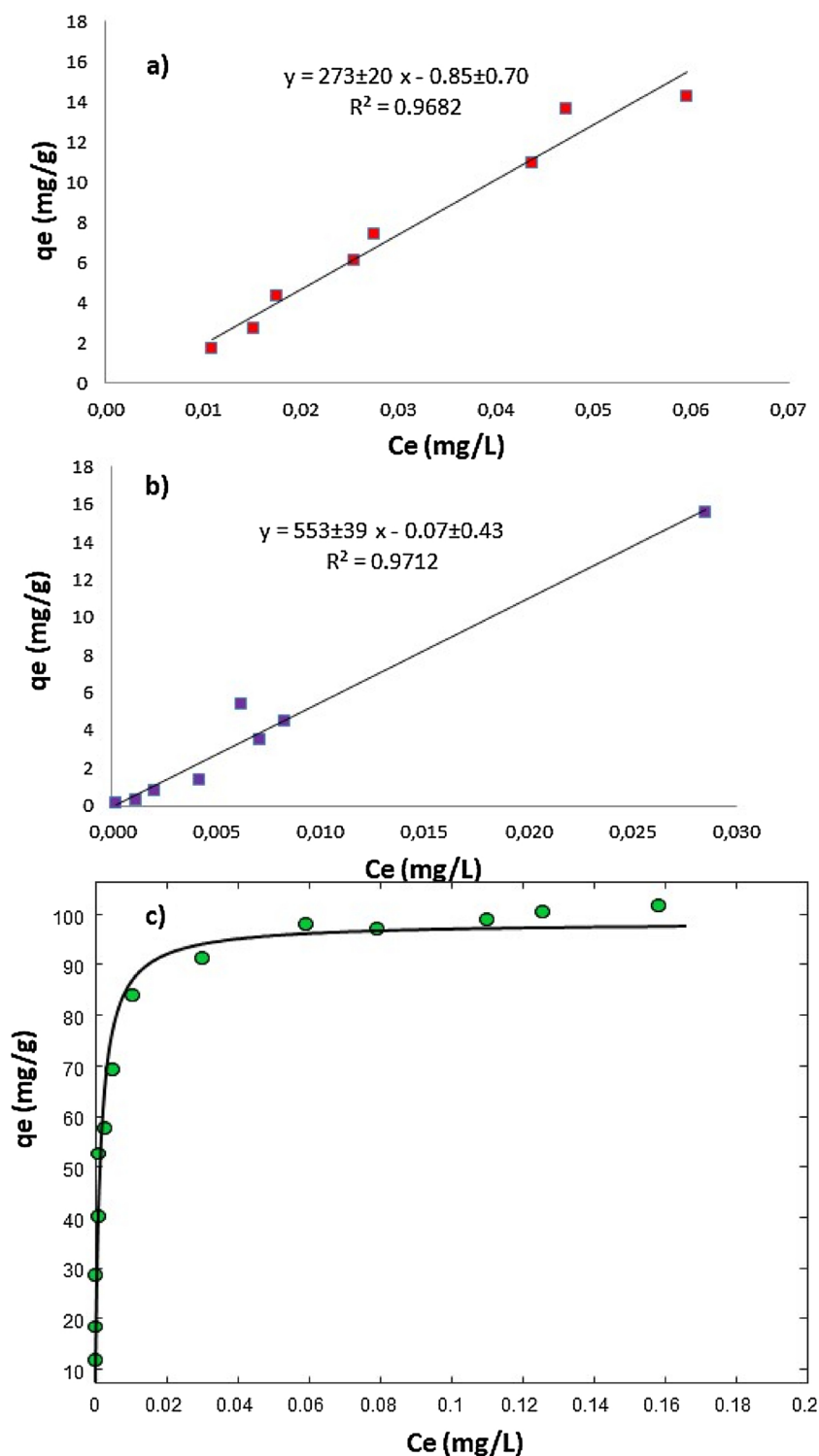


Fig. 2. Adsorption isotherms (a) ZSM-5-TOL in low concentration range, ZSM-5-HEX in: (b) low concentration range, (c) wide concentration range.

HEX and HEX-TOL mixture adsorption were investigated by X-ray powder diffraction (XRPD). According to Rodeghero et al. [35], toluene molecules in the TOL-ZSM-5 system are spread over two crystallographic independent sites: at the straight channel (TOL1 = C1, C2, C3, C4, C5, C6, C7 sites) and at the intersection between straight and sinusoidal channels (TOL2 = C8, C9, C10, C11, C12, C13, C14 sites), respectively. Refinements of the atomic occupancy factors confirm the presence of 6 toluene molecules per unit cell (corresponding to about 8% in weight). Moreover, as already highlighted by Rodeghero et al. [35], the occurrence of co-adsorbed-water-toluene oligomers

interacting with framework oxygens was also confirmed (Fig. 4a). Regarding the distribution of *n*-hexane molecules (Fig. 4b), the refined atomic occupancy factors indicate 8 molecules per unit cell spread over two fully occupied crystallographic independent sites: the first (i.e., HEX1) hosts 4 molecules at the intersection of straight and sinusoidal channels (in analogous way to what reported by Fujiyama et al. [51]); the second (i.e., HEX2) is occupied by 4 molecules embedded in the sinusoidal channel. The refined total *n*-hexane amount (about 10.7% in weight) well matches with the weight loss observed through the thermal analysis as shown in Fig. 5a. The TG curve shows a gradual

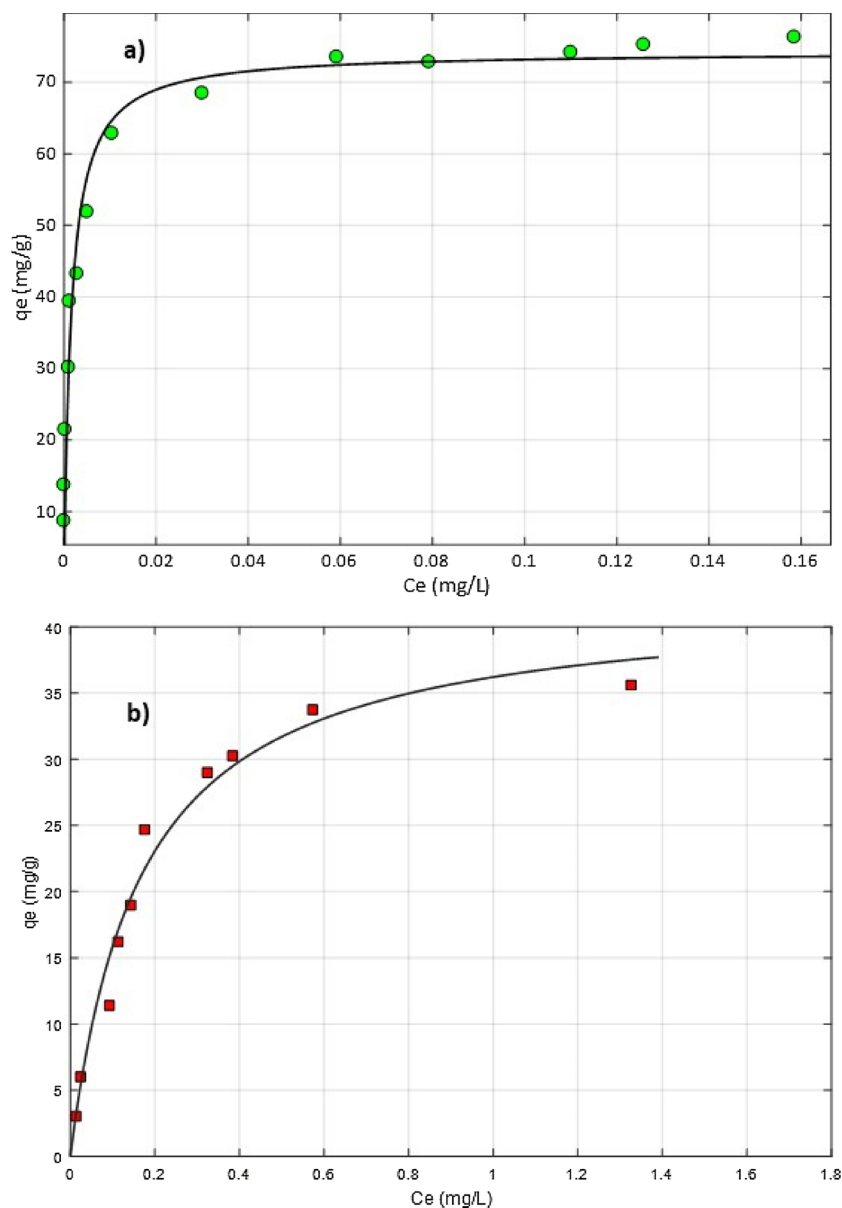


Fig. 3. Adsorption isotherms of binary equimolar mixtures of HEX-TOL on ZSM-5: a) HEX; b) TOL.

Table 2

Isotherm parameters for the adsorption of hexane and hexane-toluene mixture on ZSM-5 (@25 °C).

			$R^2$	SSE	
ZSM-5-HEX		Qsb	1019.4	0.9512	595
ZSM-5-HEX_TOL	HEX	qsb	73.57.3	0.9432	384
	TOL	qsb	422.4	0.9750	38

weight loss up to 300 °C, after which the instrument recorded a plateau with 11.14% total weight loss until the end of the measurement. As regards the relation between the adsorbed organic and the ZSM-5 structure, the refined distances among the carbon sites and the framework oxygen atoms (C1-O31 2.58(1), C1-O44 2.32(1), C9-O25 2.77(1)) revealed the occurrence of host-guest interactions. No evidence of H<sub>2</sub>O molecules is recognized, but the analysis of difference Fourier maps highlights slight disorder which could be attributed to the presence of co-adsorbed water. In both ZSM-5 loaded with unary mixtures a good correspondence with the saturation capacity estimated from the adsorption data was highlighted. After the analysis on the adsorption of

samples characterized by a single organic component, attention was paid on the structural answer to organic adsorption of HEX-TOL-ZSM-5 sample, in order to test the possible competitive behavior during the adsorption in water solution. The first evidence of effective embedding of both organics was obtained by the comparison of the collected powder diffraction patterns (Fig. 6a, b) which show slight differences in both intensity and peaks position especially at lower 2theta values. Peaks position of collected patterns scale in the following order (moving toward high 2theta values): TOL-ZSM-5 > HEX-ZSM-5 > HEX-TOL-ZSM-5, meaning that a volumetric expansion occurs from TOL-ZSM-5 to HEX-ZSM-5 samples. On the other hand, HEX-ZSM-5 show pattern very similar to that of HEX-TOL-ZSM-5 and characterized by the same peaks intensity, whereas the peaks of the TOL-ZSM-5 sample have lower intensity values. Strong similarity was also reported for lattice parameters ( $a$ ,  $b$ ,  $c$ , and  $\beta$  in Table 1) and this finding suggests a higher ZSM-5 adsorption affinity towards *n*-hexane. Rietveld structure refinements provided information about the relative position of molecules inside the structure after HEX and TOL binary mixture adsorption. Residuals of electron density calculated by mean of delta Fourier maps indicated the presence of both guest molecules but with a clear

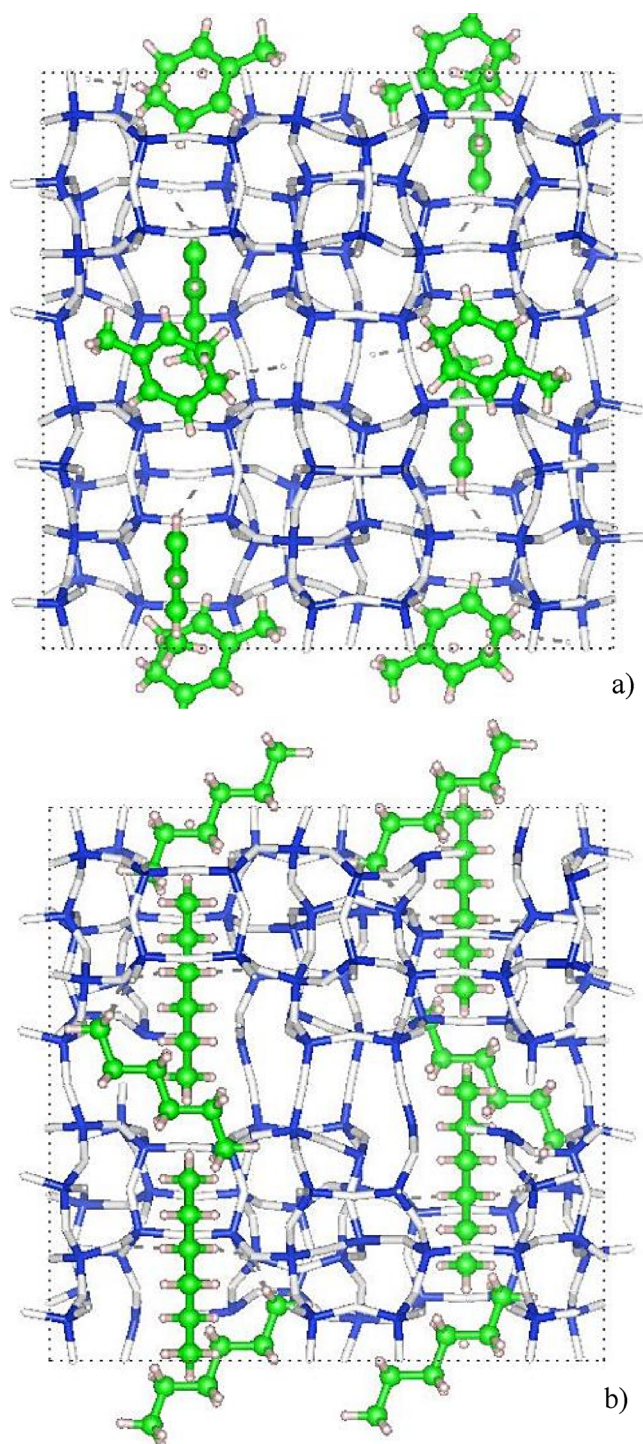


Fig. 4. Rietveld structure refinements of single component systems: a) adsorption sites of TOL in ZSM-5 structure; b) adsorption sites of HEX in ZSM-5 structure.

indication of preferential and differential adsorption site distribution (Fig. 7). Toluene molecules are located only in the straight channel (TOL1 site, about 0.8 molecules, corresponding to approx. 1.2% in zeolite dry weight (dw)), whereas TOL2 site (located at the channels intersections) is now empty (Fig. 7a). Molecules of *n*-hexane are always hosted at both HEX1 and HEX2 sites (7.2 HEX molecules per unit cell, corresponding to approx. 9.4% in zeolite dw) (Fig. 7b). The concentration of *n*-hexane in HEX1 site is unchanged with respect after only HEX adsorption, whereas the short distances between HEX2 and

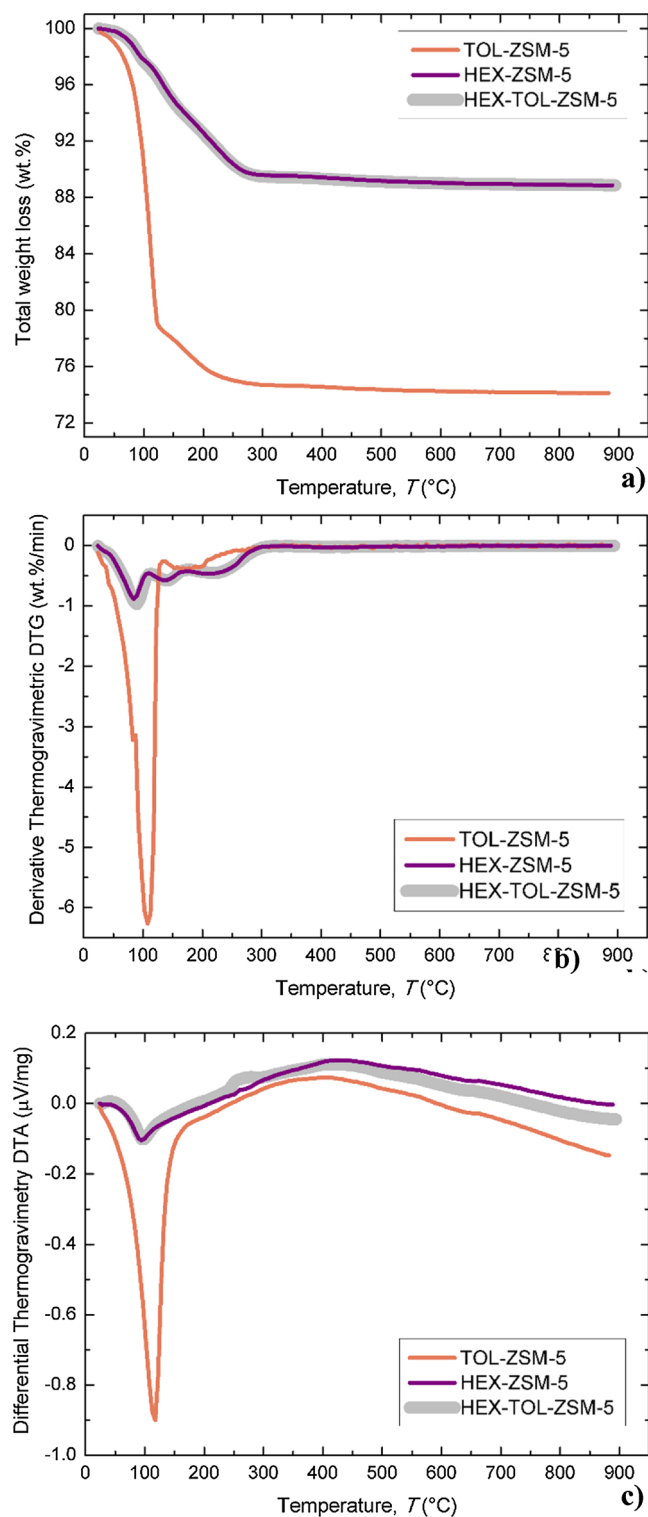


Fig. 5. Simultaneous Thermogravimetry (TG) (a); Differential Thermogravimetry (DTG) (b); Differential Thermal analyses (DTA) (c) of ZSM-5 in the temperature range 25–900 °C.

TOL1 sites prevent their simultaneous presence at the intersection of straight and sinusoidal channels; the loading of *n*-hexane in HEX2 gives rise to 3.2 molecules per unit cell. Delta Fourier maps highlight the presence of 8 co-adsorbed H<sub>2</sub>O molecules (W1 and W2 sites, respectively), corresponding to ≈2.2% in zeolite dw. The total refined amount of adsorbed organic molecules is of about 12.5% in weight (Fig. 5a, b), in good agreement with the total weight loss (wt. %) that

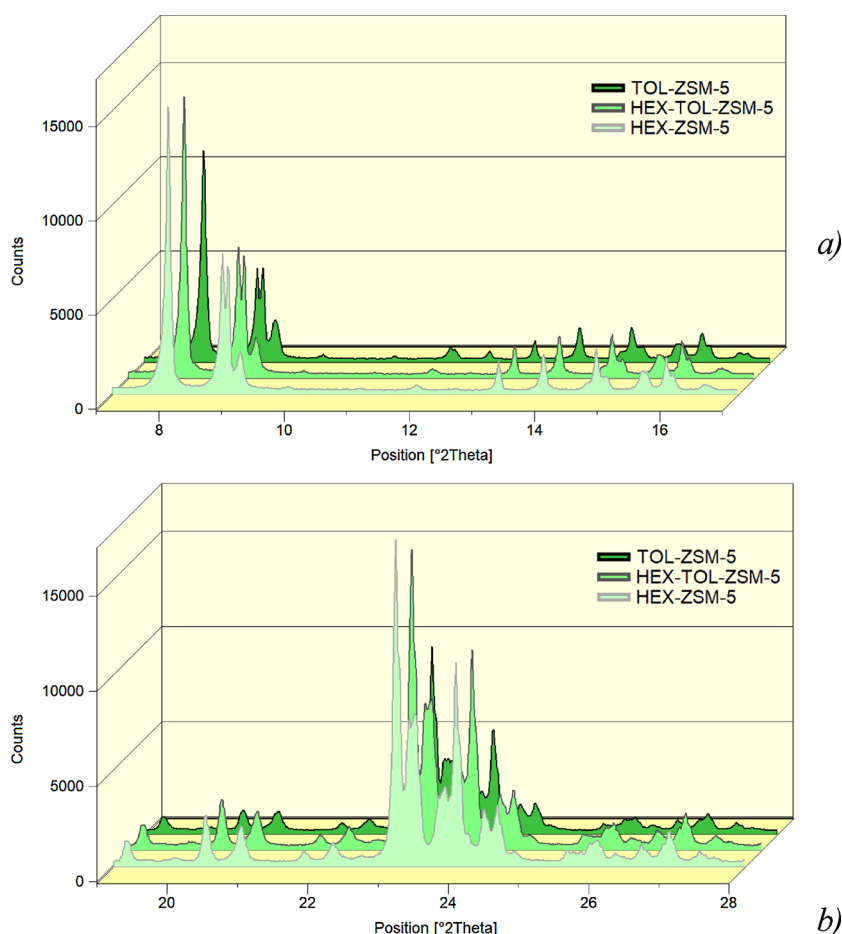


Fig. 6. Cascade plot of ZSM-5 samples in selected angular ranges (7–17 °2θ, (a); and 19–28 °2θ, (b) at room temperature.

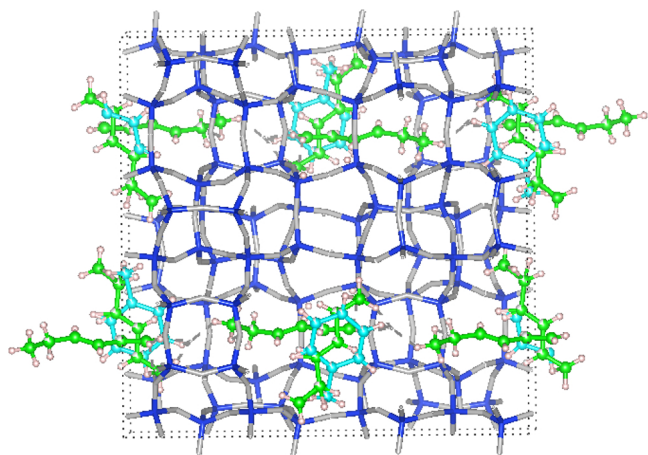


Fig. 7. Adsorption sites for HEX and TOL in binary mixture along the c axis.

was estimated by means of thermal analysis as well as by adsorption methodologies. In particular, the ZSM-5-mixture DTA curve (Fig. 5c) shows a trend very similar to that obtained for HEX-ZSM-5 sample with a TOL desorption smaller contribute at the same time. The refined distances between the framework oxygen, water oxygen atoms and organic molecules suggested the occurrence of water-TOL (W1-TOL1 2.52 Å, W2-TOL2 2.96 Å) and water-HEX (W1-C3 2.94 Å, W1-C9 2.87 Å, W1-C12 2.72 Å, W2-C4 2.94 Å, W2-C9 2.83 Å, respectively) oligomers interacting with the framework (O20-C9-HEX2 2.89 Å, O25-C12-HEX2 2.66 Å, O26-C11-HEX2 2.34 Å, O28-C9-HEX2 2.95 Å, O31-C10-HEX2 2.84 Å, O41-C11-HEX2 2.62 Å, O44-C10-HEX2 2.94 Å, respectively). In

conclusion, the integration of these structural information to adsorption data allowed us to provide insights into zeolite selectivity for aromatic and alkanes hydrocarbon, respectively.

#### 4. Conclusions

This work focused on the study of HEX and TOL absorption, in particular on the aspect of the selective behavior of zeolite ZSM-5 regarding the adsorption of aliphatic and aromatic compounds. The evaluation of adsorption isotherm data of HEX-TOL binary mixture have suggested a higher selectivity of ZSM-5 for the alkane with respect to aromatic compound a selective. Indeed, results pointed out that with respect to the single-component systems data (HEX-ZSM-5 and TOL-ZSM-5), the loading of both compounds in a mixture reduces the absorption of the other one. These data were resulted in a very good agreement with that was obtained both from X-ray powder diffraction and from thermal analyzes. As a matter of fact, the study of residual intensities obtained through the difference Fourier maps and the Rietveld structural investigation provided information about the relative position of HEX and TOL molecules inside the ZSM-5 adsorption sites. In particular, the refined host-guests interactions revealed a more affinity towards HEX with respect to toluene TOL ones. This information can help with the selection of optimal adsorbent material for water remediation technology as a function of the pollutants composition.

#### Acknowledgements

Research funded by Research Center for Non-Conventional Energy, Istituto ENI Donegani-Environmental Technologies (San Donato Milanese, Italy).

## Appendix A. Supplementary data

Supplementary material related to this article can be found, in the online version, at doi:<https://doi.org/10.1016/j.cattod.2019.09.015>.

## References

- M.E. Davis, Ordered porous materials for emerging applications, *Nature* 417 (2002) 813 <https://www.nature.com/articles/nature00785>.
- I. Braschi, S. Blasioli, L. Gigli, C.E. Gessa, A. Alberti, A. Martucci, Removal of sulfonamide antibiotics from water: evidence of adsorption into an organophilic zeolite Y by its structural modifications, *J. Hazard. Mater.* 178 (2010) 218–225, <https://doi.org/10.1016/j.jhazmat.2010.01.066>.
- A. Martucci, I. Braschi, L. Marchese, S. Quartieri, Recent advances in clean-up strategies of waters polluted with sulfonamide antibiotics: a review of sorbents and related properties, *Mineral. Mag.* 78 (2014) 1115–1140, <https://doi.org/10.1180/minmag.2014.078.5.03>.
- A. Martucci, L. Pasti, N. Marchetti, A. Cavazzini, F. Dondi, A. Alberti, Adsorption of pharmaceuticals from aqueous solutions on synthetic zeolites, *Microporous Mesoporous Mater.* 148 (2012) 174–183, <https://doi.org/10.1016/j.micromeso.2011.07.009>.
- B.A. Stein, Advanced materials progress report on advances in microporous and mesoporous solids—highlights of recent progress, *Adv. Mater.* (2003) 763–775, <https://doi.org/10.1002/adma.200300007>.
- A. Corma, State of the art and future challenges of zeolites as catalysts, *J. Catal.* 216 (2003) 298–312, [https://doi.org/10.1016/S0021-9517\(02\)00132-X](https://doi.org/10.1016/S0021-9517(02)00132-X).
- J. Pérez-Ramírez, C.H. Christensen, K. Egeblad, C.H. Christensen, J.C. Groen, Hierarchical zeolites: enhanced utilisation of microporous crystals in catalysis by advances in materials design, *Chem. Soc. Rev.* 37 (2008) 2530–2542, <https://doi.org/10.1039/b809030k>.
- I. Ali, M. Asim, T.A. Khan, Low cost adsorbents for the removal of organic pollutants from wastewater, *J. Environ. Manage.* 113 (2012) 170–183, <https://doi.org/10.1016/j.jenvman.2012.08.028>.
- A. Rosner, S.A. Snyder, D.R. Knappe, State of the art and future challenges of zeolites as catalysts, *Water Res.* 43 (2009) 3787–3796, <https://doi.org/10.1016/j.watres.2009.06.009>.
- L. Pasti, E. Rodeghero, E. Sarti, V. Bosi, A. Cavazzini, R. Bagatin, A. Martucci, Competitive adsorption of VOCs from binary aqueous mixtures on zeolite ZSM-5, *RSC Adv.* 6 (59) (2016) 54544–54552, <https://doi.org/10.1039/c6ra08872d>.
- K. Nishi, A. Hidaka, Y. Yokomori, Structure of toluene6.4-ZSM-5 and the toluene disproportionation reaction on ZSM-5, *Acta Crystallogr. Sect. B: Struct. Sci.* 61 (2005) 160–163, <https://doi.org/10.1107/S0108768105003186>.
- E. Sarti, T. Chenet, L. Pasti, A. Cavazzini, E. Rodeghero, A. Martucci, Effect of silica alumina ratio and thermal treatment of beta zeolites on the adsorption of toluene from aqueous solutions, *Minerals* 7 (2017), <https://doi.org/10.3390/min7020022>.
- A.A. Costa, W.B. Wilson, H. Wang, A.D. Campiglia, J.A. Dias, S.C.L. Dias, Comparison of BEA, USY and ZSM-5 for the quantitative extraction of polycyclic aromatic hydrocarbons from water samples, *Microporous Mesoporous Mater.* 149 (2012) 186–192, <https://doi.org/10.1016/j.micromeso.2011.06.016>.
- M. Khalid, G. Joly, A. Renaud, P. Magnoux, State of the art and future challenges of zeolites as catalysts, *Ind. Eng. Chem. Res.* 43 (2004) 5275–5280, <https://doi.org/10.1021/ie0400447>.
- C. Perego, R. Bagatin, M. Tagliabue, R. Vignola, Zeolites and related mesoporous materials for multi-talented environmental solutions, *Microporous Mesoporous Mater.* 166 (2013) 37–49, <https://doi.org/10.1016/j.micromeso.2012.04.048>.
- E. Atasoy, T. Döğeroğlu, S. Kara, State of the art and future challenges of zeolites as catalysts, *Water Res.* 38 (2004) 3265–3274, <https://doi.org/10.1016/j.watres.2004.04.036>.
- N.S. Chary, A.R. Fernandez-Alba, Determination of volatile organic compounds in drinking and environmental waters, *TrAC – Trends Anal. Chem.* 32 (2012) 60–75, <https://doi.org/10.1016/j.trac.2011.08.011>.
- W. Makowski, D. Majda, Equilibrated thermodesorption studies of adsorption of n-hexane and n-heptane on zeolites Y, ZSM-5 and ZSM-11, *Appl. Surf. Sci.* 252 (2005) 707–715, <https://doi.org/10.1016/j.apsusc.2005.02.052>.
- X.Y. Sun, J.W. Li, Y.X. Li, S.C. Yang, B.H. Chen, Adsorption of benzene and propylene in zeolite ZSM-5: grand canonical Monte Carlo simulations, *Chem. Res. Chin. Univ.* 25 (2009) 377–382 [https://scholar.google.it/scholar?cluster=6994539969316821427&hl=fr&as\\_sdt=2005&sciold=0.5](https://scholar.google.it/scholar?cluster=6994539969316821427&hl=fr&as_sdt=2005&sciold=0.5).
- N. Floquet, J.P. Coulomb, J.P. Bellat, J.M. Simon, G. Weber, G. Andre, Heptane adsorption in silicalite-1: neutron scattering investigation, *J. Phys. Chem. C* 111 (2007) 18182–18188, <https://doi.org/10.1021/jp0746502>.
- N. Floquet, J.M. Simon, J.P. Coulomb, J.P. Bellat, G. Weber, G. Andre, Heptane adsorption in silicalite-1: molecular dynamics simulation, *Microporous Mesoporous Mater.* 122 (2009) 61–71, <https://doi.org/10.1016/j.micromeso.2009.02.009>.
- R. Krishna, S. Calero, B. Smit, Investigation of entropy effects during sorption of mixtures of alkanes in MFI zeolite, *Chem. Eng. J.* 88 (2002) 81–94, [https://doi.org/10.1016/S1385-8947\(01\)00253-4](https://doi.org/10.1016/S1385-8947(01)00253-4).
- L. Song, Z.L. Sun, H.Y. Ban, M. Dai, L.V.C. Rees, Benzene adsorption in microporous materials, *Adsorption* 11 (2005) 325–339, <https://doi.org/10.1007/s10450-005-5400-2>.
- S. Calero, M. Schenk, D. Dubbeldam, T.L.M. Maesen, B. Smit, The selectivity of n-hexane hydroconversion on MOR-, MAZ-, and FAU-type zeolites, *J. Catal.* 228 (2004) 121–129, <https://doi.org/10.1016/j.jcat.2004.08.019>.
- J.F.M. Denayer, L.I. Devriese, S. Couck, J. Martens, R. Singh, P.A. Webley, G.V. Baron, Cage and window effects in the adsorption of n-alkanes on chabazite and SAPO-34, *J. Phys. Chem. C* 112 (2008) 16593–16599, <https://doi.org/10.1021/jp804349v>.
- F. Hibbe, C. Chmelik, L. Heinke, S. Pramanik, J. Li, D.M. Ruthven, et al., The nature of surface barriers on nanoporous solids explored by microimaging of transient guest distributions, *J. Am. Chem. Soc.* 133 (2011) 2804–2807, <https://doi.org/10.1021/ja108625z>.
- R. Krishna, B. Smit, S. Calero, Entropy effects during sorption of alkanes in zeolites, *Chem. Soc. Rev.* 31 (2002) 185–194, <https://doi.org/10.1039/b101267n>.
- A. Martucci, L. Pasti, M. Nassi, A. Alberti, R. Arletti, R. Bagatin, R. Vignola, R. Sticca, Adsorption mechanism of 1,2-dichloroethane into an organophilic zeolite mordenite: a combined diffractometric and gas chromatographic study, *Microporous Mesoporous Mater.* 151 (2012) 358–367, <https://doi.org/10.1016/j.micromeso.2011.10.010>.
- R. Arletti, A. Martucci, A. Alberti, L. Pasti, M. Nassi, Location of MTBE and toluene in the channel system of the zeolitemordenite: adsorption and host–guest interactions, *J. Solid State Chem.* (2019).
- L. Pasti, A. Martucci, M. Nassi, A. Cavazzini, A. Alberti, R. Bagatin, The role of water in DCE adsorption from aqueous solutions onto hydrophobic zeolites, *Microporous Mesoporous Mater.* 160 (2012) 182–193, <https://doi.org/10.1016/j.micromeso.2012.05.015>.
- A. Martucci, L. Leardini, M. Nassi, E. Sarti, R. Bagatin, L. Pasti, Removal of emerging organic contaminants from aqueous systems: adsorption and location of methyl-tertiary-butylether on synthetic ferrierite, *Mineral. Mag.* 78 (2014) 1161–1176.
- N. Kamiya, T. Oshiro, S. Tan, K. Nishi, Y. Yokomori, Adsorption process of phenol on silicalite-1 and crystal structure of phenol8.0-silicalite-1 using a single crystal X-ray diffraction method, *Microporous Mesoporous Mater.* 169 (2013) 168–175, <https://doi.org/10.1016/j.micromeso.2012.11.006>.
- A. Martucci, E. Rodeghero, L. Pasti, V. Bosi, G. Cruciani, Adsorption of 1,2-dichloroethane on ZSM-5 and desorption dynamics by in situ synchrotron powder X-ray diffraction, *Microporous Mesoporous Mater.* 215 (2015), <https://doi.org/10.1016/j.micromeso.2015.05.035>.
- N. Kamiya, W. Iwama, T. Kudo, T. Nasuno, S. Fujiyama, K. Nishi, Y. Yokomori, Determining the structure of a benzene7.2-silicalite-1 zeolite using a single-crystal X-ray method, *Acta Crystallogr. Sect. B: Struct. Sci.* 67 (2011) 508–515, <https://doi.org/10.1107/S0108768111038560>.
- E. Rodeghero, A. Martucci, G. Cruciani, R. Bagatin, E. Sarti, V. Bosi, L. Pasti, Kinetics and dynamic behaviour of toluene desorption from ZSM-5 using in situ high-temperature synchrotron powder X-ray diffraction and chromatographic techniques, *Catal. Today* 277 (2016), <https://doi.org/10.1016/j.cattod.2015.11.031>.
- C.H. Giles, D. Smith, A. Huitson, A general treatment and classification of the solute adsorption isotherm. I. Theoretical, *J. Colloid Interface Sci.* 47 (3) (1974) 755–765.
- I.J. Gomez, B. Arnaiz, M. Cacioppo, F. Arcudi, M. Prato, Nitrogen-doped Carbon Nanodots for bioimaging and delivery of paclitaxel, *J. Mater. Chem. B* 6 (2018), <https://doi.org/10.1039/x0xx00000x>.
- I. Ali, V.K. Gupta, Advances in water treatment by adsorption technology, *Nat. Protoc.* 1 (2007) 2661–2667, <https://doi.org/10.1038/nprot.2006.370>.
- V.K. Gupta, I. Ali, T.A. Saleh, A. Nayak, S. Agarwal, State of the art and future challenges of zeolites as catalysts, *RSC Adv.* 2 (2012) 6380–6388, <https://doi.org/10.1039/C2RA20340E>.
- C.T. Laurencin, S.F. El-Amin, S.E. Ibim, D.A. Willoughby, M. Attawia, H.R. Alcock, A.A. Ambrosio, A highly porous 3-dimensional polyphosphazene polymer matrix for skeletal tissue regeneration, *J. Biomed. Mater. Res.* 30 (1996) 133–138, [https://doi.org/10.1002/\(SICI\)1097-4636\(199602\)30:2<133::AID-JBMM1>3.0.CO;2-S](https://doi.org/10.1002/(SICI)1097-4636(199602)30:2<133::AID-JBMM1>3.0.CO;2-S).
- I. Ali, Water treatment by adsorption columns: evaluation at ground level, *Sep. Purif. Rev.* 43 (2014) 175–205, <https://doi.org/10.1080/15422119.2012.748671>.
- V.K. Gupta, P.J.M. Carrott, M.M.L. Ribeiro Carrott, Suhas, Low-cost adsorbents: growing approach to wastewater treatment—a review, *Crit. Rev. Environ. Sci. Technol.* 39 (2009) 783–842, <https://doi.org/10.1080/10643380801977610>.
- B. Smith, T.L.M. Maesen, Commensurate freezing of alkanes in channels of zeolite, *Nature* (1995).
- E.G. Derouane, The energetics of sorption by molecular sieves: surface curvature effects, *Chem. Phys. Lett.* 142 (1987) 200–204, [https://doi.org/10.1016/0009-2614\(87\)80922-3](https://doi.org/10.1016/0009-2614(87)80922-3).
- G.J. Dollard, P. Dumitrescu, S. Telling, J. Dixon, R.G. Derwent, Observed trends in ambient concentrations of C2–C8 hydrocarbons in the United Kingdom over the period from 1993 to 2004, *Atmos. Environ.* 41 (2007) 2559–2569, <https://doi.org/10.1016/j.atmosenv.2006.11.020>.
- H. Morell, K. Angermund, A.R. Lewis, D.H. Brouwer, C.A. Fyfe, H. Gies, Structural investigation of silicalite-1 loaded with n-hexane by X-ray diffraction, 29Si MAS NMR, and molecular modeling, *Chem. Mater.* 14 (2002) 2192–2198, <https://doi.org/10.1021/cm011267f>.
- A.C. Larson, R.B. Von Dreele, L. Alamos, Laur 86-748 ©, Structure, (2000).
- B.H. Toby, EXPGUI, a graphical user interface for GSAS, *J. Appl. Crystallogr.* 34 (2001) 210–213, <https://doi.org/10.1107/s0021889801002242>.
- A. Altomare, C. Cuocci, C. Giacobozzo, A. Moliterni, R. Rizzi, N. Corriero, A. Falcicchio, EXPO2013: a kit of tools for phasing crystal structures from powder data, *J. Appl. Crystallogr.* 46 (2013) 1231–1235, <https://doi.org/10.1107/s0021889813013113>.
- H. Zhao, J. Ma, Q. Zhang, Z. Liu, R. Li, Adsorption and diffusion of n-heptane and toluene over mesoporous ZSM-5 zeolites, *Ind. Eng. Chem. Res.* 53 (2014) 13810–13819, <https://doi.org/10.1021/ie502496v>.
- Y. Fujiyama, S. Seino, S. Kamiya, N. Nishi, K. Yoza, Y. Yokomori, Adsorption structures of non-aromatic hydrocarbons on silicalite-1 using the single-crystal X-ray diffraction method, *Phys. Chem. Chem. Phys.* 16 (2014) 15839–15845, <https://doi.org/10.1039/C4CP01860E>.

## Supplementary Information

---

### **Selective adsorption of toluene and *n*-hexane binary mixture from aqueous solution on zeolite zsm-5: evaluation of competitive behavior between aliphatic and aromatic compounds.**

E. Rodeghero<sup>a</sup>, T. Chenet<sup>b</sup>, A. Martucci<sup>a\*</sup>, M. Ardit<sup>a</sup>, E. Sarti<sup>b</sup>, and L. Pasti<sup>b\*\*</sup>

<sup>a</sup>Department of Physics and Earth Sciences, University of Ferrara, Via Saragat, 1, I-44122 Ferrara, Italy

<sup>b</sup>Department of Chemistry and Pharmaceutical Sciences, University of Ferrara, Via L. Borsari, 46, I-44123 Ferrara, Italy

#### **Corresponding authors:**

\*Annalisa Martucci, [mrs@unife.it](mailto:mrs@unife.it)

\*\*Luisa Pasti, [psu@unife.it](mailto:psu@unife.it)

**Table 1 SI.** Framework and extraframework fractional coordinates, atomic displacement parameters ( $U_{\text{iso}}$  in  $\text{\AA}^2 \times 100$ ), and atomic site fractional occupancy (s.o.f) for the TOL-ZSM-5 system. Calculated hydrogen atoms for TOL1 (C1 C2, C3, C4, C5, C6, C7) and TOL2 (C8, C9, C10, C11, C12, C13, C14) extraframework molecules are also reported.

<b>Label</b>	<b><math>x_{\text{frac}}</math></b>	<b><math>y_{\text{frac}}</math></b>	<b><math>z_{\text{frac}}</math></b>	<b><math>U_{\text{iso}}</math></b>	<b>s.o.f.</b>
<b>Framework</b>					
<b>SI1</b>	1.0539	0.4211	0.6729	0.31	1.00
<b>SI2</b>	1.0314	0.3149	0.8293	0.31	1.00
<b>SI3</b>	1.0634	0.2783	1.0461	0.31	1.00
<b>SI4</b>	1.0657	0.1246	1.0319	0.31	1.00
<b>SI5</b>	1.0267	0.0773	0.8229	0.31	1.00
<b>SI6</b>	1.0561	0.1949	0.6836	0.31	1.00
<b>SI7</b>	0.8281	0.4258	0.6786	0.31	1.00
<b>SI8</b>	0.8744	0.3115	0.8203	0.31	1.00
<b>SI9</b>	0.8260	0.2705	1.0312	0.31	1.00
<b>SI10</b>	0.8232	0.1172	1.0330	0.31	1.00
<b>SI11</b>	0.8709	0.0717	0.8260	0.31	1.00
<b>SI12</b>	0.8355	0.1890	0.6842	0.31	1.00
<b>SI13</b>	0.9437	0.0724	0.1616	0.31	1.00
<b>SI14</b>	0.9739	0.1890	0.3092	0.31	1.00
<b>SI15</b>	0.9391	0.2211	0.5279	0.31	1.00
<b>SI16</b>	0.9339	0.3761	0.5326	0.31	1.00
<b>SI17</b>	0.9749	0.4271	0.3219	0.31	1.00
<b>SI18</b>	0.9386	0.3126	0.1813	0.31	1.00
<b>SI19</b>	1.1707	0.0767	0.1855	0.31	1.00
<b>SI20</b>	1.1321	0.1892	0.3293	0.31	1.00
<b>SI21</b>	1.1694	0.2275	0.5446	0.31	1.00
<b>SI22</b>	1.1692	0.3803	0.5362	0.31	1.00
<b>SI23</b>	1.1318	0.4257	0.3202	0.31	1.00
<b>SI24</b>	1.1802	0.3060	0.1983	0.31	1.00
<b>O1</b>	1.0609	0.3777	0.7718	0.51	1.00
<b>O2</b>	1.0657	0.3103	0.9372	0.51	1.00
<b>O3</b>	1.0449	0.2012	1.0384	0.51	1.00
<b>O4</b>	1.0690	0.1019	0.9178	0.51	1.00
<b>O5</b>	1.0433	0.1224	0.7280	0.51	1.00
<b>O6</b>	1.0488	0.2480	0.7711	0.51	1.00
<b>O7</b>	0.8429	0.3762	0.7689	0.51	1.00
<b>O8</b>	0.8358	0.3010	0.9227	0.51	1.00
<b>O9</b>	0.8457	0.1935	1.0336	0.51	1.00
<b>O10</b>	0.8279	0.0867	0.9234	0.51	1.00
<b>O11</b>	0.8462	0.1188	0.7373	0.51	1.00
<b>O12</b>	0.8654	0.2471	0.7524	0.51	1.00
<b>O13</b>	0.9523	0.3245	0.8428	0.51	1.00
<b>O14</b>	0.9489	0.0825	0.8497	0.51	1.00
<b>O15</b>	1.1230	0.4190	0.6136	0.51	1.00
<b>O16</b>	0.9964	0.3883	0.6058	0.51	1.00

<b>O17</b>	0.8660	0.4019	0.5811	0.51	1.00
<b>O18</b>	1.1296	0.1992	0.6382	0.51	1.00
<b>O19</b>	1.0052	0.2091	0.5935	0.51	1.00
<b>O20</b>	0.8758	0.1897	0.5824	0.51	1.00
<b>O21</b>	1.0464	0.0023	0.7985	0.51	1.00
<b>O22</b>	0.8583	-0.0034	0.7933	0.51	1.00
<b>O23</b>	0.7492	0.4283	0.6576	0.51	1.00
<b>O24</b>	0.7575	0.2003	0.6624	0.51	1.00
<b>O25</b>	0.7494	0.2796	1.0619	0.51	1.00
<b>O26</b>	0.7480	0.1108	1.0717	0.51	1.00
<b>O27</b>	0.9502	0.1222	0.2543	0.51	1.00
<b>O28</b>	0.9488	0.1857	0.4222	0.51	1.00
<b>O29</b>	0.9263	0.2986	0.5101	0.51	1.00
<b>O30</b>	0.9450	0.4152	0.4305	0.51	1.00
<b>O31</b>	0.9371	0.3811	0.2419	0.51	1.00
<b>O32</b>	0.9403	0.2520	0.2575	0.51	1.00
<b>O33</b>	1.1609	0.1226	0.2813	0.51	1.00
<b>O34</b>	1.1457	0.1877	0.4471	0.51	1.00
<b>O35</b>	1.1494	0.3037	0.5314	0.51	1.00
<b>O36</b>	1.1646	0.4135	0.4280	0.51	1.00
<b>O37</b>	1.1677	0.3790	0.2406	0.51	1.00
<b>O38</b>	1.1706	0.2517	0.2839	0.51	1.00
<b>O39</b>	1.0537	0.1961	0.3051	0.51	1.00
<b>O40</b>	1.0532	0.4098	0.3206	0.51	1.00
<b>O41</b>	0.8717	0.0789	0.1099	0.51	1.00
<b>O42</b>	1.0003	0.0860	0.0814	0.51	1.00
<b>O43</b>	1.1318	0.1071	0.0918	0.51	1.00
<b>O44</b>	0.8722	0.3045	0.1154	0.51	1.00
<b>O45</b>	1.0016	0.3123	0.1091	0.51	1.00
<b>O46</b>	1.1327	0.2916	0.1046	0.51	1.00
<b>O47</b>	0.9632	0.5033	0.2939	0.51	1.00
<b>O48</b>	1.1445	0.5012	0.2895	0.51	1.00

**TOL1**

<b>C7</b>	0.8922	0.4610	0.0514	12.69	1.00
<b>H7</b>	0.9226	0.4724	-0.0148	19.04	1.00
<b>H7A</b>	0.9137	0.4827	0.1202	19.04	1.00
<b>H7B</b>	0.8857	0.4080	0.0582	19.04	1.00
<b>C5</b>	0.7140	0.4835	-0.0469	12.69	1.00
<b>H5</b>	0.6750	0.4448	-0.0353	15.23	1.00
<b>H5A</b>	0.7181	0.4976	-0.1269	15.23	1.00
<b>C6</b>	0.7800	0.4541	-0.0200	12.69	1.00
<b>H6</b>	0.7928	0.4063	-0.0509	15.23	1.00
<b>C4</b>	0.8251	0.4870	0.0361	12.69	1.00
<b>C2</b>	0.6961	0.5430	0.0135	12.69	1.00
<b>H2</b>	0.6738	0.5253	0.0885	15.23	1.00
<b>H2A</b>	0.6613	0.5747	-0.0321	15.23	1.00
<b>C3</b>	0.8116	0.5537	0.0722	12.69	1.00
<b>H3</b>	0.8505	0.5825	0.1107	15.23	1.00

<b>C1</b>	0.7518	0.5817	0.0500	12.69	1.00
<b>H1</b>	0.7450	0.6299	0.0726	15.23	1.00
<b>TOL2</b>					
<b>C14</b>	1.2342	0.0059	-0.2443	17.18	1.00
<b>H14</b>	1.2023	0.0135	-0.3110	25.77	1.00
<b>H14A</b>	1.2125	-0.0338	-0.1976	25.77	1.00
<b>H14B</b>	1.2873	-0.0045	-0.2628	25.77	1.00
<b>C8</b>	1.2301	0.1853	-0.1815	17.18	1.00
<b>H8</b>	1.2261	0.2288	-0.2267	20.62	1.00
<b>C9</b>	1.2330	0.1261	-0.2370	17.18	1.00
<b>H9</b>	1.2322	0.1289	-0.3164	20.62	1.00
<b>C10</b>	1.2336	0.1237	-0.0273	17.18	1.00
<b>H10</b>	1.2344	0.1217	0.0531	20.62	1.00
<b>C11</b>	1.2320	0.1841	-0.0777	17.18	1.00
<b>H11</b>	1.2319	0.2296	-0.0362	20.62	1.00
<b>C12</b>	1.2335	0.0649	-0.0816	17.18	1.00
<b>H12</b>	1.2344	0.0179	-0.0429	20.62	1.00
<b>C13</b>	1.2330	0.0666	-0.1851	17.18	1.00
<b>Water molecules</b>					
<b>W1</b>	0.7016	0.6975	0.1752	14.65	1.00
<b>W2</b>	0.5636	0.5075	0.0258	10.00	1.00

---

**Table 2 SI.** Framework and extraframework fractional coordinates, atomic displacement parameters ( $U_{\text{iso}}$  in  $\text{\AA}^2 \times 100$ ), and atomic site fractional occupancy (s.o.f) for the HEX-ZSM-5 system. Calculated hydrogen atoms for HEX1 (C1 C2, C3, C4, C9, C10) and HEX2 (C5, C6, C7, C8, C11, C12) extraframework molecules are also reported.

<b>Label</b>	$x_{\text{frac}}$	$y_{\text{frac}}$	$z_{\text{frac}}$	$U_{\text{iso}}$	<b>s.o.f.</b>
<b>Framework</b>					
<b>SI1</b>	1.0547	0.4224	0.6652	0.13	1.00
<b>SI2</b>	1.0337	0.3155	0.8241	0.13	1.00
<b>SI3</b>	1.0677	0.2784	1.0374	0.13	1.00
<b>SI4</b>	1.0668	0.126	1.0291	0.13	1.00
<b>SI5</b>	1.0282	0.0741	0.8224	0.13	1.00
<b>SI6</b>	1.0602	0.1934	0.6877	0.13	1.00
<b>SI7</b>	0.8297	0.4256	0.6761	0.13	1.00
<b>SI8</b>	0.8762	0.3095	0.8154	0.13	1.00
<b>SI9</b>	0.8280	0.2701	1.0246	0.13	1.00
<b>SI10</b>	0.8204	0.1184	1.0224	0.13	1.00
<b>SI11</b>	0.8727	0.0683	0.8215	0.13	1.00
<b>SI12</b>	0.8365	0.1856	0.6838	0.13	1.00
<b>SI13</b>	0.9427	0.0768	0.1671	0.13	1.00
<b>SI14</b>	0.9750	0.1897	0.3130	0.13	1.00
<b>SI15</b>	0.9422	0.2212	0.5327	0.13	1.00
<b>SI16</b>	0.9335	0.3751	0.5284	0.13	1.00
<b>SI17</b>	0.9742	0.4252	0.3170	0.13	1.00
<b>SI18</b>	0.9390	0.3092	0.1806	0.13	1.00
<b>SI19</b>	1.1714	0.0784	0.1868	0.13	1.00
<b>SI20</b>	1.1326	0.1924	0.3253	0.13	1.00
<b>SI21</b>	1.1689	0.2285	0.5411	0.13	1.00
<b>SI22</b>	1.1700	0.3810	0.5311	0.13	1.00
<b>SI23</b>	1.1314	0.4255	0.3162	0.13	1.00
<b>SI24</b>	1.1812	0.3084	0.1933	0.13	1.00
<b>O1</b>	1.0629	0.3764	0.7616	0.24	1.00
<b>O2</b>	1.0652	0.3165	0.9333	0.24	1.00
<b>O3</b>	1.0468	0.2026	1.0216	0.24	1.00
<b>O4</b>	1.0697	0.0941	0.9203	0.24	1.00
<b>O5</b>	1.0497	0.12	0.7308	0.24	1.00
<b>O6</b>	1.0549	0.2462	0.7755	0.24	1.00
<b>O7</b>	0.8424	0.3711	0.7599	0.24	1.00
<b>O8</b>	0.8394	0.3045	0.9197	0.24	1.00
<b>O9</b>	0.8464	0.1932	1.0179	0.24	1.00
<b>O10</b>	0.8309	0.0806	0.9199	0.24	1.00
<b>O11</b>	0.8436	0.1145	0.7348	0.24	1.00
<b>O12</b>	0.8665	0.2411	0.7567	0.24	1.00
<b>O13</b>	0.9542	0.3237	0.8342	0.24	1.00
<b>O14</b>	0.9500	0.0836	0.8437	0.24	1.00
<b>O15</b>	1.1232	0.4225	0.6042	0.24	1.00
<b>O16</b>	0.9975	0.3924	0.5953	0.24	1.00

<b>O17</b>	0.8676	0.4050	0.5772	0.24	1.00
<b>O18</b>	1.1321	0.1987	0.6366	0.24	1.00
<b>O19</b>	1.0065	0.2100	0.6031	0.24	1.00
<b>O20</b>	0.8791	0.1859	0.5843	0.24	1.00
<b>O21</b>	1.0436	-0.0016	0.7961	0.24	1.00
<b>O22</b>	0.8635	-0.0074	0.7897	0.24	1.00
<b>O23</b>	0.7510	0.4296	0.6541	0.24	1.00
<b>O24</b>	0.7594	0.2000	0.6595	0.24	1.00
<b>O25</b>	0.7513	0.2794	1.0548	0.24	1.00
<b>O26</b>	0.7422	0.1184	1.0448	0.24	1.00
<b>O27</b>	0.9469	0.1237	0.2625	0.24	1.00
<b>O28</b>	0.9572	0.1861	0.4289	0.24	1.00
<b>O29</b>	0.9247	0.2967	0.5189	0.24	1.00
<b>O30</b>	0.9400	0.4075	0.4209	0.24	1.00
<b>O31</b>	0.9405	0.3802	0.2326	0.24	1.00
<b>O32</b>	0.9395	0.2532	0.2646	0.24	1.00
<b>O33</b>	1.1669	0.1278	0.2796	0.24	1.00
<b>O34</b>	1.1423	0.1908	0.4438	0.24	1.00
<b>O35</b>	1.1486	0.3048	0.5317	0.24	1.00
<b>O36</b>	1.1681	0.4105	0.4204	0.24	1.00
<b>O37</b>	1.1653	0.3818	0.2314	0.24	1.00
<b>O38</b>	1.1694	0.2568	0.282	0.24	1.00
<b>O39</b>	1.0547	0.1944	0.2962	0.24	1.00
<b>O40</b>	1.0534	0.4065	0.3234	0.24	1.00
<b>O41</b>	0.8716	0.0841	0.1134	0.24	1.00
<b>O42</b>	0.9997	0.0958	0.0904	0.24	1.00
<b>O43</b>	1.1359	0.1109	0.0918	0.24	1.00
<b>O44</b>	0.8726	0.3013	0.1152	0.24	1.00
<b>O45</b>	1.0023	0.3030	0.1099	0.24	1.00
<b>O46</b>	1.1358	0.2907	0.0988	0.24	1.00
<b>O47</b>	0.9640	0.5009	0.2934	0.24	1.00
<b>O48</b>	1.1402	0.5023	0.2902	0.24	1.00

**HEX1**

<b>C1</b>	0.6234	-0.0156	1.4525	5.91	1.00
<b>H1</b>	0.6053	0.0255	1.4357	7.10	1.00
<b>C2</b>	0.6958	-0.0238	1.4591	5.91	1.00
<b>H2</b>	0.7150	-0.0651	1.4716	7.10	1.00
<b>C3</b>	0.7336	0.0300	1.4465	5.91	1.00
<b>H3</b>	0.7127	0.0704	1.4336	7.10	1.00
<b>C4</b>	0.8062	0.0275	1.4520	5.91	1.00
<b>H4</b>	0.8284	-0.0126	1.4620	7.10	1.00
<b>C9</b>	0.8405	0.0839	1.4426	5.91	1.00
<b>H9A</b>	0.8179	0.1238	1.4327	7.10	1.00
<b>H9B</b>	0.8872	0.0834	1.4460	7.10	1.00
<b>C10</b>	0.5833	-0.0663	1.4703	5.91	1.00
<b>H10A</b>	0.6013	-0.1075	1.4871	7.10	1.00
<b>H10B</b>	0.5370	-0.0609	1.4660	7.10	1.00

**HEX2**

<b>C5</b>	0.7622	-0.0080	1.2529	9.94	1.00
<b>H5</b>	0.7562	-0.0168	1.3204	11.93	1.00
<b>C6</b>	0.7605	-0.1844	1.1662	9.94	1.00
<b>H6</b>	0.7193	-0.1970	1.1306	11.93	1.00
<b>H6A</b>	0.7976	-0.1813	1.1187	11.93	1.00
<b>C7</b>	0.7517	-0.1214	1.2195	9.94	1.00
<b>H7</b>	0.7319	-0.1225	1.2821	11.93	1.00
<b>C8</b>	0.7701	-0.0633	1.1838	9.94	1.00
<b>H8</b>	0.7868	-0.0580	1.1196	11.93	1.00
<b>C11</b>	0.7633	0.0539	1.2222	9.94	1.00
<b>H11A</b>	0.7692	0.0633	1.1549	11.93	1.00
<b>H11B</b>	0.7581	0.0883	1.2677	11.93	1.00
<b>C12</b>	0.7767	-0.2333	1.2482	9.94	1.00
<b>H12</b>	0.8170	-0.2193	1.2833	14.91	1.00
<b>H12A</b>	0.7838	-0.2769	1.2195	14.91	1.00
<b>H12B</b>	0.7396	-0.2352	1.2945	14.91	1.00
<b>Water molecules</b>					
<b>W1</b>	0.7347	-0.3386	1.1373	5.69	1.00
<b>W2</b>	0.9476	0.0011	1.5060	4.12	1.00

---

**Table 3 SI.** Framework and extraframework fractional coordinates, atomic displacement parameters ( $U_{\text{iso}}$  in  $\text{\AA}^2 \times 100$ ), and atomic site fractional occupancy (s.o.f) for the HEX-TOL-ZSM-5 system. Calculated hydrogen atoms for each HEX (HEX1 = C8, C9, C10, C11, C16, C17; HEX2 = C12, C13, C14, C15, C18, C19) and TOL (C1, C2, C3, C4, C5, C6, C7) extraframework molecules are also reported.

<b>Label</b>	$x_{\text{frac}}$	$y_{\text{frac}}$	$z_{\text{frac}}$	$U_{\text{iso}}$	<b>s.o.f.</b>
<b>Framework</b>					
<b>SI1</b>	1.0528	0.4221	0.6675	0.13	1.00
<b>SI2</b>	1.0324	0.3152	0.8250	0.13	1.00
<b>SI3</b>	1.0683	0.2801	1.0439	0.13	1.00
<b>SI4</b>	1.0653	0.1216	1.0368	0.13	1.00
<b>SI5</b>	1.0269	0.0698	0.8202	0.13	1.00
<b>SI6</b>	1.0553	0.1913	0.6852	0.13	1.00
<b>SI7</b>	0.8276	0.4270	0.6739	0.13	1.00
<b>SI8</b>	0.8735	0.3149	0.8200	0.13	1.00
<b>SI9</b>	0.8238	0.2721	1.0291	0.13	1.00
<b>SI10</b>	0.8219	0.1170	1.0309	0.13	1.00
<b>SI11</b>	0.8687	0.0690	0.8203	0.13	1.00
<b>SI12</b>	0.8296	0.1905	0.6880	0.13	1.00
<b>SI13</b>	0.9398	0.0748	0.1689	0.13	1.00
<b>SI14</b>	0.9692	0.1908	0.3098	0.13	1.00
<b>SI15</b>	0.9365	0.2207	0.5330	0.13	1.00
<b>SI16</b>	0.9333	0.3779	0.5246	0.13	1.00
<b>SI17</b>	0.9721	0.4276	0.3121	0.13	1.00
<b>SI18</b>	0.9401	0.3129	0.1724	0.13	1.00
<b>SI19</b>	1.1745	0.0752	0.1809	0.13	1.00
<b>SI20</b>	1.1279	0.1873	0.3253	0.13	1.00
<b>SI21</b>	1.1714	0.2246	0.5412	0.13	1.00
<b>SI22</b>	1.1725	0.3813	0.5334	0.13	1.00
<b>SI23</b>	1.1294	0.4276	0.3149	0.13	1.00
<b>SI24</b>	1.1763	0.3066	0.1938	0.13	1.00
<b>O1</b>	1.0623	0.3770	0.7652	0.24	1.00
<b>O2</b>	1.0694	0.3159	0.9333	0.24	1.00
<b>O3</b>	1.0529	0.2010	1.0229	0.24	1.00
<b>O4</b>	1.0675	0.0886	0.9257	0.24	1.00
<b>O5</b>	1.0514	0.1165	0.7348	0.24	1.00
<b>O6</b>	1.0490	0.2437	0.7721	0.24	1.00
<b>O7</b>	0.8424	0.3794	0.7647	0.24	1.00
<b>O8</b>	0.8387	0.3090	0.9258	0.24	1.00
<b>O9</b>	0.8437	0.1942	1.0270	0.24	1.00
<b>O10</b>	0.8315	0.0827	0.9242	0.24	1.00
<b>O11</b>	0.8438	0.1181	0.7361	0.24	1.00
<b>O12</b>	0.8667	0.2473	0.7581	0.24	1.00
<b>O13</b>	0.9542	0.3256	0.8410	0.24	1.00
<b>O14</b>	0.9496	0.0758	0.8420	0.24	1.00
<b>O15</b>	1.1242	0.4215	0.6088	0.24	1.00
<b>O16</b>	0.9892	0.4054	0.6025	0.24	1.00

<b>O17</b>	0.8629	0.4048	0.5707	0.24	1.00
<b>O18</b>	1.1294	0.1947	0.6364	0.24	1.00
<b>O19</b>	0.9988	0.1951	0.6010	0.24	1.00
<b>O20</b>	0.8677	0.1906	0.5817	0.24	1.00
<b>O21</b>	1.0498	-0.0055	0.7921	0.24	1.00
<b>O22</b>	0.8512	-0.0060	0.7853	0.24	1.00
<b>O23</b>	0.7460	0.4294	0.6538	0.24	1.00
<b>O24</b>	0.7513	0.2029	0.6693	0.24	1.00
<b>O25</b>	0.7468	0.2886	1.0592	0.24	1.00
<b>O26</b>	0.7456	0.1036	1.0667	0.24	1.00
<b>O27</b>	0.9345	0.1249	0.2624	0.24	1.00
<b>O28</b>	0.9419	0.1907	0.4244	0.24	1.00
<b>O29</b>	0.9275	0.2986	0.5281	0.24	1.00
<b>O30</b>	0.9389	0.4059	0.4186	0.24	1.00
<b>O31</b>	0.9372	0.3869	0.2273	0.24	1.00
<b>O32</b>	0.9433	0.2596	0.2600	0.24	1.00
<b>O33</b>	1.1642	0.1217	0.2787	0.24	1.00
<b>O34</b>	1.1460	0.1851	0.4444	0.24	1.00
<b>O35</b>	1.1520	0.3030	0.5314	0.24	1.00
<b>O36</b>	1.1640	0.4119	0.4227	0.24	1.00
<b>O37</b>	1.1657	0.3821	0.2335	0.24	1.00
<b>O38</b>	1.1560	0.2551	0.2827	0.24	1.00
<b>O39</b>	1.0471	0.1798	0.3111	0.24	1.00
<b>O40</b>	1.0508	0.4127	0.3166	0.24	1.00
<b>O41</b>	0.8672	0.0779	0.1071	0.24	1.00
<b>O42</b>	1.0009	0.0942	0.0962	0.24	1.00
<b>O43</b>	1.1337	0.1034	0.0849	0.24	1.00
<b>O44</b>	0.8707	0.3055	0.1105	0.24	1.00
<b>O45</b>	1.0040	0.3111	0.1011	0.24	1.00
<b>O46</b>	1.1362	0.2952	0.0920	0.24	1.00
<b>O47</b>	0.9543	0.5053	0.2948	0.24	1.00
<b>O48</b>	1.1475	0.5052	0.2904	0.24	1.00

**TOL**

<b>C1</b>	0.9031	-0.4989	1.0658	3.36	0.20
<b>H1</b>	0.9066	-0.5396	1.1043	5.03	0.20
<b>H2</b>	0.9226	-0.4626	1.1036	5.03	0.20
<b>H3</b>	0.9271	-0.5041	1.0037	5.03	0.20
<b>C2</b>	0.7185	-0.5233	1.0060	3.36	0.20
<b>H4</b>	0.6888	-0.5581	0.9940	4.03	0.20
<b>C3</b>	0.7861	-0.5364	1.0265	3.36	0.20
<b>H5</b>	0.8015	-0.5801	1.0283	4.03	0.20
<b>C4</b>	0.8305	-0.4843	1.0440	3.36	0.20
<b>C5</b>	0.6956	-0.4581	1.0036	3.36	0.20
<b>H6</b>	0.6507	-0.4493	0.9895	4.03	0.20
<b>C6</b>	0.8074	-0.4189	1.0420	3.36	0.20
<b>H7</b>	0.8370	-0.3840	1.0539	4.03	0.20
<b>C7</b>	0.7400	-0.4061	1.0221	3.36	0.20
<b>H8</b>	0.7245	-0.3626	1.0212	4.03	0.80

**HEX**

<b>C8</b>	0.8766	-0.5156	1.0475	5.91	0.80
<b>H9</b>	0.8947	-0.4745	1.0643	5.91	0.80
<b>C9</b>	0.8042	-0.5238	1.0409	5.91	0.80
<b>H10</b>	0.7850	-0.5651	1.0284	5.91	0.80
<b>C10</b>	0.7664	-0.4700	1.0535	5.91	0.80
<b>H11</b>	0.7873	-0.4296	1.0664	5.91	0.80
<b>C11</b>	0.6938	-0.4725	1.0480	5.91	0.80
<b>H12</b>	0.6716	-0.5126	1.0380	5.91	1.00
<b>C12</b>	0.7622	-0.0080	1.2529	5.91	1.00
<b>H13</b>	0.7562	-0.0168	1.3204	5.91	1.00
<b>C13</b>	0.7605	-0.1844	1.1662	5.91	1.00
<b>H14</b>	0.7193	-0.1970	1.1306	5.91	1.00
<b>H15</b>	0.7976	-0.1813	1.1187	5.91	1.00
<b>C14</b>	0.7517	-0.1214	1.2195	5.91	1.00
<b>H16</b>	0.7319	-0.1225	1.2821	5.91	0.80
<b>C15</b>	0.7701	-0.0633	1.1838	5.91	1.00
<b>H17</b>	0.7868	-0.0580	1.1196	5.91	0.80
<b>O49</b>	0.7347	-0.3386	1.1373	3.16	1.00
<b>O50</b>	0.5524	-0.4989	0.9940	3.16	1.00
<b>C16</b>	0.6595	-0.4161	1.0574	5.91	0.80
<b>H18</b>	0.6821	-0.3762	1.0673	5.91	1.00
<b>H19</b>	0.6128	-0.4166	1.0540	5.91	1.00
<b>C17</b>	0.9167	-0.5663	1.0297	5.91	0.80
<b>H20</b>	0.8987	-0.6075	1.0129	5.91	1.00
<b>H21</b>	0.9630	-0.5609	1.0340	5.91	1.00
<b>C18</b>	0.7633	0.0539	1.2222	5.91	1.00
<b>H22</b>	0.7692	0.0633	1.1549	5.91	1.00
<b>H23</b>	0.7581	0.0883	1.2677	5.91	1.00
<b>C19</b>	0.7767	-0.2333	1.2482	5.91	1.00
<b>H24</b>	0.8170	-0.2193	1.2833	5.91	1.00
<b>H25</b>	0.7838	-0.2769	1.2195	5.91	1.00
<b>H26</b>	0.7396	-0.2352	1.2945	5.91	1.00

---

**Table 4 SI.** Selected atomic bond distances for the TOL-ZSM-5 system.

<b>Atom 1</b>	<b>Atom 2</b>	<b>Distance (Å)</b>
SI1	O1	1.591
SI1	O15	1.595
SI1	O16	1.592
SI2	O1	1.595
SI2	O2	1.595
SI2	O6	1.595
SI2	O13	1.598
SI3	O2	1.595
SI3	O3	1.597
SI4	O3	1.598
SI4	O4	1.597
SI5	O4	1.597
SI5	O5	1.599
SI5	O14	1.597
SI5	O21	1.594
SI6	O5	1.596
SI6	O6	1.593
SI6	O18	1.592
SI6	O19	1.594
SI7	O7	1.593
SI7	O17	1.589
SI7	O23	1.594
SI8	O7	1.598
SI8	O8	1.592
SI8	O12	1.592
SI8	O13	1.598
SI9	O8	1.591
SI9	O9	1.598
SI9	O25	1.594
SI10	O9	1.599
SI10	O10	1.594
SI10	O26	1.594
SI11	O10	1.596
SI11	O11	1.594
SI11	O14	1.597
SI11	O22	1.592
SI12	O11	1.595
SI12	O12	1.595
SI12	O20	1.589
SI12	O24	1.593
SI13	O27	1.600
SI13	O41	1.591
SI13	O42	1.588
SI14	O27	1.601
SI14	O28	1.600
SI14	O32	1.589

SI14	O39	1.596
SI15	O19	1.594
SI15	O20	1.593
SI15	O28	1.598
SI15	O29	1.597
SI16	O16	1.596
SI16	O17	1.592
SI16	O29	1.595
SI16	O30	1.595
SI17	O30	1.595
SI17	O31	1.598
SI17	O40	1.597
SI17	O47	1.595
SI18	O31	1.600
SI18	O32	1.590
SI18	O44	1.591
SI18	O45	1.591
SI19	O33	1.594
SI19	O43	1.591
SI20	O33	1.595
SI20	O34	1.598
SI20	O38	1.596
SI20	O39	1.597
SI21	O18	1.594
SI21	O34	1.599
SI21	O35	1.593
SI22	O15	1.595
SI22	O35	1.592
SI22	O36	1.597
SI23	O36	1.598
SI23	O37	1.595
SI23	O40	1.597
SI23	O48	1.594
SI24	O37	1.594
SI24	O38	1.596
SI24	O46	1.591
C7	H7	1.102
C7	H7A	1.102
C7	H7B	1.078
C7	C4	1.447
C5	H5	1.111
C5	H5A	1.112
C5	C6	1.482
C5	C2	1.490
C6	H6	1.078
C6	C4	1.340
C4	C3	1.452
C2	H2	1.158

C2	H2A	1.119
C2	C1	1.437
C3	H3	1.093
C3	C1	1.348
C1	H1	1.025
C14	H14	1.102
C14	H14A	1.105
C14	H14B	1.108
C14	C13	1.456
C8	H8	1.067
C8	C9	1.405
C8	C11	1.391
C9	H9	1.065
C9	C13	1.384
C10	H10	1.077
C10	C11	1.390
C10	C12	1.389
C11	H11	1.071
C12	H12	1.078
C12	C13	1.386

---

**Table 5 SI.** Selected atomic bond distances for the HEX-ZSM-5 system.

<b>Atom 1</b>	<b>Atom 2</b>	<b>Distance (Å)</b>
SI1	O1	1.597
SI1	O15	1.596
SI1	O16	1.588
SI2	O1	1.597
SI2	O2	1.588
SI2	O6	1.598
SI2	O13	1.598
SI3	O2	1.593
SI3	O3	1.595
SI4	O3	1.596
SI4	O4	1.595
SI5	O4	1.597
SI5	O5	1.598
SI5	O14	1.597
SI5	O21	1.595
SI6	O5	1.601
SI6	O6	1.590
SI6	O18	1.596
SI6	O19	1.588
SI7	O7	1.589
SI7	O17	1.586
SI7	O23	1.594
SI8	O7	1.593
SI8	O8	1.587
SI8	O12	1.597
SI8	O13	1.597
SI9	O8	1.585
SI9	O9	1.594
SI9	O25	1.594
SI10	O9	1.594
SI10	O10	1.586
SI10	O26	1.588
SI11	O10	1.585
SI11	O11	1.594
SI11	O14	1.595
SI11	O22	1.593
SI12	O11	1.592
SI12	O12	1.597
SI12	O20	1.587
SI12	O24	1.593
SI13	O27	1.591
SI13	O41	1.590
SI13	O42	1.584
SI14	O27	1.591
SI14	O28	1.598
SI14	O32	1.596

SI14	O39	1.607
SI15	O19	1.600
SI15	O20	1.605
SI15	O28	1.591
SI15	O29	1.570
SI16	O16	1.591
SI16	O17	1.589
SI16	O29	1.593
SI16	O30	1.588
SI17	O30	1.596
SI17	O31	1.593
SI17	O40	1.623
SI17	O47	1.569
SI18	O31	1.590
SI18	O32	1.593
SI18	O44	1.588
SI18	O45	1.588
SI19	O33	1.596
SI19	O43	1.592
SI20	O33	1.594
SI20	O34	1.599
SI20	O38	1.601
SI20	O39	1.597
SI21	O18	1.597
SI21	O34	1.596
SI21	O35	1.593
SI22	O15	1.594
SI22	O35	1.592
SI22	O36	1.599
SI23	O36	1.600
SI23	O37	1.592
SI23	O40	1.603
SI23	O48	1.595
SI24	O37	1.596
SI24	O38	1.598
SI24	O46	1.591
C1	H1	0.929
C1	C2	1.453
C1	C10	1.319
C2	H2	0.930
C2	C3	1.330
C3	H3	0.929
C3	C4	1.448
C4	H4	0.930
C4	C9	1.332
C5	H5	0.931
C5	C8	1.458
C5	C11	1.313

C6	H6	0.979
C6	H6A	0.981
C6	C7	1.467
C6	C12	1.509
C7	H7	0.930
C7	C8	1.317
C8	H8	0.931
C9	H9A	0.930
C9	H9B	0.931
C10	H10A	0.930
C10	H10B	0.930
C11	H11A	0.930
C11	H11B	0.929
C12	H12	0.969
C12	H12A	0.969
C12	H12B	0.969

---

**Table 6 SI.** Selected atomic bond distances for the HEX-TOL-ZSM-5 system.

<b>Atom 1</b>	<b>Atom 2</b>	<b>Distance (Å)</b>
SI1	O1	1.604
SI1	O15	1.623
SI1	O16	1.568
SI2	O1	1.594
SI2	O2	1.625
SI2	O6	1.637
SI2	O13	1.581
SI3	O2	1.649
SI3	O3	1.644
SI4	O3	1.626
SI4	O4	1.632
SI5	O4	1.669
SI5	O5	1.560
SI5	O14	1.567
SI5	O21	1.626
SI6	O5	1.647
SI6	O6	1.576
SI6	O18	1.612
SI6	O19	1.591
SI7	O7	1.576
SI7	O17	1.616
SI7	O23	1.641
SI8	O7	1.616
SI8	O8	1.584
SI8	O12	1.598
SI8	O13	1.639
SI9	O8	1.600
SI9	O9	1.616
SI9	O25	1.616
SI10	O9	1.612
SI10	O10	1.600
SI10	O26	1.612
SI11	O10	1.603
SI11	O11	1.578
SI11	O14	1.636
SI11	O22	1.617
SI12	O11	1.617
SI12	O12	1.651
SI12	O20	1.616
SI12	O24	1.592
SI13	O27	1.612
SI13	O41	1.661
SI13	O42	1.606
SI14	O27	1.622
SI14	O28	1.631
SI14	O32	1.619

SI14	O39	1.561
SI15	O19	1.618
SI15	O20	1.631
SI15	O28	1.580
SI15	O29	1.578
SI16	O16	1.619
SI16	O17	1.622
SI16	O29	1.600
SI16	O30	1.533
SI17	O30	1.634
SI17	O31	1.561
SI17	O40	1.591
SI17	O47	1.618
SI18	O31	1.661
SI18	O32	1.591
SI18	O44	1.612
SI18	O45	1.591
SI19	O33	1.624
SI19	O43	1.621
SI20	O33	1.629
SI20	O34	1.637
SI20	O38	1.581
SI20	O39	1.621
SI21	O18	1.641
SI21	O34	1.602
SI21	O35	1.628
SI22	O15	1.612
SI22	O35	1.626
SI22	O36	1.615
SI23	O36	1.629
SI23	O37	1.598
SI23	O40	1.588
SI23	O48	1.635
SI24	O37	1.623
SI24	O38	1.631
SI24	O46	1.595
C1	H2	0.969
H1	C8	1.079
H1	C17	1.153
H3	C8	1.186
H3	C17	1.315
C2	H4	0.929
C2	C5	1.388
C2	C9	1.762
C2	C10	1.567
C2	H12	1.048
H5	C9	1.146
C4	C6	1.393

C4	C8	1.111
C4	H9	1.317
C4	C9	0.951
C4	C10	1.310
C5	H6	0.927
C5	C7	1.389
C5	C10	1.572
C5	H12	1.281
C5	C16	1.323
H6	C16	1.142
C6	H7	0.929
C6	C7	1.387
C6	C10	1.320
C7	H8	0.927
C7	C10	1.450
C7	C16	1.679
C8	H9	0.929
C8	C9	1.448
C8	C17	1.316
C9	C10	1.327
C12	H13	0.930
C12	C15	1.456
C12	C18	1.311
C13	H14	0.979
C13	H15	0.977
C13	C14	1.465
C13	C19	1.509
C14	H16	0.928
C14	C15	1.315
C15	H17	0.930
C16	H18	0.929
C16	H19	0.928
C17	H20	0.930
C17	H21	0.927
C18	H22	0.930
C18	H23	0.928
C19	H24	0.968
C19	H25	0.968
C19	H26	0.965

---

**Table 7 SI.** The ellipticity ( $\varepsilon$  = largest/shortest oxygen–oxygen bond distances) and C.F.A. (Crystallographic Free Area in Å<sup>2</sup> calculated assuming an oxygen ionic radius of 1.35 Å) of the apertures for the ZSM-5 systems here investigated (*i.e.*, after the adsorption of TOL, HEX, and HEX-TOL).

$\varepsilon$ <b>Straight Channel (SC)</b> <b>TOL-ZSM-5</b>	$\varepsilon$ <b>Straight Channel (SC)</b> <b>HEX-ZSM-5</b>	$\varepsilon$ <b>Straight Channel (SC)</b> <b>HEX-TOL-ZSM-5</b>
1.07	1.08	1.06
1.05	1.03	1.04
$\varepsilon$ <b>Sinusoidal Channel (ZZ)</b> <b>TOL-ZSM-5</b>	$\varepsilon$ <b>Sinusoidal Channel (ZZ)</b> <b>HEX-ZSM-5</b>	$\varepsilon$ <b>Sinusoidal Channel (ZZ)</b> <b>HEX-TOL-ZSM-5</b>
1.06	1.05	1.08
1.10	1.10	1.11
<b>C.F.A.</b> <b>Straight Channel (SC)</b> <b>TOL-ZSM-5</b>	<b>C.F.A.</b> <b>Straight Channel (SC)</b> <b>HEX-ZSM-5</b>	<b>C.F.A.</b> <b>Straight Channel (SC)</b> <b>HEXTOL-ZSM-5</b>
24.48	24.40	23.35
23.64	23.42	22.92
<b>C.F.A.</b> <b>Sinusoidal Channel (ZZ)</b> <b>TOL-ZSM-5</b>	<b>C.F.A.</b> <b>Sinusoidal Channel (ZZ)</b> <b>HEX-ZSM-5</b>	<b>C.F.A.</b> <b>Sinusoidal Channel (ZZ)</b> <b>HEXTOL--ZSM-5</b>
24.17	24.78	23.05
23.25	22.98	22.20



ELSEVIER

Contents lists available at ScienceDirect

Catalysis Today

journal homepage: [www.elsevier.com/locate/cattod](http://www.elsevier.com/locate/cattod)

## Insights on Ga-zeolite catalysts: X-ray powder diffraction and absorption spectroscopy characterization at ambient conditions

G. Beltrami<sup>a,\*</sup>, T. Chenet<sup>b</sup>, L. Pasti<sup>b,\*\*</sup>, L. Gigli<sup>c</sup>, S. Pollastri<sup>d,\*\*\*</sup>, A. Martucci<sup>a</sup>

<sup>a</sup> Dept. of Earth Sciences, University of Ferrara, Via Saragat, 1, I-44122 Ferrara, Italy

<sup>b</sup> Dept. of Chemical and Pharmaceutical Sciences, University of Ferrara, Via Luigi Borsari, 43, I-44122 Ferrara, Italy

<sup>c</sup> Elettra - Sincrotrone Trieste S.C.p.A. Strada Statale 14 34149 Basovizza, Trieste, Italy

<sup>d</sup> CERIC-ERIC Strada Statale 14 34149 Basovizza, Trieste, Italy

### ARTICLE INFO

#### Keywords:

Gallium substituted zeolite  
XRPD  
Adsorption isotherm  
XAS  
Gallium location

### ABSTRACT

Gallium substituted L, mordenite and ferrierite zeolites, obtained through wet impregnation, were characterized combining adsorption isotherms, X-ray powder diffraction (XRPD) and X-ray absorption spectroscopy (XAS) to elucidate nature and structure of the Ga<sup>+3</sup> sites of the materials. The saturation capacity of L was higher than those of mordenite and ferrierite. Rietveld refinements on saturated materials confirm the presence of Ga<sup>+3</sup> within the zeolites pores system. Besides, the analysis of the structural features (*i.e.*, lightening of tetrahedral bond distances and narrowing of intertetrahedral angles) suggest that small fractions of metal cation have been also incorporated in tetrahedral sites. This is corroborated by XAS analysis, which confirms the effective inclusion of gallium into the zeolites frameworks, thus indicating that the incorporation of Ga<sup>+3</sup> from wet impregnation within the zeolite structures occurs in both framework and non-framework positions.

### 1. Introduction

Zeolite are crystalline microporous materials whose framework is build up by corner-sharing TO<sub>4</sub> tetrahedra, where T usually contain Si<sup>+4</sup> or Al<sup>+3</sup>. The insertion of other tetrahedral coordinated heteroatoms (*e.g.*, Fe, Ga, Ge, B, Ti, *etc*) provides a means to modify their physicochemical properties as well as to increase their catalytic activity [1]. In addition, zeolite properties can be also modified by cation exchange process, in such a case, the type and localization of extra-framework cations control and influence their selectivity and catalytic activity [2]. An interesting family of catalysts is that of Ga-loaded zeolites due to their excellent performances in isomerization, disproportionation and alkylation of aromatics and aromatization of alkanes and/or alkenes [3–6]. Gallium-containing zeolites have been widely investigated in the last decades and newest applications concerning the removal of NO<sub>x</sub> from gas streams of exhaust engine and the conversion of biomass into biofuels and bio-based chemicals have been proposed [5,7,8]. Ga-zeolite catalysts can be obtained through hydrothermal crystallization in presence of the suitable template agent or post synthesis treatments, such as galliation, recrystallization, wet impregnation, chemical vapor deposition (CVD) and ion exchange [5,9].

The ion exchange process is suitable to introduce gallium into both tetrahedral coordinated framework and interstitial non-framework positions. Besides, the precipitation on the external surface of the zeolite crystal of a separate gallium phase in aqueous solution, depending on the pH value during the exchange process, has to be foreseen. Substitution of Al<sup>+3</sup> with Ga<sup>+3</sup> cations [10] into framework positions is the main source of lattice charge defects, which give rise to Brønsted acidic Si–OH–Ga bridging hydroxyl group and, consequently, to modification of catalytic properties. To understand the precise nature and functioning of the active sites in working zeolites, incorporation of Ga<sup>+3</sup> into the zeolite framework has been highlighted by means of solid-state NMR, EXAFS, *in situ* X-ray photoelectron spectroscopy, IR spectroscopy and DFT calculations [11–17]. Along with the segregate gallium phase, excess gallium not incorporated in tetrahedral sites is trapped within the zeolite pores system as substituent of metal cations, ammonium ions or protons. The presence of gallium cations in extraframework positions introduces Lewis acidity, which is also originated from oxo cations GaO<sup>+</sup> in exchanged framework positions. Due to its size, gallium in framework positions is metastable; hence, the thermal treatment can cause the migration of Ga<sup>+3</sup> to extraframework positions and its progressive aggregation in form of isolated, dimeric and polymeric species up to

\* Corresponding author.

\*\* Corresponding author.

\*\*\* Corresponding author.

E-mail address: [bltgd@unife.it](mailto:bltgd@unife.it) (G. Beltrami).

<https://doi.org/10.1016/j.cattod.2019.09.016>

Received 13 July 2019; Received in revised form 3 September 2019; Accepted 11 September 2019

0920-5861/ © 2019 Elsevier B.V. All rights reserved.

oxide nanoparticles [18–20]. This migration leads to the appearance of a different type of acid sites of Lewis nature [21]. As a consequence, Ga exchanged zeolites can possess both Brønsted and Lewis acid sites, working separately or in a synergistic way in acid catalysed reactions [22,23]. To our knowledge, in spite of the large number of both spectroscopic and computational studies, very few detailed structural investigations have been conducted so far to explore the gallium centres using X-ray diffraction methods. With this aim, in this work we intend to investigate the structural features of Ga-loaded zeolites in order to elucidate the nature of the gallium active sites combining X-ray powder diffraction (XRPD), X-ray absorption spectroscopy (XAS) and adsorption study.

Among zeolites, gallium modified L (LTL), mordenite (MOR) and ferrierite (FER), have been employed as catalysts [24]. Consequently, these large and medium pore materials were selected in this work to: 1) investigate the adsorptive properties of hydrophobic synthetic zeolites; 2) characterize zeolites structure at ambient conditions, 3) locate and quantify  $\text{Ga}^{+3}$  cations in framework and non-framework positions, 4) determine the presence of water molecules completing the extra-framework  $\text{Ga}^{+3}$  coordination, 5) determine unit cell dimensions as well as host-guest interactions by the analysis of bond length distances. All these information are essential not only for their characterization but also for their industrial applications.

## 2. Materials and methods

### 2.1. Zeolites

The synthetic zeolite L sample (HSZ-500KOA code) was purchased by Tosoh Corporation in the K form, with a  $\text{SiO}_2/\text{Al}_2\text{O}_3$  (SAR) ratio of 6.1, an  $\text{Na}_2\text{O}$  content of 0.25 wt % and a surface area of about  $290 \text{ m}^2/\text{g}$ . MOR (CBV10A code) and FER (CP914C code) samples were supplied by Zeolyst International in  $\text{Na}^+$  and ammonium forms, respectively. The first is characterized by a SAR equal to 13, a  $\text{Na}_2\text{O}$  content of 6.5 wt % and a surface area of  $425 \text{ m}^2/\text{g}$ , whereas the second by a SAR equal to 20,  $\text{Na}_2\text{O}$  content lower than 0.05 wt % and surface area of  $400 \text{ m}^2/\text{g}$ .

### 2.2. Cation exchange

As-received L and MOR zeolites were exchanged with ammonium by the following procedure: 1 g of zeolite was stirred in 200 mL of 0.5 M solution of ammonium nitrate (> 99%, Sigma Aldrich) in MilliQ water at 343 K for 24 h. The suspension was then filtered, by using a Nylon filter  $0.22 \mu\text{m}$  (Sigma Aldrich) at room temperature and rinsed with 300 mL of MilliQ water. This procedure was repeated twice. The ammonium form of L and MOR and the as-received FER were heated in a furnace for five hours at  $\sim 600 \text{ }^\circ\text{C}$  in order to obtain the calcined-form.

**Table 1**

Crystallographic data obtained from the Rietveld refinements of Ga-L, Ga-MOR and Ga-FER systems.

Parameter	Ga-L $\text{Ga}_{2.57}\text{K}_2((\text{GaAlSi})_{36}\text{O}_{72}) \cdot 14\text{H}_2\text{O}$	Ga-MOR $\text{Ga}_{1.16}\text{Na}_2((\text{GaAlSi})_{48}\text{O}_{96}) \cdot 13\text{H}_2\text{O}$	Ga-FER $\text{Ga}_{1.3}((\text{GaAlSi})_{36}\text{O}_{72}) \cdot 5\text{H}_2\text{O}$
Wavelength ( $\text{\AA}$ )	1.54059	1.54059	1.54059
$2\theta$ ( $^\circ$ ) range	5.5-100	5.5-100	5.5-100
$N_{\text{obs}}$	1339	1482	1564
$N_{\text{var}}$	56	76	64
$R_{\text{wp}}$ (%)	14.45	13.35	14.59
$R_p$ (%)	10.83	10.17	11.34
$R_F^2$ (%)	16.85	11.32	12.29
$R_p = \sum  Y_{io} - Y_{ic}  / \sum Y_{io}$ ; $R_{\text{wp}} = [\sum w_i(Y_{io} - Y_{ic})^2 / \sum w_i Y_{io}^2]^{0.5}$ ; $R_F^2 = \sum  F_o^2 - F_c^2  / F_o^2$			

## 3. Experimental techniques

### 3.1. Wet impregnation

Cation exchange capacity was determined by using aqueous solutions of gallium nitrate ( $\text{Ga}(\text{NO}_3)_3 \cdot x\text{H}_2\text{O}$ , Aldrich 99.9%) at different initial concentrations (5, 10, 20, 50, 70, 100, 150 and  $200 \text{ mg L}^{-1}$ ), placed in contact with zeolites (L, FER and MOR) with a solid/liquid ratio of 1:1 ( $\text{mg/mL}$ ). The suspensions were kept at 343 K under stirring during the contact time at pH 4.3, the pH was monitored during the contact and variation of 0.3 pH unit occur from the beginning to the end of the contact. All batch experiments were carried out in duplicate. The concentrations of  $\text{Ga}^{+3}$  in the solutions after the contact with zeolites and in the reference solutions obtained by keeping solutions in the same conditions of the adsorption experiments but without the addition of zeolites, were quantified by ICP-OES (Perkin-Elmer Optima 3100 XL) (axial view) equipped with a solid-state charge-coupled device detector (CCD), a peristaltic pump and a low-flow GemCone nebulizer coupled to a cyclonic spray chamber. Background correction was carried out using a two-points method. Analytical line 294.364 nm was selected for quantitative determination. The amount of exchanged cations at equilibrium,  $q_e$  ( $\text{mg g}^{-1}$ ), was calculated from the mass balance equation, Eq. (1):

$$q_e = \frac{(C_i - C_e)V}{M} \quad (1)$$

where  $C_i$  and  $C_e$  ( $\text{mg L}^{-1}$ ) are the liquid-phase concentrations of Ga in the reference solution and at equilibrium respectively;  $V$  (L) is the volume of the solution and  $M$  (g) is the mass of dry zeolite used. Samples of saturated zeolite exchanged with Ga were used for structural and spectroscopic investigations. Calcined Mordenite, Ferrierite and L zeolites (0.5 g) were suspended with stirring in 500 ml of an aqueous solution of gallium nitrate ( $\text{Ga}(\text{NO}_3)_3 \cdot x\text{H}_2\text{O}$ , Aldrich 99.9%) at pH 4.2, 343 K for 24 h. The zeolites were recovered by filtration, washed with 200 mL of MilliQ water and dried in oven at 383 K overnight.

### 3.2. X-ray powder diffraction and Rietveld refinements

Powder patterns of the Ga-exchanged zeolites, here after called Ga-L, Ga-MOR and Ga-FER were collected on a Bruker D8 Advance diffractometer equipped with a Si/Li solid state detector (Sol-X). Measurements were performed at Room Temperature, using the  $\text{CuK}\alpha 1, \alpha 2$  wavelength, in a  $3\text{--}100^\circ 2\theta$  range. Full profile Rietveld refinements were performed through the GSAS software [25] and the EXPGUI graphical interface [26], using the hexagonal  $P6/mmm$  and the orthorhombic  $Cmcm$  and  $Immm$  space groups for Ga-L, Ga-MOR and Ga-FER systems, respectively. Details on the refined parameters are reported in Table 1 and below:

**Ga-L.** Peak profiles were modelled through the Pseudo-Voigt function with 0.1% cut-off peak intensity. The profile function selected was the number 2 and the coefficients refined were: Gaussian  $\theta$ -independent  $GW$ , Lorentian  $\cos\theta^{-1}$   $LX$  and  $\tan\theta$ -dependent  $LY$  terms, peak

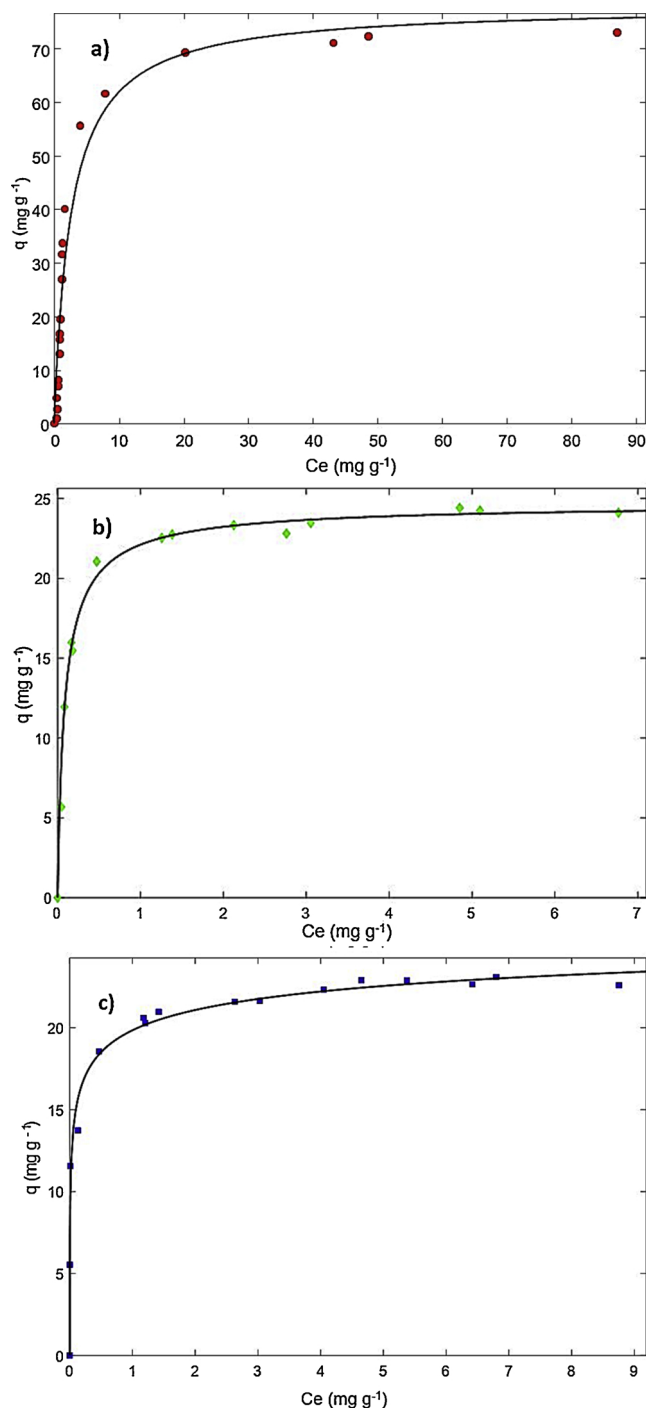


Fig. 1. Adsorption of gallium on a) L zeolite, b) Ferrierite and c) Mordenite.

asymmetry and  $ptec$  parameters. The empirical background was fitted through the Chebyshev polynomial function and 18 coefficients.

**Ga-MOR.** Peak profiles were modelled through the Pseudo-Voigt function with 0.5% cut-off peak intensity. The profile function selected was the number 2 and the coefficients refined were: Gaussian  $\theta$ -independent  $GW$ ,  $\tan^2\theta$ -dependent  $GU$ ,  $\tan\theta$ -dependent  $GV$  and Lorentian  $\cos\theta^{-1}$  dependent  $LX$  terms, peak asymmetry and  $ptec$  parameters. The empirical background was fitted through the Chebyshev polynomial function and 26 coefficients.

**Ga-FER.** Peak profiles were modelled through the Pseudo-Voigt function with 0.1% cut-off peak intensity. The profile function selected was the number 2 and the coefficients refined were: Gaussian  $\theta$ -independent  $GW$ , Lorentian  $\cos\theta^{-1}LX$  and  $\tan\theta$ -dependent  $LY$  terms, peak

asymmetry,  $ptec$  and  $stec$  parameters. The empirical background was fitted through the Chebyshev polynomial function and 15 coefficients.

Scale factor and  $2\theta$  zero shift were also accurately refined for all the systems. Besides, in all the structural refinements soft constraints were initially imposed on tetrahedral distances ( $\sigma = 0.04 \text{ \AA}$ ) and completely removed in the last refinement cycles. Whereas, atomic coordinates, site occupancies and isotropic atomic displacement parameters (UIISO) were refined, constraining equivalent UIISO for framework oxygen atoms of each system. Framework and extraframework fractional coordinates of Ga-L, Ga-MOR and Ga-FER systems are reported in Tables S11–S13, respectively.

### 3.3. X-ray absorption spectroscopy

Ga K-edge XAS spectra were collected at the XAFS beamline (ELETTRA, Trieste, Italy) [27] in transmission mode using fixed exit double crystal Si(111) monochromator. For all the samples, energy calibration was accomplished by collecting simultaneously a reference spectrum of a GaAs pellet placed in a second experimental chamber after the sample and after the I1 ionization chamber, with the position of the first inflection point taken at 10,369.0 eV. All spectra were collected at room temperature and in vacuum conditions, with a variable energy step as a function of the energy: large step (5 eV) in the first 200 eV of the spectrum, smaller step (0.2 eV) in the XANES region and a  $k$ -constant step of  $0.03 \text{ \AA}^{-1}$  (up to 1.8 eV) in the EXAFS region.

For each sample, 4 spectra have been collected and merged in order to increase the signal to noise ratio; merged spectra were then normalized with respect to the high-energy side of the curve and EXAFS signals have been extracted using the Athena software [28]. The extracted EXAFS signals were then Fourier transformed using a Hanning window in the  $k$  range  $3\text{--}15 \text{ \AA}^{-1}$  and quantitative analysis were carried out using the Artemis software (Demeter 0.9.25 package) [28,29].

Structural model for the calculation of the theoretical paths were retrieved by Rietveld refinements of the XRPD data of Ga-FER, Ga-MOR, Ga-L. Along with the samples, the compound  $\text{Ga}(\text{NO}_3)_3 \cdot x\text{H}_2\text{O}$  used for the sample preparation was also measured as reference for octahedral coordinated gallium.

## 4. Results and discussion

### 4.1. Adsorption of gallium on calcined zeolites

The gallium exchanged zeolites were obtained by wet impregnation by placing in contact aqueous solution of gallium nitrate with zeolites. During this process, the solution pH can affect the adsorption, since in very acidic media ( $\text{pH} < 2$ ) the stability of zeolite diminished and dissolution phenomena occur with change in crystallinity and in composition (dealumination) of the adsorbent material [30]. On the other hand, Gallium undergoes hydrolysis and polymerization in aqueous solution, with increasing pH. Starting from  $\text{pH} > 2$ , a progressive formation of hydroxylated monomeric specie occurs and at slightly acid pH polymeric polycations are the dominant species. Therefore, a compromise pH value equal to 4 was selected for the experiments. The total quantity of gallium adsorbed from the solution at different concentrations were evaluated by atomic spectroscopy. In Fig.1(a–c) the adsorption isotherms are reported, it can be seen that all the three zeolites show an L-Type isotherm, and zeolite L is characterized by a higher saturation capacity. The data were fitted by Langmuir and Töth isotherm models given respectively by Eqs. (2) and (3):

$$q_e = \frac{q_s K_L c_e}{1 + b c_e} \quad (2)$$

$$q_e = \frac{q_s K_T c_e}{(1 + (b c_e)^v)^{1/v}} \quad (3)$$

where,  $q_s$  is the saturation capacity and  $K_L$  and  $K_T$  the affinity constant

**Table 2**

Gallium cation exchange isotherm parameters.  $q_e$  ( $\text{mg g}^{-1}$ ): exchanged concentration at equilibrium;  $C_e$  ( $\text{mg dm}^{-3}$ ): concentration in the solution at equilibrium;  $K_L, K_T$  ( $\text{dm}^3 \text{mg}^{-1}$ ): affinity constants for the Langmuir and the Tóth models, respectively;  $q_s$  ( $\text{mg g}^{-1}$ ) cation exchange capacity;  $\nu$  heterogeneity parameter in the Tóth model (see text for further details). Confidence bounds at 95% of probability are reported in parenthesis.

Parameters	L	FER	MOR
$q_s$ ( $\text{mg g}^{-1}$ )	78.02 (70.71, 85.33)	24.52 (23.86, 25.17)	21.36 (20.07, 22.65)
$K_L$ ( $\text{dm}^3 \text{mg}^{-1}$ )	0.3841 (0.2723, 0.4959)	9.946 (8.329, 11.56)	34.9 (17.87, 51.9)
$R^2$	0.9505	0.9913	0.9328
$q_s$ ( $\text{mg g}^{-1}$ )	71.16 (65.61, 76.71)	24.76 (23.72, 25.8)	30.47 (21.88, 39.07)
$K_T$ ( $\text{dm}^3 \text{mg}^{-1}$ )	0.2788 (0.2191, 0.3385)	14.14 (7.92, 20.36)	38.4 (25.7 52.3)
$\nu$	0.83 (0.42, 1.24)	0.86 (0.64, 1.08)	0.2291 (0.1135, 0.3447)
$R^2$	0.9696	0.9954	0.9874

for the Langmuir and the Tóth models, respectively, in Eq. 3  $\nu$  represent the heterogeneity parameter. The fitting results are reported in Table 2, the values in parenthesis indicate the confidence limits at 95 % of probability. As can be seen from the coefficient of determination listed in this table, both the Langmuir and the Tóth models fit quite well the experimental data. In particular, for both L and FER, the heterogeneity parameter  $\nu$  appearing in the Tóth isotherm (see Table 2) is not significantly different from 1 and for  $\nu = 1$ , the Tóth isotherm corresponds to the Langmuir one. On the contrary, for MOR a  $\nu$  value lower than 1 was found. The heterogeneity parameter is related to the width of the energy distribution function, and lower value correspond to larger distribution and, therefore, to energetically heterogeneous sites on the surface. From the adsorption data therefore it seems that the adsorption onto MOR could involve sites of different energies. However, it should be mentioned that Langmuir isotherm has also been employed to describe the adsorption on multiple sites [31], in such cases it is supposed that their interactions energies are similar and they can be averaged to give a single averaged energy for all the sites. To gain more information on the involved site, a structural investigation on the Ga-exchanged zeolites were carried out.

#### 4.2. X-ray powder diffraction results

##### 4.2.1. Ga-L system

Zeolite L (ideal formula  $\text{K}_6\text{Na}_3\text{Al}_9\text{Si}_{27}\text{O}_{72} \cdot 21\text{H}_2\text{O}$ , framework-type LTL) is a large pore material whose framework is built from columns of cancrinite cages stacked with double six membered rings (D6R) along the  $c$  axis [32]. The 4-rings in these columns are cross-linked to form continuous 12-ring channels along the  $c$ -direction with a maximum diameter of 12.6 Å [33]. The Ga-L crystal structure was refined in the  $P6/mmm$  space group, starting from the atomic coordinates reported by Barrer and Villiger, H. (1969) [33]. The refined Ga-L lattice parameters are the following:  $a = b = 18.2177(24)$  Å,  $c = 7.5538(15)$  Å and  $V = 2171.1(6)$  Å<sup>3</sup>. According to Newsam [34] the framework bond distances confirm the not random distribution of Al (and/or Ga) in the tetrahedral sites (Table SI4). The T1-O bond lengths range from 1.630(4) and 1.668(3) Å (mean distance of 1.650 Å); whereas the T2-O ranges from 1.639(6), Å and 1.846(1) Å (mean distance 1.722 Å). Compared with the mean  $\langle \text{T-O} \rangle$  bond lengths refined for the L-LTL precursor ( $\langle \text{T1-O} \rangle = 1.640$  Å and  $\langle \text{T2-O} \rangle = 1.654$  Å, *in preparation*), a lightening of both tetrahedral distances is observed. This result suggests the incorporation of gallium in both tetrahedral sites and a Ga-enrichment in the T2 one due to the longer average  $\langle \text{T2-O} \rangle$  bond length. From the structural point of view, noteworthy are the very narrow T-O-T angles centred on the O1 and O5 framework oxygen atoms ( $\text{T1-O1-T1} = 112.6(5)$  and  $\text{T2-O5-T2} = 115.4(3)^\circ$ ), even if they

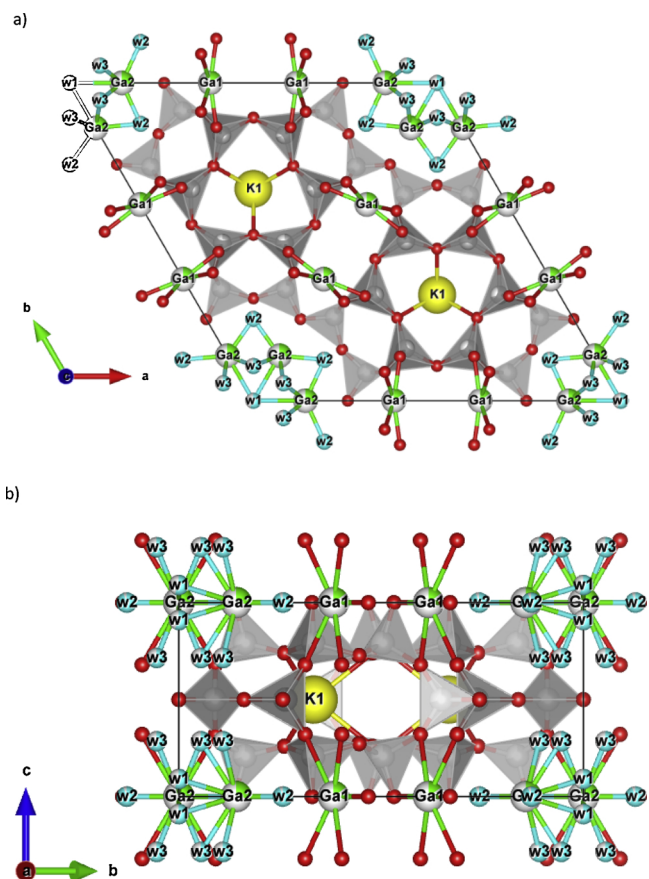


Fig. 2. Extraframework content distribution of Ga-L system. Projection along  $c$  (a) and  $a$  (b) axis.

are not the narrowest found in zeolites [35–38] (Table SI4). The difference Fourier map generated using the GSAS package [25,26] highlights the presence of six extraframework sites, which were distributed among  $\text{K}^+$  and  $\text{Ga}^{+3}$  cations, and water molecules (Fig. 2). The non-exchanged  $\text{K}^+$  was localized at the centre of the 6MR (corresponding to the KB site in the L-LTL zeolite [33], within the cancrinite cage. Two extraframework sites were assigned to  $\text{Ga}^{+3}$  ions (*i.e.*, labelled Ga1 and Ga2, respectively) and were located not far from the centre of the 8MR (Ga1) and close to the edge of the 12MR channel (Ga2), respectively. The remaining three partially occupied sites were all positioned within the 12MR channel and were attributed to  $\text{H}_2\text{O}$  molecules (*i.e.*, W1, W2 and W3 sites, respectively).  $\text{K}^+$  is six-fold coordinated to six framework oxygens, as suggested by the  $\text{K1-O3} = 2.92[x6]$  Å distance. Ga1 is six-fold coordinated to O4 and O6 framework oxygen atoms ( $\text{Ga1-O4} = 2.85[x4]$  Å and  $\text{Ga1-O6} = 2.21[x2]$  Å). The refined bond distances ( $\text{Ga2-W1} = 2.67[x2]$  Å,  $\text{Ga2-W2} = 2.23[x2]$  Å and  $\text{Ga2-W3} = 2.56[x4]$  Å) and occupancies of W1, W2 and/or W3 water molecules indicate that Ga2 is four (with W1 and W2, or only W3) or six-fold coordinated (with W1 or W2 and W3) to water. Indeed, bond distances suggest also the presence of short W1-W3-W3 water oligomers developing along the [001] direction, as testified by the  $\text{W1-W3} = 2.26$  and  $\text{W3-W3} = 2.98$  Å distances. On the whole, Rietveld refinement reveals the presence of  $\sim 14$  water molecules, 2  $\text{K}^+$  and 2.57 atoms of  $\text{Ga}^{+3}$  per unit cell, respectively. The K and Ga values are consistently lower than the theoretical concentration, which can be calculated on the basis of the aluminium content of the L precursor. This discrepancy cannot be attributed to an underestimation of the cations sites found in our refinements, neither to an incomplete  $\text{NH}_4^+$  ion exchange or dehydroxylation and/or dealumination during calcination, as well as residual  $\text{NH}_4^+$  after calcination. Moreover, difference Fourier (DF) map does not show any indication of extraframework sites, attributable to

$\text{NH}_4^+$  groups. The hypothesis of extraframework  $\text{Al}^{+3}$  atoms is also disregarded by the DF synthesis that does not show any maximum that can be interpreted as oxygen atoms coordinated to  $\text{Al}^{+3}$ . We suggest that the lattice charge defects give rise to Brønsted acidic  $\text{Si}-\text{OH}-\text{Ga}$  bridging hydroxyl group, whose occurrence is confirmed by the lengthening of the T-O distance after gallium incorporation. Recently, Beltrami et al. [personal communication] demonstrated the presence of Brønsted acid sites through neutron powder diffraction on the acidic form of zeolite L. The first site (D1) was located on the framework oxygen O5, not far from the centre of the 8-ring of the cancrinite cage. The second (D2 site) on the framework oxygen O1, heading towards the centre of the 12MR channel. On the whole, 7.6 Brønsted sites were recognized, in consistence with the tetrahedral aluminium content determined starting from the Si/Al ratio. In our refinement, the T-O distances involving the O5 and O1 framework oxygens were always among the largest of the tetrahedra (Table S14). At the same time, the attractive force of Brønsted acid sites could reasonably be responsible of the very narrow T-O-T angles centred on the O1 and O5 framework oxygen atoms ( $\text{T1-O1-T1} = 112.7(5)$  and  $\text{T2-O5-T2} = 115.4(3)^\circ$ ).

As reported by Fricke et al. (2000) [5], the excess of gallium determines the formation of a segregate phase coexisting with the main zeolitic one. In this case, a phase of gallium hydroxide ( $\text{GaO}(\text{OH})$ ) was recognized through the qualitative analysis, which highlights the presence of some extra peaks (i.e., [101], [200] and [201] *hkl* reflections at the 21.41 and 18.06 and 26.68°  $2\theta$  angles, respectively) not attributable to the L zeolite (Fig. 3). The semi-quantitative analysis reveals the presence of 83 and 17 wt % of L zeolite and  $\text{GaO}(\text{OH})$ , respectively.

#### 4.2.2. Ga-MOR system

Mordenite (ideal formula  $[\text{Na}_8^+][\text{Al}_8\text{Si}_{40}\text{O}_{96}]\cdot 24\text{H}_2\text{O}$ , framework type MOR) is a medium pore zeolite characterized by a monodimensional channel system, which consists of 12-membered rings running parallel to the [001] direction interconnected along the [010] direction through 8MR side pockets [32]. The crystal structure of the gallium-exchanged mordenite was refined using the topological orthorhombic *Cmcm* symmetry starting from the structural model of Alberti et al. (1986) [39]. After the Ga-exchange, lattice parameters highlight a slight reduction of the unit cell volume (Ga-MOR = 2766.35(25) Å<sup>3</sup>, Na-MOR = 2781.58(25) Å<sup>3</sup>) compared to the ones of the starting Na-MOR sample, due to the decrease of *b* and *c* parameters (Ga-MOR: *b* = 20.3510(9) Å, *c* = 7.4940(4) Å; Na-MOR: *b* = 20.4447(10) Å, *c* = 7.5152(4) Å). On the contrary, along *a* direction, a small increase is observed (18.1387(9) and 18.1038(10) for Ga-MOR and Na-MOR, respectively). The comparison of the mean tetrahedral distances between the exchanged ( $\langle \text{T1-O} \rangle = 1.662$  Å,  $\langle \text{T2-O} \rangle = 1.654$  Å,  $\langle \text{T3-O} \rangle = 1.658$  Å,  $\langle \text{T4-O} \rangle = 1.657$  Å) and the Na-form ( $\langle \text{T1-O} \rangle = 1.654$  Å,  $\langle \text{T2-O} \rangle = 1.650$  Å,  $\langle \text{T3-O} \rangle = 1.657$  Å,  $\langle \text{T4-O} \rangle = 1.656$  Å) does not show any indication about a preferential siting of gallium in framework positions. On the contrary, intertetrahedral angles of the Ga-MOR are narrower than those of the starting material. Among them, noteworthy is the shrinkage of the T3-O9-T3 angle, which moves from 165.5° in the Na-MOR to 151.9° in the Ga-MOR (Table S15). The analysis of the difference Fourier map allows to detect the presence of extraframework sites assigned to residual  $\text{Na}^+$  cation,  $\text{Ga}^{+3}$  and water molecules, respectively (Fig. 4). Not exchanged

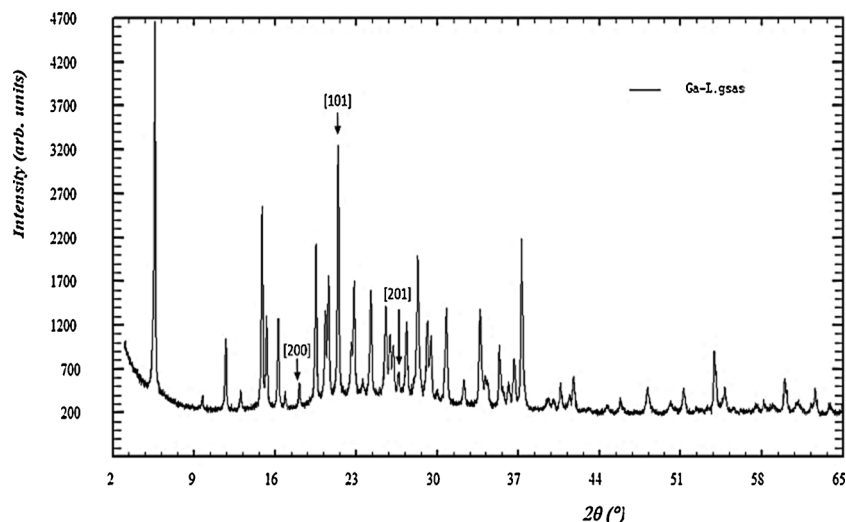


Fig. 3. Powder diffraction pattern of Ga-L system.

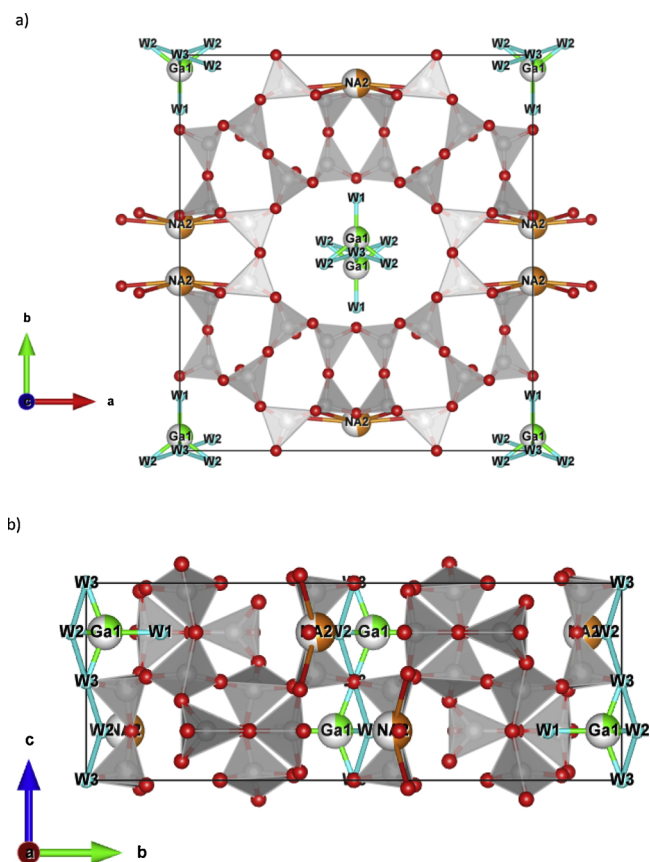


Fig. 4. Extraframework content distribution of Ga-MOR system. Projection along *c* (a) and *a* (b) axis.

exchanged

$\text{Na}^+$  (labelled Na2) is located within the 8MR in a six-fold coordination with O1 ( $\text{Na2-O1} = 3.06 \text{ \AA}$  [x4]) and O6 ( $\text{Na2-O6} = 3.01 \text{ \AA}$  [x2]) framework oxygen atoms. Gallium site (labelled Ga1) is positioned within the 12MR channel, along with all the three sites attributed to water molecules (W1, W2 and W3), which have a fundamental role in the completion of the gallium cation coordination. In this case, gallium is five-fold coordinated, as testified by the following bond distances:  $\text{Ga1-W1} = 2.10 \text{ \AA}$ ,  $\text{Ga1-W2} = 2.09 \text{ \AA}$  [x2] and  $\text{Ga1-W3} = 2.00 \text{ \AA}$  [x2]. Furthermore, W2 and W3 show to be hydrogen bonded each other ( $\text{W2-W3} = 2.56 \text{ \AA}$  [x4]), thus forming short W2-W3 water oligomers running along the 12MR. No further residual electron density, attributable to  $\text{NH}_4^+$  groups, were detected through the DF map, thus indicating that all the ammonium content has been substituted by  $\text{Ga}^{+3}$  and that the extraframework gallium quantified is the maximum exchangeable for our mordenite. Concerning the amount of the extraframework content, refined occupancies indicate the presence of 2 and 1.16 a.u.c of  $\text{Na}^+$  and  $\text{Ga}^{+3}$  cations, respectively, along with 13 water molecules per unit cell.  $\text{Na}^+$  and  $\text{Ga}^{+3}$  values obtained are lower than the theoretical concentration, hence also in this case the presence of Brønsted acidic Si-OH-Ga bridging hydroxyl group has to be supposed to counterbalance the framework charge defect. Martucci et al. (2000) [40] reports that the position of Brønsted acid sites does not strictly depends on the nature of the zeolite (natural or synthetic) and on its Si/Al ratio. Indeed, in all the three samples considered in that work (with Si/Al ratio equal to 5.5, 5.6 and 10, respectively), the four Brønsted acid sites detected were constantly located on the same framework oxygen atoms. The first, D1, was on framework oxygen O10 and headed towards the center of the 12-ring; the second, D2, was on the framework oxygen O6 and headed towards the side pocket; the third, D3, was on O5 and headed towards the center of the 12-ring; the last, D4, was on O9 and headed toward the center of the eight-ring. Hence, it is reasonable to assume the presence of charge compensator protons in these sites. The comparison of powder patterns before and after gallium exchange shows the occurrence of [301] and [200]  $hkl$  reflections at the  $33.64$  and  $18.09^\circ$   $2\theta$  angles, respectively. This testifies the presence of the segregate gallium hydroxide phase arising from the gallium-exchange process (Fig. 5). The semi-quantitative analysis reveals the presence of 74 and 26 wt % of mordenite and  $\text{GaO}(\text{OH})$ , respectively.

#### 4.2.3. Ga-FER system

Ferrierite (ideal formula  $[\text{Mg}_2^{+2}\text{Na}_2^+] [\text{Al}_6\text{Si}_{30}\text{O}_{72}] \cdot 18\text{H}_2\text{O}$ , framework type FER) is a medium pore pentasil zeolite, characterized by a two dimensional channel system built on the intersection of 10-membered and 8-membered ring (10 and 8MR) channels running parallel to the [001]

and [010] crystallographic directions, respectively. 10MR alternating along the  $b$  direction with the so-called ferrierite cages, structural units originated by the intersection of 8MR and 6MR channels [32]. In this work, due to the absence of  $l$ -centering forbidden peaks ( $h+k+l = 2n+1$  reflections), the Ga-FER crystal structure was refined in the  $Immm$  space group, starting from the atomic coordinates reported by Dalconi et al. (2003) [41]. From the analysis of the lattice parameters obtained through the Rietveld refinement, not noteworthy differences can be detected between the starting  $\text{NH}_4$ -ferrierite [42] and Ga-exchanged sample. Indeed, it is highlighted a very small reduction of the unit cell volume ( $\text{NH}_4\text{-FER} = 1978.6(1) \text{ \AA}^3$ ,  $\text{Ga-FER} = 1977.20(15) \text{ \AA}^3$ ) principally attributable to the slight decrease of  $a$  and  $b$  parameters, whereas  $c$  remains almost unchanged ( $\text{NH}_4\text{-FER}$ :  $a = 18.8477(8) \text{ \AA}$ ,  $b = 14.1049(5) \text{ \AA}$ ,  $c = 7.4425(2) \text{ \AA}$ ;  $\text{Ga-FER}$ :  $a = 18.8394(10) \text{ \AA}$ ,  $b = 14.0885(6) \text{ \AA}$ ,  $c = 7.4494(2) \text{ \AA}$ ). On the contrary, the comparison of framework bond distances and angles between them, suggests that the metal-exchange process has led to the incorporation of gallium within tetrahedral sites. After the Ga-exchange,  $\langle \text{T-O} \rangle$  distances of the four tetrahedral sites appear homogeneously longer ( $\text{Ga-FER}$ :  $\langle \text{T1-O} \rangle = 1.651 \text{ \AA}$ ,  $\langle \text{T2-O} \rangle = 1.654 \text{ \AA}$ ,  $\langle \text{T3-O} \rangle = 1.653 \text{ \AA}$  and  $\langle \text{T4-O} \rangle = 1.635 \text{ \AA}$ ;  $\text{NH}_4\text{-FER}$ :  $\langle \text{T1-O} \rangle = 1.607 \text{ \AA}$ ,  $\langle \text{T2-O} \rangle = 1.607 \text{ \AA}$ ,  $\langle \text{T3-O} \rangle = 1.609 \text{ \AA}$  and  $\langle \text{T4-O} \rangle = 1.607 \text{ \AA}$ ), whereas T-O-T angles result narrower than that of the precursor (Table S16), thus suggesting the presence of tetrahedral  $\text{Ga}^{+3}$  cations. Indeed, according to Fricke et al. (2000) [5], structural modifications strongly depend on the concentration of gallium and on the degree of substitution achieved. The analysis of the difference Fourier map reveals the presence of five partially occupied extraframework sites: three of them are occupied by water molecules (sites labelled W1, W2 and W3), the remaining by gallium cations (sites labelled Ga1 and Ga2). W1, W2 and Ga1 are located within the 10-membered ring, whereas W3 and Ga2 close to the edges of the 8-membered ring window, which defines the limits of the ferrierite cage (Fig. 6). As already observed in Ga-L system, no evidences of ammonium are highlighted by the DF analysis, thus indicating that all the  $\text{NH}_4$  content has been replaced by gallium after the exchange. Along with the  $\sim 5$  water molecules per unit cell, the refinement of the extraframework  $\text{Ga}^{+3}$  occupancies highlighted the presence of 1.3 ions per unit cell, in good agreement with the amount of ammonium calculated in the precursor sample ( $\sim 1.2$  ions per unit cell; [42]). The analysis of the extraframework bond lengths reveals the existence of strong interactions among water molecules and  $\text{Ga}^{+3}$  cations. Distances refined indicate that Ga1 site is four-fold coordinated exclusively to water molecules ( $\text{Ga1-W1} = 2.09 \text{ \AA}$  [x2] and  $\text{Ga1-W2} = 2.09 \text{ \AA}$  [x2]). Besides, W1 and W2 interact between, them thus creating W1-W2-W1 short oligomers ( $\text{W1-W2} = 2.96 \text{ \AA}$  [x2]) oriented

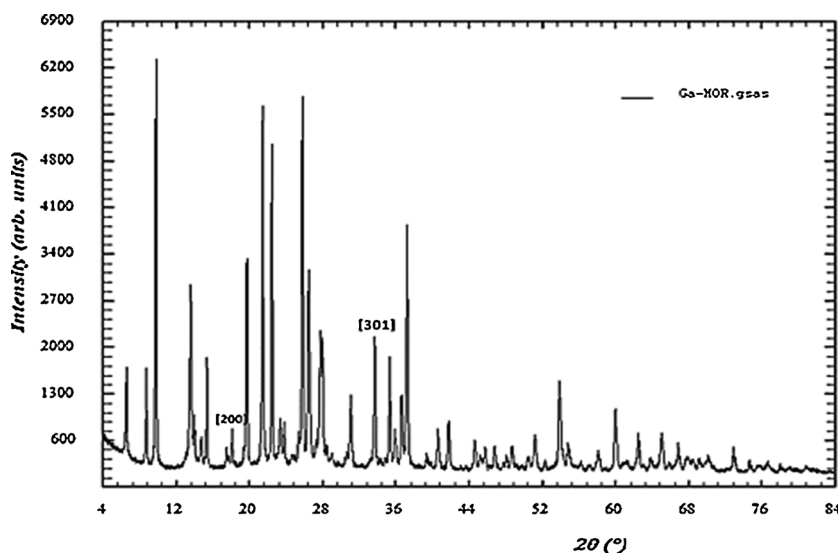


Fig. 5. Powder pattern of Ga-MOR system.

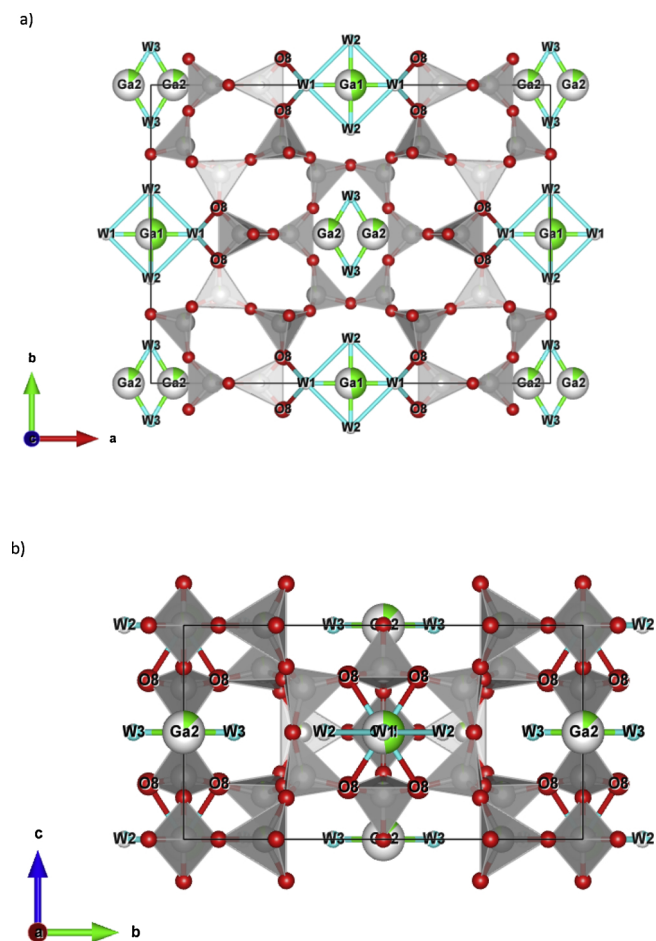


Fig. 6. Extraframework content distribution of Ga-FER system: projection along c (a) and a (b) axis.

parallel to the 10MR channel and hydrogen bonded to the O8 framework oxygen atom ( $O8-W1 = 2.53 \text{ \AA}$  [x4]). Ga2 site is coordinated by the W3 site, as testified by the  $Ga2-W3 = 2.06 \text{ \AA}$  [x2] distance. No other interactions between Ga2 and  $H_2O$  were detected and no additional reasonable electronic density residues to be attributed to water were recognized. Considering that, the four-fold coordination is the lowest for  $Ga^{+3}$  cations,

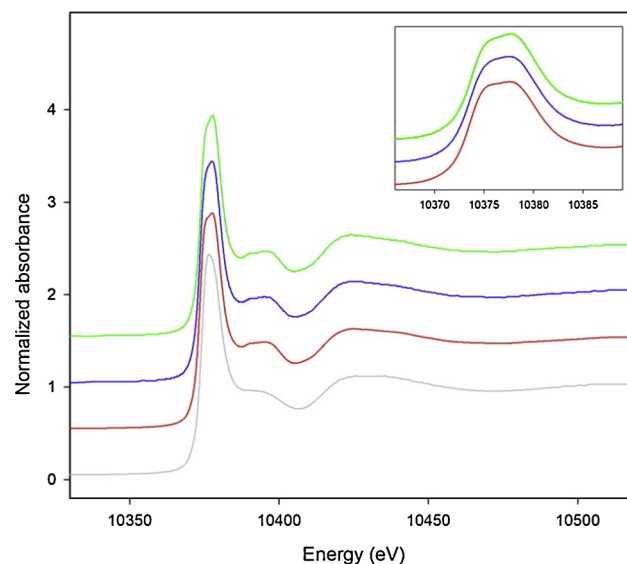


Fig. 8. Normalized spectra (from the top to the bottom) of: Ga-MOR (green), Ga-FER (blue), Ga-L (red) and  $Ga(NO_3)_3$  reference (grey). Small box on the top right is a zoom around the edge area of Ga-exchanged zeolite samples (For interpretation of the references to colour in this figure legend, the reader is referred to the web version of this article).

the presence of some not detectable protons completing the gallium coordination has to be assumed [43]. Also in this case, the segregate phase of gallium hydroxide was recognized through the qualitative analysis. It has been highlighted by the occurrence of two extra reflections (*i.e.*, [101] and [301] *hkl* at the  $21.41$  and  $33.61^\circ$   $2\theta$  angles, respectively) not attributable to the ferrierite and not present in the  $NH_4$ -FER powder pattern (Fig. 7). The semi-quantitative analysis reveals the 96 and 4 wt % of ferrierite and  $GaO(OH)$ , respectively.

#### 4.3. XAS

Fig. 8 shows the normalized spectra of all samples and  $Ga(NO_3)_3 \cdot xH_2O$  whereas the corresponding  $k^2\chi(k)$  experimental data are reported in Fig. 9. As can be seen in the zoom area of Fig. 8, the two peaks in the white line of Ga-exchanged zeolites (at energies of 10,375 and 10,379 eV) are a preliminary indication of the fact that Ga is present in both tetrahedral and octahedral geometry, according to previous

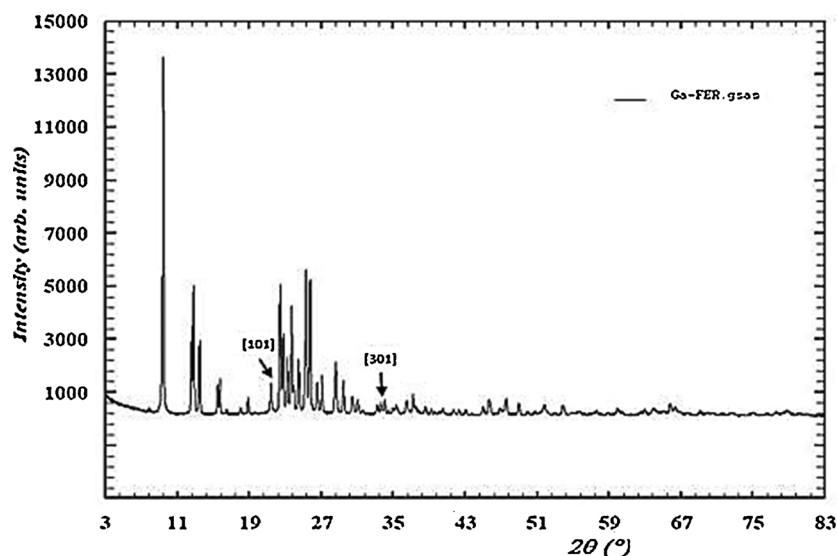
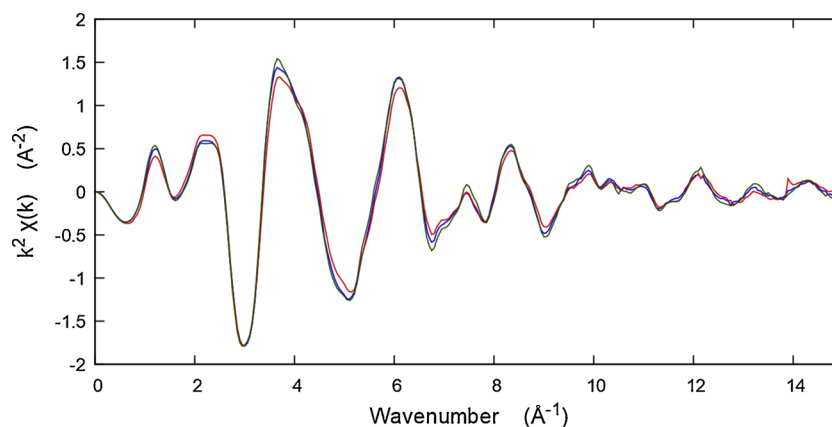


Fig. 7. Powder pattern of Ga-FER system.



**Fig. 9.**  $k^2\chi(k)$  experimental data of Ga-MOR (green), Ga-FER (blue) and Ga-L (red) (For interpretation of the references to colour in this figure legend, the reader is referred to the web version of this article).

studies [44,45]. The presence of Ga atoms in non-equivalent crystallographic sites, due to the symmetry of the zeolites, together with the secondary phase GaO(OH) in various amount in all the samples (as evidenced by the XRPD data) complicated the EXAFS refinements, so we focused only on the first shell. First-shell contribution has been modelled using Ga–O bond distances coming from the Ga in tetrahedral sites of the zeolite (as the Ga atoms in extraframework sites have longer bond distances) and the octahedral Ga in GaO(OH) impurity (structural model taken from [46]).

This strategy has been adopted as Ga–O bond distances in tetrahedral and octahedral coordination are quite similar and partially overlapping [47], confirmed also by our quantitative EXAFS results on the first-shell, summarized in Table 3 (fits are shown in Fig. 10a–c).

The obtained average bond lengths are of  $1.928 \pm 0.01 \text{ \AA}$ ,  $1.937 \pm 0.02 \text{ \AA}$ ,  $1.925 \pm 0.02 \text{ \AA}$  for Ga-Ferr, Ga-Mor and Ga-L respectively; the refined value (1.04) of the amplitude factor  $S_0^2$  on the Ga(NO<sub>3</sub>)<sub>3</sub>·xH<sub>2</sub>O reference compound is almost identical to that obtained for the zeolite samples.

As can be seen in Table 3, the major contribution to the EXAFS signal is due to Ga in GaO(OH) impurity, being about 80% in all the samples; nevertheless, a good fit cannot be achieved without introducing also tetrahedral Ga contribution. This fact, together with the XANES information of the splitted peak of the white line (zoom area in Fig. 8), allows us to confirm the presence of tetrahedral Ga and consequent incorporation into the zeolite framework.

**Table 3**

Crystallographic data and structural parameters as obtained from the R-space fit by using the theoretical references [46,48].

Sample	Shells	%	Ref.	N	$R(\text{\AA})^a$	$S_0^2$	R-factor	$\sigma^2(\text{\AA}^2)$	$\Delta E_0(\text{eV})$
Ga(NO <sub>3</sub> ) <sub>3</sub> ·xH <sub>2</sub> O			[48]			1.04 (8)	0.012	0.007 (1)	6 (1)
	Site1 - Ga - O <sub>1</sub>	0.5		6	1.939 (4)				
	Site2 - Ga - O <sub>4</sub>	0.5		4	1.935 (4)				
	Site2 - Ga - O <sub>5</sub>			2	1.961 (4)				
Fer						1.05 (5)	0.003	0.002 (2)	2 (2)
	Site1 <sup>b</sup> - Ga - O	0.2 (1)*0.5		4	1.93 (1)				
	Site2 <sup>b</sup> - Ga - O	0.2 (1)*0.5		3	1.91 (1)				
	Site2 <sup>b</sup> - Ga - O			1	1.94 (1)				
	GaO(OH) contamination:		[46]					0.005 (1)	
	Ga - O <sub>1</sub>	0.8 (1)		3	1.904 (6)				
	Ga - O <sub>2</sub>			3	2.031 (6)				
Mor						1.05 (4)	0.003	0.001 (3)	3 (1)
	Site1 <sup>b</sup> - Ga - O	0.15 (8)*0.5		4	1.96 (2)				
	Site2 <sup>b</sup> - Ga - O	0.15 (8)*0.5		4	1.92 (2)				
	GaO(OH) contamination:		[46]					0.005 (2)	
	Ga - O <sub>1</sub>	0.85 (8)		3	1.912 (8)				
	Ga - O <sub>2</sub>			3	2.040 (8)				
L						1.05 (9)	0.004	0.001 (3)	3 (1)
	T1 - Ga - O <sub>4</sub>	0.16 (4)*0.5		4	1.93 (2)				
	T2 - Ga - O <sub>5</sub>	0.16 (4)*0.5		2	1.91 (2)				
	T2 - Ga - O <sub>6</sub>			2	1.94 (2)				
	GaO(OH) contamination:		[46]					0.007 (2)	
	Ga - O <sub>1</sub>	0.84 (4)		3	1.900 (3)				
	Ga - O <sub>2</sub>			3	2.026 (3)				

<sup>a</sup>All the bond lengths values are in excellent agreement with the mean values reported by Gagné and Hawthorne (2018) [47] for Ga<sup>+3</sup> ion in both tetrahedral and octahedral coordination.

<sup>b</sup>These sites represent an average of the Ga atoms in tetrahedral coordination and did not refer to the real crystallographic sites.

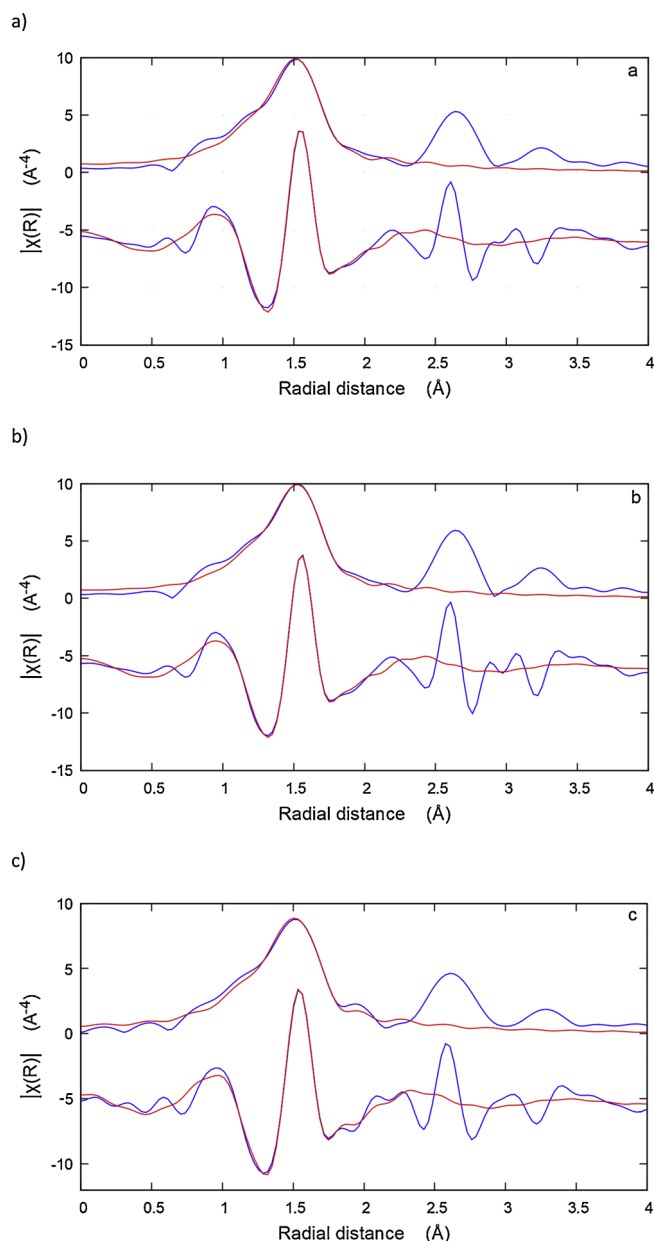


Fig. 10. The obtained EXAFS fit on the three samples: a) Ga-FER; b) Ga-MOR; c) Ga-L.

## 5. Conclusions

In this work the investigation of the structural features of Gallium substituted L, mordenite and ferrierite zeolites allowed us to elucidate the nature of the gallium active sites combining X-ray powder diffraction (XRPD), X-ray absorption spectroscopy (XAS) and adsorption study. Rietveld structure refinements allowed us to locate and quantify  $\text{Ga}^{+3}$  cations in framework and non-framework positions as well as determine the presence of water molecules completing the extra-framework  $\text{Ga}^{+3}$  coordination. The lightening of tetrahedral bond distances and narrowing of intertetrahedral angles suggest that the metal cation was incorporated in tetrahedral sites. This is corroborated by EXAFS results, which show that the average bond lengths of the first-shell are longer than the  $\langle \text{T-O} \rangle$  distances expected in presence of

$\text{Si}^{+4}$  and  $\text{Al}^{+3}$  as framework cations. All these information are essential not only for their characterization but also for their industrial applications.

## Acknowledgements

This study was carried out within a project funded by the “SoWaZe” and grant agreement n° 2017Y2PAB8\_003 PRIN program of the Italian Ministry for University and Research (MIUR). We acknowledge Dr. Giuliana Aquilanti (Elettra, Trieste) for the precious suggestions.

## Appendix A. Supplementary data

Supplementary material related to this article can be found, in the online version, at doi:<https://doi.org/10.1016/j.cattod.2019.09.016>.

## References

- [1] R. Szostak, Handbook of Molecular Sieves, Van Nostrand Reinhold, New York, 1992.
- [2] R. Guzzinati, E. Sarti, M. Catani, V. Costa, A. Pagnoni, A. Martucci, E. Rodeghero, D. Capitani, M. Pietrantonio, A. Cavazzini, L. Pasti, ChemPhysChem 19 (17) (2018) 2208–2217.
- [3] A. Ausavasukhi, T. Sooknoi, D.E. Resasco, J. Catal. 268 (1) (2009) 68–78.
- [4] V. Kanazirev, V. Mavrodinova, L. Kosova, G.L. Price, Catal. Lett. 9 (1-2) (1991) 35–42.
- [5] R. Fricke, H. Kosslick, G. Lischke, M. Richter, Chem. Rev. 100 (6) (2000) 2303–2406.
- [6] A. Bhan, W. Nicholas Delgass, Catal. Rev. 50 (1) (2008) 19–151.
- [7] K. Yogo, S. Tanaka, M. Ihara, T. Hishiki, E. Kikuchi, Chem. Lett. 21 (6) (1992) 1025–1028.
- [8] M. Shanzhy, M. Opanasenko, P. Concepción, A. Martínez, Chem. Soc. Rev. 48 (2019) 1095–1149.
- [9] E.A. Uslamin, B. Luna-Murillo, N. Kosinov, P.C. Bruijninx, E.A. Pidko, B.M. Weckhuysen, E.J.M. Hensen, Chem. Eng. Sci. 198 (2019) 305–316.
- [10] V.B. Kazansky, I.R. Subbotina, R.A. Van Santen, E.J.M. Hensen, J. Catal. 233 (2) (2005) 351–358.
- [11] R. Szostak, V. Nair, D.K. Simmons, T.L. Thomas, R. Kuvadia, B. Dunson, D.C. Shieh, Stud. Surf. Sci. Catal. 37 (1988) 403–411.
- [12] C. Otero Arean, G. Turnes Palomino, F. Geobaldo, A. Zecchina, J. Phys. Chem. 100 (16) (1996) 6678–6690.
- [13] C.R. Bayense, A.P. Kentgens, J.W. De Haan, L.J. Van de Ven, J.H. Van Hooff, J. Phys. Chem. 96 (2) (1992) 775–782.
- [14] C. Lamberti, G. Turnes Palomino, S. Bordiga, D. Arduino, A. Zecchina, G. Vlaic, Jpn. J. Appl. Phys. 38 (S1) (1999) 55–58.
- [15] V.D.O. Rodrigues, A.C.F. Júnior, Appl. Catal. A-Gen. 435 (2012) 68–77.
- [16] A.I. Serykh, M.D. Amiridis, Surf. Sci. 603 (13) (2009) 2037–2041.
- [17] E.A. Pidko, R.A. van Santen, J. Phys. Chem. C 113 (11) (2009) 4246–4249.
- [18] G. Berlier, G. Spoto, P. Fiscaro, S. Bordiga, A. Zecchina, E. Giamello, C. Lamberti, Microchem. J. 71 (2-3) (2002) 101–116.
- [19] G. Berlier, G. Spoto, S. Bordiga, G. Ricchiardi, P. Fiscaro, A. Zecchina, I. Rossetti, E. Selli, L. Forni, E. Giamello, C. Lamberti, J. Catal. 208 (1) (2002) 64–82.
- [20] K. Sun, H. Xia, E.J.M. Hensen, R.A. van Santen, C. Li, J. Catal. 238 (1) (2006) 186–195.
- [21] N. Rane, A.R. Overweg, V.B. Kazansky, R.A. Van Santen, E.J.M. Hensen, J. Catal. 239 (2) (2006) 478–485.
- [22] E.A. Pidko, V.B. Kazansky, E.J.M. Hensen, R.A. van Santen, J. Catal. 240 (1) (2006) 73–84.
- [23] A. Ausavasukhi, T. Sooknoi, Appl. Catal. A-Gen. 361 (1-2) (2009) 93–98.
- [24] J. Přeč, P. Pizarro, D.P. Serrano, J. Čejka, Chem. Soc. Rev. 47 (2018) 8263–8306.
- [25] A.C. Larson, General structure analysis system (GSAS), Los Alamos Nat. Lab. Rep. LAUR (2000) 86–748.
- [26] B.H. Toby, J. Appl. Cryst. 34 (2001) 210–213.
- [27] A. Di Cicco, G. Aquilanti, M. Minicucci, E. Principi, N. Novello, A. Cognigni, L. Olivi, J. Phys. Conf. Ser. 190 (1) (2009) 012043.
- [28] B. Ravel, M. Newville, J. Synchrotron Rad. 12 (2005) 537–541.
- [29] M. Newville, IFEFFIT: interactive XAFS analysis and FEFF fitting, J. Synchrotron Rad. 8 (2001) 322–324.
- [30] A. Petushkov, J. Freeman, S.C. Larsen, Langmuir 26 (9) (2010) 6695–6701.
- [31] M. Ardit, A. Martucci, L. Pasti, E. Rodeghero, G. Beltrami, G. Cruciani, J. Phys. Chem. C. 122 (13) (2018) 7249–7259.
- [32] C. Baerlocher, L.B. McCusker, D.H. Olson, Atlas of Zeolite Framework Types, 6<sup>th</sup> rev. ed., Elsevier, Amsterdam, 2007.
- [33] R.M. Barrer, H. Villiger, Z. Krist - Cryst Mater. 128 (1-6) (1969) 352–370.
- [34] J.M. Newsam, J. Chem. Soc. Chem. Commun. 2 (1987) 123–124.
- [35] E. Stuckenschmidt, W. Joswig, W.H. Baur, Eur. J. Miner. 8 (1996) 85–92.
- [36] E. Cannillo, A. Coda, G. Fagnani, Acta Cryst. 20 (2) (1966) 301–309.
- [37] A. Sani, G. Cruciani, Phys. Chem. Miner. 29 (5) (2002) 351–361.

- [38] G. Cruciani, A. Martucci, C. Meneghini, *Eur. J. Miner.* 15 (2) (2003) 257–266.
- [39] A. Alberti, P. Davoli, G. Vezzalini, *Z. Krist - Cryst Mater.* 175 (1-4) (1986) 249–256.
- [40] A. Martucci, G. Cruciani, A. Alberti, C. Ritter, P. Ciambelli, M. Rapacciuolo, *Microporous Mesoporous Mater.* 35 (2000) 405–412.
- [41] M.C. Dalconi, A. Alberti, G. Cruciani, P. Ciambelli, E. Fonda, *Microporous Mesoporous Mater.* 62 (3) (2003) 191–200.
- [42] A. Martucci, L. Leardini, M. Nassi, E. Sarti, R. Bagatin, L. Pasti, *Miner. Mag.* 78 (5) (2014) 1161–1176.
- [43] Y.V. Joshi, K.T. Thomson, *Catal. Today* 105 (1) (2005) 106–121.
- [44] K. Nishi, K. Shimizu, M. Takamatsu, H. Yoshida, A. Satsuma, T. Tanaka, S. Yoshida, T. Hattori, *J. Phys. Chem. B* 102 (50) (1998) 10190–10195.
- [45] M. Akatsuka, T. Yoshida, N. Yamamoto, M. Yamamoto, S. Ogawa, S. Yagi, *J. Phys. Conf. Ser.* 712 (1) (2016) 012056.
- [46] S.J. Li, C. Zheng, K.C. Lohring, *Z. Krist -New Cryst. St.* 218 (JG) (2003) 11–12.
- [47] O.C. Gagné, F.C. Hawthorne, *Acta Crystallogr. B* 74 (1) (2018) 63–78.
- [48] A.D. Hendsbee, C.C. Pye, J.D. Masuda, *Acta Crystallogr. E* 65 (8) (2009) i65–i65.

## SUPPLEMENTARY INFORMATION

### **INSIGHTS ON GA-ZEOLITE CATALYSTS: X-RAY POWDER DIFFRACTION AND ABSORPTION SPECTROSCOPY CHARACTERIZATION AT AMBIENT CONDITIONS**

G. Beltrami<sup>1\*</sup>, T. Chenet<sup>2</sup>, L. Pasti<sup>2\*\*</sup>, L. Gigli<sup>3</sup>, S. Pollastri<sup>4\*\*\*</sup> and A. Martucci<sup>1</sup>

<sup>1</sup>Dept. of Earth Sciences, University of Ferrara, Via Saragat, 1, I-44122 Ferrara, Italy.

<sup>2</sup>Dept. of Chemical and Pharmaceutical Sciences, University of Ferrara, Via Luigi Borsari, 43, I-44122 Ferrara, Italy.

<sup>3</sup>Elettra - Sincrotrone Trieste S.C.p.A. Strada Statale 14 34149 Basovizza, Trieste, Italy.

<sup>4</sup>CERIC-ERIC Strada Statale 14 34149 Basovizza, Trieste, Italy.

\*Corresponding author: [bltgd@unife.it](mailto:bltgd@unife.it)

\*\*Corresponding author: [psu@unife.it](mailto:psu@unife.it)

\*\*\*Corresponding author: [simone.pollastri@elettra.eu](mailto:simone.pollastri@elettra.eu)

Table S11: Fractional coordinates, fraction and thermal displacement parameters of Ga-L framework and extraframework atoms

<b>Atom</b>	<b>x/a</b>	<b>y/b</b>	<b>z/c</b>	<b>Ui/Ue*100</b>	<b>Fraction</b>
<b>KB</b>	2/3	1/3	1/2	8.89(2)	1.0
<b>Ga1</b>	0.3824(24)	0.0	0.0	8.96(2)	0.15(1)
<b>Ga2</b>	0.1418(25)	0.0	0.0	13.3(1)	0.28(1)
<b>T1</b>	0.0879(5)	0.3516(5)	1/2	0.82(32)	1.0
<b>T2</b>	0.1635(4)	0.4961(4)	0.2079(4)	0.82(32)	1.0
<b>O1</b>	0.0	0.2569(5)	1/2	1.67(6)	1.0
<b>O2</b>	0.1610(2)	0.3219(4)	1/2	1.67(6)	1.0
<b>O3</b>	0.2608(3)	0.5216(6)	0.2594(14)	1.67(6)	1.0
<b>O4</b>	0.0907(2)	0.4028(3)	0.3208(5)	1.67(6)	1.0
<b>O5</b>	0.4454(1)	0.8907(1)	0.2728(1)	1.67(6)	1.0
<b>O6</b>	0.1390(4)	0.4684(5)	0.0	1.67(6)	1.0
<b>W1</b>	0.0	0.0	0.090(20)	3.33(8)	0.55(1)
<b>W2</b>	0.1286(17)	0.2572(34)	0.0	13.0(4)	0.93(1)
<b>W3</b>	0.1093(26)	0.0546(13)	0.2851(6)	13.36(4)	0.60(1)

Table S12: Fractional coordinates, fraction and thermal displacement parameters of Ga-MOR framework and extraframework atoms

<b>Atom</b>	<b>x/a</b>	<b>y/b</b>	<b>z/c</b>	<b>Ui/Ue*100</b>	<b>Fraction</b>
<b>Na2</b>	0.0	0.4283(34)	3/4	19.20(5)	0.49(2)
<b>Ga1</b>	0.0	0.0349(2)	3/4	12.1(2)	0.296(7)
<b>T1</b>	0.1947(2)	0.4248(2)	0.5406(2)	1.88(11)	1.0
<b>T2</b>	0.1944(1)	0.1876(1)	0.5395(1)	1.88(11)	1.0
<b>T3</b>	0.0890(2)	0.3859(2)	1/4	1.88(11)	1.0

<b>T4</b>	0.0826(1)	0.2240(1)	1/4	1.88(11)	1.0
<b>O1</b>	0.1146(5)	0.3991(8)	0.4595(7)	2.12(27)	1.0
<b>O2</b>	0.1240(7)	0.1778(4)	0.4020(17)	2.12(27)	1.0
<b>O3</b>	0.2714(5)	0.3876(3)	0.4748(22)	2.12(27)	1.0
<b>O4</b>	0.0791(12)	0.3052(2)	1/4	2.12(27)	1.0
<b>O5</b>	0.1728(12)	0.2047(11)	3/4	2.12(27)	1.0
<b>O6</b>	0.1654(8)	0.4155(12)	3/4	2.12(27)	1.0
<b>O7</b>	0.2269(9)	1/2	1/2	2.12(27)	1.0
<b>O8</b>	1/4	1/4	1/2	2.12(27)	1.0
<b>O9</b>	0.0	0.4058(10)	1/4	2.12(27)	1.0
<b>O10</b>	0.0	0.1889(4)	1/4	2.12(27)	1.0
<b>W1</b>	0.0	0.1381(3)	3/4	11.45(23)	1.0
<b>W2</b>	0.0917(14)	-0.0278(15)	3/4	8.89(29)	0.68(2)
<b>W3</b>	1/2	1/2	0.0	16.27(32)	0.98(5)

Table SI3: Fractional coordinates, fraction and thermal displacement parameters of Ga-FER framework and extraframework atoms

<b>Atom</b>	<b>x/a</b>	<b>y/b</b>	<b>z/c</b>	<b>Ui/Ui*100</b>	<b>Fraction</b>
<b>Ga1</b>	1/2	0.0	0.0	10.30(10)	0.447(9)
<b>Ga2</b>	0.556(2)	0.0	1/2	16.05(30)	0.123(6)
<b>T1</b>	0.1528(4)	0.0	0.0	1.78(11)	1.0
<b>T2</b>	0.0855(3)	0.2041(3)	0.0	1.78(11)	1.0
<b>T3</b>	0.2735(2)	0.0	0.2908(2)	1.78(11)	1.0
<b>T4</b>	0.3258(1)	0.2015(1)	0.2086(1)	1.78(11)	1.0
<b>O1</b>	0.0	0.2316(14)	0.0	2.02(20)	1.0
<b>O2</b>	0.2437(4)	0.0	0.5	2.02(20)	1.0

<b>O3</b>	0.0943(4)	0.0875(3)	0.0	2.02(20)	1.0
<b>O4</b>	0.1945(4)	0.0	0.1947(10)	2.02(20)	1.0
<b>O5</b>	1/4	1/4	1/4	2.02(20)	1.0
<b>O6</b>	0.1543(6)	0.2729(8)	1/2	2.02(20)	1.0
<b>O7</b>	0.1023(3)	0.2568(6)	0.1936(8)	2.02(20)	1.0
<b>O8</b>	0.3303(3)	0.0879(2)	0.2584(13)	2.02(20)	1.0
<b>W1</b>	0.1114(1)	1/2	1/2	13.22(30)	0.148(20)
<b>W2</b>	0.0	0.3509(1)	1/2	19.10(10)	0.305(25)
<b>W3</b>	0.0	0.1270(1)	1/2	15.27(50)	0.767(10)

Table SI4: Framework bond distances and angles of Ga-L zeolite

Bond distances (Å) and angles (°)	Ga-L
<b>T1-O1</b>	1.666(8)
<b>T1-O2</b>	1.668(3)
<b>T1-O4 [x2]</b>	1.630(4)
<b>T2-O3</b>	1.639(6)
<b>T2-O4</b>	1.765(6)
<b>T2-O5</b>	1.846(1)
<b>T2-O6</b>	1.641(5)
<b>T1-O1-T1</b>	112.6(5)
<b>T1-O2-T1</b>	147.5(8)
<b>T2-O3-T2</b>	140.0(6)
<b>T1-O4-T2</b>	138.2(4)
<b>T2-O5-T2</b>	115.4(3)
<b>T2-O6-T2</b>	146.1(6)

Table SI5: Framework bond distances and angles of Na-MOR and Ga-MOR zeolites

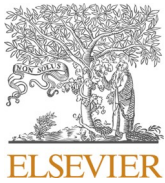
Bond distances (Å) and angles (°)	Na-MOR	Ga-MOR
<b>T1-O1</b>	1.647(2)	1.659(4)
<b>T1-O3</b>	1.647(2)	1.658(4)
<b>T1-O6</b>	1.666(2)	1.667(4)
<b>T1-O7</b>	1.657(2)	1.664(4)
<b>T2-O2</b>	1.644(2)	1.651(4)

T2-O3	1.649(2)	1.656(4)
T2-O5	1.667(2)	1.662(3)
T2-O8	1.642(2)	1.647(3)
T3-O1 [x2]	1.659(1)	1.658(2)
T3-O4	1.654(2)	1.653(4)
T3-O9	1.656(2)	1.665(4)
T4-O2 [x2]	1.656(1)	1.657(2)
T4-O4	1.656(2)	1.653(4)
T4-O10	1.664(2)	1.660(4)
<hr/>		
T1-O1-T3	134.9(4)	129.9(6)
T2-O2-T4	136.2(2)	135.3(5)
T1-O3-T2	143.5(3)	139.0(5)
T3-O4-T4	178.1(8)	171.5(1)
T2-O5-T2	137.7(4)	143.2(7)
T1-O6-T1	139.6(5)	140.4(8)
T1-O7-T1	131.3(5)	138.9(8)
T2-O8-T2	180.0	180.0
T3-O9-T3	165.5(1)	151.9(1)
T4-O10-T4	133.5(6)	129.0(1)

Table SI6: Framework bond distances and angles of NH<sub>4</sub>-FER and Ga-FER

Bond distances (Å) and angles (°)	NH <sub>4</sub> -FER	
	Martucci et al.,(2014) [42]	Ga-FER
T1-O3 [x2]	1.609(1)	1.653(2)
T1-O4 [x2]	1.608(1)	1.649(2)
T2-O1	1.606(1)	1.658(2)
T2-O3	1.608(1)	1.651(3)
T2-O7 [x2]	1.608(1)	1.653(2)
T3-O2	1.615(1)	1.656(2)
T3-O4	1.608(1)	1.650(3)
T3-O8 [x2]	1.609(1)	1.655(2)
T4-O5	1.613(1)	1.612(1)
T4-O6	1.605(1)	1.639(2)
T4-O7	1.610(1)	1.645(2)
T4-O8	1.605(1)	1.644(2)
<hr/>		
T2-O1-T2	174.12(1)	152.9(1)
T3-O2-T3	151.74(1)	140.4(7)

<b>T1-O3-T2</b>	152.31(1)	143.9(4)
<b>T1-O4-T3</b>	157.70(1)	144.1(9)
<b>T4-O5-T4</b>	180.0	180.0
<b>T4-O6-T4</b>	139.96(1)	143.0(7)
<b>T2-O7-T4</b>	149.77(1)	134.6(6)
<b>T3-O8-T4</b>	143.71(1)	136.6(4)



## Adverse effects of plastic ingestion on the Mediterranean small-spotted catshark (*Scyliorhinus canicula*)

Annalaura Mancia<sup>a,\*</sup>, Tatiana Chenet<sup>b</sup>, Gioacchino Bono<sup>c</sup>, Michele Luca Geraci<sup>c</sup>, Carmela Vaccaro<sup>d</sup>, Cristina Munari<sup>b</sup>, Michele Mistri<sup>b</sup>, Alberto Cavazzini<sup>b</sup>, Luisa Pasti<sup>b</sup>

<sup>a</sup> Department of Life Sciences and Biotechnology, University of Ferrara, Via L. Borsari 46, 44121, Ferrara, Italy

<sup>b</sup> Department of Chemistry and Pharmaceutical Sciences, University of Ferrara, Via L. Borsari 46, 44121, Ferrara, Italy

<sup>c</sup> Institute for Biological Resources and Marine Biotechnologies - IRBIM, National Research Council (CNR), Via Vaccara, 61, 91026, Mazara del Vallo (TP), Italy

<sup>d</sup> Department of Physics and Earth Sciences, University of Ferrara, Via L. Borsari 46, 44121, Ferrara, Italy

### ARTICLE INFO

#### Keywords:

Microplastics  
Macroplastics  
 $\mu$ -Raman spectroscopy  
Small-spotted catshark  
Immunity

### ABSTRACT

Plastics are widely diffused in the oceans and their ingestion by marine organisms is raising concern for potentially adverse effects. The risk of harmful interactions with marine plastic pollution depends on the biology of the species as well as the distribution and abundance of the different plastic types.

The aim of this study was to assess the occurrence of plastic ingestion by the small-spotted catshark (*Scyliorhinus canicula*), one of the most abundant elasmobranchs in the Mediterranean Sea. The expression levels of genes indicative of total immune system function were analyzed to gather preliminary data for further investigation of any potential correlations between plastic presence and immune activation.

One hundred catsharks were collected during the Spring 2018 in two geographic locations in the southern region of the central Mediterranean Sea: 1) near Mazara del Vallo, SW Sicily and 2) near Lampedusa island, Italy's southernmost. Standard measurements were recorded for each specimen and its organs and sex was determined. The gastrointestinal tract (GIT) was preserved for plastic detection and identification. Where present, plastics (macro- and micro-) were characterized in terms of size, shape and polymer typology through microscopy and  $\mu$ -Raman spectroscopy. Spleen from a subset of thirty samples was preserved for RNA extraction, then used to quantify by real time PCR the transcripts of T cell receptor beta (TCRB), T cell receptor delta (TCRD) and IgM genes.

The results indicated that ingestion of plastic is widespread, with microplastics (MP, from 1  $\mu$ m to <1 mm) abundantly present in nearly all samples and macroplastic (MaP, > 1 cm) in approximately 18% of the specimens collected. A significant increase in the expression of TCRB, TCRD and IgM was observed in the spleen of MaP + specimens from Mazara del Vallo waters, in parallel with 67% increase in liver weight.

While the presence of MP alone is not enough to induce a strong activation of the immunity, some type of plastics falling into the MaP category may be more toxic than others and crucial in the activation of the immune response.

The results of this study represent a first evidence that plastic pollution represents an emerging threat to *S. canicula*, the Mediterranean food web and human consumers.

### 1. Introduction

The abundance of plastic debris floating in Mediterranean waters was first reported in 1980 (Morris RJ, 1980). Later studies confirmed the distribution, abundance and characteristics of plastic debris in the basin thanks to visual counts supported by surface nets tows allowing detection and quantification of microplastics, (MP, from 1  $\mu$ m to <1 mm)

(Aliani et al., 2003; Suaria et al., 2014; Faure et al., 2015; Ruiz-Orejón et al., 2016; Zeri et al., 2018). Plastic particles are in fact typically grouped into categories from macro (MaP >1 cm) to nano (from 1 to <1000 nm) depending on their size (as measured by their diameter or by considering the larger dimension as classifier for irregular or fiber debris) according to the classification proposed by Hartmann et al. (2019).

\* Corresponding author. University of Ferrara, via L. Borsari 46, 44121, Ferrara, Italy.

E-mail address: [annalaura.mancia@unife.it](mailto:annalaura.mancia@unife.it) (A. Mancia).

<https://doi.org/10.1016/j.marenvres.2020.104876>

Received 5 September 2019; Received in revised form 9 January 2020; Accepted 9 January 2020

Available online 14 January 2020

0141-1136/© 2020 Elsevier Ltd. All rights reserved.

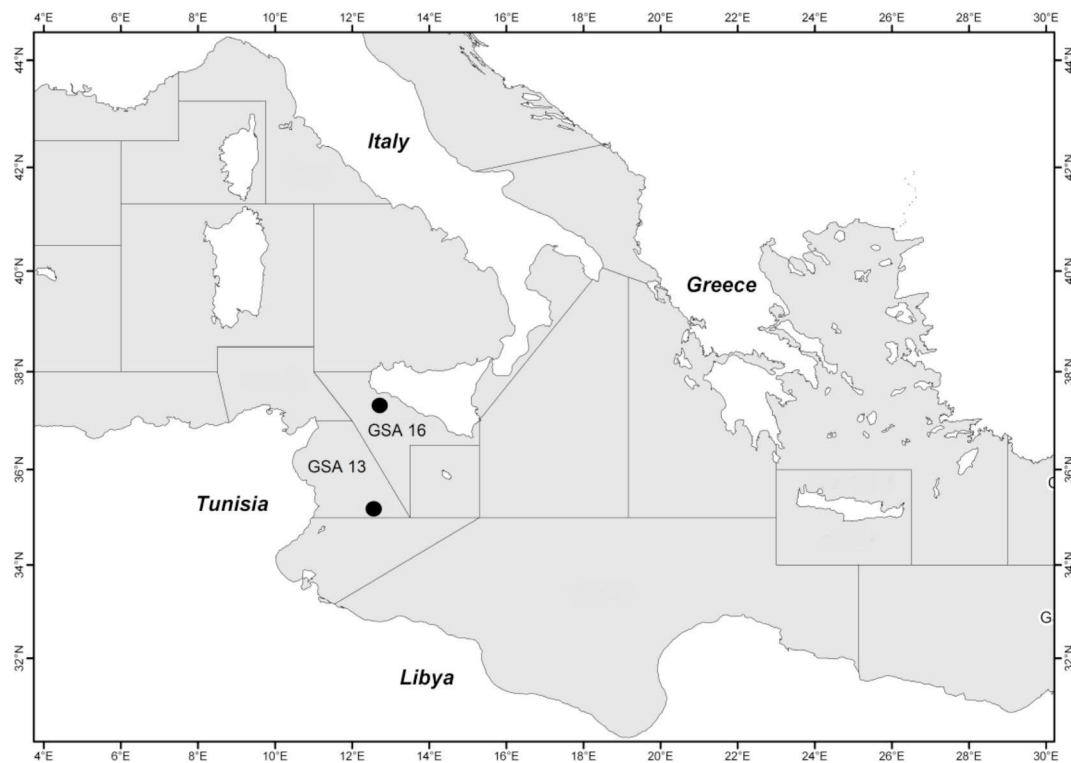


Fig. 1. Sampling sites, located within FAO GFCM GSAs. Dots represent the 2 locations of sampling, south of Mazara del Vallo, GSA 16 and south of Lampedusa, GSA 13. Lampedusa samples were collected in deep water. GFCM, General Fisheries Commission for the Mediterranean; GSA, Geographical Sub-Area.

In the Mediterranean Sea, MP concentrations is ranging from tens to hundreds of thousands of items per square kilometer; this abundant presence of buoyant plastic debris is likely related to the high human pressure and the hydrodynamics of this semi-enclosed basin (Eriksen et al., 2014; Cozar et al., 2015) which is also one of world's busiest shipping routes, receiving waters from densely populated river shorelines (e.g., Nile, Ebro, Rhone and Po) while being connected to the Atlantic Ocean only by the Strait of Gibraltar. For its characteristics, the Mediterranean basin has a water residence time as long as a century (Lacombe et al., 1981) and its shores house 10% of the global coastal population (ca. 100 million people within the 10-km coastal strip (CIESIN, 2012)).

MP are divided in two types: 1) primary, found in most commonly utilized products (e.g. cosmetic and personal care products, insect repellents, sunscreens, products for children), and 2) secondary, originating from the fragmentation of larger plastic debris through biological degradation, photo-degradation, chemical deposition and physical fragmentation (Auta et al., 2017). Both primary and secondary MP are present in sea water where the most represented synthetic polymers are polypropylene (PP), polyethylene (PE), polystyrene (PS), polyvinylchloride (PVC) and polyethylene terephthalate (PET) (Rocha-Santos and Duarte, 2015).

MP in the marine environment are dispersed via oceanic currents and wind patterns throughout the water column (Lebreton et al., 2012), in a variety of colors, shapes, sizes and densities (Reisser et al., 2014). Their persistence, availability and the biomagnification of the associated harmful chemicals, represent a potential hazard to marine life throughout the food web also if there is very few studies in field (Lusher et al., 2017; Romeo et al., 2015). MP interaction with marine organisms has been described for zooplankton (Botterell et al., 2019), invertebrates (Avio et al., 2015; Digka et al., 2018), fish (Digka et al., 2018; Compa et al., 2018; Renzi et al., 2019), turtles (Domenech et al., 2019), birds (Wilcox et al., 2015) and mammals (Fossi et al., 2016), including endangered species (Deudero and Alomar, 2016).

Fish may accidentally ingest particulate while they are feeding on

their prey or ingest plastic debris because of their resemblance to prey: the first report of MP ingestion in fish was in 1972 (Carpenter et al., 1972). Depending on plastic size and species, particles may be expelled or accumulate in the gastrointestinal tract (GIT), where could cause physical damage (e.g. block of feeding appendages or filters, and obstruction of GIT), and in some cases inflammation leading to death (Li et al., 2016; Werner et al., 2016).

In the last few years, the presence of plastics debris in fish has been described in species captured in the oceans, seas and freshwater raising concerns on their potential negative effects (e.g Ory et al., 2018; Bessa et al., 2018; Pellini et al., 2018; Silva-Cavalcanti et al., 2017). In addition, several authors have studied in controlled conditions the effects of virgin MP intake or as vehicles of other toxic compounds. Potential damage is related to the physical properties, regarding the interaction of the particles with the organism tissues and to the chemical properties, concerning the transfer of contaminants or leaching of plastic additives (Rochman et al., 2013; Pedà et al., 2016; Limonta et al., in review). Indeed, plastics, due to their lipophilic nature, have the potential to adsorb many hydrophobic persistent organic pollutants which may increase their harmful effect on biota. Up to now, it has not been completely elucidated the contribution of chemicals to plastic toxicity. Recent studies suggest that the two main routes of uptake in fish are represented by the ingestion and inhalation, since MP were found to accumulate and cause tissue damage in GIT and gills (Li et al., 2016; Pedà et al., 2016). Histological observations on exposed fish confirmed that MP were able to induce a strong inflammatory response in the target tissues (Limonta et al., 2019). The transcriptomic profiling of zebrafish larvae exposed to PS also suggested the activation of immune response, with the up-regulation of genes related to the complement system (Veneman et al., 2017; Pitt et al., 2018). Lu et al. (2016) reported how the accumulation of PE in gills, gut and liver of zebrafish causes oxidative stress, inflammation in fish liver and a disturbed lipid and energy metabolism (Lu et al., 2016).

Besides inflammation and metabolic disorders, MP absorption and distribution in different tissues and cells can result in several types of

effects, such as behavior alterations, predatory performance reduction, neurotoxicity, decreased growth (Rochman et al., 2013, 2014; Ferreira et al., 2016; Pedà et al., 2016; Barboza et al., 2018a, 2018b). Moreover, given the chemical properties, the MP uptake by aquatic organisms with other contaminants is a route to harmful chemicals including styrene, metals, phthalates, bisphenol A, polycyclic aromatic hydrocarbons (PAHs), polychlorinated biphenyls (PCBs) or polybrominated diphenyl ethers (PBDEs) (Koelmans et al., 2014; Barboza et al., 2018c). For example, the Japanese medaka (*Oryzias latipes*), exposed for short-time to both virgin and marine PE fragments, showed bioaccumulation of PAHs, PCBs and PBDEs, with signs of liver stress and early tumor formation (Rochman et al., 2013, 2014).

The small-spotted catshark (*Scyliorhinus canicula*, Linnaeus, 1758, SC) is a species of the family Scyliorhinidae. It is one of the most abundant cartilaginous fish in the central Mediterranean Sea (Ragonese et al., 2013) and inhabits the continental shelves off the coasts of Norway and the British Isles up to Senegal. It is a small, shallow-water shark inhabiting waters of depths ranging from a few meters (mt) down to 400 mt (Geraci et al., 2017; Rodríguez-Cabello et al., 2007). SC feeds opportunistically on a wide range of macrobenthic fauna, with Crustacea, Mollusca, Annelida, and Echinodermata as preferred prey. Feeding preference may depend on SC age and feeding intensity is highest during the summer due to the higher availability of living preys (Rodríguez-Cabello et al., 2007).

Given their low commercial value and abundance in the Mediterranean Sea (this species is currently listed as “Least Concern” on the IUCN Red List of Threatened Species), SC has been chosen as model in this study, as representative sample of the potential hazard fish in the southern waters of Italy are subject.

Here we present the description and analysis of effects of plastics (MP and MaP) in SC from two different geographic locations in the southern region of the central Mediterranean Sea, near: 1) Mazara del Vallo (MDV), SW Sicily and 2) Lampedusa (LMP), Italy’s southernmost island.

Plastics have been isolated from the GIT of SC, quantified and analyzed with Raman spectroscopy to identify the polymer category. *S. canicula* was further investigated through the analysis of spleen transcripts of key genes involved in adaptive and innate immunity to evaluate the potential of future research hypothesis linking plastic presence to health status.

## 2. Materials and methods

### 2.1. Samples collection

One hundred specimens of SC were collected on March 16, 2018 near Mazara del Vallo (N = 48, N = 25 females, F, and N = 23 males, M), SW Sicily, Italy and on May 7th, 2018, near Lampedusa island (N = 52, N = 14 females, F, and N = 38 males, M), Italy’s southernmost island, in the FAO General Fisheries Commission for the Mediterranean (GFCM) areas marked as Geographical Sub-Area (GSA) 16 and GSA13 in Fig. 1, respectively (Fig. 1; Supplementary Table 1).

### 2.2. Morphometric indices

Fish total length (TL), body weight (BW), spleen weight (SPL W), liver weight (LIV W) and GIT weight (GIT W), gender and maturity stage were recorded. Visceral weight (VW) was calculated subtracting the carcass weight (CW) to the BW. Fish were weighed after sampling, then spleen, liver and GIT were removed by dissection and weighted after evisceration. All the weights were measured using Sartorius balance (model: MSEE6202P-000-D0) to an accuracy of 0.01 g.

Sexual maturity was defined by 6 stages of gonadic development according to the Medits (International Bottom Trawl Survey in the Mediterranean) scale (MEDITS, 2016).

Condition factor (CF) was calculated as follows:  $(BW \cdot 100) / TL^3$ . The hepato-somatic index (HSI), the spleno-somatic index (SSI) and the GIT

**Table 1**

Sample subset of *S. canicula* used in the chemistry and gene expression analyses.

Sample ID	Gender	MAT	TL	BW	CW	VW	CF	SPL W	SSI	LIV W	HSI	GIT W	GSI (g)	Date 2018	LS
SC1	M	1	42,00	245,10	200,62	44,48	0,33	0,66	0,27	17,17	7,01	16,78	6,85	16-mar	MDV
SC2	M	2	39,00	186,11	157,77	28,34	0,31	0,75	0,40	10,34	5,56	11,01	5,92	16-mar	MDV
SC3	F	4	45,00	294,11	230,23	63,88	0,32	0,79	0,27	14,39	4,89	20,60	7,00	16-mar	MDV
SC4	F	5	43,00	254,05	198,29	55,76	0,32	0,98	0,39	26,66	10,49	19,43	7,65	16-mar	MDV
SC5	M	2	39,50	182,92	155,00	27,92	0,30	0,66	0,36	10,58	5,78	10,50	5,74	16-mar	MDV
SC6	M	1	33,50	104,68	91,01	13,67	0,28	0,37	0,35	4,76	4,55	7,72	7,37	16-mar	MDV
SC7	F	3	40,50	245,02	187,62	57,40	0,37	0,88	0,36	24,58	10,03	14,43	5,89	16-mar	MDV
SC8	F	2	33,50	118,53	99,08	19,45	0,32	0,78	0,66	6,08	5,13	11,09	9,36	16-mar	MDV
SC9	M	4	45,00	303,99	248,30	55,69	0,33	0,67	0,22	14,10	4,64	13,57	4,46	16-mar	MDV
SC10	M	1	39,50	209,30	166,67	42,63	0,34	0,79	0,38	13,16	6,29	15,38	7,35	16-mar	MDV
SC11	F	3	41,00	260,30	205,87	54,43	0,38	0,78	0,30	21,25	8,16	17,17	6,60	16-mar	MDV
SC12	F	1	34,50	127,30	110,60	16,70	0,31	0,51	0,40	6,03	4,74	8,87	6,97	16-mar	MDV
SC13	F	1	35,50	137,50	118,32	19,18	0,31	0,57	0,41	10,01	7,28	8,23	5,99	16-mar	MDV
SC14	M	4	40,50	197,58	159,56	38,02	0,30	0,60	0,30	10,95	5,54	10,36	5,24	16-mar	MDV
SC15	F	4	41,00	267,70	186,99	80,71	0,39	0,43	0,16	14,07	5,26	24,32	9,08	16-mar	MDV
SC49	M	4	36,50	151,80	127,41	24,39	0,31	0,36	0,24	5,14	3,39	7,97	5,25	7-mag	LMP
SC50	F	3	35,00	151,82	118,48	33,34	0,35	0,54	0,36	15,59	10,27	10,66	7,02	7-mag	LMP
SC51	F	2	32,00	121,80	98,75	23,05	0,37	0,45	0,37	10,85	8,91	8,87	7,28	7-mag	LMP
SC52	M	2	36,00	155,08	130,58	24,50	0,33	0,68	0,44	7,03	4,53	9,13	5,89	7-mag	LMP
SC53	F	2	37,00	157,90	131,39	26,51	0,31	0,67	0,42	10,87	6,88	11,62	7,36	7-mag	LMP
SC54	M	2	38,00	173,59	138,99	34,60	0,32	0,51	0,29	9,66	5,56	11,92	6,87	7-mag	LMP
SC55	M	4	35,50	129,70	105,39	24,31	0,29	0,29	0,22	6,76	5,21	9,87	7,61	7-mag	LMP
SC56	M	2	36,00	144,72	115,63	29,09	0,31	0,57	0,39	9,42	6,51	13,71	9,47	7-mag	LMP
SC57	F	4	36,50	161,30	122,43	38,87	0,33	0,56	0,35	13,03	8,08	8,64	5,36	7-mag	LMP
SC58	M	2	35,50	147,88	126,27	21,61	0,33	0,40	0,27	7,39	5,00	6,83	4,62	7-mag	LMP
SC59	M	5	38,50	206,30	167,04	39,26	0,36	0,62	0,30	10,38	5,03	12,78	6,19	7-mag	LMP
SC60	F	5	35,50	155,94	123,01	32,93	0,35	0,63	0,40	15,95	10,23	10,13	6,50	7-mag	LMP
SC61	F	3	36,50	174,00	131,86	42,14	0,36	0,53	0,30	20,13	11,57	8,77	5,04	7-mag	LMP
SC62	M	2	35,50	120,46	102,45	18,01	0,27	0,62	0,51	6,21	5,16	6,62	5,50	7-mag	LMP
SC63	M	4	38,50	171,80	145,30	26,50	0,30	0,55	0,32	10,25	5,97	6,59	3,84	7-mag	LMP

SC, *S. canicula*. Gender: M, male sample, F, female sample. MAT, stage of gonadal maturity (1–5). L, total length; W, total weight. CW, carcass weight. VW, visceral weight. SPL W, spleen weight. LIV W, liver weight. GIT W, gastro-intestinal tract weight. SSI, spleno-somatic index. HIS, hepato-somatic index. GSI, GIT somatic index. Length is measured in centimeters (cm); weight is measured in grams (g). LS, location of sampling. MDV, Mazara del Vallo; LMP, Lampedusa.

**Table 2**  
Sequences and amplification efficiency of primers used in q-PCR analysis.

Label	Gene Description	Sequence (5' -> 3')	Acc. n.	Slope	R <sup>2</sup>	Eff	Amp
RPL13	Large Ribosomal Subunit Protein 13	F: GCTCCAAGTTAATCATCTTCCCA R: GCCTTGAAATTCCTTCATCCTC	AY130423	-3,2	0,91	104	2,0
ACTb	Actin beta	F: CGAGACCTTCAATACCCCTGC R: CATAACCTTCGTAGATGGGCACAG	AJ312004	-3,1	0,95	110	2,1
RPS29	Large Ribosomal Subunit Protein 29	F: CATCAGCAGCTTACTGGTCTCATC R: GAAGCCGATGCTTTAGCGTATTG	n/a	-3,0	0,95	114	2,1
TCRB	T cell receptor beta, B (TCRbB)	F: CGTCAATGGCGAAGAAATGC R: TGTCAATGTTGCGTCTCTGG	KY434203	-3,1	0,9	110	2,1
IgM	Immunoglobulin M heavy chain	F: CGATGGACTACTCCCAGAA R: CACAGCTGATTTGCTGCAT	JX555996	-3,1	0,97	110	2,1
TCRD	T cell receptor delta (TCRD)	F: TGCTTGGCATCAGACTTCTACCC R: TTACCCAGGTGAGATTTCCGG	KY434205	-3,2	0,98	100	2,0

Slopes (-3.1, -3.6), R<sup>2</sup>, efficiencies (Eff, 90–110) and amplification (Amp) for each primer couple was checked through the creation of a five points standard curve with serially diluted 1:5 cDNA from 5 samples (MDV: SC7, SC9, SC11 and LMP: SC56, SC57). Amplification and efficiency were calculated using the equation from Dhar et al. (2009).

somatic index (GSI) were calculated as follows: HSI = liver weight (g) × 100/body weight (g), SSI = spleen weight (g) × 100/body weight (g), GSI = GIT weight (g) × 100/body weight (g) (Supplementary Table 1).

### 2.3. Chemistry: Plastic isolation and identification in the GIT

After sampling, fish were quickly frozen and stored at -20 °C. Successively, they were processed in the laboratory, where they were washed with MilliQ water, sectioned and the entire GIT (esophagus to vent), liver and spleen were removed. Liver and spleen were fixed in RNAlater® and stored in separated closed container at -20 °C for subsequent isolation of RNA, whereas GIT was wrapped in aluminum foil and then frozen at -20 °C in a closed container.

GIT samples were digested at 60 °C for 24 h in 10% KOH (Merck) in MilliQ® water, filtered with 0.45 µm nitrocellulose filter before use, according to the protocol published by Dehaut A et al. (2016). Following digestion, samples were filtered on 8 µm cellulose nitrate filters (Whatman). In the case of the presence of debris in the digestate, a density-based separation step using a ipersaline solution of NaCl (Sigma Aldrich) was performed. The solution was added to the digestate (2:1, v/v) and stirred for 10 min before being left to settle for 1 h. The supernatant, containing the floating plastic particles was collected and filtered, as previously described. Plastic debris of big size that could not be digested nor filtered were isolated and analyzed as undigested MaP. The filters that by visual inspection contained plastic debris contaminated with undigested organic residues or minerals were subject to an additional basic digestion step according to the procedure reported in Roch et al. (2017) and washed by a dilute acid aqueous solution (HCl 0.1M); it was observed that even after this treatment plastic debris were not broken into smaller fragments. Blank samples were prepared and analyzed in parallel as controls to account for MP contamination from the digestion and filtering processes (i.e., 'digestion control'). In detail, digestion solutions were placed into a clean beaker, heated at 60 °C for 24 h, and vacuum filtered onto a nitrocellulose filter 0.45 µm, (the procedure was repeated ten times; n = 10). MP was quantified and characterized for fish samples (see below). The blank samples contamination (mean No. filter-1) consisted only of fibers with average values of 4.2 (±0.5).

Measure to avoid contamination were adopted during all the extraction procedure, cotton lab coat and nitrile gloves were used and glassware equipment were thoroughly washed and rinsed with MilliQ water before use, all materials were covered between use with aluminum foils, and filters were stored in glass petri dishes.

Filters were first examined and sorted by visual inspection with a stereo microscope following protocol (Dehaut A et al., 2016). Microscopic analysis of the filters was performed with a Nikon SMZ745T stereomicroscope, equipped with a Nikon Digital Sight DS-F12 camera.

All the MaP, fragments and filaments, were analyzed with Raman

spectroscopy. The size of the analyzed subset should insure a representative view of the particle size distribution and chemical nature as suggested by Kedzierski M et al., 2019. Spectra were generated with a LabRam HR800 micro-Raman instrument from Horiba Scientific equipped with an air-cooled CCD detector at -70 °C, an Olympus BXFM microscope, a 600 groove/mm grating and a 50 × objective were used to collect the Raman scattering signals. The excitation source was a He-Ne laser (632.8 nm line) with a maximum laser power of 20 mW. A minimal spectral accumulation of 10 times 1 s was used; if a high background was recorded the accumulations were increased to a maximum of 100 times 1 s to improve the signal-to-noise ratio.

### 2.4. Gene expression analysis

**RNA Extraction.** Total RNA from spleen samples of thirty selected samples (Table 1) was extracted using RNeasy Plus Mini Kit (Qiagen, Hilden, Germany) following the manufacturer's instructions. Tissue (about 30 mg) lysis and homogenization was performed with T 10 basic ULTRA-TURRAX® (IKA, Staufen, Germany). Genomic DNA was removed through an in-column DNase I digestion (Qiagen). The RNA concentration and the quality of the extractions were assessed with a BioSpec-nano UV-Vis spectrophotometer (Shimadzu Italia S.r.l., Milan, Italy). The RNA samples that did not meet the absorbance ratio cutoff (1.8-2.0 for the 280/260; 2.0-2.2 for the 260/230) were extracted more than once.

**Quantitative real time PCR (q-PCR).** A panel of immunity genes [*T cell receptor beta (TCRB)*, *T cell receptor delta (TCRD)* and *immunoglobulin M (IgM)*], and housekeeping genes [*ribosomal protein 13 (RPL13)*, *actin beta 1 (ACTb)* and *ribosomal protein L29 (RPL29)*] was selected from the literature.

Primers for the selected genes were obtained from literature or designed with Primer 3 on different exons to exclude any genomic DNA co-amplification: ncbi accession numbers of the sequences used were KY434203 (TCRB); KY434205 (TCRD); JX555996 (µ heavy chain IgM) (Crouch et al., 2013; Li et al., 2015; Pettinello et al., 2017) (Table 2). Reverse transcription was performed using iScript™ cDNA synthesis kit (Bio-Rad, California, USA) according to the manufacturer's instructions using 1 µg total RNA. The qPCR reaction was performed in triplicates in 96 wells plates, using the EvaGreen Dye Master mix (Bio-Rad) on CFX Connect Real-Time Detection system (Bio-Rad). qPCR efficiencies were calculated using the equation from Dhar et al. (2009). The amplification efficiency of each primer couple was checked through the creation of a five points standard curve with serially diluted 1:5 cDNA from 5 samples (MDV: SC7, SC9, SC11 and LMP: SC56, SC57) (Table 2). cDNA was reverse transcribed from 1 µg of total RNA using SsoFast™ EvaGreen® Supermix (Bio-Rad) in a total volume of 10 µl of a reaction mix containing 10 ng cDNA, 0.3 µM of each primer, 2 × Evagreen enzyme and DNase-free sterile water. qPCR reactions were run as follows: 1 cycle of

**Table 3**

Percentage of change in MDV samples compared to LMP samples.

Md Diff	MAT	CF	HSI
F	- 34%	0%	- 24%
M	- 34%	- 3%	+20%

MD, Morphometric data. Diff, % of change in MDV vs LMP. F, females; M, males. MAT, gonadal maturity. CF, condition factor. HSI, hepato-somatic index.

98 °C for 30 min, 49 cycles of 95 °C for 5 s, 60 °C for 10 s; melting curve 65 °C–95 °C: increment 0.5 °C every 5 min. Each reaction was run in triplicate, together with a tri-plicate of no-template controls. The average Ct values were normalized to the values of the housekeeping genes RPL13. RPL13 was the most stable house-keeping gene amongst those tested (e.g RPL13, ACTb, RPL29). Comparative Ct method of analysis ( $2^{-\Delta\Delta Ct}$ ) was used to determined changes of expression between control and treated samples on CFX connect manager software 3.1 (Bio-Rad). Fold differences were calculated accounting for differences in primer efficiencies using the Pfaffl method (Pfaffl, 2001).

### 2.5. Statistical analysis

Data were analyzed within and between locations. Morphometric data were analyzed within MDV and LMP, related to gender (male and females) and/or presence or absence of MaP in the GIT. Student t-test and ANOVA were used in comparison to detect significant differences between groups compared, for morphometric data and for gene expression analysis.

## 3. Results and discussion

### 3.1. Morphometric data analysis

All the morphometric data for the 100 samples were analyzed to examine if significant differences exist between the samples from the two locations studied. Variation in TL and BW did not account for a difference in CF between MDV and LMP while the gonadal maturity and liver size had interesting dissimilarities (Table 3, Supplementary Table 2).

In detail: MDV, both females and males SC have smaller (<34%) index of gonadal maturity when compared to samples from LMP. Moreover, MDV males have bigger liver (HSI > 20%), while females have smaller liver (HSI < 24%) compared to LMP specimens.

The smaller gonadal maturity in MDV specimens may be linked to the great difference in the existing anthropogenic activities in the two locations of sampling. MDV sampling site is close to a port with the largest fishing fleet in Italy, while LMP sampling site is in a pristine area, near Lampedusa, the Italian southernmost island inhabited by only 6.000 people in an area of 20.2 square kilometers. The difference in human activity, contamination and consequently greater stress conditions in MDV, may have an effect on the appropriate development of the

MDV fish and may correlate to the overall differences we observed amongst the two shark's populations. The translation of stress to the organismal/population level and higher is not straightforward. In teleosts, acute and chronic stressors can stimulate physiological changes at the organismal level, impacting growth rate, reproductive output or investments, and disease resistance (Davis, 2002; Iwama et al., 2006; Ramsay et al., 2009). In contrast, very little is known about the physiological changes linked to stress in elasmobranchs. Indeed, the extent to which elasmobranchs are affected by pervasive anthropogenic threats, such as habitat degradation, climate change and pollution and its transient or prolonged impacts on health and fitness (e.g., somatic growth and reproduction) remains poorly understood (Skomal and Mandelman, 2012). We could assume that they respond to threats in a similar way teleosts do, but the nature and magnitude of the response could be highly species-specific and related to ecological factors and the type and duration of the stressors. Plastic contamination and the ingestion by aquatic organisms, including species of commercial importance for fisheries, are well documented in the Mediterranean Sea (Lusher et al., 2017) and we can reasonably assume that it will continue to increase in the foreseeable future; filling the knowledge gaps on the occurrence and adverse effects caused by (of the) polymers actually present in the environment is necessary to assess/understand the impact of these contaminants on biota (degree of the biological impact).

### 3.2. Effects and composition of plastics in the GIT of *S. canicula*

The GIT of 50 selected specimens was analyzed for plastic presence, quantity and type. Plastic were either grouped as fibers, MP fragments or MaP (Fig. 2 and Fig. 3) following the classification proposed by Hartmann et al. (2019). The occurrence of plastic was considered by the number of ingested plastics as well as the frequency of ingestion (Avio et al., 2020).

We found debris in the shape of fibers (filaments and lines) and fragments in about 80% of the samples analyzed (86.3% of the MDV samples, and 75.7% from LMP samples), both colored and clear (Fig. 3; Table 4). Artificially dyed debris and filaments identified by Raman spectroscopy were referred as plastic particles. Fibers in most cases were characterized by a not regular diameter along the particle, with diameter values lower than 10 µm. A total number of 138 particles were counted by visual inspection: 115 fibers shape (83.3%; which were classified based on the diameter size in 68 fibers and 59 filaments) and fragments (16.7%). According to size classes, the plastic debris were divided up as follows: 17 were in the range 1–10 µm, 72 were in the range 20 µm e 100 µm, 38 the range 20 µm e 100 µm and 11 were in the range 1 cm–5 cm (MaP). Considering the color, 88 debris were dark colored (63.8%), 30 were light colored (21.7%) and 20 were transparent (14.5%).

All fragments and filaments were analyzed by Raman micro-spectroscopy: fibers identification resulted in many cases problematic possibly due to additive/pigments contained in the fibers or to adhesion of organic residues. The uncertainty in identification of fibers

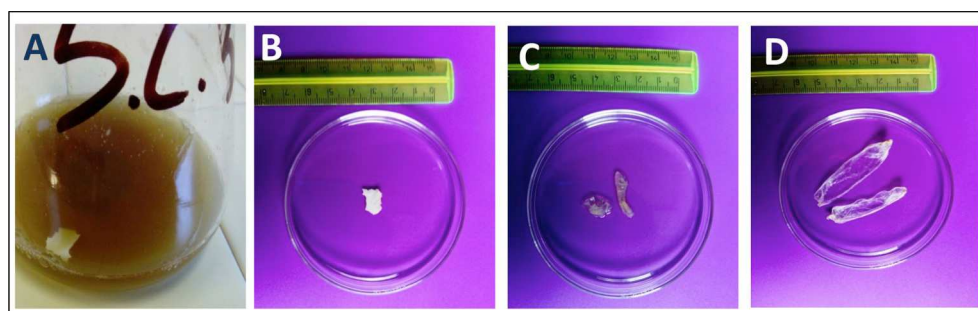


**Fig. 2.** Images of undigested plastics MaP from 3 different samples. A, Digested GIT tissue with undigested plastic; same specimen is shown in B. C–D MaP found in the GIT of two other specimens. MaP were identified by Raman spectroscopy: B (polypropylene), C (Polyethylene terephthalate), D (polyethylene).

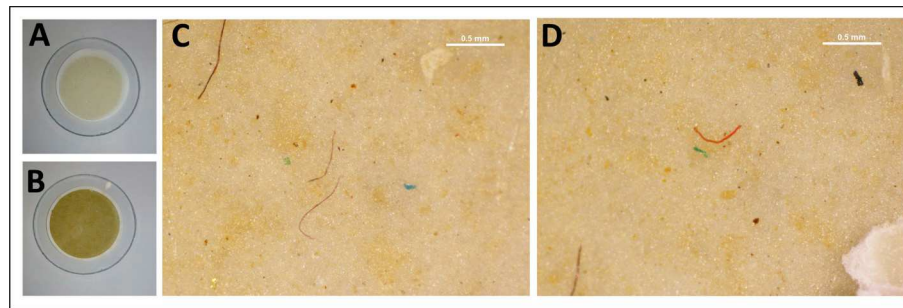


**Fig. 3.** Microscope images of MP debris found on filters in 2 different samples. A, B. Filters after digestion of SC6 and SC7. C, D. Microscope image of plastic debris on filters.

**Table 4**

Microplastic (MP) and Macroplastic (MaP) total number, particles, fibers, average ingested by individual fish and frequency of ingestion.

Catch area	N. specimens	Total number MP	Filaments	Fragments	Average/fish	Frequency of ingestion
GSA 16 MDV	25	33	24	9	1.32	71%
GSA 13 LMP	25	26	19	7	1.04	62%
Catch area	N. specimens	Total number MaP	Filaments	Fragments	Average/fish	Frequency of ingestion
GSA 16 MDV	25	6	–	6	0.24	20%
GSA 13 LMP	25	5	–	5	0.2	16%

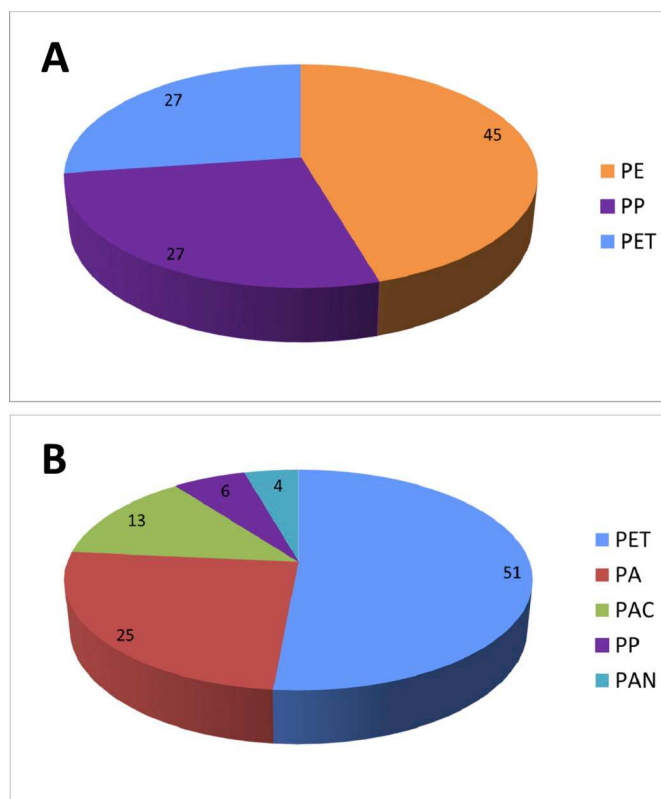


**Fig. 4.** Plastic debris composition. A, B. MaP and MP composition: PE polyethylene, PP polypropylene, PET Polyethylene terephthalate, PA Polyamide, PAC Polyacrylate, PAN Polyacrylonitrile. The numbers refer to percentage values.

constituents and therefore the bias induced by a partial identification of the samples, combined with the fact that fibers can also derive from contamination during the sample preparation procedure suggest us to limit the data only to MaP, fragments and filaments.

In addition, in the present work we aimed to investigate possible

correlation of MaP presence and variation of immune-related gene expression in *S. canicula*.

MP filaments and fragments accounted for a similar number in the two location with an ingested average by individual of 1.32 items in MDV vs 1.04 items in LMP and a frequency of ingestion of 71% in MDV vs 62% in LMP (Table 4).

Differently, MaP were detected in 18% of the samples analyzed. Specifically, in 20% of the MDV samples, and 16% from LMP samples (Table 4). All specimens with MaP from MDV were females, while those with MaP from LMP were 50% males and 50% females (Supplementary Table 3).

MaP were composed of the polymers polypropylene, polyethylene and polyethylenterephthalate whereas MP were mainly identified as polyester, acrylic and nylon 6 (Fig. 4). Average values of MP composition were not significantly different in the two sites.

The analysis of morphological data associated to the presence of MaP in samples from both locations showed no correlation to CF and VW. However, a significant increase in liver weight (49%,  $p < 0.05$ ) and HIS (26%,  $p < 0.01$ ) was observed (Supplementary Table 4A). In the correlation to MaP, MDV specimens showed an increase in the weight of all organs, although only the liver and HSI returned a significant increase of 67% and 34%, respectively of the total weight ( $p < 0.005$ ) (Fig. 5, Supplementary Table 4B). In LMP, the MaP specimens showed an increase of VW but the variation was non-significant; nevertheless, the liver was still subject to the highest increase (Fig. 5, Supplementary Table 4C).

In general, females from both location have higher VW probably due to higher structural and functional demands linked to vitellogenesis and maternal immunity (LIV W is 25% and 44% higher in females than males in MDV and LMP, respectively) (Supplementary Tables 4D and 4E).

The analysis of morphometric data of specimens sampled at MDV and LMP related to both MaP detection and gender, resulted in non-significant differences although it is evident that MDV females have an increase of BW that is only in part related to the increase in VW (Supplementary Table 5A). In LMP the increase of VW is more evident in females than males (Supplementary Table 5B). The females have VW that is 31% ( $p < 0.05$ ) than males (Supplementary Table 5C). BW and VW were higher in samples with MaP females and lower in males (Supplementary Tables 5D and 5E). The correlation analysis is clearly showing that females in MDV have smaller liver activity than those in

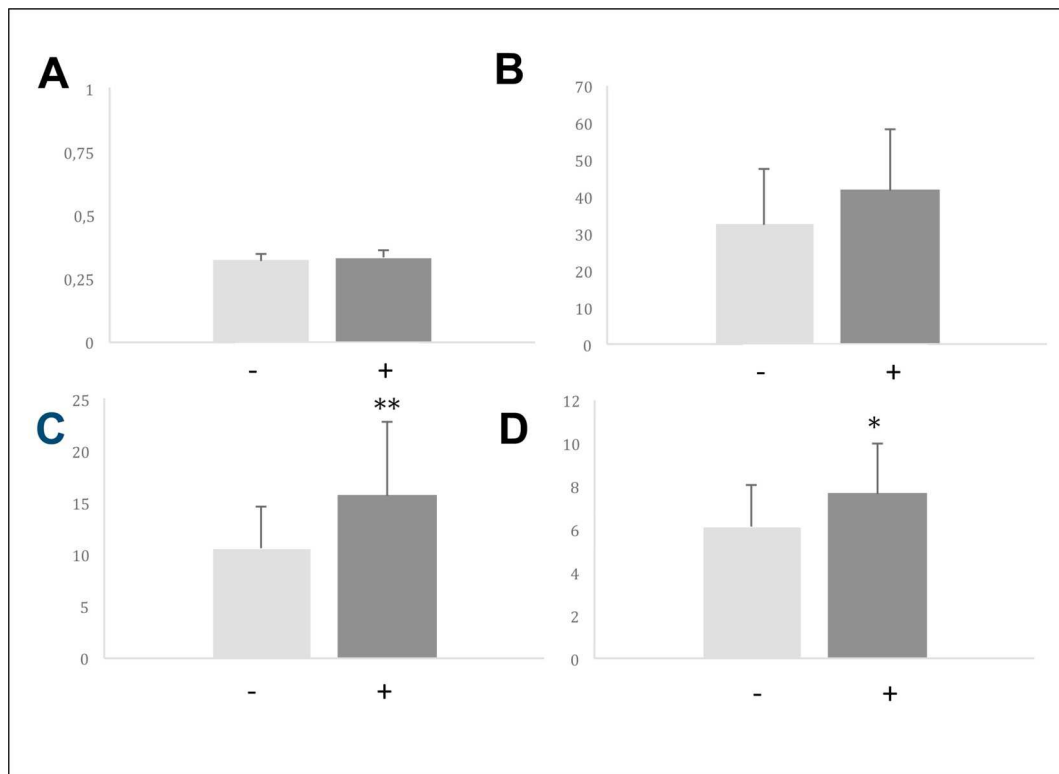


**Fig. 5.** Morphometric changes correlated to the presence of MaP in GIT samples from both locations. A, Condition factor, CF. B, Viscera weight. C, liver weight, LIV W. D, Hepato-somatic index, HSI. (+), MaP isolated; (-), no MaP detected. \* $p < 0.05$ , \*\* $p < 0.01$ . 30. Samples/individuals: MDV, N = 15; LMP, N = 15. MDV: N = 10 MaP (+), N = 5 MaP (-); LMP: N = 4 MaP (+), N = 11 MaP (-).

LMP, while the males in MDV have higher liver activity, almost as the males in MDV are stimulated to invest more in liver functions, which is usually a female feature (e.g. vitellogenesis) rather than in male characters (in males the body weight should be higher because is correlated to bones and muscles, for examples). The feminization-like evidence and the smaller gonadal maturity overall observed could severely impact the reproduction rate and fitness of the SC population in MDV. It has been previously observed that the exposure to endocrine disrupting chemicals (additives of plastics) can strongly influence the course of sex differentiation and unbalance the sex ratio in zebrafish populations; in other freshwater species vitellogenin concentration in male fish have been described in correlation to the exposure to estrogenic contaminants (Von Hippel et al., 2017; Santos et al., 2017). Decreased growth rate, decreased fecundity and negative impacts on subsequent generations have also been linked to plastic exposure in both marine and terrestrial species (Huerta-Lwanga et al., 2016; Sussarellu et al., 2016).

### 3.3. Gene expression

In order to move beyond simply studying the presence and type of plastics, the effects on the underlying physiological and biochemical mechanisms should be investigated. The effects can be many and diverse, and may involve a stress response implicating several systems, such as the immune, the endocrine or reproductive one. A first step to identify changes that may be associated to the presence of plastic described was to evaluate changes in the expression of genes known linked to the immune system. There are two main layers of immune responses: innate immune responses and adaptive immune responses. The innate immune system creates a fast, non-specific reaction to the pathogen infecting the host organism. If the pathogen persists despite innate defenses, then the adaptive immune system will engage the microbe with specificity and memory. The adaptive (or acquired) immune system mounts to a discriminating long lasting immune response

directed by two types of lymphocytes, T cells (cell-mediated immunity) and B cells producing immunoglobulins (Ig) (humoral immune response) (Rauta et al., 2012). Cartilaginous fish and elasmobranchs (sharks, skates and rays), in particular, are the first jawed vertebrate group to emerge in evolution and are the oldest group relative to mammals having an immune system grounded upon Ig, T cell receptors (TCR), the major histocompatibility complex (MHC), as well as RAG-mediated rearrangement, somatic hypermutation and the presence of primary and secondary lymphoid tissues (Flajnik MF, 2002). Immunoglobulins (IgM) were discovered in sharks almost 40 years ago and while some features of the immune system are simple and primordial, other features, including the Ig system, can be quite complex (e.g. the presence of two non-IgM isotypes, IgW and IgNAR) (Dooley and Flajnik, 2006; Flajnik MF, 2002). It is highly probable that each of these isotypes evolved to mediate a particular type of defense mechanism, although there are no functional data as yet for the non-IgM isotypes. The genes that were analyzed in this study were those related to canonical immune response pathways, *IgM*, *TCRB* and *TCRD* (Pettinello et al., 2017; Crouch et al., 2017).

RNA extraction from spleen of the 30 specimens was successful and all samples were retrotranscribed and used as template in the real time qPCR of *TCRB* and *IgM*, specifically related to adaptive immunity activity and *TCRD*, linked to innate immunity activity. Samples analyzed within location group (MDV and LMP separately), considering the presence (MaP +) or absence (MaP -) of plastics, showed differences in the expression of the genes (immune-related) tested.

In MDV (5 MaP + and 8 MaP -) specimens, MaP + spleens showed a significant increase in the expression of all immune-related genes: fold increases were: 1.2 for *TCRB* ( $p < 0.02$ ), 2.1 for *TCRD* ( $p < 0.01$ ) and 3.1 for *IgM* ( $p < 0.01$ ) (Fig. 6). When the analysis was restricted to only females (5 MaP + and MaP -), fold increases were: 3.5 for *TCRB* (not significant), 6.3 for *TCRD* ( $p < 0.02$ ), and 16.4 for *IgM* ( $p < 0.02$ ) (Fig. 6).

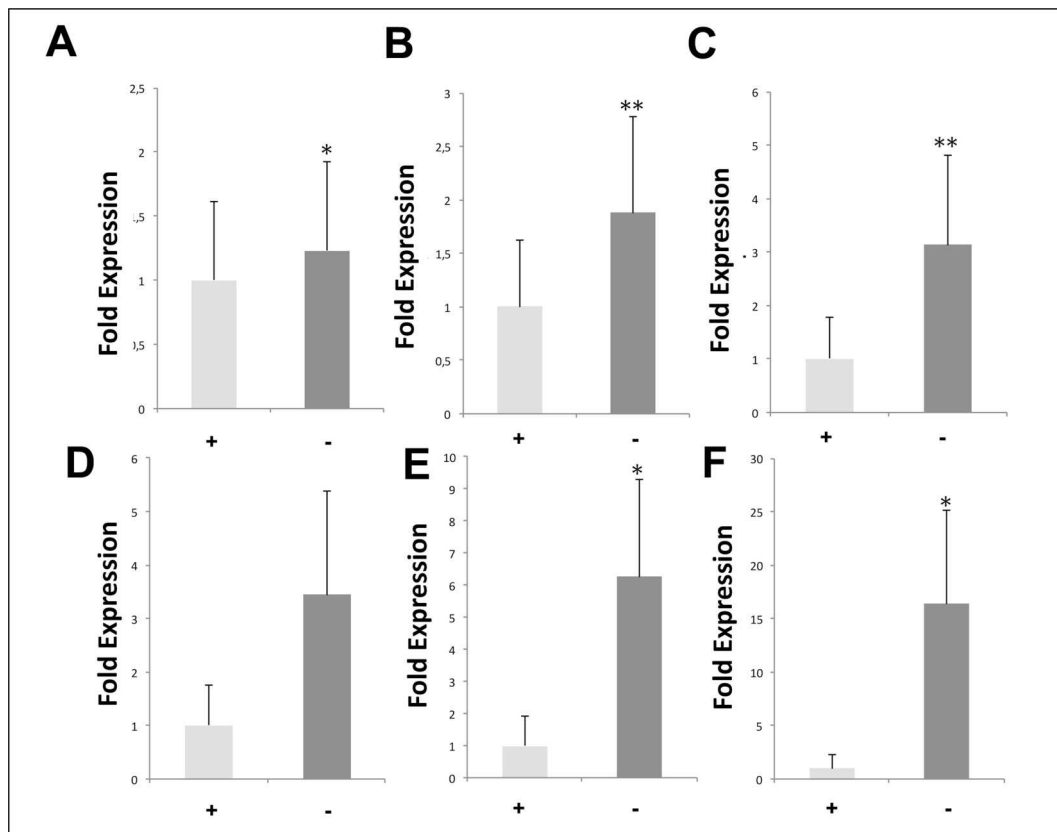


**Fig. 6.** Expression of immune-related genes in *S. canicula* spleen samples from MDV. A, D, TCRB; B, E, TCRD; C, F, IgM. Normalized fold expression relative to HK gene (RPL13) in spleen of specimens with macroplastic MaP (+) vs specimens without MaP (–) in the digested GIT of all MDV samples (A–C) or only female MDV samples (D–F). Statistically different comparison are represented by asterisks: \*,  $p < 0.02$ ; \*\*,  $p < 0.01$ . MDV, 1, Mazara del Vallo.

In LMP specimens (4 MaP + and 11 MaP –), MaP + spleens showed minimal and not significant variations of immune-related gene transcripts: fold increases were 0.13 (*TCRB*), 0.23 (*TCRD*) and 0.18 (*IgM*). Data analyzed separating males and females gave the same outcome (data not shown).

Results from spleen gene expression were somewhat correlated with what we observed in the previous analyses. The changes observed in the expression of the three immune-related genes in spleen were greater in MDV samples than in LMP samples, consistent with the hypothesis that the adverse effects observed may be correlated to the highest degree of MDV anthropogenic pollution, in which MaP, co-present with MP (detected in on nearly all samples) are most likely additive for chemical co-contaminants.

#### 4. Conclusion

The present study reports high frequencies of microplastic consumption as well as the presence of macroplastic ingestion in the small spotted shark, *S. canicula*, sampled in two different locations of the Mediterranean Sea. From a first examination, it may be hypothesized that sharks could be less susceptible to microplastic ingestion than macroplastics, given the potential correlation of macroplastic presence to changes in expression of immune-related genes. But the link between plastics and the unavoidable absorbed chemicals, differently distributed in the locations examined, needs to be specifically addressed, given the estrogenic effects hereby reported on maturity and gender development that could be caused, for example, by endocrine disruptors present in the most contaminated site. Correspondingly, immunology data describing the full functionality of T- and B-cells needs to be specifically gathered and integrated.

To our knowledge, this is the first study to explore the influence that

plastic ingestion by a shark species in the Mediterranean Sea. The occurrence and high frequency of ingested plastic debris hereby reported highlights the ubiquitous nature of this pollutant throughout the Mediterranean Sea and the importance of targeting plastics and their co-contaminants in future pollution control efforts.

#### CRediT authorship contribution statement

**Annalaura Mancía:** Formal analysis, Writing - original draft. **Tatiana Chenet:** Formal analysis. **Gioacchino Bono:** Formal analysis. **Michele Luca Geraci:** Formal analysis. **Carmela Vaccaro:** Formal analysis. **Luisa Pasti:** Formal analysis.

#### Acknowledgments

The research leading to these results has received funding from the Ministry of Education, University and Research (MIUR) under the PRIN 2017 program grant agreement n 2017Y2PAB8\_003.

#### Appendix A. Supplementary data

Supplementary data to this article can be found online at <https://doi.org/10.1016/j.marenvres.2020.104876>.

#### References

- Aliani, S., Griffo, A., Molcard, A., 2003 Sep. Floating debris in the ligurian sea, north-western mediterranean. *Mar. Pollut. Bull.* 46 (9), 1142–1149. PubMed PMID: 12932495.
- Autá, H.S., Emenike, C.U., Fauziah, S.H., 2017 May. Distribution and importance of microplastics in the marine environment: a review of the sources, fate, effects, and potential solutions. *Environ. Int.* 102, 165–176. <https://doi.org/10.1016/j.envint.2017.02.013>. Epub 2017 Mar 9. Review. PubMed PMID: 28284818.

- Avio, C.G., Gorbí, S., Milan, M., Benedetti, M., Fattorini, D., d'Errico, G., Pautetto, M., Bargelloni, L., Regoli, F., 2015 Mar. Pollutants bioavailability and toxicological risk from microplastics to marine mussels. *Environ. Pollut.* 198, 211–222. <https://doi.org/10.1016/j.envpol.2014.12.021>. Epub 2015 Jan 28. PubMed PMID: 25637744.
- Avio, C.G., Pittura, L., d'Errico, G., Abel, S., Amorello, S., Marino, G., Gorbí, S., Regoli, F., 2019 Dec 9. Distribution and characterization of microplastic particles and textile microfibrils in Adriatic food webs: general insights for biomonitoring strategies. *Environ. Pollut.* 258, 113766. <https://doi.org/10.1016/j.envpol.2019.113766> [Epub ahead of print] PubMed PMID: 31855672.
- Barboza, L.G.A., Vieira, L.R., Branco, V., Figueiredo, N., Carvalho, F., Guilhermino, L., 2018a. Microplastics cause neurotoxicity, oxidative damage and energy-related changes and interact with the bioaccumulation of mercury in the European seabass, *Dicentrarchus labrax* (Linnaeus, 1758). *Aquat. Toxicol.* 195, 49–57. <https://doi.org/10.1016/j.aquatox.2017.12.008>. Epub 2017 Dec 20. PubMed PMID: 29287173.
- Barboza, L.G.A., Vieira, L.R., Guilhermino, L., 2018b. Single and combined effects of microplastics and mercury on juveniles of the European seabass (*Dicentrarchus labrax*): changes in behavioural responses and reduction of swimming velocity and resistance time. *Environ. Pollut.* 236, 1014–1019. <https://doi.org/10.1016/j.envpol.2017.12.082>. Epub 2018 Feb 12. PubMed PMID: 29449115.
- Barboza, L.G.A., Vieira, L.R., Branco, V., Carvalho, C., Guilhermino, L., 2018 Oct 23. Microplastics increase mercury bioconcentration in gills and bioaccumulation in the liver, and cause oxidative stress and damage in *Dicentrarchus labrax* juveniles. *Sci. Rep.* 8 (1), 15655. <https://doi.org/10.1038/s41598-018-34125-z>. PubMed PMID: 30353126; PubMed Central PMCID: PMC6199270.
- Bessa, F., Barriá, P., Neto, J.M., Frias, J.P.G.L., Otero, V., Sobral, P., Marques, J.C., 2018 Mar. Occurrence of microplastics in commercial fish from a natural estuarine environment. *Mar. Pollut. Bull.* 128, 575–584. <https://doi.org/10.1016/j.marpolbul.2018.01.044>. Epub 2018 Feb 7. PubMed PMID: 29571409.
- Botterell, Z.L.R., Beaumont, N., Dorrington, T., Steinke, M., Thompson, R.C., Lindeque, P. K., 2019 Feb. Bioavailability and effects of microplastics on marine zooplankton: a review. *Environ. Pollut.* 245, 98–110. <https://doi.org/10.1016/j.envpol.2018.10.065>. Epub 2018 Oct 17. Review. PubMed PMID: 30415037.
- Carpenter, E.J., Anderson, S.J., Harvey, G.R., Miklas, H.P., Peck, B.B., 1972 Nov 17. Polystyrene spherules in coastal waters. *Science* 178 (4062), 749–750. PubMed PMID: 4628343.
- CIESIN, Center for International Earth Science Information Network. National Aggregates of Geospatial Data: Population, Landscape and Climate Estimates Version 3. National Aeronautics and Space Administration Socioeconomic Data and Applications Center, Palisades, NY. Available: <http://sedac.ciesin.columbia.edu/data/set/nagdc-population-landscape-climate-estimates-v3>. Accessed 2012 Oct 16.
- Compa, M., Ventero, A., Iglesias, M., Deudero, S., 2018 Mar. Ingestion of microplastics and natural fibres in *Sardina pilchardus* (Walbaum, 1792) and *Engraulis encrasicolus* (Linnaeus, 1758) along the Spanish Mediterranean coast. *Mar. Pollut. Bull.* 128, 89–96. <https://doi.org/10.1016/j.marpolbul.2018.01.009>. Epub 2018 Jan 12. PubMed PMID: 29571417.
- Cózar, A., Sanz-Martín, M., Martí, E., González-Gordillo, J.I., Ubeda, B., Gálvez, J.Á., Irgoien, X., Duarte, C.M., 2015 Apr 1. Plastic accumulation in the Mediterranean sea. e0121762 *PLoS One* 10 (4). <https://doi.org/10.1371/journal.pone.0121762>. eCollection 2015. PubMed PMID: 25831129; PubMed Central PMCID: PMC4382178.
- Crouch, K., Smith, L.E., Williams, R., Cao, W., Lee, M., Jensen, A., Dooley, H., 2013 May. Humoral immune response of the small-spotted catshark, *Scyliorhinus canicula*. *Fish Shellfish Immunol.* 34 (5), 1158–1169. <https://doi.org/10.1016/j.fsi.2013.01.025>. Epub 2013 Feb 21. Erratum in: *Fish Shellfish Immunol.* 2013 Aug;35(2):623. PubMed PMID: 23439398.
- Davis, M.W., 2002. Key principles for understanding fish bycatch discard mortality. *Can. J. Fish. Aquat. Sci.* 59, 1834–1843. PMC6823372.
- Dehaut, A., Cassone, A.L., Frère, L., Hermabessiere, L., Himber, C., Rinnert, E., Rivière, G., Lambert, C., Soudant, P., Huvet, A., Duflos, G., Paul-Pont, I., 2016 Aug. Microplastics in seafood: benchmark protocol for their extraction and characterization. *Environ. Pollut.* 215, 223–233. <https://doi.org/10.1016/j.envpol.2016.05.018>. Epub 2016 May 19. PubMed PMID: 27209243.
- Deudero, S., Alomar, C., 2015 Sep 15. Mediterranean marine biodiversity under threat: reviewing influence of marine litter on species. *Mar. Pollut. Bull.* 98 (1–2), 58–68. <https://doi.org/10.1016/j.marpolbul.2015.07.012>. Epub 2015 Jul 13. Review. PubMed PMID: 26183308.
- Dhar, A.K., Bowers, R.M., Licon, K.S., Veazey, G., Read, B., 2009 May. Validation of reference genes for quantitative measurement of immune gene expression in shrimp. *Mol. Immunol.* 46 (8–9), 1688–1695. <https://doi.org/10.1016/j.molimm.2009.02.020>. Epub 2009 Mar 17. PubMed PMID: 19297025.
- Digka, N., Tsangaris, C., Torre, M., Anastasopoulou, A., Zeri, C., 2018 Oct. Microplastics in mussels and fish from the Northern Ionian sea. *Mar. Pollut. Bull.* 135, 30–40. <https://doi.org/10.1016/j.marpolbul.2018.06.063>. Epub 2018 Jul 4. PubMed PMID: 30301041.
- Dooley, H., Flajnik, M.F., 2006. Antibody repertoire development in cartilaginous fish. *Dev. Comp. Immunol.* 30 (1–2), 43–56. Review. PubMed PMID: 16146649.
- Eriksen, M., Lebreton, L.C., Carson, H.S., Thiel, M., Moore, C.J., Borero, J.C., Galgani, F., Ryan, P.G., Reisser, J., 2014 Dec 10. Plastic pollution in the world's oceans: more than 5 trillion plastic pieces weighing over 250,000 tons afloat at sea. e111913 *PLoS One* 9 (12). <https://doi.org/10.1371/journal.pone.0111913>. eCollection 2014. PubMed PMID: 25494041; PubMed Central PMCID: PMC4262196.
- Faure, F., Saini, C., Potter, G., Galgani, F., de Alencastro, L.F., Hagmann, P., 2015 Aug. An evaluation of surface micro- and mesoplankton pollution in pelagic ecosystems of the Western Mediterranean Sea. *Environ. Sci. Pollut. Res. Int.* 22 (16), 12190–12197. <https://doi.org/10.1007/s11356-015-4453-3>. Epub 2015 Apr 19. PubMed PMID: 25893619.
- Ferreira, P., Fonte, E., Soares, M.E., Carvalho, F., Guilhermino, L., 2016 Jan. Effects of multi-stressors on juveniles of the marine fish *Pomatoschistus microps*: gold nanoparticles, microplastics and temperature. *Aquat. Toxicol.* 170, 89–103. <https://doi.org/10.1016/j.aquatox.2015.11.011>. Epub 2015 Nov 28. PubMed PMID: 26642093.
- Flajnik, M.F., 2002 Sep. Comparative analyses of immunoglobulin genes: surprises and portents. *Nat. Rev. Immunol.* 2 (9), 688–698. Review. PubMed PMID: 12209137.
- Fossi, M.C., Marsili, L., Bani, M., Giannetti, M., Coppola, D., Guerranti, C., Caliani, I., Minutoli, R., Lauriano, G., Finoia, M.G., Rubegni, F., Panigada, S., Bérubé, M., Urbán Ramírez, J., Panti, C., 2016 Feb. Fin whales and microplastics: the Mediterranean Sea and the sea of cortex scenarios. *Environ. Pollut.* 209, 68–78. <https://doi.org/10.1016/j.envpol.2015.11.022>. Epub 2015 Dec 7. PubMed PMID: 26637933.
- Geraci, M.L., Ragonese, S., Norrito, G., Scannella, D., Falsone, F., Vitale, S., 2017. [Chapter 2] A tale on the demersal and bottom dwelling Chondrichthyes in the south of Sicily through 20 scientific survey. In: Rodrigues-Filho, L.F., de Luna Sales, J.B. (Eds.), *Chondrichthyes—Multidisciplinary Approach*. IntechOpen, London, UK, pp. 13–37. <https://doi.org/10.5772/intechopen.69333> doi: 10.5772/65879.
- Hartmann, N.B., Hu, T., Thompson, R.C., Hassello, M., Verschoor, A., Daugaard, A.E., et al., 2019. Are we speaking the same language? Recommendations for a definition and categorization framework for plastic debris, 2015 *Environ. Sci. Technol.* 53 (3), 1039–1047. <https://doi.org/10.1021/acs.est.8b05297> PMID: 30608663.
- Huerta Lwanga, E., Gertsen, H., Gooren, H., Peters, P., Salánki, T., van der Ploeg, M., Besseling, E., Koelmans, A.A., Geissen, V., 2016 Mar 1. Microplastics in the terrestrial ecosystem: implications for lumbricus terrestris (Oligochaeta, lumbricidae). *Environ. Sci. Technol.* 50 (5), 2685–2691. <https://doi.org/10.1021/acs.est.5b05478>. Epub 2016 Feb 8. PubMed PMID: 26852875.
- Iwama, G.K., Afonso, L.O.B., Vijayan, M.M., 2006. Stress in fish. In: Evans, D.E., Claiborne, J.B. (Eds.), *The Physiology of Fishes*, 3 ed. CRC Press, Boca Raton, FL, pp. 319–342.
- Kedzierski, M., Villain, J., Falcou-Préfou, M., Kerros, M.E., Henry, M., et al., 2019. Microplastics in Mediterranean Sea: a protocol to robustly assess contamination characteristics. *PLoS One* 14 (2). <https://doi.org/10.1371/journal.pone.0212088> e0212088.
- Koelmans, A.A., Besseling, E., Foekema, E.M., 2014 Apr. Leaching of plastic additives to marine organisms. *Environ. Pollut.* 187, 49–54. <https://doi.org/10.1016/j.envpol.2013.12.013>. Epub 2014 Jan 16. PubMed PMID: 24440692.
- Lacombe, H., Gascard, J.C., Gonella, J., Bethoux, J.P., 1981. Response of the Mediterranean to the water and energy fluxes across its surface, on seasonal and interannual scales. *Oceanol. Acta* 4 (2), 247–255.
- Lebreton, L.C., Greer, S.D., Borrero, J.C., 2012 Mar. Numerical modelling of floating debris in the world's oceans. *Mar. Pollut. Bull.* 64 (3), 653–661. <https://doi.org/10.1016/j.marpolbul.2011.10.027>. Epub 2012 Jan 20. PubMed PMID: 22264500.
- Li, R., Redmond, A.K., Wang, T., Bird, S., Dooley, H., Secomb, C.J., 2015 Nov. Characterisation of the TNF superfamily members CD40L and BAFF in the small-spotted catshark (*Scyliorhinus canicula*). *Fish Shellfish Immunol.* 47 (1), 381–389. <https://doi.org/10.1016/j.fsi.2015.09.033>. Epub 2015 Sep 16. PubMed PMID: 26386192.
- Li, W.C., Tse, H.F., Fok, L., 2016 Oct 1. Plastic waste in the marine environment: a review of sources, occurrence and effects. *Sci. Total Environ.* 566–567, 333–349. <https://doi.org/10.1016/j.scitotenv.2016.05.084>. Epub 2016 May 24. Review. PubMed PMID: 27232963.
- Limonta, G., Mancía, A., Benkhalqui, A., Bertolucci, C., Abelli, L., Fossi, M.C., Panti, C., 2019 Oct 31. Microplastics induce transcriptional changes, immune response and behavioral alterations in adult zebrafish. *Sci. Rep.* 9 (1), 15775. <https://doi.org/10.1038/s41598-019-52292-5>. PubMed PMID: 31673028; PubMed Central PMCID: PMC6823372.
- Lu, Y., Zhang, Y., Deng, Y., Jiang, W., Zhao, Y., Geng, J., Ding, L., Ren, H., 2016 Apr 5. Uptake and accumulation of polystyrene microplastics in zebrafish (*Danio rerio*) and toxic effects in liver. *Environ. Sci. Technol.* 50 (7), 4054–4060. <https://doi.org/10.1021/acs.est.6b00183>. Epub 2016 Mar 17. PubMed PMID: 26950772.
- Lusher, A.L., Hollman, P.C.H., Mendoza-Hill, J.J., 2017. *Microplastics in Fisheries and Aquaculture: Status of Knowledge on Their Occurrence and Implications for Aquatic Organisms and Food Safety*. FAO Fisheries and Aquaculture Technical Paper. No. 615. Rome, Italy.
- MEDITS, 2016. *International Bottom Trawl Survey in the Mediterranean. Instruction Manual. Version 8. [MEDITS—handbook. Version n. 8]. MEDITS Working Group*. Morris, R.J., 1980. Floating debris in the mediterranean. *Mar. Pollut. Bull.* 11, 125.
- Ory, N., Chagnon, C., Felix, F., Fernández, C., Ferreira, J.L., Gallardo, C., Garcés Ordóñez, O., Henostroza, A., Laaz, E., Mizraji, R., Mojica, H., Murillo Haro, V., Ossa Medina, L., Preciado, M., Sobral, P., Urbina, M.A., Thiel, M., 2018 Feb. Low prevalence of microplastic contamination in planktivorous fish species from the southeast Pacific Ocean. *Mar. Pollut. Bull.* 127, 211–216. <https://doi.org/10.1016/j.marpolbul.2017.12.016>. Epub 2017 Dec 21. PubMed PMID: 29475656.
- Pedà, C., Caccamo, L., Fossi, M.C., Gai, F., Andaloro, F., Genovese, L., Perdicchi, A., Romeo, T., Maricchiolo, G., 2016 May. Intestinal alterations in European sea bass *Dicentrarchus labrax* (Linnaeus, 1758) exposed to microplastics: preliminary results. *Environ. Pollut.* 212, 251–256. <https://doi.org/10.1016/j.envpol.2016.01.083>. Epub 2016 Feb 4. PubMed PMID: 26851981.
- Pellini, G., Gomiero, A., Fortibuoni, T., Ferrà, C., Grati, F., Tassetti, A.N., Polidori, P., Fabi, G., Scarcella, G., 2018 Mar. Characterization of microplastic litter in the gastrointestinal tract of Solea solea from the Adriatic Sea. *Environ. Pollut.* 234, 943–952. <https://doi.org/10.1016/j.envpol.2017.12.038>. Epub 2017 Dec 21. PubMed PMID: 29665634.
- Pettinello, R., Redmond, A.K., Secomb, C.J., Macqueen, D.J., Dooley, H., 2017 Sep. Evolutionary history of the T cell receptor complex as revealed by small-spotted

- catshark (*Scyliorhinus canicula*). *Dev. Comp. Immunol.* 74, 125–135. <https://doi.org/10.1016/j.dci.2017.04.015>. Epub 2017 Apr 19. PubMed PMID: 28433528.
- Pfaffl, M.W., 2001 May 1. A new mathematical model for relative quantification in real-time RT-PCR. *Nucleic Acids Res.* 29 (9), e45. PubMed PMID: 11328886; PubMed Central PMCID: PMC55695.
- Pitt, J.A., Kozal, J.S., Jayasundara, N., Massarsky, A., Trevisan, R., Geitner, N., Wiesner, M., Levin, E.D., Di Giulio, R.T., 2018 Jan. Uptake, tissue distribution, and toxicity of polystyrene nanoparticles in developing zebrafish (*Danio rerio*). *Aquat. Toxicol.* 194, 185–194. <https://doi.org/10.1016/j.aquatox.2017.11.017>. Epub 2017 Nov 24. PubMed PMID: 29197232.
- Ragonese, S., Vitale, S., Dimech, M., Mazzola, S., 2013 Sep 23. Abundances of demersal sharks and chimaera from 1994–2009 scientific surveys in the central Mediterranean Sea. *e74865 PLoS One* 8 (9). <https://doi.org/10.1371/journal.pone.0074865>. eCollection2013. PubMed PMID: 24086386; PubMed Central PMCID: PMC3781099.
- Ramsay, J.M., Watral, V., Schreck, C.B., Kent, M.L., 2009 Dec 22. Pseudoloma neurophilia infections in zebrafish *Danio rerio*: effects of stress on survival, growth, and reproduction. *Dis. Aquat. Org.* 88 (1), 69–84. <https://doi.org/10.3354/dao02145>. PubMed PMID:20183967; PubMed Central PMCID: PMC4752113.
- Rauta, P.R., Nayak, B., Das, S., 2012 Nov-Dec. Immune system and immune responses in fish and their role in comparative immunity study: a model for higher organisms. *Immunol. Lett.* 148 (1), 23–33. <https://doi.org/10.1016/j.imlet.2012.08.003>. Epub 2012 Aug 10. Review. PubMed PMID: 22902399.
- Reisser, J., Slat, B., Noble, K., du Plessis, K., Epp, M., Proietti, M., de Sonneville, J., Becker, T., Pattiaratchi, C., 2014. The vertical distribution of buoyant plastics at sea. *Biogeosci. Discuss.* 11, 16207–16226.
- Renzi, M., Specchiulli, A., Blašković, A., Manzo, C., Mancinelli, G., Cilenti, L., 2019 Jan. Marine litter in stomach content of small pelagic fishes from the Adriatic Sea: sardines (*Sardina pilchardus*) and anchovies (*Engraulis encrasicolus*). *Environ. Sci. Pollut. Res. Int.* 26 (3), 2771–2781. <https://doi.org/10.1007/s11356-018-3762-8>. Epub 2018 Nov 27. PubMed PMID: 30484055.
- Roch, S., Brinker, A., 2017 Apr 7. Rapid and efficient method for the detection of microplastic in the gastrointestinal tract of fishes. *Environ. Sci. Technol.* 51 (8), 4522–4530. <https://doi.org/10.1021/acs.est.7b00364>. PubMed PMID: 28358493.
- Rocha-Santos, Duarte, 2015. A critical overview of the analytical approaches to the occurrence, the fate and the behavior of microplastics in the environment. *Trends Anal. Chem.* 65, 47–53.
- Rochman, C.M., Hohn, E., Kurobe, T., Teh, S.J., 2013 Nov 21. Ingested plastic transfers hazardous chemicals to fish and induces hepatic stress. *Sci. Rep.* 3, 3263. <https://doi.org/10.1038/srep03263>. PubMed PMID: 24263561; PubMed Central PMCID: PMC3836290.
- Rochman, C.M., Kurobe, T., Flores, I., Teh, S.J., 2014 Sep 15. Early warning signs of endocrine disruption in adult fish from the ingestion of polyethylene with and without sorbed chemical pollutants from the marine environment. *Sci. Total Environ.* 493, 656–661. <https://doi.org/10.1016/j.scitotenv.2014.06.051>. Epub 2014 Jul 1. PubMed PMID: 24995635.
- Rodriguez-Cabello, C., Sanchez, F., Olaso, I., 2007. Distribution patterns and sexual segregations of *Scyliorhinus canicula* (L.) in the Cantabrian Sea. *J. Fish Biol.* 70, 1568–1586. <https://doi.org/10.1111/j.1095-8649.2007.01444.x>.
- Romeo, T., Pietro, B., Pedà, C., Consoli, P., Andaloro, F., Fossi, M.C., 2015 Jun 15. First evidence of presence of plastic debris in stomach of large pelagic fish in the Mediterranean Sea. *Mar. Pollut. Bull.* 95 (1), 358–361. <https://doi.org/10.1016/j.marpolbul.2015.04.048>. Epub 2015 Apr 30. PubMed PMID: 25936574.
- Ruiz-Orejón, L.F., Sardá, R., Ramis-Pujol, J., 2016 Sep. Floating plastic debris in the central and western Mediterranean Sea. *Mar. Environ. Res.* 120, 136–144. <https://doi.org/10.1016/j.marenvres.2016.08.001>. Epub 2016 Aug 2. PubMed PMID: 27540696.
- Santos, D., Luzio, A., Coimbra, A.M., 2017 Oct. Zebrafish sex differentiation and gonad development: a review on the impact of environmental factors. *Aquat. Toxicol.* 191, 141–163. <https://doi.org/10.1016/j.aquatox.2017.08.005>. Epub 2017 Aug 10. Review. PubMed PMID: 28841494.
- Silva-Cavalcanti, J.S., Silva, J.D.B., França, E.J., Araújo, M.C.B., Gusmão, F., 2017 Feb. Microplastics ingestion by a common tropical freshwater fishing resource. *Environ. Pollut.* 221, 218–226. <https://doi.org/10.1016/j.envpol.2016.11.068>. Epub 2016 Dec 1. PubMed PMID:27914860.
- Skomal, G.B., Mandelman, J.W., 2012 Jun. The physiological response to anthropogenic stressors in marine elasmobranch fishes: a review with a focus on the secondary response. *Comp. Biochem. Physiol. Mol. Integr. Physiol.* 162 (2), 146–155. <https://doi.org/10.1016/j.cbpa.2011.10.002>. Epub 2011 Oct 10. Review. PubMed PMID: 22008842.
- Suaría, G., Aliani, S., 2014 Sep 15. Floating debris in the Mediterranean Sea. *Mar. Pollut. Bull.* 86 (1–2), 494–504. <https://doi.org/10.1016/j.marpolbul.2014.06.025>. Epub 2014 Aug 10. PubMed PMID: 25127501.
- Sussarellu, R., Suquet, M., Thomas, Y., Lambert, C., Fabioux, C., Pernet, M.E., Le Goïc, N., Quillien, V., Mingant, C., Epelboin, Y., Corporeau, C., Guyomarch, J., Robbins, J., Paul-Pont, I., Soudant, P., Huvet, A., 2016 Mar 1. Oyster reproduction is affected by exposure to polystyrene microplastics. *Proc. Natl. Acad. Sci. U. S. A.* 113 (9), 2430–2435. <https://doi.org/10.1073/pnas.1519019113>. Epub 2016 Feb 1. PubMed PMID: 26831072; PubMed Central PMCID: PMC4780615.
- Veneman, W.J., Spaink, H.P., Brun, N.R., Bosker, T., Vijver, M.G., 2017 Sep. Pathway analysis of systemic transcriptome responses to injected polystyrene particles in zebrafish larvae. *Aquat. Toxicol.* 190, 112–120. <https://doi.org/10.1016/j.aquatox.2017.06.014>. Epub 2017 Jul 4. PubMed PMID: 28704660.
- Von Hippel, F.A., Miller, P.K., Carpenter, D.O., Dillon, D., Smayda, L., Katsiadaki, I., Titus, T.A., Batzel, P., Postlethwait, J.H., Buck, C.L., 2018 Mar. Endocrine disruption and differential gene expression in sentinel fish on St. Lawrence Island, Alaska: health implications for indigenous residents. *Environ. Pollut.* 234, 279–287. <https://doi.org/10.1016/j.envpol.2017.11.054>. Epub 2017 Dec 21. PubMed PMID: 29182972; PubMed Central PMCID: PMC5809177.
- Werner, S., Budziak, A., Franeker, J., van Galgani, F., Hanke, G., Maes, T., Matiddi, M., Nilsson, P., Oosterbaan, L., Priestland, E., Thompson, R., Veiga, J., Vlachogianni, T., 2016. Harm Caused by Marine Litter: MSFD GES TG Marine Litter - Thematic Report.
- Wilcox, C., Van Sebille, E., Hardesty, B.D., 2015 Sep 22. Threat of plastic pollution to seabirds is global, pervasive, and increasing. *Proc. Natl. Acad. Sci. U. S. A.* 112 (38), 11899–11904. <https://doi.org/10.1073/pnas.1502108112>. Epub 2015 Aug 31. Erratum in: *Proc Natl Acad Sci U S A.* 2016 Jan 26;113(4):E491. PubMed PMID: 26324886; PubMed Central PMCID: PMC4586823.
- Zeri, C., Adamopoulou, A., Bojanić Varezić, D., Fortibuoni, T., Kovač Viršek, M., Kržan, A., Mandić, M., Mazziotti, C., Palatinus, A., Peterlin, M., Prvan, M., Ronchi, F., Siljic, J., Tutman, P., Vlachogianni, T., 2018 Nov. Floating plastics in Adriatic waters (Mediterranean Sea): from the macro- to the micro-scale. *Mar. Pollut. Bull.* 136, 341–350. <https://doi.org/10.1016/j.marpolbul.2018.09.016>. Epub 2018 Sep 22. PubMed PMID: 30509816.

## **ACKNOWLEDGEMENTS**

First of all, I am deeply grateful to my supervisor, Prof. Luisa Pasti, for her guidance and precious lessons during these three years.

Many thanks to Prof. Alberto Cavazzini and all the group of Analytical Chemistry for the assistance and advice given to me during the course of my studies.

I would like to thank the Earth Science group, in particular Prof. Annalisa Martucci, for their collaboration.

I would like to thank Prof. Detlef Günther, Dr. Bodo Hattendorf and all the members of the research group at ETH in Zürich for the opportunity to work in their laboratories during my study period abroad.

Lots of thanks to my family and friends for their affection and support.